Transactions of the ASME®

FLUIDS ENGINEERING DIVISION
Technical Editor
DEMETRI P. TELIONIS (1999)
Executive Secretary
PAT WHITE (1999)
Assistant to the Editor
N. W. SCHAEFFLER
Calendar Editor
M. F. ACKERSON

Associate Technical Editors
P. R. BANDYOPADHYAY (1998)
S. BANERJEE (1999)
P. W. BEARMAN (1998)
P. BRADSHAW (2000)
M. S. CRAMER (1998)
M. N. DHAUBHADEL (1999)
J. K. EATON (1998)
G. ERLEBACHER (2000)
J. A. C. HUMPHREY (1998)
F. HUSSAIN (1998)
J. KATZ (1998)
C. L. MERKLE (2000)
B. SCHIAVELLO (1999)
P. M. SOCKOL (1998)
M. SOMMERFELD (1999)
M. S. TRIANTAFYLLOU (1998)
F. K. WASDEN (2000)
D. R. WILLIAMS (2000)

BOARD ON COMMUNICATIONS
Chairman and Vice-President
R. MATES

OFFICERS OF THE ASME
President, **KEITH B. THAYER**
Exec. Director
D. L. BELDEN
Treasurer
J. A. MASON

PUBLISHING STAFF
Managing Director, Engineering
CHARLES W. BEARDSLEY
Director, Technical Publishing
PHILIP DI VIETRO
Managing Editor, Technical Publishing
CYNTHIA B. CLARK
Managing Editor, Transactions
CORNELIA MONAHAN
Production Assistant
MARISOL ANDINO

Transactions of the ASME, Journal of Fluids Engineering (ISSN 0098-2202) is published quarterly (Mar., June, Sept., Dec.) for $195.00 per year by The American Society of Mechanical Engineers, 345 East 47th Street, New York, NY 10017. Periodicals postage paid at New York, NY and additional mailing offices. POSTMASTER: Send address changes to Transactions of the ASME, Journal of Fluids Engineering, c/o THE AMERICAN SOCIETY OF MECHANICAL ENGINEERS, 22 Law Drive, Box 2300, Fairfield, NJ 07007-2300.
CHANGES OF ADDRESS must be received at Society headquarters seven weeks before they are to be effective. Please send old label and new address.
PRICES: To members, $40.00, annually: to nonmembers, $195.00. Add $40.00 for postage to countries outside the United States and Canada.
STATEMENT from By-Laws. The Society shall not be responsible for statements or opinions advanced in papers or . . . printed in its publications (B7.1, Par. 3).

INDEXED by Applied Mechanics Reviews and Engineering Information, Inc. Canadian Goods & Services Tax Registration #126148048.

Journal of Fluids Engineering

Published Quarterly by The American Society of Mechanical Engineers

VOLUME 120 • NUMBER 2 • JUNE 1998

Technical Papers

(Contents continued on p. 273)

This journal is printed on acid-free paper, which exceeds the ANSI Z39.48-1992 specification for permanence of paper and library materials. ♾™

♻ 85% recycled content, including 10% post-consumer fibers.

(Contents continued)

Technical Briefs

Announcements and Special Notices

F. Ballio
Assistant Professor.

C. Bettoni
Researcher.

S. Franzetti
Professor.

Department I.I.A.R., Politecnico di Milano,
Piazza Leonardo da Vinci, 32,
20133 Milano, Italy

A Survey of Time-Averaged Characteristics of Laminar and Turbulent Horseshoe Vortices

(Data Bank Contribution)*

The time-averaged kinematical and dynamical characteristics of the junction vortex system in front of a symmetrical obstacle are systematically analyzed for both laminar and turbulent flows. A wide set of experimental and numerical results from the literature is coordinated in nondimensional form together with some new computational data. In turbulent flows the dimensions of the vortex system in the symmetry plane depend only on the obstacle geometry; in laminar systems they are also correlated with the Reynolds number and the thickness of the incoming boundary layer. The horseshoe vortices induce shear stresses on the bottom several times higher than those of the undisturbed boundary layer.

1 Introduction

When a two-dimensional laminar or turbulent boundary layer encounters a body rising from a surface, a complex vortical flow field is created in the junction region. Owing to the combined effects of the longitudinal and vertical pressure gradients, due respectively to the blockage effect of the body and to the momentum deficit in the boundary layer, the latter separates and forms one or more vortices which stretch around and downstream the obstacle, in the typical horseshoe configuration (Fig. 1).

The presence of these necklace vortices increases local shear stresses, heat transfer, drag and noise, and modifies the lift characteristics of wings. These phenomena occur in many real cases, including naval and aircraft design, turbomachinery, buildings, bridge piers, meteorological and geological applications. Moreover, since a complex highly three-dimensional vortical flow can be generated by this simple geometrical configuration, the junction vortex system is often taken as a test case for numerical simulation codes and for measurement and visualization techniques, while its formation, structure, and topology have been the objects of several theoretical and conceptual analyses. Junction flows are often studied in a cross-stream symmetrical configuration, so that the plane of symmetry ahead of the obstacle can be considered to be the "origin" of the horseshoe vortices, and some of their properties can be therefore analyzed in two dimensions only.

In spite of the many studies on this topic published in the last decades, the mechanisms of formation and development of the vortices are still only partially understood. The spanwise vorticity generated in the incoming boundary layer is transported toward the leading edge of the obstacle and reorganized into discrete vortices; vorticity of the opposite sign is generated on the surfaces of the junction, so that a complex pattern of primary and secondary vortices undergoes a process of mutual annihilation and of deformation by the main flow, while turning around the obstacle (Mason and Morton, 1987; Seal et al., 1995). Starting from a no-recirculation pattern, the number of primary and secondary vortices in the symmetry plane grows as the Reynolds number increases (up to six vortices have been observed for laminar flows); for higher Re_{δ^*} the vortex system becomes unsteady (eventually oscillating) and finally turbulent. Apparently though, the Reynolds number is not the only parameter related to the structure of the vortex system: the boundary layer thickness seems to have similar effects to those of the Reynolds number, while, to our knowledge, there is no evidence of the effects of any other flow parameter.

The structural evolution described above is supported by many works (Baker, 1979 and 1991; Thomas, 1986; Visbal, 1991; Bain and Fletcher, 1993; Khan et al., 1995; Seal et al., 1995), but there is no quantitative agreement about the relationships between the flow parameters and the number, the topology, and the time behavior of the vortices (see the analysis in Ballio, 1995); particularly, the possible unsteadiness of the system is surely one of the most difficult and intriguing aspects of the problem.[1]

Turbulent systems are even more complicated. Mean flow measurements and calculations always indicate either no vortices in the symmetry plane[2] (Eckerle and Langston, 1987; Eckerle and Awad, 1991) or a single primary vortex, possibly coupled with some hints of a corner secondary circulation (Abid and Schmitt, 1986; Kubendran et al., 1986; Pierce and Tree, 1990; Devenport and Simpson, 1990; Larousse et al., 1991; Eckerle and Awad, 1991; Rizzetta, 1994; Khan and Ahmed, 1995). More complicated configurations have been inferred from visualizations of shear stresses on the bottom surface (Baker, 1980; Abid and Schmitt, 1986; De Ponte et al., 1994), but the topological interpretation of surface visualizations for turbulent systems is controversial (Devenport and Simpson, 1990; Martinuzzi and Tropea, 1993). Moreover, it has been shown that the relation between flow and surface topologies is not univocal (Hung et al., 1991; Ballio, 1995), so that the information from the surface stresses can be extrapolated to the flow field only with extreme care. Instantaneous visualizations and measurements of turbulent flow fields have indicated complex vortex patterns, whose topology is hardly recognizable (Baker, 1980; Kubo and Takezawa, 1988; Darghai, 1989; Agui

* Data have been deposited to the JFE Data Bank. To access the file for this paper, see instructions on p. 416 of this issue.

Contributed by the Fluids Engineering Division for publication in the JOURNAL OF FLUIDS ENGINEERING. Manuscript received by the Fluids Engineering Division June 27, 1996; revised manuscript received July 3, 1997. Associate Technical Editor: P. W. Bearman.

[1] All studies agree on the actual independence of the vortex system in front of the obstacle from the possible vortex shedding in the wake, both for laminar and turbulent cases.

[2] Even if no vortices are formed in the symmetry plane, nevertheless a horseshoe vortex system is normally recognizable aside of the obstacle, possibly originated by an open separation on the bottom surface at some distance from the symmetry line.

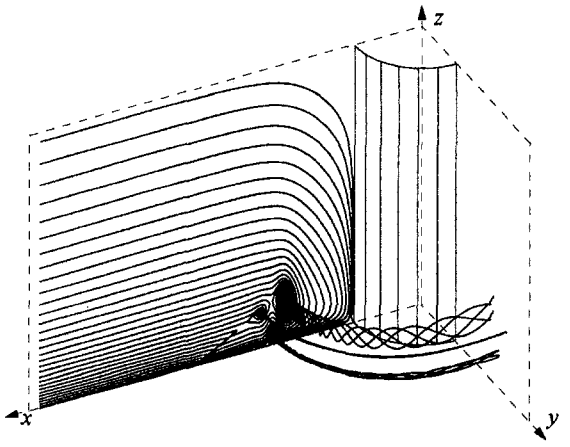

Fig. 1 Horseshoe vortex system. From the computational results in Ballio (1995); $Re_{\delta^*} = 409$, $\delta^*/b = 0.094$, $h/b = 0.95$. Enlarged vertical scale.

and Andreopulos, 1992); finally, from the time series analysis, the dynamics of the flow has been described in terms of a succession of relatively simple "modes" (Baker, 1979; Devenport and Simpson, 1990; Larousse et al., 1991; Martinuzzi and Tropea, 1993; Ölçmen and Simpson, 1994; Khan and Ahmed, 1995), while no turbulent steady vortex system has ever been documented. In the light of such results, it is at least doubtful whether mean flow topologies have any significance at all with respect to the actual flow structures; on the other hand, the dimension, position, and intensity of the mean structures may at least constitute imperfect indicators for identifying a much more complex unsteady system.

The difficulties and uncertainties, which are involved in studying the turbulent junction vortex, explain the interest of many researchers for the laminar case: steady laminar structures can be relatively well identified, and they can therefore represent meaningful examples for the study of the three-dimensional evolution and mutual interaction of vortices. On the other hand, it is true that, in spite of the significant efforts in the literature, still little is known of the 3-D characteristics of the horseshoe vortex system, of its interactions with the vortices of the wake, and of its effects on the solid boundaries in terms of normal and shear stresses (see, for example, Kaul et al., 1985; Mason and Morton, 1986; Eckerle and Langston, 1987; Merati et al., 1991; Pierce and Shin, 1992; Fleming et al., 1993; Martinuzzi and Tropea, 1993; Rizzetta, 1994; Ballio, 1995).

In this paper, a wide set of numerical and experimental data from the literature is reviewed, with the addition of the computations in Ballio (1995), still unpublished. Only subsonic vortex systems around cross-stream symmetrical obstacles will be considered, for both laminar and turbulent flows. Some of the mean characteristics in the symmetry plane will be systematically analyzed in nondimensional form, comparing experimental and numerical results for both prismatic and shaped obstacles. To our knowledge, comprehensive comparisons and analyses of such a wide data set have never been published.

2 Definition Sketch

Three Cartesian axes xyz are respectively aligned with the longitudinal, vertical and transversal direction of the flow (Fig. 1). The flow is identified by a limited number of control variables (see Fig. 2): the fluid density ρ and viscosity μ, the characteristics of the incoming boundary layer[3] (free-stream velocity U, displacement thickness δ^*, form parameter H, turbulence intensity, and length scales), the obstacle shape, its width b and height h, the transversal and vertical dimensions of the stream (L_g, d_o), and the roughness of the solid boundaries. The obstacle will be said to be "submerged" when the fluid can overtop it, i.e., when $d_o > h$. When $h > d_o$, which can only happen with free surface liquid flows, only the submerged part of the obstacle can influence the junction vortex; hence, it can be set $h = d_o$. Finally, the obstacle and the flow can be delimited by two parallel solid surfaces; in this case two symmetrical vortex systems are formed at the two junctions, so that it is reasonable to set $h = \frac{1}{2} d_o$. Since a free surface approximately behaves as a symmetry condition,[4] the last two configurations will be called "symmetrical."

The 3-D evolution of the junction vortices is obviously influenced by the obstacle shape; nevertheless, it has been shown that the vortical flow in front of the obstacle is determined only by the characteristics of its leading edge (bluntness and transversal dimension), so that all the remaining shape parameters, and particularly the obstacle chord, can be omitted from the analysis inasmuch as the flow field is considered in proximity to the symmetry plane (see, for example, Darghai, 1989).

The influence of the boundary layer form and turbulence intensity on the junction flow is not really clear: these parameters are often considered to have a negligible, or at least minor effect on the system, although, as a matter of fact, very little attention has been paid to them (see Baker, 1980 and 1985; Martinuzzi and Tropea, 1993; Bettoni, 1995). Similar arguments can be repeated for the surface roughness: since in most of the works no indications about this parameter are given, it seems reasonable to assume that smooth surface was used; the consequences of different conditions are unknown.[5] It is to be noticed that the surface roughness, the boundary layer form, and its turbulence characteristics are mutually correlated for developed turbulent boundary layers for given U and δ^*. Finally, it can be assumed that the stream transversal dimension L_g does not affect the vortex system in front of the obstacle for large values of the blockage ratio L_g/b: for most of the data sets that will be analyzed it is $L_g/b > 4$, which is normally considered sufficient to exclude major effects of this parameter.[6]

From the foregoing considerations, the main parameters affecting the vortex system in the symmetry plane are therefore:

$$[b, h, \delta^*, U, \mu, \rho]$$

which can be combined in dimensionless groups as:

$$[h/b, \delta^*/b, \mathrm{Re}_{\delta^*} = U\delta^*/\nu].$$

The Reynolds number Re_{δ^*} has been shown to be a better choice than the perhaps more obvious $\mathrm{Re}_b = Ub/\nu$ for the analysis of the results: Re_{δ^*} is related to the characteristics of

[3] Boundary layer parameters, and particularly δ^*, are referred to an undisturbed boundary layer, in the position of the obstacle axis.

[4] In free surface flow with very small d_o/b ratios surface waves could have not negligible effects.

[5] The experiments in Kubo and Takezawa (1988) and in Darghai (1989) were run on a rough bottom; the corresponding points show no difference with all the other data.

[6] West and Apelt (1982) indicate that λ_s varies for $7 \leq L_g/b < 51$.

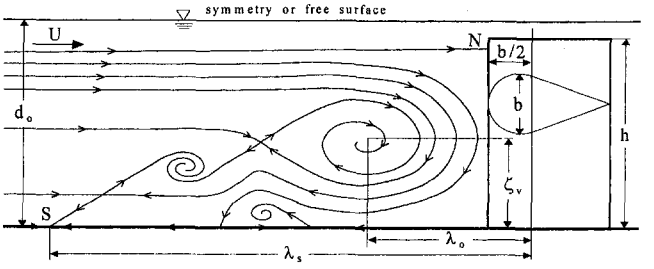

Fig. 2 Vertical symmetry plane: flow pattern of the vortex system in Fig. 1 and definition sketch (submerged body)

the incoming boundary layer, surely influencing the junction vortex, while Re_b mainly dominates the wake, which is only weakly correlated with the flow pattern in front of the obstacle.

If the control variables of the system can be restricted to a few dimensionless groups, the same is not true for the state variables: the brief discussion in the previous paragraph has shown that the flow can be very complex with respect to both space and time. In this work, three state variables have been chosen to characterize the dimensions of the time-averaged junction vortex system, and one to characterize its dynamical properties.

(a) The position of the primary separation, λ_s (Fig. 2). The point is recognizable as the outermost saddle in the shear stress field on the bottom wall; in the velocity field it is usually pointed out as the saddle where the incoming boundary layer separates, but some authors (Hung et al., 1991; Visbal, 1991; Rizzetta, 1994; Ballio, 1995; Coon and Tobak, 1995) have detected a node of attachment at this point, as in Fig. 2 (point S), placing the separation in an internal saddle. In spite of its not univocal nature, the point will be conventionally addressed as "primary separation."

The position of λ_s is identified either from surface stress visualizations on the bottom or from flow field measurements and visualizations in the symmetry plane.

(b) The longitudinal and vertical coordinates of the main vortex center, λ_o, ζ_v. When multiple vortex patterns arise, a dominant vortex can usually be recognized.

The position of the vortex center has been found approximately to coincide with both the minimum in the pressure distribution and the maximum reverse shear stress on the bottom, so that λ_o can be identified from velocity measurements and visualizations in the symmetry plane, or from pressure measurements on the bottom surface; only flow measurements or visualizations can locate ζ_v.

For the sake of comparability of the different obstacle shapes, λ_s and λ_o are measured from an ideal axis placed inside the obstacle at a distance of $b/2$ from the leading edge.

(c) The maximum value of the shear stress τ at the intersection of the symmetry plane with the bottom surface in front of the body.

For submerged bodies, the position of the attachment point on the obstacle leading edge (point N in Fig. 2) may be another meaningful vertical length scale, but this point is either nonsignificant or not well defined for symmetrical obstacles.

Some kinematical or dynamical parameters other than τ have been used in the literature to describe the system; among them the circulation of the main vortex, its circumferential velocity, and its vorticity. These quantities have not been chosen in this paper because their definition is not always straightforward and/or it is often difficult to infer them from the available data.

3 Data Collection

The sources of the data elaborated in this paper, together with some of the flow parameters and indications on experimental or numerical techniques, are listed in the Appendix. The values of λ_s, λ_o, ζ_v, and τ have been either directly drawn out of the text and of plots, or "measured" from velocity vector plots and flow visualizations. Most of the values for the control parameters were given directly by the authors; in a few cases they have been inferred by cross-comparisons of different plots showing the same data, or from different papers. Digitalization of pictures was performed with extreme care, so that the accuracy of the data can be considered to be that of the original works.

Apart from some uncertainties in the interpretation of the available information, the most frequent and serious problem has been caused by missing or improper data for the boundary layer thickness. Typically δ was available, but neither was δ^* nor any form parameter. Sometimes these last values were referred to positions other than the obstacle axis. If such problems are easily solved for laminar cases, transforming the data by means of the Blasius solution, the situation is more uncertain for turbulent boundary layers. Power law profiles have been used, tuning the coefficient on the available data (e.g., some form parameter). Even if the values thus obtained were sometimes affected by significant errors, they were believed to be acceptable for most of the analyses, since the phenomenon proved to be quite insensitive to the boundary layer thickness, for turbulent flows. For details about the accuracy of the data see Bettoni (1995).

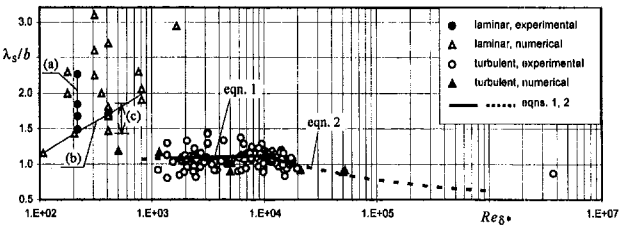

Fig. 3 Variation of λ_s/b with Re_{δ^*}, laminar and turbulent flows, $h/b > 0.6$. The lines of Eq. (1) and Eq. (2) are dotted out of the validity ranges of the formulas. Labels indicate homogeneous series: (a) Peake and Galway, $Re_{\delta^*} = 217$, $\delta^*/b = 0.047 \rightarrow 0.17$; ($b$) Ballio, $Re_{\delta^*} = 107 \rightarrow 815$, $\delta^*/b = 0.094$; (c) Ballio, $Re_{\delta^*} = 409$, $\delta^*/b = 0.037 \rightarrow 0.30$.

4 Results: λ_s, λ_o—Turbulent Flows

Position of Primary Separation: λ_s. Figure 3 plots all the available data for the coordinate of the primary separation λ_s in the $\lambda_s/b - Re_{\delta^*}$ plane. The transition between laminar and turbulent vortex systems occurs for $400 < Re_{\delta^*} < 1000$. The different behavior of the two regimes is evident from the figure: while for turbulent systems λ_s can be considered primarily scaling with b for a wide range of Reynolds numbers ($Re_{\delta^*} \cong 10^3 \rightarrow 10^7$), the scatter of laminar data does not allow to draw even a qualitative relationship with Re_{δ^*}, nor does it confirm the significance of b as the main scale parameter for λ_s. The correlations for turbulent experimental data of λ_o and λ_s proposed in the literature are collected in Table 1; besides the equations, their validity ranges are indicated.

The choice of b as the main scale parameter for λ_s is possibly the only result widely accepted in the literature for the position of the primary separation of turbulent junction vortices. Consider the dependence of λ_s/b on Re_{δ^*} and δ^*/b, which are usually pointed out as the main nondimensional groups governing the flow system. Baker (1980) suggests a "certain tendency" of λ_s/b to decrease as δ^*/b decreases and Re_{δ^*} increases. In a later work (1985) this author indicates two opposite effects of the Reynolds number: λ_s/b would grow with Re_{δ^*} for $Re_{\delta^*} < 10^4$ (Eq. (1)), while diminishing for $Re_{\delta^*} > 10^4$ (Eq. (2)). In addition to the relationships in Table 1, single data sets with constant values for either Re_{δ^*} or δ^*/b have been directly analyzed here: the results of the exercise show that the points in Belik (1973) and in Lai and Makomaski (1989) are qualitatively consistent with the indications of Baker for the effects of δ^*/b, and that Belik's and Monti's (1994) points seem to confirm Baker's result of a positive effect of Re_{δ^*} on λ_s/b for small Re_{δ^*} values. On the contrary, Lai and Makomaski find an inverse correlation between λ_s/b and Re_{δ^*} for $Re_{\delta^*} < 6000$. Finally, Darghai (1989) claims that λ_s/b increases for increasing Re_b ($\lambda_s/b = 0.73 \rightarrow 0.93$ for $Re_\delta = 6600 \rightarrow 65000$).

As a matter of fact, the whole turbulent data set in Fig. 3 do not suggest any dependence of λ_s/b on the Reynolds number within the range $10^3 < Re_{\delta^*} < 10^7$; the same points have been analyzed controlling for different classes of δ^*/b, and no effects of the boundary layer thickness have been detected: although single data sets may show some weak trend of λ_s/b as a function of Re_{δ^*} and/or δ^*/b, the result cannot be generalized to all the

Table 1 Turbulent flows: literature formulas for λ_s and λ_0

Baker (1985)	$\lambda_s/b = 0.5 + 0.46\ \mathrm{Re}_{\delta^*}^{0.033}$	$\mathrm{Re}_{\delta^*} = 1.5\cdot10^3 \rightarrow 1\cdot10^4$	(1)
Baker (1985)	$\lambda_s/b = 0.5 + 15.6\ \mathrm{Re}_{\delta^*}^{-0.35}$	$\mathrm{Re}_{\delta^*} = 1\cdot10^4 \rightarrow 1.8\cdot10^4$	(2)
Baker (1985)	$\lambda_s/b - 0.5 = \tanh(3.0\ h/b)[\lambda_s/b - 0.5]_{h/b\rightarrow\infty}$	$h/b = 0.03 \rightarrow 2.5$	(3)
Belik (1973)	$\lambda_s/b = 0.5 + 0.57(2\cdot10^{-5}\ \mathrm{Re}_\delta)^{0.19}$	$\mathrm{Re}_\delta = 1.4\cdot10^4 \rightarrow 1.3\cdot10^5$ $\mathrm{Re}_b = 3.6\cdot10^4 \rightarrow 2.2\cdot10^5$	(4)
Belik (1973)	$\lambda_s/b = 0.5 + (0.516 + 0.111\cdot10^{-5}\ \mathrm{Re}_b)(2\cdot10^{-5}\ \mathrm{Re}_\delta)^{0.19}$	$\mathrm{Re}_\delta = 1.4\cdot10^4 \rightarrow 1.3\cdot10^5$ $\mathrm{Re}_b = 3.6\cdot10^4 \rightarrow 2.2\cdot10^5$	(5)
Monti (1994)	$\lambda_s/b = 0.48 - 6.35\cdot10^{-6}\ \mathrm{Re}_b + 0.005\ \mathrm{Re}_b^{0.5}$	$\mathrm{Re}_b = 1\cdot10^4 \rightarrow 1\cdot10^5$	(6)
Baker (1985)	$\lambda_0/b = 0.5 + 0.10\ \mathrm{Re}_{\delta^*}^{0.10}$	$\mathrm{Re}_{\delta^*} = 1\cdot10^3 \rightarrow 1\cdot10^4$	(7)

Note: in Baker (1985) Eq. (1) is reported as $\lambda_s/b = 0.5 + 0.373\ \mathrm{Re}_{\delta^*}^{0.033}$; this formula clearly appears a misprint, since it does not fit the author's experimental points, nor agrees with the line plotted in Fig. 3 of his article. The value 0.46 for the coefficient seems an appropriate correction of the formula.

sets. On the other hand, an influence of the boundary layer thickness on the vortex system can be expected for $\delta^*/b \rightarrow 0$, the incoming flow field tending to that of a 2-D infinite cylinder with no bottom solid boundary, for which there is no vortex formation in front of the obstacle. For the smaller values of δ^*/b it is therefore reasonable that the dimensions of the separation zone scale not only with b but also with δ^*, but no evidence of such a trend can be drawn from the available data ($\delta^*/b \geq 0.011$ for points with $h/b \geq 0.6$).

In Fig. 4 the effects of small values for the relative obstacle height h/b on the primary separation are shown. The data in Baker (circular cylinder) and in Larousse et al. (prism) suggest that h/b has a negligible influence on the primary separation for $h/b > 1$, while λ_s/b decreases with h/b for the smaller height-to-width ratios. Since both sets tend to the asymptotic value $\lambda_s/b \cong 1.3$ for large h/b, this value has been assumed for the term $[\lambda_s/b]_{h/b\rightarrow\infty}$ in Eq. (3) instead of the original expression of Baker (Eq. (1)).

Even if the obstacle height has some distinguishable effects on λ_s for values smaller than the above-mentioned threshold ($h/b = 1$), such effects appear modest already for $h/b = 0.5 \rightarrow 0.7$, when compared with the general spread of the data characterized by higher values for the same ratio. Therefore, in this work it has been chosen to discuss results for obstacles with h/b larger or smaller than 0.6.

Larousse et al. show that λ_s scales with h more than with b for $h/b < 0.5$, resulting in $(\lambda_s - 0.5b)/h \cong$ const; the same is not strictly true for Baker's data which, even if heavily influenced by h, keep at least part of their dependence on b even for the smaller values of h/b. It is to be noticed that all data in Fig. 4 correspond to submerged bodies, i.e., $h < d_o$; the effect of h/b on the vortex system is not necessarily the same for setups where $h = d_o$ (symmetrical). In the submerged case, as h becomes small compared to b, most of the fluid is diverted to the top of the obstacle rather than to its side, tending to the limit of a 2-D flow over a transversally indefinite obstacle, with h becoming the scaling factor instead of b. On the contrary, for symmetrical patterns the fluid must flow laterally even for the smallest obstacle height, so that both h and b reasonably keep some influence on the dimensions of the vortex system.

The effect of the obstacle shape on the primary separation can be analyzed in Fig. 5. A blunt obstacle distorts the incoming flow field and generates vorticity more than an airfoil with the same transversal dimension b; therefore the former induces a larger separation zone than the latter. This effect can be recognized in the figure: although the values of λ_s/b for prisms, cylinders, and airfoils are similar, prisms tend to gather in the upper part of the rather dispersed cloud of cylinders, while wing-shaped obstacles lay somehow in the lower part of it. Moreover, the six points from Ölçmen and Simpson (1994) ($\mathrm{Re}_{\delta^*} \cong 10^4$) clearly confirm this trend (recall that b is defined as the maximum thickness of the airfoil). A positive correlation between the bluntness of the obstacle and the dimensions and intensity of the vortex system is also confirmed by the measurements of the flow field around differently shaped airfoils in Kubendran et al. (1986) and Metha (1984).

Position of the Main Vortex: λ_o. The longitudinal coordinate of the main vortex λ_o can be discussed along similar lines as λ_s. In Fig. 6 laminar and turbulent data are shown in the $\lambda_o/b - \mathrm{Re}_{\delta^*}$ plane: the general pattern resembles that of λ_s very closely, with the laminar-turbulent transition occurring at

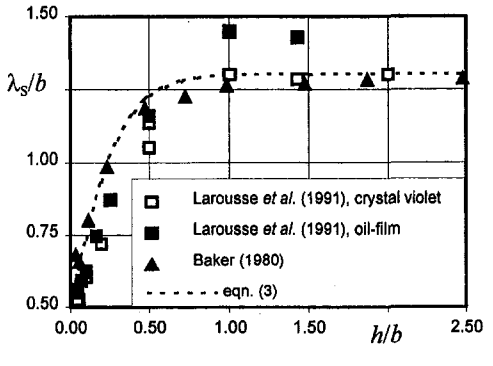

Fig. 4 Variation of λ_s/b with h/b, turbulent flows, submerged obstacles. $[\lambda_s/b]_{h/b\rightarrow\infty} = 1.3$ in Eq. (3). Larousse et al. (1991): prism, $\mathrm{Re}_{\delta^*} = 3.1\cdot10^3$, $\delta^*/b = 0.0052 \rightarrow 0.25$; Baker (1980): cylinder, $\mathrm{Re}_{\delta^*} = 9.5\cdot10^3$, $\delta^*/b = 0.066$.

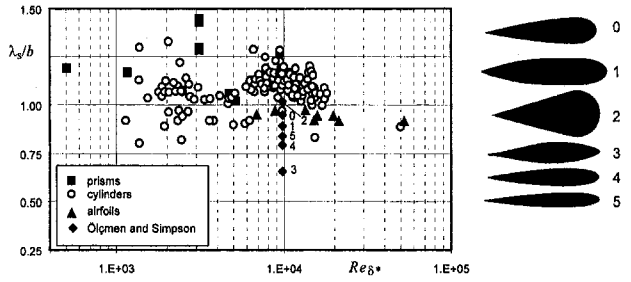

Fig. 5 Effect of the obstacle shape on λ_s/b, turbulent flows. The labels in the plot correspond to the airfoil shapes on the right (Ölçmen and Simpson).

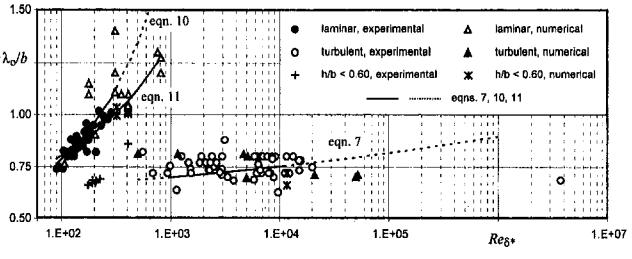

Fig. 6 Variation of λ_o/b with Re_{δ^*}, laminar and turbulent flows. The lines of Eq. (7) and Eq. (10) are dotted out of the validity ranges of the formulas.

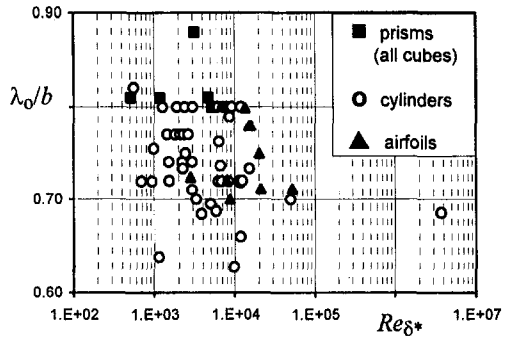

Fig. 7 Effect of the obstacle shape on λ_o/b, turbulent flows

$300 < Re_{\delta^*} < 500$. If we consider that numerical points have little significance in determining the flow regime, from Figs. 3 and 6 the transition can be placed around $Re_{\delta^*} \cong 500$, not too differently from the values for boundary layers on a flat plate. For the turbulent regime, b appears to be the main parameter influencing the values of λ_o. Baker (1985) proposes a positive correlation between λ_o/b and Re_{δ^*} (Eq. (7), $Re_{\delta^*} = 10^3 \rightarrow 10^4$); on the contrary, Kubo and Takezawa (1988) suggest a constant value for λ_o/b ($\lambda_o/b = 0.65 \rightarrow 0.75$ for $Re_b = 5 \cdot 10^3 \rightarrow 3.5 \cdot 10^5$), confirmed by the calculations of Lai and Makomaski (1989) for a cube ($\lambda_o/b \equiv 0.80$ for $Re_{\delta^*} = 5 \cdot 10^2 \rightarrow 5 \cdot 10^3$). No direct effect of the boundary layer thickness has ever been indicated on λ_o.

The observation of the overall data set in Fig. 6 suggests conclusions similar to those for λ_s: even if some authors noticed an influence of the Reynolds number on λ_o, the only expression which appears to be valid on the whole range of Reynolds ($Re_{\delta^*} = 5 \cdot 10^2 \rightarrow 4 \cdot 10^6$) is the simple $\lambda_o/b = \text{const}$. The partition of the data in different classes for δ^*/b (not shown here) has confirmed no influence of this parameter on λ_o/b.

No data are available for the influence of h/b on the position of the main vortex; the effects of the obstacle shape can be seen in Fig. 7: blunt obstacles (cubes) tend to induce larger values for λ_o/b and therefore larger vortices, while no significant difference arises between cylinders and airfoils (all the airfoils in Fig. 7 have an approximately round leading edge).

Discussion. In Bettoni (1995) the experimental and numerical data for λ_s and λ_o relative to turbulent flows have been thoroughly examined, inquiring their possible relations with b, h, the boundary layer thickness (δ and δ^*) and form parameter ($H = \delta^*/\theta$), the flow-field width (L_g), and the Reynolds numbers (Re_b, Re_δ, Re_{δ^*}). Many functional correlations have been estimated and different dimensionless coordinations have been tried, both over the whole data set and over particular selections of more homogeneous data.[7] All analyses have confirmed that, with the exception of the effect of small h/b and of the obstacle shape, the only significative relation for both λ_s and λ_o is proportionality with b.

The constants have been estimated with ordinary least squares; the residual distribution of λ_o has been shown to be Gaussian, while that of λ_s deviates from normality[8]; the estimators for the constants and the standard deviations are respectively:

$$\lambda_s/b = 1.1 \quad \sigma_s = 0.11$$

$$\lambda_o/b = 0.74 \quad \sigma_o = 0.05$$

[7] Such as cylinders alone, or large h/b and/or L_g/b ratios alone.

[8] It has been conjectured that, due to the various experimental/numerical conditions and techniques, data from different setups could not be fully comparable. In the λ_s sample a significant part of the data comes from a limited number of literature data sets; the uneven size distribution of the sets in the sample could therefore be a reason for the deviation from normality. This hypothesis has been tested by averaging the data of each set into one single value: the sample thus obtained was robustly normal, giving: $\lambda_s/b = 1.0 \quad \sigma_s = 0.11$.

The dispersion of the values is to be interpreted as the normal experimental or numerical scatter, in addition to the effects of a sum of various parameters whose influence on the system has never been clearly detected: among them, the surface roughness, the geometrical boundary conditions, the form and the turbulence of the incoming boundary layers, or the compressibility effects.

The qualitative and quantitative (Table 1) correlations of λ_o/b or λ_s/b with the different dimensionless numbers indicated in the literature and previously discussed cannot be extrapolated nor generalized to all the data: trends are clearly distinguishable within a single data set, but they look weak when compared with all the other points (see, for example, Eqs. (1) and (2) in Fig. (3) and Eq. (7) in Fig. 6), if not even in contrast with each other. Only homogeneous data sets with one (nondimensional) free parameter show correlations between the vortices characteristics and the flow parameters. For example, small values of L_g/b may be expected to affect the vortex system, but sets where all the parameters other than L_g/b are fixed do not exist, and the analysis of the entire group of data do not show any effect within the available range for this ratio ($L_g/b = 3 \rightarrow 30$). On the other hand, the relationship between h/b and λ_s/b in Fig. 4 is distinguishable because either h alone or b alone have been varied in the sets; if the same data sets are plotted together with all the other points, the spread of the values cancels any significant trend.

The observed incoherence of behavior may be explained in terms of the structural characteristics of the vortices. While the main time-averaged properties of the system are fundamentally stable, i.e., they scatter within a confined range independently of most of the flow parameters, the instantaneous structure of the often (if not always) unsteady vortex pattern appears unstable, as it changes dramatically from one experiment to the other, and possibly also for different values of the control parameters. This topological instability may be the cause of the spread in the values for λ_s and λ_o found by different authors and the apparent impossibility to repeat their trends in similar but distinct flow conditions.

5 Results: λ_s, λ_o—Laminar Flows

Among the available data for laminar flows, only two data sets are experimental: four points for the primary separation from Peake and Galway (1965) (Fig. 3) and a richer group for the position of the main vortex center from Baker (1979, 1985) (Fig. 6). Table 2 collects literature formulas for λ_s and λ_o.

Any attempt to coordinate the whole group of the laminar points for λ_s in Fig. 3 with the flow parameters has been unsuccessful. Therefore, the only possible indications come from the three available sets with constant values for either Re_{δ^*} or δ^*/b (Peake and Galway, experimental, $Re_{\delta^*} = 217$; Ballio, numerical, $\delta^*/b = 0.094$ and $Re_{\delta^*} = 409$), see Figs. 3 and 8. Ballio's set with $\delta^*/b = 0.094$ in Fig. 3 and the two sets in Fig. 8 clearly indicate a positive correlation of λ_s/b with both Re_{δ^*} and δ^*/b, the effect of the last parameter being noticeably different for the two data sets. In Fig. 8 the data are also compared with Eq. (8): Peake and Galway's points satisfactorily match the formula, while Ballio's show a different pattern. In particular, these last points suggest that the effect of the boundary layer thickness would vanish as δ^*/b is increased, while Eq. (8) does not include any saturation level for higher δ^*/b. Finally, if the laminar data are plotted in a $\lambda_s/b - (Re_{\delta^*})(\delta^*/b)$ plane (not shown here), Eq. (8) appears incapable to coordinate the whole group of points; no better result is achieved by Eq. (9) (Belik, 1973).

The dependence of the position of the vortex center on the characteristics of the flow is better defined than that of λ_s. In Baker (1985), λ_o/b is shown to be an increasing function of Re_{δ^*} alone, without any significant dependence on the boundary layer thickness (Eq. (10)); this trend is confirmed by the nu-

Table 2 Laminar flows: literature formulas for λ_s and λ_0

Baker (1985)	$\lambda_s/b = 0.5 + 0.338(\delta^*/b\ \mathrm{Re}_{\delta^*})^{0.48}$	$\mathrm{Re}_{\delta^*} = 210$ $\delta^*/b = 0.045 \rightarrow 0.17$	(8)
Belik (1973)	$\lambda_s/b = 0.5 + 35.5\ \mathrm{Re}_b^{-0.424}$	$\mathrm{Re}_b = 1200 \rightarrow 4700$	(9)
Baker (1985)	$\lambda_o/b = 0.5 + 0.013\ \mathrm{Re}_{\delta^*}^{0.67}$	$\mathrm{Re}_{\delta^*} = 90 \rightarrow 300$ $\delta^*/b = 0.03 \rightarrow 0.09$	(10)

Note: Equation (8) has been derived by Baker from analytical considerations. The author proposed to correct the coefficient 0.338 to 0.30 for a better fit of Peake and Galway's points; however, the accuracy of these data, and specifically of the boundary layer thickness, does not really allow a preference between the two values of the coefficient, so that the original analytical one has been adopted here.

merical results in Ballio ($\mathrm{Re}_{\delta^*} = 107 \rightarrow 815$, $\delta^*/b = 0.037 \rightarrow 0.30$), which closely agree quantitatively with Baker's. The scatter of some of the remaining numerical points in Fig. 6 that lie above those in Baker and in Ballio is not explained by any of the flow parameters. For example, the three points with $\mathrm{Re}_{\delta^*} = 311$, $\lambda_o/b = 1.1 \rightarrow 1.4$, correspond to the calculations by Chen et al. (1992) and Visbal (1989), all with identical flow conditions ($\delta^*/b = 0.21$, $h/b > 2.0$, Blasius profile for the incoming boundary layer): the difference in the results on λ_o apparently is caused only by the different numerical schemes used in the three cases; the same holds true for λ_s.

An ordinary least squares regression on Baker's and Ballio's data with $h/b > 0.6$ has confirmed that δ^*/b is not correlated with λ_o/b, while the coefficients of Eq. (10) may be corrected as:

$$\lambda_o/b = 0.5 + 0.038\ \mathrm{Re}_{\delta^*}^{0.45} \quad \mathrm{Re}_{\delta^*} = 90 \rightarrow 800 \qquad (11)$$

For the higher Reynolds numbers Eq. (11) gives a better fit of the points than Eq. (10), whose validity range is limited within $\mathrm{Re}_{\delta^*} < 300$.

In Fig. 9 a set of results with constant values for δ^*/b and Re_{δ^*} from the calculations in Ballio (1995), shows that the effect of h/b on laminar vortex systems is analogous to the effect on turbulent ones, with both λ_o/b and λ_s/b decreasing with the obstacle height for $h/b < 1$. Finally, the similarity of the behavior of λ_o and λ_s with respect to h/b for the laminar flows suggests that the same may happen for turbulent flows, thus suggesting to extend the $\lambda_s(h/b)$ function in Fig. 4 also to λ_o; moreover, the correction proposed by Baker for turbulent systems (Eq. (3)) is compared to the data in Fig. 9 (asymptotical values: $[\lambda_s/b]_\infty = 1.70$; $[\lambda_o/b]_\infty = 1.05$), showing that the formula, which has been estimated for turbulent systems in front of submerged obstacles, may be applied with reasonable approximation also to laminar symmetrical flows.

Discussion. The analysis of the laminar values for λ_o and λ_s has not offered fully definite results. More experimental data are needed to quantify the dependencies on the main parameters of the system. The main issues that arose from the data analysis are the following.

1) Analogously to turbulent systems, the longitudinal dimensions of the laminar vortices scale primarily with the obstacle width b.
2) λ_o and λ_s are positively correlated with the Reynolds number, although this dependency has not been completely quantified.
3) No effects of the boundary layer thickness have been detected on λ_o; on the contrary, λ_s/b appears to increase with δ^*/b, but the trend is unclear even from a qualitative point of view.
4) The available data provide no evidence about the effects of $L_g(L_g/b \geq 6)$[9], of the form of the incoming boundary layer (Blasius profile for all data), and of the obstacle shape (cylinders or rounded-nose airfoils).

The wide scatter of the data for λ_o and λ_s may be explained in terms of topological instability of the vortex system: the transition from one structure to the other would imply a discrete jump in the vortices dimensions, so that the different topological patterns would result quantitatively incomparable. This hypothesis has been examined, but no relation between λ_o or λ_s and the topological parameters has been found, nor topological anomalies justify any of the most scattering values. This topic anyway requires some deeper investigation within the general topological definition of the flow.

6 Results: ζ_v

Turbulent Flows. In spite of the scantiness of the data and of the scatter of the values, the dependence on Re_{δ^*} of the coordinate ζ_v of the main primary vortex, chosen as the vertical scale of the vortex system, can be recognized to resemble those of the longitudinal scales λ_o and λ_s (Fig. 10). With the exception of a single point far above the others (Larousse et al., 1991; $\mathrm{Re}_{\delta^*} = 3.1 \cdot 10^3$, $\zeta_v/b = 0.13$), turbulent values vary within the range $\zeta_v/b = 0.028 \rightarrow 0.073$ without any evident dependence on the Reynolds number; the wide scatter of the points corresponding to laminar systems suggests a significant correlation

[9] Baker (1979) presents a data set with $L_g/b = 2$, $h/b = 0.5$ (submerged cylinder); it is difficult to separate the effects of the two ratios on the characteristics of the vortices, so that this set is hardly comparable with the other points. See also the results for ζ_v.

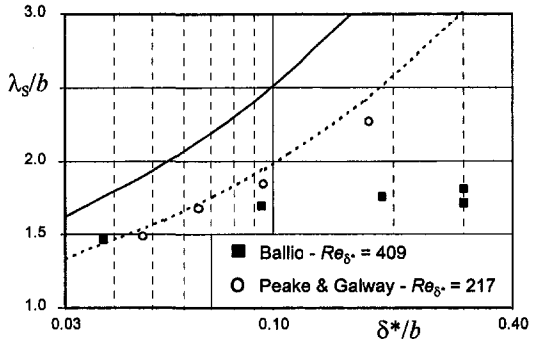

Fig. 8 Effect of δ^*/b on λ_s/b, laminar flows; comparison with Eq. (8): dashed line–$\mathrm{Re}_{\delta^*} = 217$, solid line–$\mathrm{Re}_{\delta^*} = 409$

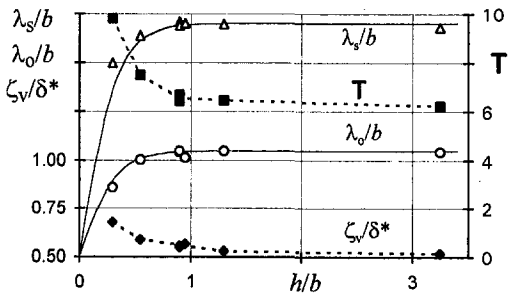

Fig. 9 Effect of h/b on the vortex system. Data from Ballio (1995), laminar flow around a cylinder, $\mathrm{Re}_{\delta^*} = 409$; $\delta^*/b = 0.094$. Solid lines: Eq. (3), asymptotic values: $[\lambda_s/b]_{h/b\rightarrow\infty} = 1.70$, $[\lambda_o/b]_{h/b\rightarrow\infty} = 1.05$.

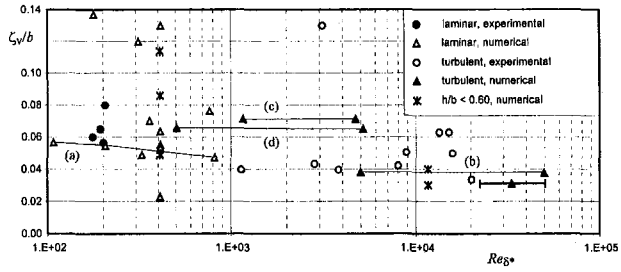

Fig. 10 Variation of ζ_v/b with Re_{δ^*}, laminar and turbulent flows. Labels indicate homogeneous series: (*a*) and (*b*) Ballio (1995), cylinder, $\delta^*/b = 0.094$ and $\delta^*/b = 0.031$; (*c*) and (*d*) Lai and Makomaski (1991), prism, $\delta^*/b = 0.17 \rightarrow 0.18$ and $\delta^*/b = 0.073 \rightarrow 0.074$.

with some other flow parameters. The result for turbulent flows is confirmed by the numerical sets in Ballio (1995) and Lai and Makomaski (1991): for constant geometry and constant δ^*/b, Re_{δ^*} has been widely varied without any effect on ζ_v. Lai and Makomaski's points indicate a weak positive correlation between ζ_v/b and δ^*/b (Fig. 11).

Further analysis of the data in Fig. 10 has shown that turbulent values for ζ_v scale primarily with the obstacle dimension b, and that they are not significantly correlated with δ^*/b, either alone (see Fig. 11) or in conjunction with Re_{δ^*}. If only cylinders and airfoils are considered, the data scatter around a constant value for ζ_v/b is reduced, while prisms lie above the other points (Fig. 11), similarly to what happens to λ_o and λ_s. To our knowledge, no attempt of coordinating the values for ζ_v has been carried out in the literature, except for the study of Kubo and Takezawa (1988), where ζ_v/b has been shown to be independent of Re_b with $\zeta_v/b = 0.028 \rightarrow 0.038$ for a Reynolds number range $Re_b = 5 \cdot 10^3 \rightarrow 3.5 \cdot 10^5$, thus confirming the analysis here developed. Notice that for the points in Kubo and Takezawa neither the δ^*/b nor the Re_{δ^*} values are known, so that they do not appear in the plots of this paper.

Laminar Flows. Literature studies do not suggest any kind of correlation of laminar values of ζ_v with the flow parameters. In Fig. 12 the data are plotted in the $\zeta_v/\delta^* - Re_{\delta^*}$ plane: a comparison between Fig. 10 and Fig. 12 shows that ζ_v is better scaled by δ^* instead of b. The four experimental points in Baker are isolated from the others (numerical), and are characterized by a strong variation of ζ_v/δ^*, which cannot be correlated with the flow parameters; these experiments correspond to the small group of points in Fig. 6 which lay lower than the other laminar data ($Re_{\delta^*} \cong 200$, $\lambda_o/b < 0.7$), and it seems reasonable to assume that, due to their peculiar geometrical conditions (submerged circular cylinder, $h/b = 0.5$, $L_g/b = 2$), they are not fully comparable with data characterized by larger h/b and L_g/b ratios. All the remaining points in Fig. 12 come from computation (cylinders or airfoils) and are somewhat randomly distributed in the range $\zeta_v/\delta^* \cong 0.4 \rightarrow 0.8$. The two sets in

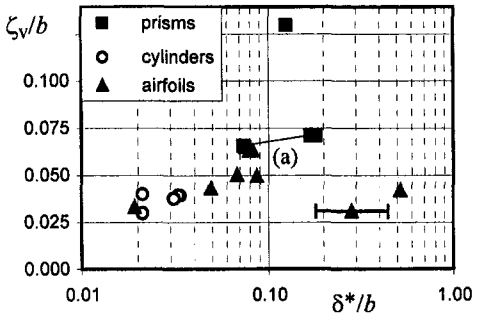

Fig. 11 Effect of the obstacle shape on ζ_v/b, turbulent flows. Label (*a*): Lai and Makomaski (1991), prism, $Re_{\delta^*} = 500 \rightarrow 5000$.

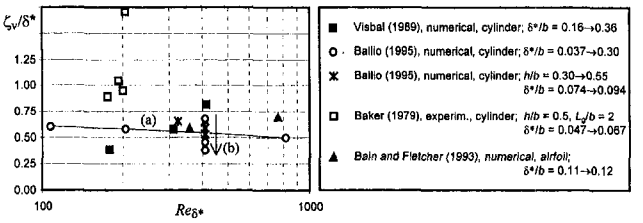

Fig. 12 Effect of Re_{δ^*} on ζ_v/δ^*, laminar flows; $h/b \geq 0.6$ if not differently specified. Labels indicate homogeneous series in Ballio: (*a*) $\delta^*/b = 0.094$; (*b*) $Re_{\delta^*} = 409$, $\delta^*/b = 0.037 \rightarrow 0.30$.

Ballio (1995) with $Re_{\delta^*} = \text{const}$ and $\delta^*/b = \text{const}$ suggest that ζ_v/δ^* decreases as both δ^*/b and Re_{δ^*} increase.

The effect of h/b on ζ_v can be evaluated from Fig. 9: the vortex system is not influenced by the height of the obstacle for large values of h/b, while for $h/b < 1$ the scale ζ_v grows when h/b decreases. This result is in contrast with the behavior of the longitudinal scales and somewhat surprising, since ζ_v, like all the dimensions of the vortex system, can be expected to vanish as $h/b \rightarrow 0$. It must be noticed that the data in Fig. 9 have $\delta/b \equiv 0.28$, so that necessarily it is $h/b > 0.28$, since δ/h cannot be larger than unity for symmetrical flow systems like the one in the figure. As a consequence of this, the trends in the figure cannot be extrapolated to smaller values of h/b, since the parameter would lose its significance for the fixed value of $\delta^*/b = 0.094$. The situation would be different for submerged obstacles, where the height of the obstacle is not limited by the boundary layer thickness; unfortunately, no data are available to evaluate the effect of h in this case.

Discussion. Turbulent ζ_v values show a behavior similar to that of the coordinates λ_s and λ_o, the ratio ζ_v/b resulting independent of both δ^*/b and Re_{δ^*}. The average value of the ratio for the turbulent data of cylinders and airfoils (comprehensive of the above-mentioned Kubo and Takezawa's points) has been found to be:

$$\zeta_v/b = 0.040 \quad \sigma = 0.010$$

The high value of the standard deviation is an index of the scatter of the data; the residual distribution cannot be assumed normal.

Indications for laminar flows are less conclusive. The main scale factor is probably δ^* more than b, but ζ_v/δ^* seems to be influenced by both Re_{δ^*} and δ^*/b, thus keeping some dependence on b. Further experimental data are needed for a better definition of the problem.

It is perhaps worthwhile to emphasize that ζ_v values are small if compared with the overall dimensions of the separation zone, so that their estimation from velocity measurements or flow visualizations is affected by a larger inaccuracy than that of λ_s or λ_o.

7 Results: τ

The data available in the literature for the maximum shear stress induced by the vortices on the symmetry line of the solid bottom are scarce. The attempt of an analysis looks attractive, since none of the parameters that characterize the dynamic properties of the vortex system has ever been systematically investigated. It seems reasonable to normalize τ with some characteristic parameter of the shear stress of the undisturbed boundary layer; two possible nondimensional groups are typically:

$$\mathbf{T} = \frac{\tau}{\mu U/\delta^*} \qquad C_f = \frac{\tau}{0.5\rho U^2}$$

In Fig. 13 all the data are plotted in the $\mathbf{T} - Re_{\delta^*}$ plane. Apart

from identifying the laminar-turbulent transition, no conclusions can be drawn from the three turbulent points.

Some observations are possible for the laminar systems. From the numerical results in Ballio (1995) in Figs. 13 and 14, **T** appears to be positively correlated both with δ^*/b and Re_{δ^*}; the few data from other authors are quantitatively poorly coordinated with Ballio's, but they do not contradict their qualitative trends. No better coordination is achieved if δ^* is replaced by δ or by b in the normalization of τ.

The shear stress on the solid boundary for a Blasius velocity profile is $\tau = 1.66\mu U/\delta = 0.57\mu U/\delta^*$; stresses induced by laminar vortex systems are therefore five to twenty times larger than for the corresponding undisturbed boundary layers. For the turbulent flows, if the boundary layer profiles are approximated with a power low $u(\zeta)/U = (\zeta/\delta)^{1/n}$, the undisturbed stress can be expressed as:

$$n = 7 \quad \frac{\delta}{\delta^*} = 8$$

$$\frac{\tau}{0.5\rho U^2} = 0.027\ \mathrm{Re}_{\delta^*}^{-1/4} \quad \frac{\tau}{\mu U/\delta^*} = 0.014\ \mathrm{Re}_{\delta^*}^{3/4}$$

$$n = 10 \quad \frac{\delta}{\delta^*} = 11$$

$$\frac{\tau}{0.5\rho U^2} = 0.013\ \mathrm{Re}_{\delta^*}^{-1/6} \quad \frac{\tau}{\mu U/\delta^*} = 0.0065\ \mathrm{Re}_{\delta^*}^{5/6}$$

The ratio between the shear stresses for the three turbulent points in Fig. 13 and their corresponding stresses in the absence of the obstacle decreases from 3 to 1.5 as the Reynolds number increases ($\mathrm{Re}_{\delta^*} = 5 \cdot 10^3 \rightarrow 5 \cdot 10^4$), as already noticed by Monti (1994).

It may be worth mentioning that the maximum value of the shear stress on the solid bottom is not reached in the symmetry plane, but beside the obstacle and close to it, at an angle of 45 → 60 deg with the flow direction; for both laminar and turbulent flows the lateral peaks are three to five times higher than the values in the plane of symmetry (Carstens and Sharma, 1975; Darghai, 1989; Ballio, 1995).

The effect of the h/b ratio on shear stresses (Fig. 9, laminar) is similar to that on ζ_v: larger values of **T** are generated as h/b decreases, while the effect of the obstacle height tends to vanish for $h/b > 1$. As previously discussed, these results should not be extrapolated for smaller values of h/b since δ^*/b could not be kept constant.

The τ values in Ballio require some further consideration. Although the numerical solutions have been checked to be grid-independent as far as the streamlines and therefore the dimensions of the separation zone are concerned, bottom shear stresses may be quite sensitive to the dimensions of the cells; a computation with a refined grid has given higher values for τ[10]. The spatial resolution requirements and the quantification of the discretization effects on computed or measured shear stresses require further investigation.

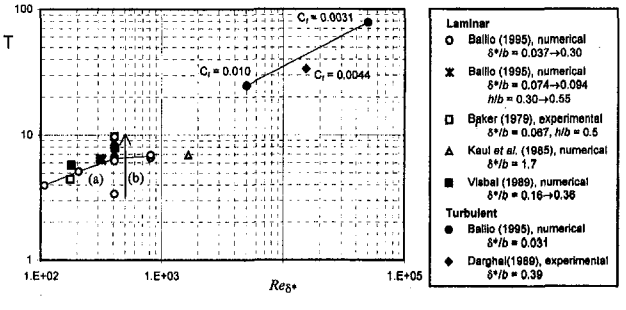

Fig. 13 Effect of Re_{δ^*} on T. Cylinders, $h/b \geq 0.6$ if not differently specified. Labels indicate homogeneous series in Ballio: (a) $\delta^*/b = 0.094$; (b) $\delta^*/b = 0.037 \rightarrow 0.30$.

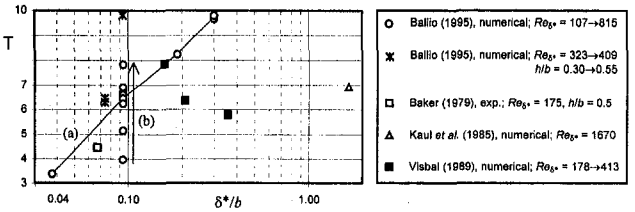

Fig. 14 Effect of δ^*/b on T, laminar flows. Cylinders, $h/b \geq 0.6$ if not differently specified. Labels indicate homogeneous series in Ballio: (a) $\mathrm{Re}_{\delta^*} = 409$; (b) $\mathrm{Re}_{\delta^*} = 107 \rightarrow 815$.

8 Conclusions

1) For both laminar and turbulent flows, the obstacle width b is the main length scale parameter for the vortex system, except for the vertical coordinate ζ_v of laminar vortices, which apparently scales with the boundary layer thickness (δ or δ^*) better than with b.
2) The longitudinal and vertical dimensions of turbulent junction vortices are not significantly correlated with most flow parameters; extreme values of the ratios between some geometrical flow parameters (h/b, L_g/b, δ^*/b, δ^*/h, ...) are expected to affect the system, but evidence of such effects have been found for h/b only. The different relationships proposed in the literature between λ_o/b or λ_s/b and both the Reynolds number and the boundary layer thickness appear not to be of general value.
3) Laminar junction vortices are more evidently influenced by the characteristics of the flow than turbulent ones. λ_o/b is positively correlated with Re_{δ^*} but presumably not with δ^*/b, while λ_s/b seems to be correlated with both. Due to the scatter of the available points, interpolation formulas need further validation. Scarcity of data does not allow definite conclusions on ζ_v, although there is some evidence of a negative correlation between ζ_v/δ^* and both Re_{δ^*} and δ^*/b.
4) For small values of the ratio h/b, the obstacle height h becomes a significant length scale for the longitudinal dimensions of the vortical pattern, so that λ_o/b and λ_s/b decrease for decreasing h/b. This dependence is similar for laminar and turbulent systems, and for submerged and symmetrical obstacles. Almost no effects are detected for $h/b > 1$. Unlike λ_o and λ_s, increasing values of ζ_v have been found for $h/b < 1$, but the trend has not been checked for the smallest values of the ratio.
5) Blunt obstacles distort the flow more than slender ones, and therefore generate larger vortex systems. With the exception of "sharp" airfoils, the results for differently shaped obstacles are anyway comparable, with prisms generally giving larger λ_o, λ_s and ζ_v values than cylinders and round-nosed wings.
6) The shear stresses induced by the horseshoe vortex on the bottom surface are several times higher than those of the undisturbed flow; when normalized with the undisturbed values, the stresses appear to be positively correlated with Re_{δ^*} and δ^*/b for laminar flows. It does not seem appropriate to draw any definite conclusion for turbulent systems on the base of the only three available points.

[10] For constant flow and geometrical conditions ($\mathrm{Re}_{\delta^*} = 409$, $\delta^*/b = 0.094$, $h/b = 0.9$) the grid resolution has been approximately doubled, giving maximum τ values 20 percent higher than those here shown. The cell dimensions ($\Delta x \times \Delta y \times \Delta z$) at the location of the maximum stress were, respectively ($0.020 \times 0.020 \times 0.005$)$b$ and ($0.012 \times 0.010 \times 0.0025$)$b$.

7) As repeatedly noticed in the literature, since in turbulent flows the vertical dimensions of the vortices are independent of the boundary layer thickness, for smaller δ^*/b the fluid entering the vortex system comes from higher momentum zones of the flow; consequently, higher dynamical effects may be expected, and also higher turbulence and vorticity values. However, the same is not necessarily true for laminar flows, for which ζ_v is presumably dependent on δ.
8) Numerical solutions for laminar flows are in some cases dependent on the computational scheme; the problem is worsened by the possible instability and/or unsteadiness of the vortex structures for the different flow conditions. On the contrary, the performance of computations is unexpectedly good for turbulent flows. Reynolds stress measurements and analyses in the junction region (Metha, 1984; Devenport and Simpson, 1992) indicate that eddy viscosity models, and specifically the κ-ϵ model, may not be suited for this flow. The results of turbulent computations, at least on a global scale, are fully comparable with experimental data, in spite of the fact that they were mostly obtained using the κ-ϵ model; eddy viscosity models could be inadequate to reproduce correctly some details of the vortex structures here not analyzed. It is to be noticed that, although the vortex pattern has a complex unsteady dynamics, its mean characteristics have been properly captured by the solutions of the steady form of the Reynolds equations; when computed on an unsteady base (Rizzetta, 1994; Deng and Piquet, 1992), the solution has turned out to be time-independent.

9 Data Bank Contribution

The data bank collects the values for the flow parameters and the results of literature data shown in the paper. In a single large table each line contains one experiment/numerical simulation and columns show all the parameters and result values.

10 Acknowledgments

This paper was partially supported by the Italian Ministry of University and Research (MURST). The authors wish to thank two anonymous referees for their pertinent suggestions.

References

(Numbers refer to the list of data sources in the Appendix)

Abid, R., and Schmitt, R., 1986, "Experimental Study of a Turbulent Horseshoe Vortex Using a Three Component Laser Velocimeter," AIAA Paper 86-1069, May. (1)

Agui, J. H., and Andreopoulos, J., 1992, "Experimental Investigation of a Three-Dimensional Boundary Layer Flow in the Vicinity of an Upright Wall Mounted Cylinder," ASME JOURNAL OF FLUIDS ENGINEERING, Vol. 114, pp. 566–576. (2)

Baker, C. J., 1979, "The Laminar Horseshoe Vortex," *Journal of Fluid Mechanics,* Vol. 95, Part 2, pp. 347–367. (3)

Baker, C. J., 1980, "The Turbulent Horseshoe Vortex," *Journal of Wind Engineering and Industrial Aerodynamics,* Vol. 6, 9–23. (4)

Baker, C. J., 1985, "The Position of Points of Maximum and Minimum Shear Stress Upstream of Cylinders Mounted Normal to Flat Plates," *Journal of Wind Engineering and Industrial Aerodynamics,* Vol. 18, pp. 263–274. (5)

Bain, J. G., and Fletcher, C. A. J., 1993, "A Computational Study of the Flow in a Bluff Body/Flat Plate Junction," *Journal of Wind Engineering and Industrial Aerodynamics,* Vol. 46–47, pp. 121–127. (6)

Ballio, F., 1995, "Caratterizzazione cinematica e dinamica del campo di moto all'intersezione ostacolo-parete," Ph.D. thesis, Politecnico di Milano. (7)

Belik, L., 1973, "The Secondary Flow About Circular Cylinders Mounted Normal to a Flat Plate," *The Aeronautical Quarterly,* Vol. 24, No. 1, pp. 47–54. (8)

Bettoni, C., 1995, "Analisi del campo di moto attorno ad un ostacolo cilindrico su fondo piano," *Tesi di Laurea,* Politecnico di Milano.

Carstens, T., and Sharma, H. R., 1975, "Local Scour Around Large Obstructions," *Proceedings of the XVI Congress of IAHR,* July 27–Aug. 1st, San Paolo, Brasil, B32, pp. 251–262.

Chen, C. H., and Hung, C. M., 1992, "Numerical Study of Juncture Flows," *AIAA Journal,* Vol. 30, No. 7, pp. 1800–1807. (9)

Chima, R. V., and Yokota, J. W., 1990, "Numerical Analysis of Three-Dimensional Viscous Internal Flows," *AIAA Journal,* Vol. 28, No. 5, 798–806. (10)

Coon, M. D., and Tobak, M., 1995, "Experimental Study of Saddle Point of Attachment in Laminar Juncture Flow," *AIAA Journal,* Vol. 33, No. 12, pp. 2288–2292.

Dargahi, B., 1989, "The Turbulent Flow Field Around a Circular Cylinder," *Experiments in Fluids,* Vol. 8, pp. 1–12. (11)

Deng, G. B., and Piquet, J., 1992, "Navier-Stokes Computations of Horseshoe Vortex Flows," *International Journal for Numerical Methods in Fluids,* Vol. 15, pp. 99–124. (12)

De Ponte, S., Gibertini, G., Cerchiari, M., Franzetti, S., and Monti, R., 1994, "Vortical Flow and Skin Friction in a Surface-body Intersection. An Aeronautical and Hydraulic Cooperation," *Proceedings of the 2nd International Conference on Experimental Fluid Mechanics,* July 4–8, Torino, Italy.

Devenport, W. J., and Simpson, R. L., 1990, "Time-Dependent and Time-Averaged Turbulence Structure Near the Nose of a Wing-Body Junction," *Journal of Fluid Mechanics,* Vol. 210, pp. 23–55. (14)

Devenport, W. J., Simpson, R. L., Dewitz, M. B., and Agarwal, N. K., 1992, "Effects of a Leading-Edge Fillet on the Flow Past an Appendage-Body Junction," *AIAA Journal,* Vol. 30, No. 9, pp. 2177–2179. (15)

Eckerle, W. A., and Awad, J. K., 1991, "Effect of Freestream Velocity on the Three-Dimensional Separated Flow Region in Front of a Cylinder," ASME JOURNAL OF FLUIDS ENGINEERING, Vol. 113, pp. 37–44. (16)

Eckerle, W. A., and Langston, L. S., 1987, "Horseshoe Vortex Formation Around a Cylinder," ASME *Journal of Turbomachinery,* Vol. 109, No. 2, pp. 278–285. (17)

Fleming, J. L., Simpson, R. L., Cowiing, J. E., and Davenport, W. J., 1993, "An Experimental Study of a Turbulent Wing-Body Junction and Wake Flow," *Experiments in Fluids,* No. 14, pp. 366–378.

Hölscher, N., and Niemann, H. J., 1987, "Some Aspects About the Flow Around a Surface-Mounted Circular Cylinder in Turbulent Shear Flows," *Proceedings of the 6th Symposium on Turbulent Shear Flows, Toulouse,* France, 7–9 Sept. (18)

Hung, C. M., Sung, C. H., and Chen, C. L., 1991, "Computation of Saddle Point of Attachment," AIAA Paper 91-1713.

Khan, M. J., Ahmed, A., and Trosper, J. R., 1995, "Dynamics of the Juncture Vortex," *AIAA Journal,* Vol. 33, No. 7, pp. 1273–1278. (19)

Kaul, U. K., Kwak, D., and Wagner, G., 1985, "A Computational Study of Saddle Point Separation and Horseshoe Vortex System," AIAA-Paper n. 85-0182, Jan. (20)

Kubo, K., and Takezawa, M., 1988, "Experimental Study on Horseshoe Vortex in the Upstream Front of Cylindrical Structure," *Modelling Soil-Water-Structure Interactions,* Kolkman et al., eds., Balkema, Rotterdam, pp. 117–126. (21)

Kubrendran, L. R., McMahon, H. M., and Hubbartt, J. E., 1986, "Turbulent Flow Around a Wing-Fuselage Type Juncture," *AIAA Journal,* Vol. 24, No. 9, pp. 1447–1452. (22)

Lai, K. Y. M., and Makomaski, A. H., 1989, "Three-Dimensional Flow Pattern Upstream of a Surface-Mounted Rectangular Obstruction," ASME JOURNAL OF FLUIDS ENGINEERING, Vol. 111, pp. 449–455. (23)

Larousse, A., Martinuzzi, R., and Tropea, C., 1991, "Flow Around Surface-Mounted, Three-Dimensional Obstacles," *Proceedings of the 8th Symposium on Turbulent Shear Flow.* (24)

Martinuzzi, R., and Tropea, C., 1993, "The flow Around Surface-Mounted, Prismatic Obstacles Placed in a Fully Developed Channel Flow," ASME JOURNAL OF FLUIDS ENGINEERING, Vol. 115, pp. 85–92. (25)

Mason, P. J., and Morton, B. R., 1987, "Trailing Vortices in the Wakes of Surface-Mounted Obstacles," *Journal of Fluid Mechanics,* Vol. 175, pp. 247–293.

Merati, P., McMahon, H. M., Yoo, K. M., 1991, "Experimental Investigation of a Turbulent Flow in the Vicinity of an Appendage Mounted on a Flat Plate," ASME JOURNAL OF FLUIDS ENGINEERING, Vol. 113, pp. 635–642.

Metha, R. D., 1984, "Effect on a Wing Nose Shape on the Flow in a Wing/Body Junction," *Aeronautical Journal,* Dec.

Monti, R., 1994, "Indagine sperimentale delle caratteristiche fluidodinamiche del campo di moto intorno ad una pila circolare," Ph.D. thesis, Politecnico di Milano. (26)

Ölçmen, S. M., and Simpson, R. L., 1994, "Influence of Wing Shapes on Surface Pressure Fluctuations at Wing-Body Junctions," *AIAA Journal,* Vol. 32, No. 1, pp. 6–15. (27)

Peake, D. J., and Galway, R. D., 1965, "The Three-Dimensional Separation of a Plane Incompressible Laminar Boundary Layer Produced by a Circular Cylinder Mounted to a Flat Plate," *Recent Developments in Boundary Layer Research—AGARDOGRAPH 97,* Part 11, pp. 1049–1080. (28)

Pierce, F. J., and Harsh, M. D., 1988, "The Mean Flow Structure Around and Within a Turbulent Junction of Horseshoe Vortex—Part II. The Separated and Junction Vortex Flow," ASME JOURNAL OF FLUIDS ENGINEERING, Vol. 110, pp. 415–423. (29)

Pierce, F. J., and Shin, J., 1992, "The Development of a Turbulent Junction Vortex System," ASME JOURNAL OF FLUIDS ENGINEERING, Vol. 114, pp. 559–521. (30)

Pierce, F. J., and Tree, I. K., 1990, "The Mean Flow Structure on the Symmetry Plane of a Turbulent Junction Vortex," ASME JOURNAL OF FLUIDS ENGINEERING, Vol. 112, pp. 16–22. (31)

Qadar, A., 1981, "The Vortex Scour Mechanism at Bridge Piers," *Proceedings Institution of Civil Engineers,* Vol. 71, Part 2, pp. 739–757.

Rizzetta, D. P., 1994, "Numerical Simulation of Turbulent Cylinder Juncture Flowfields," *AIAA Journal,* Vol. 32, No. 6, pp. 1113–1119. (32)

Seal, C. V., Smith, C. R., Akin, O., and Rockwell, D., 1995, "Quantitative Characteristics of Laminar, Unsteady Necklace Vortex System at a Rectangular Block-Flat Plate Juncture," *Journal of Fluid Mechanics,* Vol. 286, pp. 117–135.

Thomas, A. S. W., 1987, "The Unsteady Characteristics of Laminar Juncture Flows," *The Physics of Fluids,* Vol. 30 (2), pp. 283–285.

Visbal, M. R., 1989, "Numerical Investigation of Laminar Juncture Flows," AIAA-Paper n. 89-1873, June. (33)

West, G. S., and Apelt, C. J., 1982, "The Effects of Tunnel Blockage and Aspect Ratio on the Mean Flow Past a Circular Cylinder with Reynolds Numbers Between 10^4 and 10^5," *Journal of Fluid Mechanics,* Vol. 114, pp. 361–377.

APPENDIX

Data Sources and Flow Parameters

(A)	(B)	(C)	h/b	L_f/b	$\delta^*/b \cdot 10^2$	$Re_{\delta^*} \cdot 10^{-2}$	λ_s	λ_o	ζ_v	τ	b (cm)	Experimental techniques
Experimental, laminar												
3	C	A	0.5→4.8	2.0→8.0	3.0→9.3	0.9→2.9	x	x	x	x	6.4→7.6	FV, IP, PT
5	C	A	0.03→12	2.0→8.0	2.7→8.3	1.1→1.8		x			2.5→10	PT
28	C	W	2.0→7.4		4.7→17	2.2	x				1.9→7.0	BSV
Experimental, turbulent												
1	A	A	2.1	4.6	1.9	200	x	x	x		36	BSV, LDV, PT
2	C	A	2.0	4.0	1.1	25	x	x			31	BSV, IP, PT
4	C	A	0.03→4.8	5.0→8.0	2.3→38	5.6→170	x	x			6.4→15	FV, BSV, PT
5	C	A	0.03→12	2.0→8.0	2.1→50	14→180	x	x			2.5→10	FV, BSV, PT
8	C	A	1.7→5.0		1.2→21	21→150	x				2→6	BSV
11	C	W	1.3		39	150	x	x	x	x	15	FV, HV, PT, PR
14	A	A	3.2	12→25	4.5→6.8	69→88	x	x	x		7.2	BSV, LDV, PT
15	A	A	3.2	25	4.5	69	x				7.2	BSV
16	C	A	1.5	4.0	2.9→3.5	11→62	x	x	x		15	BSV, LDV, PT
17	C	A	0.5	6.0	2.1	120	x	x			30	BSV, 5HP, PT
18	C	A	1.9		60	37200	x	x			32	BSV, PT
19	A	A	> 0.38	7.4	8.4→52	80		x	x		12	BSV, IP
21	C	W	0.6						x		64	FV
22	A	A		63	5.0	28		x			5.8	HV
24	P	A	0.04→2.0	1.0→48	0.5→25	31	x	x	x		1.3→60	BSV, LDV
26	C	A	2.3→5.0	14		27→62	x	x	x		5.0→5.6	5HP
27	A	A		13	3.9→9.6	97	x				4.9→13	BSV
29	A	A	1.8	7.2	7.9	130	x	x	x		13	BSV, 5HP, PT
30	A	A	1.8	7.2	8.3	150	x	x	x		13	BSV, LDV, 5HP
31	A	A	1.8	28	8.6	160	x	x	x		13	BSV, LDV, PT

(A)	(B)	(C)	h/b	L_f/b	$\delta^*/b \cdot 10^2$	$Re_{\delta^*} \cdot 10^{-2}$	λ_s	λ_o	ζ_v	τ	CD $\cdot 10^3$	Numerical techniques
Numerical, laminar												
6	C	E		7.0	10→11	3.6→7.6	x	x	x		120x120x??	
7	C	V	0.5→3.3	5.8→10	3.7→30	1.1→8.1	x	x	x	x	20x20x5 13x10x2.5	IC, ST, HY or 2^{nd}
9	C	V	3	40	21→36	1.8→3.1	x	x			??x??x??	CP, UT, 1^{st}→3^{rd}
20	C		5	50	170	17	x			x	100x100x15	IC, UT
33	C	V	2	31	16→36	1.8→4.1	x	x	x	x	5x5x0.5	IC, UT, 2^{nd}
Numerical, turbulent												
7	C	V	0.6	5.0	3.1	50→500	x	x	x	x	7.5x10x1	IC, ST, HY, κ-ε + WF
10	C	V	0.5	6.0	2.1	120	x	x	x		57x68x??	IC, ST, 2^{nd}, Baldwin-Lomax
12	A	V	2.1	3.6	18→45	210→520	x	x	x		70x70x??	IC, UT, EXP, Baldwin-Lomax
23	P	V	0.66	3.3	7.3→18	5.0→51	x	x	x		30x??x30	IC, ST, HY, κ-ε + WF
32	C	V	0.5	> 4	2.1	120	x	x			4x0.2x0.1	IC, UT, 2^{nd}, κ-ε + TLM

Legend for the table:

Column (A): source; see numbers in the bibliography;

Column (B): obstacle shape; Cylinder/Airfoil/Prism;

Column (C): Air/Water (experimental); finite Elements/Volumes (numerical);

Columns "λ_s", "λ_o", "ζ_v", "τ": x if available;

Column "CD" (numerical): approximate cell dimensions in the symmetry plane, $0.5b$ ($b = 1$) ahead of the obstacle leading edge;

Column "experimental techniques": FV = flow visualization, *BSV* = bottom shear stresses visualization, IP = image processing, LDV = laser doppler velocimetry, HV = hot wire/film velocimetry, 5HP = 5-hole probe, PT = pressure tap, PR = preston probe;

Column "numerical techniques": IC = incompressible, CP = compressible; ST = steady, UT = unsteady; interpolation procedure: HY = hybrid, EXP = exponential, nth = nth order; wall treatment: WF = wall function, TLM = two-layer model.

A Large-Eddy Simulation of the Near Wake of a Circular Cylinder

S. A. Jordan
Mechanical Engineer,
Naval Undersea Warfare Center,
Newport, RI 02841

S. A. Ragab
Professor,
Department of Engineering Science and Mechanics,
Virginia Polytechnic Institute and State University,
Blacksburg, VA 24061

The formation and the downstream transport of the Strouhal vortices in the near wake of a circular cylinder are investigated using the large-eddy simulation (LES) method. The governing equations are formulated in curvilinear coordinates to accommodate a nonorthogonal grid with formal development of a dynamic model to account for the subgrid turbulent scales. Results were produced with and without use of the model. The focus of the investigation is at a subcritical Reynolds number of 5600. Using the dynamic model, the LES results compared best to the published experimental data in terms of both the global and local wake characteristics such as the drag and base pressure coefficients, shedding and detection frequencies, peak vorticity, and the downstream mean velocity-defect and Reynolds stresses. The results further showed streamwise filaments that connect subsequent Strouhal vortices. Qualitatively, the time-averaged Reynolds stresses of the formation region revealed similar symmetric characteristics over the range $525 \leq Re \leq 140{,}000$.

Introduction

A detailed study of the turbulent vortex formation regime behind a circular cylinder and the subsequent transport of the vortices downstream has many important and practical implications. Resolution of the corresponding local turbulent characteristics poses a true challenge for the large-eddy simulation (LES) methodology. The vortices themselves derive most of their large-scale vorticity from the separated shear layers, which constitute the transverse outer regions of the formation regime. Except for only minor dispersion, their large-scale motion remains strongly coherent for many diameters downstream. Since the purpose of the LES approach is full resolution of the large-scale turbulent motion, the numerical results can provide useful physics regarding the cyclic formation of the vortices as well as their near downstream transport.

Only three LES investigations of the cylinder near wake flow have been formally published above the low Reynolds number regime. The first was a two-dimensional (2D) study by Song and Yuan (1990) at a high Reynolds number. Since vortex stretching strongly dominates the turbulent production in the near wake (Cantwell and Coles, 1983), their simulation appears quite inadequate for capturing the important scales of the turbulent physics. A second study by Kato et al. (1993) concentrated on predicting the aerodynamic noise in the near wake using the finite element method. Their LES results served as input into the Lighthill-Curle equation for predicting the radiated far field acoustic pressures. However, due to their highly dissipative subgrid-scale turbulence model and their relatively coarse mesh of the wake region, agreement with the experimental data in terms of the spectral physics was obtained only at the very low frequency levels. Contrasting the predictive accuracy of second-order central and fifth-order upwind-biased schemes for the convective terms was the focus of an LES study by Mittal and Moin (1997). They concluded that both schemes will give similar predictions of the turbulent Reynolds stress statistics where the spatial resolution is moderate, provided a 20–30 percent finer grid spacing is coupled with the lower order scheme.

The present LES investigation attempts to resolve the organized vortex motion in the near wake of the circular cylinder with special emphasis placed on the turbulent statistics of the formation region. The Reynolds number is 5600, which is based on the cylinder diameter (D) and a uniform freestream velocity (U_∞). This Reynolds number is subcritical, meaning that the cylinder boundary layers are strictly laminar at separation. According to the experimental data reported by Bloor (1964), Unal and Rockwell (1968), and Wei and Smith (1986), the shear layer immediately downstream of separation develops 2D small-scale instabilities which quickly amplify to produced high-frequency disturbances that comprise a discernible spanwise component (see Fig. 1). Wei and Smith (1968), in particular, correlated these disturbances with their observation of small-scale secondary eddies. Further downstream within the shear layer, these eddies lead to the formation of the large-scale periodic vortices. At Re = 5600, the shedding of the primary vortices occurs at a dimensionless frequency (Strouhal number, S_t) of approximately 0.205; $S_t = fD/U_\infty$.

The experimental measurements of the near wake turbulent statistics at a Reynolds number of 5600 were published by Zhou and Antonia (1993). They reported the near wake as being fully turbulent over a downstream distance (x) increasing from 10 to 60 diameters referenced to the cylinder center. Over that range, their data showed little variation in the cross-sectional area of the primary vortices. At $x = 10$, the convection velocity (U_c) of the vortices was found to be 85 percent of the freestream velocity and slowly increased downstream to 92 percent at $x = 60$. The experimental measurements also indicated that the individual vortices experienced a downstream exponential decay of their peak vorticity with the relative internal distribution remaining essentially unchanged. Moreover, the time-averaged turbulent quantities showed a relative decrease with distance downstream. While the peak horizontal components occurred at the vortex center, the circumferential fluctuations closely mimic that of an Oseen vortex. Zhou and Antonia focused much of their work on developing an empirically-based Oseen vortex model to correctly predict the turbulent wake physics and the transport of the shed vortices.

In the present investigation, we will use the experimental data just discussed to verify the LES predictions of the shed vortex characteristics. Inasmuch as these characteristics are derived directly from the formation region, we can then extend the present study to include new physics of that region. Thus, the combined experimental and present numerical results will give us an understanding of the turbulent physics over the entire near wake region. To adequately resolve the flow, we generated a nonorthogonal O-type grid topology. The corresponding equa-

Contributed by the Fluids Engineering Division for publication in the JOURNAL OF FLUIDS ENGINEERING. Manuscript received by the Fluids Engineering Division February 14, 1997; revised manuscript received March 2, 1998. Guest Editor: C. Dolton.

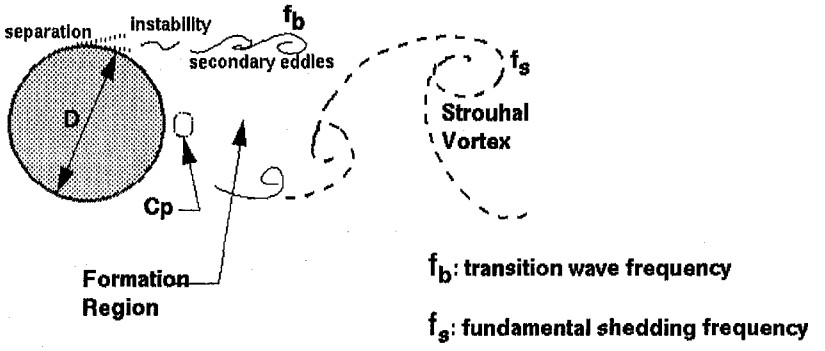

Fig. 1 Large-scale physics of the cylinder near wake flow

tions were therefore solved in a generalized curvilinear coordinate framework. Additionally, the dynamic subgrid scale turbulence model of Germano et al. (1991) was reformulated for application in the curvilinear space. Since nonorthogonal topologies are often necessary to properly resolve the flow characteristics in many complex domains like the cylinder wake, the present LES formulation with the dynamic model has extensive applicability.

Governing Equations and Numerical Method

Development of a LES formulation applicable to nonorthogonal grid topologies begins with a transformation of the incompressible Navier-Stokes and continuity equations to curvilinear coordinates. This system appears as

$$\frac{\partial \sqrt{g} u_i}{\partial t} + \frac{\partial \sqrt{g} \xi^k_{x_j} u_j u_i}{\partial \xi^k} = \frac{\partial \sqrt{g} \xi^k_{x_i} p}{\partial \xi^k} + \frac{1}{\mathrm{Re}} \frac{\partial}{\partial \xi^k} \left[\sqrt{g} g^{kl} \frac{\partial u_i}{\partial \xi^l} \right] \quad (1)$$

$$\frac{\partial \sqrt{g} \xi^k_{x_i} u_i}{\partial \xi^k} = 0 \quad (2)$$

where each term is shown in its nondimensional strong conservation-law form (Vinokur, 1974). The coefficients $\xi^k_{x_j}$ and $\sqrt{g}$ denote the metrics and the Jacobian of the transformation, respectively. To obtain a LES formulation, the system in (1) and (2) must now be spatially filtered. For the present, we will assume that the filter width and local grid spacing are equal; thus, the resolved and filtered turbulent fields are mathematically the same. Along the curvilinear lines, the filter operation proceeds according to

$$\overline{g(\xi^k)\phi(\xi^k)} = \int H(\xi^k - \xi'^k) g(\xi'^k) \phi(\xi'^k) d\xi'^k \quad (3)$$

where $H(\xi^k - \xi'^k)$ is the homogenous filtering kernel, $g(\xi'^k)$ is the metric coefficient, and $\phi(\xi'^k)$ is an arbitrary turbulent quantity. By applying the filter in this manner, the differentiation and filtering will commute similar to the filter operation applied to the Navier-Stokes equations in Cartesian coordinates (Jordan, 1996). The resultant grid-filtered equations in curvilinear coordinates become

$$\frac{\partial}{\partial t} (\sqrt{g} \overline{u_i}) + \frac{\partial}{\partial \xi^k} (\overline{U}^k \overline{u_i}) = \frac{\partial}{\partial \xi^k} (\sqrt{g} \overline{\xi}^k_{x_i} \overline{p}) + \frac{\partial}{\partial \xi^k} \left(\sigma^k_i + 1/\mathrm{Re} \sqrt{g} g^{kl} \frac{\partial \overline{u_i}}{\partial \xi l} \right) \quad (4)$$

$$\frac{\partial \overline{U}^k}{\partial \xi^k} = 0 \quad (5)$$

where the convective term is redefined in terms of the resolvable contravariant velocity components ($\overline{U}^k$); $\overline{U}^k = \sqrt{g} \overline{\xi}^k_{x_j} \overline{u_j}$. Under this derivation, the subgrid scale (SGS) stress tensor σ^k_i is defined as $\sigma^k_i = \overline{U^k u_i} - \overline{U}^k \overline{u}_i$. We note that because the metric quantities are evaluated at discrete points along the curvilinear lines, they can be considered as filtered quantities. This representation is justified due to the analogy that can be drawn between implicit filtering and their discrete approximation (Rogallo and Moin, 1984 and Jordan, 1996).

To resolve the cylinder wake flow, the above LES system was time-advanced by a variant of the fractional-step method (Jordan and Ragab, 1996). Their technique is an extension of the finite-difference scheme of Rai and Moin (1989) to a semi-staggered discretization molecule and reformulated in generalized curvilinear coordinates. The Crank-Nicolson scheme was applied to the diffusive terms to eliminate the high viscous stability restriction particularly near the cylinder surface. An explicit Adams-Bashforth scheme was used for the convective terms. Spatially, the convective terms were approximated by third-order-accurate upwind-biased finite differences while the diffusive terms were discretized using standard second-order-accurate central differences. All terms in the pressure-Poisson equation of the fractional-step procedure were central differenced to the second order. Strong coupling between the pressure and the velocity components was maintained using a fourth-order accurate compact differencing scheme for the pressure gradient at the cell interfaces. The overall discretization scheme is second-order accurate in both space and time. Through extensive testing of this fractional-step method for the cylinder wake flow, we have ascertained an error tolerance (residual) of 10^{-4} to be acceptable for terminating convergence of the pressure-Poisson equation. Under these criteria, incompressibility was reached usually in less than 100 iterations at each time increment. On a CRAY Y/MP platform, the code required approximately 2.5×10^{-5} CPU sec/grid point/time step. Further details of the solution methodology, along with several test cases, can be found in Jordan (1996) or Jordan and Ragab (1996).

Curvilinear Form of the Dynamic Subgrid Scale Model

Smagorinsky's eddy viscosity model (Smagorinsky, 1963), modified by Germano et al. (1991) for dynamic computation of the model coefficient, was used to represent the SGS stress field. This model gives the correct asymptotic behavior of the turbulent stresses when approaching solid walls and can distinguish between laminar and turbulent flow regimes. For the present application, their model was transformed to the computational space. To accomplish this transformation, we expressed the SGS stress tensor σ^k_i as a function of its Cartesian counter-

part τ_{ij}; $\tau_{ij} = \overline{u_i u_j} - \overline{u_i}\,\overline{u_j}$. We begin by showing the SGS stress tensor σ_i^k written in its original grid-filtered form,

$$\sigma_i^k = \overline{\sqrt{g}\,\xi^k_{x_j} u_j u_i} - \overline{\sqrt{g}\,\xi^k_{x_j}}\,\overline{u_j u_i} \tag{6}$$

Since the metric quantities are smooth (devoid of fluctuations), we can redefine σ_i^k as

$$\sigma_i^k = \sqrt{\bar{g}}\,\bar{\xi}^k_{x_j}(\overline{u_j u_i} - \overline{u_j}\,\overline{u_i}) \tag{7}$$

which can be further shown in terms of τ_{ij} as $\sigma_i^k = \sqrt{\bar{g}}\bar{\xi}^k_{x_j}\tau_{ij}$. Using this expression, we can now write a curvilinear dynamic model (CDM) for the SGS stress tensor as

$$\sigma_i^k + \tfrac{1}{3}\bar{\zeta}_i^k \tau_{ll} = 2C\bar{\Delta}^2 |\bar{S}|\,\bar{S}_i^k \tag{8}$$

where C is still considered as Smagorinsky's coefficient and the filtered metric term $\bar{\zeta}_i^k$ is defined as $\bar{\zeta}_i^k = \sqrt{\bar{g}}\bar{\xi}^k_{x_j}\delta_{ij} = \bar{\xi}^k_{x_i}$. In this model, the turbulent eddy viscosity is defined as $\nu_T = C\bar{\Delta}^2|\bar{S}|$ where $|\bar{S}| = \sqrt{2\bar{S}_{ij}\bar{S}_{ij}}$ and $\bar{\Delta}$ is the grid-filter width. The filtered strain-rate tensor $\bar{S}_{ij}$ is defined by

$$\bar{S}_{ij} = \frac{1}{2}\left(\frac{\partial \bar{u}_i}{\partial x_j} + \frac{\partial \bar{u}_j}{\partial x_i}\right) = \frac{1}{2}\left(\bar{\xi}^k_{x_j}\frac{\partial \bar{u}_i}{\partial \xi^k} + \bar{\xi}^k_{x_i}\frac{\partial \bar{u}_j}{\partial \xi^k}\right) \tag{9}$$

Like the SGS stress tensor σ_i^k, the contravariant form of the resolvable strain-rate field $\bar{S}_i^k$ can be expressed as $\bar{S}_i^k = \sqrt{\bar{g}}\bar{\xi}^k_{x_j}\bar{S}_{ij}$. By combining this transformation with Eq. (9), the complete definition of the tensor $\bar{S}_i^k$ is

$$\bar{S}_i^k = \frac{\sqrt{\bar{g}}}{2}\left(\bar{\xi}^k_{x_j}\bar{\xi}^l_{x_j}\frac{\partial \bar{u}_i}{\partial \xi^l} + \bar{\xi}^k_{x_j}\bar{\xi}^l_{x_i}\frac{\partial \bar{u}_j}{\partial \xi^l}\right) \tag{10}$$

Knowing that the contravariant metric tensor g^{kl} is defined as $g^{kl} = \xi^k_{x_j}\xi^l_{x_i}$, the resolvable strain-rate field in the computational space can be reformulated as

$$\bar{S}_i^k = \frac{1}{2}\left(\sqrt{\bar{g}}\bar{g}^{kl}\frac{\partial \bar{u}_i}{\partial \xi^l} + \bar{U}_f^k\right) \tag{11a}$$

$$\bar{U}_f^k = \bar{\xi}^k_{x_j}\bar{u}_f^j \tag{11b}$$

$$\bar{u}_f^j = \frac{\partial \sqrt{\bar{g}}\,\bar{\xi}^l_{x_i}\bar{u}_j}{\partial \xi^l} \tag{11c}$$

One can now easily see that the first term in Eq. (11a) is a direct contribution of the CDM to the transformed molecular diffusion term in Eq. (1). The second term represents the contravariant components of the cell flux vector gradients ($\bar{u}_f^j$). After substituting Eqs. (8) and (11) into Eq. (4), the final form of the governing LES equations in the computational space is

$$\frac{\partial}{\partial t}(\sqrt{\bar{g}}\bar{u}_i) + \frac{\partial}{\partial \xi^k}(\bar{U}^k\bar{u}_i) = \frac{\partial}{\partial \xi^k}\left[\sqrt{\bar{g}}\,\bar{\xi}^k_{x_i}\left(\bar{p} + \frac{1}{3}\tau_{ll}\right)\right] + \frac{\partial}{\partial \xi^k}\left[(\nu_T + 1/\mathrm{Re})\sqrt{\bar{g}}\bar{g}^{kl}\frac{\partial \bar{u}_i}{\partial \xi^l} + \nu_T\bar{U}_f^k\right] \tag{12}$$

along with continuity as defined in Eq. (5). To maintain second-order accuracy in time, the Crank-Nicolson and Adams-Bashforth schemes were applied to the first and second components of the total viscous term, respectively.

Smagorinsky's Coefficient

The procedures of Germano et al. (1991) and Lilly (1992) were used to derive an expression for Smagorinsky's coefficient in the CDM. To implement their procedures directly however, the SGS stress tensor σ_i^k was kept in the form comprising the product of the Cartesian and the contravariant velocity components. The governing LES equations in curvilinear coordinates were then filtered a second time (by a test filter). This third operation produced resolvable tensors similar to those obtained by Germano et al. (1991) in the Cartesian coordinate system. In the generalized curvilinear coordinates however, these tensors are the modified Reynolds stress tensor T_i^k

$$T_i^k = \overline{\bar{u}_i\bar{U}^k} - \overline{\bar{u}_i}\,\overline{\bar{U}^k} \tag{13}$$

and the modified Leonard tensor L_i^k

$$L_i^k = \overline{\bar{u}_i\bar{U}^k} - \overline{\bar{u}_i}\,\overline{\bar{U}^k} \tag{14}$$

where the second overbar indicates the test filter operation. Both tensors L_i^k and T_i^k are computed by test filtering the Cartesian and the contravariant velocity components of the resolved field. The identity derived by Germano (1992) for the Leonard term has a similar form in the computational space, which is here defined as $L_i^k = T_i^k - \bar{\sigma}_i^k$. To be consistent with the eddy viscosity law previously shown for σ_i^k, the Reynolds stress tensor T_i^k is modeled as

$$T_i^k - \tfrac{1}{3}\zeta_i^k T_{ll} = 2C\bar{\bar{\Delta}}^2|\bar{\bar{S}}|\,\bar{\bar{S}}_i^k \tag{15}$$

Using the new identity, the Leonard term in the computational space can be represented as

$$L_i^k - \tfrac{1}{3}\zeta_i^k L_{ll} = 2C\bar{\Delta}^2 M_i^k \tag{16a}$$

$$M_i^k = \alpha^2|\bar{\bar{S}}|\,\bar{\bar{S}}_i^k - \overline{|\bar{S}|\,\bar{S}_i^k} \tag{16b}$$

where the filter width ratio is $\alpha = \bar{\bar{\Delta}}/\bar{\Delta}$. Following the least-squares minimization procedure of Lilly (1992), the CDM coefficient shown in Eq. (16a) is computed as

$$C = -\frac{L_i^k M_i^k}{2\bar{\Delta}^2 M_i^k M_i^k} \tag{17}$$

In this expression, the tensorial components of L_i^k and M_i^k are given in Eqs. (14) and (16b), respectively. Because the model coefficient reflects the local instantaneous strain-rates of the resolved field, it can yield either positive or negative values. Physically, the positive values denote dissipation which mirror energy cascading down to the finest scales the turbulent field. Negative values, on the other hand, symbolize backscatter (or negative dissipation) and indicate energy transfer locally up the cascade; specifically, from the modeled scales to the finest scales of the resolved field. When no intrinsic mechanism exists in the solution algorithm for guaranteeing stability in local regions of high negative dissipation, "ad hoc" measures are commonly exercised to control the range and the distribution of the model coefficient.

We note that the filtering necessary to compute the model coefficient can be performed along the curvilinear lines in either the physical domain or the computational space. In the latter case, transformation of the physical variable is necessary before and after filtering. Also, because the grid is regular and uniform in the computational space, the associated filter is identical in form to its Cartesian counterpart. Jordan (1996) designed two explicit filters (one for each domain) having forms similar to the standard box-type filter that essentially implements volume-averaging (Schumann, 1975) of either the physical or transformed quantity. Using the results from a direct numerical simulation of the cylinder wake flow at Re = 3400, no discernible differences were detected in the attenuated spectral energy of the fluctuating velocities using either box filter. Conversely, the computational cost of the physical-based filter was nearly twice that of the other including the cost associated with the transfor-

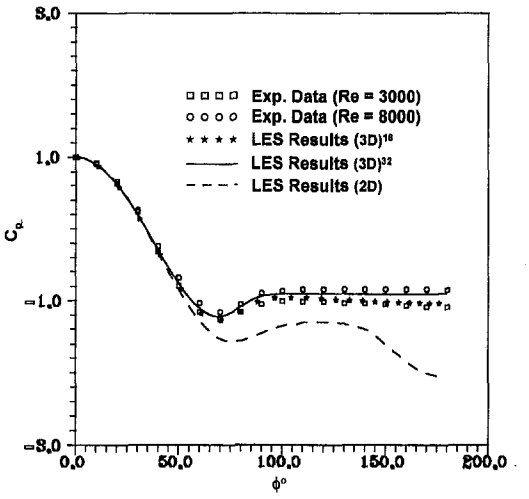

Fig. 2 Comparison of the computed mean pressure coefficient to the experimental results of Norberg (1992); (3D)^{16} depicts 16 spanwise points over length π and (3D)^{32} denotes 32 points over spanwise length $\frac{2}{3}\pi$

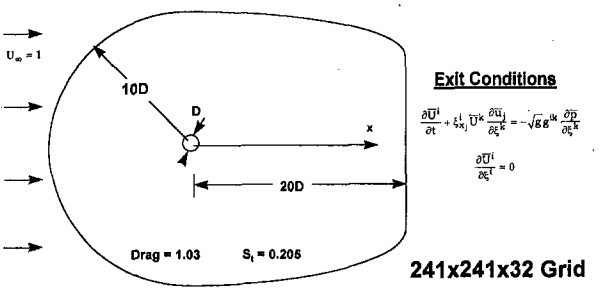

Fig. 4 Geometric and flow conditions of the LES computation of the cylinder near wake at Re = 5600

mations. Using the same database, a filter width ratio of $\alpha = 2$ gave acceptable global correlations between the exact and model Reynolds stresses of the SGS field. Locally, negative values were observed, however, that often sustained long correlation times.

Based on the above analyses, all explicit filtering in the present simulation was conducted in the computational space using the box-type filter. In the expression for the model coefficient, the filter width ratio was set at a value of 2. Moreover, backscatter effects in this first application of the CDM were truncated to zero to inhibit the potential for diverging solutions. This conservative measure enforced a minimum level of dissipation of the turbulent kinetic energy at all computational points within the physical domain as delivered by the kinematic viscosity. Finally, the importance and contributions of the CDM relative to the remaining terms in the governing transformed equations will be address in the next section.

Results and Discussion

In this section, we will present our investigation of the turbulent physics in the near cylinder wake at Re = 5600 followed by an examination of the Reynolds stress statistics within the formation region over a range of Re from 525 to 140,000. When 2D simulations are performed of the cylinder wake flow within this range, both the minimum and the base pressure coefficients will be over-predicted (Mittal and Balachandar, 1996). The base pressure coefficient $(Cp)_b$ in this case refers to the mid-plane region directly behind the cylinder (see Fig. 1). In view of the experimental data, this parameter strongly correlates with the formation length, Strouhal number, and strength of the primary vortices. Typically, a 2D simulation under-predicts the formation length while over-predicting the strength and the shedding frequency. Resolving the correct base pressure is therefore an essential prerequisite of the three-dimensional (3D) computation.

A second concern of the 3D computation is adequate resolution of the streamwise near-wake structures, which are spanwise periodic. According to the experimental results reported by Mansy et al. (1994) and Williamson et al. (1995), the spanwise wavelength (λ_z) of these large eddies scale as $\lambda_z/D \sim 20\ \mathrm{Re}^{-1/2}$. In our simulations, we used 32 points over length $\frac{2}{3}\pi$ in the spanwise direction to satisfy this requirement. This spacing should give seven streamwise eddies each resolved by a minimum of four spanwise points.

Evidence indicating proper resolution of the base pressure is illustrated in Fig. 2 where the mean pressure coefficients (time-averaged over six shedding cycles) are compared to the experimental data published by Norberg (1992) for Re = 3000 and Re = 8000. In our simulations, we found time-averaging over six cycles sufficient to establish the mean velocity and pressure fields downstream of the cylinder. Similar results from a respective 3D computation with 16 points over spanwise length π as

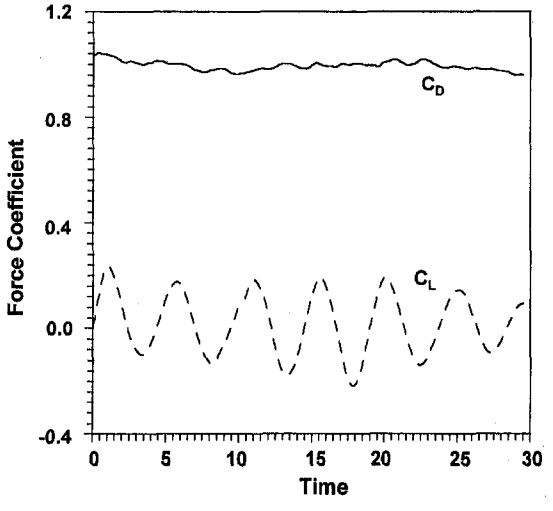

Fig. 3 Profiles of the lift and drag force coefficient over approximately six shedding cycles for Re = 5600; $\langle C_D \rangle$ = 1.01 and S_t = 0.206

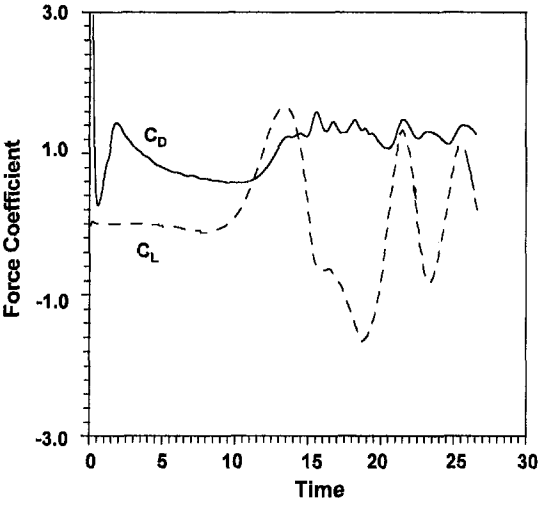

Fig. 5 Profiles of the early lift and drag force coefficients for flow over a circular cylinder at Re = 5600

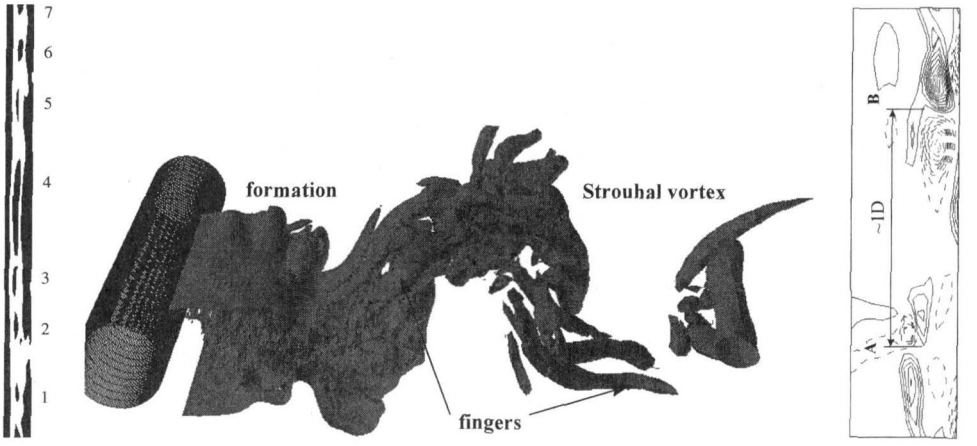

Fig. 6 Typical snapshots of the three-dimensionality of the cylinder near wake; (*a*) streamwise vorticity ($r/D \sim 1.1$), (*b*) isosurfaces of vorticity magnitude ($\omega = 2$) revealing streamwise "fingers" and (*c*) streamwise vorticity contours through "fingers" ($r/D \sim 4$); max. 4.5, min. −4.5, incr. 0.45 (dash contours depict negative vorticity)

well as a 2D computation are also included in the figure. The 2D profile clearly illustrates the gross errors attained after separation when the three-dimensionality of the wake flow is ignored while the poor spanwise resolution slightly over-predicts the downstream pressure. Under the higher spanwise resolution, the drag coefficient profile plotted in Fig. 3 averaged to approximately $\langle C_D \rangle = 1.01$, which is within 2 percent of the experimental value shown in Fig. 4 (White, 1974). Later in this section, we will further show that the higher spanwise resolution adequately captured the large-scale wake eddies and gave accurate predictions of the mean turbulent statistics.

The final grid was $241 \times 241 \times 32$ (x, y, z directions) with the inflow and outflow boundaries set at 10 and 20 diameters, respectively (see Fig. 4). These boundaries were established through comparisons of the pressure coefficient profiles and the experimental data of Zhou and Antonia (1993) in terms of the peak vorticity decay of the Strouhal vortices. The inner boundary representing the cylinder surface was no-slip. Along the cylinder periphery (s), the distribution of points was $\Delta s \cong 0.011\,\pi$ within the upstream laminar boundary layer and $(\Delta s)_{\min} \cong 0.003\pi$ in the formation region. We note that Jordan (1996) found this circumferential resolution satisfactory for resolving Kolmorgorov's scale within the formation region at Re = 3400. All the circumferential lines were clustered toward the cylinder surface to insure a first-point field condition in wall units of $\langle \Delta y^+ \rangle < 4$ within the turbulent regions. To complete the kinematic definition, we applied periodic end conditions in the spanwise direction.

The flow over the cylinder was impulsively started with unit velocity, zero reference pressure and a fixed nondimensional time step of $\Delta T = 0.002$; $T = tU_\infty/D$. Once the wake destabilized ($T \sim 10$ in Fig. 5), new velocity and pressure conditions were imposed only along the downstream outflow boundary. Specifically, the continuity and Euler equations were found satisfactory to exit shed vortices with minimum distortion (see Fig. 4 for the explicit equations). Euler's equation was applied for the streamwise and spanwise velocities based on the successful application of the linear convection equation by Pauley et al. (1990) for exiting vortices downstream of a flat plate. The continuity equation was invoked for the transverse velocity to maintain an incompressibility condition even at exit. Finally, an exit pressure gradient was computed via the velocity update equation of the fractional-step method to serve as a Neuman boundary condition for the pressure field solution. Before collecting the field data, the computation was examined over four shedding cycles to insure adequacy of these exit conditions (see the lift and drag force coefficients profiles in Fig. 5). The entire computation required approximately 60 time units to achieve statistical steady-state of the near wake turbulence at Re = 5600.

A useful quantity for visualizing the three-dimensionality of the near wake is the magnitude of vorticity (ω); $\omega = (\omega_x^2 + \omega_y^2 + \omega_z^2)^{1/2}$. This parameter is shown in Figs. 6(a) and 6(b) which are snapshots locally through the upper separated shear layer (radial plane $r/D \sim 1.1$) and globally of the near wake, respectively. Typically, seven small-scale streamwise eddies appear inside the separated shear-layers that transverse the lateral limits of the formation region. The spanwise locations of the secondary eddy structures specifically shown in Fig. 6(a) are illustrated in Fig. 7. This profile represents the average vorticity taken along each circumferential line of the plane (ω_m) scaled by the average vorticity of the entire radial plane (ω_a). Capturing seven streamwise eddies gives an average spanwise wavelength ($\lambda_z \sim 0.29$) that agrees closely with the criteria discussed earlier; but more importantly, they confirm our selection of the spanwise length and resolution of the cylinder near-wake structure at Re = 5600.

The snapshot of the near wake in Fig. 6(b) clearly shows the formation region structure, Strouhal vortices, and large-scale streamwise structures connecting the alternating shed vortices. Gerrard (1978) regularly observed these elongated filaments in his flow visualization experiments and termed them as "fin-

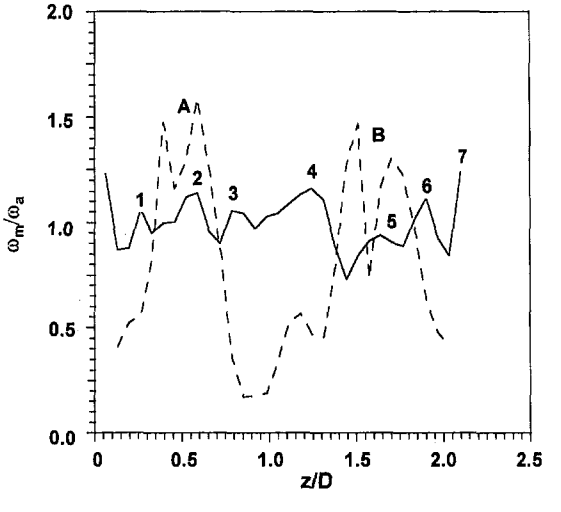

Fig. 7 Spanwise vorticity magnitude (ω_m) scaled by the average value (ω_a) taken of radial plane; —— plane in Fig. 5(a) ($r/D \sim 1.1$, $\Delta s \sim 0.18$), ----- plane in Fig. 5(c) ($r/D \sim 4$, $\Delta s \sim 0.75$)

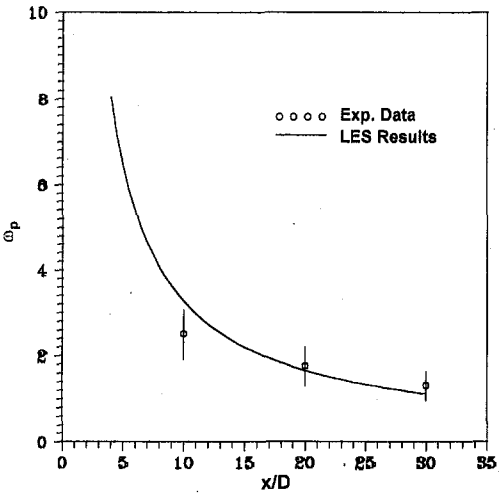

Fig. 8 Time-averaged downstream decay of the peak vorticity of the shed vortices; experimental measurements by Zhou and Antonia (1993)

gers." These intermediate structures of the near wake persist downstream and posses a high degree of streamwise vorticity, but low streamwise velocity. In terms of the helicity quantity $(\vec{v}\cdot\vec{\omega})$, they are on the same local scale as the adjacent Strouhal vortices, which by comparison contain a high degree of spanwise vorticity, but low spanwise velocity. Each finger comprises a pair of counter-rotating vortices, as shown in Fig. 6(*c*), which is a circumferential plane of radius 4D through the first set of fingered structures (the dashed lines indicate contours of negative streamwise vorticity). The respective vorticity magnitudes shown in Fig. 7 reveal a spanwise separation length of approximately one diameter. This periodicity is typical of the wake computation and it agrees with the observations made by Bays-Muchmore and Ahmed (1993) who reported similar separation lengths near this Re.

As mentioned earlier, the experimental measurements of Zhou and Antonia (1993) detected little variation in the relative size of the Strouhal vortices beyond ten diameters. This result implies a probable balance of influencing factors such as the vorticity diffusion and the spanwise stretching of the large-scale structures. They also noticed only a gradual decay of the peak vorticity of the shed vortices over the measurement range $10 \le x/D \le 60$. The present computations (time-averaged over six shedding cycles) plotted in Fig. 8 confirm their observation. However, nearly fifty percent of the peak vorticity (ω_p) decays within the first six diameters after complete formation ($x/D \sim 2$). Using both the numerical and experimental results, ω_p decays according to the relationship $\omega_p = Ax^{\alpha}$ over the wake region $2 \le x \le 30$ ($A = 31.4$, $\alpha = -0.982$).

Before presenting our statistical results of the near wake, we must first address the question regarding the significance of the SGS model relative to the truncation error and the artificial dissipation associated with the upwind approximation of the convective terms. In Table 1, typical values of the globally-averaged L_2 norm are listed for the convection (C_v), molecular diffusion (D_m), SGS, truncation error (TE), and artificial dissipation (D_a) terms. At the outset, the relative orders-of-magnitude suggest that the near wake flow is dominated by convection with an inconsequential contribution by the SGS terms. This conclusion was also reached by Olsson and Fuchs (1994) who approximated the SGS and diffusion terms to the fourth-order for solving an axi-symmetric jet flow. To appreciate the model's quality, one must investigate the SGS term locally. A fair example is the phase-averaged results (five shedding cycles), as shown in Fig. 9, where homogeneity is assumed in the spanwise direction. The ν_T contours (scaled by ν) illustrate the model's ability to correctly contribute negligible eddy viscosity in regions of known laminar flow conditions or where the turbulence is adequately resolved by the local grid spacing. Moreover, nearly ten percent of all the phase-averaged values are above 0.1 with approximately six percent being positive. The corresponding streamwise term $(\mathrm{SGS})_u$ along the wake centerline (scaled by D_m) suggest a dominant role played by the model locally in regions of high strain-rate activity. Like the ν_T contours, only slightly more than one-half of these scaled terms were positive. As noted previously, however, all negative turbulent eddy viscosity was truncated to zero in the LES computations.

Besides affecting certain regions of the near wake, the SGS model also directly influenced other wake properties, four examples of which are listed in Table 2. Better predictions of the drag force (C_d), Strouhal frequency (f_s), base pressure coefficient, and separation angle (θ_s) are suggested with use of the CDM even when the grid spacing was doubled (noted as LES_2 using a $121 \times 121 \times 16$ coarse grid). Although the LES_n computation (coarse grid with no model) remained stable, it gave the least accurate wake properties. With grid refinement and the use of the SGS model, improved predictions of these four basic properties are illustrated in the table; $\mathrm{LES}_{1.5}$ denotes results from an intermediate grid ($161 \times 161 \times 24$) computation. Locally, the LES_f computation (final grid) produced superior solutions of the wake statistics compared to that using the coarse and intermediate grids as exemplified by the transverse profiles shown in Fig. 10 of the mean velocity-defect ($\bar{U}_d/\bar{U}_m$) and in Fig. 11 of the normal Reynolds stresses ($\langle u'^2\rangle/U_c^2$ and $\langle v'^2\rangle/U_c^2$); U_c is the mean streamwise velocity along the wake centerline. At ten diameters downstream, stronger peaks and sharper gradients of the fluctuating quantities were predicted by the LES_2 and $\mathrm{LES}_{1.5}$ computations. With reference to the experimental measurements, the LES_f computation produced reasonable accuracy of these wake statistics.

We note that the insert of Fig. 11(*a*) shows two-point spanwise correlations at $x/D = 10$ of the streamwise fluctuations (R_{uu}); for the definition of R_{uu} see Beaudan and Moin, (1994). The insert depicts a profile of R_{uu} resulting from phase-averages taken of six shedding cycles. At one-half the span length, R_{uu} reduces to less than five percent, which was considered negligible for the present computation.

As discussed earlier, past experimental observations and measurements conclude that the most fundamental physics of Strouhal vortices originate from the region immediately behind the cylinder. Consequently, by previously verifying our LES predictions using the published experimental evidence of the near wake region, we can now direct our investigation to the turbulent characteristics of the formation region where no conclusive experimental data currently exists. We begin by examining the turbulent statistics of the region (spatially averaged in the spanwise direction) in terms of the total Reynolds stresses ($\tilde{u}_i\tilde{u}_j + u_i'u_j'$); $u_i = \bar{u}_i + \tilde{u}_i + u_i'$ where the instantaneous velocity (u_i) equals the sum of the mean ($\bar{u}_i$), periodic ($\tilde{u}_i$) and random (u_i') components. Contours of the mean streamwise ($\langle\tilde{u}^2 + u'^2\rangle/U_\infty^2$), transverse ($\langle\tilde{v}^2 + v'^2\rangle/U_\infty^2$) and shearing ($\langle\tilde{u}\tilde{v} + u'v'\rangle/U_\infty^2$) stresses are plotted in Fig. 12. The contours represent time-averaged results of six shedding cycles which appear to be sufficient to reach statistical steady-state in the formation region by evidence of their distinct symmetric character. The

Table 1 Relative importance of terms (Re = 5600); convection (C_v), molecular diffusion (D_m), subgrid-scale stress (SGS), truncation error (TE) and artificial dissipation (D_a)

C_v	D_m	SGS	TE	D_a
O(1)	$O(10^{-1})$	$O(10^{-2})$	$O(10^{-2})$	$O(10^{-2})$

$C_v = (\tilde{U}^k\tilde{u}_i)_{\xi^k}$ $\quad D_m = 1/\mathrm{Re}\,[\sqrt{g}g^{k\ell}(\tilde{u}_i)_{\xi^\ell}]_{\xi^k}$ $\quad \mathrm{SGS} = (\sigma_i^k)_{\xi^k}$

$\mathrm{TE} = \frac{u_{BA} - u_A}{\beta^4 - 1}$; $\beta = \Delta\xi/\Delta\ell$ $\quad D_a = [(\tilde{U}^k\tilde{u}_i)_{\xi^k}]^{O(3)} - [(\tilde{U}^k\tilde{u}_i)_{\xi^k}]^{O(4)}$

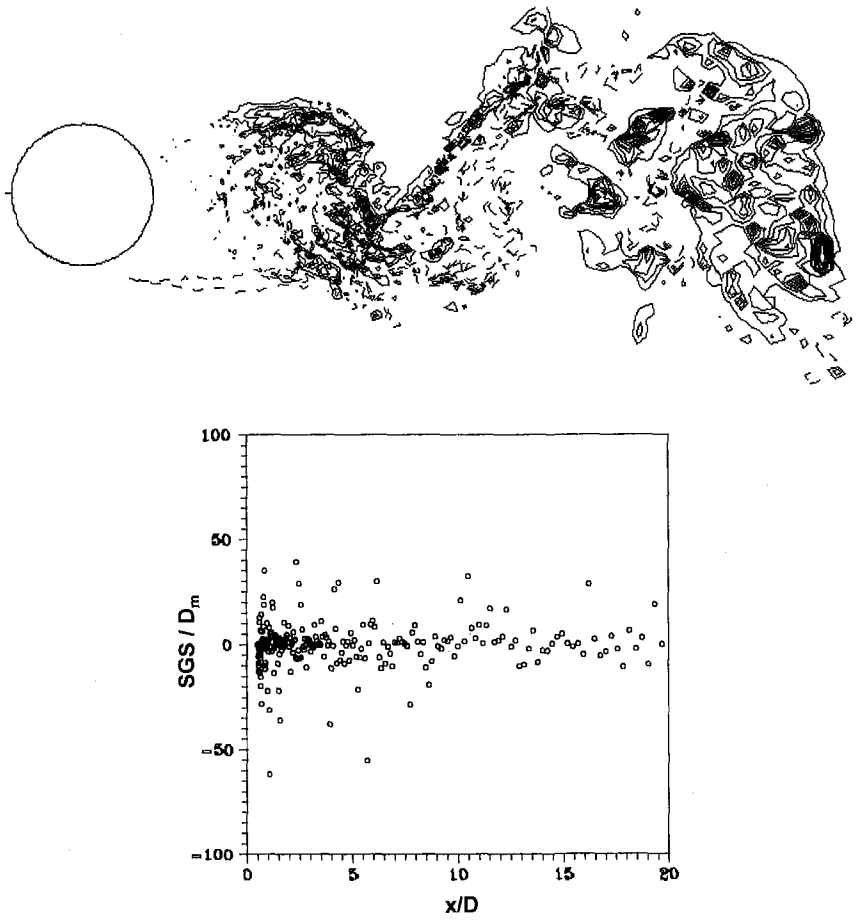

Fig. 9 Phase-averaged SGS model results; (*a*) ν_T/ν contours, max. 0.2, min. −0.2, and incr. 0.02, (*b*) SGS/D_m through wake centerline

figure shows negligible levels of total stress within the upstream laminar regimes and along the cylinder periphery, suggesting again that the CDM performed well by responding correctly to the local strain-rates. All three stress components share similar orders of magnitude with their maximums reached near the downstream limit of the formation region. The sharp contours of increasing streamwise fluctuations especially trace the path leading to final formation of the Strouhal vortices. Notably, the regional distributions of all three stress components distinctly differ. For example, the maximum value of the transverse component occurs along the wake centerline where the streamwise and shearing components decline to their near minimums. The adjacent smaller peaks of opposite sign and lesser magnitude in the shearing stress distributions directly affects the production of turbulence inside the formation region. This topic will be address later in this section.

Cantwell and Coles (1983) reported mean Reynolds stresses within the formation region at Re = 140,000, but measured the periodic components separately from the purely random ones. In the present simulation, only the total Reynolds stresses of the formation region were continuously stored. However, because both Reynolds numbers of 5600 and 140,000 are below critical (Re ≅ 300,000), they should qualitatively share similar dynamics. A visual inspection of the present total Reynolds stress results shown in Fig. 12 and the summed periodic and random data reported in Cantwell and Coles do reveal similar distributions of the mean normal and shear Reynolds stress components within the formation region. Moreover, the DNS

Table 2 List of the numerical and experimental data (Re = 5600) for drag force (C_d), shedding frequency (f_s), base pressure coefficient (C_{pb}) and separation angle (θ_s); LES_n: no model, coarse grid; LES_2: model, coarse grid; $LES_{1.5}$: model, intermediate grid; LES_f: model, final grid

	LES_n	LES_2	$LES_{1.5}$	LES_f	Exper.
C_d	1.11	1.08	1.03	1.01	1.03[1]
f_s	0.190	0.193	0.203	0.206	0.205[2]
$-C_{pb}$	0.96	1.08	1.04	1.02	0.99[3]
θ_s	89	89	88	87	86[4]

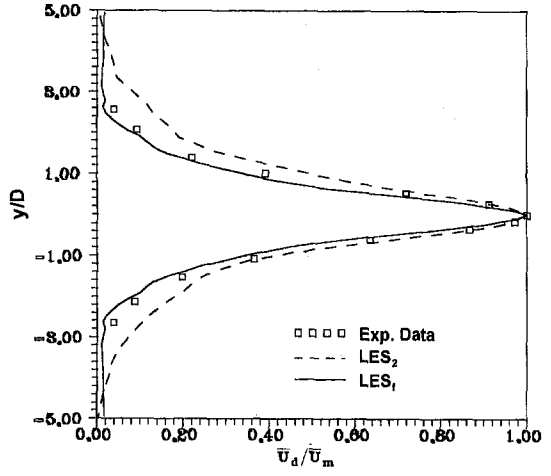

Fig. 10 Mean velocity-defect at ten diameters downstream of centerline. Experimental measurements by Zhou and Antonia (1993).

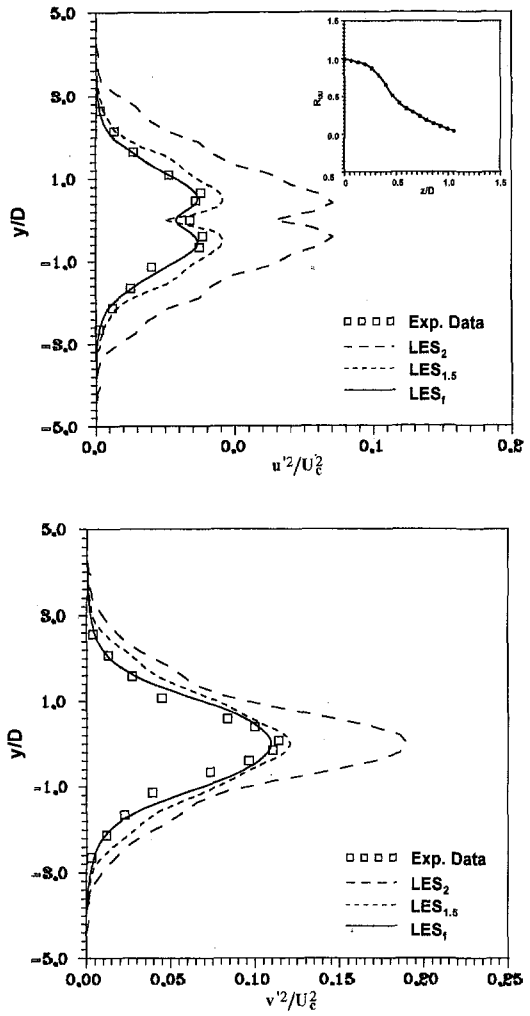

Fig. 11 Time-averaged Reynolds normal stresses at ten diameters downstream of cylinder centerline; (*a*) horizontal components ($\langle u'^2\rangle/U_c^2$) with spanwise correlation R_{uu} and (*b*) vertical components ($\langle v'^2\rangle/U_c^2$). Experimental data taken from Zhou and Antonia (1993).

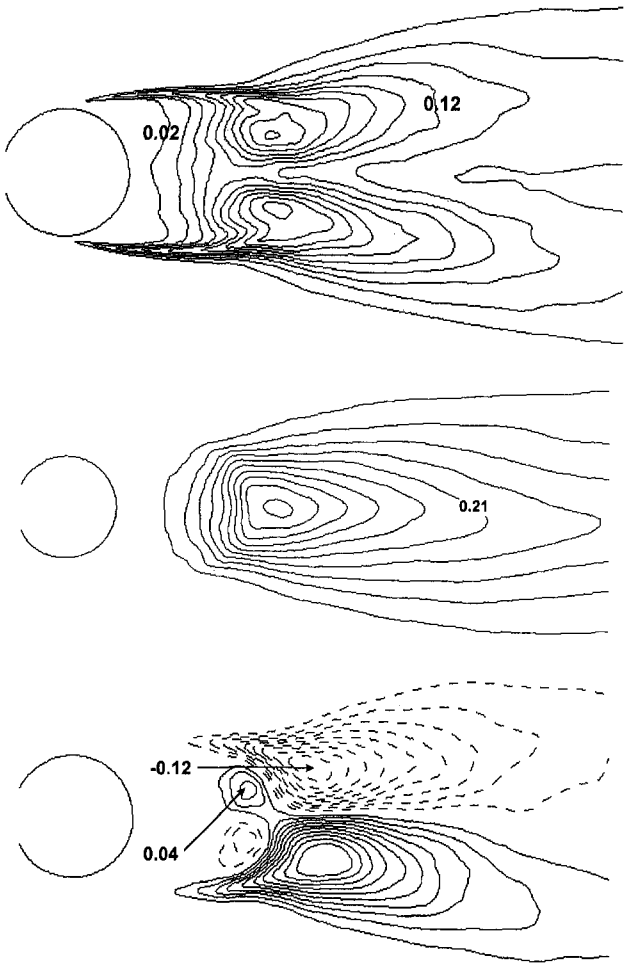

Fig. 12 Reynolds stress statistics within the formation region; (*a*) $\langle u'^2\rangle/U_\infty^2$ contour max. 0.2. incr. 0.02, (*b*) $\langle v'^2\rangle/U_\infty^2$ contour max. 0.42, incr. 0.042 and (*c*) $\langle u'v'\rangle/U_\infty^2$ contour max. 0.12, min. −0.12, incr. 0.012. Contours time-averaged over six shedding cycles.

data at subcritical Reynolds numbers of 525 (Mittal and Balachandar, 1995) and 3400 (Jordan, 1996) and the LES results at 3900 (Beaudan and Moin, 1994) also qualitatively agree with this observation thereby extending the range of this similarity to $525 \leq \mathrm{Re} \leq 140{,}000$. Quantitatively, the peak magnitudes of each stress listed in Table 3 share similar orders, but not their respective downstream locations. As shown in Fig. 13, the downstream locations of the peak total stresses within the formation region are dependent on the Reynolds number. But more importantly, their locations correlate well with the base pressure coefficient, as do the global wake properties presented earlier. As depicted in the figure, the position of each peak is inversely proportional to the base pressure coefficient; the additional data point at Re = 2600 is taken from Prasad and Williamson (1997).

From the viewpoint of engineering design, understanding the local mechanism of turbulence production is an important ingredient. Shown in Fig. 14 is the global mean of turbulent energy production $\langle -P\rangle$ of the formation region along with the analogous experimental data from Cantwell and Coles (1983) at Re = 140,000; $\langle -P\rangle = \langle \tau_{ij}\rangle \partial\langle u_i\rangle/\partial x_j\,(i,j=1,2)$. The qualitative agreement indicated by the figures further supports the conclusion that the turbulent activity inside the formation region share similar dynamics at both sub-critical Reynolds numbers. The figures show strongest production levels along the wake centerline near the formation closure point; 2.0D (Re = 5600) and 1.3D (Re = 140,000). We note that the last term $\langle \tau_{22}\rangle \partial\langle v\rangle/\partial y$ of the energy production definition accounts for over 90 percent of the produced turbulence near the closure point. Downstream of this point, both figures show the production of turbulence declining rapidly and reaching near negligible levels after only one diameter. The negative levels indicated for the present Re were not detected by Cantwell and Coles, however their locations may have been outside the measurement domain. Unlike the centerline peaks, only the first and middle terms of the production equation contributed to the negative turbulent energy with the former streamwise term $\langle \tau_{11}\rangle \partial\langle u\rangle/\partial x$ dominating these levels by over 80 percent. Although the respective three vortex stretching terms ($\partial\langle u\rangle/\partial x$, $\partial\langle v\rangle/\partial x$, $\partial\langle u\rangle/\partial y$) were relatively on the same order, the shearing stresses shown in Fig. 12(*c*) were concurrently one order less thereby minimizing the importance of the middle term.

Table 3 Peak normal and shear Reynolds total stresses within the formation region

Total Stress	Reynolds Number				
	525[1]	3,400[2]	3,900[3]	5,600[4]	140,000[5]
$\langle \overline{u}^2 + u'^2\rangle/U_\infty^2$	0.21	0.17	0.18	0.20	0.22
$\langle \overline{v}^2 + v'^2\rangle/U_\infty^2$	0.60	0.35	0.40	0.42	0.43
$\langle \overline{u}\overline{v} + u'v'\rangle/U_\infty^2$	0.15	0.10	0.12	0.12	0.19

[1]Mittal and Balachandar (1995) [2]Jordan (1996),
[3]Beaudan and Moin (1994) [4]Present Simulation [5]Cantwell and Coles, (1983).

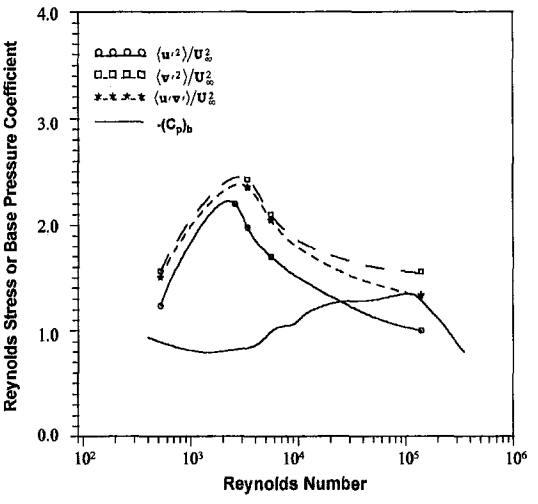

Fig. 13 Downstream location (referenced to cylinder centerline) of peak Reynolds stresses and base pressure coefficient (Williamson, 1995) as a function of Reynolds number (refer to Table 3 for the reference source of the data points)

Concluding Remarks

In view of the experimental data and the supporting numerical results just presented, we offer the following concluding remarks regarding the flow characteristics of cylinder near wake region at Re = 5600.

1. The primary Strouhal vortices were shed at a nondimensional time-averaged frequency of 0.206. Their time-averaged peak vorticity (ω_p) exponentially decayed with downstream distance (x/D) over the near wake region of interest $2 \leq x/D \leq 30$; specifically, $\omega_p = 31.4x^{-0.982}$.
2. Between subsequent shed vortices are pairs of connecting intermediate structures (or "fingers") having streamwise counter-rotating vorticity that are approximately one diameter apart spanwise. Finer-scale streamwise structures also exist within the separated shear layers whose spanwise wavelength comply with the empirical relationship reported by Mansy et al. (1994) and Williamson et al. (1995).
3. The distributions of the normal and shearing Reynolds stress components in the formation region at Re = 5600 agree qualitatively with the published experimental data of Cantwell and Coles (1983) and the numerical results of Mittal and Balachandar (1995), Jordan (1996), and Beaudan and Moin (1994). This agreement indicates that the near wake over a range of Reynolds numbers from full-turbulence inception (Re $\cong$ 300) up to critical (Re $\cong$ 300,000) share similar structural dynamics.
4. Although peak magnitudes of the turbulent statistics inside the formation region appear independent of Reynolds number, their downstream location is inversely proportional to the base pressure coefficient. The distribution of the mean turbulent production within the formation region was also quite similar for subcritical Reynolds numbers examined with peak levels occurring along the wake centerline near formation closure. The negative production levels indicated by the present simulation require further study.

We close this section with the following final comment. The experimental evidence tells us that an accurate prediction of the base pressure coefficient directly behind the cylinder is a prerequisite of any near wake simulation because this parameter is well-known to strongly correlate with the most fundamental characteristics of the Strouhal vortices, such as their formation length, shedding, and local detection frequency, and their internal strength. We found in our simulation that at least 32 points uniformly distributed in the spanwise direction over length $\frac{2}{3}\pi$ was sufficient to correctly resolve not only this coefficient but also the entire pressure distribution on the cylinder surface. Moreover, this resolution captured the salient large-scale streamwise structures of the near wake. We therefore conclude that the grid spacing used herein sufficiently resolve the large-scale turbulence that one needs to meaningfully understand the dynamics of the vortex formation region and the subsequent downstream transport of the shed vortices. We further note that these dynamics are very useful for engineering design purposes while concurrently minimizing the total CPU demand for their numerical simulation.

Acknowledgments

The authors would like to express our sincere appreciation to the reviewers of this manuscript for providing important and helpful comments to improve its content. The first author gratefully acknowledges the support of the Office of Naval Research (Contract No. N0001495-WX20147; Dr. L. P. Purtell, Science Officer) and the In-House Laboratory Independent Research Program (Dr. S. Dickinson, Coordinator) at the Naval Undersea Warfare Center Division Newport. The second author has been supported by the Office of Naval Research, under grant No. N00014-92-J-4087.

References

Bays-Muchmore, B., and Ahmed, A., 1993, "On Streamwise Vortices in Turbulent Wakes of Cylinders," *Physics of Fluids,* Series A, Vol. 5, pp. 387–392.

Beaudan, P., and Moin, P., 1994, "Numerical Experiments on the Flow Past a Circular Cylinder a Sub-Critical Reynolds Number," Report No. TF-62, Stanford University, Stanford, CA.

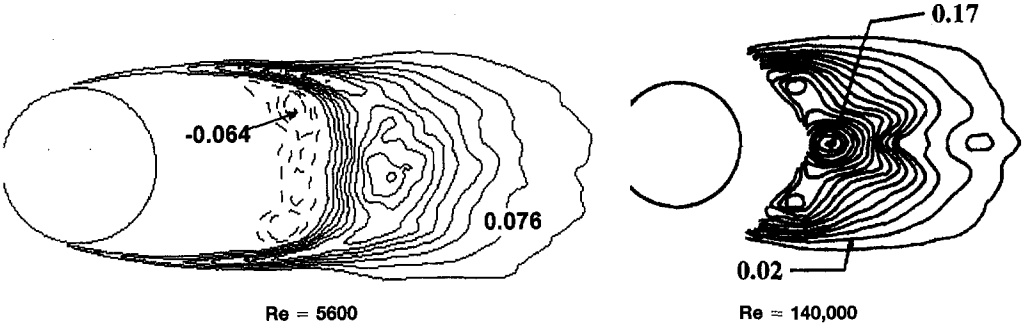

Fig. 14 Mean turbulent-energy production; (*a*) contour max. 0.38, incr. 0.038; min. −0.064, incr. −0.016 and (*b*) contour max. 0.17, incr. 0.01 (Cantwell and Coles, 1983).

Bloor, M. S., 1964, "The Transition to Turbulence in the Wake of a Circular Cylinder," *Journal of Fluid Mechanics,* Vol. 19, p. 290.

Cantwell, B., and Coles, D., 1983, "An Experimental Study of Entrainment and Transport in the Turbulent Near Wake of a Circular Cylinder," *Journal of Fluid Mechanics,* Vol. 136, pp. 321–374.

Germano, M., 1992, "Turbulence: The Filtering Approach," *Journal of Fluid Mechanics,* Vol. 238, pp. 325–336.

Germano, M., Piomelli, U., Moin, P., and Cabot, W. H., 1991, "A Dynamic Subgrid-Scale Eddy Viscosity Model," *Physics of Fluids,* Series A, Vol. 3, pp. 1760–1765.

Gerrard, J. H., 1978, "The Wakes of Cylindrical Bluff Bodies at Low Reynolds Number," *Phil. Transactions Royal Society of London,* Vol. 288, pp. 351–382.

Jordan, S. A., 1996, 'A Large-Eddy Simulation Methodology for Incompressible Flows in Complex Domains,' NUWC-NPT Technical Report 10,592.

Jordan, S. A., and Ragab, S. A., 1996, "An Efficient Fractional-Step Technique for Unsteady Three-Dimensional Flows," *Journal of Computational Physics,* Vol. 127, pp. 218–225.

Kato, C., Iida, A., Takano, Y. Fujita, H., and Ikegawa, M., 1993, "Numerical Prediction of Aerodynamic Noise Radiated from Low Mach Number Turbulent Wake," *AIAA 93-0145.*

Lilly, D. K., 1992, "A Proposed Modification of the Germano Subgrid-Scale Closure Method," *Physics of Fluids,* Series A, Vol. 4, pp. 633–635.

Mansy, H., Yang, P., and Williams, D. R., 1990, "Quantitative Measurements of Three-Dimensional Structures in the Wake of a Circular Cylinder," *Journal of Fluid Mechanics,* Vol. 270, pp. 277–296.

Mittal, R., and Balachandar, S. 1996, "Effect of Three-dimensionality on the Lift and Drag of Nominally Two-dimensional Cylinders," *Physics of Fluids,* Vol 7, No. 8, pp. 1841–1865.

Mittal, R., and Moin, P. 1997, "Suitability of Upwind-Biased Finite Difference Schemes for Large-Eddy Simulation of Turbulent Flows," *AIAA Journal,* Vol 35, No. 8, pp. 1415–1417.

Norberg, C., 1992, "Pressure Forces on a Circular Cylinder in Cross Flow," *IUTAM Symposium on Bluff-Body Wakes, Dynamics and Instabilities,* Eckelmann ed., et al., Springer-Verlag, pp. 275–278.

Olsson, M., and Fuchs, L., 1994, "Significant Terms in Dynamic Modeling SGS-Modeling," First ERCOFTAC Workshop on Direct and Large-Eddy Simulation, Voke et al., eds, Kluwer Academic Publishers, pp. 73–84.

Pauley, L. L. Moin, P., and Reynolds, W. C., 1990, "The Structure of Two-dimensional Separation," *Journal of Fluid Mechanics,* Vol. 220, pp. 397–411.

Prasad, A., and Williamson, C. H. K., 1997, "Three-Dimensional Effects in Turbulent Bluff-Body Wakes," *Journal of Mechanics,* Vol. 343, pp. 235–265.

Rai, M. M., and Moin, P., 1989, "Direct Simulations of Turbulent Flow Using Finite-difference Schemes," *AIAA-89-0369.*

Rogallo, R. S., and Moin, P., 1984, "Numerical Simulation of Turbulent Flows," *Annual Review of Fluid Mechanics,* Vol. 16, pp. 99–137.

Schumann, U., 1975, "Subgrid Scale Model for Finite Difference Simulation of Turbulent Flows in Plane Channel and Annuli," *Journal of Computational Physics,* Vol. 18, pp. 376–404.

Smagorinsky, J., 1963, "General Circulation Experiments with the Primitive Equations, I. The Basic Experiment," *Monthly Weather Review,* Vol. 91, pp. 99–164.

Son, J. S., and Hanratty, T. J., 1969, "Velocity Gradients at the Wall for Flow around a Cylinder at Reynolds Number from 5×10^3 to 10^5," *Journal of Fluid Mechanics,* Vol. 35, pp. 353–368.

Song, C. C. S., and Yuan, M., 1990, "Simulation of Vortex-Shedding flow About a Circular Cylinder at High Reynolds Number," ASME *Journal of Fluids Engineering,* Vol. 112, pp. 155–163.

Szepessy, S., 1994, "On the Spanwise Correlation of Vortex Shedding from a Circular Cylinder at High Subcritical Reynolds Number," *Physics of Fluids,* Series A, Vol. 6, pp. 2406–2416.

Unal, M. F., and Rockwell, D., 1988, "On Vortex Formation From a Cylinder. Part 1. The Initial Instability," *Journal of Fluid Mechanics,* Vol. 190, pp. 491–512.

Vinokur, M., 1974, "Conservative Form of Gas Dynamics Equations," *La Recherche Aerospatiale,* No. 1974-1, pp. 65–68.

Wei, T., and Smith, C. R., 1986, "Secondary Vortices in the Wake of Circular Cylinders," *Journal of Fluid Mechanics,* Vol. 169, pp. 513–533.

White, F. W., 1974, *Viscous Fluid Flow,* McGraw-Hill, NY.

Williamson, C. H., 1995, "Vortex Dynamics in the Wake of a Cylinder," *Fluid Vortices: Fluid Mechanics and Its Application,* Vol. 30, ed. S. L. Green, ed., Kluwer Academic Publishers, pp. 155–134.

Williamson, C. H. K., Wu, J., and Sheridan, J., 1995, "Scaling of the Streamwise Vortices in Wakes," *Physics of Fluids,* Series A, Vol. 7, pp. 112–122.

Zhou, Y., and Antonia, R. A., 1993, "A Study of Turbulent Vortices in the Near Wake of a Cylinder," *Journal of Fluid Mechanics,* Vol. 253, pp. 643–661.

Lance H. Benedict
Post-Doctoral Assistant.

Richard D. Gould
Associate Professor.

Mechanical and Aerospace Engineering Department,
North Carolina State University,
Raleigh, NC 27695-7910

Enhanced Power Spectrum Estimates Using Kalman Reconstruction

A number of power spectral density (PSD) estimators were assessed using real laser Doppler anemometer (LDA) data from grid generated turbulence. PSD estimates from the raw data via the slotting technique and direct transform method were compared to those estimated from sample and hold, linear, and Kalman reconstructed velocity time histories. Of the reconstruction schemes, only Kalman reconstruction was shown to significantly reduce the effects of noise on the measurements leading to an additional 2 decades in power of high frequency information.

Introduction

"Reconstruction" is a term given to the creation of an equal-time-spaced velocity record from the randomly arriving velocity measurements made by a burst mode laser-Doppler anemometer (LDA). It is well known that the processing of burst mode LDA data is complicated by the Poisson distributed arrival times of the measurements. Recently, much of the work in reconstruction techniques (Müller et al., 1994) for LDA data has been directed at overcoming the high data density requirement. This approach might be likened to the "filling in" of missing information and generally makes use of advanced statistical schemes to predict the signal behavior between observations.

A promising technique for reconstruction under *high data density* conditions in the presence of noise is the application of the Kalman filter (van Maanen and Tulleken, 1994). This technique not only creates an equi-time-spaced data set, it also creates optimal estimates of the velocity time history by making use of information concerning the noise variance inherent in the original data. Based on this it is felt that the technique holds promise for enhancing power spectrum estimates. To test this, a variety of signal reconstruction and power spectrum estimation techniques, using real LDA measurements made in grid generated turbulence with data density sufficient to resolve all energy containing scales and complemented by hot-wire measurements, were examined. This paper is a slightly different and abridged version of our previous paper (Benedict and Gould, 1995), where more details may be found. In particular, a more complete literature review and discussion on conventional PSD techniques are given in this earlier work.

Facility and Measurement Technique

An open circuit low-speed wind tunnel with a centrifugal blower was used to provide room temperature air flow for this investigation (Benedict et al., 1994). A biplane round rod grid, 6.35 mm between rod centers with rod diameter of 1.59 mm, was situated following an 18:1 contraction ratio nozzle immediately upstream of a glass windowed test section of 15.24 cm by 10.16 cm cross section. Flow speed was maintained at 11.7 m/s for all measurements made in this study, giving a mesh Reynolds number (based on distance between rod centers, M) of approximately 4950.

Both LDA and hot-wire measurements were made in this study for comparative and validative purposes. A one-component dual-beam LDA system operating in forward scatter mode and with a net fringe shift of 10 MHz was used in this study. A TSI model 1990C counter processor set to sample in single measurement per burst mode was used to count 32 fringes to determine each velocity measurement. Oil particles approximately 1 μm in diameter, having a 3 dB down response of 50 to 60 kHz (Goldstein, (1983)), were used to seed the flow. At 12 m/s, single measurement per burst average data validation rates of up to 60 kHz were possible.

The hot-wire equipment consisted of a TSI 1054 anemometer with a TSI platinum P2 sensor. The sensor diameter was 5 μm and the length was 1.25 mm. Frequency response of this wire at 11.7 m/s was approximately 50 kHz.

Power Spectral Density Techniques

Procedures for estimating the power spectral density (PSD) are well established for equi-spaced data (Bendat and Piersol, 1986). Just as in the case of equi-spaced data, the estimation of the PSD from data with Poisson arrival time statistics (i.e., LDV data) follows one of two approaches, either a direct transformation from the data or a Fourier transform of the autocovariance function. The latter approach is due to Mayo (1974) where in the case of Poisson distributed time spacing, a method known as the slotting technique is used to estimate the autocovariance function, $C_{uu}(\tau)$. In the slotting technique, a discretized estimate of $C_{uu}(\tau)$ is made by summing lag products over equi-spaced slots of interval $\Delta\tau$. The direct method for estimating the PSD of Poisson spaced samples is due to Gaster and Roberts (1977).

Conventional Estimators. Figure 1 shows typical discrete autocovariance estimates in grid generated turbulence made from hot-wire and LDA velocity measurements. For the LDA data 95 percent confidence limits are given for the expected values of each covariance where the variance of the slotting technique estimator has been determined from the formula due to Scott (1974). Note the significant uncertainty despite the fact that 60,000 samples were used to build the covariance estimates. This is due mainly to the relatively short observation time (1.2 s), a consequence of the high mean sampling rate (50 kHz). This illustrates the difficulty of making characterizations of high frequency turbulent behavior. The confidence bounds on the hot-wire measurements would be somewhat narrower but are not shown in the figure for the sake of clarity.

Typically, LDA covariance estimates (especially at low turbulence intensity as is the case for grid generated turbulence) reveal a noise spike in the zero-lag slot which corresponds to the estimated variance of the flow velocity. The spike occurs due to the squaring of uncorrelated noise in the LDA signal.

Contributed by the Fluids Engineering Division for publication in the JOURNAL OF FLUIDS ENGINEERING. Manuscript received by the Fluids Engineering Division September 27, 1996; revised manuscript received February 25, 1998. Associate Technical Editor: D. P. Telionis.

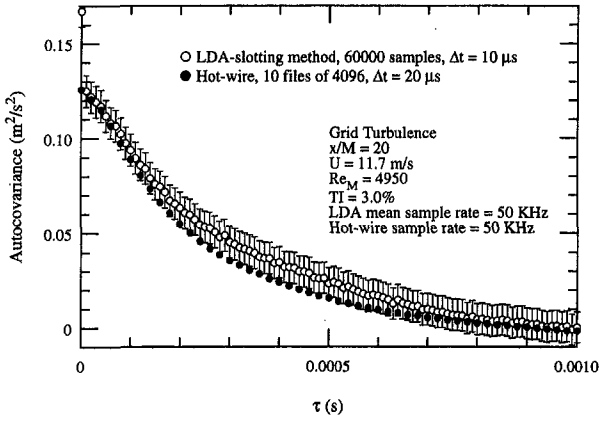

Fig. 1 LDA and hot-wire autocovariance estimates

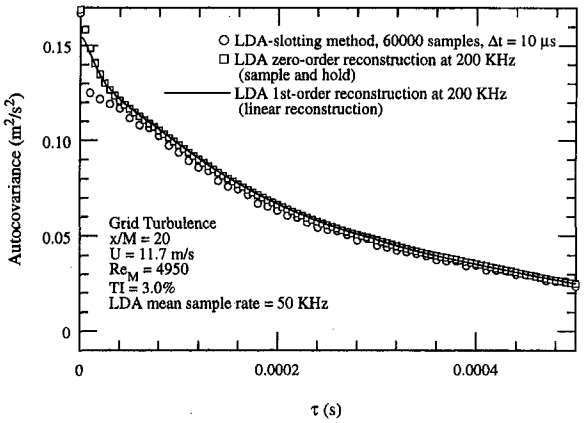

Fig. 3 Autocovariance using conventional reconstruction schemes

The variance is thus overestimated under noisy conditions and should be corrected (i.e. "back-fitting" the covariance function to zero time lag) when estimating time scales or making precise characterizations of turbulence level (Benedict et al., 1994). Hot-wire signals also contain noise, but at a much lower level than LDA signals.

Figure 2 shows the best results for the PSD which can be obtained by essentially decreasing $\overline{u'^2}$ to account for the noise variance. In the slotting method, this amounts to either omitting the zero-lag term altogether, or correcting it to a level similar to the "lag 1" covariance. Omitting the zero-lag term causes the slotting method PSD estimates to behave like the original direct transform estimates (not shown here) as one might have expected, while "correcting" the zero-lag term offers some minor improvement in the range of frequencies which may be evaluated. "Correcting" the direct transform method amounts to multiplying the ratio of the "lag 1" covariance and the noise corrupted zero-lag term by the $\overline{u'^2}$ in Gaster's formula. This improves the direct transform estimates as well, but none of the results presented thus far offers significant enhancement of PSD estimates for LDA data. This can be seen by comparing the PSDs in Fig. 2 with the baseline PSD shown in Fig. 8 for the slotting method case without zero-lag correction. It is important to note that the hot wire data also contains noise, albeit at a lower level than the LDA data. Careful inspection of Fig. 2 shows that the PSDs obtained using the direct transform method behave quite differently from those obtained using the slotting method. Both methods agree well with each other and with the hot wire data out to approximately 1 kHz, after which the direct transform method gives a PSD which shows ocsillatory behavior. Furthermore, the PSD obtained using the zero-lag corrected slotting method agrees well with the hot wire PSD out to ~5 kHz, while the corrected direct transform method gives a PSD which is biased low (~factor of 5–10) and which shows severe ocsillatory behavior beginning at ~4 kHz.

Conventional Reconstruction Techniques. Sample and hold (zero-order) reconstruction implies "holding" the most recent velocity measurement until a new one is available. Such a data set can be created either in real time with appropriate processor inhibit hardware or in the post-processing stage by skipping through a data set at equal times. Linear reconstruction is none other than the typical interpolation procedure used to interpolate values between those given in a table.

In terms of enhancing PSD estimates for real data, Figs. 3 and 4 show that sample and hold reconstruction and linear reconstruction do nothing to improve the estimates but simply *add a finite correlation time* to the signal noise. This is in agreement with the results of van Maanen and Tulleken (1994) who used simulated LDA data. From Fig. 3 it can be seen that the original noise "spike," denoting uncorrelated noise, now appears as an exponential decay for sample and hold reconstruction, while for linear reconstruction, more complicated behavior results. Sample and hold reconstruction is equivalent to a low-pass filter with cut-off frequency of $1/(2\pi t_0)$ (where t_0 is the mean time spacing) leading to a roll-off in the power spectrum. It is also noted that the linear interpolation (1st order) seems to reduce the noise variance to some extent; however, this results in only slight improvement in the PSD estimates shown in Fig. 4.

The correlation behaviors introduced to the measurement noise as *a result of these conventional signal reconstruction techniques manifest themselves as a change of slope in the PSD*

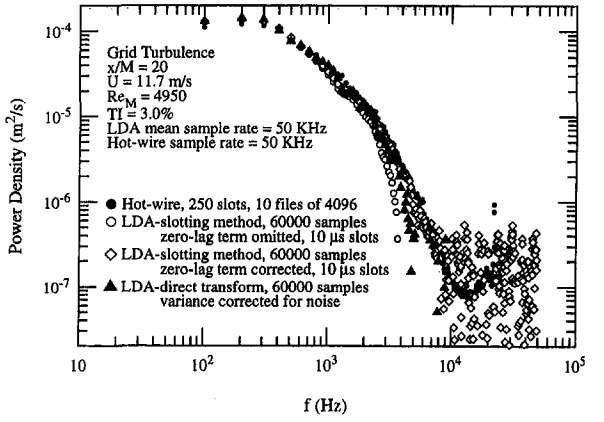

Fig. 2 Comparison of PSD results from modified estimators

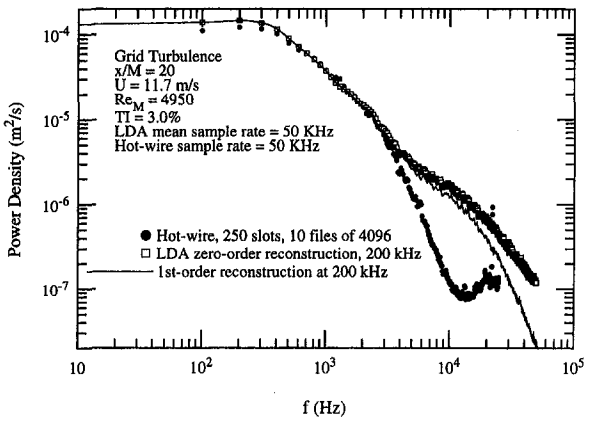

Fig. 4 PSD estimates from conventional reconstruction schemes

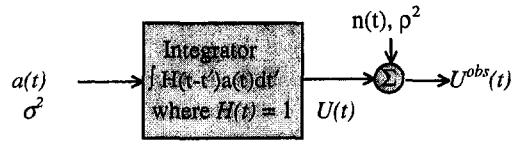

Fig. 5 Model for single input, single output system

estimates which could be interpreted as a legitimate turbulence characteristic by unwary investigators. Given a high enough reconstruction data rate the sample and hold estimates will "roll off" at slope of -2 while the linear reconstruction will "roll off" at a steeper rate until aliasing effects begin near $\frac{1}{2}\Delta\tau_{\text{recon.}}$ (100 kHz in Fig. 4).

Application of the Kalman Filter

The Kalman filter (Kalman, 1960) is an optimal linear filter in that it minimizes the mean square prediction error in the class of all linear filters. It is used in the prediction and control of linear systems by creating optimal estimates of the output of a linear system based on observations of the output in the presence of noise and the system transfer function operating on an input variable to produce the given output. The Kalman filter consists of a general state space model describing the state of the system and an observation equation describing the influence of the system transfer function and measurement noise on the system output. Unlike with many standard filter algorithms, users of a Kalman filter do not need to set cut-off frequencies and roll-off rates a priori. The filter seeks a minimum noise value in a least squared sense.

Such a situation is described by Fig. 5 illustrating the process of making noise corrupted velocity measurements in a turbulent flow. Here, $a(t)$, represents the flow accelerations (which following van Maanen and Tulleken (1994) are assumed to be generated by a white noise process) operated on by the "system transfer function," $H(t)$ (in this case a simple integrator from acceleration to velocity). The variable of interest, $U(t)$, cannot be measured directly but rather, $U^{obs}(t)$, the velocity corrupted by noise, n, is the output of the LDA. The variable t denotes time here. For this simple case, the state space equation may be represented following van Maanen and Tulleken (1994) as,

$$\frac{dU(t)}{dt} = a(t) \tag{1}$$

and the observation equation by,

$$U^{obs}(t) = U(t) + n(t) \tag{2}$$

Statistical requirements for application of the filter are that the noise and accelerations have zero mean, and are uncorrelated with themselves, each other, or the velocity. The filter is expressed as:

$$\frac{dU(t)}{dt} = L(U^{obs}(t) - H(t)U(t)) \tag{3}$$

where L is the filter gain and $H(t) = 1$ for an integrator. For this simple model, L is expressed as σ/ρ where $\sigma = \sqrt{a^2}$ and $\rho = \sqrt{n^2}$. This differential equation is solved recursively with linear interpolation used to estimate $U^{obs}(t)$ between measurements to develop the filtering algorithm given in van Maanen and Tulleken (1994). Here we focus on the performance of the scheme and specification of σ/ρ which is only alluded to in the original paper by the creators of the algorithm.

Essentially, ρ^2 is the variance of the noise, n, and can be determined by the spike in the autocovariance function as seen in Fig. 1. In all methods of specifying the filter gain, this is the starting point. Determining σ^2, the variance of the flow accelerations is more complicated since there is no obvious indicator of this quantity from the raw data. Three techniques will be described for estimating σ^2 to determine the filter gain, however the best method is still open to some discussion.

Method 1. One cannot differentiate the measured time history to retrieve σ^2 since the measurements are corrupted by noise. This, however, is a starting point for an algorithm which might converge on σ^2. Specifically, one may estimate σ^2 to a first approximation from differencing the $U^{obs}(t)$ time series. This gives an initial estimate of the filter gain which may be used in the Kalman filter to create an initial estimate of the optimal reconstruction of the series. From this reconstructed set, a new estimate of σ^2 is made and the above process is repeated until convergence.

Method 2. In this method, use is made of the relationship which exists between the PSD of a variable and its derivative (Bendat and Piersol, 1986), and the spectral properties of white noise processes. From Fourier principals,

$$G_{aa}(f) = (2\pi f)^2 G_{uu}(f) \tag{4}$$

where f is the circular frequency. If $G_{uu}(f)$ (one-side PSD of velocity) is available, then $G_{aa}(f)$ is known, and since the accelerations are assumed to be white noise, their variance is,

$$\sigma^2 = \int_0^\infty G_{aa}(f)df = \int_0^\infty (2\pi f)^2 G_{uu}(f)df \tag{5}$$

The reasoning here seems circular, since use is made of a quantity of interest, $G_{uu}(f)$; however an estimate of $G_{uu}(f)$, $G_{u^{obs}u^{obs}}(f)$, is available and may be corrected by subtracting a white level to account for the measurement noise. Generally, $(2\pi f)^2 G_{uu}(f)$ decays so quickly, that its integral is negligible above a cut-off frequency well below the point at which the estimate of $G_{uu}(f)$ begins to deteriorate.

Method 3. This method follows from Method 2. From Hinze (1975), it can be shown that,

$$\frac{1}{\tau_E^2} = \frac{2\pi^2}{\overline{u'^2}} \int_0^\infty f^2 G_{uu}(f)df \tag{6}$$

where τ_E is the Eulerian micro(time)scale of the flow and u' fluctuation about the mean velocity. This quantity is also available as,

$$\frac{1}{\tau_E^2} = -\frac{1}{2\overline{u'^2}}\left[\frac{\partial^2 C_{uu}}{\partial t^2}\right]_{t=0} \tag{7}$$

Thus by fitting a parabola to the discrete autocovariance function (with noise spike removed) near $t = 0$ to determine the microscale, a value of σ^2 may also be found using Eqs. (6) and (5).

Comparison of PSD Results

Methods 2 and 3 determine a single value of the filter gain parameter; however, the filter gain parameter has units of 1/time and its optimum value seems to vary with reconstruction time spacing. Method 1 gives a filter gain which varies according to reconstruction time spacing but with variation opposite to that desired. Coincidentally, if the reconstruction time spacing is chosen to be on the order of the minimum time spacing in the raw LDA data set ($\approx$1/250 kHz), all three methods agree and give results which seem to be optimal. It is unknown whether this is a fortuitous occurrence or not, but this fact has been used to create the reconstruction, a portion of

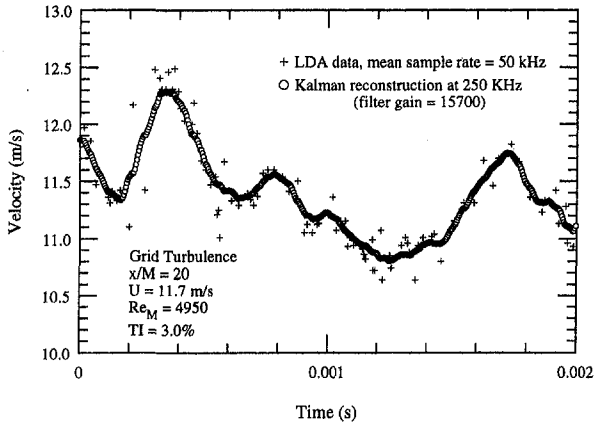

Fig. 6 Kalman-reconstructed velocity time history

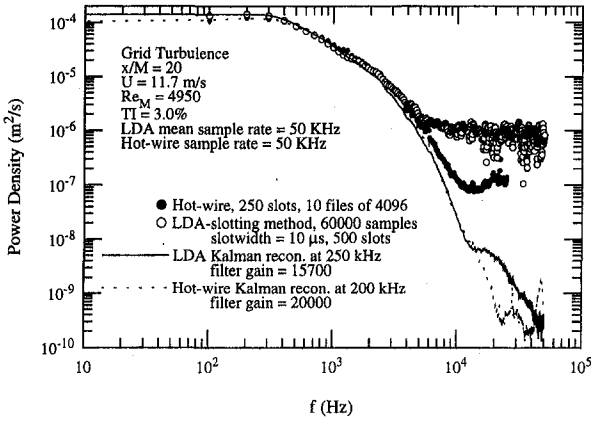

Fig. 8 Original and Kalman-reconstructed PSD estimates

which is shown in Fig. 6. It can be seen that the reconstruction smoothes out unrealistic accelerations in the flow to an extent determined by the filter gain. A remarkable improvement in the noise characteristics of the velocity time history can be noted from the autocovariances plotted in Fig. 7. Finally, this leads to the improved PSD estimate shown in Fig. 8. Note that the frequency range is extended to ≈12 kHz for the LDV data and to ≈20 kHz for the hot wire data before oscillations in the PSDs occur when using Kalman reconstruction. The PSDs obtained using the Kalman reconstructed velocites appear to be biased low relative to the PSDs obtained using the unfiltered and uncorrected velocities. Purists may argue that the unfiltered hot wire data is the only true comparison to which the filtered data should be compared. It is important to note that noise will always bias the PSD upward and that the original hot wire data is corrupted by a finite level of noise. The fact that two different instruments with entirely different noise characteristics (i.e., the hot wire and LDA) produce virtually the same PSD is proof that the Kalman filter seeks the minimum noise value of the original signal regardless of how much noise is in the original signal. It does this on its own without prescribing a filter shape.

Conclusions

Comparisons between the slotting technique of Mayo and the direct transform method of Gaster under actual flow measurement conditions show both methods to be adversely affected by measurement noise. The direct transform method does not, as claimed by other authors, "filter" white noise present in LDA signals. The noise rather manifests itself differently in the direct transform algorithm such that PSD estimates drastically underestimate the spectrum rather than overestimate it as in the case of the slotting technique. The slotting technique is also found to be more convenient and able to resolve somewhat higher frequency information in general.

Simple reconstruction algorithms, which do not attempt to account for noise present in LDA measurements, do little to enhance PSD estimates and even display misleading behavior which could lead to false conclusions concerning high frequency behavior of turbulence. Kalman reconstruction on the other hand allows for significant improvement in the high frequency end of PSD estimates for both LDA and hot-wire data (in this investigation over 2 decades in amplitude were recovered).

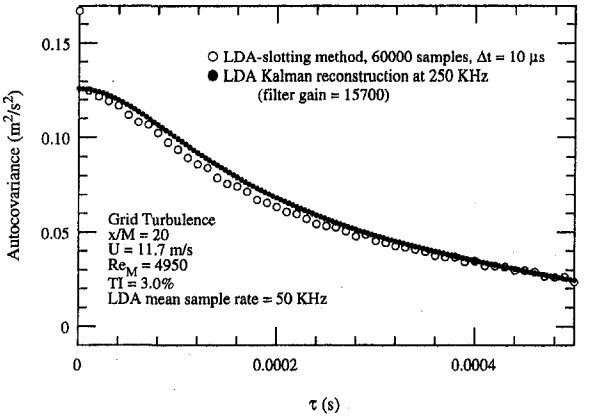

Fig. 7 Autocovariance from Kalman reconstruction

Acknowledgments

This work was supported in part by the United States Air Force Office of Scientific Research through the Summer Research Extension Program.

References

Benedict, L. H., Yearling, P. R., and Gould, R. D., 1994, "Concerning Taylor Time and Length Scale Estimates Made from Counter-Process Autocorrelation Measurements in Gas Flows," *Proceedings of the 7th International Symposium on Applications of Laser Techniques to Fluid Mechanics,* Lisbon, Portugal, July 11–14, also to appear in, *Experiments in Fluids,* 1998.

Benedict, L. H., and Gould, R. D., 1995 "Experiences using Kalman Reconstruction for Enhanced Power Spectrum Estimates," ASME 1995 *Laser Anemometry,* FED-Vol. 229, pp. 1–7.

Bendat, J. S., and Piersol, A. G., 1986, *Random Data, Analysis and Measurement Procedures,* Wiley, New York.

Gaster, M., & Roberts, J. B., 1977, "The Spectral Analysis of Randomly Sampled Records by a Direct Transform," *Proceedings of the Royal Society of London,* Series A, Vol. 354, pp. 27–58.

Goldstein, R. J., 1983, *Fluid Mechanics Measurements,* Hemisphere Publishing Corporation, New York.

Hinze, J. O., 1975, *Turbulence,* McGraw-Hill, New York.

Kalman, R. E., 1960, "A New Approach to Linear Filtering and Prediction Theory," ASME *Journal of Basic Engineering,* Vol. 83, pp. 95–108.

van Maanen, H. R. E., and Tulleken, H. J. A. F., 1994, "Application of Kalman Reconstruction to Laser-Doppler Anemometry Data for Estimation of Turbulent Velocity Fluctuations," *Proceedings of the 7th International Symposium on Applications of Laser Techniques to Fluid Mechanics,* Lisbon, Portugal, July 11–14.

Mayo, W., Shay, M., and Riter, S., 1974, "The Development of New Digital Data Processing Techniques for Turbulence Measurements with a Laser Velocimeter," AEDC-TR-74-53.

Müller, E., Nobach, H., and Tropea, C., 1994, "LDA Signal Reconstruction: Application to Moment and Spectral Estimation," *Proceedings of the 7th International Symposium on Applications of Laser Techniques to Fluid Mechanics,* Lisbon, Portugal, July 11–14.

Scott, P. F., 1974, "Random Sampling Theory and its Application to Laser Velocimeter Turbulent Spectral Measurements," Report No. 74CRD216, Tech, Info Series, General Electric Co., Corporate Res. and Development.

An Implicit Multigrid Scheme for the Compressible Navier-Stokes Equations With Low-Reynolds-Number Turbulence Closure

Peter Gerlinger
Researcher.

Dieter Brüggemann
Professor.

Institut für Thermodynamik
der Luft- und Raumfahrt,
Universität Stuttgart,
Pfaffenwaldring 31, 70550 Stuttgart,
Germany

A multigrid method for convergence acceleration is used for solving coupled fluid and turbulence transport equations. For turbulence closure a low-Reynolds-number q-ω turbulence model is employed, which requires very fine grids in the near wall regions. Due to the use of fine grids, convergence of most iterative solvers slows down, making the use of multigrid techniques especially attractive. However, special care has to be taken on the strong nonlinear turbulent source terms during restriction from fine to coarse grids. Due to the hyperbolic character of the governing equations in supersonic flows and the occurrence of shock waves, modifications to standard multigrid techniques are necessary. A simple and effective method is presented that enables the multigrid scheme to converge. A strong reduction in the required number of multigrid cycles and work units is achieved for different test cases, including a Mach 2 flow over a backward facing step.

Introduction

Multigrid methods are widely used for convergence acceleration in subsonic flows where excellent results can be achieved. Even the treatment of supersonic and hypersonic flows became possible during recent years (Turkel et al., 1991, Radespiel and Swanson, 1995). Such progress in numerical schemes, as well as in available computer capability, enables the use of more complicated turbulence models. Presently, two-equation turbulence closures seem to be favored because of their generality in comparison to algebraic models and their economy in comparison to the more complicated and less investigated Reynolds stress models. Among two-equation models, low-Reynolds-number versions do not need any wall functions and do not depend on validity of a local equilibrium of turbulence in the near wall region. On the other hand, most of the ad hoc low-Reynolds-number damping functions used in these models are calibrated on equilibrium turbulent boundary layers (Speziale and Abid, 1993) and, as such, are not suited for the study of separated flows. In the present q-ω model (Coakley and Huang, 1992), damping functions are introduced in order to account for the dominance of viscous effects near solid walls. In most cases low-Reynolds-number models have proved to be more accurate than the standard high-Reynolds-number formulations (Martelli and Michelassi, 1990). However, the integration of the governing equations to solid walls requires very fine grids, leading to high cell aspect ratios. This is due mainly to the steep gradient of the dissipation rate ϵ that has to be resolved by the computational grid. The introduction of low-Reynolds-number damping terms, which include exponential functions, additionally causes the system of governing equations to become numerically stiff. Therefore it is desirable to use an implicit or at least point implicit solver for numerical time integration.

Convergence acceleration becomes an important factor when numerical methods are applied to complicated problems, especially when low-Reynolds-number terms are included in the turbulence model. Convergence slows down because of the need to employ extremely fine grids. From a theoretical point-of-view, the convergence rate for multigrid methods should be independent of grid size, which is normally a very limiting factor for wall bounded turbulent flows. In practice, the strong nonlinear source terms may reduce the effectiveness of the multigrid technique. For this reason, most authors use algebraic or high-Reynolds-number turbulence models or limit the multigrid method to the treatment of the fluid equations (Dick et al., 1994).

Description of the Algorithm

Navier-Stokes Equations and Numerical Scheme. An implicit LU-SGS (lower-upper symmetric Gauss-Seidel) method (Jameson and Yoon, 1987 and Shuen, 1992) is used for solving the compressible Navier-Stokes and species transport equations, which are given by

$$\frac{\partial \mathbf{Q}}{\partial t} + \frac{\partial (\mathbf{F} - \mathbf{F}_\nu)}{\partial x} + \frac{\partial (\mathbf{G} - \mathbf{G}_\nu)}{\partial y} = 0. \qquad (1)$$

Because the code was developed for multicomponent flows, the conservative variable vector $\mathbf{Q} = [\rho, \rho u, \rho v, \rho E, \rho Y_i]'$ includes species densities. The variables are the density ρ, the velocity components u, and v in x- and y-direction, respectively, the total specific energy E, and the species mass fractions Y_i. $\mathbf{F}$ and $\mathbf{G}$ are the inviscid, $\mathbf{F}_\nu$ and $\mathbf{G}_\nu$ are the viscous fluxes in x- and y-direction, respectively. Central difference is used for space discretization and first and third-order artificial viscosity is added to enable good shock capturing and prevent odd-even decoupling (Gerlinger et al., 1995). More details on the finite volume scheme may be found in Gerlinger and Algermissen (1993).

The q-ω Turbulence Model. The q-ω turbulence model was first introduced by Coakley (1983) to overcome the stiffness problems associated with other low-Reynolds-number turbulence closures. For this study, the 1992 version of the q-ω model is employed. For a variety of different test cases (Gerlinger et al., 1996), we found it to be very stable from a numerical point of view, especially when compared to a k-ϵ model (Gerlinger and Algermissen, 1993). This is a desirable feature

Contributed by the Fluids Engineering Division for publication in the JOURNAL OF FLUIDS ENGINEERING. Manuscript received by the Fluids Engineering Division December 4, 1996; revised manuscript received October 15, 1997. Associate Technical Editor: M. M. Sindir.

when multigrid methods are used. The turbulent transport variables for the q-ω model are $q = \sqrt{k}$ and $\omega = \epsilon/k$, where k is the turbulent kinetic energy and ϵ its rate of dissipation. For the two-dimensional case the field equations for the q-ω model are given by

$$\frac{\partial \mathbf{Q}_{q\omega}}{\partial t} + \frac{\partial(\mathbf{F}_{q\omega} - \mathbf{F}_{q\omega_v})}{\partial x} + \frac{\partial(\mathbf{G}_{q\omega} - \mathbf{G}_{q\omega_v})}{\partial y} = \mathbf{S}_{q\omega} \quad (2)$$

where $\mathbf{Q}_{q\omega} = [\rho q, \rho\omega]^t$ is the conservative turbulent variable vector,

$$\mathbf{F}_{q\omega} = \begin{bmatrix} \rho u q \\ \rho u \omega \end{bmatrix}, \quad \mathbf{G}_{k\omega} = \begin{bmatrix} \rho v q \\ \rho v \omega \end{bmatrix} \quad (3)$$

are the inviscid fluxes,

$$\mathbf{F}_{q\omega_v} = \begin{bmatrix} \left(\mu_m + \frac{\mu_t}{\sigma_q}\right)\frac{\partial q}{\partial x} \\ \left(\mu_m + \frac{\mu_t}{\sigma_\omega}\right)\frac{\partial \omega}{\partial x} \end{bmatrix}, \quad \mathbf{G}_{q\omega_v} = \begin{bmatrix} \left(\mu_m + \frac{\mu_t}{\sigma_q}\right)\frac{\partial q}{\partial y} \\ \left(\mu_m + \frac{\mu_t}{\sigma_\omega}\right)\frac{\partial \omega}{\partial y} \end{bmatrix} \quad (4)$$

are the viscous fluxes, μ_m and μ_t are the molecular and turbulent viscosity, and

$$\mathbf{S}_{q\omega} = \begin{bmatrix} C_{q1}\left(C_\mu D_q \frac{S}{\omega^2} - \frac{2}{3}\frac{D}{\omega} - 1\right)\rho\omega q \\ \left[C_{\omega 1}\left(C_\mu \frac{S}{\omega^2} - C_{\omega 3}\frac{D}{\omega}\right) - C_{\omega 2}\right]\rho\omega^2 \end{bmatrix} \quad (5)$$

is the turbulent source vector. The problems for the multigrid technique are mainly caused by the strain invariant

$$S = \left[2\frac{\partial u}{\partial x} - \frac{2}{3}\left(\frac{\partial u}{\partial x} + \frac{\partial v}{\partial y}\right)\right]\frac{\partial u}{\partial x} + \left(\frac{\partial u}{\partial y} + \frac{\partial v}{\partial x}\right)^2 + \left[2\frac{\partial v}{\partial y} - \frac{2}{3}\left(\frac{\partial u}{\partial x} + \frac{\partial v}{\partial y}\right)\right]\frac{\partial v}{\partial y} \quad (6)$$

and the exponential damping functions D_q and $C_{\omega 1}$

$$D_q = 1 - \exp(-0.022\, R_q), \quad C_{\omega 1} = 0.5\, D_q + 0.055 \quad (7)$$

which depend on the turbulent Reynolds number $R_q = (\rho q l_w)/\mu_m$ (l_w is the vertical distance to the nearest wall). If these terms (S, D_q, and $C_{\omega 1}$) are recalculated on coarse grids, already small changes in the variable vector, in addition to the changed values of l_w, will cause great changes in R_q and S which can destroy convergence. Therefore, such terms require special treatment and will be described later. Finally, the divergence of the velocity field is given by $D = \partial u/\partial x + \partial v/\partial y$ and the eddy viscosity is calculated by

$$\mu_t = C_\mu D_q \frac{\rho q^2}{\omega}. \quad (8)$$

The boundary conditions at solid walls are $q = 0$ and $\omega_n = 0$ where n is normal to the solid wall. For inflow conditions we used fixed freestream values for the first test case and calculated fully developed turbulent inlet profiles for the second. At the exit the primitive variables are extrapolated. The model constants were chosen as

$$C_{q1} = 0.5, \quad C_{\omega 2} = 0.833, \quad C_{\omega 3} = 2/3$$
$$\sigma_q = 0.8, \quad \sigma_\omega = 2.0, \quad C_\mu = 0.09. \quad (9)$$

Coakley and Huang (1992) reported that when y^+ for the first cell center is greater than one, errors in skin friction were noted. Therefore all grids employed conformed to this requirement.

The Multigrid Method

The current multigrid method follows the Full Approximation Storage (FAS) scheme of Brandt (1977) for nonlinear problems and the work of Jameson and Yoon (1986). It is incorporated into the implicit LU-SGS algorithm to accelerate the removal of low frequency errors with the consequence that a steady state is more rapidly attained. The iterative scheme works effectively only on high frequency error components. Therefore a hierarchy of five grid levels is used in which the low frequencies are resolved as increasingly higher frequencies and thus may be more effectively damped. One condition for the multigrid to work is the ability of the driving scheme to rapidly damp out high frequency errors. A sequence of grids is formed by eliminating every other grid line in every coordinate direction (full coarsening). The calculation is started on the finest grid. For complicated geometries and simple flow field initializations, the calculation is started with several fine grid iterations before changing to coarser grids. Further convergence acceleration is achieved by a local time stepping.

The implicit LU-SGS algorithm may symbolically be expressed by

$$LU(\mathbf{Q}^k)\,\Delta\mathbf{Q}^k = \mathbf{R}(\mathbf{Q}^k) \quad (10)$$

where LU is the implicit operator, $\mathbf{R}$ the residual, k indicates the level of the grid, and $\Delta\mathbf{Q}^k$ is the correction of one LU-sweep. After one relaxation sweep is performed on the finest level, the FAS V-cycle strategy is as follows:

Step 1: The solution and the recalculated residuals are transferred from the finest to the next coarser grid by

$$\mathbf{Q}_0^{k+1} = I_k^{k+1}\,\mathbf{Q}^k, \; \mathbf{R}_c^{k+1} = r_k^{k+1}\,\mathbf{R}(\mathbf{Q}^k) \quad (11)$$

where the subscripts 0 and c stand for the initialized coarse grid solution at the present time step (using present finer grid values) and the collected residuals, respectively. I_k^{k+1} and r_k^{k+1} are restriction operators for the change from fine to coarse grids.

Step 2: According to Jameson and Yoon (1986) a forcing function is defined (for $k = 1$) by

$$\mathbf{P}^{k+1} = \mathbf{R}_c^{k+1} - \mathbf{R}(\mathbf{Q}_0^{k+1}) \quad (12)$$

which is the difference between the transferred residuals from the fine grid and the new calculated coarse grid residuals for which the transferred variables $\mathbf{Q}_0^{k+1}$ are used. The residual error

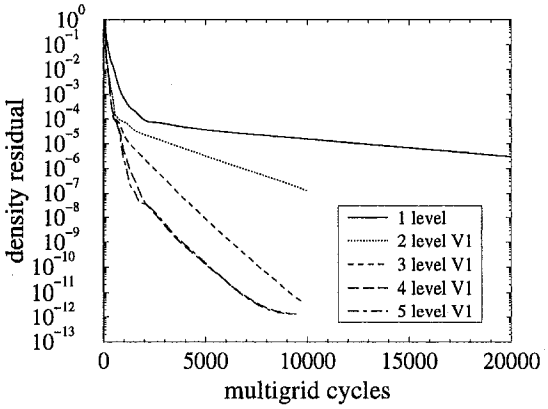

Fig. 1 Convergence histories for the density residual

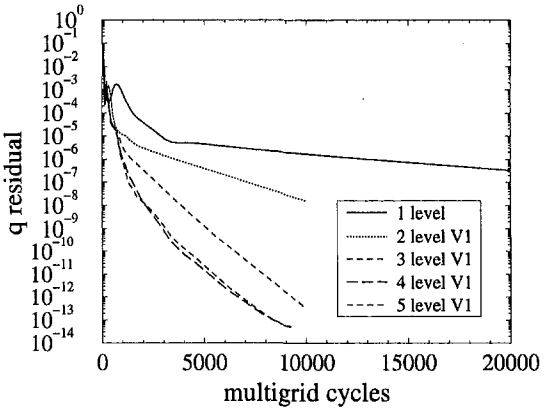

Fig. 2 Convergence histories for the q residual

for the coarse grid is the sum of the forcing function and the calculated residual

$$\mathbf{T}^{k+1} = \mathbf{R}(\mathbf{Q}^{k+1}) + \mathbf{P}^{k+1}. \tag{13}$$

Step 3: The coarse grid solution is updated by

$$\mathrm{LU}(\mathbf{Q}^{k+1})\,\Delta\mathbf{Q}^{k+1} = \mathbf{T}^{k+1}. \tag{14}$$

Steps 1 to 3 are repeated successively until the coarsest grid level is reached. However, the forcing function for $k > 1$ is now calculated by

$$\mathbf{P}^{k+1} = r_k^{k+1}\,\mathbf{T}(\mathbf{Q}^k) - \mathbf{R}(\mathbf{Q}_0^{k+1}). \tag{15}$$

instead of Eq. (12).

Step 4: Finally, the obtained coarse grid corrections are prolongated back to the finer grids by

$$\mathbf{Q}_{\text{new}}^k = \mathbf{Q}^k + p_{k+1}^k\,(\mathbf{Q}_{\text{new}}^{k+1} - \mathbf{Q}_0^{k+1}) \tag{16}$$

where p_{k+1}^k is a prolongation operator from coarse to fine grids. While one or more iterations may be performed after every restriction step no additional relaxation sweeps are performed during prolongation. The primitive variables, pressure, temperature, and gas properties are calculated from transferred conservative variables. The boundary conditions are treated in the same way at all grid levels.

According to Jameson and Yoon (1986) a cell area weighted restriction operator (Ω is the corresponding cell area) is employed for the transfer of the conservative variables

$$I_k^{k+1}\,\mathbf{Q}^k = \frac{1}{\Omega^{k+1}} \sum_{l=1}^{4} \Omega_l^k\,\mathbf{Q}_l^k \tag{17}$$

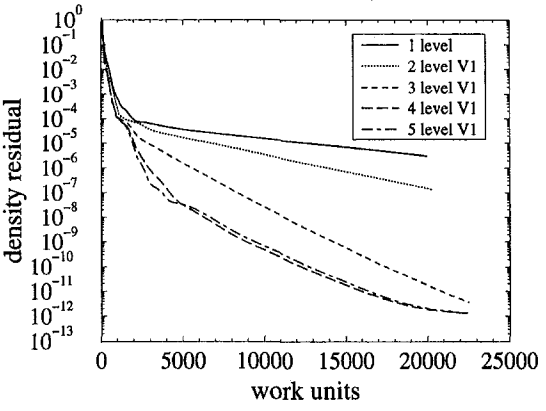

Fig. 3 Convergence histories for the density residual

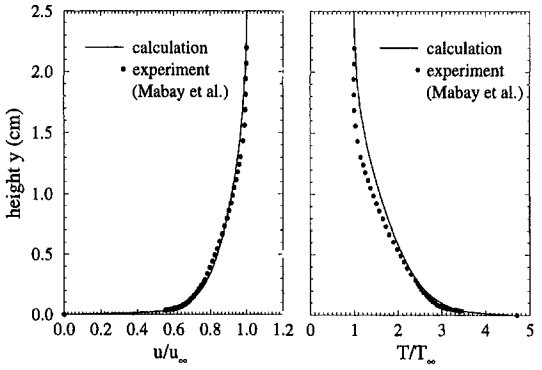

Fig. 4 Normalized velocity and temperature profiles

while the residuals **R** and **T** are restricted by simply adding up four fine grid values. Multigrid methods had first been developed for elliptic equations, but they also work in supersonic or hypersonic flows, however with reduced effectivity. If shock waves occur and the computational grid is not extremely fine at the shock wave, we found it necessary to use the following modifications:

- the transferred residuals from fine to coarse grids are damped (reduced) near shock waves
- the time step for time integration near shock waves is reduced on coarse grids
- a simple form of an upwind prolongation is employed.

All these points work on reducing or neglecting the upwind influence at shock waves during restriction or prolongation. In the present work, central differences are used for space discretization making the addition of artificial viscosity necessary. First-order terms are added near shock waves, while a weak third-order background damping is necessary to reduce odd-even oscillations and enable convergence to machine accuracy. To locate shock waves, a pressure based sensor is used, being a blend between the standard (Jameson et al., 1981) and a total variation diminishing sensor (Sanson and Turkel, 1990, Gerlinger et al., 1995). This sensor is also used to reduce the transferred residuals (Radespiel and Swanson, 1995) as well as the time step (Gerlinger and Brüggemann, 1997) at shock waves. The reduction in time step is only necessary for implicit schemes where information may be passed through shock waves, even if the residuals directly at the shock would become zero. The prolongation of corrections from coarse to fine grids is performed by bilinear interpolation in subsonic flow regimes. When the flow is supersonic, only the upwind cell centers are included into the prolongation process. The contravariant velocity between two coarse grid centers serves as an identificator for the switch. This treatment is much simpler than the mathematically exact characteristic upwind prolongation proposed by Leclercq and Stoufflet (1993).

If multigrid is used for solving the turbulence transport equations, the source terms require special treatment. Due to the

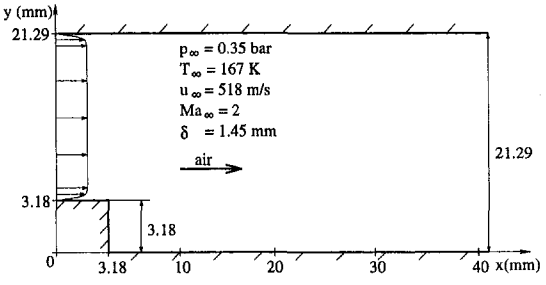

Fig. 5 Geometry (mm) and inflow conditions

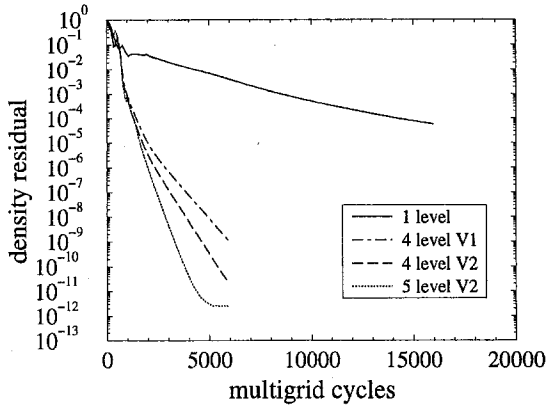

Fig. 6 Convergence histories for the density residual

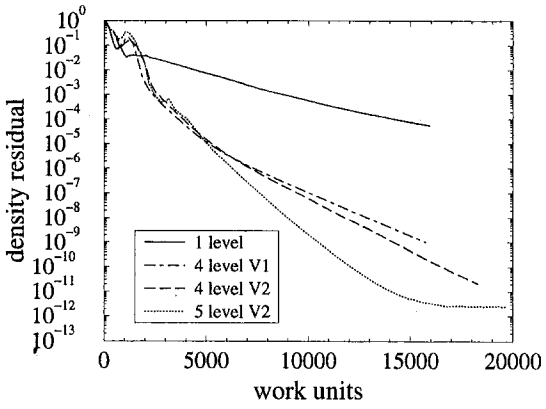

Fig. 8 Convergence histories for the density residual

included exponential functions (depending on the turbulent Reynolds-number) and production terms (depending on the square of velocity gradients) the nonlinear behavior of these terms may prevent the multigrid from converging. Small changes in the coarse grid variable vector may drastically affect the source terms with the result that such terms no longer represent the problem on the fine grid. It is possible to collect the fine grid source terms and treat them as constants on coarser grids. Thus reduces the source Jacobian to zero. If the solution is already near the stationary condition, this method works quite well. However, such an explicit treatment does not work in the transient phase of integration or if the calculation is started from uniform flow. A turbulent source term Jacobian is also required on coarse grids to handle numerical stiffness. Cell area weighted fine grid Jacobians as approximation for coarser grid Jacobians did not work well in the investigated test cases.

Another simple, but very effective, technique is to treat only the nonlinear parts of the source vector as constants on coarse grids. The term S, the exponential function D_q (see Eqs. (6) and (7)), and also for simplicity, the divergence of the velocity field D is calculated only on the finest grid. They are transferred to coarser grids (according to Eq. (17)) in the same way as the conserved variables but are held constant while the turbulence variables are allowed to change. The advantage of this method is that the turbulent source Jacobian for the q-ω model can therefore be calculated in the same way at all grid levels. Using

$$N_q = (\rho q)\,\frac{\partial D_q}{\partial(\rho q)} = 0.022\ \mathrm{Re}_t \exp(-0.022\ \mathrm{Re}_t) \quad (18)$$

the source Jacobian $\mathbf{H}_{q\omega} = \partial S_{q\omega}/\partial \mathbf{Q}_{q\omega}$ is given by

$$\mathbf{H}_{q\omega} = \begin{bmatrix} C_{q1}\left(C_\mu \frac{S}{\omega}[D_q + N_q] - \frac{2}{3}D - \omega\right) & -C_{q1}\left(C_\mu q D_q \frac{S}{\omega^2} + q\right) \\ 0.5\,N_q \frac{1}{q}(C_\mu S - C_{\omega 3} D\omega) & -C_{\omega 3}C_{\omega 1}D - 2C_{\omega 2}\omega \end{bmatrix}. \quad (19)$$

However, N_q may be set to zero for most cases because it is different from zero only in a very limited range of Re_t.

We finally summarize the modifications used for the nonlinear turbulent source vector in conjunction with the multigrid technique:

- The turbulence equations are solved and updated in the usual way on the finest grid.
- The nonlinear parts D_q, S and term D are calculated only on the finest grid. They are restricted to the next coarser grid and are kept constant.
- The turbulence equations are solved and updated on the coarse grid. The updated solution as well as the parts of the source vector kept constant are restricted again to still coarser grids, until the coarsest level is reached.

The foregoing method is used for all calculations within this paper. It is easy to implement, very robust, and works without further modifications even when the calculations are initialized with the freestream values.

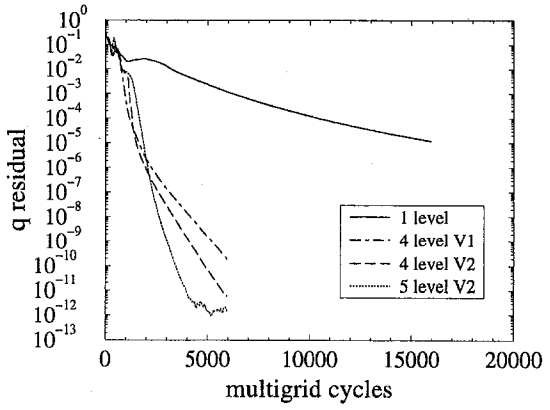

Fig. 7 Convergence histories for the q residual

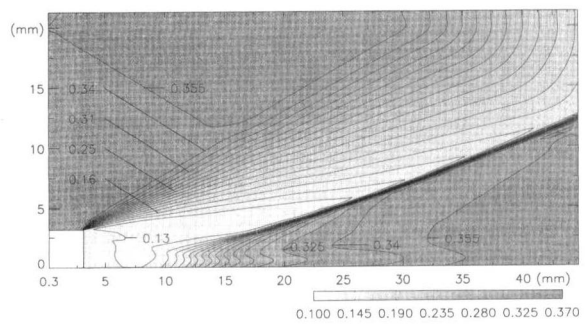

Fig. 9 Pressure contours (Δ = 0.015 bar)

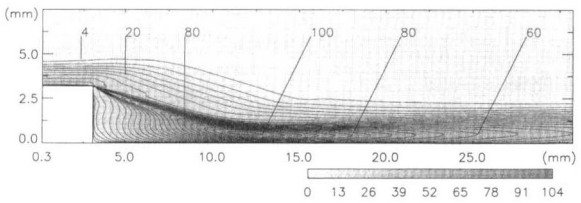

Fig. 10 q contours (Δ = 4 m/s)

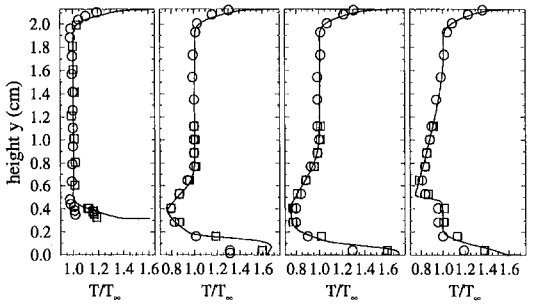

Fig. 12 Temperature profiles at the locations x = 3.1, 8.8, 12.7 and 24.4 mm (— calculation, □ LIIF, ○ PLIIF)

Results and Discussion

Flat Plate. While the flow over a flat plate is the most simple test case for the turbulence model, severe difficulties may occur for the multigrid method. Due to the strong mesh clustering normal to the wall and the high cell aspect ratios the damping properties of the driving numerical scheme are degraded (Edwards, 1995). A second problem called *strong alignment* by Brandt (1979), results when the direction of the flow aligns with one coordinate direction. The coupling between the different coordinate directions becomes too small and the multigrid method is not able to remove oscillatory components of the error. Mulder (1989) proposed a semi-coarsening in two coordinate directions to solve this problem. Another possibility is the use of implicit, more global relaxation schemes (Mulder, 1989). The employed implicit LU-algorithm offers good damping properties as shown by Jameson and Yoon (1986) and allows the use of full coarsening.

The following test case is a Mach 4.5 adiabatic flow over a flat plate. The experiment was performed by Mabey et al. (1974) and is also documented by Fernholz and Finley (1977). The freestream temperature and pressure are 62 K and 3.2 kPa, respectively. In the experiment, a roughness band was used to move transition forward toward the leading edge of the plate and thus increase the length of turbulent flow. The calculation was performed with constant inflow conditions (turbulence inflow intensity Tu = 1 percent) and transition took place about 0.18 m downstream of the leading edge. Pressure and temperature profiles are compared with experimental data for the same turbulent boundary layer thickness. The computational grid consists of 192 · 80 volumes for a length of 1.62 m in x- and 0.86 m in y-direction. The grid is highly refined near the leading edge. The distance of the first cell center to the solid wall is 0.001 mm. Thus all y^+ values for first cell centers are smaller than 0.32, even near the leading edge of the plate. This results in cell aspect ratios up to 2400. Figures 1 and 2 show convergence histories for the density and q-residuals calculated by using 1 to 5 grid levels. Given are the absolute averaged normalized residuals for V-cycles with one coarse grid iteration starting on the finest grid. As can be seen from these figures, turbulence and density residuals converge with nearly the same rate. This is the advantage if multigrid is used for all conservation equations. No improvement could be achieved by a second coarse grid iteration. The use of 5 instead of 4 grid level also resulted in no significant improvement. It is possible that grid alignment is responsible for these properties. Figure 3 shows the convergence history of the density residual versus the necessary number of work units. One work unit represents the computational effort for one fine grid iteration. The computations are performed on a NEC-SX4 using a fully vectorized code. Because of the shorter vector length on coarse grids the computational effort for the multigrid method is higher than its theoretical value. Figure 4 compares normalized computational and experimental velocity and temperature profiles for the boundary layer thickness δ = 2.195 cm. Both profiles show that the computation is in reasonably good agreement with the experiment.

Backward Facing Step. A turbulent Mach 2 flow over a backward facing step is investigated numerically and compared with experimental data of McDaniels et al. (1991). Figure 5 shows the geometry and inflow conditions for the computed domain. A two block grid with 112 · 80 for the lower and 144 · 112 volumes for the upper part is used. A further grid refinement resulted in no significant changes of the flow variable profiles. The distance from the upper and lower wall to the first cell center is about 0.002 mm. Again, very fine grids are necessary near solid walls to assure y^+ values below 1. With the exception of the last volumes at the lower wall upstream of the step, this requirement on y^+ was met throughout. However, the expansion fan accelerates the upstream boundary layer leading to an increase in y^+ values up to 2 in the last volume directly at the step. The grid near the step is also strongly refined in the x-direction. The maximum value for the cell aspect ratio is 850 and the used CFL number is 6. Inlet profiles are calculated with the same code to match the experimental measured boundary layer thickness δ = 1.45 mm at the x = 0 location, which is 3.18 mm upstream of the rearward facing step. Although not shown in this paper, the calculated inlet pressure, temperature, and velocity profiles agree very well with experimental data.

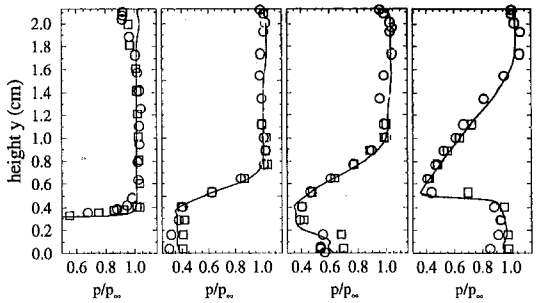

Fig. 11 Pressure profiles at the locations x = 3.1, 8.8, 12.7 and 24.4 mm (— calculation, □ LIIF, ○ PLIIF)

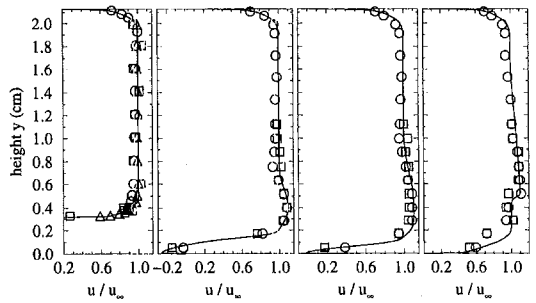

Fig. 13 u-velocity profiles at the locations x = 3.1, 8.8, 12.7 and 24.4 mm (— calculation, ○ PLIIF, □ LIIF, Δ LDA)

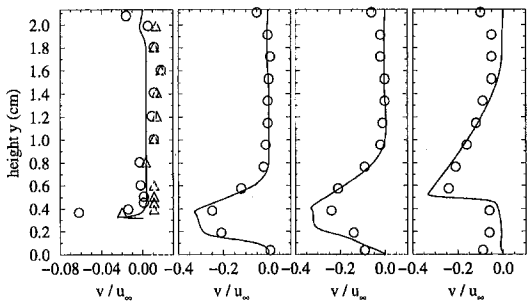

Fig. 14 *v*-velocity profiles at the locations x = 3.1, 8.8, 12.7 and 24.4 mm (— calculation, ○ PLIIF, Δ LDA)

Again calculations are performed using V-cycles with up to 5 grid levels and full coarsening. Figures 6 and 7 show convergence histories for the density and q-residuals, respectively. It is noted that the achieved convergence acceleration for this more complicated flow field is better than for the flat plate, thus confirming that the strong grid alignment in the first case may be responsible for degradation in convergence. For this case, further improvement was achieved by a second coarse grid iteration being shown for the 4 level calculation. Also, the change from 4 to 5 levels led to an additional reduction in multigrid cycles and work units to converge to machine accuracy. Again, convergence of the turbulence equations has not lagged in comparison to the fluid equations. In Fig. 8 the convergence history of the continuity equations is plotted against the number of work units. Because of the additional effort for solving the equations on coarser grids, the difference between the multi and 1 grid solution decreases. However, there is still a strong reduction (at least by a factor of 3) in CPU-time.

Figures 9 and 10 show pressure and q contours for the whole and lower channel area, respectively. At the backward facing step an expansion fan is obtained lowering the pressure in the base of the step to about 35 percent of its freestream value. This lower pressure is responsible for the boundary layer reduction at the step and the flow acceleration, which lead to an increase in y^+ values. Downstream of the rearward facing step an oblique shock wave is formed with beginning reattachment. The calculated point of reattachment agrees well with the experimentally measured value. Due to the strong velocity gradients associated with the changes in flow direction at the step and with beginning reattachment, high production rates in the turbulent kinetic energy occur. The maximum values for q of about 100 m/s are reached during reattachment. In the experiment, several different measurement techniques have been used, a pointwise (LIIF) and a planar (PLIIF) laser-induced iodine fluorescence technique for pressure, temperature, and velocity measurements, and laser Doppler aneometry (LDA) for velocity measurements (McDaniels et al., 1991). Figures 11 and 12 show calculated and measured pressure and temperature profiles at different x-locations. The formation of the shock wave can be clearly seen in the last two pressure profiles and its location is given very exactly by the calculation. According to McDaniels et al. (1991) the PLIF temperatures in the vicinity of walls are too low for the first profile and for the remaining profiles at the upper wall. This is due to wall scattering and the used coating. Finally, Figs. 13 and 14 show calculated and measured velocity profiles in x- and y-direction, respectively.

Conclusion

A method for treating the turbulent source trems of a low-Reynolds-number q-ω model is presented which enables the use of multigrid for convergence acceleration. A strong reduction in the necessary number of multigrid cycles and CPU-time is achieved for different test cases. The method works well for supersonic flows if restriction and prolongation operator are slightly modified. In conjunction with an implicit LU-SGS algorithm, the multigrid technique is robust and offers good damping properties necessary for highly stretched grids or cases with strong grid alignment. Comparisons with experiments have demonstrated the high numerical stability and accuracy of the q-ω model for turbulent separated flows.

Acknowledgment

This research was supported by the Deutsche Forschungsgemeinschaft (DFG) within the special research programme SFB 259 at the University of Stuttgart.

References

Brandt, A., 1977, "Multi-Level Adaptive Solutions to Boundary-Value Problems," *Math. Comp.,* Vol. 31, pp. 333–390.

Brandt, A., 1979, "Multi-Level Adaptive Solutions in Fluid Dynamics," INKA-Conf.-79, 351-010, 79-1455.

Coakley, T. J., 1983, "Turbulence Modeling Methods for the Compressible Navier-Stokes Equations," AIAA-Paper 83-1693.

Coakley, T. J., and Huang, P. G., 1992, "Turbulence Modeling for High Speed Flows," AIAA-Paper 92-0436.

Dick, E., Herbosch, P., Steelant, J., and Lacor, C., 1994, "Comparison of Multigrid Solutions of the Compressible Navier-Stokes Equations Coupled to the $k - \epsilon$ Turbulence Equations for Upwind and Central Difference Schemes," *Proc. ECOMAS 2nd European Computational Fluid Dynamics Conference,* Wagner, Hirschel, Periaux, Piva, eds., Vol. 1, pp. 356–362.

Edwards, J. R., 1995, "Development of an Upwind Relaxation Multigrid Method for Computing Three-Dimensional, Viscous Internal Flows," AIAA-paper 95-0208.

Fernholz, H. H., and Finley, P. J., 1977, "A Critical Compilation of Compressible Boundary Layer Data," AGARD-AG-223.

Gerlinger, P., and Algermissen, J., 1993, "Numerical Simulation of Supersonic Combustion Problems Using an Implicit LU-SGS Scheme and $k - \epsilon/q - \omega$ Turbulence Closure," AIAA-Paper 93-5021.

Gerlinger, P., Algermissen, J., and Brüggemann, D., 1995, "Matrix Dissipation for Central Difference Schemes with Combustion," *AIAA Journal,* Vol. 33, pp. 1865–1870.

Gerlinger, P., Algermissen, J., and Brüggemann, D., 1996, "Numerical Simulation of Mixing for Turbulent Slot Injection," *AIAA Journal,* Vol. 34, pp. 73–78.

Gerlinger, P., and Brüggemann, D., 1997, "Multigrid Convergence Acceleration for Turbulent Supersonic Flows," *International Journal of Numerical Methods of Fluids,* Vol. 24, pp. 1019–1035.

Jameson, A., and Yoon, S., 1986, "Multigrid Solution of the Euler Equations Using Implicit Schemes," *AIAA Journal,* Vol. 24, pp. 1737–1743. 1737–1743.

Jameson, A., Schmidt, W., and Turkel, E., 1981, "Numerical Solution of the Euler Equations by Finite Volume Methods using Runge-Kutta Time Stepping Schemes," AIAA-Paper 81-1259.

Leclercq, M. P., and Stoufflet, B., 1993, "Characteristic Multigrid Method Application to Solve the Euler Equations with Unstructured and Unnested Grids," *J. Comp. Phys.,* Vol. 104, pp. 329–346.

Martelli, F., and Michelassi, V., 1990, "3-D Implicit Navier-Stokes Solver for Internal Turbulent Compressible Flows," *Recent Advances and Applications in Computational Fluid Dynamics,* O. Baysal, ed., ASME, New York, pp. 233–241.

McDaniels, J., Fletcher, D., Hatfield, Jr., R., and Hallo, S., 1991, "Staged Transverse Injection Into Mach 2 Flow Behind a Rearward-Facing Step: A 3-D Compressible Test Case for Hypersonic Combustion Code Validation," AIAA-paper 91-5071.

Mulder, W. A., 1989, "A New Multigrid Approach to Convection Problems," *Journal of Computational Physics,* Vol. 83, pp. 303–323.

Mabay, D. G., Meier, H. U., and Sawyer, W. G., 1974, "Experimental and Theoretical Studies of the Boundary Layer on a Flat Plate at Mach Numbers from 2.5 to 4.5," RAE TR 74127.

Radespiel, R., and Swanson, R. C., 1995, "Progress with Multigrid for Hypersonic Flow Problems," *Journal of Computational Physics,* Vol. 116, pp. 103–122.

Shuen, J. S., 1992, "Upwind Differencing and LU Factorization for Chemical Non-equilibrium Navier-Stokes Equations," *Journal of Computational Physics,* Vol. 99, pp. 233–250.

Speziale, C. G., Abid, R., 1995, "Near-Wall Integration of Reynolds Stress Turbulence Closures with No Wall Damping," *AIAA Journal,* Vol. 33, pp. 1974–1977.

Swanson, R., C., Turkel, E., "On Central Difference and Upwind Schemes," 1992, *Journal of Computational Physics,* Vol. 101, pp. 292–306.

Turkel, E., Swanson, R. C., Vatsa, V. N., and White, J. A., 1991, "Multigrid for Hypersonic Viscous Two- and Three-Dimensional Flows," ICASE Report No. 91-57.

Statistical Model of a Self-Similar Turbulent Plane Shear Layer

Zuu-Chang Hong
Professor.

Ming-Hua Chen
Ph.D. Student.

Department of Mechanical Engineering,
National Central University,
Chungli, Taiwan

A turbulence probability density function (pdf) equation model is employed to solve a self-similar turbulent plane shear layer. The proper similarity variable was introduced into the problem of interest to reduce the pdf equation into a spatially one-dimensional equation, which is still three dimensional in velocity space. Then the approximate moment method is employed to solve this simplified pdf equation. By the solutions of this equation, the various one-point mean quantities are immediatelly available. Agreement of the calculated mean velocity, turbulent energy and Reynolds stress with the available experimental data is generally satisfactory indicating that the pdf equation model and the moment method can quantitatively describe the statistics of free turbulence. Additionally, the balance of turbulence energy was calculated and discussed subsequently. It shows that the pdf methods are of more potential in revealing turbulence structure than conventional turbulence models.

I Introduction

Conventional turbulence models (Launder and Spalding, 1972; Lakshminarayana, 1986; Pollard and Martinuzzi, 1989) are extensively employed to predict a wide variety of turbulent flows of engineering interest. Their basis is to close a set of transport equations for turbulence mean quantities by making use of gradient type molecular transport assumptions. Some inadequacies of the gradient type transport assumptions on turbulent transfer, in which the higher-order correlations are in terms of lower order mean gradients, are well pointed out by many researchers (Hinze, 1959; Tennekes and Lumley, 1972; Cebeci and Smith, 1974; Chung, 1972). Alternatively, probability density function (pdf) methods can provide more statistical information than is provided in conventional turbulence models. This is due to the fact that once the pdf is determined, any order means can be constructed from the pdf. In this paper, we will employ a turbulent pdf equation model to construct the one-point moments of a self-similar turbulence plane shear layer flow.

Mixing phenomena in a free turbulent shear layer has been of engineering interests since early 1920's (Tollmien, 1926; Gortler, 1942). It is of basic importance to the description of the phenomena occurring in the flow field downstream of an aerodynamic body and about the interaction between fuel and oxidizer in a combustion system. So far, there is no complete analytical solution for this problem. Most of the analyses are phenomenological approaches to solve the closure problem of the moments equations derived from the Navier-Stokes equations. Some experimental and analytical investigations were carried out by many researchers (Lee and Harsha, 1970; Spencer and Jones, 1971; Jones, 1976; Mohammadian et al., 1976; Batt, 1977; Hong, 1975; Bywater, 1981; Hong and Lai, 1983; Haworth and Pope, 1987). Reviews of the experimental data are given by Rodi (1975) and Batt (1977). The kinetic theory due to Chung (1967) was employed by Hong (1975) to solve two-dimensional shear layer using a Green's function method. Its calculations are very tedious and the calculations of high order correlation are not very successful. However, the pdf of the fluid elements and the chemical species in the flow field are revealed for the first time. Later on the Green's function method was modified to solve an unsteady two half space instantaneous mixing problem to simulate the half plane two streams steady mixing problem (Hong and Lai, 1983). The numerical calculation time was reduced and higher order correlations calculation are improved. Bywater (1981) used Chung's kinetic theory (1967) to solve the two-dimensional free shear layer by direct numerical method for the normal component of the turbulence velocity pdf.

More recently, a generalized Langevin equation due to Pope (Haworth and Pope, 1986) was employed to solve the self-similar turbulent free shear flows (Haworth and Pope, 1987). The generalized Langevin equation was rewritten from the Navier-Stokes equation by analogy to Langevin equation of Brownian motion. This was based on the assumption that the Langevin equation, originally proposed to describe the Brownian motion of small particles owing to collisions with gaseous or liquid molecules, can be used to describe turbulent flows. The major difference between Haworth and Pope's model and Chung's model is that the characteristic relaxation rate of energy containing eddies, β, of Chung's model was replaced by a more flexible, undetermined 2nd order tensor G_{ij}. With different choices of G_{ij}, the Reynolds-stress equations derived from Haworth and Pope's model can be fitted to a variety of existing Reynolds-stress models. However, the above-mentioned models can provide no information on length and time scales. To remedy this deficiency, Pope and Chen (1990) recently developed a model based on the joint pdf of velocity and the instantaneous dissipation rate. This model was developed by reference to the known statistics of homogeneous turbulence, and in its original form it is restricted to homogeneous turbulence. Subsequently, Pope (1991) extended the model to the general case of inhomogeneous flows, and calculations are made to demonstrate its performance. The major advantage of this approach is that no assumption was specified for pdf, therefore the unphysical behaviors of pdf would not appear. Regarding the theoretical foundations of the pdf approach, Pope (1985) has provided a comprehensive, understandable and thorough introduction. In addition, Pope (1994) reviewed the more recent and sophisticated stochastic models regarding Lagrangian pdf methods that also is good reference.

In contrast to Lagrangian pdf models, the pdf model used here is an Eulerian one. The detailed derivation and properties are presented by Hong et al. (1993, 1995). This paper presents

Contributed by the Fluids Engineering Division for publication in the JOURNAL OF FLUIDS ENGINEERING. Manuscript received by the Fluids Engineering Division April 23, 1996; revised manuscript received January 19, 1998. Associate Technical Editor: P. R. Bandyopadhyay.

current results of a continuing effort to describe the significant engineering aspects of turbulent flowfields using this pdf model. The previous application (Hong et al., 1995) based on this model has focused primarily upon the ability of such a pdf approach to model the wall-bounded turbulent flows. The tools employed were the QUICKER (Pollard and Siu, 1982) scheme and dimensionality reduction, which was used to determine the statistical characteristics of one-dimensional turbulence flowfield structure. The success of that work suggests the value of exploring further applications of this pdf equation model. In this paper, the two-dimensional free shear layer was solved by this pdf equation model in more direct and efficient way. A proper similarity variable is introduced into the problem of interest to reduce the pdf equation into an equation that is one-dimensional spatially and still three dimensional in velocity space. The bimodal method after Liu and Lees (1961) is employed to solve this simplified pdf equation. The calculated one-point means are compared with the available experimental data. The generally satisfactory agreement between the present calculations and the available experimental data indicates the potential ability of this pdf model to reveal free turbulence statistic.

II General Theory

In this section, the general velocity pdf equation model for turbulent flows is outlined. The basic theory and model equations upon which the present study is built have been described in detail in the two previous papers (Hong et al., 1993, 1995).

The model equation that forms the basis for the present study uses a pdf, $f(\tilde{U}; t, \tilde{x})$, to describe the turbulence velocity field. The $f(\tilde{U}; t, \tilde{x})d\tilde{U}$ gives the probability of a fluid element at time t and location $\tilde{x}$ having its fluctuating velocity in the range $\tilde{U}$ to $\tilde{U} + d\tilde{U}$. It is related to the mean quantities (correlations) through the ensemble average:

$$\overline{Q(\tilde{U})} = \int Q(\tilde{U}) f(\tilde{U}) d\tilde{U} \tag{1}$$

where the overscores denote the mean quantities. It is seen from equation (1) that if a solution of f can be obtained, all higher order moments (mean quantities) are immediately available.

The derivation of the governing equation for $f(\tilde{U}; t, \tilde{x})$ used here is divided into two fractional steps. A dynamic equation for the fluid element was proposed in the first step by modeling the fluctuating part of Navier-Stokes equation. Under some assumptions and with the aid of an auxiliary mathematical lemma (Hong et al., 1993, 1995), a transition probability density function (tpdf) was constructed through the solution of the modeled dynamic equation of a fluid element. A Fokker-Planck type pdf equation was then obtained by gradually unfolding the pdf of a fluid element from one phase point to its neighboring phase point through the assistance of tpdf. In view of the effects of fluctuating pressure and molecular viscous transport not being considered in first modeled dynamic equation of the fluid elements, subsequently, the pdf equation was further modified by the assistance of Lundgren's formal pdf model for ensuring that it could properly describe these effects. The final pdf model is then constructed. Details of the derivation can be found in Hong et al. (1993, 1995), with only the results presented here:

$$\frac{Df}{Dt} = \frac{\partial}{\partial V_i}\left[(1 - C_p)\frac{\partial \overline{u_i}}{\partial X_j} V_j f + C_{f1}\frac{\epsilon}{k} V_i f - \frac{\partial \overline{U_i U_j}}{\partial X_j} f \right]$$

$$(a) \qquad (b) \quad (c) \qquad (d) \qquad (e)$$

$$+ \nu \frac{\partial^2 f}{\partial X_i \partial X_i} + \left(C_{f2}\epsilon - \frac{C_p}{3}\frac{\partial \overline{u_m}}{\partial X_n}\overline{U_m U_n} \right) \frac{\partial^2 f}{\partial V_i \partial V_i} . \tag{2}$$

$$(f) \qquad (g) \qquad (h)$$

where upper and lower cases u's denote fluctuating and mean components of velocity, and $D/Dt = (\partial/\partial t) + u_i(\partial/\partial X_i)$ is the instantaneous substantial derivative. Cartesian tensor notation and the summation convention for repeated indices were used in equation (2). V_i, $i = 1 - 3$, is the coordinate in the velocity space corresponding to U_i, $i = 1 - 3$, respectively. C_{f_1}, C_{f_2}, and C_p are three modeling constants, and k and ϵ are the turbulent kinetic energy and its dissipation rate.

The physical interpretation of each term in Eq. (2) is as follows. The term (a) represents the change in f along a streamline, and (b) represents the transport in V-space due to the interaction of mean velocity gradient with turbulence. The terms (c) and (h) denote the transport in V-space due to the forced interaction part of fluctuating pressure effect, and (d) and (g) denote the transport in V-space by the viscous dissipation effect and the free interaction part of redistribution effect. The terms (e) and (f) represent the transport in V-space by turbulence energy gradient and the viscous diffusion effects, respectively. The modeling processes which the above relations are built have been described in detail in the two previous papers (Hong et al., 1993, 1995). These, therefore, will not be repeated here.

A comparison of the turbulent energy equations obtained from Eq. (2) and from the Navier-Stokes equations yields,

$$C_{f2} = \frac{(2C_{f1} - 1)}{3} . \tag{3}$$

The constant C_{f_1} can be determined from Rotta's model (1951) as 0.75, and then $C_{f_2} = \frac{1}{6}$ by manipulating equation (3). The value of C_p is as follows.

$$C_p = \begin{cases} \dfrac{-3C_{f_2}\epsilon}{Prod} & \text{for } Prod < 0 \text{ and } \dfrac{-3C_{f_2}\epsilon}{Prod} < \alpha, \\ \alpha & \text{otherwise,} \end{cases}$$

where $\alpha = 0.4 \sim 0.6$ (Naot et al., 1970) and

$$Prod = -\frac{\partial \overline{u_m}}{\partial X_n}\overline{U_m U_n} .$$

Subsequently, we will devote this section to the comparison of the fundamental aspects of the present pdf model with those of the Haworth and Pope's generalized Langevin model (1986, hereafter designated HP model). We will briefly discuss the major differences between these two models. Their differences can be seen clearly from the starting point, modeling procedure, and the final form of each model.

The starting point of present model is Navier-Stokes equation. Although Haworth and Pope also claimed that the Navier-Stokes equation is the starting point of their model, they just rewrote the Navier-Stokes equation to the generalized Langevin equation by analogy to Langevin equation. It seems that their model can be viewed as an analogy between turbulent velocity of a fluid particle and the velocity of a particle undergoing Brownian motion. The generalized Langevin equation actually is the starting point of HP model.

In the present modeling procedure, the Navier-Stokes equation was simplified by some assumptions. A Fokker-Planck type pdf equation was constructed from this simplified equation. This Fokker-Planck type pdf equation was modified by Lundgren's formal pdf equation to ensure it can be used to represent the pdf behavior of turbulence properly. Finally, the model constants were determined with the aid of Reynolds-stress model so that the Reynolds-stress equation deduced from the present pdf model can be compared to some proven Reynolds-stress models. In Haworth and Pope's work, the generalized Langevin equation proposed by Pope was employed to construct a Fokker-Planck type pdf model. In their model, a second-order tensor term G_{ij} was left undetermined. With different choices of G_{ij}, the Reynolds-stress equations deduced from their model can be fitted to different requirements on Reynolds-stress models. Haworth and Pope claimed that their model is physically justi-

fied in two respects. The first one is that the stochastic term in their generalized Langevin equation is consistent with Kolmogorov's inertial range scaling law. The second justification is that an arbitrary initial distribution of velocity could relax to a joint normal distribution for homogeneous turbulence. As one can see there are many equations that could contain the above two characteristics and yet could have nothing to do with turbulence. The two justifications serve as the necessary conditions not as the sufficient conditions for an equation to describe turbulence. Besides, the inside mechanisms of turbulent fluctuation and Brownian fluctuation are different from each other. It seems that the HP model is rather a Reynolds-stress model than a pdf model.

Concerning the final forms, two major differences arise between the present model and HP model. The first discrepancy is that the highest derivative order with respective to physical space in the present model is two and in the HP model it is one. The second order derivative term, although being negligible in most regions of the flow field, becomes important near a solid wall region and keeps the elliptic characteristic of pdf equation. The other difference is the modeling of the forced interactive pressure term. The contribution for forced interactive pressure from both large and small eddies is considered in the present model, whereas, only the former effects were contained in HP model.

III Plane Free Turbulent Shear Layer

In this section, the similarity flow description of two-dimensional free shear layer is presented. The mathematical formulation based on the present pdf model for this flowfield of interest is derived to facilitate later application of the reduction technique employed to obtain the solution. The similarity form of the turbulence energy equation derived from the pdf model also is presented. This equation gives particular insight into the nature of energy balance. Every term in this equation was computed for showing their similarity features which will be discussed in next section.

Flow Descriptions. Two-dimensional free turbulent shear layer is a boundary-layer (or a thin-shear-layer) flow. This flow is characterized by being remote from walls and by having a single predominant flow direction, the streamwise direction being denoted by x. In addition, this flow has a direction of statistical homogeneity, which is denoted by z, and the flow is statistical stationary. The transverse direction is denoted by y. Corresponding velocity components of x, y, and z are u, v and w, respectively, and their mean parts are u_o, v_o and w_o where $w_o = 0$. As is well known, in the self-similar regimes (implied by the order-of-magnitude analysis) of thin-shear-layer flow, profiles of any one-point statistic of an Eulerian velocity field can be rendered independent of x by introducing a dimensionless similarity coordinate η, which is defined as $\eta = y/(x - x_o)$ where x_o is the axial virtual origin location. It is useful to define a characteristic velocity difference $\Delta u = u_\infty - u_{-\infty}$, width $\delta = y_{0.95} - y_{0.1}$, and the velocity ratio $r = u_{-\infty}/u_\infty$ for mixing layer flow, where u_∞ and $u_{-\infty}$ are the velocities of the high- and low-speed streams, respectively, and y_a denotes the cross-stream location at which the mean velocity is equal to $u_{-\infty} + a\Delta u$. The flow regime investigated is illustrated in Fig. 1.

Mathematical Formulation. In this paper, a steady, incompressible turbulent two-dimensional free mixing layer flow is solved by the pdf equation shown in Eq. (2). The terms involved in $\partial/\partial t$, $\partial/\partial z$, are zero, and w_o is also zero. In addition, since the problem to be considered is remote from walls, the viscous term is neglected. Thus Eq. (2) becomes:

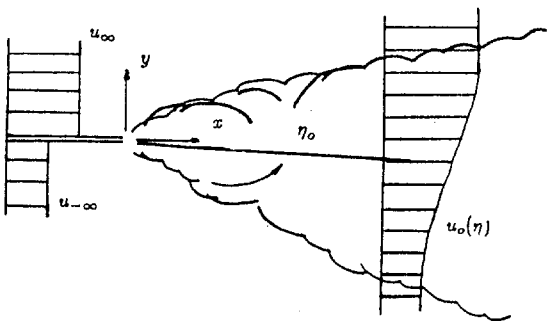

Fig. 1 Turbulent plane shear layer

$$u\frac{\partial f}{\partial x} + v\frac{\partial f}{\partial y} = \frac{\partial}{\partial U}\left[(1 - C_p)\left(\frac{\partial u_o}{\partial x}U + \frac{\partial u_o}{\partial y}V\right)f + C_{f1}\frac{\epsilon}{k}Uf - \left(\frac{\partial \overline{UU}}{\partial x} + \frac{\partial \overline{UV}}{\partial y}\right)f\right] + \frac{\partial}{\partial V}\left[(1 - C_p)\left(\frac{\partial v_o}{\partial x}U + \frac{\partial v_o}{\partial y}V\right)f + C_{f1}\frac{\epsilon}{k}Vf - \left(\frac{\partial \overline{UV}}{\partial x} + \frac{\partial \overline{VV}}{\partial y}\right)f\right] + \frac{\partial}{\partial W}\left[C_{f1}\frac{\epsilon}{k}Wf - \left(\frac{\partial \overline{UW}}{\partial x} + \frac{\partial \overline{VW}}{\partial y}\right)f\right] + \left[C_{f2}\epsilon - \frac{C_p}{3}\left(\frac{\partial u_o}{\partial x}\overline{UU} + \left(\frac{\partial v_o}{\partial x} + \frac{\partial u_o}{\partial y}\right)\overline{UV} + \frac{\partial v_o}{\partial y}\overline{VV}\right)\right]\cdot\left(\frac{\partial^2 f}{\partial U^2} + \frac{\partial^2 f}{\partial V^2} + \frac{\partial^2 f}{\partial W^2}\right). \quad (4)$$

The free shear layer coordinate η defined in above subsection is used to transform (4), resulting in

$$(v - \eta u)\frac{\partial f}{\partial \eta} = \frac{\partial}{\partial U}[A_U(\eta)fU + B_U(\eta)fV + C_U(\eta)fW + D_U(\eta)f] + \frac{\partial}{\partial V}[A_V(\eta)fU + B_V(\eta)fV + C_V(\eta)fW + D_V(\eta)f] + \frac{\partial}{\partial W}[A_W(\eta)fU + B_W(\eta)fV + C_W(\eta)fW + D_W(\eta)f] + E(\eta)\left[\frac{\partial^2 f}{\partial U^2} + \frac{\partial^2 f}{\partial V^2} + \frac{\partial^2 f}{\partial W^2}\right] \quad (5)$$

where the following relations have been used to obtained (5):

$$A_U(\eta) = C_{f1}U_e - (1 - C_p)\eta\frac{\partial u_o}{\partial \eta}$$

$$B_U(\eta) = (1 - C_p)\frac{\partial u_o}{\partial \eta}$$

$$C_U(\eta) = 0$$

$$D_U(\eta) = \eta\frac{\partial \overline{UU}}{\partial \eta} - \frac{\partial \overline{UV}}{\partial \eta}$$

$$A_V(\eta) = -(1 - C_p)\eta \frac{\partial v_o}{\partial \eta}$$

$$B_V(\eta) = C_{f_1} U_e + (1 - C_p) \frac{\partial v_o}{\partial \eta}$$

$$C_V(\eta) = 0$$

$$D_V(\eta) = \eta \frac{\partial \overline{UV}}{\partial \eta} - \frac{\partial \overline{VV}}{\partial \eta}$$

$$A_W(\eta) = 0$$

$$B_W(\eta) = 0$$

$$C_W(\eta) = C_{f_1} U_e$$

$$D_W(\eta) = \eta \frac{\partial \overline{UW}}{\partial \eta} - \frac{\partial \overline{VW}}{\partial \eta}$$

$$E(\eta) = C_{f_2} U_e k + \frac{C_p}{3}\left[\frac{\partial u_o}{\partial \eta}\eta \overline{UU} + \left(\frac{\partial v_o}{\partial \eta}\eta - \frac{\partial u_o}{\partial \eta}\right)\overline{UV} - \frac{\partial v_o}{\partial \eta}\overline{VV}\right]$$

$$U_e = \frac{\epsilon(x - x_o)}{k}$$

Previous studies (Pope, 1984; Haworth and Pope, 1987) have shown that, for thin free shear flow, it is reasonable to argue that the turbulent time scale τ $(=k/\epsilon)$ is constant across the flow, at least in the fully turbulent core of the flow. In terms of the characteristic velocity Δu and characteristic length δ, we can write

$$\frac{\epsilon}{k} = \omega^* \left(\frac{\Delta u}{\delta}\right), \tag{6}$$

where the constant ω^* takes the value 0.2. Spencer's experiment data (1970, 1971) have shown δ to be proportional to $(x - x_o)$ and could be specified as such while performing the solution.

$$\delta = 0.213 \frac{(1 - r)}{(1 + r)}(x - x_o). \tag{7}$$

Using Eqs. (6) and (7), and solving for U_e yields

$$\frac{U_e}{u_\infty} = 0.939(1 + r). \tag{8}$$

Equation (5) which is a integrodifferential equation is difficult to solve. The chief reason is the dimensionality of $f(U, V, W, \eta)$ being large. In this paper, therefore, the pdf f is not solved directly from Eq. (5). Instead, the moment equations derived from Eq. (5) is solved by an approximate moment method. Thus, a generalized moment equation for a generic function $Q(U, V, W)$ is obtained by multiplying Eq. (5) by Q and integrating over all U, V and W as follows:

$$-\eta \frac{\partial}{\partial \eta}\int uf Q d\vec{U} + \frac{\partial}{\partial \eta}\int vf Q d\vec{U}$$

$$= -\int \frac{\partial Q}{\partial U}[A_U(\eta)fU + B_U(\eta)fV + C_U(\eta)fW + D_U(\eta)f]d\vec{U} - \int \frac{\partial Q}{\partial V}[A_V(\eta)fU + B_V(\eta)fV + C_V(\eta)fW + D_V(\eta)f]d\vec{U} - \int \frac{\partial Q}{\partial W}[A_W(\eta)fU + B_W(\eta)fV + C_W(\eta)fW + D_W(\eta)f]d\vec{U} + E(\eta)\int f\left(\frac{\partial^2 Q}{\partial U^2} + \frac{\partial^2 Q}{\partial V^2} + \frac{\partial^2 Q}{\partial W^2}\right)d\vec{U}, \tag{9}$$

where $d\vec{U} = dUdVdW$.

Equation (9) was solved for the distribution function f by the moment method of Liu and Lees (1961). The solution was obtained first by approximating the distribution function by two half-Maxwellian functions as,

$$f = f_1 + f_2, \tag{10}$$

where

$$f_1 = \frac{1}{(\frac{2}{3}\pi E_1)^{3/2}}\exp\left[-\frac{(u - u_{o1})^2 + V^2 + W^2}{2E_1/3}\right] \quad \text{for} \quad V > 0,$$

$$f_2 = \frac{1}{(\frac{2}{3}\pi E_2)^{3/2}}\exp\left[-\frac{(u - u_{o2})^2 + V^2 + W^2}{2E_2/3}\right] \quad \text{for} \quad V \le 0,$$

and f_1 and f_2 are considered to be zero for $V \le 0$ and $V \ge 0$, respectively. The present moment method of solution entails the determination of the four unknown functions $E_1(\eta)$, $E_2(\eta)$, $u_{o1}(\eta)$ and $u_{o2}(\eta)$ by substituting the assumed form of the distribution function, equation (10), into a set of four particular moment equations to be deduced from Eq. (9), which is the generalized moment form of Eq. (5). By approximating the distribution function by (10), we are conceptually implying that the flow field is a shear layer of infinite extent formed between two isotropic turbulent parallel streams with the turbulence energies of $E_1(-\infty)$ and $E_2(\infty)$, respectively, and with the mean velocities of $u_{o1}(-\infty)$ and $u_{o2}(\infty)$, respectively.

With the preceding distribution function of Eq. (10), as an example, the following mean quantities can readily be evaluated according to Eq. (1)

$$\frac{\bar{u}}{u_\infty} = \frac{u_o}{u_\infty} = \int_{-\infty}^{\infty}\int_{0}^{\infty}\int_{-\infty}^{\infty} uf_1 dUdVdW + \int_{-\infty}^{\infty}\int_{-\infty}^{0}\int_{-\infty}^{\infty} uf_2 dUdVdW = \frac{\alpha_1 + \alpha_2}{2} \tag{11}$$

$$\frac{\overline{UU}}{u_\infty^2} = \frac{\alpha_3^2 + \alpha_4^2}{6} + \frac{(\alpha_1 - \alpha_2)^2}{4} \tag{12}$$

$$\frac{\overline{UV}}{u_\infty^2} = \frac{(\alpha_1 - \alpha_2)(\alpha_3 + \alpha_4)}{2\sqrt{6\pi}} \tag{13}$$

$$\frac{\overline{U_i U_i}}{u_\infty^2} = \frac{\bar{E}}{u_\infty^2} = \frac{\alpha_3^2 + \alpha_4^2}{2} + \frac{(\alpha_1 - \alpha_2)^2}{4} - \frac{(\alpha_3 - \alpha_4)^2}{6\pi} \tag{14}$$

$$\frac{\overline{U^2 V}}{u_\infty^3} = \frac{(\alpha_3 - \alpha_4)(\alpha_3 + \alpha_4)^2}{6\sqrt{6\pi}} \tag{15}$$

where α_i, $i = 1 - 4$, are defined as follows:

$$\alpha_1 = \frac{u_{o1}}{u_\infty}, \quad \alpha_2 = \frac{u_{o2}}{u_\infty}, \quad \alpha_3 = \frac{E_1^{1/2}}{u_\infty}, \quad \alpha_4 = \frac{E_2^{1/2}}{u_\infty}.$$

As we successively let $Q = 1$, U^2, V^2 and UV in Eq. (9), and by making use of Eq. (10), the following four equations result:

$$\sum_{j=1}^{4} A_{ij} \cdot \frac{d\alpha_j}{d\eta} = B_i, \quad i = 1\text{–}4 \tag{16}$$

where A_{ij}, for different i, and B_j are functions of α_j. For the convenience of specifying initial conditions, a simple transformation, which introduces new dependent variables, β_i, $i = 1-4$, and a new independent variable, ξ, as follows:

$$\xi = \eta - \eta_o, \tag{17}$$

$$\beta_1 = \alpha_1 + \alpha_2, \tag{18}$$

$$\beta_2 = \alpha_1 - \alpha_2, \tag{19}$$

$$\beta_3 = \alpha_3, \tag{20}$$

$$\beta_4 = \alpha_4. \tag{21}$$

where η_o is similarity coordinate corresponding to $u_o = \frac{1}{2}(u_\infty + u_{-\infty})$. Substituting this transformation into Eqs. (11)–(15) yields

$$\frac{u_o}{u_\infty} = \frac{\beta_1}{2} \tag{22}$$

$$\frac{\overline{UU}}{u_\infty^2} = \frac{\beta_3^2 + \beta_4^2}{6} + \frac{\beta_2^2}{4} \tag{23}$$

$$\frac{\overline{UV}}{u_\infty^2} = \frac{\beta_2(\beta_3 + \beta_4)}{2\sqrt{6\pi}} \tag{24}$$

$$\frac{\overline{U_iU_i}}{u_\infty^2} = \frac{\overline{E}}{u_\infty^2} = \frac{\beta_3^2 + \beta_4^2}{2} + \frac{(\beta_2)^2}{4} - \frac{(\beta_3 - \beta_4)^2}{6\pi} \tag{25}$$

$$\frac{\overline{U^2V}}{u_\infty^3} = \frac{(\beta_3 - \beta_4)(\beta_3 + \beta_4)^2}{6\sqrt{6\pi}} \tag{26}$$

And Eq. (16) becomes

$$\sum_{j=1}^{4} C_{ij} \cdot \beta_j' = D_i, \quad i = 1-4 \tag{27}$$

where the prime ($'$) denotes derivatives with respect to the independent variable ξ.

Initial Conditions. The above system of the resulting equations must be solved with appropriate initial conditions in ξ direction. Physically, it is expected that both upper and lower streams should impact the mechanics occurring within the mixing layer. Therefore, there is a need for two initial conditions in ξ direction reflecting the influence of the two bounding streams. However, the imposition of two ξ initial conditions upon Eq. (27) would seem to overspecify this problem because Eq. (27) is first order in ξ. Moreover, in practice it is difficult to locate the position and to specify the initial ξ_i values of the edges in the plane mixing layer. As for examples, Liepmann and Laufer (1947), Hackett and Cox (1967), and Spencer and Jones (1971) had experienced this difficulty in calculating the Reynolds stress distributions from the measured mean velocity profile in a plane mixing layer. As noted by Hackett and Cox (1967), their calculation is very sensitive to a small change in the position of the edge on the streaming side.

Table 1 Empirical inputs and initial conditions

	$r = 0$	$r = 0.3$	$r = 0.61$
ξ_o	0.022	0.	0.
$(k/\Delta u^2)_{\xi_o}$	0.0275*	0.0355†	0.0325†
$(-\overline{UV}/\Delta u^2)_{\xi_o}$	0.0103*	0.0132†	0.011†
$(\overline{UU}/\Delta u^2)_{\xi_o}$	0.032*	0.0375†	0.0287†
$(u_o/u_\infty)_{\xi_o}$	0.635*	0.64†	0.8†
$\beta_1(\xi_o)$	1.27	1.28	1.6
$\beta_2(\xi_o)$	0.24	0.179	0.0798
$\beta_3(\xi_o)$	0.186	0.157	0.091
$\beta_4(\xi_o)$	0.186	0.157	0.091

(* Patel, 1973; † Spencer, 1970).

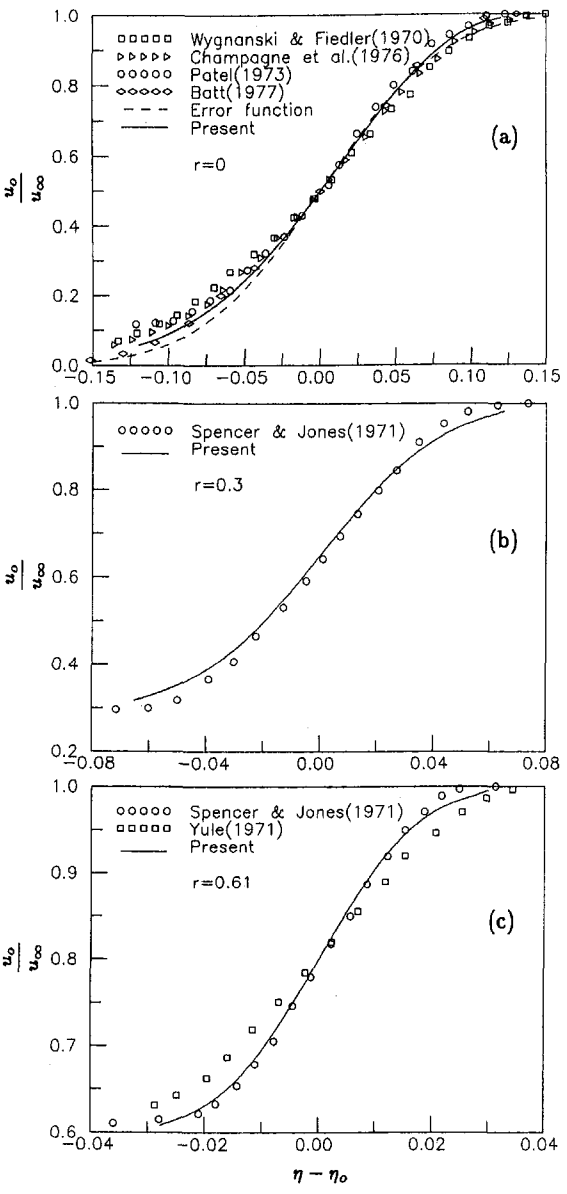

Fig. 2 Normalized profiles of the mean velocity

This difficulty is overcome by making use of an alternate initial condition in the present calculation. This specification involves empirical inputs as an initial condition. The initial conditions are to specify the values of β_i, $i = 1-4$, at the maximum $\overline{UV}$ point at which the streamwise component of the normal stresses is maximum, as observed in plane mixing layers (Bradshaw et al., 1964; Spencer and Jones, 1971; Patel, 1973). Furthermore, since experimental data indicates $V^2 \simeq W^2 \simeq \frac{1}{2} U^2$ and the maximums of V^2 and W^2 occurring near the half velocity point (Sami et al., 1967; Spencer and Jones, 1971; Patel, 1973), the peak position of turbulent kinetic energy, $k = \frac{1}{2}(U^2 + V^2 + W^2)$, may coincide approximately with that of $\overline{U^2}$. In addition, measured $\overline{U^2V}$ profile reveals antisymmetry about the zero axis that coincides approximately with the maximum $\overline{UV}$ point.

On the basis of the above indication of experimental data, accompanied by the inspection of Eqs. (22) through (26), the initial conditions may be readily determined. Regarding the peak values and their occurring positions of U^2, k and $\overline{UV}$ for different velocity ratio, the Rodi's review (1975) is used as a guideline. The data of Patel (1973) for the $r = 0$ layer and

Spencer (1970) for the $r = 0.61$ layer, which are recommended by Rodi (1975) based on the $\overline{UV}$ consistency check, are used to determined the initial conditions, β_{i_o}, $i = 1-4$, as shown in Table 1. For the $r = 0.3$ layer, Spencer's data (1970) are used again because the $r = 0.61$ layer performed by him are recommended by Rodi (1975). It is first observed that $\beta_{3_o} = \beta_{4_o}$ according to Eq. (26) because $\overline{U^2V}$ is zero at ξ_o where the subscript 'o' denotes the initial condition. Subsequently, subtracting Eq. (23) from equation (25) yields readily β_{3_o} ($= \beta_{4_o}$). β_{1_o} may be determined from Eq. (22) at ξ_o. Finally β_{2_o} at ξ_o is determined with the aid of Eq. (24). The resulting empirical inputs and initial conditions are tabulated in Table 1.

The initial conditions specified above are consistent with the mathematical character of equation (27) which requires only one initial condition in ξ direction. On the basis of these initial conditions, in the positive and negative ξ directions the solutions for the system of Eq. (27) may be easily obtained by using the finite difference technique. The split initial condition is therefore seen to provide for a consistent set of initial condition without overspecification.

IV Results and Discussion

The system of the resulting four equations satisfying the appropriate boundary conditions given in Table 1 was solved for four unknown functions, β_i, $i = 1-4$, by using the Runge-Kutta fourth-order numerical scheme. A uniform spacing of mesh points of 301 both in the positive and negative ξ directions were chosen in the present calculation after checking the grid independence. Subsequently, α_i, $i = 1-4$, and then the various mean quantities can be obtained by manipulating Eqs. (18)–(21) and Eq. (1), respectively.

In this section, various mean quantities calculated according to equation (1) are presented and discussed for the turbulence plane mixing layer geometry as shown in Fig. 1 with comparisons made when experimental data available. The study cases include the velocity ratio $r = 0$, 0.3 and 0.61 layers. The abscissa in the following figures is chosen as $(y - y_{0.5})/(x - x_o)$ $(=\eta - \eta_o)$ because deviation from similarity are easy to discern in such plots, even though Rodi (1975) argued that the velocity profiles agree well only when y is nondimensionalized by a characteristic flow width defined by $y_{0.9}-y_{0.1}$.

The streamwise mean velocity profiles for various velocity ratios are presented in Fig. 2. The calculated mean velocities are in close agreement with experimental data except at the low velocity edge, where the present calculation shows a slightly faster approach to the free-stream velocity than do the measurements. Also shown on Fig. 2(*a*) is Gortler's error function (Schlichting, 1960) for comparison with the present calculation. The calculated spreading rates along with the corresponding measurements are tabulated in Table 2. The calculated spreading rates for the $r = 0$ layer is in good agreement with the target value of 0.18–0.19, which 0.16 is recommended by Rodi (1975) based on $y_{0.9}-y_{0.1}$. The large scatter of experimental data as shown in Table 2 is attributed to the different initial conditions upstream of the splitter plate discontinuity (Bradshaw, 1966; Batt et al., 1970; Batt, 1975). For the $r = 0.3$ and $r = 0.61$ layers, an intermediate value of calculated spreading rate is obtained in the present calculation. In addition, for the $r = 0$ layer, the somewhat low spreading rate calculated by Haworth and Pope (1987) is also included for comparison.

Table 2 Measured and calculated spreading rates for plane mixing layer

$r = 0$ $\frac{d(y_{.95} - y_{.1})}{dx}$	Measured	Liepmann and Laufer (1947)	0.17
		Wygnanski and Fiedler (1970)	0.23
		Patel (1973)	0.19
		Champagne et al. (1976)	0.208
		Batt (1977)	0.18
	Calculated	Haworth and Pope (1987)	0.125–0.15
		Present	0.182
$r = 0.3$ $\frac{d(y_{.9} - y_{.1})}{dx}$	Measured	Spencer and Jones (1971)	0.078
		Yule (1971)	0.095
	Calculated	Present	0.0886
$r = 0.61$ $\frac{d(y_{.9} - y_{.1})}{dx}$	Measured	Spencer and Jones (1971)	0.0328
		Yule (1971)	0.046
	Calculated	Present	0.0345

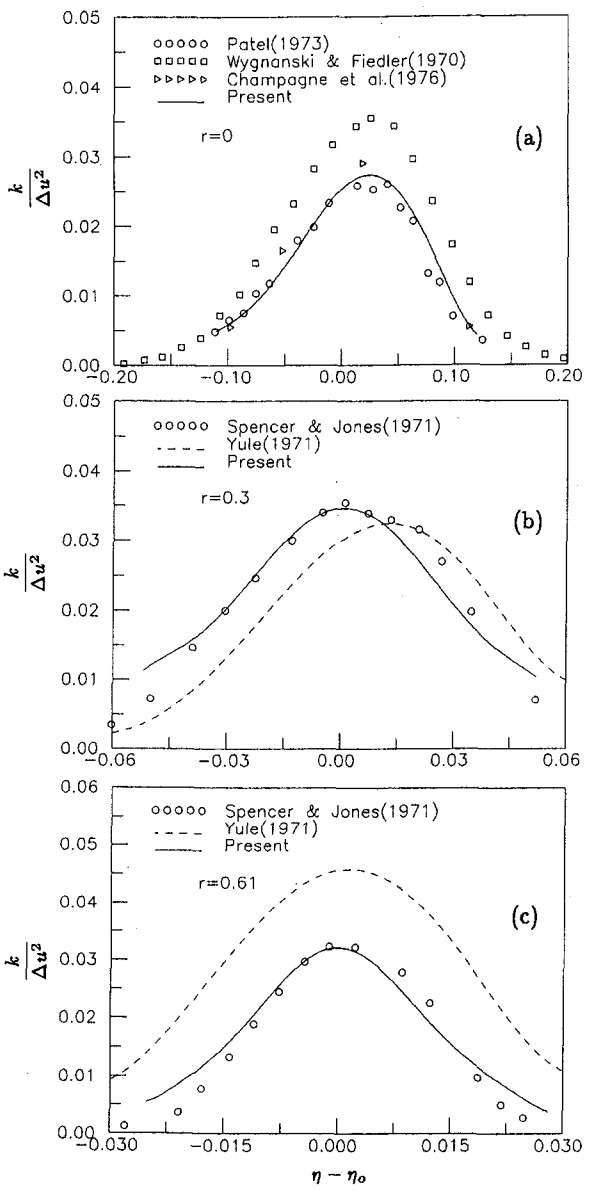

Fig. 3 Normalized profiles of the turbulence kinetic energy

Figure 3 shows the normalized turbulence energy profiles for three velocity ratios (the dashed lines indicate Yule's experimental data (1971) with hot wire yaw effect correction). It is obvious that the calculated k profiles agree with the experimental data whose peak values are the empirical inputs for the determination of the initial conditions for the present calculation. However, the calculated results extend too far into the edges of the mixing layer for $r = 0.3$ and $r = 0.61$ cases. For the $r = 0$ layer, the calculated profile compares better with the data of Champagne et al. (1976) at the high velocity side, whereas for $\eta - \eta_o < 0$ the calculated results and the experimen-

tal data appear to collapse together on the low velocity side. Also shown in Fig. 3(a) for comparison are the Wygnanski and Fiedler's data (1970) which its peak value is about 25 percent greater than that of Patel (1973) and the present calculation. Figure 3(b) shows the calculated results agreement with Spencer and Jones' data (1971) in the central region while the Yule's data tend to be shifted toward the high velocity side. For the $r = 0.61$ layer, for comparison, the Yule's data (1971) is also included whose peak value is about 40 percent greater than that of Spencer and Jones and the present calculation. These differences will be discussed later.

For comparison with the Haworth and Pope calculation (1987), their prediction and the present calculated profiles of normal stresses are depicted in Fig. 4 (the dashed lines indicates Haworth and Pope's calculation (1987) with GL model). As shown in Haworth and Pope's paper (1987), by plotting their calculated normal stresses vs $(y - y_{0.5})/(y_{0.9} - y_{0.1})$ the comparison showed a good agreement with the experimental data of Wygnanski and Fiedler (1970), Patel (1973), and Champagne et al. (1976). It can be seen from Fig. 4 that when their calculated distributions are replotted the agreement with these data

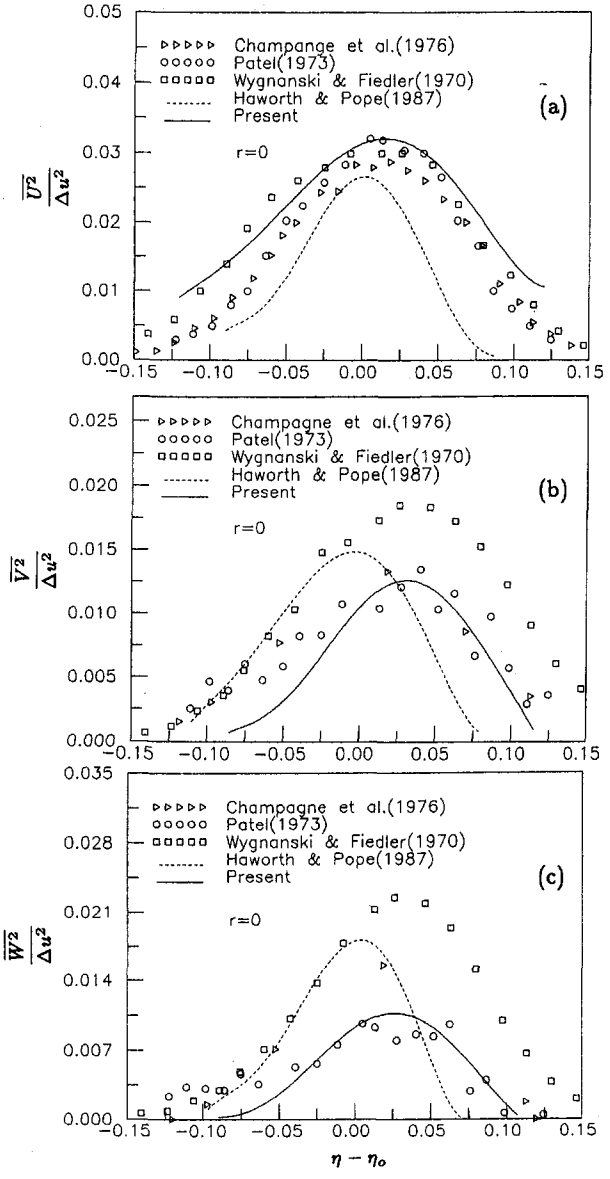

Fig. 4 Normalized profiles of the normal stresses for the $r = 0$ layer

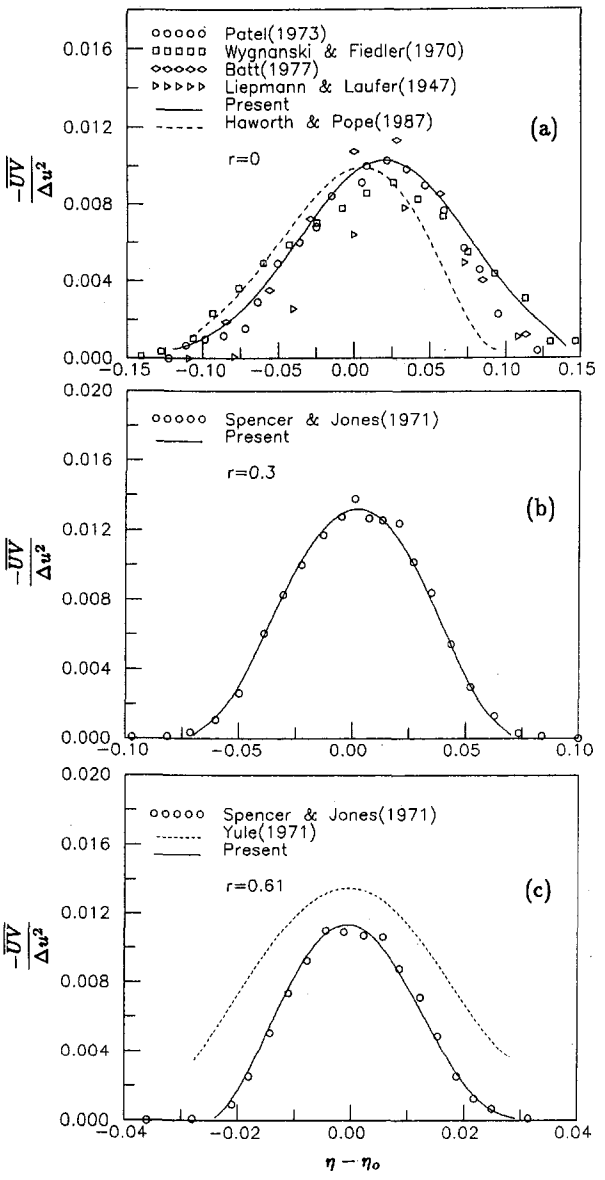

Fig. 5 Normalized profiles of the Reynolds shear stress

is poor. It should be noted that the present way of plotting the results is preferred because deviation from similarity are easy to discern in such plots. Unlike the Haworth and Pope's calculation (1987), the present calculation shows general agreement with these experimental data.

The solution of Reynolds stress that is presented in Fig. 5 is compared with the experimental data and the available calculated profiles. Agreement with the experimental data as to both profiles shape and magnitude of the shear stresses is quite good for three velocity ratios. In Fig. 5(a), for comparison, the calculated Reynolds stresses profiles by Haworth and Pope (1987) using pdf method is also included. Their prediction in the present similarity plot exhibits a rather poor agreement at the high velocity side than do the present calculation. Also shown in Fig. 5(c) is Yule's data presented by dashed line for the velocity ratio 0.61 case. The greater magnitude of $\overline{UV}$ (Fig. 5(c)) and k (Fig. 3(c)) of Yule's data is attributed to the effect of free-stream turbulence generated by the duct boundary layers, as argued by Rodi (1975). For the $r = 0$ layer, the calculated maximum value of the correlation coefficient $\overline{UV}/((\overline{U^2})^{1/2}(\overline{V^2})^{1/2})$ was 0.52 comparable with 0.57 and 0.54

measured by Liepmann and Laufer (1947) and Patel (1973), respectively.

In view of the general agreement in turbulence structure (u_o, k and $\overline{UV}$) discussed above, it was felt that it might be instructive to compare further the higher-order moments of available experimental data with the present calculation. Therefore, the comparisons for moments to fourth order are presented in the following. Most investigators, except Spencer (1970), Wygnanski and Fiedler (1970) and Champagne et al. (1976), ignored correlation functions higher than second order in both their theoretical and experimental analyses. The higher the orders of the correlations, the harder the measurements, and more difficult is analytical analysis by the conventional mean gradient type approach, which would require more parameters to be determined by experiments. In this paper the higher order moments also were calculated.

The third-order correlation $\overline{UE}$ and $\overline{VE}$, where $\bar{E} = U^2 + V^2 + W^2$, represent physically the transport of turbulence energy by the U- and V-component velocity fluctuations while the correlation $\overline{WE}$ is zero by symmetry. The directions and magnitudes of the turbulence energy transport can be illustrated by the knowledge of the third-order correlations. Moreover, it is necessary to know their distributions to evaluate the diffusion term in the turbulence energy balance. These U- and V-component transport of turbulent kinetic energy (TKE) in transverse direction and their breakdown into component for the $r = 0$ layer are shown in Figs. 6 and 8, respectively. Both correlations in Fig. 6 show antisymmetry about the zero axes indicating uniform transport of turbulence energy away from the mixing layer centerline. That the direction of transport is indeed away from the central region is easily verified by noting the correlations of $\overline{VE}$ and its breakdown into component to be positive on the high velocity side and negative on the low velocity side. Hence higher than locally average $\bar{E}$ is correlated with outwardly directed V. Similarly the transport of energy toward the boundaries by V is accompanied on the high velocity side by a negative (or slower than local average) U-component fluctuation, and oppositely on the low velocity side. As shown in Fig. 6, a better agreement with available data is predicted at the low velocity side.

A lateral convection velocity V^* may be defined to represent the lateral transport of turbulence energy (Townsend, 1956; Hinze, 1959):

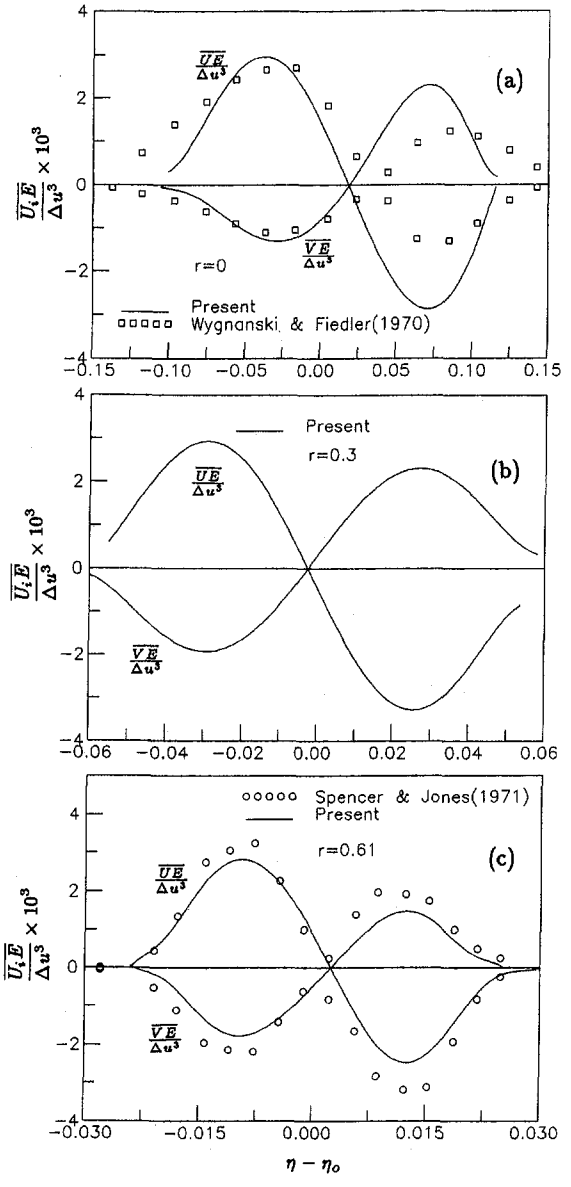

Fig. 6 Transport of turbulence kinetic energy by velocity fluctuations

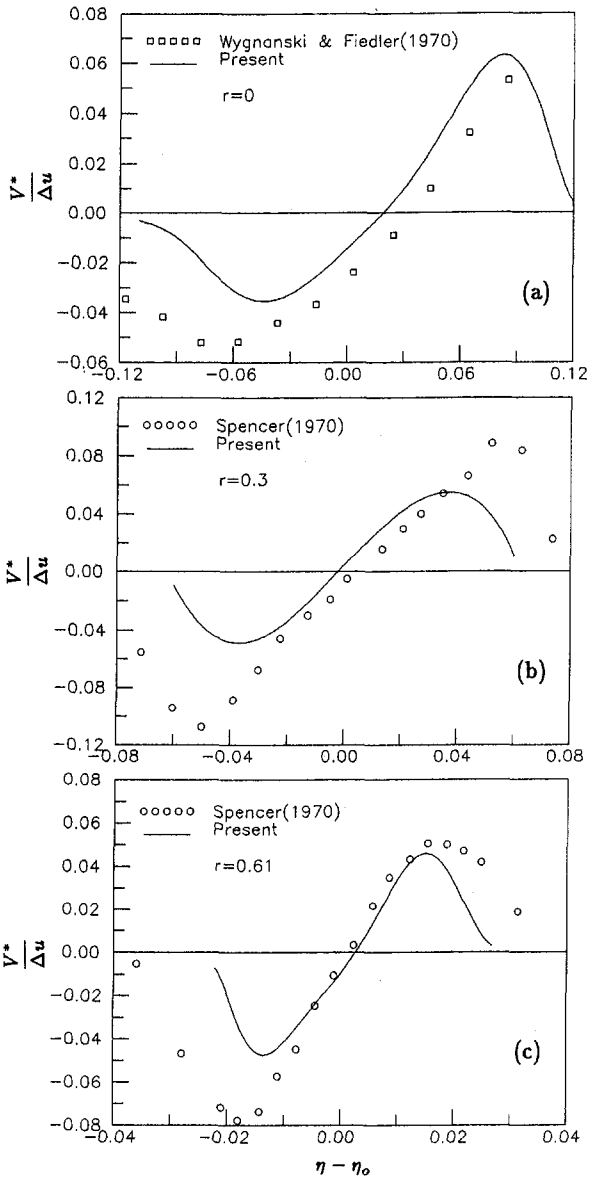

Fig. 7 Normalized profiles of the bulk convection velocity

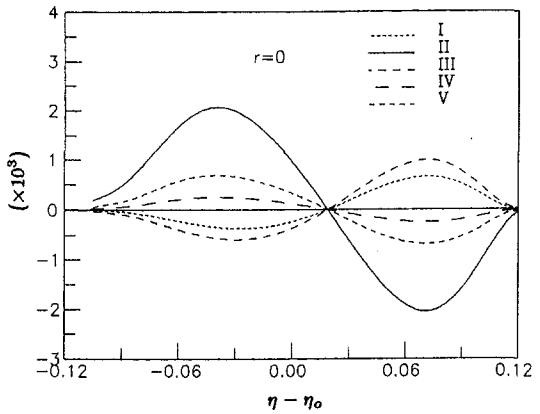

Fig. 8 Normalized profiles of the third-order cross products. I, $\overline{U^2V}/\Delta u^3$, $\overline{VW^2}/\Delta u^3$; II, $\overline{U^3}/\Delta u^3$; III, $\overline{V^3}/\Delta u^3$; IV, $\overline{UV^2}/\Delta u^3$; V, $\overline{UW^2}/\Delta u^3$.

$$V^* = \frac{\overline{VE}}{\overline{E}} \tag{28}$$

This calculated quantity, normalized by the velocity difference across the mixing layer, is presented in Fig. 7. As expected, the effective transport velocity is directed toward the mixing layer boundaries. Agreement between the prediction and measurements is generally satisfactory in the central region though the calculation displays a somewhat large difference at both edges of the mixing layer. Figure 9 illustrates the calculated distributions of the various fourth-order correlations for the $r = 0$ layer. The distributions of U^4, UV^3 and U^3V shown in this figure show symmetry about the zero axis whereas V^4 and W^4 tend to be shifted toward the high velocity side.

The calculated vs measured skewness and flatness factors for the $r = 0.61$ layer are tabulated in Table 3. As the table indicates, in the central region of the flow ($\eta - \eta_o = 0.002$) the U-component fluctuations are nearly Gaussian. When away from the central region of the flow, the non-Gaussian nature of the flow appears. Agreement of this calculated statistical quantities with experiments is generally satisfactory in the central region ($\eta - \eta_o = 0.002$) of the mixing layer though the calculated results display a somewhat larger difference at the intermittent edges ($\eta - \eta_o = -0.0145, 0.0185$). The skewness of the velocity is explained with the turbulence emanating from the central region of the flow. The convected turbulent elements have an impelling effect on the low velocity side and a retarding effect on the high velocity side; hence the corresponding positive and negative skewness factors in these regions.

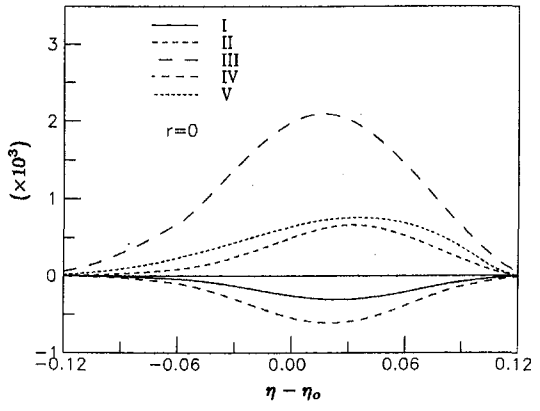

Fig. 9 Normalized profiles of the fourth-order cross products. I, $\overline{UV^3}/\Delta u^4$; II, $\overline{V^4}/\Delta u^4$; III, $\overline{U^4}/\Delta u^4$; IV, $\overline{U^3V}/\Delta u^4$; V, $\overline{W^4}/\Delta u^4$.

Table 3 Measured versus calculated skewness and flatness for plane mixing layer with velocity ratio r of 0.61

		u-component fluctuations		v-component fluctuations		w-component fluctuations	
	$\eta - \eta_0$	Spencer (1970)	Present	Spencer (1970)	Present	Spencer (1970)	Present
Skewness	−0.0145	1.38	0.86	−0.85	−1.04	0.16	0
	0.002	0.01	0.015	0.23	−0.019	0	0
	0.0185	−1.5	−0.87	0.99	1.33	−0.17	0
Flatness	−0.0145	5.56	3	4.42	3.78	5.45	4.97
	0.002	2.59	2.5	3.11	3.29	3.18	3
	0.0185	6.5	3.2	6.41	4.97	5.76	4.81

To check the turbulent kinetic energy (TKE) balance, the nondimensionalized TKE equation derived from (8) by substituting $Q = E = U^2 + V^2 + W^2$ is obtained as,

$$\left(\eta\frac{u_o}{u_\infty} - \frac{v_o}{u_\infty}\right)\frac{d}{d\eta}\left(\frac{\overline{E}/2}{\Delta u^2}\right) + \frac{\overline{UV}}{\Delta u^2}\left[\eta\frac{d}{d\eta}\left(\frac{v_o}{u_\infty}\right) - \frac{d}{d\eta}\left(\frac{u_o}{u_\infty}\right)\right]$$

$$+ \frac{(\overline{U^2} - \overline{V^2})}{\Delta u^2}\eta\frac{d}{d\eta}\left(\frac{u_o}{u_\infty}\right) + (1 - r)\left[\eta\frac{d}{d\eta}\left(\frac{\overline{UE}/2}{\Delta u^3}\right)\right.$$

$$\left. - \frac{d}{d\eta}\left(\frac{\overline{VE}/2}{\Delta u^3}\right)\right] - \frac{\epsilon(x - x_o)}{u_\infty \Delta u^2} = 0 \tag{29}$$

The above equation serves as a basis for evaluating the contribution of turbulence characteristics to TKE balance. The terms, in turn, denote the contribution of the convection by mean flow, the production by Reynolds stress, the production by mean flow, the turbulent diffusion, and the viscous dissipation. The contribution of the pressure diffusion, which is not included in the present model, will be determined by what is required to establish the energy balance.

All the terms in Eq. (29) have been calculated and the pressure diffusion also was determined by energy balance. For clarity, Eq. (29) is condensed to the following form:

$$C + P + T + D = 0 \tag{30}$$

where $C = \eta(u_o/u_\infty)(d/d\eta)((\overline{E}/2)/\Delta u^2) - (v_o/u_\infty)(d/d\eta)((\overline{E}/2)/\Delta u^2)$ denote the convection of TKE by the mean flow, while $P = -(\overline{UV}/\Delta u^2)(d/d\eta)(u_o/u_\infty)$ the production by Reynolds stress, $T = T_p - (1 - r)(d/d\eta)((\overline{VE}/2)/\Delta u^3)$ the diffusion by fluctuating velocity and fluctuating pressure gradients, $D = -(\epsilon(x - x_o)/u_\infty \Delta u^2)$ the viscous dissipation, and T_p the diffusion by fluctuating pressure gradient that is determined by what is required to establish the energy balance. Figure 10 shows the TKE balance for three velocity ratios. It is first observed that the overall trend of the calculated distributions is similar, regardless of the different velocity ratio. This character of the energy balance is consistent with the argument by Rodi (1975). In the figure, as anticipated, the production of TKE exceeds the viscous dissipation that is underpredicted in the present calculation. Since the mixing layer is self-preserving this net accumulation of energy in the central region must be transported toward the boundaries to participate in the mixing layer spread. The role of the diffusion term T is to do exactly this. The net effect of the mean flow is the removal of energy from the edge regions as shown in this figure.

V Concluding Remarks

The pdf turbulent equation model developed earlier by the present authors have been solved with an approximate moment method to calculate the one-point statistical quantities of a turbulent plane free mixing layer flow. The solutions of this equation yield the various one-point mean quantities for

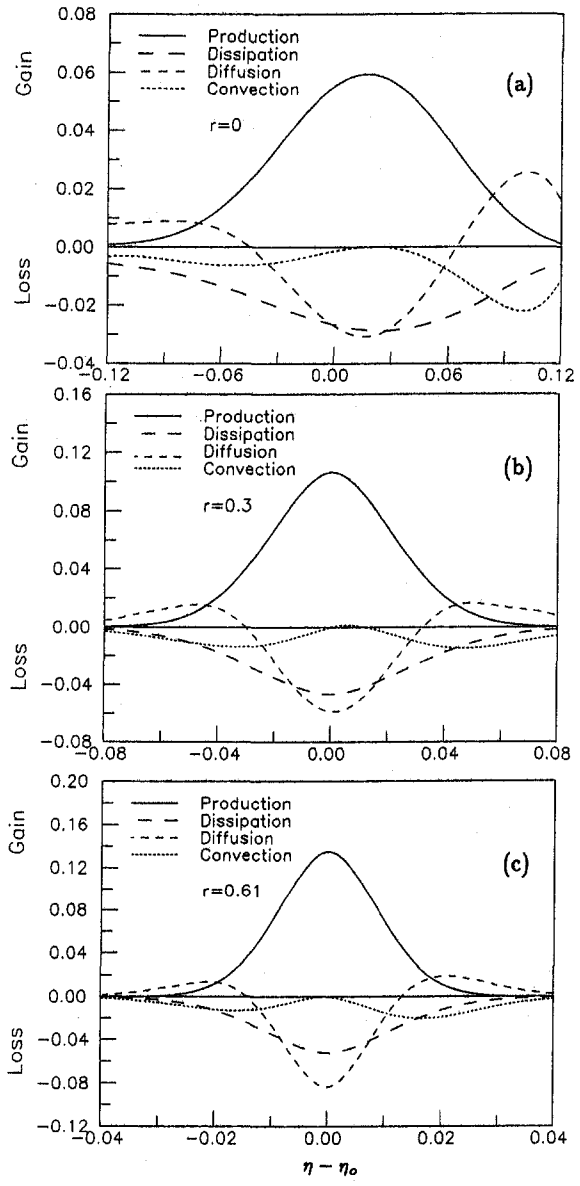

Fig. 10 The turbulence kinetic energy balance

the flow problem of the present interest. The calculated mean velocity, turbulent energy, Reynolds stress, turbulent energy transport, skewness factors are compared with the available experimenta data and show generally satisfactory agreements. These agreements show that the pdf equation model can satisfactorily describe the statistics of free turbulence. Besides these results, the turbulence energy balance were also calculated and discussed. It shows that the pdf methods are of more potential in revealing turbulence structure than conventional turbulence models.

References

Batt, R. G., Kubota, T., and Laufer, J., 1970, "Experimental Investigation of the Effect of Shear Flow Turbulence on a Chemical Reaction," AIAA Paper 70–721.

Batt, R. G., 1975, "Some Measurements on the Effect of Tripping the Two-Dimensional Shear Layer," *AIAA Journal,* Vol. 13, No. 2, pp. 245–247.

Batt, R. G., 1977, "Turbulent Mixing of Passive and Chemically Reacting Species in a Low-Speed Shear Layer," *Journal of Fluid Mechanics,* Vol. 82, pp. 53–95.

Bradshaw, P., 1966, "The Effect of Initial Conditions on the Development of a Free Shear Layer," *Journal of Fluid Mechanics,* Vol. 26, pp. 225–236.

Bradshaw, P., Ferriss, D. H., and Johnson, R. F., 1964, "Turbulence in the Noise-producing Region of a Circular Jet," *Journal of Fluid Mechanics,* Vol. 19, pp. 591–624.

Bywater, R. J., 1981, "Velocity Space Description of Certain Turbulent Free Shear Flow Characteristics," *AIAA Journal,* Vol. 19, No. 8, pp. 969–975.

Cebeci, T., and Smith, A. M. O., 1974, *Analysis of Turbulent Boundary Layers,* Academic Press, New York.

Champagne, F. H., Pao, Y. H., and Wygnanski, I. J., 1976, "On the Two-Dimensional Mixing Region," *Journal of Fluid Mechanics,* Vol. 74, pp. 209–250.

Chung, P. M., 1967, "A Simplified Statistical Description of Turbulence Chemically Reacting Flows," Aerospace Report TR-1001-S2855-20-5.

Chung, P. M., 1972, "Diffusion Flames in Homologous Turbulent Shear Flows," *The Physics of Fluids,* Vol. 15, No. 10, pp. 1735–1746.

Gortler, H., 1942, "Brechnung von Aufgaben der freien Turbulenz auf Grund eines neuen Naherungsansatzes," *Zeitschrift fur Angewandte Mathematik und Mechanik,* Vol. 22, pp. 244–254.

Hackett, J. E., and Cox, D. K., 1967, "Measurements in a Three-dimensional Mixing Layer Between Two Grazing Perpendicular Streams," Aero Report 1248-A.R.C. 29544, N.P.L. Aerodynamics Division, England.

Haworth, D. C., and Pope, S. B., 1986, "A Generalized Langevin Model for Turbulent Flows," *Physics of Fluids,* Vol. 29, pp. 387–405.

Haworth, D. C., and Pope, S. B., 1987, "A pdf Modeling Study of Self-similar Turbulent Free Shear Flows," *Physics of Fluids,* Vol. 30, pp. 1026–1044.

Hinze, J. O., 1959, *Turbulence,* McGraw-Hill, New York, N.Y.

Hong, Z. C., 1975, "Turbulent Reacting Flows According to a Kinetic Theory," Ph.D. thesis, University of Illinois.

Hong, Z. C., and Lai, Z. C., 1983, "On the Mixing Analysis of a Free Turbulence Shear Layer," *The Chinese Journal of Mechanics,* Vol. 1, No. 1, pp. 25–33.

Hong, Z. C., Lin, C., and Chen, M. H., 1993, "An Eulerian One-point Velocity Probability Density Function Model for Turbulent Flows," *The Chinese Journal of Mechanics,* Vol. 9, No. 3, pp. 167–179.

Hong, Z. C., Lin, C., and Chen, M. H., 1995, "A PDF Description of Turbulent Plane Couette Flow," *International Journal of Numerical Methods for Heat and Fluid Flow,* Vol. 5, No. 9, pp. 757–779.

Jones, I. S. F., 1976, "The Maintenance of Turbulent Shear Stress in a Mixing Layer," *Journal of Fluid Mechanics,* Vol. 74, pp. 269–295.

Lakshminarayana, B., 1986, "Turbulence Modeling for Complex Shear Flows," *AIAA Journal,* Vol. 24, No. 12, pp. 1900–1917.

Launder, B. E., and Spalding, D. E., 1972, *Mathematical Models of Turbulence,* Academic, New York.

Lee, S. C., and Harsha, P. T., 1970, "Use of Turbulent Kinetic Energy in Free Mixing Studies," *AIAA Journal,* Vol. 8, No. 6, pp. 1026–1032.

Liepmann, H. W., and Laufer, J., 1947, "Investigation of Free Turbulent Mixing," NACA TN 1257.

Liu, C. Y., and Lees, L., 1961, "Kinetic Theory Description of Plane Compressible Couette Flow," *Rarefied Gas Dynamics,* L. Talbot, ed., Academic Press, New York, pp. 391–428.

Mohammadian, S., Saiy, M., and Peorless, S. J., 1976, "Fluid Mixing with Unequal Free-stream Turbulence Intensities," ASME JOURNAL OF FLUIDS ENGINEERING, pp. 229–242.

Naot, D., Shavit, A., and Wolfshtein, M., 1970, "Interactions between Components of the Turbulent Velocity Correlation Tensor," *Israel Journal of Technology,* Vol. 8, pp. 259–265.

Patel, R. P., 1973, "An Experimental Study of a Plane Mixing Layer," *AIAA Journal,* Vol. 11, No. 1, pp. 67–73.

Pollard, A., and Martinuzzi, R., 1989, "Comparative Study of Turbulence Models in Predicting Turbulent Pipe Flow Part II: Reynolds Stress and k–ϵ Models," *AIAA Journal,* Vol. 27, No. 12, pp. 1714–1721.

Pollard, A., and Siu, A. L.-W., 1982, "The Calculation of Some Laminar Flows Using Various Discretisation Schemes," *Computer Methods in Applied Mechanics and Engineering,* Vol. 35, pp. 293–313.

Pope, S. B., 1984, "Calculations of a Plane Turbulent Jet," *AIAA Journal,* Vol. 22, pp. 896–904.

Pope, S. B., 1985, "PDF Methods for Turbulent Reactive Flows," *Progress in Energy and Combustion Science,* Vol. 11, pp. 119–192.

Pope, S. B., and Chen, Y. L., 1990, "The Velocity-dissipation Probability Function Model for Turbulent Flows," *Physics of Fluids A,* Vol. 2, pp. 1437–1449.

Pope, S. B., 1991, "Application of the Velocity-dissipation Probability Density Function Model to Inhomogeneous Turbulent Flows," *Physics of Fluids A,* Vol. 3, pp. 1947–1957.

Pope, S. B., 1994, "Lagrangian PDF Methods for Turbulent Flows," *Annual Review of Fluid Mechanics,* Vol. 26, pp. 23–63.

Rodi, W., 1975, "A Review of Experimental Data of Uniform Density Free Turbulent Boundary Layers," *Studies in Convection,* B. E. Launder, ed., Academic, New York, pp. 79–165.

Rotta, J. C., 1951, "Statistische Theorie Nichthomogener Turbulenz," *Zeitschrift fuer Physik,* Vol. 192, pp. 547–572.

Sami, S., Carmody, T., and Rouse, H., 1967, "Jet Diffusion in the Region of Flow Establishment," *Journal of Fluid Mechanics,* Vol. 27, pp. 231–252.

Schlichting, H., 1960, *Boundary Layer Theory,* McGraw-Hill, New York, N.Y.

Spencer, B. W., 1970, "Statistical Investigation of Turbulent Velocity and Pressure Fields in a Two-stream Mixing Layer," Ph.D. thesis, University of Illinois.

Spencer, B. W., and Jones, B. C., 1971, "Statistical Investigation of Pressure and Velocity Fields in the Turbulent Two-stream Mixing Layer," AIAA paper 71-613.

Tennekes, H., and Lumley, J. L., 1972, *A First Course in Turbulence,* MIT Press, Cambridge, MA.

Tollmien, W., 1926, "Berechnung Turbulenter Ausbreitungsvorgange," *Zeitschrift fur Angewandte Mathematik und Mechanik,* Vol. 6, pp. 468–478.

Townsend, A. A., 1956, *The Structure of Turbulent Shear Flow,* Cambridge University Press, London.

Wygnanski, I., and Fiedler, H. E., 1970, "The Two-Dimensional Mixing Region," *Journal of Fluid Mechanics,* Vol. 41, pp. 327–361.

Yule, A. J., 1971, "Two-Dimensional Self-Preserving Turbulent Mixing Layers at Different Free-Stream Velocity Ratios," ARC 32 732, FM 4213.

Numerical Calculation of the Fully Developed Turbulent Flow in an Axially Rotating Pipe With a Second-Moment Closure

K.-J. Rinck
Research Associate.

H. Beer
Professor.

Technische Universität Darmstadt,
Institut für Technische Thermodynamk,
Petersenstr. 30,
64287 Darmstadt, Germany

The effect of axial tube rotation on the fully developed pipe flow is analyzed by a low-Reynolds-number turbulence closure and compared with experimental results. A flow which is initially turbulent is stabilized by the rotation leading to a laminarized mean axial velocity distribution. The applied second-moment closure reveals an encouraging ability to capture this phenomenon as well as other features of the mentioned flow configuration. The "rapid" part of the pressure-strain correlation model is found to have a significant influence on the numerical results and seems to be the key for further improvements concerning highly swirling flows.

1 Introduction

The turbulent fluid flow in a circular pipe, which rotates around its axis, is a basic engineering problem arising frequently in the field of rotating machinery.

Comprehensive experimental investigations are known by Murakami and Kikuyama (1980), Kikuyama et al. (1983), and Reich and Beer (1989). In the two latter papers the authors were also engaged in calculating the fully developed turbulent flow numerically by using a mixing length hypothesis, modified by the introduction of the Richardson number, which was required to capture the influence of streamline curvature on the axial turbulent shear stress $\overline{v_r v_z}$. Numerical approaches using a $k-\epsilon$-model were performed by Hirai et al. (1988). Because the sensitivity of the standard $k-\epsilon$-model to the streamline curvature is much too weak, they also had to introduce a correction term proportional to the Richardson number.

Though the flow geometry is quite simple, the theoretical analysis is complicated. There exist two counter effects imposed by the rotation having a strong influence on the distribution of the Reynolds stresses: On the one hand, additional terms in the transport equations for $\overline{v_i v_j}$, similar to the centrifugal and the coriolis force in the momentum equations, lead to a flow laminarization suppressing the fluctuation velocities (Hirai et al., 1988). On the other hand, the rotation of the pipe wall causes a tangential shear stress which represents an additional source of turbulence energy and destabilizes the flow. Provided that the rotational Reynolds number Re_φ is sufficiently large the latter effect causes a reduction of the critical Reynolds number of the pipe flow from the empirical value of $\mathrm{Re}_{cr} = 2300$ for the nonswirling flow to values below 200, which was shown by Nagib et al. (1971) experimentally and by Mackrodt (1976) numerically.

In a flow which is initially turbulent the stabilizing effect prevails (Nishibori et al., 1987). Hence, for the fully developed rotating pipe flow one can observe a laminarized axial velocity distribution and, therefore, a reduced pressure loss as compared to the flow in a stationary pipe.

Due to a linear distributed tangential Reynolds shear stress $\overline{v_r v_\varphi}$ in the fully developed flow, the mean tangential velocity profile becomes parabolic. Hirai et al. (1988) showed that any eddy viscosity model fails to calculate this tangential velocity distribution correctly predicting a rigid body rotation, which corresponds to a vanishing Reynolds stress $\overline{v_r v_\varphi}$. Moreover, they showed that a Reynolds stress turbulence model captures this phenomenon as well as the laminarization effect.

This paper intends to provide a comprehensive investigation for various Reynolds numbers and rotation rates N using the low-Reynolds-number second-moment closure of Launder and Shima (1989) in a slightly modified form.

2 Analysis

2.1 Basic Equations in Cylindrical Coordinates. The analysis is based on a time-smoothed fully developed axisymmetric pipe flow with or without rotation, which means that the time-smoothed radial velocity V_r and all derivatives $\partial/\partial t$, $\partial/\partial\varphi$ and $\partial/\partial z$, except the term $\partial P/\partial z$, become zero in the entire solution domain. Therefore, the conservation equation of mass vanishes as well.

Considering a Newtonian fluid with constant properties, the conservation equations of momentum in cylindrical coordinates take the following form:

$$\frac{r}{\rho}\frac{\partial P}{\partial r} = V_\varphi^2 - \frac{\partial}{\partial r}\left(r\overline{v_r v_r}\right) + \overline{v_\varphi v_\varphi} \tag{1}$$

$$0 = \nu\frac{\partial}{\partial r}\left(r^3\frac{\partial}{\partial r}\left(\frac{V_\varphi}{r}\right)\right) - \frac{\partial}{\partial r}\left(r^2\overline{v_r v_\varphi}\right) \tag{2}$$

$$\frac{r}{\rho}\frac{\partial P}{\partial z} = \nu\frac{\partial}{\partial r}\left(r\frac{\partial V_z}{\partial r}\right) - \frac{\partial}{\partial r}\left(r\overline{v_r v_z}\right) \tag{3}$$

The transport equations for the Reynolds stresses of a fully developed flow in cylindrical coordinates can be written as

$$\frac{D\overline{v_i v_j}}{Dt} = 0 = P_{ij} + \nu_{ij} + \Phi_{ij} + d_{ij} - \epsilon_{ij} + R_{ij}. \tag{4}$$

In this equation

$$P_{ij} \equiv -\left[\overline{v_i v_r}\frac{\partial V_j}{\partial r} + \overline{v_j v_r}\frac{\partial V_i}{\partial r}\right] \tag{5}$$

Contributed by the Fluids Engineering Division for publication in the JOURNAL OF FLUIDS ENGINEERING. Manuscript received by the Fluids Engineering Division March 4, 1997; revised manuscript received January 12, 1998. Associate Technical Editor: C. L. Merkle.

is the stress generation rate by mean shear,

$$\nu_{ij} = \nu \frac{\partial}{\partial r}\left(\frac{\partial \overline{v_i v_j}}{\partial r}\right) \tag{6}$$

the viscous diffusion,

$$\Phi_{ij} \equiv \overline{\frac{p}{\rho}\left(\frac{\partial v_i}{\partial x_j} + \frac{\partial v_j}{\partial x_i}\right)} \tag{7}$$

the pressure-strain correlation,

$$d_{ij} \equiv -\frac{\partial}{\partial r}\left(\overline{v_i v_j v_r} + \frac{1}{\rho}\overline{p v_i}\delta_{jr} + \frac{1}{\rho}\overline{p v_j}\delta_{ir}\right) \tag{8}$$

the turbulent diffusion and

$$\epsilon_{ij} \equiv 2\nu \overline{\frac{\partial v_i}{\partial x_k}\frac{\partial v_j}{\partial x_k}} \tag{9}$$

the dissipation rate. In

$$R_{ij} = P_{ij,\text{add}} + \nu_{ij,\text{add}} - C_{ij,\text{add}} + \Phi_{ij,2,\text{add}} + d_{ij,\text{add}} \tag{10}$$

all additional terms that arise due to the transformation from the cartesian into the cylindrical coordinate system are summarized. These terms are listed in Table 1.

2.2 Turbulence Model. In a second-moment closure the stress generation rate P_{ij} and the viscous diffusion ν_{ij} can be calculated exactly, whereas for the pressure strain correlation Φ_{ij}, the turbulent diffusion d_{ij} and the dissipation rate ϵ_{ij} a modelling is required. In this investigation, a slightly modified form of the second-moment closure proposed by Launder and Shima (1989) is adopted, which has proved to be reliable in its almost original version (only the chosen models for d_{ij} are different) for the complex swirling flow in an axially rotating annulus (Rothe and Beer, 1994).

Concerning the modeling of the pressure-strain correlation one distinguishes four different terms:

$$\Phi_{ij} = \Phi_{ij,1} + \Phi_{ij,2} + \Phi^w_{ij,1} + \Phi^w_{ij,2} \tag{11}$$

where $\Phi_{ij,1}$ denotes the so-called "return-to-isotropy" part, $\Phi_{ij,2}$ represents the "rapid" term and $\Phi^w_{ij,1}$ as well as $\Phi^w_{ij,2}$ are supposed to capture the "echo" effects caused by the reflection of pressure fluctuations from a rigid wall.

For $\Phi_{ij,1}$ the "return-to-isotropy" model proposed by Rotta (1951) is adopted

$$\Phi_{ij,1} = -c_1 \epsilon a_{ij} \tag{12}$$

with the dimensionless anisotropic parts of the Reynolds stresses

$$a_{ij} = \frac{\overline{v_i v_j}}{k} - \frac{2}{3}\delta_{ij}. \tag{13}$$

In Launder and Shima's model the isotropization of production (IP) model is suggested for the "rapid" term, but the isotropization of production and convection (IPC) model was found to provide better results in complex swirling flows (Eggels, 1994; Ohtsuka, 1995):

$$\Phi_{ij,2} = -c_2(P_{ij} - \tfrac{2}{3}\delta_{ij}P_k - C_{ij} + \tfrac{2}{3}\delta_{ij}C_k). \tag{14}$$

P_k and C_k can be reduced to

$$P_k \equiv \frac{1}{2}P_{kk} = -\overline{v_r v_z}\frac{\partial V_z}{\partial r} - \overline{v_r v_\varphi}\frac{\partial V_\varphi}{\partial r} \quad \text{and}$$

$$C_k \equiv \frac{1}{2}C_{kk} = 0 \tag{15}$$

for this application. In a fully developed flow the regular convective terms C_{ij} vanish, in contrast to the additional terms $C_{ij,\text{add}}$ which result from the coordinate transformation and arise in $\Phi_{ij,2,\text{add}}$ (see Eq. (10) and Table 1).

The "echo" effects, which become dominant in the vicinity of a solid wall, are expressed by (Launder and Shima, 1989):

$$\Phi^w_{ij,1} = c_1^w \frac{\epsilon}{k}\left(\overline{v_k v_m}n_k n_m \delta_{ij} - \frac{3}{2}\overline{v_k v_i}n_k n_j - \frac{3}{2}\overline{v_k v_j}n_k n_i\right) f \tag{16}$$

$$\Phi^w_{ij,2} = c_2^w(\Phi_{km,2}n_k n_m \delta_{ij} - \tfrac{3}{2}\Phi_{ik,2}n_k n_j - \tfrac{3}{2}\Phi_{jk,2}n_k n_i) f \tag{17}$$

with the near-wall damping function

$$f = 0.4\frac{k^{3/2}}{\epsilon x_2}, \tag{18}$$

where x_2 represents the distance normal to the wall.

In order to extend the turbulence model to the near-wall sublayer, Launder and Shima suggest expressing c_1, c_2, c_1^w, and c_2^w in the pressure-strain correlation as functions of the turbulent Reynolds number

$$\mathrm{Re}_t \equiv \frac{k^2}{\nu\epsilon} \tag{19}$$

and the two independent Reynolds stress invariants

$$A_2 \equiv a_{ik}a_{ki} \quad \text{and} \quad A_3 \equiv a_{ik}a_{kj}a_{ji}. \tag{20}$$

The parameter

$$A \equiv 1 - \tfrac{9}{8}(A_2 - A_3) \tag{21}$$

represents the "flatness" of the turbulence and ranges from

Nomenclature

C_{ij} = convection terms for $\overline{v_i v_j}$
k = turbulent kinetic energy $\frac{1}{2}\overline{v_i v_i}$
N = rotation rate $V_{\varphi,w}/\bar{V}_z$
n_i = component in i-direction of the unit vector normal to wall
P = time mean pressure
p = pressure fluctuation
P_k = shear generation rate of k
R = pipe radius
r = radial coordinate
Re = Reynolds number $\bar{V}_z 2R/\nu$
Re_{cr} = critical Reynolds number
Re_φ = rotational Reynolds number $V_{\varphi,w}2R/\nu$
t = time
V_i = time mean velocity in direction i
$\bar{V}_z$ = mean axial velocity over the pipe cross section
v_* = friction velocity $\sqrt{\tau_w/\rho}$
$\overline{v_i v_j}$ = Reynolds stress
z = axial coordinate
δ_{ij} = kronecker delta
ϵ = dissipation rate of turbulence energy
φ = tangential coordinate
ν = kinematic viscosity
τ = viscous shear stress
ρ = density

Subscripts

add = additional
w = pipe wall

Table 1 Additional terms R_{ij} in the Reynolds stress transport Eqs. (4)

$\overline{v_iv_j}$	$P_{ij,\mathrm{add}}$	$\nu_{ij,\mathrm{add}}$	$C_{ij,\mathrm{add}}$	$\Phi_{ij,2,\mathrm{add}}$
$\overline{v_rv_r}$	$2\overline{v_rv_\varphi}\,\frac{V_\varphi}{r}$	$2\,\frac{\nu}{r^2}\,(\overline{v_\varphi v_\varphi}-\overline{v_rv_r})$	$-2\overline{v_rv_\varphi}\,\frac{V_\varphi}{r}$	$-2c_2\overline{v_rv_\varphi}\,\frac{V_\varphi}{r}$
$\overline{v_\varphi v_\varphi}$	0	$2\,\frac{\nu}{r^2}\,(\overline{v_rv_r}-\overline{v_\varphi v_\varphi})$	$2\overline{v_rv_\varphi}\,\frac{V_\varphi}{r}$	$2c_2\overline{v_rv_\varphi}\,\frac{V_\varphi}{r}$
$\overline{v_zv_z}$	0	0	0	0
$\overline{v_rv_z}$	$\overline{v_\varphi v_z}\,\frac{V_\varphi}{r}$	$-\frac{\nu}{r^2}\,\overline{v_rv_z}$	$-\overline{v_\varphi v_z}\,\frac{V_\varphi}{r}$	$-c_2\overline{v_\varphi v_z}\,\frac{V_\varphi}{r}$
$\overline{v_rv_\varphi}$	$\overline{v_\varphi v_\varphi}\,\frac{V_\varphi}{r}$	$-4\,\frac{\nu}{r^2}\,\overline{v_\varphi v_\varphi}$	$(\overline{v_rv_r}-\overline{v_\varphi v_\varphi})\,\frac{V_\varphi}{r}$	$c_2(\overline{v_rv_r}-\overline{v_\varphi v_\varphi})\,\frac{V_\varphi}{r}$
$\overline{v_\varphi v_z}$	0	$-\frac{\nu}{r^2}\,\overline{v_\varphi v_z}$	$\overline{v_rv_z}\,\frac{V_\varphi}{r}$	$-c_2\overline{v_rv_z}\,\frac{V_\varphi}{r}$

$\overline{v_iv_j}$	$d_{ij,\mathrm{add}}$
$\overline{v_rv_r}$	$-\frac{2}{r}c_s\frac{\partial}{\partial r}\left(\frac{k}{\epsilon}\overline{v_rv_\varphi}^2\right)+2c_s\frac{k}{\epsilon}\left[-\frac{\overline{v_rv_\varphi}}{r}\frac{\partial\overline{v_rv_\varphi}}{\partial r}+\frac{\overline{v_\varphi v_\varphi}}{r^2}(\overline{v_\varphi v_\varphi}-\overline{v_rv_r})\right]$
$\overline{v_\varphi v_\varphi}$	$\frac{2}{r}c_s\frac{\partial}{\partial r}\left(\frac{k}{\epsilon}\overline{v_rv_\varphi}^2\right)+2c_s\frac{k}{\epsilon}\left[\frac{\overline{v_rv_\varphi}}{r}\frac{\partial\overline{v_rv_\varphi}}{\partial r}+\frac{\overline{v_\varphi v_\varphi}}{r^2}(\overline{v_rv_r}-\overline{v_\varphi v_\varphi})\right]$
$\overline{v_zv_z}$	0
$\overline{v_rv_z}$	$-\frac{1}{r}c_s\frac{\partial}{\partial r}\left(\frac{k}{\epsilon}\overline{v_rv_\varphi}\,\overline{v_\varphi v_z}\right)+c_s\frac{k}{\epsilon}\left[-\frac{\overline{v_rv_\varphi}}{r}\frac{\partial\overline{v_\varphi v_z}}{\partial r}-\frac{\overline{v_\varphi v_\varphi}}{r^2}\overline{v_rv_z}\right]$
$\overline{v_rv_\varphi}$	$\frac{1}{r}c_s\frac{\partial}{\partial r}\left(\frac{k}{\epsilon}\overline{v_rv_\varphi}\,(\overline{v_rv_r}-\overline{v_\varphi v_\varphi})\right)+c_s\frac{k}{\epsilon}\left[\frac{\overline{v_rv_\varphi}}{r}\left(\frac{\partial\overline{v_rv_r}}{\partial r}-\frac{\partial\overline{v_\varphi v_\varphi}}{\partial r}\right)-4\frac{\overline{v_\varphi v_\varphi}}{r^2}\overline{v_rv_\varphi}\right]$
$\overline{v_\varphi v_z}$	$\frac{1}{r}c_s\frac{\partial}{\partial r}\left(\frac{k}{\epsilon}\overline{v_rv_\varphi}\,\overline{v_rv_z}\right)+c_s\frac{k}{\epsilon}\left[\frac{\overline{v_rv_\varphi}}{r}\frac{\partial\overline{v_rv_z}}{\partial r}-\frac{\overline{v_\varphi v_\varphi}}{r^2}\overline{v_\varphi v_z}\right]$

zero in the two-component limit to unity in isotropic turbulence. Therefore, this parameter offers the possibility to make the stress equations consistent with the two-component limit of the turbulence as the wall is approached.

Of course, not only the pressure-strain correlation is affected by a rigid wall but also the dissipation rate ϵ_{ij} and the turbulent diffusion d_{ij}. Launder and Shima propose to omit the wall effect on d_{ij}, because the stress equations are source-term dominated in this area. And, in order to keep the number of empirical constants small, they suggest to regard Φ_{ij} as including the wall effects on the dissipation rate as well.

The following equations for the coefficients in the Φ_{ij}-model are taken over from the original recommendation without any change:

$$c_1 = 1 + 2.58AA_2^{1/4}(1 - \exp[-(0.0067\ \mathrm{Re}_t)^2]) \quad (22)$$

$$c_2 = 0.75\sqrt{A} \quad (23)$$

$$c_1^w = -\tfrac{2}{3}c_1 + 1.67 \quad (24)$$

$$c_2^w = \max\left[\left(\frac{2}{3}-\frac{1}{6c_2}\right), 0\right] \quad (25)$$

The turbulent diffusion is modelled by the generalized gradient diffusion hypothesis by Daly and Harlow (1970)

$$d_{ij} = \frac{\partial}{\partial x_k}\left(c_s\frac{k}{\epsilon}\overline{v_kv_l}\frac{\partial\overline{v_iv_j}}{\partial x_l}\right), \quad (26)$$

which can be reduced to

$$d_{ij} = \frac{\partial}{\partial r}\left(c_s\frac{k}{\epsilon}\overline{v_rv_r}\frac{\partial\overline{v_iv_j}}{\partial r}\right) \quad (27)$$

in a fully developed pipe flow. For c_s a value of 0.11 was chosen, which is only half as large as the usually employed value. The reason for this measure will be described later.

Concerning the dissipation rate ϵ_{ij} local isotropy is assumed

$$\epsilon_{ij} = \tfrac{2}{3}\delta_{ij}\epsilon. \quad (28)$$

The energy dissipation rate of turbulence ϵ can be calculated by solving

$$\frac{D\epsilon}{Dt} = \frac{\partial}{\partial x_k}\left[\left(c_\epsilon\frac{k}{\epsilon}\overline{v_kv_l}+\nu\delta_{kl}\right)\frac{\partial\epsilon}{\partial x_l}\right] + (c_{\epsilon 1}+\psi_1+\psi_2)\frac{\epsilon}{k}P_k - c_{\epsilon 2}\frac{\epsilon\tilde{\epsilon}}{k} \quad (29)$$

with

$$\tilde{\epsilon} \equiv \epsilon - 2\nu\left(\frac{\partial\sqrt{k}}{\partial x_j}\right)^2 \quad (30)$$

$$\psi_1 = 2.5A\left(\frac{P_k}{\epsilon}-1\right) \quad (31)$$

$$\psi_2 = 0.3(1 - 0.3A_2)\exp[-(0.002\ \mathrm{Re}_t)^2]. \quad (32)$$

The quantity $\tilde{\epsilon}$, which vanishes at the wall, was first introduced instead of ϵ by Hanjalic and Launder (1976) in order to avoid that the last term in Eq. (29) tends to minus infinity as the wall is approached. The standard values of 0.18, 1.45, and 1.9 are taken for the coefficients c_ϵ, $c_{\epsilon 1}$, and $c_{\epsilon 2}$, respectively. For the fully developed pipe flow Eqs. (29) and (30) can be reduced to

$$0 = \frac{\partial}{\partial r}\left[\left(c_\epsilon \frac{k}{\epsilon}\overline{v_r v_r} + \nu\right)\frac{\partial \epsilon}{\partial r}\right] + (c_{\epsilon 1} + \psi_1 + \psi_2)\frac{\epsilon}{k}P - c_{\epsilon 2}\frac{\epsilon\tilde{\epsilon}}{k} \quad (33)$$

$$\tilde{\epsilon} \equiv \epsilon - 2\nu\left(\frac{\partial\sqrt{k}}{\partial r}\right)^2. \quad (34)$$

The transformation from the Cartesian into the cylindrical coordinate system causes additional terms in the transport equations for the Reynolds stresses. These terms are summarized for every component $\overline{v_i v_j}$ in Table 1. In modeling the "rapid" term $\Phi_{ij,2}$ the additional terms of the stress generation rate $P_{ij,\text{add}}$ were omitted, a measure that was recommended by Hogg and Leschziner (1989) and confirmed by Rothe and Beer (1994) for highly swirling flows. The inclusion of $P_{ij,\text{add}}$ has the advantage that the model is frame-invariant and provides reasonable results as well, but it leads to a very low Reynolds shear stress $\overline{v_r v_\varphi}$ in the vicinity of the centerline and to a nearly linear tangential velocity in this area, which does not occur in the experiments. In contrast to this the additional convection terms $C_{ij,\text{add}}$ were not left out in the model for the "rapid" part. They are proportional to the local mean tangential velocity V_φ and can be regarded as a correction term due to mean flow rotation. It will be shown later that these terms lead to an improved agreement with experimental results.

2.3 Boundary Conditions. Boundary conditions can be provided at the centerline, which is an axis of symmetry and at the rotating pipe wall, where all velocities, expect V_φ, have to vanish.

$$r = 0: \quad V_\varphi = 0; \quad \frac{\partial V_z}{\partial r} = 0; \quad \frac{\partial \overline{v_r v_r}}{\partial r} = \frac{\partial \overline{v_\varphi v_\varphi}}{\partial r} = \frac{\partial \overline{v_z v_z}}{\partial r} = 0;$$

$$\overline{v_r v_z} = \overline{v_r v_\varphi} = \overline{v_\varphi v_z} = 0; \quad \frac{\partial \epsilon}{\partial r} = 0;$$

$$r = R: \quad V_\varphi = V_{\varphi,w}; \quad V_z = 0; \quad \overline{v_i v_j} = 0; \quad \tilde{\epsilon} = 0. \quad (35)$$

3 Numerical Method

In order to solve the presented system of the ten differential equations, another equation, i.e., the integral continuity equation

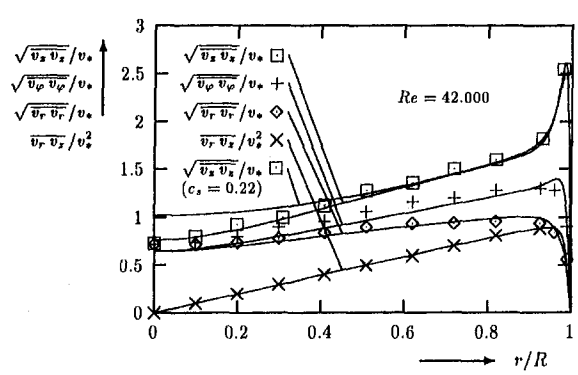

Fig. 1 Radial distribution of the Reynolds stresses in a fully developed nonrotating pipe flow at Re = 42.000. Symbols: Laufer's experimental results, solid lines: computations.

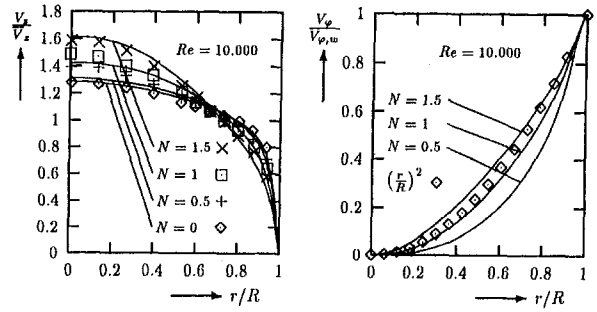

Fig. 2 Mean axial and tangential velocity profiles for various rotation rates N at Re = 10.000. Symbols: Kikuyama's experimental results, solid lines: computations.

$$\int_{r=0}^{R} V_z(r) r dr = \frac{1}{2}\bar{V}_z R^2 \quad (36)$$

is required, which provides the global conservation of mass.

The equations were approximated by difference equations using central differences at each nodal point. During the iteration procedure the new values were computed with the aid of the Successive Over-Relaxation (SOR) method. The mesh size was decreased in geometric proportion with a length ratio of 0.95 from a maximum value at the centerline toward the pipe wall. The computations were performed with 80 nodes across the pipe radius which was found to ensure a negligible discretization error.

The Reynolds stresses and the dissipation rate were placed at nodes midway between those of the mean axial and tangential velocity. This staggered-grid formation has proved to increase the stability of the equation systems in many applications (Hogg and Leschziner, 1989; Launder and Shima, 1989; Rothe and Beer, 1994).

4 Results and Discussion

4.1 Stationary Pipe Flow. In order to check the performance of the described turbulence model for a standard case, calculations of a fully developed stationary turbulent pipe flow are compared with Laufer's (1954) comprehensive experimental investigations. Figure 1 shows the calculated and the measured radial distributions of the Reynolds stresses for a Reynolds number of 42.000. When a value of $c_s = 0.11$ is chosen for the coefficient in the turbulent diffusion model, which is only half the usually applied value, the agreement between theory and experiment is excellent. This can be explained by bearing in mind that the gradient diffusion model exhibits a singularity for $r = 0$ in a cylindrical coordinate system leading to an overprediction of turbulent diffusion in the vicinity of the symmetry axis. This is shown in Fig. 1 for the streamwise fluctuation $\overline{v_z v_z}$. The coincidence of the calculations and the experimental results in the near-wall region is very good, too, and this confirms the approach of Launder and Shima to capture the wall effects upon the flow by the Reynolds stress invariants.

It should be mentioned that all other coefficients proposed by the authors were taken over unchanged and that for $c_s = 0.11$ the agreement concerning the mean axial velocity is excellent as well.

3.2 Rotating Pipe Flow. The numerical calculations of the fully developed flow in an axially rotating pipe are compared with the experimental results of Kikuyama et al. (1983). Figure 2 shows the influence of the rotation Rate N on the dimensionless time mean axial velocity distribution $V_z/\bar{V}_z$ at Re = 10.000. For the non-rotating case ($N = 0$) the deviations between theory and experiment are less than 5 percent. The same figure also reveals a small weakness of the applied turbulence model: For the low rotation rate $N = 0.5$ the predicted laminar-

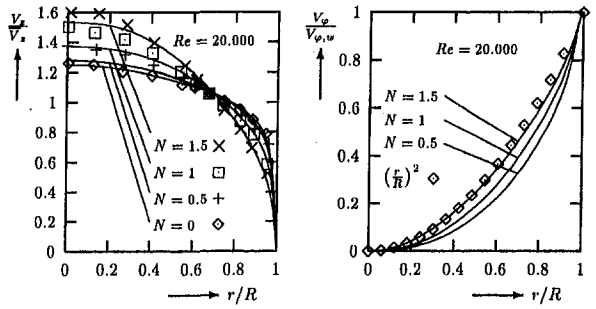

Fig. 3 Mean axial and tangential velocity profiles for various rotation rates at Re = 20.000. Symbols: Kikuyama's experimental results, solid lines: computations.

ization effect is slightly too weak, whereas at the high rotation rate $N = 1.5$ the suppression of turbulence is somewhat overpredicted. But, at the moderate rotation rate of $N = 1$ the coincidence between the numerical and the experimental axial velocity distribution is very good. This tendency is confirmed by the results for the same rotation rates at Re = 20.000 (Fig. 3), where the best agreement can be found for $N = 1.5$, and by the comparison for Re = 50.000 and $N = 1$ in Fig. 4.

Generally, one can see that the second-moment closure is able to capture the laminarization effect due to rotation without any flow-specific extension of the terms which have to be modeled, as it is necessary for any eddy viscosity model. The reason for this is that the additional terms in the stress budgets, which arise "naturally" due to the coordinate transformation, do not occur in the kinetic energy equation (Launder, 1989). These terms, however, were found to cause the laminarization effect of the rotating pipe flow in the numerical analysis (Hirai, 1988).

In the right-hand plots of Fig. 2–4 the computed time mean tangential velocity profiles are also compared with the experimental results of Kikuyama, which provide a parabolic distribution independent of the rotation rate and the Reynolds number. One can see that, in contrast to an eddy viscosity model (Hirai, 1988), a Reynolds stress turbulence closure does not predict a profile corresponding to a rigid body rotation. For the cases where the agreement concerning the laminarization effect is very good ($N = 1$ at Re = 10.000 and $N = 1.5$ at Re = 20.000), the tangential velocity profiles are in excellent agreement with the experiments, too. Moreover, the overprediction of the turbulent shear stresses at low rotation rates, as well as the too strong laminarization effect at high rotation rates can be observed here once again.

The comparison of the measured and computed friction coefficients is summarized in Table 2. For the non-rotating flows an excellent agreement exists between the calculations and the experimental values, which may be represented by the empirical formula of Blasius

Table 2 Comparison of computed and measured friction coefficients λ. Experimental values of the swirling flows by Kikuyama et al. (1983) and for the non-rotating flows by Blasisus' law.

	Re = 10.000		*Re* = 20.000		*Re* = 50.000	
N	Calc.	Exp.	Calc.	Exp.	Calc.	Exp.
0	0.0326	0.0316	0.0268	0.0266	0.0218	0.0212
0.5	0.0283	0.028	0.0242	0.022	—	—
1	0.0238	0.022	0.0193	0.017	0.0127	0.013
1.5	0.0162	0.017	0.0135	0.012	—	—

$$\lambda = 0.3164\ \mathrm{Re}^{-0.25}. \tag{37}$$

Concerning the swirling pipe flows the coincidence is good, too, the deviations are less than 12%.

Figure 5 demonstrates clearly the improvement of the turbulence model by introducing the IPC-model for the "rapid" part in the pressure-strain correlation $\Phi_{ij,2}$ instead of the basic IP-model: The computed radial distribution of the streamwise velocity fluctuations is in much better agreement with the experiments of Nishibori et al. (1987), when the additional convective terms are taken into account. The IP-model provides a much too high turbulence intensity in the vicinity of the symmetry axis, whereas in the near-wall area the streamwise fluctuations are underpredicted. In contrast to this the IPC-model coincides with the measured values satisfactorily.

Moreover, it should be mentioned that for the investigated case (Re = 30.000 and $N = 1$) a much too strong laminarization of the mean axial velocity profile is predicted by the IP-model. Further, the same model computes a total breakdown of the turbulence for $N = 1.5$, independent of the Reynolds number, leading to a Hagen-Poiseuille flow with superimposed rigid rotation, which is in total disagreement with the experiments.

5 Conclusions

The fully developed flow in an axially rotating pipe was calculated with the aid of a low-Reynolds-number turbulence model and compared with experimental results for Reynolds numbers between 10.000 and 50.000. The second-moment closure was found to capture the laminarization effect of the mean axial velocity profile and the non-linear mean tangential velocity profile which are observed in the experiments. Concerning the original turbulence model proposed by Launder and Shima (1989) two modifications were made: The first one was to chose the constant for the turbulent diffusion model of Daly and Harlow (1970) only half as large as the usual value of $c_s = 0.22$. This measure avoids an overprediction of the Reynolds stresses in the vicinity of the symmetry axis and might be appro-

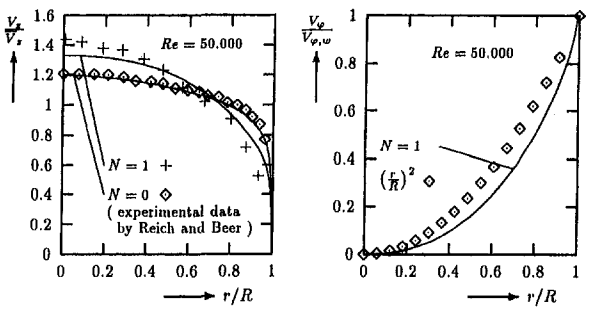

Fig. 4 Mean axial and tangential velocity profiles for $N = 0$ and $N = 1$ at Re = 50.000. Symbols: experimental results mentioned by Kikuyama ($N = 1$) and performed by Reich and Beer (1989) ($N = 0$), solid lines: computations.

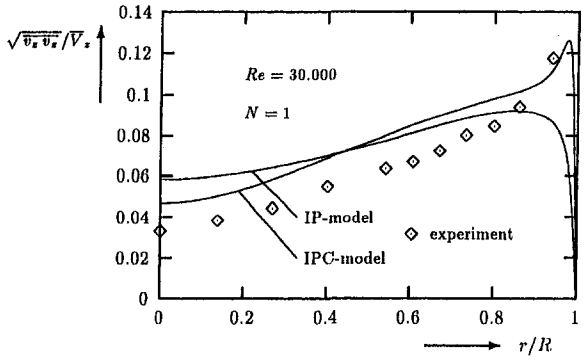

Fig. 5 Radial distribution of the streamwise velocity fluctuations in a fully developed axially rotating pipe flow at Re = 30.000 and $N = 1$. Symbols: Nishibori's (1987) experimental results, Solid lines: Computations with the IP- and the IPC-model for $\Phi_{ij,2}$.

priate for similar applications in cylindrical coordinates, too. The second measure was to replace the basic isotropization of production (IP) model for the "rapid" part in the pressure-strain correlation $\Phi_{ij,2}$ by the isotropization of production and convection (IPC) model. The latter model has proved to provide much better results concerning the streamwise velocity fluctuations $\overline{v_z v_z}$ and the laminarization effect of the mean axial velocity profile in the rotating pipe flow.

Finally, it should be mentioned that even the application of the IPC-model leads to a slight underprediction of the flow laminarization at low rotation rates, whereas at high rotation rates the turbulence suppression due to swirl is still somewhat overpredicted. A further improvement might be achieved by a more sophisticated model for the rapid term which has a strong influence on the numerical results of the investigated flow configuration.

References

Daly, B. J. and Harlow, F. H., 1970, "Transport Equations in Turbulence," *Physics of Fluids,* Vol. 13, pp. 2634–2649.

Eggels, J. M., 1994, "Direct and Large Eddy Simulation of Turbulent Flow in a Cylindrical Pipe Geometry," Doctoral thesis, Delft University Press.

Hanjalic, K., and Launder, B. E., 1976, "Contribution Towards a Reynolds-Stress Closure for Low-Reynolds-Number Turbulence," *Journal of Fluids Mechanics,* Vol. 74, pp. 593–610.

Hirai, S., Takagi, T., and Matsumoto, M., 1988, "Predictions of the Laminarization Phenomena in an Axially Rotating Pipe Flow," ASME JOURNAL OF FLUIDS ENGINEERING, Vol. 110, pp. 424–430.

Hogg, S., and Leschziner, M. A., 1989, "Computation of Highly Swirling Confined Flow with a Reynolds Stress Turbulence Model," *AIAA Journal,* Vol. 27, pp. 57–63.

Kikuyama, K., Murakami, M., Nishibori, K., and Maeda, K., 1983, "Flow in an Axially Rotating Pipe," *Bulletin of the JSME,* Vol. 26, pp. 506–513.

Laufer, J., 1954, "The Structure of Turbulence in Fully Developed Pipe Flow," NACA Report 1174 (Supersedes NACA TN 2954).

Launder, B. E., 1989, "Second-Moment Closure: Present . . . and Future?," *International Journal of Heat and Fluid Flow,* Vol. 10, pp. 282–300.

Launder, B. E., and Shima, N., 1989, "Second-Moment Closure for the Near-Wall Sublayer: Development and Application," *AIAA Journal,* Vol. 27, pp. 1319–1325.

Mackrodt, P.-A., 1976, "Stability of Hagen-Poiseuille Flow with Superimposed Rigid Rotation," *Journal of Fluid Mechanics,* Vol. 73, Part 1, pp. 153–164.

Murakami, M. and Kikuyama, K., 1980, "Turbulent Flow in Axially Rotating Pipes," ASME JOURNAL OF FLUIDS ENGINEERING, Vol. 102, pp. 97–103.

Nagib, H. M., Lavan, Z., Fejer, A. A., and Wolf, L., 1971, "Stability of Pipe Flow with Superposed Solid Body Rotation," *Physics of Fluids,* Vol. 14, pp. 766–768.

Nishibori, K., Kikuyama, K., and Murakami, M., 1987, "Laminarization of Turbulent Flow in the Inlet Region of an Axially Rotating Pipe," *Bulletin of the JSME,* Vol. 30, pp. 255–262.

Ohtsuka, M., 1995, "Numerical Analysis of Swirling Non-Reacting and Reacting Flows by the Reynolds Stress Differential Method," *International Journal of Heat and Mass Transfer,* Vol. 38, pp. 331–337.

Reich, G., and Beer, H., 1989, "Fluid Flow and Heat Transfer in an Axially Rotating Pipe I. Effect of Rotation on Turbulent Pipe Flow," *International Journal of Heat and Mass Transfer,* Vol. 32, pp. 551–562.

Rothe, T., and Beer, H., 1994, "An Experimental and Numerical Investigation of Turbulent Flow and Heat Transfer in the Entrance Region of an Annulus Between Rotating Tubes," *Proceedings 5th International Symposium on Transport Phenomena and Dynamics of Rotating Machinery,* Vol. A, pp. 548–560.

Rotta, J. C., 1951, "Statistische Theorie nichthomogener Turbulenz," *Zeitschrift für Physik,* Vol. 129, p. 547.

Anisotropy Invariants of Reynolds Stress Tensor in a Duct Flow and Turbulent Boundary Layer

A. Mazouz

L. Labraga

C. Tournier

Laboratoire de Mécanique
des Fluides, L.A.M.I.H.,
Université de Valenciennes
et du Hainaut Cambrésis,
le Mont Houy, B.P. 311, 59304
Valenciennes Cedex, France

The present study shows that the Reynolds stress anisotropy tensor for turbulent flow depends both on the nature of the surface and the boundary conditions of the flow. Contrary to the case of turbulent boundary layers with k-type surface roughness, the measured anisotropy invariants of the Reynolds stress tensor over a series of spanwise square bars separated by rectangular cavities (k-type) in duct flows show that roughness increases the anisotropy. There is a similarity between the effect of roughness on channel flow turbulence and that on pipe flow turbulence. The present data show that the effect of introducing a surface roughness significantly perturbs the entire thickness of the turbulent flow.

1 Introduction

In spite of the large number of numerical and experimental investigations on turbulent shear flow, it is reasonable to assert that our knowledge of the turbulence structure still remains limited. A great deal of attention has been given to the study of the structure of the turbulent boundary layer over smooth walls. By contrast, the corresponding boundary layer over rough walls has received far less attention. It has long been considered that the effect of wall roughness on turbulent flows is restricted to the flow region extending out to about five times the roughness height, known as the "roughness sublayer." Outside this region, smooth- and rough-wall boundary layers are assumed to have the same structure. This hypothesis was labeled "similarity hypothesis." Raupach (1981) carried out measurements over rough surfaces consisting of cylindrical roughness elements in different arrays and found that outside a region twice the roughness height, second-order moments of the velocity normalized by the friction velocity are universal and independent of roughness. The observations of Djenidi and Antonia (1996) over both a smooth-wall and ribletted surface for drag reduction, suggest that there is no significant structural change in the turbulence structure between the two types of walls. Simulations have also been carried out on riblet walls for a channel flow (Choi et al., 1993; Chu and Karniadakis, 1993). The latter data, which was limited to low Reynolds numbers, emphasized that the riblets inhibit the spanwise motions of the wall streaks, leading to reductions in Reynolds stress and surface drag. Wood and Antonia (1975) concluded that the influence of the roughness on the flow is largely confined to the wall region, while the data of Osaka and Mochizuki (1988) showed that, even in the outer region at $y/\delta = 0.6$, differences could be detected between smooth and d-type rough walls (d-type are characterized by $w < k$, where w is the width of the roughness). Later measurements by Djenidi et al. (1994) in smooth wall and d-type rough wall boundary layers have shown that differences in the turbulence intensities persist over a significant distance above the two surfaces. Recently, Krogstad et al. (1992a) questioned the similarity hypothesis in the outer region on the basis of differences observed between turbulent boundary layers over smooth- and rough-walls. They showed that the streamwise turbulence intensity distribution over rough- and smooth-wall turbulent boundary layers was the same for both surfaces. However, the rough-wall distribution of v^{+2} (+ denotes normalization by U_τ) is significantly larger than for the smooth wall. A similar increase has been detected by Acharya and Escudier (1987) in rough-wall turbulent boundary layers. Outer region behavior depends on the nature of the surface. Sabot et al. (1977) found large differences in the experimental profiles of $\sqrt{v^{+2}}$ and $\sqrt{w^{+2}}$ for fully developed smooth- and rough-pipe turbulent flows, although the $\sqrt{u^{+2}}$ profiles were similar. Their experiments were carried out for a Reynolds number Re_R ($\equiv U_0 R/\nu$), where U_0 is the centerline velocity and R the pipe radius) equal to 67500 and with k-type roughness (for the k-type, $w > k$). In this study, the anisotropy was much larger for the rough pipe than for the smooth pipe, even in the core flow. Contrary to the results of Sabot et al. (1977), Shafi and Antonia (1995) ($\mathrm{Re}_\theta \cong 17420$) have found that the surface mesh roughness reduces the anisotropy of u^{+2} and v^{+2} significantly, everywhere in the boundary layer, although the effect on w^{+2} and uv^{+} is less marked. The latter authors showed that the anisotropy is smaller for rough than for smooth walls. This observation suggests a relation between the nature of the surface and the outer flow region. Antonia et al. (1990) have shown that the Reynolds number effect is very small when Re_θ is greater than about 3000. The nature of the flow is probably a parameter to be taken into account in the behavior of the components of the Reynolds stress anisotropy tensor. In order to examine the influence of the k-type surface roughness, as well as the flow type on the turbulence structure, we have calculated the anisotropy invariants, introduced by Lumley and Newman (1977) and Lumley (1978) in both rough- and smooth-channel flows. The smooth wall results provide a basis of comparison for the rough wall. From the viewpoint of the duct flow anisotropy, we also have calculated the anisotropy invariant map, which consists in plotting the second invariant ($II = -b_{ij}b_{ji}/2$) versus the third invariant ($III = b_{ij}b_{jk}b_{ki}/3$) of b_{ij}. The Reynolds stress anisotropy tensor permits one to quantify the anisotropy of each Reynolds stress component. The b_{ij} components are calculated according to $b_{ij} = \overline{u_i u_j}/q^2 - \delta_{ij}/3$, where $q^2 \equiv 2k \equiv \overline{u_i u_i}$ is the average turbulent kinetic energy and $\delta_{ij} = 1$ when $i = j$ and $\delta_{ij} = 0$ when $i \neq j$; quantities $u_1 \equiv u$, $u_2 \equiv v$ and $u_3 \equiv w$ denote the velocity fluctuations in the streamwise (x), wall normal (y) and spanwise (z) directions, respectively.

Contributed by the Fluids Engineering Division for publication in the JOURNAL OF FLUIDS ENGINEERING. Manuscript received by the Fluids Engineering Division July 8, 1996; revised manuscript received December 4, 1997. Associate Technical Editor: M. S. Triantafyllou.

2 Experimental Setup

The experiments were performed in an open wind tunnel with a working section composed of two parallel plates which formed a two-dimensional rectangular channel. The test section is 2 m long with an aspect ratio of 16:1. The static pressure was measured along the channel as well as in spanwise z direction showing good symmetry and two-dimensionality of the turbulent flow. In the case of the smooth channel, the boundary layer was tripped using a 1 mm square trip bar spanning each entire plate, followed by a 10 cm wide strip of sandpaper. For the rough-channel, the k-type roughness consisted of two-dimensional bars of square cross-section uniformly distributed over both plates. The transversely grooved surface is illustrated in Fig. 1. The k-type roughness elements have a height k (= width w) = 2 mm and span the full (800 mm) width of the working section. The gap between consecutive elements was equal to four times the element width w (λ = 10 mm). Rough and smooth channel measurements were carried out at a Reynolds number Re_{2h} ($\equiv U_0 2h/\nu$, where h is the channel half-height) of 113000. The Reynolds number based on the momentum thickness Re_θ ($\equiv U_0\theta/\nu$) were, respectively, 5300 and 6864 for the smooth and rough channels. The turbulent flow was fully developed and representative of the fully rough regime. Under these conditions, for the present measurements the Reynolds number k^+ ($\equiv ku_\tau/\nu$), based on the element roughness height and friction velocity was 335. Comte-Bellot (1965) found that when the values of the skewness and flatness factors on the channel centerline of the channel cease to vary, the turbulent flow can be considered to be fully developed. The present measurements were carried out at a position x/h = 65, downstream of the inlet, where the variation of the third and fourth-order statistical moments on the centerline are negligible beyond x/h = 57. Measurements of mean velocity and turbulence moments were obtained using 5 μm wire probes with 90 deg apex angles. The probes had a length to wire diameter ratio l_w/d_w = 250. The hot wires were run by constant temperature anemometers whose outputs were linearized and filtered. The analog outputs of the wires were digitized by a data acquisition system. A computer was used to process the data. The friction velocity u_τ for both the smooth and rough walls was deduced from the longitudinal static pressure measurements. The shift in origin ϵ (cf. Fig. 1) required in the case of a rough wall was determined using the semi-logarithmic form of the velocity distribution. The mean value of the shift obtained from the fitted profile was ϵ/k = 0.29. The uncertainty factor in the pitot tube centerline velocity measurements is ±2 percent. The overall uncertainties with the hot wire measurement are: $\sqrt{\overline{u^2}}$, ±1 percent; $\sqrt{\overline{v^2}}$, ±2 percent; $\sqrt{\overline{w^2}}$, ±2 percent.

3 Results and Discussion

3.1 Turbulence Intensities. Distributions of $\sqrt{\overline{v^{+2}}}$ and $\sqrt{\overline{w^{+2}}}$, shown in Fig. 2(a), indicate that the magnitude of the smooth-wall turbulence intensities is slightly larger than for the rough-wall. This observation applies over the whole of the channel. However, the differences between the rough- and smooth-channel data are very small in the case of the $\sqrt{\overline{u^{+2}}}$ profiles. The results from the X-wire probe agree well with the data obtained using a single normal wire (not shown). Also included are the data obtained in the region of the fully developed smooth channel turbulent flow by Comte-Bellot (1965) for a Reynolds number Re_h = 57000. Our data for the smooth channel agree reasonably with those of Comte-Bellot. The r.m.s. profiles obtained by Sabot et al. (1977) in turbulent flows in a k-type rough and smooth pipe, shown in Fig. 2(b) present a similar trend to that of the channel flow. Over a large part of the pipe radius, the k-type roughness strongly decreases the turbulence intensities $\sqrt{\overline{v^{+2}}}$ and $\sqrt{\overline{w^{+2}}}$ in the pipe flow, while the $\sqrt{\overline{u^{+2}}}$ profiles remain the same for both the smooth and rough pipe. However, the measurements obtained by Krogstad et al. (1992a) in the outer region ($y/\delta > 0.2$) of a turbulent boundary layer show that the mesh roughness geometry increases the normal turbulence intensities $\overline{v^{+2}}$, and the rough-wall data for $\overline{u^{+2}}$ are slightly higher than for the smooth wall (not shown). These differences were caused by an increase in the energy content at high wave numbers and a different entrainment rate, manifesting itself in a stronger wake component in the case of the rough wall (Krogstad et al., 1992a). Results obtained for $\overline{w^{+2}}$ are not reported in their paper. Contrary to the generally accepted idea that a k-type roughness only influences the flow structure in the vicinity of the wall (Raupach, 1981 and Bandyopadhyay and Watson, 1987), these different results show that the roughness effect on the turbulence structure extends well into the core region of the duct flows and in the outer region of the boundary layer. As noted by Krogstad et al. (1992a), the mesh roughness may be described as a k-type roughness because the classification of rough walls is based solely on the effect of the roughness on the mean velocity. Contrary to turbulent boundary layers, the k-type roughness decreases the values of $\overline{v^{+2}}$ and $\overline{w^{+2}}$ for a turbulent duct flows. The present results suggest that the normal turbulence intensity distribution is influenced by the flow type and the roughness geometry. The roughness has a tendency to strongly affect a flow and particularly influence the overall anisotropy of the diagonal Reynolds stress components. On the other hand, we observe that the longitudinal turbulence intensity is essentially independent of roughness and remains the same for either rough or smooth walls.

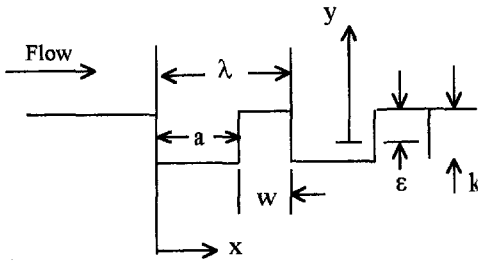

Fig. 1 Two-dimensional roughness geometry

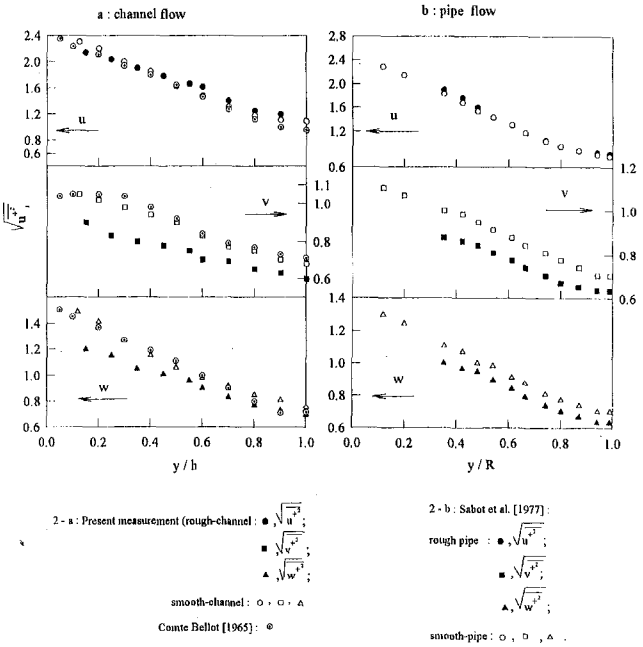

Fig. 2 (a) and (b). Distributions of turbulence intensities in duct flows

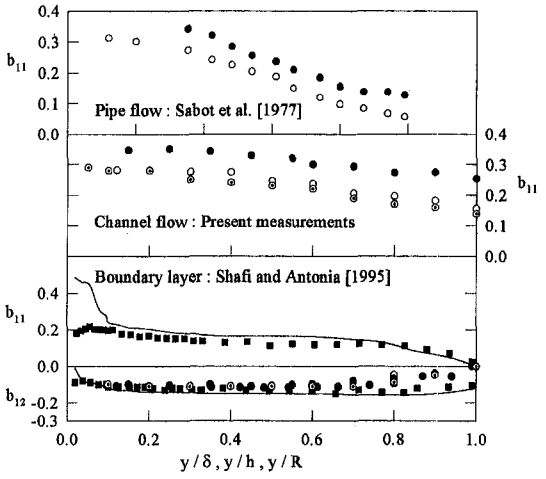

Fig. 3 Distributions of b_{11} and b_{12} components of b_{ij} tensor for different flow types

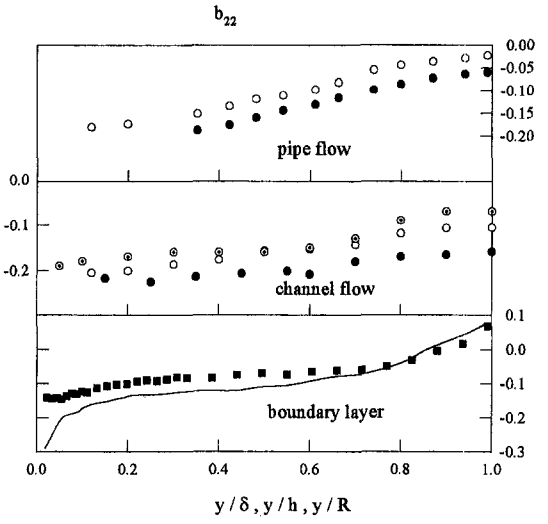

Fig. 4 Distributions of b_{22} components of b_{ij} tensor for different flow types

3.2 b_{ij} Component for Reynolds Stress. In order to quantify the differences in turbulence intensities in turbulent duct flows, the components of the Reynolds stress anisotropy tensor b_{ij} have been calculated. Profiles of b_{11}, b_{12}, b_{22}, and b_{33} are presented in Figs. 3, 4, and 5. Also included are the calculated components using experimental data of Comte-Bellot (1965) in smooth channel flow and Sabot et al. (1977) in rough and smooth pipes. Shafi and Antonia (1995) reported experimental data for a rough wall turbulent boundary layer and Spalart (1988) ($Re_\theta \cong 1410$) numerical data computed from DNS for a smooth wall turbulent boundary layer. The b_{ij} values of Comte-Bellot are in good agreement with the present data for the smooth channel. Distributions of b_{11} and b_{22} and b_{33} anisotropy invariants calculated from our present data indicate differences between the rough and smooth channel flows. The roughness significantly increases the values of b_{11} and b_{22}, although the b_{12} profiles seem to be nearly the same for both surfaces. This shows that anisotropy of turbulence intensities is probably affected by both wall roughness and flow type. The nearly constant value of the b_{12} profiles over a significant distance normal to the wall, for different experiments, indicates that the ratio of the shear stress and turbulent kinetic energy varies in the same manner for different flows.

A first observation is the opposing trend between the results of b_{11} and b_{22} obtained in turbulent boundary layers compared with turbulent duct flows. Compared to Spalart's (1988) numerical data, Shafi and Antonia (1995) have shown that the inner region is characterized by values of b_{11} and b_{22} significantly smaller in the case of rough walls. In the outer region these components are closer to an isotropic value for a rough wall than for a smooth wall. Differences between the b_{11} and b_{22} profiles obtained in turbulent boundary layers and ducts (pipe or channel) illustrate the influence of both the type of flow and roughness geometry on the behaviour of the Reynolds stress tensor anisotropy components.

The data of Shafi and Antonia (1995) for b_{33} are not influenced by the wall roughness. This observation applies only to the turbulent boundary layer. No marked important differences can be observed between the values of b_{33} in the outer regions of smooth and rough walls turbulent boundary layers. In the $0.15 < y/h(\delta) < 0.8$ region, the b_{12} values of Spalart (1988) for a smooth wall seem higher than those of Shafi and Antonia (1995) for a rough wall. This lower value of the ratio b_{12} has been observed in Antonia and Luxton's (1971) k-type grooved surface (not shown here). Bandyopadhyay and Watson (1987) mentioned in their paper Bradshaw's suggestion that lower values of b_{12} are to be expected near rough walls because the extra turbulence generated near the roughness elements is not likely to contribute proportionately to the stress. The b_{ij} components of the Reynolds stress anisotropy tensor are in fact quite sensitive indicators to changes in turbulence structure.

We have calculated the ratio $\Delta b_{ii}/b_{ii} = (b_{iir} - b_{iis})/b_{iir}$ between $y/h = 0.2$ and $y/h = 0.8$ (the subscript ii does not indicate summation and varies from 1 to 3, the subscripts r and s refer to the rough and smooth wall case). This ratio represents the differences between the invariants of the Reynolds stress tensor between rough and smooth ducts. The resulting values of $\Delta b_{11}/b_{11}$ in this region highlight variations of 20 to 33 percent

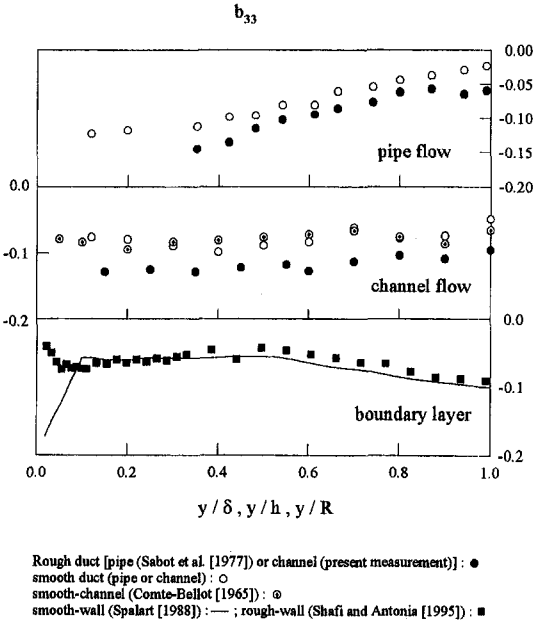

Fig. 5 Distributions of b_{33} components of b_{ij} tensor for different flow types

and a slight increase in the $\Delta b_{22}/b_{22}$ ratio in the case of the channel flow. These same ratios calculated from experimental data of Sabot et al. (1977) vary from 23 percent at $y/R = 0.35$ to 38 percent at $y/R = 0.80$ for $\Delta b_{11}/b_{11}$, and between 20 and 49 percent over the same range for $\Delta b_{22}/b_{22}$ in the pipe flow. The duct roughness significantly increases the anisotropy of u^{+2} and v^{+2} in the core region, which signifies that the turbulence structure in the rough duct is influenced significantly. Moreover, for rough walls the ejections are relatively violent, rising almost vertically into the outer flow. The $\Delta b_{33}/b_{33}$ values for pipe flows exhibit differences between rough and smooth walls extending over the whole pipe. The channel data for $\Delta b_{33}/b_{33}$ present the same behaviour in the core region.

According to Shafi and Antonia (1995) the ratio $\Delta b_{ii}/b_{ii} = (b_{ii\,s} - b_{ii\,r})/b_{ii\,s}$ highlights the difference between the smooth and rough wall data because the wall-roughness decreases the anisotropy of the streamwise and normal-wall intensities in the case of the turbulent boundary layer. The ratio $\Delta b_{11}/b_{11}$ in a turbulent boundary layer varies between 21 percent at $y/\delta \cong 0.2$ to 33 percent at $y/\delta \cong 0.6$. Over the same range, the previous authors indicate that the $\Delta b_{22}/b_{22}$ ratio varies from 30 to 47 percent. However, these latter values were calculated using Erm and Joubert's (1991) ($Re_\theta \cong 2700$) data over a smooth wall. The difference between this data and the numerical data of Spalart (1988) is about 15 percent. Between $y/\delta \cong 0.6$ and $y/\delta \cong 0.8$, the $\Delta b_{22}/b_{22}$ values calculated using Spalart's numerical data and Shafi and Antonia's measurements indicate a faster decrease in the vicinity of the boundary layer interface with the outer flow. The interface between the turbulent and the non turbulent flow leads to scattering in $\Delta b_{22}/b_{22}$ values for $y/\delta > 0.8$. In the wall vicinity ($y/\delta \leq 0.15$), the $\Delta b_{33}/b_{33}$ values decrease rapidly from 70 to 18 percent and tend to be scattered across the whole boundary layer.

3.3 Anisotropy Invariant Map. The anisotropy invariant map obtained from the present measurements is shown in Fig. 6. This presentation is independent of the y axis. Also included are data from the mesh screen experiments of Shafi and Antonia (1995) and Spalart (1988) from smooth walls and Sabot et al. (1977) for a smooth pipe. The invariant map of the smooth-channel data of Comte-Bellot (1965) are also included. The rough-wall data of Shafi and Antonia (1995) indicate that the values of (III, $-II$) at $y/\delta \cong 0.2$ and $y/\delta \cong 0.6$ are (0.002, 0.034) and (0.0016, 0.029), respectively. At the same locations, the corresponding smooth wall values of Erm and Joubert are (0.0025, 0.054) and (0.0018, 0.046). This shows that the anisotropy in the outer region of the boundary layer of a rough wall is smaller than that of a smooth wall (1995). We have included in figure 6 Spalart's (1988) values of (III, $-II$) obtained in the inner region where the maximum occurs at $y^+ \cong 8$.

Table 1 Anisotropy invariant values for the Reynolds stress tensor

	(III, −II) at $y/h \cong 0.2$	(III, −II) at $y/h \cong 0.6$
Rough channel turbulent flow (present measurements)	= (0.0112, 0.10)	= (0.062, 0.08)
Smooth channel turbulent flow (present measurements)	= (0.0054, 0.07)	= (0.004, 0.05)
Comte-Bellot (1965) (smooth channel turbulent flow)	= (0.006, 0.07)	= (0.003, 0.05)
Sabot et al. (1977) (smooth pipe turbulent flow)	= (0.007, 0.07)	= (0.002, 0.04)
Shafi and Antonia (1995) (rough-wall turbulent boundary layer)	= (0.002, 0.034)	= (0.0016, 0.0029)
Erm and Joubert (1991) (smooth-wall turbulent boundary layer)	= (0.0025, 0.054)	= (0.0018, 0.046)

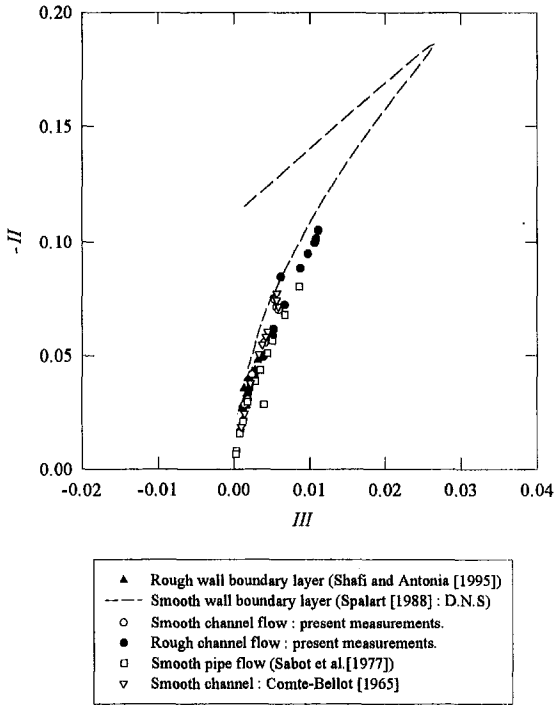

Fig. 6 Anisotropy invariant map for the Reynolds stress tensor

The values of (III, $-II$) for turbulent duct flows are given in Table 1. Note that there is an increase in the anisotropy for rough-wall channel flows. At the same locations the (III, $-II$) values of Comte-Bellot (1965) agree reasonably with the present data for the smooth channel. The corresponding smooth pipe values (Sabot et al., 1977) are also in good agreement with the smooth channel data.

The magnitudes of the invariants obtained in smooth and rough ducts and rough wall boundary layers are to be found near the bottom region of the triangle in Fig. 6. It should be noted that the mechanisms of kinetic energy distribution among its components depend on both the boundary conditions and flow types. This has been underlined by Teitel and Antonia (1991) by measuring the ratio $\alpha(\equiv \overline{(uv)_2}/\overline{(uv)_4})$ which allows one to distinguish differences in the structure of the outer layers of turbulent channel flows and turbulent boundary layers. The quantities $(\overline{uv})_2$ and $(\overline{uv})_4$ are the average values of the product uv in quadrants 2 (Q_2) and 4 (Q_4), respectively, of the (u, v) plane.

4 Conclusions

Measurements of the turbulence intensities in smooth and rough channels have been compared with the corresponding data in both smooth and rough pipes. The roughness at the wall decreases v^{+2} and w^{+2} values over a significant distance for both turbulent flows. Streamwise intensities do not seem to be dependent on the roughness in duct flows (pipe or channel). Generally, in turbulent boundary layer flows, the inverse trend has been observed by many authors (Krogstad et al., 1992a; Acharya and Escudier, 1987). The components of the Reynolds stress anisotropy tensor have been calculated from the turbulence intensities for different type flows. The present data indicate that wall roughness in turbulent duct flows increases the anisotropy of v^{+2}, across the whole duct. The roughness effect on w^{+2} seems to be important in the inner region and relatively lower in the core region of the channel flow, although a difference exists between the data in rough and smooth pipes. The data of Shafi and Antonia (1995) for a rough-wall turbulent boundary layer exhibit an opposite trend for the roughness effect

on the anisotropy of $\overline{u^{+2}}$ and $\overline{v^{+2}}$. The difference results from the existence of a turbulent or nonturbulent interface. The presence of an opposite shear stress on either side of the duct leads to a large contribution to the anisotropic behavior of this tensor. The *II* magnitudes of the rough wall invariants of different flow types are quite close to zero, compared to the data of Erm and Joubert for a smooth wall presented in Shafi and Antonia's paper's (1995). The data of b_{22} and b_{11} over smooth walls are significantly higher than in the case of rough wall boundary layers and rough duct flows. The b_{ij} components and anisotropy invariants map of the Reynolds stress tensor provides a good criterium for indicating the influence of the flow type and nature of the surface in the outer region.

Acknowledgement

The authors would like to acknowledge many useful constructive comments made by Professor R. A. Antonia and the Dr. H. S. Shafi (Dept. of Mechanical Engineering, University of Newcastle, N.S.W., 2308, Australia) and Professor J. Dickinson (Dept. of Mechanical Engineering, University of Laval, Canada).

References

Acharya, M., and Escudier, M., 1987, "Turbulent Flow Over Mesh Roughness," F. Durst, B. E. Launder, J. L. Lumley, F. W. Schmidt, J. H. Whitelaw, eds., *Turbulent Shear Flow 5,* Berlin, Springer, pp. 176–185.

Antonia, R. A., Bisset, D. K., and Browne, L. W. B., 1974, "Effect of Reynolds Number on the Topology of the Organized Motion in a Turbulent Boundary Layer," *Journal of Fluid Mechanics,* Vol. 213, pp. 267–286.

Antonia, R. A., and Luxton, R. E., 1971, "The Response of a Turbulent Boundary Layer to a Step Change in Surface Roughness, Part 1. Smooth to Rough," *Journal of Fluid Mechanics,* Vol. 48, pp. 721–761.

Bandyopadhyay, P. R., and Watson, R. D., 1987, "Measurements of Turbulence Moments in Boundary Layers over Transversely Grooved Surfaces," *Forum on Turbulent Flows,* Cincinnati, June 14–17 New York, ASME, pp. 19–23.

Choi, H., Moin, P., and Kim, J., 1993, "Direct Numerical Simulation of Turbulent Flow Over Riblets," *Journal of Fluid Mechanics,* Vol. 255, pp. 503–539.

Chu, D. C., and Karniadakis, G. E., 1993, "A Direct Numerical Simulation of Laminar and Turbulent Flow Over Riblet-Mounted Surfaces," *Journal of Fluid Mechanics,* Vol. 250, pp. 1–42.

Comte-Bellot, G., 1965, "Ecoulement Turbulent Entre Deux Parois Parallèles," Publication Scientifique et Technique du Ministère de l'Air, No 419.

Djenidi, L., Anselmet, F., and Antonia, R. A., 1994, "LDA Measurements in a Turbulent Boundary Layer over a d-Type Rough Wall," *Experiments in Fluids,* Vol. 16, pp. 323–329.

Djenidi, L., and Antonia, R. A., May 1996, "Laser Doppler Anemometer Measurements of Turbulent Boundary Layer over a Riblet Surface," *AIAA Journal,* Vol. 34, No. 5, pp. 1007–1012.

Erm, L. P., and Joubert, P. N., 1991, "Low-Reynolds Number Turbulent Boundary Layer," *Journal of Fluid Mechanics,* Vol. 230, pp. 1–44.

Krogstad, P. Å., Antonia, R. A., and Brown, L. W. B., 1992a, "Comparison Between Rough- and Smooth-Wall Turbulent Boundary Layers," *Journal of Fluid Mechanics,* Vol. 245, pp. 599–617.

Lumley, J. L., and Newman, G. R., 1977, "The Return to Isotropy of Homogeneous Turbulence," *Journal of Fluid Mechanics,* Vol. 82, pp. 161–178.

Lumley, J. L., 1978, "Computational Modelling of Turbulent Flows," *Advances in Applied Mechanics,* Vol. 18, pp. 123–176.

Osaka, H., and Mochizuki, S., 1988, "Coherent Structure of a d-Type Rough Wall Boundary Layer," Hirata and N. Kasagi, eds., *Transport Phenomena in Turbulent Flow: Theory, Experiments and Numerical Simulation.* New York, Hemisphere, pp. 199–211.

Raupach, M. R., 1981, "Conditional Statistics of Reynolds Stress in Rough-Wall and Smooth-Wall Turbulent Boundary Layers," *Journal of Fluid Mechanics,* Vol. 108, pp. 363–381.

Sabot, J., Saleh, I., and Comte-Bellot, G., 1977, "Effects of Roughness on the Intermittent Maintenance of Reynolds Shear Stress in Pipe Flow," *Physics of Fluids,* Vol. 20, No. 10, pp. S150–S155.

Shafi, H. S., and Antonia, R. A., 1995, "Anisotropy of the Reynolds Stresses in a Turbulent Boundary Layer on a Rough Wall," *Experiments in Fluids,* Vol., pp. 213–215.

Spalart., 1988, "Direct Simulation of a Turbulent Boundary Layer up to R_θ = 1410," *Journal of Fluid Mechanics,* Vol. 187, pp. 61–98.

Teitel, M., and Antonia, R. A., 1991, "Comparison between a Turbulent Boundary Layer and a Turbulent Duct Flow," *Experiments in Fluids,* 11, pp. 203–204.

Wood, D. H., and Antonia, R. A., 1975, "Measurements in a Turbulent Boundary Layer Over a d-Type Surface Roughness," ASME *Journal of Applied Mechanics,* Vol. 42, pp. 591–597.

Numerical Simulation of Turbulent Jets With Rectangular Cross-Section[1]

R. V. Wilson
Graduate Student.

A. O. Demuren
Professor.

Department of Mechanical Engineering,
Old Dominion University,
Norfolk, VA 23529

Three-dimensional turbulent jets with rectangular cross-section are simulated with a finite-difference numerical method. The full Navier-Stokes equations are solved at a low Reynolds number, whereas at a higher Reynolds number filtered forms of the equations are solved along with a sub-grid scale model to approximate effects of the unresolved scales. A 2-N storage, third-order Runge-Kutta scheme is used for temporal discretization and a fourth-order compact scheme is used for spatial discretization. Divergence-free velocity field is obtained by solving a Poisson equation for pressure with the same spatial discretization scheme for consistent accuracy. Computations are performed for different inlet conditions which represent different types of jet forcing within the shear layer. The phenomenon of axis-switching is observed in some cases. At low Reynolds numbers, it is based on self-induction of the vorticity field, whereas at higher Reynolds numbers, the turbulent structure becomes the dominant mechanism in natural jets. Budgets of the mean streamwise velocity show that convection is balanced by gradients of the Reynolds stresses and the pressure.

Introduction

Turbulent jets are present in many physical processes and technological applications. Turbulent jets can be found in combustors where the fuel and oxidizer are introduced as coflowing jets. The efficiency of such a process is largely determined by the mixing of the jets. Recently, jet aircraft noise has received much attention due to plans for a high-speed civil transport vehicle. A critical issue for the project's success is reducing jet noise to acceptable levels near populated areas. The belief is that acoustic patterns can be altered by manipulating the large scale structures in turbulent jet flows through external forcing. Noncircular jets can also be used to enhance the mixing of hot jet gases with the surroundings and thus avoid aircraft detection. In industrial applications, efficient mixing is required to dilute pollutants issuing from smokestacks with the ambient air to minimize its harmful effects or to promote fuel-oxidant mixing in combustion chambers.

Experiments (Tsuchiya et al., 1986, 1989, Quinn, 1989, 1994) have shown that three-dimensional (3-D) jets can be used to enhance mixing and entrainment rates in comparison to nominally two-dimensional (2-D) jets. A fundamental understanding of the dynamics of complex, turbulent jets is required for their prediction and control. The present study is concerned with the understanding of the roles of vorticity and turbulence in the spatial evolution of incompressible 3-D jets in the near to medium field and the effects of external forcing and Reynolds number thereupon. Previous numerical simulations of such flows have been performed by Grinstein (1995), with emphasis on the vorticity dynamics in the near field (less than 5 diameters), and Miller et al. (1995), who studied coflowing jets at a low Reynolds number of 800. In the latter, examination of instantaneous vorticity fields show symmetries which are not indicative of turbulent flow. This work extends those studies into the medium field, beyond the extent of the potential core, and into truly turbulent flows.

Some analytical studies have used vortex-induction arguments or stability analysis to explain some observed phenomena in complex jets, such as axis-switching and enhanced mixing. In the former category are works by Viets and Sforza (1972) and Dhanak and DeBernandis (1981) who applied the Biot-Savart law to predict the evolution of elliptic vortex rings. Jets are of course not vortex rings. Though with some particular type of inlet forcing, vortex rings could be superposed on the jet periphery, and thereby jets can be made to evolve to some extent like vortex rings. In the latter category are studies by Koshigoe and coworkers (1987, 1989) who used a shooting method to analyze instability modes in complex jets, and Tam and Thies (1993) who used a vortex sheet model to analyze the "very" near field of rectangular jets where the boundary layer thickness was still very small. These methods yield useful results, but cannot be used for highly nonlinear situations, especially at higher Reynolds numbers where inviscid and turbulent structure mechanisms compete to determine the jet evolution, nor can they be used for quantitative predictions. On the other hand, conventional RANS (McGuirk and Rodi, 1979) failed to predict observed axis-switching and saddle-shaped velocity profiles in turbulent rectangular jets.

Mathematical Formulation

Governing Equations. The partial differential equations governing the incompressible jet fluid flow are the Navier-Stokes equations which can be written in Cartesian tensor form, for dimensionless variables as:

$$\frac{\partial u_i}{\partial t} + u_j \frac{\partial u_i}{\partial x_j} = -\frac{\partial p}{\partial x_i} + \frac{1}{\mathrm{Re}_{D_e}} \frac{\partial^2 u_i}{\partial x_j \partial x_j} \tag{1}$$

where, u_i are the Cartesian velocity components in the Cartesian coordinate directions x_i, p is the pressure and Re_{D_e} is the Reynolds number based on the equivalent diameter. These equations must be solved in conjunction with the continuity equation:

$$\frac{\partial u_i}{\partial x_i} = 0 \tag{2}$$

which expresses the divergence-free velocity condition.

[1] The authors were partially supported by the National Aeronautics and Space Administration under NASA Contract No. NAS1-19480 while the authors were in residence at the Institute for Computer Applications in Science and Engineering (ICASE), NASA Langley Research Center, Hampton, VA 23681-0001. Additional support was provided by the NASA Graduate Student Research Program.

Contributed by the Fluids Engineering Division for publication in the JOURNAL OF FLUIDS ENGINEERING. Manuscript received by the Fluids Engineering Division November 7, 1996; revised manuscript received March 2, 1998. Associate Technical Editor: S. P. Vanka.

At higher Reynolds numbers, all scales present in the flow cannot be resolved on computational grids that present resources would allow, so a large eddy simulation (LES) must be utilized. The application of a grid filter to Eqs. (1) and (2) results in the filtered equations of motion, in which the overbar indicates a filtered variable:

$$\frac{\partial \bar{u}_i}{\partial t} + \bar{u}_j \frac{\partial \bar{u}_i}{\partial x_j} = -\frac{\partial}{\partial x_i}\bar{p} + \frac{1}{\mathrm{Re}_{D_e}} \frac{\partial^2 \bar{u}_i}{\partial x_j \partial x_j} - \frac{\partial \tau_{ij}}{\partial x_j} \quad (3)$$

and

$$\frac{\partial \bar{u}_i}{\partial x_i} = 0 \quad (4)$$

where $\bar{u}_i$ represents components of the filtered velocity which is resolved in the computation, and τ_{ij} is the subgrid scale (SGS) Reynolds stress which is approximated with the Smagorinsky eddy-viscosity model in the present study.

The Navier-Stokes Eq. (1) and the filtered Eq. (3) are discretized temporally with an explicit Runge-Kutta scheme, and spatially with an implicit, fourth-order, compact finite-difference scheme (see Wilson et al., 1998). The divergence-free velocity condition is satisfied indirectly through the solution of a Poisson equation for pressure, derived by taking the divergence of the momentum equations. In order to maintain consistent global accuracy, this equation is also discretized with the fourth-order compact scheme.

Boundary Conditions. In order to solve a well-posed problem, the boundary and initial conditions for the jet simulations are defined. The ellipticity in the spatial terms of the governing equations requires that boundary conditions be defined on all boundaries. In the laboratory, jet flows are commonly generated by the use of a fan which forces fluid along an enclosed duct of nozzle. The jet leaves the exit plane of the nozzle where it interacts with the ambient fluid. Prior to exit, the jet can be considered to consist of a relatively uniform core with a curved thin boundary layer at the walls of the nozzle. A short distance downstream of the nozzle exit, the boundary layer is smoothened so that the streamwise velocity can be modeled at the periphery with a hyperbolic tangent (tanh) function. The tanh function enables the streamwise velocity to transition in the radial direction from the uniform velocity at the core of the jet to that of the ambient fluid in the freestream. The inflow boundary of the computational domain is placed at a short distance downstream of the nozzle exit which is not actually included in the jet simulations.

The mean or time-averaged streamwise velocity component at the inflow boundary is given by:

$$\bar{u}_1(0, x_2, x_3) = U_c + \frac{(U_H - U_L)}{2} \tanh\left(\frac{r}{2\theta_o}\right) \quad (5)$$

where $U_C = (U_H + U_L)/2$ is the convective velocity and U_H, U_L, represent the velocities of the jet core, and ambient fluid, respectively. The variable r, represents the minimum directed distance from the point, $(0, x_2, x_3)$ to the line of constant convective velocity of the boundary layer. The momentum thickness of the boundary layer at the inflow plane, θ_o is used to normalize the directed distance, r. If the point $(0, x_2, x_3)$ is "outside" the shear layer, r is defined to be negative, otherwise, if the point lies on the inside of the shear layer r is defined to be positive. Equation (5) produces a constant thickness shear layer if the momentum thickness, θ_o, is constant at all azimuthal locations along the jet periphery. Variable-thickness shear layers can be generated by specifying the desired variation of θ_o along the perimeter of the jet. The mean cross-plane velocity components at the inflow plane, $u_2(0, x_2, x_3)$ and $u_3(0, x_2, x_3)$ are specified from experiment. They are close to zero in nozzle jets, but may deviate substantially from zero in orifice jets or in jets with tabs or other vortex generators.

To simulate instabilities in the shear layer, a time dependent forcing function of low intensity is added to the mean velocity components at the inflow boundary to promote unsteady motion. At higher Reynolds numbers or large computational lengths small round-off errors would grow to produce unsteady motion of the unstable shear layers thus obviating the need for forcing functions. Two classes of perturbations are used in the current study; (i) sinusoidal perturbations with frequency and amplitudes related to the most unstable modes found from viscous stability analysis (Wilson and Demuren, 1996); (ii) perturbations having an experimentally measured velocity spectrum and transverse root mean square (rms) value. Perturbations which have a broad spectrum resembling that of fully-developed, mostly random, 3-D turbulence were generated (Wilson, 1993). These perturbations are typical of those found in the experimental jets originating from contoured nozzles. The power spectrum and rms values are taken from experiment. Because phase information is not included in the power spectrum, a random phase relationship for the modes comprising the spectrum was assumed. The random inlet boundary conditions are the spatial analog to the random perturbations generated for use as initial conditions in temporal simulations of mixing layers (Rogers and Moser, 1995). Class (i) represents jets issuing from a nozzle with laminar boundary layers, whereas class (ii) represents jets issuing from a nozzle with turbulent boundary layers.

At lateral boundaries, located sufficiently far from the jet shear layers, freestream conditions prevail, and entrainment velocities are calculated via the corresponding momentum equation in the direction normal to the respective boundary. The downstream boundary is an artificial one. The main requirement is that waves or disturbances not propagate upstream from this boundary, i.e., it should be an absorbent plane. This is achieved with the buffer domain technique proposed by Street and Macareg (1990). In the buffer layer, which was two diameters thick in the present simulations, ellipticity in the governing equations, which appears in diffusion and pressure terms, is gradually eliminated, and the convection velocity also transitions to the local mean streamwise velocity.

Model Problems

Spatial simulations of rectangular jet flows are performed in this study in which a fixed region of the flow is computed and disturbances grow in the streamwise direction. This can be contrasted with a temporal simulation in which a small region of the flow is followed in time and the domain moves in the streamwise direction. Spatial simulations are closer to reality, but are computationally more demanding. As a result of the spatial reference frame, initial conditions are of minor importance because they are quickly convected out of the domain and the dynamics of the jet flow are determined by the forcing functions applied at the inflow plane, until the inherent instabilities of the flow take over or the onset of transition to turbulent flow. Simulations are started on coarser grids with the velocities specified at the inflow plane used to initialize the velocity field in the interior at $t = 0$. After several flow through times (the time required for a fluid particle to convect from the inflow to the outflow plane at the jet core velocity, U_e) the initial conditions are "washed" from the domain. Simulations on finer grids are commenced with initial fields obtained by prolongating the coarser grid results using a standard, 2nd-order accurate interpolation formula.

The rectangular jet of the present study has a nominal aspect ratio of 2:1. This corresponds to the configuration of some jet issuing from contoured nozzle studied by Quinn (private communication). Cases with both low and high Reynolds numbers are considered. In the former, the flow is fully resolved and no sub-grid scale model is required, but in the latter, filtered

Table 1 Grid parameters for resolution study

Grid level	$\Delta x, \Delta y, \Delta z$	N_x, N_y, N_z	L_x, L_y, L_z	Points per wave (PPW)
1	0.386×0.313^2	26×32^2	10^3	1.25
2	0.193×0.156^2	52×64^2	10^3	2.5
3	0.096×0.078^2	104×128^2	10^3	5
4	0.048×0.039^2	104×128^2	5^3	10

equations are solved and an SGS model is utilized. Reynolds numbers based on the core velocity and the equivalent diameter are 750 and 75,000, respectively. In each case, the momentum thickness is constant around the jet and equal to $\frac{1}{30}$th of the jet diameter. The four cases presented in this paper correspond to the two Reynolds numbers and the different types of inlet forcing functions, as explained previously, namely; (i) sinusoidal perturbations with the fundamental mode at an rms of 3 percent of mean jet velocity, and Re = 750; (ii) sinusoidal perturbation with the fundamental and first subharmonic modes, each at an rms of 1.5 percent, and Re = 750; (iii) same perturbations as in (ii), but at Re = 75000; (iv) random broad-mode perturbations with an rms of 3 percent of mean jet velocity, and Re = 75000.

Computational Details. Case (i) was simulated in a domain with size $(10 \times 5 \times 5)$ on a uniform computational grid of $(80 \times 65 \times 65)$, whereas all other cases were simulated on a $(10 \times 10 \times 10)$ domain with computational grids of $(104 \times 129 \times 129)$. The computational grids correspond to 5 points per wavelength (PPW) of the fundamental shear layer instability, in the transverse direction, and 10 PPW in the streamwise direction. Analysis of the fourth-order compact scheme in use here, in several benchmark problems (Wilson et al., 1998), has shown that roughly 6 PPW are sufficient for accurate simulation. The compact scheme is inherently non-diffusive and non-dissipative, and with adequate resolution dispersive errors are minimized. In contrast, a second-order central-difference scheme required about 32 PPW. In a previous study (Wilson and Demuren, 1996), growth rates of fundamental and subharmonic instability modes, predicted by viscous and inviscid stability theory, were accurately reproduced by direct simulation.

Grid Resolution Study. A grid sensitivity test was performed for the model problem of case (iv). The grids are refined by halving the spacing in each direction. Table 1 summarizes the grid parameters. Due to computational cost, the full domain could not be used for the finest grid resolution, hence the domain was reduced in size so that only the first 5 diameters could be compared in this case. Computed results are compared in Fig. 1. The two coarsest grids are clearly inadequate. These correspond to the use of 1.25, and 2.5 PPW in the shear layers, respectively, and so these are grossly underresolved. Hence, the limited jet growth and mixing. However, on the two finest grids, with 5 and 10 PPW, respectively, the shear layers are well resolved and reasonable growth is seen. The main difference between them is that at the finest resolution there is a shift of about 0.7 diameters in the length of the potential core from 4.1 De on the level 3 grid to 3.4 De. It is not clear what influence the limited streamwise extent (5 De) of the computational domain in the level 4 grid played in this. If the results are plotted relative to the end of the potential core, they lie almost on top of each other. Hence, the resolution of the level 3 grid is considered adequate and is utilized in all other simulations reported here.

Results and Discussion

Low Reynolds Number Jets. Figures 2 and 3 show computed instantaneous vorticity fields for the low Reynolds number cases (i) and (ii), respectively. In case (i), the flow remains

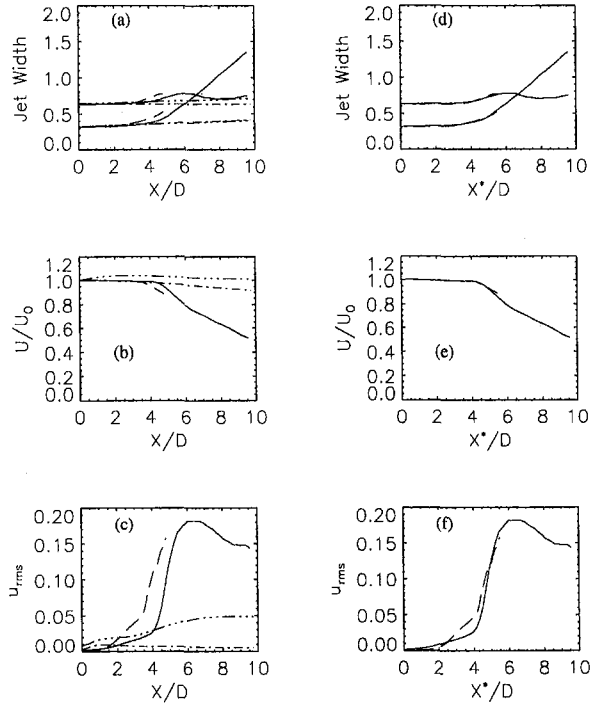

Fig. 1 Effect of grid resolution, (a)–(c) time-averaged quantities versus x, (d)–(f) level 4 grid corrected for length of potential core; (dot-dash: level 1 grid; 3 dots-dash: level 2 grid; solid: level 3 grid; dash: level 4 grid)

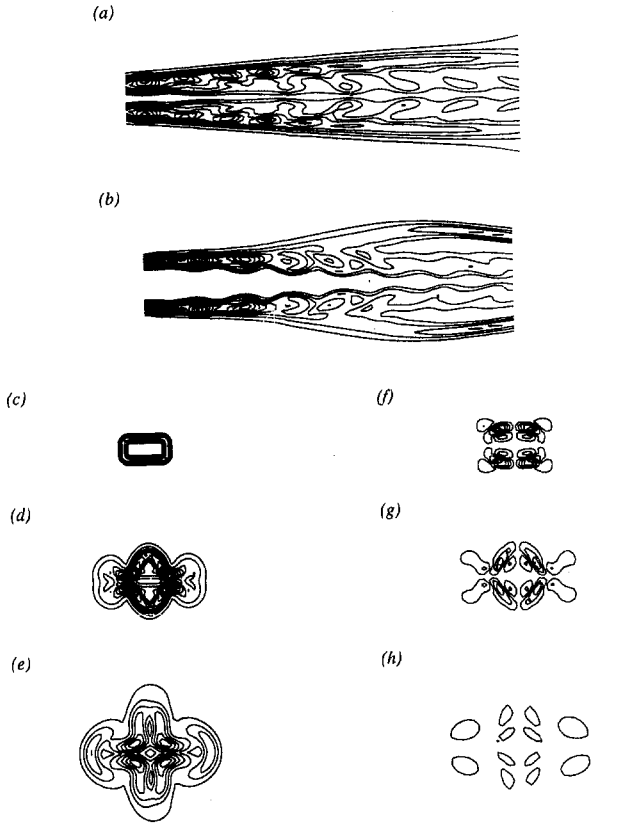

Fig. 2 Contours of vorticity magnitude, (a)–(e) and streamwise vorticity, (f)–(h) for case (i) at $t = 2$ flow through times, for fundamental forcing function. (a) Minor axis plane, $z/D_e = 0$, (b) major axis plane, $y/D_e = 0$, (c) cross flow plane, $x/D_e = 0$, (d) $x/D_e = 5$, (e) $x/D_e = 10$, (f) $x/D_e = 2.5$, (g) $x/D_e = 5$, and (h) $x/D_e = 10$.

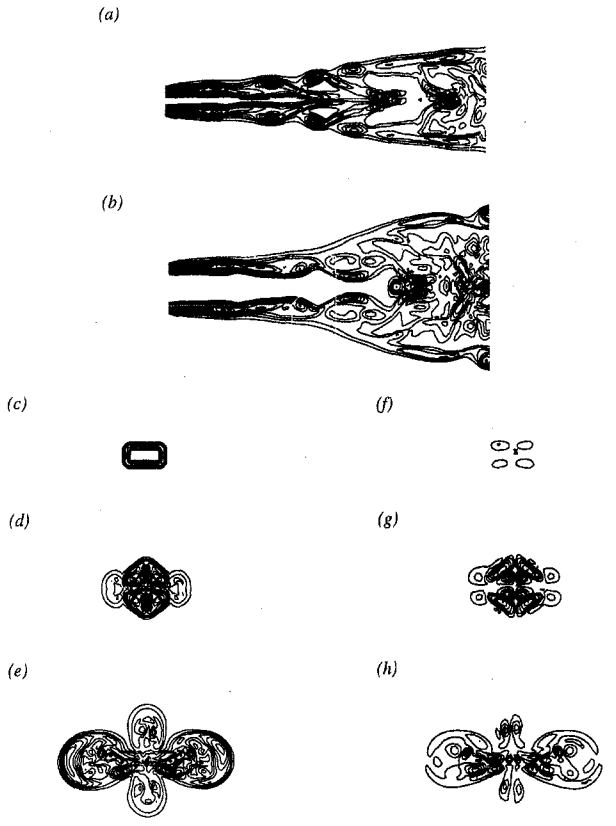

Fig. 3 Contours of vorticity magnitude, (*a*) – (*e*) and streamwise vorticity, (*f*) – (*h*) for case (ii) at $t = 2$ flow through times, for fundamental and first subharmonic forcing function. (*a*) Minor axis plane, $z/D_e = 0$, (*b*) major axis plane, $y/D_e = 0$, (c) cross flow plane, $x/D_e = 0$, (d) $x/D_e = 5$, (e) $x/D_e = 10$, (*f*) $x/D_e = 2.5$, (*g*) $x/D_e = 5$, and (*h*) $x/D_e = 10$.

symmetrical about the major and minor axes, just like the inlet mean flow and perturbation velocities, hence the flow has remained laminar and transition to turbulence did not occur in the 10 diameters computed. The phenomenon of axis switching is observed to be taking place near the end of the domain. The source of this is seen to be clearly in the complex vorticity field. It is most likely due to self-induction, since there is no streamwise vorticity at the inlet plane. It appears that the effect of the induced streamwise vorticity field is to pump fluid from the major axis to the minor axis. This process can be explained with deformation of vortex rings as described by Dhanak and DeBernardis (1981). Spanwise rollers are seen in Figs. 2(*a*) and (*b*) which form superelliptical vortex rings. Through self-induction, the narrow ends will move faster in the streamwise direction than the wider sides; a process which will eventually lead to axis-switching. In case (ii), the vortex field is even more complex. Self-induction must now compete with the instability mechanism which produces vortex pairing in 2D mixing layers. In the latter (see Wilson and Demuren, 1996), the presence of the sub-harmonic disturbance mode produces a transverse shift, into faster moving fluid, in every other spanwise roller which eventually catches up with the preceding roller and pairs with it. The effect of this process, in this 3D case, is that two subsequent vortex rings now have different shapes and the interaction between them produces neither pairing nor axis-switching. Rather, as seen in Fig. 3(*a*), along the minor axis plane, each pair of spanwise rollers is sucked in between the proceeding pair, thereby producing a reduction in width. Correspondingly, the pair of rollers, along the major axis plane are pushed out, thereby producing an increase in width in the plane. The net effect is opposite to the tendency towards axis-switching in the single mode case of (i). In fact, Fig. 3(*e*) shows that the jet is moving toward bifurcation. A similar phenomenon was observed by Zaman (1996) in experiments in rectangular jets in which tabs were placed in the exit plane along the wider sides. In that case, the jet bifurcation was caused by the streamwise vorticity induced by the tabs, whereas in the present case, the streamwise vorticity inducing bifurcation, evolved naturally. Zaman also observed axis-switching, similar to our case (i), when the tabs were placed along the narrow sides of the rectangular plane. Hence, the natural processes simulated in cases (i) and (ii) can be achieved experimentally by selective placement of tabs. The effects are of course stronger in the latter, but at the expense of higher pressure losses. Now, since the flow remains laminar, these processes are inviscid and are unrelated to turbulence-generated secondary flow as found in streamwise corners, the so-called secondary flow of Prandtl's second kind, (e.g., Demuren and Rodi 1984). The role of viscosity is to promote the eventual decay of this secondary motion. We can speculate that in the presence of more sub-harmonic modes, self-induction will not lead to axis-switching. The result was confirmed by further simulation by Wilson (1996), not reported here. Thus natural jets at low Reynolds numbers, with a broad mode of disturbances in the shear layer are not expected to undergo axis-switching.

High Reynolds Number Jets. At higher Reynolds numbers, transition to turbulence occurs in the near field. There is then a competition between largely inviscid mechanisms and turbulent mechanisms in the subsequent evolution of the jet. The question is which mechanism dominates, under what condi-

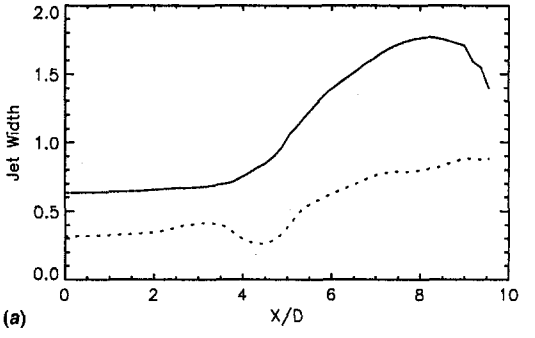

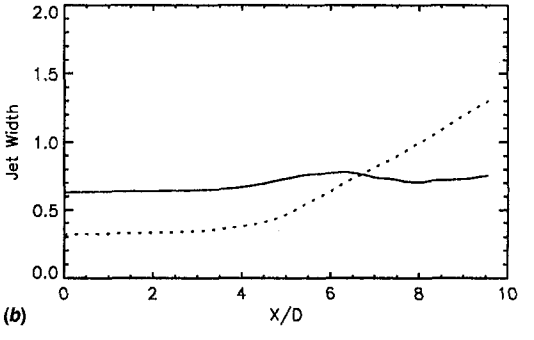

Fig. 4 Jet half-widths for (*a*) case (iii), (*b*) case (iv) (solid—major axis plane, dashed–minor axis plane)

tions? Time-averaged jet half-widths are shown for the two high Reynolds number cases, (iii) and (iv) in Fig. 4. We see that in case (iii), with discrete two-mode forcing, no axis-switching occurred up to ten diameters downstream. This result is in agreement with that of case (ii), and is confirmation that in this case the phenomenon of axis-switching is not controlled by inviscid mechanisms rather than turbulence structure. Grinstein (1995) has also demonstrated axis-switching in simulations of turbulent jets with strong axial single-mode forcing. This is similar to our non-turbulent case above, so self-induction is again responsible. On the other hand, in case (iv) axis-switching occurred at about 7 diameters, in contrast to the nonturbulent case. This inlet condition, with a broad-mode spectrum of perturbations is indicative of a jet evolving from a nozzle with turbulent boundary layers. Experimental data from similar conditions (Tsuchiya and Horikoshi, 1986, and Quinn, 1995) suggest that axis-switching was observed at 6 and 11 diameters, respectively. Figure 5 shows a comparison of the computed time-averaged streamwise velocity and the jet half-widths to experimental data. The potential core lengths are roughly the same in computed and experimental results, but the computations indicate a faster rate of velocity decay, subsequently. This would indicate higher entrainment and associated spread rates. Figure 5(*b*) shows that computed half-widths along the major axis plane are comparable to experimental data, but they are much larger along the minor-axis plane, which is indicative of much stronger axis-switching effect and higher entrainment rates. We should, of course, not expect perfect agreement with experimental data. Our computations were performed with a constant momentum thickness around the periphery of the jet, whereas the momentum thickness was not constant in the experiments. Analyses and experimental data of Koshigoe et al. had shown significant influence of the momentum thickness distribution in subsequent jet evolution. However, the presence of axis-switching should not be equated directly with increased entrainment of ambient fluid, which is desired in several engineering applications. Integration of the entrained flow shows that more ambient fluid was entrained in case (iii) than in case (iv).

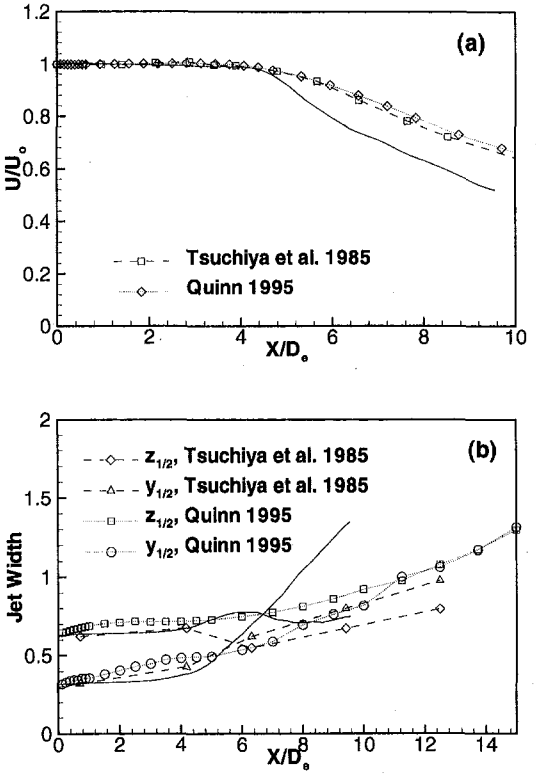

Fig. 5 Comparison of (*a*) jet mean velocity decay and (*b*) jet half-widths to experimental data

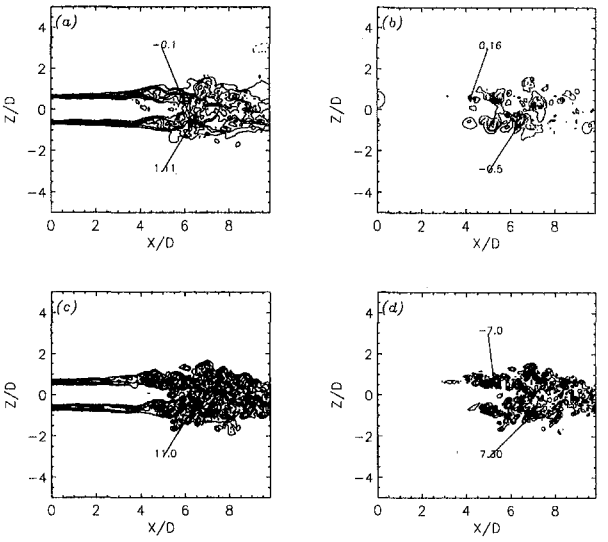

Fig. 6 Instantaneous contours of dimensionless (*a*) streamwise velocity, (*b*) pressure, (*c*) total vorticity, (*d*) streamwise vorticity along major axis plane at $t = 9$ flow through times, for case (iv). (Numbers represent peak values.)

All subsequent results focus on case (iv), which is closest to experiment of unforced jets. Figures 6 and 7 show instantaneous fields of the streamwise velocity, pressure, total vorticity, and the streamwise vorticity in the major and minor axis planes, respectively, after nine flow through times. Displayed numbers correspond to peak values for each variable, and negative values are drawn with dashed lines. The potential core of the jet extends to about 4 diameters, and significant streamwise vorticity commences from this location downstream. The latter quickly reached peak values by about 6 to 7 diameters, and subsequently decayed in strength further downstream. The location of axis crossover corresponds roughly to the location of peak streamwise vorticity. Analysis of the mean streamwise vorticity equation indicates that the main generation mechanism is the anisotropy of the turbulence field, similar to that in complex duct flows. *That is, for natural turbulent jets, with a broad-mode of*

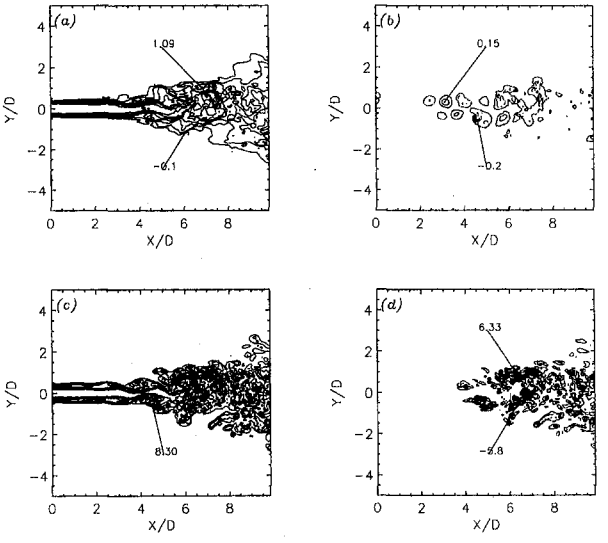

Fig. 7 Instantaneous contours of dimensionless (*a*) streamwise velocity, (*b*) pressure, (*c*) total vorticity, (*d*) streamwise vorticity along minor axis plane, at $t = 9$ flow through times, for case (iv). (Numbers represent peak values.)

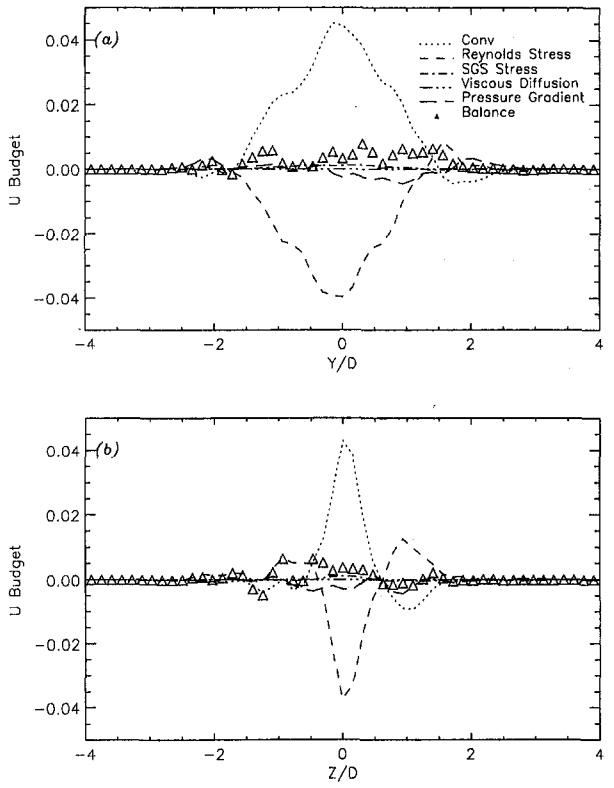

Fig. 8 Balance of terms in the mean streamwise momentum equation, for case (iv) at $x/D_e = 9.4$. (*a*) minor axis; (*b*) major axis

instabilities in the shear-layer, jet evolution is controlled by turbulence-induced secondary flow, i.e., of Prandtl's second kind, and not by self-induction as in forced jets. Hence, axis-switching in complex jets can be predicted with RANS, so long as the turbulence model utilized can reproduce the anisotropy of the turbulence. McGuirk and Rodi (1979) had utilized a $k - \epsilon$ turbulence model which is inadequate for this purpose. Therefore, their inability to predict axis-switching is not now surprising. Some form of Reynolds stress model (full or algebraic) would be required.

Figure 8 shows the balance of terms in the streamwise momentum equation, time-averaged over 6000 time steps and approximately 10 flow-through-times. We see that, by an overwhelming margin, the spatial convection is balanced by gradients of the resolved Reynolds stresses. By comparison, gradients of the SGS stresses are negligible, which would indicate the reliability of the LES approach for this problem, even at the chosen Reynolds number of 75,000. The third most important term is the pressure gradient. In fact, near the edges, it is the dominant term which balances spatial convection, i.e., it acts as the source for the entrainment of ambient fluid. The symbols, in the figure, represent the lack of balance or drift from steady state, which is indicative of the adequacy or otherwise of the sample size used in the time-averaging process. With no homogeneous direction in the present flow, the sample size seems to be adequate. Further time-averaged quantities of first and second moments, as well as budgets of the respective equations can be found in Wilson (1996).

Concluding Remarks

Numerical simulation of jets with rectangular cross-section have been performed using a third-order Runge-Kutta scheme for temporal integration and a fourth-order compact scheme for spatial discretization. Cases at low Reynolds numbers are direct simulations and those at high Reynolds number are large eddy simulations.

The phenomenon of axis-switching is observed to be dependent on instability waves present in the inlet boundary layers, and could be induced in both laminar and turbulent jets by single-mode forcing. It is confirmed that this is based on self-induction of the vorticity field. The presence of a discrete subharmonic mode led to its suppression, but entrainment of ambient fluid was still enhanced, and there was a tendency towards bifurcation.

Self-induction cannot produce axis-switching in jets which have a broad mode of instabilities in their shear layers. In non-turbulent jets, no axis-switching occurs. In turbulent jets, turbulence-induced secondary flow is responsible for axis-switching.

Budget of terms in the mean streamwise momentum equation showed that spatial convection is balanced mostly by gradients of the Reynolds stresses, with pressure gradients making a minor contribution. However, near the edges, ambient fluid entrainment is fueled by the pressure gradients. Terms involving the SGS stresses and viscous diffusion are negligible.

Acknowledgment

The authors wish to acknowledge many fruitful discussions with Dennis Bushnell. The simulations were performed on the Cray C-90 computer at NAS, NASA Ames Research Center, the use of which is gratefully acknowledged.

References

Demuren, A. O., and Rodi, W., 1984, "Calculation of Turbulence-Driven Secondary Motion in Non-Circular Ducts," *Journal of Fluid Mechanics,* Vol. 140, pp. 189–222.

Dhanak, M. R., and DeBernandis, B., 1981, "The Evolution of an Elliptic Vortex Ring," *Journal of Fluid Mechanics,* Vol. 100, pp. 189–216.

Grinstein, F. F., 1995, "Self-Induced Vortex Ring Dynamics in Subsonic Rectangular Jets," *Physics of Fluids,* Vol. 7, pp. 2519–2521.

Koshigoe, S., and Tubis, A., 1987, "Wave Structures in Jets of Arbitrary Shape. II. Application of a Generalized Shooting Method to Linear Instability Analysis," *Physics of Fluids,* Vol. 30, pp. 1715–1723.

Koshigoe, S., Gutmark, E., Schadow, K. C., and Tubis, A., 1989, "Initial Development of Noncircular Jets Leading to Axis Switching," *AIAA Journal,* Vol. 27, pp. 411–419.

McGuirk, J. J., and Rodi, W., 1979, "The Calculation of Three-Dimensional Turbulent Free Jets," *Turbulent Shear Flows I,* F. Durst, B. E. Launder, F. W. Schmidt and J. H. Whitelaw, eds., pp. 71–83.

Miller, R. S., Madnia, C. K., and Givi, P., 1995, "Numerical Simulation of Non-Circular Jets," *Comp. Fluid.,* Vol. 24, pp. 1–25.

Quinn, W. R., 1989, "On Mixing in an Elliptic Turbulent Free Jet," *Physics of Fluids A,* Vol. 1, No. 10, pp. 1716–1722.

Quinn, W. R., 1994, "Experimental Study of a Turbulent Free Jet Issuing from a Small-Aspect-Ratio Sharp-Edged Rectangular Slot," *Proc. 2nd Int. Conf. Expt. Fluid Mech.,* Turin, Italy.

Quinn, W. R., 1995, "Turbulent Mixing in a Free Jet Issuing from a Low Aspect Ratio Contoured Rectangular Nozzle," *The Aeronautical Journal of the Royal Aeronautical Society,* Vol. 99, No. 988, pp. 337–342.

Rogers, M. M., and Moser, R. D., 1994, "Direct Simulation of a Self-Similar Turbulent Mixing Layer," *Physics of Fluids,* Vol. 6, No. 2, pp. 903–923.

Street, C. L., and Macareg, M. G., 1990, "Spectral Multi-Domain for Large-Scale Fluid Dynamic Simulations," *Applied Numerical Mathematics,* Vol. 6, pp. 123–139.

Tam, C. K. W., and Thies, A. T., 1993, "Instability of Rectangular Jets," *Journal of Fluid Mechanics,* Vol. 248, pp. 425–448.

Tsuchiya, Y., and Horikoshi, C., 1986, "On the Spread of Rectangular Jets," *Expt. Fluid.,* Vol. 4, pp. 197–204.

Tsuchiya, Y., Horikoshi, C., Sato, T., and Takahashi, M., 1986, "A Study on the Spread of Rectangular Jets," *JSME Int. J.,* II, Vol. 32, pp. 11–18.

Viets, H., and Sforza, P. M., 1972, "Dynamics of Bilaterally Symmetric Vortex Rings," *Physics of Fluids,* Vol. 15, No. 2, pp. 230–240.

Wilson, R. V., 1993, "Numerical Simulation of Two-Dimensional, Spatially Developing Mixing Layers," Masters thesis, Old Dominion University.

Wilson, R. V., 1996, "Numerical Simulation of Complex Three-Dimensional Turbulent Free Jets." Ph.D. thesis, Old Dominion University.

Wilson, R. V., and Demuren, A. O., 1996, "Two-Dimensional Spatially-Developing Mixing Layers," *Numerical Heat Transfer, A.,* Vol. 29, pp. 485–509.

Wilson, R. V., Demuren, A. O., and Carpenter, M. H., 1998, "Higher-Order Compact Schemes for the Numerical Simulation of Incompressible Flows," ICASE Report 98-13.

Zaman, K. B. M. Q., 1996, "Axis Switching and Spreading of an Asymmetric Jet: The Role of Coherent Structure Dynamics," *Journal of Fluid Mechanics,* Vol. 316, pp. 1–27.

Experimental and Numerical Investigation Into the Flow Characteristics of Channels Etched in ⟨100⟩ Silicon

S. M. Flockhart
Research Student.

R. S. Dhariwal
Lecturer.

Department of Computing and Electrical Engineering, Heriot-Watt University, Riccarton, Edinburgh, Scotland, UK, EH14 4AS

This paper describes the experimental and numerical techniques utilized to determine the flow characteristics of a series of trapezoidal channels. The channels, with hydraulic diameters ranging from 50 to 120 μm, are fabricated in silicon using micro fabrication technology. During this investigation the flow results, using distilled water as the test fluid, were kept well within the laminar flow regime, with the experimental results not exceeding a Reynolds number of 600. In order to compare the experimental results to the theoretical response, a numerical technique is employed to determine the predicted flow. This essentially involves solving the unknown coefficients of the Dirichlet equation using a numerical method called the Householder Transformation. The numerical results, provide a comparison to the experimental results and allows us to determine whether flow in channels of these dimensions, fabricated in silicon, produce results comparable to the predicted theoretical response.

1 Introduction

Recent advances in microtechnology, such as the fabrication of micropumps, valves, etc. have resulted in a great deal of research being concentrated within the field of microfluids. (Gravesen (1993) reviews the advances in microfluid devices constructed using micro-fabrication techniques.) However, to design efficient micro-fluid devices it is essential to be able to predict flow in cavities of micron dimensions.

The idea that flow in cavities of micron dimensions would deviate from the classical approach is not a new concept, in fact it was first voiced by Eringen in 1964. His work provided the starting point in the investigation of microcontinuum fluid mechanics. Eringen suggested that a significant difference between the flow predicted using the conventional macro-scale laws, and the actual physical flow may occur when the flow is in a cavity of which one of the dimensions is of similar magnitude to the molecular size of the medium. Another possible reason for a deviation is that the continuity assumption of mass density is no longer applicable when the volume element approaches the size of the fluid particle. (A review detailing the developments in microcontinuum fluid mechanics was written by Ariman (1973).)

Over the years there has been a great deal of research time devoted to determining if, as predicted by Eringen, flow in cavities of micron dimensions differs greatly from that predicted using classical theories. The literature available on this topic appears to provide conflicting results. For example, Israelachvili (1986) reports that the macro-scale model holds for dimensions down to the last molecular layer. However, Harley and Bau (1989) report that for a trapezoidal channel with hydraulic diameter of 45 μm, using *n*-propanol as the test fluid, the Poiseuille number is larger then expected and concludes that further investigation is required. Also, Pfahler et al. (1991) investigated channels ranging in hydraulic diameter from 0.96 to 39.7 μm. Their results indicate that as the hydraulic diameter gets smaller, the results deviate further from the conventional macroscopic models.

This study investigates the flow in trapezoidal channels, etched in ⟨100⟩ silicon, with hydraulic diameters ranging from 50 to 120 μm. The experimental differential pressure (Δp) and volume flow rate (Q) characteristics of the channels are determined using the experimental technique detailed in this paper, which will be directly compared to the conventional macro-scale theoretical results. In predicting the theoretical $\Delta p/Q$ relationship for the trapezoidal channels a numerical technique is utilised. This is due to the fact that no simple equation or experimental data exists, as is the case for circular ducts, with which to determine the flow characteristics of trapezoidal channels. Shah and London (1978) investigated numerically the flow in various shaped ducts, including that of trapezoids, the results of which shall be used as a comparison in this study. The numerical technique utilized essentially involves solving the unknown coefficients of the Dirichlet equation using a numerical technique called the Householder Transformation (Ralston and Rabinowitz, 1978). This transformation has the effect of reducing errors as well as calculation time.

As well as comparing the theoretical results to the experimental data, a brief investigation into the losses due to the introduction of a 90 degree corner was performed. This involves only experimental analysis.

2 Experimental Procedure

The micro-channels were fabricated by Siemens in ⟨100⟩ silicon, using a two-stage wet anisotropic etching technique (Petit et al., 1985 and Allen, 1981). This results in the channels having a trapezoidal cross section, defined by the orientation of the silicon crystal planes, with $\theta = 54.74$ deg. A 500 μm Corning glass wafer is anodically bonded to complete the structure. A top view of the silicon wafer and a list of channel dimensions is provided in Fig. 1 and Table 1, respectively. All the channels on a single wafer are of the same depth, and in this study channel depths of 27 and 63 μm were investigated.

A schematic representation of the experimental apparatus is provided in Fig. 2. The basic components of the system are comprised of a constant volume fluid pump, a vacuum pump, two pressure transducers, and a set of accurate electronic scales.

Connection to the silicon test plate, on which the channels are etched, is achieved as shown in Fig. 3. The connectors, 0.8

Contributed by the Fluids Engineering Division for publication in the JOURNAL OF FLUIDS ENGINEERING. Manuscript received by the Fluids Engineering Division November 21, 1996; revised manuscript received December 4, 1997. Associate Technical Editor: P. R. Bandyopadhyay.

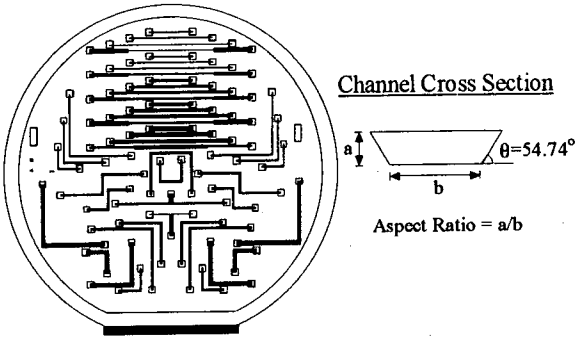

Fig. 1 Top view of silicon test plate and microchannel cross section

Table 1 Channel configuration and dimension

Channel shape	Dimensions (w = width, L = length)
	w = 100, 300, 450, 600, 1000 μm L = 12, 24, 36 mm
	w = 300, 450, 1000 μm L = 6/6, 12/12, 18/18 mm
	w = 450 μm L = 6/6/6, 12/6/12 mm
	w = 450 μm L = 6/6/6, 12/6/12 mm
	w = 1000/100/1000, 1000/300/1000, 1000/450/1000, 300/1000/300 μm L = 12/24/12 mm
	w = 100/600/100 μm w = 300/1000/300 μm L = 16/2.5/16 mm L = 6/6/6 mm

mm internal diameter LEE connectors, are inserted into the base plate which is separated from the test plate by a series of O-rings. When a vacuum is applied the silicon test plate is forced onto the O-rings, producing a tight seal which can be maintained for pressures of up to 12 Bar.

The experimental procedure involves varying the flow rate of the test fluid, in this case distilled water, and monitoring the pressure drop across the channel under test, the volume flow rate, and finally the temperature of the test fluid. The volumetric flow rate was determined by monitoring the time taken to collect a given mass of fluid, and dividing this by the temperature adjusted density value.

Losses due to the connecting system are characterized by analyzing the pressure drop, over a range of flow rates, across a short section of channel with the same internal diameter as the connectors, Fig. 3. This result is then subtracted from the

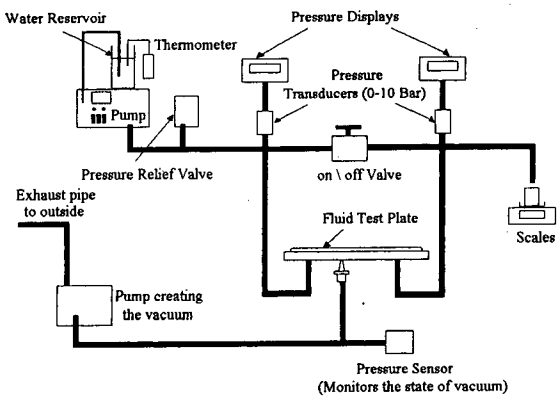

Fig. 2 Schematic of experimental apparatus

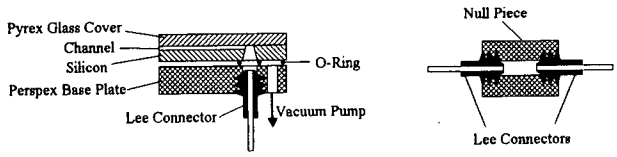

Fig. 3 Schematic of connecting system and null piece

flow results achieved for each channel in order to obtain the true flow characteristics of the channel under test.

A brief investigation was undertaken to determine experimentally the losses due to the introduction of a 90 deg corner, Fig. 4. The corner is slightly tapered due to undercutting of the mask at the fabrication stage. An estimate of the depth of taper is provided by δ, which equates to approximately 6 times the channel depth. The $\Delta p/Q$ losses due to the corner, R_{corn}, were determined by firstly calculating the hydraulic resistance, $\Delta p/Q$, of the L shaped channels, $R_{tot,sb}$. The channel was then broken into its components, i.e., straight and corner sections, resulting in the expression below, where R_{st} is the hydraulic resistance, $(\Delta p/Q)_{st}$, per mm of the straight channel, L_{st} is the total length of straight section, and finally R_{corn} is the hydraulic resistance associated with the corner. For each width of L shaped channel there are 3 lengths, producing three equations, for which the calculated value of R_{corn} should be the same, allowing R_{corn} and in turn R_{st} to be determined. The values obtained for R_{st} were then compared to the experimental and numerical results obtained during the analysis of the straight channels. It should be noted that due to the configuration of the channels, it was not possible simply to subtract the result for the straight channel from that of the L shaped channel in order to determine the corner losses.

$$R_{tot,sb} = R_{st}L_{st} + R_{corn} \quad (1)$$

The errors associated with the experimental analysis falls into two categories. First, there is an error due to experimental measurements, and second, an error associated with channel geometry. The total error due to measurement, i.e., pressure, volumetric flow, fluid temperature, etc., was calculated to be in the region of 1 percent. In considering the error in channel dimensions some thought has to be given to the technique used to fabricate the channels. As previously mentioned, the channels are etched using a two-stage wet anisotropic etching process and there is therefore going to be negligible error associated with the channel width and length, resulting in only channel depth producing a possible error. The channel is etched to the appropriate depth by monitoring time, the etch rate being 57.4 ± 0.5 micrometer per hour. This produces a possible error in result of approximately ±3.5 percent producing a total error in the range of ±4.5 percent.

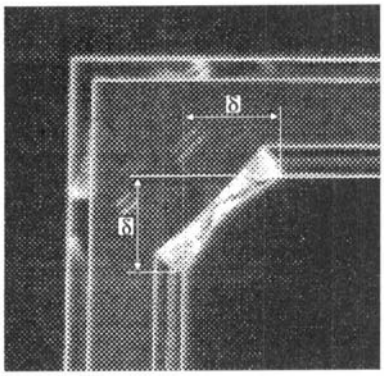

Fig. 4 Photograph of corner section in a 0.3 μm wide channel

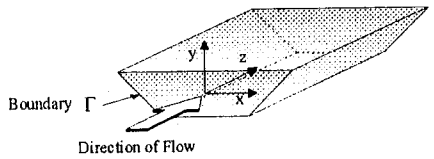

Fig. 5 Trapezoidal channel

3 The Analytical Problem

The trapezoidal channel, Fig. 5, is described in terms of polar coordinates. When considering an isothermal, Newtonian fluid, exhibiting fully developed laminar flow, in a channel of constant cross section the differential momentum equation, described in terms of polar coordinates, is provided below.

$$\nabla^2 u = \frac{1}{r}\frac{\partial}{\partial r}\left(r\frac{\partial u}{\partial r}\right) + \frac{1}{r^2}\frac{\partial^2 u}{\partial \theta^2} = \frac{1}{\mu}\cdot\frac{dp}{dz} \tag{2}$$

$$u^* = \frac{u}{dp/\mu dz} \Rightarrow \nabla^2 u^* = 1 \tag{3}$$

$$\varphi^* = u^* - \frac{r_i^2}{4} \quad \text{where} \quad \varphi^* = \frac{R_i^2}{4} \tag{4}$$

$$\nabla^2 \varphi^* = 0 \quad \textit{Laplaces Equation} \tag{5}$$

On creating a dimensionless velocity, (3), and applying the transformation stated in (4), the velocity problem reduces to solving Laplaces equation, which has a general solution described below.

$$\varphi^* = a_0 + \sum_{n=1}^{N} R_i^n [a_n \cos(n\theta_i) + b_n \sin(n\theta_i)] = \frac{R_i^2}{4} \tag{6}$$

From Eq. (6) it becomes apparent that the total number of unknown coefficients, n, is equal to $2N + 1$. If m points on the boundary are considered, where R_i and θ_i are known, there are m equations available to determine n unknowns. Equation (6) can be represented as $A\mathbf{x} = \mathbf{y}$ where A is an $m \times n$ matrix and vector $\mathbf{x}$ and $\mathbf{y}$ are column vectors having n and m components, respectively. The A matrix is constructed using the polar coordinates used to define the channel boundary, $\mathbf{x}$ contains the unknown coefficients and, finally, vector $\mathbf{y}$ comprises of the R_i values. This is essentially a least squares problem and in this investigation the Householder Transformation technique was utilized to reduce matrix A into an upper triangular matrix. On reducing matrix A the unknown coefficients of $\mathbf{x}$ can be determined using simple matrix manipulation techniques. The coefficients are then substituted into the equation below in order to construct a velocity profile describing the flow within the duct, Fig. 6. To calculate the resulting volumetric flow rate the flow through each small area, defined by the points for which the fluid velocity is computed, is determined and added together to provide the total volume flow.

$$u = -\frac{1}{\mu}\cdot\frac{dp}{dz}\left[\frac{R_i^2}{4} - (a_0 + \sum_{j=1}^{N} r_i^2(a_j \cos j\theta_i + b_j \sin j\theta_i)\right] \tag{7}$$

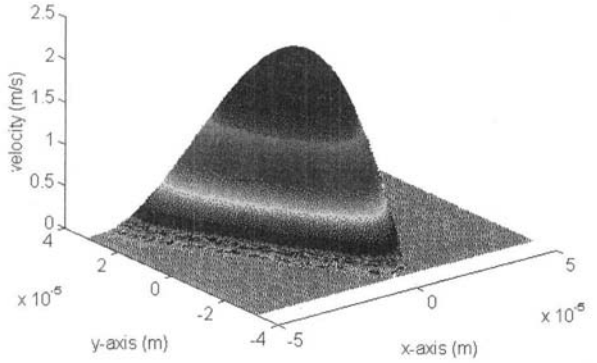

Fig. 6 Numerically determined velocity profile for a 100 μm wide, 63 μm depth, 12 mm long channel

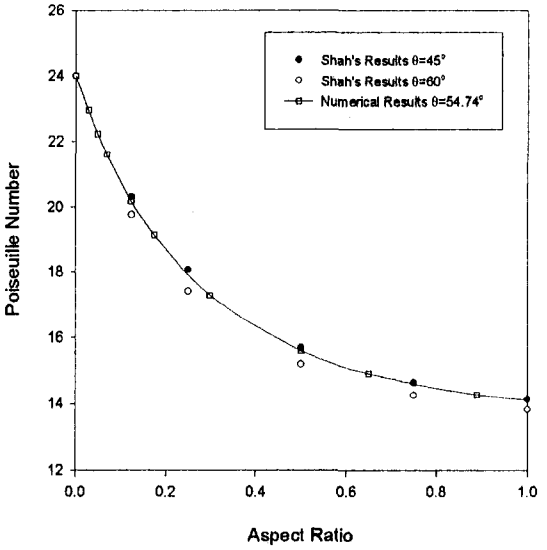

Fig. 7 Comparison between the published data of Shah and London and the numerically determined results for a channel with θ = 54.74 deg

4 The Poiseuille Number

Relatively little work has been undertaken in order to determine the flow characteristics of arbitrarily shaped ducts, therefore very little data exists to which this work can be directly compared. However, Shah and London (1978) calculated numerically the flow in various shaped ducts including that of the trapezoid, and their results will be used as a comparison in this study.

Shah and London describe the results in terms of channel cross section, i.e., aspect ratio, and the Poiseuille number, P_o. The Poiseuille number is a constant describing the flow characteristics of an isothermal, Newtonian fluid, exhibiting fully developed laminar flow, in a channel of arbitrary but constant cross section. In order to calculate the Poiseuille number the Fanning friction factor is multiplied by the Reynolds number, resulting in the equation detailed below. The Poiseuille number is described in terms of the differential pressure, Δp, channel length, L, volume flow rate, Q, fluid viscosity, μ, channel cross-sectional area, A, and, finally, hydraulic diameter, D_h.

$$P_o = \frac{AD_h^2 \Delta p}{2\mu QL} \tag{8}$$

Once the Poiseuille number is determined the flow characteristics of the channel can be calculated readily.

Shah and London calculated numerically the flow rate for various trapezoidal shapes, which include channels with θ equal to 45 and 60 degrees. The numerical results achieved in this study are plotted in Fig. 7, and compared to those detailed by Shah and London. As expected, the numerical results of this study lie between the 45 and 60 degree cases determined by Shah and London. In addition, the study of Urbanek et al. (1993) into the temperature dependence of Poiseuille numbers in microchannel flow, stated that for channels with an aspect ratio of 0.0277 the numerically determined P_o was calculated to be 22.94, which corresponds very well with the results detailed in this study. This provides confidence in the numerical

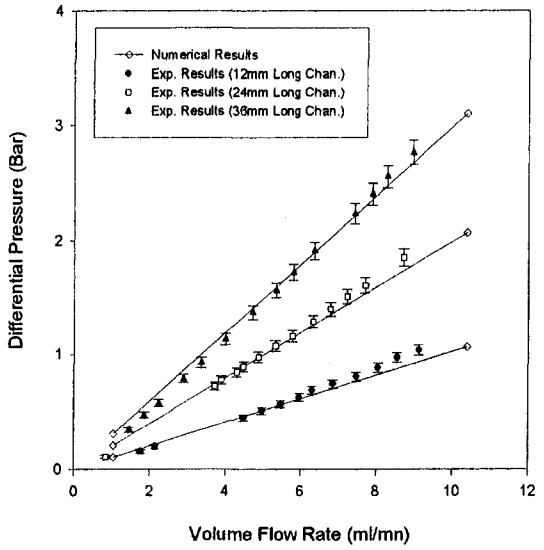

Fig. 8(*a*) Comparison between experimental and numerical results for 1 mm wide, 63 μm depth channels (aspect ratio = 0.0692)

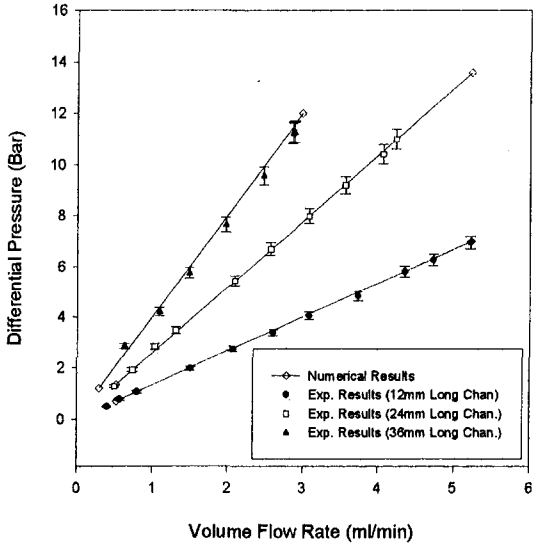

Fig. 8(*b*) Comparison between experimental and numerical results for 1 mm wide, 27 μm depth channels (aspect ratio = 0.0281)

technique and therefore in the results produced using the described analysis.

6 Results

A comparison of the experimental and numerical results for the 63 and 27 μm depth, 1 mm wide channels, is provided in Figs. 8(a) and (b), respectively. Each graph includes the results obtained for the 12, 24, and 36 mm length ducts.

Figure 9 provides a comparison, for each channel investigated, between the numerical and experimentally computed Poiseuille results. The error bars are included on the results achieved for the 36 mm length ducts. This result, coupled with those of Figs. 8(a) and (b), suggest that entry losses exist, which is particularly evident in the shorter length channels. The experimental Poiseuille numbers, for ducts of the same cross section, appear to decrease, approaching the numerical result, as the channel length increases. It is also evident from Figs. 8(a) and (b) that the numerical results coincide to a greater degree with the experimental results achieved for the 27 μm depth channel.

The estimated $\Delta p/Q$ losses due to the introduction of a 90 degree corner are provided in Fig. 10. Also included on this

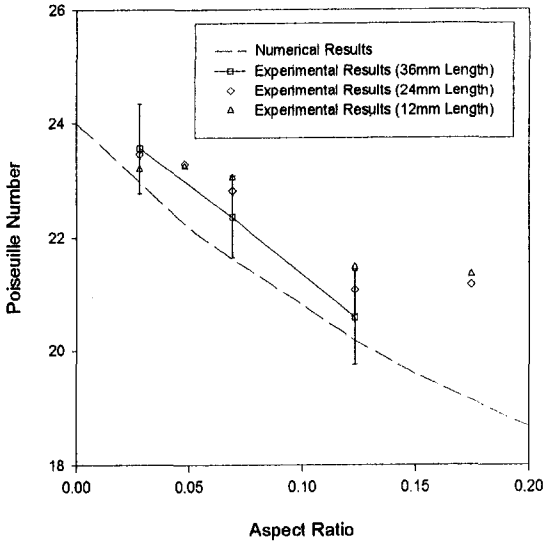

Fig. 9 Comparison between experimental and numerical Poiseuille numbers for each channel tested

graph is the flow relationship, $\Delta p/Q$, per mm length of straight channel, obtained during the analysis of the corner section, compared to the numerical results. From the data achieved for the single channels it was possible to estimate the flow characteristics for the double bend channels. The results presented in Table 2, for the 63 μm depth channels, provide a comparison between the experimental results obtained for the double bend and those estimated using the appropriate hydraulic resistances calculated from the single bend analysis. It was found that for the longer channels the results were extremely close, whereas for the shorter channels the percentage difference is slightly higher. This variation is thought to be due to entrance losses.

7 Conclusion

The main aim of this work was to investigate whether conventional macroscale fluid mechanics could accurately predict flow in channels of micron dimensions, fabricated using micro technology. A comparison is made between the experimental data obtained for channels of hydraulic diameters ranging from 50

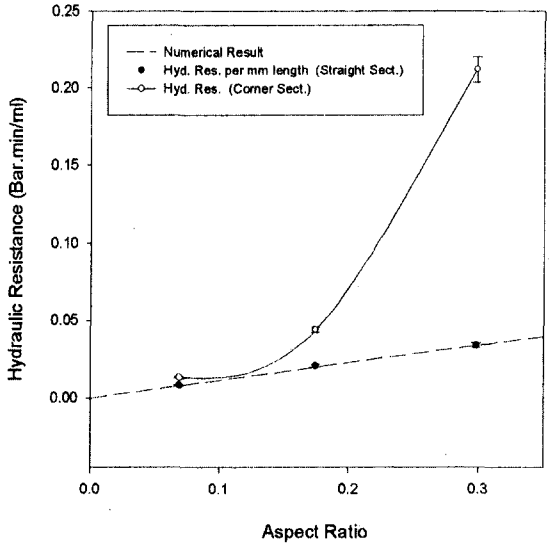

Fig. 10 Details losses due to the introduction of a 90 degree corner for channels of depth 63 μm

Table 2 Comparison of double bend results based on values determined from single bend analysis and experimental data (channel width = 450 μm, depth = 63 μm)

Channel Width (mm)	Channel Shape		Calc. Total Rest. (Bar · min/ml)	Exp. Total Rest. (Bar · min/ml)	% Diff.
0.45	*U*	6 × 6 × 6	0.43855	0.4293	2.10
0.45	*U*	12 × 12 × 12	0.82914	0.8303	0.14
0.45	*Z*	6 × 6 × 6	0.44703	0.4308	3.63
0.45	*Z*	6 × 12 × 6	0.70144	0.6965	0.70

to 120 μm, etched in ⟨100⟩ silicon, and the numerically calculated flow based on conventional fluid mechanics. The numerical technique essentially describes the channel in terms of polar coordinates, the no-slip boundary condition is then applied, reducing the problem to that of a Dirichlet equation which has a unique solution. To determine the solution a mathematical technique called the Householder Transformation was utilized. The numerical results, calculated for the θ = 54.74 deg trapezoid, were then compared to the data quoted by Shah and London for trapezoidal channels with θ equal to 45 and 60 degrees. The numerical results, for the case where θ equals 54.74 deg, were found to lie between those computed by Shah and London, and was found to correspond to a result quoted by Urbanek et al. This provides confidence in the numerical technique utilized during this investigation.

Figures 8(a)–(b) and 9 indicate that, for channels of dimensions considered, the numerical analysis utilized in this study, based on conventional fluid mechanics, can adequately predict the resulting flow characteristics of the trapezoidal ducts. It should be noted that for the shorter length channel, especially in the case of the 63 μm depth results, that entry losses are evident. Thus, in the comparison of the Poiseuille numbers (Fig. 9), the error bars were only introduced onto the results achieved for 36 mm length ducts, and were found to lie within the margin of error.

In addition to the analysis of the straight channels the losses due to the introduction of a 90 degree corner, Fig. 10, were investigated using the experimental results. Unfortunately, due to the limitation of L shaped channels only three values for each channel depth could be obtained, which is obviously not sufficient in order to determine a trend. However, based on these three points the losses, due to the corners, appear to follow a second-order polynomial trend with respect to the inverse of the channel width. Table 2 indicates that using the results from the single bend analysis it is possible to determine, with a reasonable degree of accuracy, the results of a channel incorporating two 90 degree corners. It is going to be important to microsystems, comprising of micro fluidic components, that research into the losses due to such microengineered connections is continued.

While the results in this paper conform to macro scale laws, it is still an important result. It provides a basis from which future work can be undertaken in order to precisely predict where the result moves away from that which can be accurately estimated using conventional macro scale laws.

References

Allen D. M., 1981, "Anisotropic Etching Microtechnology," *Precision Engineering,* pp. 161–166.

Ariman T, Turk M. A., and Sylvester N. D., 1973, "Microcontinuum Fluid Mechanics—A Review," *Int. Journal of Engineering Science,* Vol. 11, pp. 905–929.

Eringen A, 1964, "Simple Microfluids," *Int. Journal of Engineering Science,* Vol. 2, pp. 205–217.

Eringen A., and Suhubi E. S., 1964, "Nonlinear Theory of Simple Micro-Elastic Solids," *Int. Journal of Engineering Science,* Vol. 2, pp. 189–203.

Gravesen P., Branebjerg J., and Jensen O. S., 1993, "Microfluidics—A Review," *Journal of Micromechanics and Microengineering,* Vol. 3, pp. 168–182.

Harley J., Bau H., 1989, "Fluid Flow in Micron and Submicron Size Channels," *Proceedings IEEE MEMS,* pp. 25–28.

Israelachvili J. N., 1986, "Measurement of Viscosity in Very Thin Films," *Journal of Colloid and Interface Science,* Vol. 110, No 1, pp. 263–271.

Petit B., Pelletier J., and Mollins R., 1985, "A Novel Processing Technique for the Fabrication of Thick Silicon Grids by Anisotropic Etching," *Journal of the Electrochemical Society: Solid State Science and Technology,* Vol. 132, No. 4, pp. 982–984.

Pfahler J., Harley J., Bau H., and Zemel J., 1991, "Gas and Liquid Flow in Small Channels," DSC-Vol. 32 *Micromechanical Sensors Actuators and Systems,* ASME pp. 49–59.

Ralston A., and Rabinowitz P., 1978, *A First Course in Numerical Analysis,* McGraw-Hill, Second Edition, pp. 451–457.

Shah R. K., and London A. L., 1978, *Laminar Flow Forced Convection in Ducts,* Academic Press, New York, pp. 256–260.

Urbanek W, Zemel J. N., and Bau H. H., 1993, "An Investigation of the Temperature Dependence of Poiseuille Numbers in Microchannel Flow," *Journal of Micromechanics and Microengineering,* Vol. 3, pp. 206–209.

Study on the Deposition Profile Characteristics in the Micron-Scale Trench Using Direct Simulation Monte Carlo Method

Masato Ikegawa
Senior Researcher.

Jun'ichi Kobayashi
Department Manager 1st Department.

Mechanical Engineering Research Laboratory, Hitachi Ltd., 502 Kandatsu, Tsuchiura, Ibaraki 300-0013 Japan

Morihisa Maruko
Professor,
Hiroshima Women's Commercial College, Sakacho, Aki-gun, Hiroshima 731-4300 Japan

As integrated circuits are advancing toward smaller device features, step-coverage in submicron trenches and holes in thin film deposition are becoming of concern. Deposition consists of gas flow in the vapor phase and film growth in the solid phase. A deposition profile simulator using the direct simulation Monte Carlo method has been developed to investigate deposition profile characteristics on small trenches which have nearly the same dimension as the mean free path of molecules. This simulator can be applied to several deposition processes such as sputter deposition, and atmospheric- or low-pressure chemical vapor deposition. In the case of low-pressure processes such as sputter deposition, upstream boundary conditions of the trenches can be calculated by means of rarefied gas flow analysis in the reactor. The effects of upstream boundary conditions, molecular collisions, sticking coefficients, and surface migration on deposition profiles in the trenches were clarified.

1 Introduction

Ultra-large-scale integration (ULSI) devices are becoming more integrated and their line widths are being reduced to submicron dimensions. With the trend toward finer and finer line structures on semiconductor devices, developing deposition processes for semiconductor manufacturing is becoming more difficult. This is because deposition profiles in small trenches and holes suffer from poor step-coverage. Since poor step-coverage affects production yield and device reliability, the problem has become more and more serious for ULSI technology. Computer simulations of deposition profiles are becoming more effective for analyzing deposition profile factors because small-scale deposition phenomena cannot be analyzed easily through experiments.

So far, the conventional deposition simulator in the total process simulator SAMPLE (Neureuther et al., 1980) has been used for this analysis. Although the simulator is effective for examining features of the whole device, it is insufficient for analyzing film profiles precisely because its physical model is too simple. More accurate simulators are needed for developing deposition processes for ULSI devices with trenches and holes that are 1 μm wide or less on the substrate.

Deposition phenomena consist of gas flow in the vapor phase and film growth in the solid phase. The gas flow around a 1-μm-wide trench or hole must be analyzed as a rarefied gas flow because the mean free path of molecules cannot be dismissed in comparison with characteristic flow dimensions. The flow rarefaction degree is indicated by a Knudsen number. The Knudsen number Kn is a nondimensional parameter and is defined as λ/B where λ is the mean free path of molecules and B is characteristic dimension. The mean free path of molecule is $\lambda = 1/(\sqrt{2}\pi d^2 n)$, where d is molecular diameter, and n is number density. The characteristic dimension in the flow around the trench on the substrate is the trench width.

The flow pattern of rarefied gas is divided into three regions according to the Knudsen numbers. In the larger Kn (>10), the flow is a free molecular, or collisionless flow. In the smaller Kn (<0.01), the flow is continuous, and can be analyzed using continuum fluid dynamics. The flow region in the Knudsen numbers ($0.01 < \text{Kn} < 10$) is transitional, that is, the flow must be analyzed as a rarefied gas flow, not as a collisionless flow. The flow around a 1-μm-wide trench in sputter deposition, plasma chemical vapor deposition (PCVD), and low pressure chemical vapor deposition (LPCVD) is free molecular and the flow in atmospheric-pressure chemical vapor deposition (APCVD) is transitional. These processes must also be analyzed with molecular collisions by using the Boltzmann equation. The direct simulation Monte Carlo (DSMC) method is a powerful numerical simulation technique for solving the Boltzmann equation through molecular collisions (Bird, 1976). It is a technique for computer modeling of real gas flow based on tens of thousands of sampled molecules, and has been applied mainly to flow problems of aerospace engineering (Bird, 1979).

We developed a rarefied gas flow simulator using the DSMC method for calculating flow fields in vacuum apparatuses (Ikegawa and Kobayashi, 1990). We also developed a deposition profile simulator using the DSMC method for investigating characteristics of deposition profiles in small trenches under conditions ranging from vacuum to atmospheric pressure. The deposition profiles in trenches for several processes such as aluminum-sputter deposition, amorphous-Si PCVD, PSG (phosphosilicate glass) APCVD were successfully simulated (Ikegawa and Kobayashi, 1989).

This paper describes the effects of deposition process factors, such as incident molecule conditions, Knudsen numbers, sticking coefficients, surface migration, and ground shape, on the step-coverage in small trenches for semiconductor manufacturing processes using this deposition profile simulator with several models.

2 Modeling

Figure 1 shows a physical model for thin film deposition on a 1-μm-wide trench. Deposition phenomena consist of vapor phase processes (the incidence of reactive molecule and molecular collision), surface processes (surface migration, physical adsorption, surface reaction, and desorption of reaction product), and solid phase processes (film growth). Molecular move-

Contributed by the Fluids Engineering Division for publication in the JOURNAL OF FLUIDS ENGINEERING. Manuscript received by the Fluids Engineering Division March 7, 1997; revised manuscript received March 3, 1998. Associate Technical Editor: J. Katz.

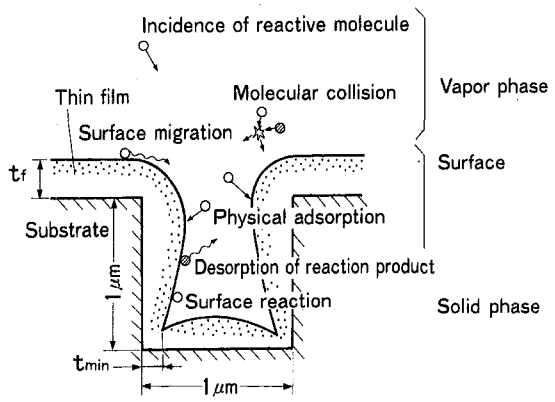

Fig. 1 Physical model for thin film deposition on a 1 μm-wide trench

ments in the vapor phase are calculated by the DSMC method. For film surfaces, the sticking coefficient, surface reaction probability, and surface migration of molecules must be considered. In the solid phase, film growth must be calculated. The film growth algorithm is based on a string model (Neureuther et al., 1980).

Film coverage (step-coverage) in the trench is defined as $t_{\min}/t_f$ ($t_{\min}$ = minimum film thickness in the trench, t_f = flat surface film thickness). The factors affecting the step-coverage in the trench are the Knudsen number, ground shape, the incident condition of molecules, sticking coefficients, and surface migration distance.

The flow pattern of rarefied gas is divided into three regions according to the Knudsen number, as shown in Table 1. The flow in the sputter deposition, PCVD, and LPCVD are free molecular and the flow in APCVD is transitional. These processes must also be analyzed using the DSMC method.

2.1 Upper Boundary Conditions of the Trench. Figure 2 shows the relation between the gas flow in the deposition reactor and the calculation domain near the small trench (the width and depth of 1 μm) on the substrate (the diameter of 150 mm). When the flow in the reactor is continuous, the molecules reach the trench with many molecular collisions during the flight from the main stream of the reactor. In this case, the Maxwell velocity distribution with a certain temperature and density can be applied to the incident molecules at the upper boundary of

Table 1 Flow regimes around the trench of 1-μm dimension in the deposition processes

Kn	∞	10	10^{-2}	0
Pressure (Ar)		0.83 kPa	830 kPa	
Flow regime	Free molecular	Transitional	Continuous	
Molecular collision	Collision less	Collision		
Gov. eq.	Boltzmann		Navier Stokes	
Deposition process	Sputter depo. PCVD LPCVD	APCVD		

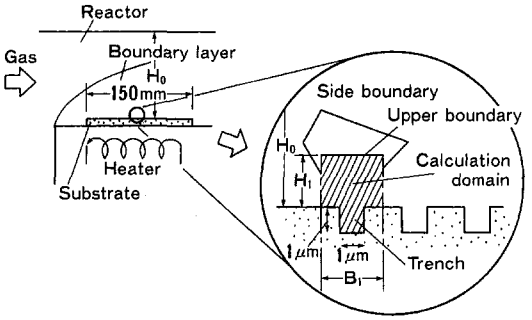

Fig. 2 Relation between the gas flow in the deposition reactor and calculation domain near the small trench

the trench. In the case of transitional or free molecular flows, the incident conditions of molecule can be determined by calculating the flow fields in the reactor, using the DSMC method. For a typical example of low-pressure deposition reactor, sputter deposition apparatus is examined here. The flow field in the sputter deposition apparatus can be calculated by the DSMC method because the reactor-Knudsen number is around 0.1, where the characteristic dimension of the flow is the distance H_0 (=55 mm) between the target and the substrate.

Figure 3 shows the calculation model and domain (two dimensions) for calculating the incident angle distribution θ of sputtered atoms onto the substrate using the DSMC method. Usually the number density of a discharge gas is 10^4 times that of sputtered atoms in the ordinary sputter deposition apparatuses. The temperature of a discharge gas is not affected by the

Nomenclature

B = trench width, or flow-characteristic dimension
C_{msp} = the most probable speed of sputtered atoms at the target
C_{m0} = the most probable speed of discharge gas atoms
d = molecular diameter
f_L = canonical distribution of migration distance
f_{sp} = velocity distribution function of atoms sputtered from the target surface
f_0 = velocity distribution function of discharge gas atoms in the space
H = trench depth
H_0 = target-substrate distance
Kn = Knudsen number
k_m = parameter of migration
L = surface migration distance ($=|x - x_0|$)
L_m = parameter of migration
$\bar{L}$ = mean surface migration distance
n = index of the cosine nth powers distribution or number density
R^* = uniform random number
Sc = sticking coefficient
S_i = ith segment on the film surface
t_b = maximum film thickness on the bottom of the trench
$t_{\min}$ = minimum film thickness in the trench
$t_{\min}/t_f$ = step-coverage in the trench
T_w = surface temperature of the substrate
u, v, w = velocity components of atoms
x = distance between the position that the molecule stopped after migration and the origin of the coordinates on the substrate
x_0 = position that the flying molecule reaches the substrate
θ = incident angle of sputtered atoms onto the substrate
λ = mean free path of molecules
ϕ = angle of trench-bottom corner
APCVD = atmospheric-pressure chemical vapor deposition
DSMC = direct simulation Monte Carlo method
LPCVD = low pressure chemical vapor deposition
PCVD = plasma chemical vapor deposition
PSG = phosphosilicate glass
ULSI = ultra large scale integration

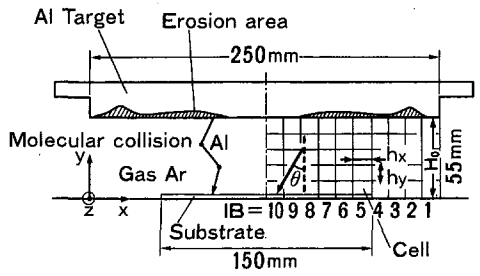

Fig. 3 Calculation model for sputtered atoms in the sputter deposition reactor

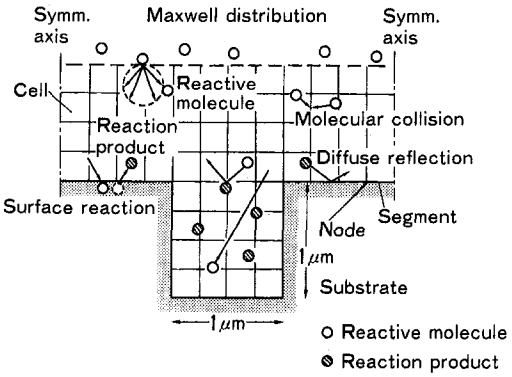

Fig. 4 Calculation model of molecular movements in the trench

sputtered atoms. Therefore an approximate DSMC method, that only movements of the low-concentration-gas atoms are pursued, is used instead of conventional one here. Here the former method is applied with the assumption that the temperature of the discharge gas atoms is constant and the molecular collisions among sputtered atoms can be ignored. Selection of two methods depends on the concentration of the gas components that be analyzed.

The form of the erosion area in the target indicates the emission distribution of sputtered atoms from the target. Therefore, the sputtered atoms (aluminum) are emitted from the target with this distribution in the simulation. Let's think of an example of sputter deposition apparatus with the dimensions of a target diameter (D_t) of 250 mm, a substrate diameter (D_s) of 150 mm, and a target-substrate distance (H_0) of 55 mm. The space between the target and the substrate is divided into many cells of which sizes are set to be smaller than the mean free path of atoms. The flights and the molecular collisions with the discharge gas atoms for the sputtered atoms are calculated sequentially in a small time interval (time step) Δt. Here Δt is set to be smaller than the mean collision time of atoms. The calculation of molecular collisions between the sputtered atoms (Aluminum) and the discharge gas atoms (Argon) is based on the Time-counter method (Bird, 1976) with a hard-sphere molecular model. The coordinate axes x, y, and z are set as seen in the Fig. 3 and the components of velocity in the their directions are u, v, and w. Aluminum sputtered atoms at the target are assumed to have the Maxwell velocity distribution with the temperature T_{sp} and zero mean velocity. The number density is not needed to be treated explicitly here because of the former assumption of very low concentration. The velocity distribution function of atoms sputtered from the target surface is written as follows.

$$f_{sp}(u, v, w) = \frac{2}{\pi C_{msp}^4} v \cdot \exp\left\{ -\frac{1}{C_{msp}^2}(u^2 + v^2 + w^2) \right\} \quad (1)$$

where, $C_{msp} = \sqrt{2kT_{sp}/m_{sp}}$ is the most probable speed, k is the Boltzmann constant, T_{sp}, m_{sp} are the initial temperature and the mass of sputtered atoms. The velocity components u, v, w of sputtered atoms are written with the uniform random number $R_i^*[0, 1]$ as follows.

$$u = C_{msp}\sqrt{-\ln(R_1^*)}\cos(2\pi R_2^*) \quad (2)$$

$$v = -C_{msp}\sqrt{-\ln(R_3^*)} \quad (3)$$

$$w = C_{msp}\sqrt{-\ln(R_1^*)}\sin(2\pi R_2^*) \quad (4)$$

The discharge gas atoms are assumed to have the Maxwell velocity distribution with room (constant) temperature and zero mean velocity. Its number density is calculated from the gas pressure. The velocity distribution function of discharge gas molecules in the space is written as follows.

$$f_0(u, v, w) = \frac{1}{\pi^{1.5} C_{m0}^3} \exp\left\{ -\frac{1}{C_{m0}^2}(u^2 + v^2 + w^2) \right\} \quad (5)$$

where, $C_{m0} = \sqrt{2kT_0/m_0}$ is the most probable speed, and T_0, m_0 are the temperature and the mass of discharge gas atoms. The velocity components u, v, w of discharge gas atoms in the space are written with the uniform random number $R_i^*[0, 1]$ as follows.

$$u = C_{m0}\sqrt{-\ln(R_4^*)}\cos(2\pi R_5^*) \quad (6)$$

$$v = C_{m0}\sqrt{-\ln(R_4^*)}\sin(2\pi R_5^*) \quad (7)$$

$$w = C_{m0}\sqrt{-\ln(R_6^*)}\sin(2\pi R_7^*) \quad (8)$$

Sputtered atoms are assumed to be adsorbed at the top, bottom, and right side boundaries, and are reflected specularly at the center axis. The velocity distribution function of the sputtered atoms onto the substrate are counted for each segment (IB) on it. Then the incident angles of the sputtered atoms onto the substrate are calculated using their velocity components u, v as follows.

$$\theta = \text{Arc tan}(u/v) \quad (9)$$

The distribution of incident angle is counted as that of frequency in the division of 0.05 π from $-\pi$ to π.

2.2 Deposition Profile. Figure 4 shows a calculation model of molecular movements in the trench. The characteristic dimension of the flow is the trench width B. The DSMC method is used to solve for the flow field by calculating the molecular flight and collisions in the smaller cells into which the flow field is divided rather than the mean free path for tens of thousands of molecules in every time step. In the deposition simulator (Ikegawa and Kobayashi, 1989), starting from an initial condition, molecular movements in the vapor phase are calculated by the DSMC method, and sticking molecules on the film surface, approximated by a series of nodes joined by straight line segments, are counted. One division of film thickness grows in proportion to the flux of sticking molecules in the direction of flux vector. The network of cells is moved and distorted in the growth of film (a moving cell network model). The growth of film is iterated until film thickness reaches the set value. Figure 5 shows the flow chart of the deposition profile simulator program. Since the velocities of molecules are much higher than the growth speed of film, the velocities of molecules are not affected by it. The number of incident molecules into the trench, however is affected by the profile of the film surface during its growth.

Reactive molecules come down to the flow field from the upper boundary with the velocity distributions that are calculated in Section 2.1. When the Maxwell velocity distribution

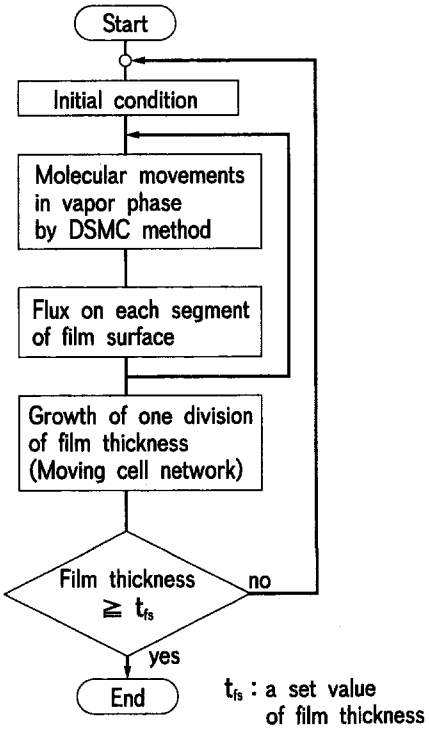

Fig. 5 Flow chart of the deposition profile simulator

with the temperature T, the number density n, and zero mean velocity can be applied to the upper boundary, the number of incident molecules into the upper boundary per unit area and time is $N_{in} = (\frac{1}{4})n\bar{C}$, where $\bar{C} = \sqrt{8kT/\pi m}$ is the average thermal speed, and m is the mass of the reactive molecule. The relation between the number density n and the Knudsen number Kn is written as $n = 1/(\sqrt{2}\pi d^2 B\mathrm{Kn})$. The molecules fly straight or reflect on the wall, or are discharged into the upper boundary in short time step. The molecules reaching the symmetrical walls (dot-dashed lines in Fig. 4) are reflected specularly. Molecules reaching the substrate stick on it according to the sticking coefficient (probability) Sc, and are reflected diffusely with probability $(1 - Sc)$. Sticking molecules on the substrate cause a chemical reaction which forms a film and the reaction product is emitted to the flow field. As all of the sticking molecules are assumed to cause chemical reactions immediately, the sticking coefficient is the same as the surface reaction probability in this model.

Next, molecular collisions are calculated in each cell by its collision probability. Molecular collisions in diluted gas are overwhelmingly like binary collisions involving just two molecules. In the following calculations, we assumed a simple monatomic gas with a hard-sphere molecular model. The molecular collision calculations are also based on the Time-counter method (Bird, 1976). In the computer program, reactive molecules and reaction products are distinguished by flags. The more minute explanation of the method is described in the previous paper (Ikegawa et al., 1989).

When the incident angle distribution is asymmetrical around the normal on the substrate, the symmetrical side boundary conditions in Fig. 4 cannot be used, and the incident molecules into each boundary must be calculated differently. In the case of a free molecular flow, this problem is solved easily by means of equalizing the upper boundary and the flat surface of film.

2.3 Surface Migration. There is a bias-sputter deposition technique that gives good step-coverage while enhancing the surface migration using ion bombardment during deposition (Homma and Tsunekawa, 1985, Blader and Lardon, 1985). The

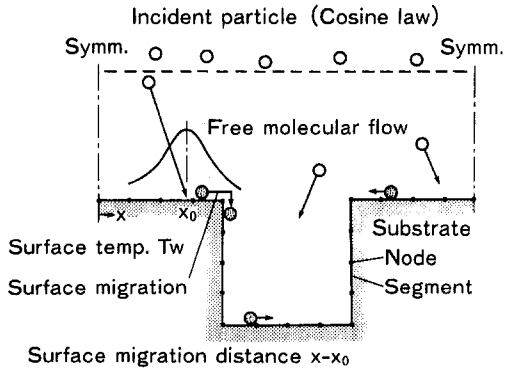

Fig. 6 Calculation model of deposition profile with surface migration

step-coverage of a bias-sputter deposition with low bias voltage is thought to be improved by the migration of sticking molecules on the surface of film (Skelly and Gruenke, 1986). Figure 6 shows the calculation model (two dimensions) of deposition with surface migration. Since the characteristic dimension (the width of the trench) B is 1 μm and the gas pressure is 1.1 Pa, the Knudsen number for the trench is larger than 6000. Therefore, the flow around the trench is a free molecular flow. As the Knudsen number for the reactor is close to 0.2, the velocity distribution of sputtered atoms at the upper boundary is assumed as the Maxwellian with zero mean velocity. The side boundaries are symmetrical.

The surface of the substrate is heated to the temperature T_w by ion bombardment. The sputtered molecules reaching the substrate obtain thermal energy and migrate on the substrate. The surface migration distance $L = |x - x_0|$ is assumed to have the following canonical distribution.

$$f_L = \frac{1}{L_m\sqrt{\pi}} \exp\left(-\frac{L^2}{L_m^2}\right) \tag{10}$$

$$= \frac{1}{L_m\sqrt{\pi}} \exp\left\{-k_m \frac{(x - x_0)^2}{T_w}\right\} \tag{11}$$

where

$$L_m = \sqrt{(T_w/k_m)}.$$

The term x_0 is the position that the flying molecule reaches the substrate and x is the distance between the position that the molecule moved and stopped and the origin of the coordinates on the substrate.

The mean surface migration distance is as

$$\bar{L} = \int_{-\infty}^{\infty} |L| f_L dL = \sqrt{\frac{T_w}{\pi k_m}} \tag{12}$$

The probability variable x is written with two uniform random numbers R_1^*, R_2^* as follows.

$$x - x_0 = L_m\sqrt{-\ln(R_1^*)} \cos(2\pi R_2^*) \tag{13}$$

Each sputtered atom that reaches the substrate can migrate the distance of $x - x_0$ on the substrate and stick to one segment S_i on the film surface. The atoms return in the residual distance if they reach the symmetrical boundaries. In the case of surface migration, the flight directions of atoms are forgot. Therefore, the film growth algorithm is such that a thin layer of film in proportion to the sticking molecules on each segment grows sequentially in the direction perpendicular to the old segment surface.

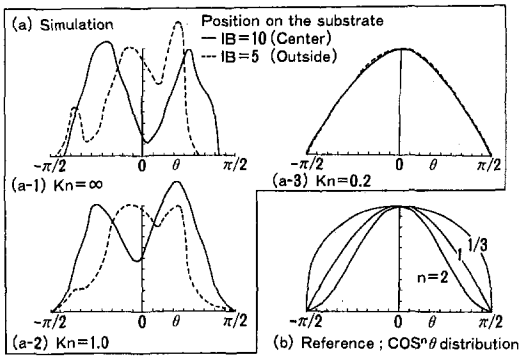

Fig. 7 Results of incident angle θ distribution of sputtered molecules on the substrate with several reactor-Knudsen numbers Kn ($=\lambda/H_0$)

3 Results and Discussion

3.1 The Effect of Upper Boundary Condition. Figure 7 shows the results of incident angle distribution of sputtered molecules on the substrate in the case of reactor-Knudsen numbers Kn ($=\lambda/H_0$) of ∞, 1.0 and 0.2. Aluminum sputtered atoms (atomic weight = 26.981, atomic diameter (d_{sp}) = 2.86 Å) at the target are assumed to have the Maxwell velocity distribution with the temperature 76,180 K. The discharge gas atoms (Ar, atomic weight = 34.948, atomic diameter (d_0) = 3.66 Å) are assumed to have the Maxwell velocity distribution of room temperature (293 K).

The emitting probability y of the sputtered atoms from the target is modeled as the following equations from one example of erosion area as shown in the Fig. 3.

$$125 < x < 180: \quad y = 0.00909(x - 125) \tag{14}$$

$$180 < x < 218: \quad y = -0.00658(x - 180) + 0.5 \tag{15}$$

$$218 < x < 230: \quad y = 0.0625(x - 218) + 0.25 \tag{16}$$

$$230 < x < 250: \quad y = -0.0526(x - 230) + 1.0 \tag{17}$$

where the unit of x is mm, and y is normalized by its maximum value.

In the case of Kn = ∞, the incident angle distribution of molecules is asymmetrical and differs from the cosine-law (n = 1) distribution. In the case of Kn = 0.2, however, the distribution is almost a cosine-law distribution, and is obtained because of many molecular collisions with discharge gas molecules. It is ascertained that this result can be applied to any erosion profile in case of Kn < 0.2. Therefore, the Maxwell velocity distribution for the incident molecules from the upper boundary of the trench can be assumed in the case of smaller reactor-Knudsen numbers (Kn < 0.2).

3.2 The Effect of Knudsen Number, Sticking Coefficient, and Ground Shape. Table 2 shows the left side of the calculated results of a deposition profile simulation for thin film growth converting *Sc* into 1.0, 0.4, and 0.2 in Kn = 0.1 (atmospheric pressure), i.e., transitional flow, and Kn = ∞ (below 0.8 kPa), i.e., free molecular flow. The characteristic dimension in the flow around the trench on the substrate is the trench width (1 μm). The Maxwell velocity distribution with zero mean velocity is used in the upper boundary condition. In Kn = 0.1, film thickness becomes uniform due to the uniformalization of reactive-molecule concentration in the trench as *Sc* becomes smaller. In Kn = ∞ and *Sc* = 1.0, cracks grow at the bottom corners and the step-coverage becomes poor because the number of molecules flying there decreases due to the shadow effect by means of overhangs grown on the shoulders. In addition, film thickness becomes uniform as *Sc* becomes smaller in the same manner as Kn = 0.1. This is because of the molecules

Table 2 Simulation results for deposition profiles (Knudsen number Kn ($=\lambda/B$) and sticking coefficient Sc effect)

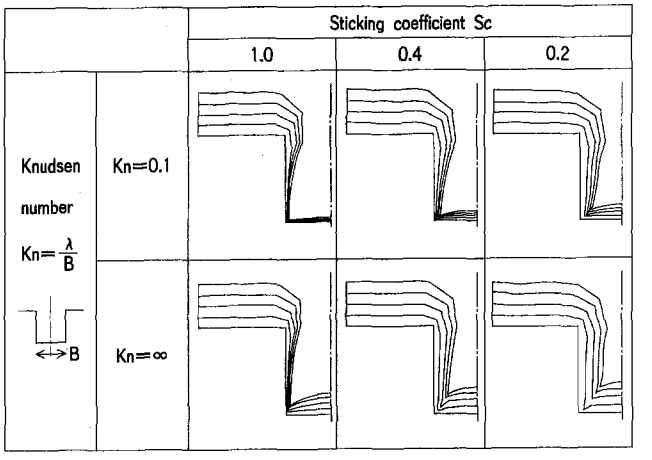

which reach the wall bottom by reflecting off the trench walls many times. A smaller Knudsen number flow (higher pressure) also makes the film thinner. This is caused by preventing reactive molecules that fly down to the trench from invading the trench by means of collisions with reaction products within the trench.

The results where Kn = ∞ and *Sc* = 1.0 agree with the experiment on sputter deposition of aluminum (Ikegawa and Kobayashi, 1989). Since the sticking coefficient of aluminum atoms to the substrate at a temperature below several hundred degrees centigrade is close to 1.0 (Redhead et al., 1968), this result is appropriate. In SiO_2 film growth at LPCVD, Watanabe and Komiyama (1990) obtained an experimental result of *Sc* = 0.2. The deposition profile is close to the simulation result shown in Table 2, *Sc* = 0.2 (Kn = ∞).

In APCVD, *Sc* measurement values have rarely been reported, but from the comparison of film growth profiles of experimental and simulation results, a value of *Sc* = 0.1 for PSG (SiO_2) film was predicted (Ikegawa and Kobayashi, 1989).

Simulation results, when *Sc* is converted, are shown in Fig. 8 using step-coverage, that is, showing the relation between

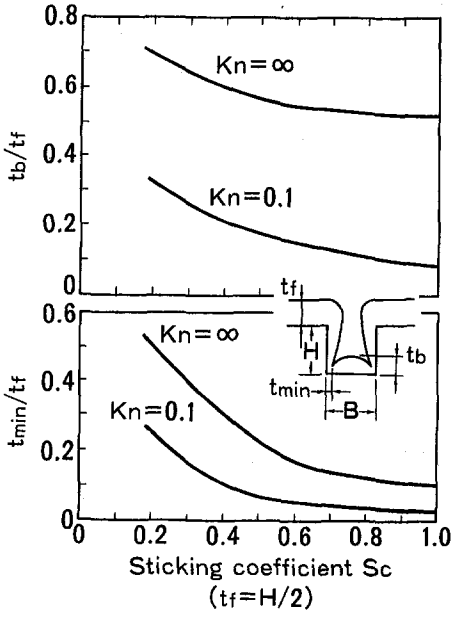

Fig. 8 The relation between *Sc* and step-coverage (t_{min}/t_f, t_b/t_f) with Knudsen numbers Kn ($=\lambda/B$)

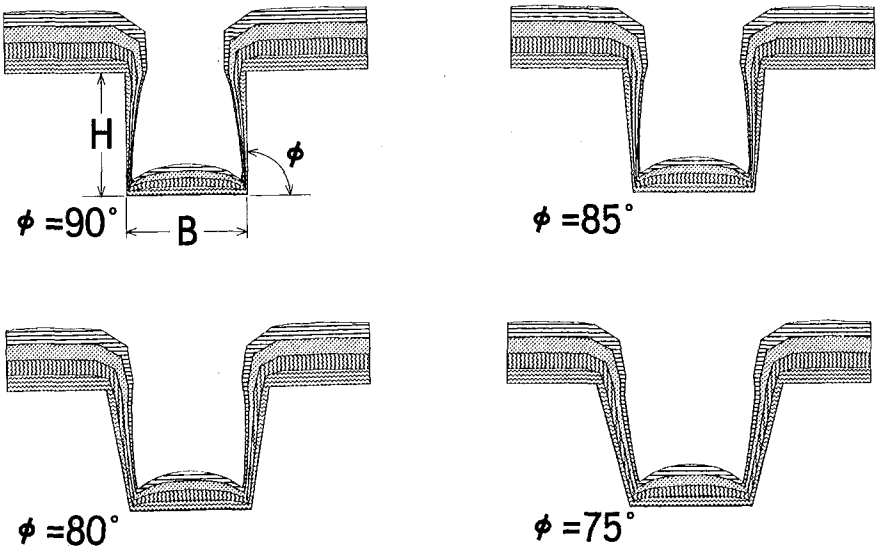

Fig. 9 Results of deposition profiles with tapered side walls (Kn = ∞, *Sc* = 1.0)

t_{min}/t_f (minimum film thickness/flat area film thickness), t_b/t_f (maximum bottom film thickness/flat area film thickness) and sticking coefficient *Sc*.

Figure 9 shows the results of deposition profiles with tapered side walls (Kn = ∞, *Sc* = 1.0). In the case of *Sc* = 1.0, the ground shape is very sensitive to the deposition profile. Slight angle differences of the side walls of the trench affect the step-coverage.

3.3 The Effect of Surface Migration. Figure 10 shows the results of the left side of deposition profile simulation with surface migration in the trench. The gas flow near the trench is a free molecular flow. As the mean surface migration distance $\bar{L}$ increases from 0.01 μm to 1.6 μm, the step-coverage increases. When the $\bar{L}$ exceeds the trench depth *H*, the film thickness in the trench approaches that of a flat surface because many molecules flow into the trench. The relation between the ratio of the mean migration distance and the trench depth $\bar{L}/H$ and the step-coverage are shown in Fig. 11.

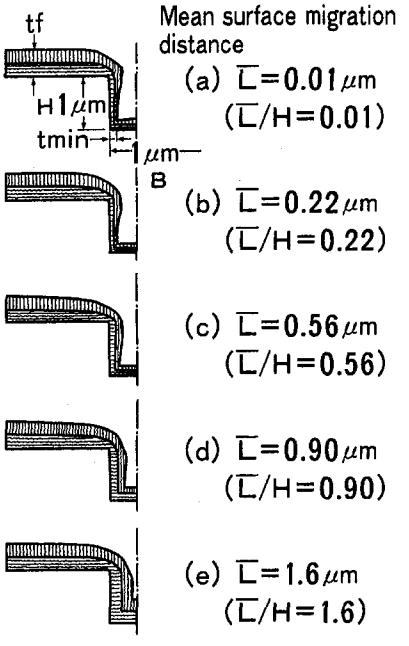

Fig. 10 Results of deposition profile simulation with surface migration (Kn = ∞)

3.4 Consideration on the Method to Increase the Step-Coverage for the Small Trench. The preceding results reveal that to increase step-coverage, it is best to increase Knudsen number Kn (low pressure), use a smaller sticking coefficient *Sc*, or increase mean surface migration distance $\bar{L}$.

In the case of aluminum sputter deposition, the sticking coefficient is close to 1.0. Therefore, the ground shape is very sensitive to step-coverage. The bottom corner angle (180 deg − φ) should be larger than 90 degrees and must be controlled precisely in the production lines. Figure 12 shows the difference of a step-coverage with a slightly different angle at the bottom corner. Recent sophisticated techniques for increasing step-coverage with an enhanced surface migration in the Al sputter deposition are bias sputter and high-temperature sputter deposition methods. When these new sputter deposition methods cannot be applied to production, the changes of the film material and the process from sputter deposition to CVD dare to be done. A recent 0.5-μm process uses tungsten-CVD instead of aluminum-sputter deposition. To increase the minimum film thickness, it proves to be more effective to use APCVD under *Sc* = 0.3 than sputter deposition with *Sc* = 1.0. Thus, the best countermeasure for obtaining better step-coverage is to find a process condition or method that lowers the sticking coefficient in LPCVD.

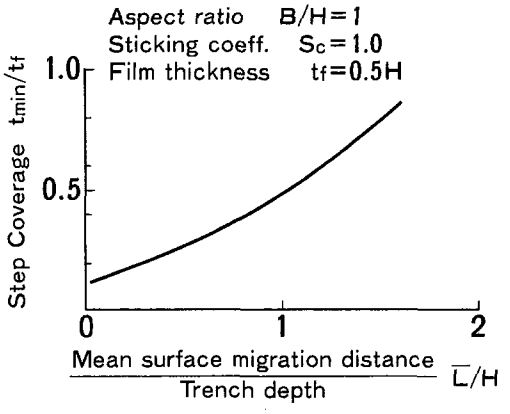

Fig. 11 The relation between the ratio $\bar{L}/H$ of the mean surface-migration distance and the trench depth, and the step coverage (Kn = ∞)

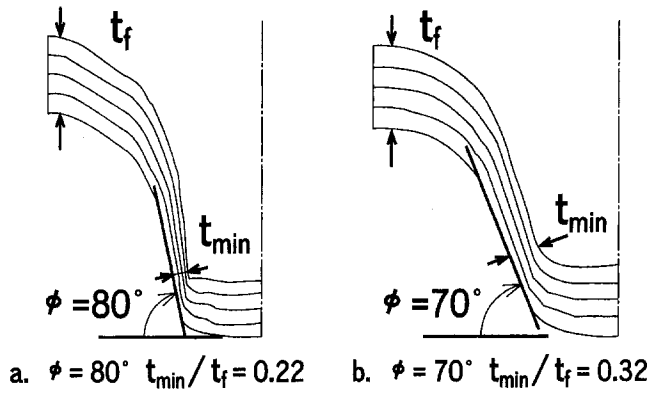

Fig. 12 Difference of step-coverage with a small angle change at the bottom corner (Kn = ∞, Sc = 1.0)

The sticking coefficient of CVD that includes chemical reaction is different from that of Al-sputter deposition. In the case of CVD using pyrolysis of SiH_4, Coltrin et al. (1986) predicted 17 chemical species for the decomposition of gases, in the vapor phases, such as Si_2H_6, Si_2H_2, SiH_2, SiH_3, and Si. These radicals have their own different sticking coefficients on the film surface and their concentrations near the substrate. The film growth rate is proportionate to the sum of the product of their sticking coefficients and their concentrations. Therefore, the total sticking coefficient of deposition is determined by the ratio of the product to its sum. Process conditions, such as temperature, pressure and initial concentration of species, affect the kinds of deposition species and their concentration and determine the value of total sticking coefficient of the deposition profiles. The method for lowering the total sticking coefficient is to decrease the concentration on the species of larger sticking coefficients or to increase the concentration of smaller sticking coefficients at the upper boundary of the trench.

4 Conclusions

(1) Deposition profiles in 1-μm-wide trenches from high degree of vacuum state to an atmospheric pressure state can be analyzed using the direct simulation Monte Carlo method with a moving cell network model during the growth.

(2) Deposition profile simulations of several processes can be performed for accurate film growth by using models of molecular collision, sticking coefficients and surface migration.

(3) Step-coverage can be increased by a larger Knudsen number, smaller sticking coefficient and greater surface migration.

Acknowledgments

The authors wish to thank Prof. Yasuhiko Aihara (Tokai University), Prof. Kenichi Nanbu (Tohoku University), and Prof. Hiroshi Komiyama (Tokyo University) for their stimulating discussions and encouragements.

References

Bird, G. A., 1976, *Molecular Gas Dynamics,* Clarendon Press.

Bird, G. A., 1979, "Simulation of Multi-Dimensional and Chemical Reacting Flows," *Rarefied Gas Dynamics,* CEA, 11th, Paris, Vol. 1, p. 365.

Bader, H. P., and Lardon, M. A., 1985, "Planalization by Radio-frequency Bias Sputtering of Aluminum as Studied Experimentally and by Computer Simulation," *Journal of the Vacuum Science and Technology,* Vol. A3, pp. 2167–2171.

Cortrin, M. E., Kee, R. J., and Miller, J. A., 1986, "A Mathematical Model Silicon Chemical Vapor Deposition," *Journal of the Electrochemical Society,* Vol. 133, No. 6, p. 1206.

Homma, Y., and Tsunekawa, S., 1985, "Planar Deposition of Aluminum by RF/DC Sputtering with RF Bias," *Journal of the Electrochemical Society,* Vol. 132, No. 6, pp. 1466–1472.

Ikegawa, M., and Kobayashi, J., 1989, "Deposition Profile Simulation Using Direct Simulation Monte Carlo Method," *Journal of the Electrochemical Society,* Vol. 136, No. 10, pp. 2983–2986.

Ikegawa, M., and Kobayashi, J., 1990, "Development of a Rarefied Gas Flow Simulator Using the Direct-Simulation Monte Carlo Method (2-D Flow Analysis with the Pressure Conditions Given at the Upstream and Downstream Boundaries)," *JSME International Journal,* Series 2, Vol. 33, No. 3, pp. 463–467.

Neureuther, A. R., Ting, C. H., and Liu, C. Y., 1980, "Application of Line-Edge Profile Simulation to Thin Film Deposition Processes," *IEEE Transactions of Electron Devices,* Vol. ED-27-8, pp. 1449–1455.

Redhead, P. A., Hobson, J. P., and Kornelsen, E. V., 1968, *The Physical Basis of Ultrahigh Vacuum,* Chapman and Hall Ltd., London.

Skelly, D. W., and Gruenke, L. A., 1986, "Significant Improvement in Step Coverage Using Bias Sputtered Aluminum," *Journal of the Vacuum Science and Technology,* Vol. A4(3), pp. 457–462.

Watanabe, K., and Komiyama, H., 1990, "Micro/Macrocavity Method Applied to the Study of the Step Coverage Formation Mechanism of SiO2 Films by LPCVD," *Journal of the Electrochemical Society,* Vol. 137, No. 4, pp. 1222–1227.

Skin Friction Measurements in a Gas-Liquid Pipe Flow Via Optical Interferometry

T. J. Garrison
Assistant Professor,
York College of Pennsylvania,
York, PA 17405

E. Manceau
Graduate Student.

D. E. Nikitopoulos
Associate Professor.

Department of Mechanical Engineering,
Louisiana State University,
Baton Rouge, LA 70803

An instrument for the measurement of wall shear stress in two-phase flows is described. The device, termed a Laser Interferometer Skin Friction (LISF) meter, determines the wall shear by optically measuring the time rate of thinning of a thin oil film placed on the wall of the flow channel. The LISF meter has proven to be a valuable tool for measurement of wall shear in single-phase gaseous flows but, to date, had not been applied to liquid or gas-liquid flows. This paper describes modifications to the LISF meter developed to facilitate its use in two-phase flows. The instrument's configuration, governing theory, and data reduction procedure are described. Additionally, results of validation experiments for a single-phase water flow are presented, which demonstrate the instrument's ability to accurately measure wall shear. Measurements are also presented for two-phase, water-air flows in a duct of square cross section at various superficial gas and liquid velocities within the bubbly flow regime. Results of the measurements confirm previous observations that the addition of a very small amount of the gaseous phase increases the wall shear significantly over that in a single-phase water flow. The two-phase wall shear saturates to a maximum and then declines again as the superficial gas velocity is increased. The peak two-phase wall shear increases as the liquid superficial velocity is decreased. These trends are qualitatively in agreement with previous measurements obtained in pipes using an electrochemical technique.

Introduction

Dispersed bubbly flow in pipes is of interest to the chemical, petrochemical, and nuclear power generation industries. A large number of experiments have been conducted thus far investigating the turbulent and phase distribution aspects of such flows. The works of Malnes (1966), Serizawa et al. (1975, 1992), Herring and Davis (1976), Nakoryakov et al. (1981), Sekoguchi et al. (1981), Theofanous and Sullivan (1982), Beyerlein et al. (1985), Wang et al. (1987), Liu and Bankoff (1990), Bataille et al. (1990), Matsui (1992), Stanley et al. (1995) and others have contributed a diverse database of bubbly-flow measurements revealing important qualitative and quantitative trends in phase distribution, bubble and liquid velocities and their dependence on bulk-flow properties. One of the most striking features of the available experimental evidence are the contradictory trends regarding the mean flow, the modification of the carrier-phase turbulence caused by the dispersed bubbles, and the phase distribution within the pipe cross section, even when the bulk flow parameters are comparable. A typical example is the disagreement regarding the existence of an off-center mean liquid velocity peak which has been observed by Malnes (1966), Nakoryakov et al. (1981), Theofanous and Sullivan (1981), and Wang et al. (1987) but was absent from the measurements of Serizawa et al. (1975) and Liu and Bankoff (1990).

Most of the past studies mentioned above have used intrusive techniques for the measurement of liquid and bubble velocity, void fraction, and occasionally bubble size. Some of the existing contradictions can possibly be attributed to the effect of probe intrusion, which can be significant, particularly in the neighborhood of the wall. The effect of bubble size is also a very important factor in determining the details of the flow and therefore measurements of bubble size are becoming a necessity in order to draw useful conclusions from a given experiment. Recently, Matsui (1992) and Serizawa et al. (1992) studied the effect of bubble size on vertical upward bubbly flow in ducts. The former used laser Doppler velocimetry without phase-discrimination to measure liquid properties. Both studies employed an intrusive resistivity probe to measure bubble properties. These investigations concluded that bubble size has a considerable effect on the flow properties. Another factor that could be responsible for the observed inconsistencies is the possibility of facility imposed initial conditions and the existence of "fully developed" bubbly flow. The results presented by Serizawa et al. (1992) indicate that initial conditions set by the injection system could be of considerable influence on the flow topology within the "bubbly" flow-regime. Recent nonintrusive measurements by Stanley et al. (1995) have observed both mean liquid velocity profiles (with and without the off-center peak) and argued that their appearance may depend on the initial (injection) conditions.

As indicated above, experimental studies focusing on the measurement of velocity and phase distributions in bubbly two-phase flow abound. However, very few studies are available that offer local and accurate data on wall shear in this class of flows. There are many studies that provide average frictional pressure-drop data but the uncertainty can be high since the result is based on the measurement of pressure differences. Furthermore, the measurement is not a local one and thus cannot be related directly to the particular flow topology near the wall. Moreover, accurate measurement of the wall shear is critical for the development of wall-shear predicting schemes in two-phase flows. Wall-shear measuring schemes are necessary for the accurate calculation of the pressure drop within two-phase flows as well as other transport properties. Such measurements would also contribute to the better understanding of the effect of the flow topology and, indirectly, the "initial" conditions discussed above, as a factor influencing this flow topology. The scarcity of wall-shear data is attributed primarily to the lack of

Contributed by the Fluids Engineering Division for publication in the JOURNAL OF FLUIDS ENGINEERING. Manuscript received by the Fluids Engineering Division May 3, 1996; revised manuscript received June 9, 1997. Associate Technical Editor: D. P. Telionis.

experimental methods capable of measuring shear stress in such flows. In the only two studies known to the present authors in which wall shear measurements were made, Nakoryakov et al. (1981) and Souhar and Cognet (1983) both used an electrochemical technique to measure shear stress in a gas-liquid flow over a relatively broad range of flow conditions. While these studies provided valuable information, the technique used suffers several drawbacks. First, an intrusive anode must be placed within the flow to facilitate the measurements. Second, the method is restricted to a limited set of liquid flows which can support the electrochemical reaction. (Nakoryakov et al. used a solution of potassium ferri- and ferro-cyanide in a background solution of sodium hydroxide and distilled water.) Finally, the cathode must be imbedded in the wall of the channel, making it difficult to reposition the measuring point at different locations which would be of value in developing regions.

The present study has focused on using a nonintrusive technique to measure the wall shear in a vertical bubbly flow. The technique used in the present study overcomes the limitations of the electrochemical technique mentioned above, providing a valuable means for accurate measurement of wall shear. The primary objective of the present paper is to describe this technique and to provide a preliminary data set which demonstrates the method's capabilities and limitations. The experiments described herein involved a rather dilute bubbly flow. Apart from the fact that the methods used here are easier to implement in dilute two-phase flow, this choice was also motivated by lack of experimental data for very dilute flows and the evidence presented by Nakoryakov et al. (1981) showing that two-phase wall shear increases sharply even with a very small addition of a gaseous phase.

Description of the Experiments

Experimental Facility. The experiments were conducted in LSU's vertical-upwards, air-water, two-phase pipe flow facility. The experimental facility, shown in Fig. 1, is an air-water loop designed and built to perform local two-phase measurements. Water is drawn from a collection tank by a single speed centrifugal pump and directed into a 406-mm diameter settling chamber. The collection tank has three baffles and a maximum capacity of approximately 490 gallons. A combination of two pipe-loops and two valves is used to control the flow rate in the test section. The first loop supplies water to the test section and the second loop is used to bypass excess water to the collection tank. A water filter bypass is also installed on the return between the pump and collection tank. The flow rate is measured by a flow meter installed between the pump and the test section. The settling chamber contains honeycomb and screen flow-straighteners. A transition section, made of fiberglass, is used to connect the test section to the settling chamber and is designed to minimize the flow development length in the test section. Bubbles are injected in the settling chamber between the transition piece and the flow straighteners. The two-phase fluid exits the test section, into an overhead tank through a diffuser section. The overhead tank consists of two concentric cylinders. The water overflows the inner cylinder, releasing the gaseous phase, and falls into the outer one to be drained back to the collection tank through a return pipe.

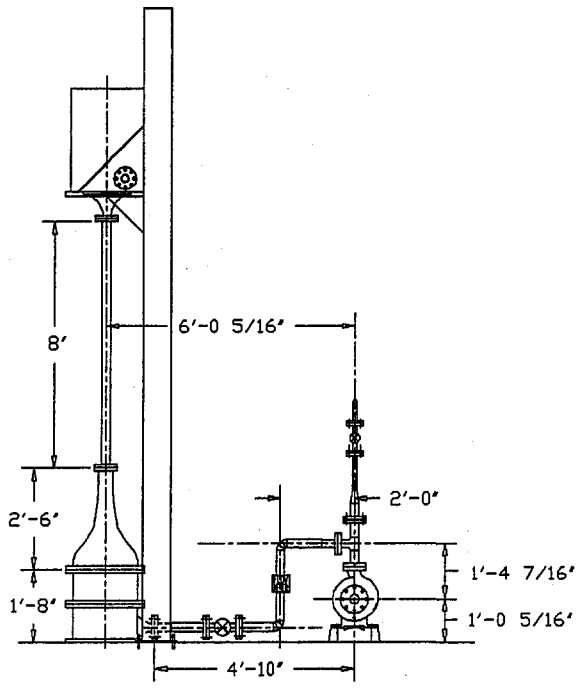

Fig. 1 Two-phase flow facility

Figure 2 shows a schematic of the test section used for the present experiments. The initial portion of the test section is comprised of a smooth acrylic channel with a square cross section having an internal dimension of 38.1 mm per side. A square test section was used to facilitate the wall shear measurements, as described in a later section. The square portion of the test section was 1.4 m long. As shown in Fig. 2, the square test section was equipped with a removable glass window to facilitate application of the oil films needed for the wall shear measurements. This aspect is discussed in more detail in the following section. All wall shear measurements were made at a distance of 370 mm from the bottom of the glass window to ensure that any disturbances created at the junction between the glass window and the acrylic test section were fully attenuated at the measurement location. Downstream of the square test section, the flow channel transitions to a circular cross section. Special care was taken to ensure that the entire test section is vertical to within less than a degree since it is well known that slight misalignment can lead to bubble migration.

Two-phase flow is produced when air-bubbles are injected into the settling chamber by using up to 30 injectors made of stainless steel tubing with fine hypodermic needle tips. These tubes are inserted through the side of the settling chamber, equidistantly and axisymmetrically with their tips forming circles concentric with the test section. The bubbles are thus injected perpendicular to the flow stream. For the present experiments, 25 gauge hypodermic needles were used for the injector tips. Two different sets of injectors were used in the present study. The first set consisted of 10 injectors equally spaced around the circular settling chamber. This set was capable of providing superficial gas velocities up to 0.017 m/s. A second set of injectors, consisting of 20 equally spaced hypodermic needles, was used to produce gas superficial velocities up to 0.05 m/s. The injectors are supplied with air through a manifold specially designed to maintain the same flow rate through each injector. Gas flow rate is measured with a rotameter placed before the manifold together with a flow regulating valve. Since the injection requires pressures on the order of 25–60 psi, a pressure transducer is used to measure the air pressure upstream of the rotameter. A small amount of surfactant was added to the water in order to produce smaller bubbles with the given injector size.

Table 1 summarizes all the test cases examined in the present study. In this table, V_L and V_g are the liquid and gas superficial velocities, respectively. The volumetric flow ratio, β, is the ratio of the gaseous volumetric flow rate, Q_g, to the total (gaseous plus liquid) flow rate, $Q_g + Q_L$. Table 1 also indicates which of the two injector sets (i.e., 10 vs. 20 injectors) were used for each experiment. As noted in the table, at one case both sets of injectors were tested independently to examine how the number of injectors influences the results.

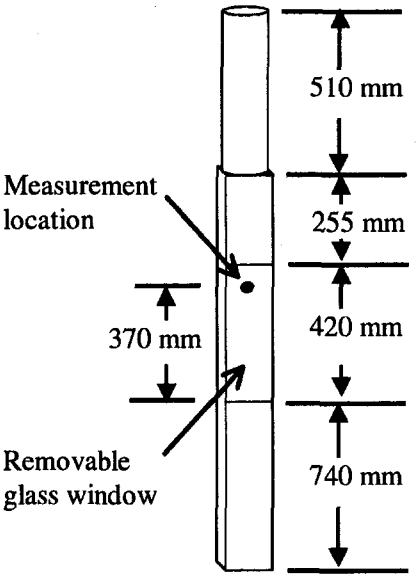

Fig. 2 Test section geometry

Bubble Size Measurements. For each of the two-phase test cases examined in the present study, bubble size measurements were made to quantify the bubble size distribution and to qualitatively assess the bubble shapes. This was accomplished using an image based analysis system. Images of the flow were recorded for each test condition using a CCD camera with a variable shutter speed to 1/16,000 of a second. The camera was used to record a sequence of frozen bubble images which were stored on SVHS video tape and later analyzed using an image processing package developed for cell sizing (JAVA by Jandel Scientific). This image-based bubble sizing system has been validated and used in previous studies by Tassin and Nikitopoulos (1995), Stanley et al. (1995), and Stanley and Nikitopoulos, (1996). The uncertainty in measuring bubble size with such a system has been shown to be less than 5 percent.

Wall Shear Measurements. Wall shear measurements within the air-water and pure water flows were made using a Laser Interferometer Skin Friction (LISF) meter. The LISF method for measuring wall shear was originally developed by Tanner and Blows (1976) for use in low-speed air flows. The basic principle of operation of the LISF meter is to optically measure the time rate of thinning of an oil film placed on a test surface subject to shear. The rate of thinning of the oil film is determined using optical interference and can be related to the applied shear stress through lubrication theory. In this way, the shear stress can be determined without any knowledge of the overlying flow properties (i.e., only properties of the oil and not properties of the outer flow are required to determine the shear).

Over time, several investigators have enhanced the LISF technique to cover a much broader range of gas flows (Tanner and Kulkarni, 1976; Monson and Higuchi, 1981; Monson, 1983; Garrison and Settles, 1994). With revisions to both the experimental setup and data reduction algorithm, the LISF instrument has been shown to provide accurate wall shear measurements in a broad range of subsonic and supersonic flows with and without flow separation.

Despite the LISF meter's many advantages and broad range of applicability, its use to date has been restricted to gaseous flows. In general, the principle of operation of the instrument itself is not limited by the specifics of the outer flow. Nonetheless, practical difficulties do arise when the instrument is used for shear measurement in liquid flows. During the instruments initial development, Tanner (1979) examined the potential for using the LISF meter in water flows. While Tanner was able to measure wall shear in a water flow, he found that stripping of the oil film from the model surface due to surface tension effects was a substantial problem and he concluded that the usefulness of the instrument in water flows was limited.

As part of the current research program, enhancements to the LISF technique have been developed which enable the instrument to work effectively in single-phase liquid flows and in two-phase gas-liquid flows. The following sections describe the instrument configuration and data analysis procedure used in the present study.

LISF Instrument Configuration. Figure 3 shows a schematic of the LISF instrument used in the present study. In this arrangement, the beam from a 5 mW Helium-Neon laser first passes through an iris diaphragm followed by a 10× microscope objective and a focusing lens. The beam is then turned horizontally by a mirror and passes through a glass window on the flow channel. The microscope objective, in combination with the focusing lens, is used to produce a precisely-focused beam on the surface of a thin oil film located on the inside wall of the glass window. By adjusting the separation between the microscope objective and the first focusing lens, a sharply focused laser spot less than 0.25 mm in diameter can be generated on the oil film. The mirror is adjusted to direct the beam nearly normal to the plate surface, resulting in an incidence angle of not more than 5 degrees.

Table 1 Experimental test matrix (typical uncertainties are 2 percent for velocity and 3–4 percent for volumetric flow ratio)

V_g	V_L = 0.66 (m/s)	V_L = 0.80 (m/s)	V_L = 1.02 (m/s)	V_L = 1.38 (m/s)
0.0 mm/s	β = 0.0	β = 0.0	β = 0.0	β = 0.0
2.3 mm/s		β = 0.0029[1]	β = 0.0023[1]	
16.1 mm/s			β = 0.0155[3]	
18.0 mm/s		β = 0.022 [2]		
29.4 mm/s		β = 0.0354[2]	β = 0.0280[2]	
43.5 mm/s			β = 0.0409[2]	
52.9 mm/s			β = 0.0493[2]	

[1] 10 hypodermic bubble injectors used
[2] 20 hypodermic bubble injectors used
[3] separate tests conducted using both sets of injectors

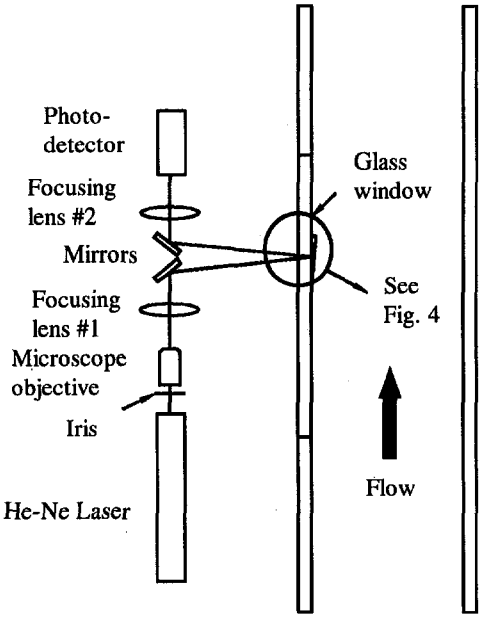

Fig. 3 LISF instrument configuration

Referring to Fig. 4, which is an enlargement of the oil film in Fig. 3, a portion of the incident laser beam is reflected from the interface between the oil film and the glass window due to differences in the index of refraction of the two materials. The transmitted portion of the beam continues through the oil film and undergoes another partial reflection at the interface between the oil film and the fluid (water in the present study). The two reflected beams, one from each surface of the oil film, then pass back out through the glass window and through a second focusing lens. This lens collects the two reflected beams (which are slightly diffused by the oil and window surfaces) and refocuses them on a photodetector.

Because the two reflected beams have traveled different optical path lengths, when they reach the photodetector and recombine, their phase angles are different. During the course of a test run, the outer flow field applies a shear on the oil film which causes it to thin. As the oil film thins, the spatial interference fringes propagate downstream. Since the laser beam is focused at a fixed location, the passing of the fringes generates a temporal variation in the intensity detected by the photodetector. The signal from the photodetector is recorded on a digital storage oscilloscope. Figure 5 shows a sample of an interference pattern generated during the present measurements.

Figure 6 shows an image of an actual oil film applied to the window surface. During a typical test run, the initial oil film thickness is on the order of 3 to 5 microns and the final thickness is approximately 0.5 microns. To help overcome the aforementioned problem of the oil film stripping, a special treatment was applied to the glass window prior to application of the oil film, which must be applied with the test section drained. A dilute solution of silicon oil in carbon tetrachloride was wiped over the window surface and then the window was baked at a temperature of 300°C for approximately 60 minutes. This treatment modified the wetting properties of the surface with respect to the oil-water pair and greatly reduced the tendency for the oil film to strip from the window surface. However, it was found that the surface treatment was not permanent and had to be repeated after approximately 5 to 10 test runs. The need for periodic surface treatment is, presently, the primary drawback of the LISF technique in two-phase flows. Additional research is in progress to optimize and simplify the surface treatment process to minimize stripping of the oil film and to eliminate the need for repeated surface treatments.

It should be noted that a rectangular test section with a removable window was used in the present study to simplify the oil application process. However, the technique can also be applied to circular pipes provided some form of oil dispensing system is incorporated into the pipe. This could be achieved by inserting a hypodermic needle through the pipe wall and then "bleeding" a small amount of oil through the needle and allowing it to drain down the inside of the pipe, forming the desired oil film. Optical lensing effects caused by a circular pipe can be minimized by positioning the optical system such that the plane containing the incident and reflected laser beam is oriented along the pipe axis as shown in Fig. 3. Furthermore, curvature effects are negligible so long as the pipe radius is large compared to the focused LISF laser-beam cross section.

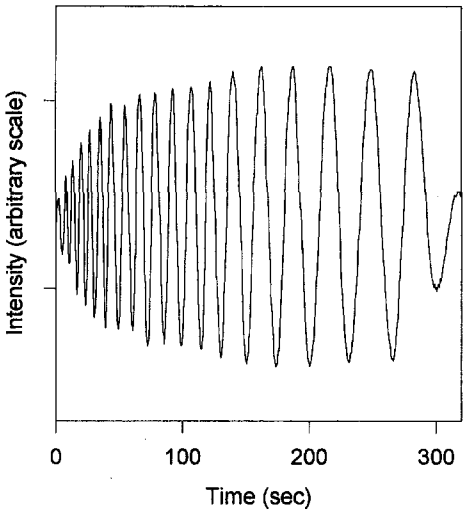

Fig. 5 Sample LISF interference signal

Data Reduction Procedure. This section describes how the shear stress is extracted from the optical inference signals such as that shown in Fig. 5. The governing theory for the flow of a thin film subject to gravity and spatially varying wall shear stress and surface pressure has been developed by previous investigators (see, e.g., Squire, 1962, Tanner and Blows, 1976). The resulting governing equation for the oil film is given below

$$h = \frac{\frac{1}{\sqrt{\tau}} \int_0^x \frac{1}{\sqrt{\tau}}\, dx}{\int_0^t \frac{dt}{\mu}} \tag{1}$$

where τ is the applied shear, x is the distance from the leading edge of the oil film to the location of the laser beam, h is the thickness of the oil film at that x location, μ is the viscosity of the oil film, and t is time. In the subject experiments, the oil film leading edge was located using a video camera equipped

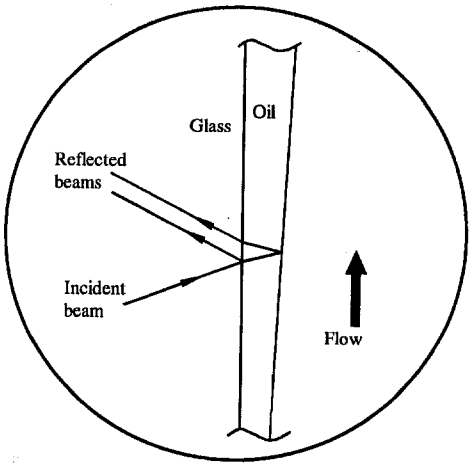

Fig. 4 Magnified view of the oil film in Fig. 3

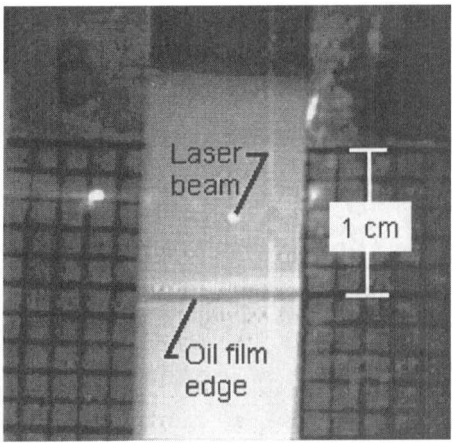

Fig. 6 Actual oil film prior to test run

with a high magnification lens. By backlighting the oil film, the oil leading edge could easily be identified. Typically, the distance from the oil leading edge to the laser spot was approximately 5 mm and could be measured using the video system to within ±0.04 mm (±0.8 percent).

In Eq. (1) it is assumed that the shear stress is the dominant driving force for the oil film and that the effects of pressure gradient and gravity are negligible. This assumption can be made provided the following relation is true.

$$\tau \gg \left| \frac{h}{2} \left[\frac{dp}{dx} - \rho g \sin \theta \right] \right| \tag{2}$$

In Eq. (2), θ is the inclination angle of the surface on which the oil film is applied and is 90 deg for the present study. Because the oil film thickness, h, is very small, Eq. (2) will be satisfied unless τ is extremely small and/or the pressure gradient is large. Such is not the case for the present experiments, and the assumption given by Eq. (2) is valid. (In the present experiments the right hand side of Eq. (2) was typically on the order of 0.01 Pa which is two to three orders of magnitude smaller than the expected shear stress.)

Further simplification of Eq. (1) can be made for flows in which the oil viscosity is constant with time (i.e., a constant temperature flow) and the wall shear does not vary spatially over the region between the oil leading edge and the laser beam location. For fully-developed pipe flows, the assumption of a constant wall shear is valid. However, this assumption can typically be invoked for other flows provided the spatial variation of the wall shear is reasonably small. This is because the integral of the wall shear in Eq. (1) is evaluated over the region between the oil film leading edge and the location of the laser beam which is typically on the order of 5 to 10 mm, as shown in Fig. 6. Hence, because this distance is small, to a first approximation τ can be assumed constant over this region for many flows unless $d\tau/dx$ is proven to be large.

With these assumptions, Eq. (1) reduces to the following

$$\tau = \frac{\mu x}{ht} \tag{3}$$

which relates the applied shear stress to the thickness of the oil film. The thickness of the oil film can be determined from the optical interference pattern (such as that shown in Fig. 5) enabling the wall shear to be calculated from Eq. (3). While the procedure to determine the oil film thickness versus time from the recorded photodetector signal is relatively straightforward, a complete discussion of the analysis steps is rather lengthy and will not be included herein. Complete details on the data reduction procedure can be found in Garrison (1994) and Manceau (1996).

Based on an uncertainty analysis of the governing equation for the LISF instrument along with previous validation experiments performed in air flows over a broad range of conditions, the uncertainty of the LISF measurement method has been estimated to be the larger of 0.2 Pa or ±15 percent of the measured shear value. The applicability of this uncertainty range to water and two-phase flows is discussed in the following section.

Results

Validation Experiments. An initial series of validation experiments were performed to evaluate the accuracy of the LISF instrument in liquid flows. Wall shear measurements were made on the surface of the glass window for a single-phase water flow at various flow rates. The measured results were compared to the theoretical wall shear values for a square duct. The theoretical wall shear results were calculated from standard pipe flow theory using the channel hydraulic diameter (38.1 mm). It is important to note that this procedure for determining the theoretical shear is itself accurate to only ±15 percent for turbulent flows (White, 1994). LISF measurements, made at four water flow rates ranging from 1.00 to 2.08 L/s (15.9 to 33 gpm), are compared to the theoretical values in Fig. 7. Each experimental data point in Fig. 7 represents an average shear value obtained from between 7 and 10 separate measurements. The standard deviation for each series of measurements was approximately 12 percent of the measured value and the error bars in Fig. 7 represent the 95 percent confidence interval. The maximum deviation between the LISF results and the theoretical values is 20 percent and the average deviation 8.2 percent; well within the uncertainty of the theoretical estimates. Thus, the results shown in Fig. 7 clearly show the LISF technique can be used to accurately measure the wall shear in liquid flows and indicate that the uncertainty levels attained in air flows appear applicable to liquid flows.

Two-Phase Experiments

Bubble Size Measurements. Figure 8 shows representative bubble images taken at three different gaseous flow rates for a single liquid superficial velocity of 1.02 m/s. These images are for volumetric flow ratios, β, of 0.0023, 0.0155, and 0.0493, respectively. At the lower volumetric flow ratio, Fig. 8(a), the bubbles are all nearly spherical and the mean bubble diameter is around 2 mm. At the intermediate volumetric flow ratio, Fig. 8(b), both the mean bubble diameter and its standard deviation increase while most of the bubbles remain nearly spherical. Finally, at the highest volumetric flow ratio, Fig. 8(c), further increase in the mean bubble diameter and its standard deviation are observed. Additionally, one can observe a significant number of nonspherical bubbles.

For each test case, a series of images such as those shown in Fig. 8 were analyzed to determine the mean bubble diameter and the range of bubble sizes present. In all the cases the bubble size distribution was nearly Gaussian. Figure 9 summarizes the mean bubble diameter for all the two-phase test cases examined in the present study. Additionally, the error bars in Fig. 9 indicate the standard deviation of the measured diameter.

Figure 9 shows that for all the present experiments, the mean bubble diameter ranged from 2 to 3 mm, and that the bubble size tended to increase with the volumetric flow ratio at a fixed liquid superficial velocity ratio. It should be noted here that, on theoretical grounds, the stable bubble size in a given bubbly flow can be bracketed by a maximum size that can resist breakup (Hinze, 1955) and a minimum size that can resist coalescence (Thomas, 1981). The relevant mechanisms that dictate both limits are related to the turbulence characteristics of the continu-

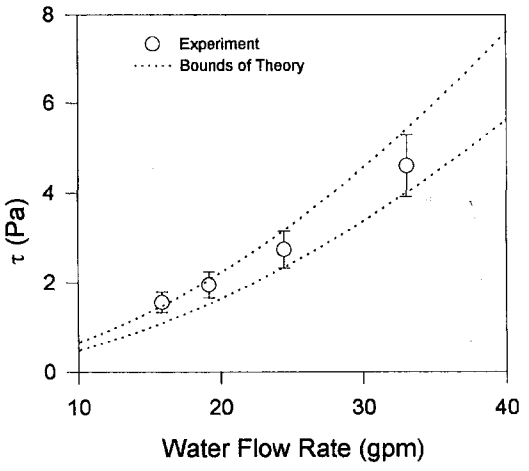

Fig. 7 Wall shear results for a single-phase water flow (error bars represent 95 percent confidence intervals based on 7 to 10 separate measurements)

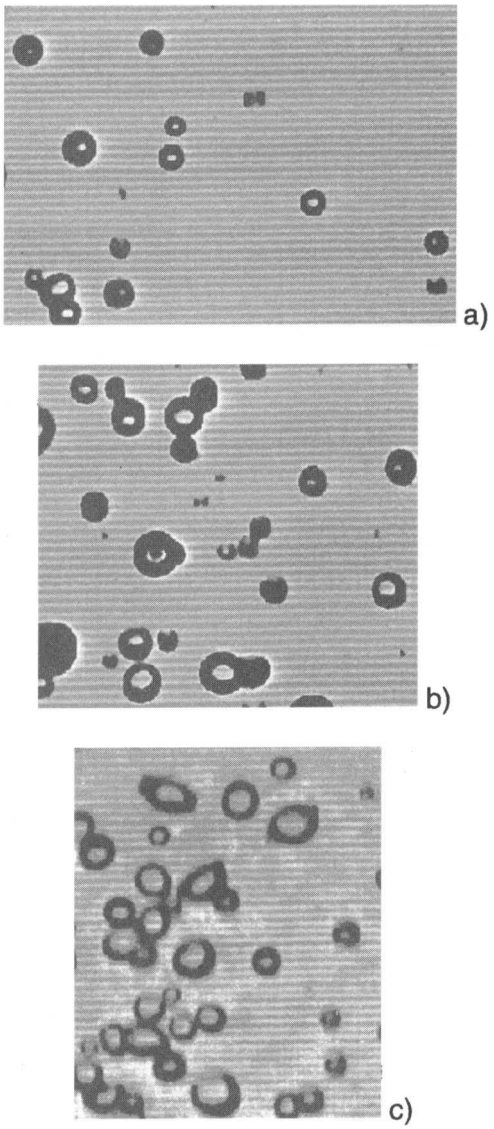

Fig. 8 Bubble images at various flow qualities for V_L = 1.02 m/s: (*a*) β = 0.0023; (*b*) β = 0.0155; and (*c*) β = 0.0493

ous phase. In bubbly duct flow these limiting sizes are well separated (by at least an order of magnitude); thus, a wide variety of stable size distributions are possible at given bulk flow conditions, and the injection (initial) conditions play a determining role as to the detailed nature of the bubbly flow topology (Nikitopoulos and Michaelides, 1995). Evidence in support of this statement can be found in Nakoryakov et al. (1981) as well as Serizawa et al. (1992). The nonmonotonic trend of the curve corresponding to a liquid superficial velocity of 1.02 m/s in Fig. 9 can be explained on these grounds as a direct result of increasing the number of bubble injectors used from 10 to 20 (i.e. the initial condition of injection). While this increase was necessary to attain higher gas flow rates, it results in different gas-injection velocities which in turn influence the bubble size (this was also observed by Serizawa et al., 1992). Also, as the volumetric flow ratio is increased at a fixed liquid superficial velocity the bubble injection frequency increases. Since, the injector tips are fairly close together the probability of bubble interaction and possible coalescence in the neighborhood of the injector tips increases. This can also contribute to the broadening of the bubble size distribution and an increase in mean size. Nevertheless, the change in the number of injectors did not influence the bubbly flow produced to a

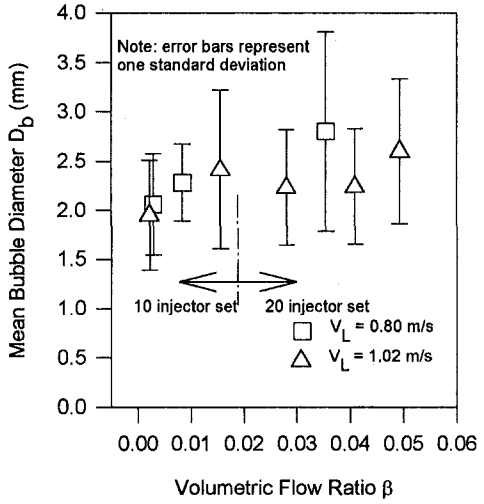

Fig. 9 Mean bubble diameters

considerable extent. Therefore, results obtained with the two sets of injectors at the same bulk flow conditions can be construed as the product of essentially the same initial conditions.

Shear Stress Measurements Figure 10 shows the results of the wall shear measurements in two-phase bubbly flow. This figure plots the wall shear at various volumetric flow ratios, β, using the liquid superficial velocity, V_L, as a parameter. It should be noted that the measured wall shear has been normalized by the shear values for the corresponding single-phase water flow (i.e., $\beta = 0$) at the same liquid velocity.

Several important observations can be made from the results shown in Fig. 10. A significant increase in the wall shear is observed due to the addition of the gaseous phase. The two-phase flow results shown are all for relatively low gas flow rates. However, even the slightest addition of the gaseous phase resulted in wall shear values up to 2.5 times that for a pure water flow. For both liquid flow rates the wall shear was observed to initially rise to a local maximum and then drop off. Additionally, decreasing the liquid flow rate resulted in increased wall shear values. All these trends are consistent with those observed by Nakoryakov et al. (1981). However, it is important to note that the peak shear values obtained in the present study are lower than those reported by Nakoryakov et al. They reported peak τ/τ_o values of approximately 3.5 and 5 for liquid velocities of

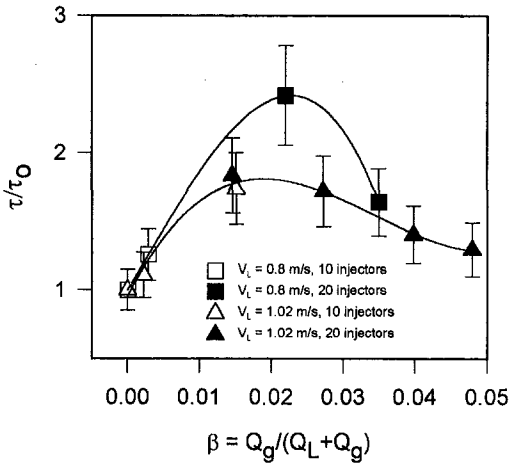

Fig. 10 Wall shear results for a two-phase air-water flow (error bars represent 95 percent confidence intervals based on 7 to 10 separate measurements)

1.05 and 0.79 m/s, respectively. Moreover, they observed the peak shear values to occur at significantly higher β values ($\approx$0.1 to 0.15) than those in the present study. There are several possible reasons why the present results may not agree quantitatively with those of Nakoryakov et al. (1981). The study by Nakoryakov. was performed in a circular tube while the present study was conducted in a square duct. The hydraulic analogy that exists between ducts of different cross sections in single phase flow may be questionable in the case of two phase flow, and thus the difference in the cross section shape may be of importance. The study of Nakoryakov et al. (1981) was conducted at a pressure different than the present one; this will certainly influence the values of β. A correction was not possible because the pressure in Nakoryakov's case was unknown. Moreover, Nakoryakov et al. (1981) used a significantly larger tube diameter than the equivalent hydraulic diameter of the present experiment (86.4 mm vs. 38.1 mm). The ratio of the bubble diameter to the tube hydraulic diameter can also be an important flow parameter that may influence the two-phase wall shear. Given that this ratio differed by more than a factor of 2 between the present experiments and those of Nakoryakov et al. (1981), it is possible that the observed differences between their study and ours could be, at least partially, attributed to this parameter mismatch. Nevertheless the trends are common between the two studies and further investigation will be necessary to quantify the influence of cross section shape and bubble-to-duct size ratio.

The possible effect of the number of injectors used to generate the bubbly flow was examined at a single test condition; the results of this test can easily be seen in Fig. 10 by comparing the two data points taken at $\beta = 0.0155$ for $V_L = 1.02$ m/s. At this test condition both sets of bubble injectors were tested while holding β and V_L constant. A measurable difference in wall shear was observed but it was within the standard deviation margins and cannot be considered significant. This is not unexpected since no radical changes were introduced in the flow topology by increasing the number of injectors, as discussed previously. Thus, we can conclude that the change in initial injection conditions brought about by increasing the number of injectors did not change the flow topology significantly and, therefore, the observed shear stress trend can be attributed to the variation of the volumetric flow ratio.

During the course of the experiments, substantial fluctuations in the wall shear were observed both during individual test runs and from one run to the next. This is reflected by the error-bars in Fig. 10, which are based on the standard deviation of the wall shear stress. These fluctuations were at a relatively large time scale and indicated an intermittent pattern. In general, the LISF instrument is designed to measure mean shear values and is not capable of resolving the fluctuating wall shear. However, at the low gas flow rate, substantial shear fluctuations were observed at a frequency low enough to be resolved by the instrument. Transitions between periods of high shear and periods of low shear, equivalent to the pure water flow, were observed at this condition. This behavior was correlated to the passage of bubbles that are moving faster than the liquid in the neighborhood of the wall. It should be noted that sizable shear-stress fluctuations with RMS values of the order of 40–100 percent were also observed by Nakoryakov et al. (1981). The trend was an increasing one with β.

At low volumetric flow ratios, the sharp increase of the two-phase shear stress with increasing volumetric flow ratio can be attributed to the increase of the concentration of faster-moving bubbles in the neighborhood of the wall. This phase distribution which manifests itself through near-wall peaks of the void fraction and highly uniform liquid velocity profiles is characteristic of low-β bubbly flows at modest superficial liquid velocities and has been amply documented by Serizawa et al. (1975, 1992), Nakoryakov et al. (1981), Wang et al. (1987), Liu and Bankoff (1990) in pipe flows and Matsui (1992) in rectangular ducts. According to these previous experimental studies, at higher values of β, the peak bubble concentration (or void fraction) near the wall diminishes while the concentration in the central region of the duct increases. The liquid velocity profiles in this case are documented to become less uniform. The saturation of the two-phase shear stress shown in Fig. 10 can be correlated with this transition and the associated arrest in the accumulation of fast-moving bubbles near the wall. Previous experiments have also shown that peak bubble concentrations are more pronounced at low liquid superficial velocities. This feature can account for the higher peak of the measured two-phase shear stress at the lower liquid superficial velocity presented in Fig. 10. Further increase of β at constant liquid superficial velocity leads to bubble "coring" where the peak bubble concentration occurs at the center of the pipe and the central peak of the liquid velocity profile becomes sharper. The drop-off in wall shear with further increase of β observed in Fig. 10 can be correlated with this flow topology. It should be noted that when β is varied the average bubble size does not remain constant. So, bubble size effects can also influence the magnitude and trend of the two-phase shear stress. Indeed Matsui (1992) has shown that the flow topologies mentioned above strongly depend on bubble size. His experiments in a square duct showed that large bubbles (>4 mm in his case) tend to move toward the center leading to a coring pattern while smaller bubbles (<2 mm) preferred the wall leading to a wall-peak pattern. Furthermore, results of a simple model by Nikitopoulos and Michaelides (1995) for bubbly pipe flow which took into account bubble size effects showed that the two-phase shear stress is indeed sensitive to bubble size at fixed β. In our study, the bubble size did not vary considerably (always between 2 mm and 2.75 mm) and the likelihood of bubble size effects being the prominent factor in defining the observed trends is not high.

These above interpretations are still of speculative nature due to the lack of a complete test matrix. Measurements of the local properties of the flow, particularly in the neighborhood of the wall, in tandem with the wall-shear measurements, are necessary in order to fully understand the source and quantify the influencing factors of this behavior.

Finally, the results shown in Fig. 10 demonstrate the ability to successfully record wall shear data using the LISF instrument. The measured results and their qualitative correlation with the trends observed by Nakoryakov et al. (1981), serve to validate the LISF technique, making it a valuable tool for measurement of wall shear in two phase flows.

Conclusions

An instrument has been developed which enables the measurement of wall shear within two-phase flows. The instrument, termed a Laser Interferometer Skin Friction meter, is essentially nonintrusive and uses the rate of thinning of a thin film to determine the shear stress. The accuracy of the instrument was verified for a single-phase water flow. Results of these tests indicate a typical uncertainty of approximately $\pm$15 percent. The instrument was also used to measure the wall shear in a two-phase bubbly flow over a range of superficial liquid and gas flow rates. Results of the two-phase measurements show that the presence of the gaseous phase, even in small amounts, can significantly increase the wall shear stress. The two-phase wall shear saturates to a maximum and then declines again as the superficial gas velocity is increased. The peak two-phase wall shear increased as the liquid superficial velocity was decreased. These trends are qualitatively in agreement with previous measurements obtained in pipes using an electrochemical technique. Additionally, the presence of the gaseous phase appears to substantially increase the wall shear fluctuation. This was clearly observed at very low volumetric gas flow ratios where the time scale associated with this fluctuation was long.

Acknowledgments

The authors gratefully acknowledge the support from La-SPACE and NASA, the Louisiana Board of Regents through research grants LEQSF(1991–1992)-ENH-21, 31, and LEQSF(1990–1992)-RD-A-07, and ARCO Chemical Company through its University Grants Program under the supervision of Mr. John Egan.

References

Bataille, J., Lance, M., and Marie, J. L., 1990, "Bubbly Turbulent Shear Flows," ASME FED-99/HTD-155, pp. 1–8.

Beyerlein, S. W., Cossman, R. K., and Richter, H. J., 1985, "Prediction of Bubble Concentration Profiles in Vertical Turbulent Two-Phase Flow," *International Journal of Multiphase Flow,* Vol. 11, pp. 629–641.

Garrison, T. J., and Settles, G. S., 1994, "Laser Interferometer Skin-Friction Measurements of Crossing-Shock Wave/Turbulent Boundary-Layer Interactions," *AIAA Journal,* Vol. 32, No. 6, pp. 1234–1241.

Garrison, T. J., 1994, "The Interaction Between Crossing-Shock Waves and a Turbulent Boundary Layer," Ph.D. thesis, The Pennsylvania State University, University Park, PA.

Hinze, J. O., 1955, "Fundamentals of the Hydrodynamic Mechanism of Splitting in Dispersion Process," *AIChE Journal,* Vol. 1, p. 289.

Herring, E. A., and Davis, M. R., 1976, "Structural Development of Gas-Liquid Mixture Flows," *Journal of Fluid Mechanics,* Vol. 73, pp. 58–70.

Liu, T. J., and Bankoff, S. G., 1990, "Structure of Air-Water Bubbly Flow in a Vertical Pipe: I and II," ASME FED-99/HTD-155, pp. 9–26.

Manceau, E., 1996, "Skin Friction Measurements in a Gas-Liquid Pipe Flow via Optical Interferometry," MS thesis, Louisiana State University, Baton Rouge, LA.

Malnes, D., 1966, "Slip Ratios and Friction Factors in the Bubble Flow Region in Vertical Tubes," Report KR-110, Institutt Atomenergi, Kjelles. Norway.

Matsui, G., 1992, "Characteristic Structure of Upward Bubble Flow," *Dynamics of Two-Phase Flows,* C. Jones and I. Michiyoshi, eds., CRC Press, pp. 359–377.

Monson, D. J., and Higuchi, H., 1981, "Skin Friction Measurements by a Dual-Laser-Beam Interferometer Technique," *AIAA Journal,* Vol. 19, No. 6, pp. 739–744.

Monson, D. J., 1983, "A Nonintrusive Laser Interferometer Method for Measurement of Skin Friction," *Experiments in Fluids,* Vol. 1, pp. 15–22.

Nakoryakov, V. E. et al. 1981, "Local Characteristics of Upward Gas-Liquid Flows," *International Journal of Multiphase Flow,* Vol. 7, pp. 63–81.

Nikitopoulos, D. E., and Michaelides, E. E., 1995, "Phenomenological Model for Dispersed Bubbly Flow in Pipes," *AIChE Journal,* Vol. 41, No. 1, pp. 12–22.

Sekoguchi, K., Fukui, H., and Sato, H., 1981, "Flow Characteristics and Heat Transfer in Vertical Bubble Flow, Two-Phase Flow," A. E. Bergles and S. Ishigai, eds., pp. 59–74.

Serizawa, A., Kataoka, I., and Michiyoshi, I. 1975a, "Turbulence Structure of Air-Water Bubbly Flow. I. Measuring Techniques," *International Journal of Multiphase Flow,* Vol. 2, pp. 235–246.

Serizawa, A., Kataoka, I., Michiyoshi, I., 1975b, "Turbulence Structure of Air-Water Bubbly Flow. II. Local Properties," *Int. J. Multiphase Flow,* Vol. 2, pp. 235–246.

Serizawa, A., Michiyoshi, I., Kataoka, I., and Zun, I., 1992, "Bubble Size Effect on Phase Distribution," *Dynamics of Two-Phase Flows,* C. Jones and I. Michiyoshi, eds., CRC Press, pp. 379–400.

Souhar, M., and Cognet, G., 1993, "Wall Shear Measurements by Electrochemical Probes in Two-Phase Flow Bubble and Slug Regimes," *Measuring Techniques in Gas-Liquid Two-Phase Flows,* Proceedings of the IUTAM Symposium, Nancy, France, 1983, pp. 723–744.

Squire, L. C., 1962, AGARDograph 70.

Stanley, K. N., Khan, M., and Nikitopoulos, D. E., 1995, "Non-Intrusive Measurements in Dispersed, Bubbly Pipe Flow," ASME FED-Vol. 233/HTD-Vol. 321, pp. 451–460.

Stanley, K. N., and Nikitopoulos, D. E., 1996, "Bubble Measurements in a Turbulent Axisymmetric Two-Phase Jet," *Chemical Engineering Communications,* Vol. 143, pp. 1–22.

Tanner, L. H., and Blows, L. G., 1976, "A Study of the Motion of Oil Films on Surfaces in Air Flow, with Application to the Measurement of Skin Friction," *Journal of Physics E: Scientific Instruments,* Vol. 9, pp. 194–202.

Tanner, L. H., and Kulkarni, V. G., 1976, "The Viscosity Balance Method of Skin Friction Measurement: Further Developments Including Applications to Three-Dimensional Flow," *Journal of Physics E: Scientific Instruments,* Vol. 9, pp. 1114–1121.

Tanner, L. H., 1977, "A Skin Friction Meter, Using the Viscosity Balance Principle, Suitable for use with Flat or Curved Metal Surfaces," *Journal of Physics E: Scientific Instruments,* Vol. 10, pp. 278–284.

Tanner, L. H., 1979, "Skin Friction Measurement by Viscosity Balance in Air and Water Flows," *Journal of Physics E: Scientific Instruments,* Vol. 12, pp. 610–619.

Tassin, A. L., and Nikitopoulos, D. E., 1995, "Non-Intrusive Measurements of Bubble Size and Velocity," *Experiments in Fluids,* Vol. 19, pp. 121–132.

Theofanous T., G., and Sullivan, J., 1982, "Turbulence in Two-Phase Flows," *Journal of Fluid Mechanics,* Vol. 116, pp. 343–362.

Thomas, R. M., 1981, "Bubble Coalescence in Turbulent Flows," *International Journal of Multiphase Flow,* Vol. 7, No. 6, p. 709.

Wang, S. L., Lee, S. J., Jones, O. C., Jr, and Lahey, R. T., Jr, 1987, "Three-Dimensional Turbulence Structure and Phase Distribution Measurements in Bubbly Two-Phase Flows," *International Journal of Multiphase Flow,* Vol. 13, pp. 327–343.

White, F. M., 1994, *Fluid Mechanics,* Third Edition, McGraw-Hill, New York, NY.

CFD Simulation and Experimental Validation of a New Closed Circuit Wind/Water Tunnel Design

Robert Gordon
Postgraduate Student.

Mohammed S. Imbabi
Lecturer.

The Department of Engineering,
The University of Aberdeen,
Aberdeen. AB24 3UE, Scotland,
United Kingdom

A new closed-circuit wind/water tunnel to support flow visualization research was designed and constructed at The University of Aberdeen. Review of existing closed-circuit tunnel designs revealed that they are large, expensive, difficult to set up and maintain, and typically employ a single working fluid. Key objectives of the work reported here were to reduce the overall cost and size of the tunnel, facilitate the use of alternative working fluids (air or water), and provide high quality flow within the test section. Conventional design methods were used initially, and computational fluid dynamics (CFD) was then employed to simulate the flow within critical sections of the tunnel. The results from CFD played a decisive role in identifying the modifications needed to achieve the compact, cost-effective tunnel design eventually built and tested. Flow quality within the test section was established using measured velocity profiles, and these are also presented.

1 Introduction

This paper presents certain aspects of the work leading to the design and construction of a new compact high-performance (uniform velocity with low turbulence in the working section) modular wind/water tunnel. The tunnel has since been used to obtain high quality images of fluid flow around bluff bodies, model aerofoil sections, and model buildings, providing an important test-bed for development of a new generation of high speed stereo flow visualization computer codes. In the future, the tunnel will be used as a general purpose teaching aid, as well as a specialist research tool.

The design of the tunnel needed to be flexible, to enable a wide range of fluid flow situations to be reproduced. In order to comply with this goal, it was decided to include the option of using either air or water (any chemically inert fluid could be used, in fact) as the working fluid. The higher absolute viscosity of water permits conventional tracer particles, such as pollen seed, to be suspended without being markedly affected by gravitational force. The low kinematic viscosity of water provides the added advantage that high Reynolds numbers can be obtained at lower flow velocities than with air (Lagarde, 1984). Conversely, using air as the working fluid has the advantage of allowing known, well-defined flows to be reproduced at higher flow velocities, thus aiding the development of the high speed element of our flow visualization algorithms. Also, with air as the working fluid the tunnel bridges an important gap in our existing large, open-circuit wind tunnel and the closed-circuit supersonic wind tunnel facilities.

There are a number of noteworthy tunnel designs in use today (Ito et al., 1992). Guidelines such as those by Mehta and Bradshaw (1979) provide information on basic design and construction, and have been widely employed. Such tunnel designs tend to be large and expensive, and use air as the working fluid. Smith et al. (1990) demonstrated that good performance trends were achieved when using a $\frac{1}{50}$th scale model of the National Full-scale Aerodynamics Complex wind tunnel, which possesses test section dimensions of 40 ft × 80 ft (≈12.2 m × 24.4 m). Their work thus suggests that flow performance is not necessarily a function of tunnel size. This being the case, there seems to be little disadvantage in considering a smaller tunnel design. Given that spatial and financial constraints are important factors for many, it was decided to investigate in greater depth the possibility of developing a compact, inexpensive tunnel design which would not compromise the flow quality within its test section.

Computational fluid dynamics (CFD) simulation was used to investigate the influence of a number of key tunnel components on flow behavior. This information was used to obtain a greater understanding of how the tunnel would perform when built. The conventional approach to such an engineering design problem in the past has been to use a combination of theory and empirical calculations to obtain an initial specification. After construction, the tunnel would then be modified and "tuned" to obtain the desired flow. This has resulted in the acceptance by some of the "black art" element in wind tunnel design, with all which this entails in terms of time, labor, and cost. In contrast, the computational approach allows different designs, or design modifications, to be investigated rapidly and economically.

CFD results are presented in detail for the most important components of the tunnel, upstream of the test section. The results are validated by comparison of experimental test section velocity profiles with velocity profiles obtained numerically. Most of the simulations were carried out using a 2-D approximation. This is justified, in part, by the tunnels symmetry about the longitudinal vertical plane, and also because of the deployment of flow straighteners to tame secondary flows at the inlet and outlet of the 180 deg upstream bend. The results further illustrate how flow through the diffuser screens can be accurately simulated using a porous model in turbulent flow. A final low Reynolds number simulation in 3D was performed to assess the effects of lateral expansion of the inlet flow into the diffuser/contraction sections and guide vanes.

2 Design Considerations

2.1 Test Section Dimensions. The tunnel was to be used in the first instance to examine flow in the wake of a circular

Contributed by the Fluids Engineering Division for publication in the JOURNAL OF FLUIDS ENGINEERING. Manuscript received by the Fluids Engineering Division April 30, 1996; revised manuscript received December 4, 1997. Associate Technical Editor: P. M. Sockol.

cylinder for Reynolds numbers in the range 10^2 to 10^4. This type of flow has been extensively investigated in the past (Braun et al., 1992; Eaton, 1987; Engelman and Jamnia, 1990; Unal and Rockwell, 1988), and therefore provides a good reference benchmark for our visualization work. The vortex-shedding mechanism also offers a logical step in developing our knowledge of more complicated turbulent flows.

Despite the economic desirability of a small tunnel design, the size is largely dependant on the cross-sectional area of the test section. In order to prevent the boundary layer from interfering with the vortex shedding mechanism, the test section dimensions were determined from the maximum boundary layer thickness and the vortex street spreading range. These calculations were performed for water as working fluid. With air as working fluid the boundary layer is less prominent at the same Reynolds number.

The maximum boundary layer thickness was calculated for Reynolds 10^2 to 10^4 from the von Karman integral momentum equation for steady, incompressible flow, using a quarter sine wave as an approximation to the velocity profile (Massey, 1989). From previously recorded experimental data on the von Karman vortex street (Hughes, 1979) the distance between each vortex can be taken as $x \approx 4.3\varnothing_c$ and the width between the vortices as $y \approx 1.2\varnothing_c$. By assuming that the diameter of each vortex can expand to a maximum mean diameter of x, an extra $5.5\varnothing_c$ must be added to the depth of the test section. Combining these gives a working section $W = 2\delta + 5.5\varnothing_c$, where δ is the maximum boundary layer thickness taken at $L = 0.5$ m. For a cylinder diameter $\varnothing_c$ of 0.02 m this resulted in a working section of 0.25 × 0.25 m. The test section depth could have been further reduced by choosing a smaller cylinder diameter, but in practice the latter had to be large enough to produce a vortex structure clearly visible to the naked eye.

The test section length needed to be sufficiently long to allow vortices downstream to be observed. The restriction of $x \approx 4.3\varnothing_c$ is not a limiting factor, and a test section length of 800 mm was chosen. This allowed objects up to 40 mm in height to be placed within the test section, allowing a minimum of four whole vortices to be visible downstream of the cylinder at any one time.

2.2 Conventional Tunnel Designs. Given the minimum size of test section required, the application of current design guidelines (Mehta and Bradshaw, 1979) would have led to a wind tunnel approximately 9 m in length and 4 m high. A classic example of such a wind tunnel is presented by Arakeri et al. (1988) and Ito et al. (1992). Due to the volume of fluid involved this was obviously not a practical design for a water tunnel. Compact water tunnels, such as the gravity fed open circuit vertical tunnel (Kerres and Grönig, 1990), were not considered a viable option due to height constraints. Other water tunnel designs do not specifically address the problem of size (Durnet, 1994). For air, an open-circuit design could have been implemented (Lam and Pomfret, 1984), reducing construction cost and size. However, this would not have been suitable for use with an optical visualization system in which the flow is seeded with tracer particles, and a closed-circuit design was deemed necessary.

The important features of a closed-circuit wind tunnel (Fig. 1) are as follows:

- An exit diffuser upstream of the fan prevents unsteady pressure recovery from perturbing the fan speed at constant input power. A diffuser screen or flow straightener can be used as an alternative.
- A wide-angled diffuser performs a similar task to the exit diffuser over a much shorter distance upstream of the test section. This wide diffusion, however, leads to unwanted boundary layer separation that must be controlled. It is therefore important to obtain the optimum profile to prevent this separation.

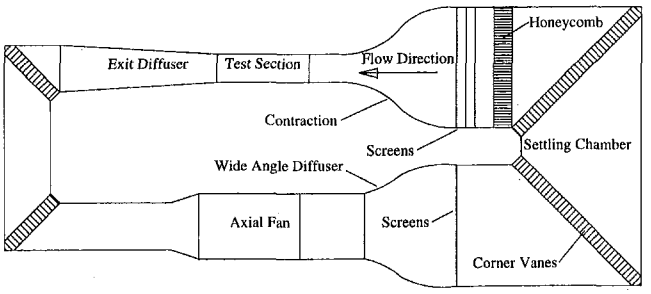

Fig. 1 Conventional wind tunnel design

- 90 deg "square" bends to channel the flow. Flow around the bend is controlled by curved corner vanes, where the tailing edge is aligned parallel to the axis of the downstream leg, and the leading edge is typically set at a positive angle of incidence of four deg to the axis of the upstream leg. Ideally the flow entering the diffuser from the bend upstream of the test section should be uniform in profile.
- A settling chamber which houses a series of flow straighteners and diffuser screens. The larger cross-sectional area results in a reduction in the flow velocity within the settling chamber, which serve to reduce nonstreamwise velocity fluctuations and turbulence.
- Diffuser screens, the pressure drop across which provides an important method for reducing streamwise velocity fluctuations.
- Flow straighteners, consisting of a large number of hexagonal or rectangular cells, typically 2500 for a small wind tunnel, which act to reduce velocity fluctuations normal to the flow direction.
- The contraction nozzle, which improves flow uniformity and steadiness and reduces turbulence in the working section. The effectiveness of the contraction nozzle is governed by its shape, or profile.

It has been pointed out by Lam and Pomfret (1984) and Su (1991) that quality of flow within the test section is, to a great extent, dependent on the contraction nozzle profile. A good contraction design should have no flow separation, a uniform and parallel flow at the exit, and should minimize the unsteadiness and degree of turbulence in the test section (Gibbings, 1993; Lam and Pomfret, 1984). Considerable effort has been devoted to establishing the optimum contraction profile. Although elegant, analytical solutions in which an infinite contraction length is assumed are mathematically complex (Albayrak, 1991). The design of contraction profiles of finite length has also been widely investigated (Downie et al., 1984; Gibbings, 1993; Morel, 1975; Su, 1991). However, none of the solutions put forward has significant performance advantage. The conclusion was that a relatively simple contraction profile, based on two elliptical curves, offered the best solution (Downie et al., 1984). For the tunnel size to remain small the contraction length was limited to less than 1.0 m, resulting in a contraction ratio of 5.6:1. Although this is slightly lower than the values recommended by Mehta and Bradshaw (1979) of 6:1 to 9:1, it should be noted that, whereas increasing the effective length of the contraction improves flow quality, the contraction ratio has only limited influence (Su, 1991). Guidelines for design of the bend, settling chamber, or diffuser are much less readily available.

Our aim was to develop a compact tunnel that retained all of the important indispensable features of a conventional tunnel, such as the contraction, diffusers, screens, and flow straighteners. In order to achieve the desired reduction in size the wide angle diffuser, contraction and test section were aligned along a single axis in the direction of the flow, and the settling chamber dispensed with. The square bends and corner vanes were replaced with full 180 deg circular bends upstream and down-

stream of the diffuser/contraction assembly, with inlet and outlet honeycomb flow straighteners for the former to reduce secondary flows. Transitions to the fan/pump were employed to close the circuit.

CFD simulations were performed to evaluate the flow within the resulting sections. For each section, the geometry was modified to match the outermost flow streamlines obtained from numerical simulation. The process was repeated until the correct shape was obtained. Guiding vanes at the inlet to the wide angle diffuser were required to provide a more robust method of diffusing the flow for the range of Reynolds number specified.

The resulting tunnel was approximately 4 m in length and 2 m high. Loss of the settling chamber was compensated for by employing additional screens. An important element of the design was modular construction, allowing the tunnel to be readily modified for use of either air or water as the working fluid.

3 Computational Model

The numerical simulations described in this paper were performed using FIDAP v 6.0–7.5, a general purpose program for the simulation of fluid flow based on the Galerkin finite element formulation. A complete description of the numerical method employed can be found in the *FIDAP Theoretical Manual* (FDI Inc., 1990), however, a brief overview will be presented.

3.1 Governing Equations. The flow within the tunnel sections is described mathematically for incompressible, isothermal flow with a constant viscosity, by the following general equations:

$$\rho_o\left(\frac{\partial u_i}{\partial t} + u_j u_{i,j}\right) = -p_{,i} + [\mu(u_{i,j} + u_{j,i})]_{,j} + \rho_o f_i \quad (1)$$

$$u_{i,i} = 0 \quad (2)$$

Equation (1) is known as the Navier-Stokes form of the momentum equation and Eq. (2) is the mass continuity equation, written in vector notation.

3.2 Turbulence Flow Equations. To mathematically simulate turbulence a standard 2-equation k-ϵ turbulence model, utilizing Prandl's mixing layer hypothesis, was used. In this case, the Navier-Stokes and continuity equations remain unchanged. To incorporate the evolution of the turbulent kinetic energy k, and the rate of dissipation ϵ, two transport equations were employed:

$$\rho\left(\frac{\partial k}{\partial t} + u_j k_{,j}\right) = \left(\frac{\mu_t}{\sigma_k} k_{,j}\right)_{,j} + \mu_t \Phi - \rho\epsilon \quad (3)$$

$$\rho\left(\frac{\partial \epsilon}{\partial t} + u_j \epsilon_{,j}\right) = \left(\frac{\mu_t}{\sigma_\epsilon} \epsilon_{,j}\right)_{,j} + c_1 \frac{\epsilon}{k} \mu_t \Phi - \rho c_2 \frac{\epsilon^2}{k} \quad (4)$$

where:

$$\Phi = 2\epsilon_{ij}\epsilon_{ij} \quad (5)$$

and:

$$\mu_t = c_\mu \rho \frac{k^2}{\epsilon} \quad (6)$$

The values of the empirical constants c_μ, σ_k, σ_ϵ, c_1, and c_2, in Eqs. (3), (4), and (6) are the default values of 0.09, 1.00, 1.30, 1.44 and 1.92, respectively. These values have been tested and optimized against a wide range of incompressible, isothermal flows.

3.3 Porous Flow Equations. In order to accurately simulate the flow through the diffuser screens further modification of the governing equations was required. FIDAP offers three permeability models: the Darcy formulation, Brinkman model, and Forchheimer-Brinkman model (FDI Inc., 1990). The Brinkman model was employed in the absence of sufficient data for the more sophisticated Forchheimer-Brinkman model. Thus,

$$\frac{\rho_o}{\phi}\frac{\partial u_i}{\partial t} + u_i \frac{\mu}{k_i} = -p_i + [\tilde{\mu}(u_{i,j} + u_{j,i})]_{,j} + \rho_o f_i \quad (7)$$

where $\mu = a\tilde{\mu}$ and the suggested value for a is 100.

Also, given the absence of experimental data for the screens employed the permeability coefficients were calculated using a capillary tube model (Bear, 1988), where the porosity was given as:

$$\phi = \frac{V_{\text{fluid}}}{V_{\text{fluid}} + V_{\text{solid}}} \quad (8)$$

and the permeability:

$$K = \frac{Cd^2\rho g}{\mu} \quad (9)$$

where $C = 6.54 \times 10^{-4}$, an empirical constant, and $d = 2$ mm, the radius of the screen wires. These equations result in porosity and permeability values of 0.56 and 1.31×10^{-4}, respectively.

4 Numerical Method

All simulations are based on the assumption of incompressible, isothermal, steady fluid flow. The upstream bend was simulated separately during the initial design stages, and the resulting flow at the outlet was used as the inflow for the more complex diffuser/contraction models.

In the 2-D laminar and turbulent simulations the nonlinear algebraic equations were solved using successive substitution. Although slow, this method provides a large radius of convergence. For the complex geometries considered, and in particular when turbulence and porosity models are included, successive substitution proved to be the most suitable. Pressure recovery, in the laminar case, was implemented from the velocity data by solving a Poisson-like equation (Giliver et al., 1991). In the turbulence and porous models, the pressure was approximated with a piecewise-constant function within each element (FDI Inc., 1990; Giliver et al., 1991).

Due to the increase in computational resources required when solving the 3-D turbulence equations it was not feasible to use successive substitution, and a segregated solver was employed. This method avoids creation of the global system matrix, solving each of the conservation equations in a sequential manner.

4.1 Boundary Conditions. In all of the simulations the velocity at solid boundaries was set to zero to represent the nonslip condition. In order to predict the flow behavior in the viscous sublayer in the turbulent models, an additional wall model was applied to all solid boundaries. These wall functions were specified along the edge of the computational grid, slightly displaced from the physical boundary. In doing so, the finite element simulation begins at the inner edge of the turbulent boundary layer and does not compute any flow quantities within the viscous sublayer. At the outflow a default stress-free boundary condition was employed (Engelman and Jamnia, 1990). Assuming temperature gradients and coriolis forces across the outlet are nonexistent, this type of boundary condition was considered adequate.

For the 180 deg circular bend the velocity profile at the inlet was assumed to be uniform. However, to accurately predict the flow behavior in the diffuser/contraction section the inlet velocity profile was taken from the 180 deg bend simulation. In all of the turbulence models the initial kinetic energy and dissipation rate were assumed constant. The values are given by:

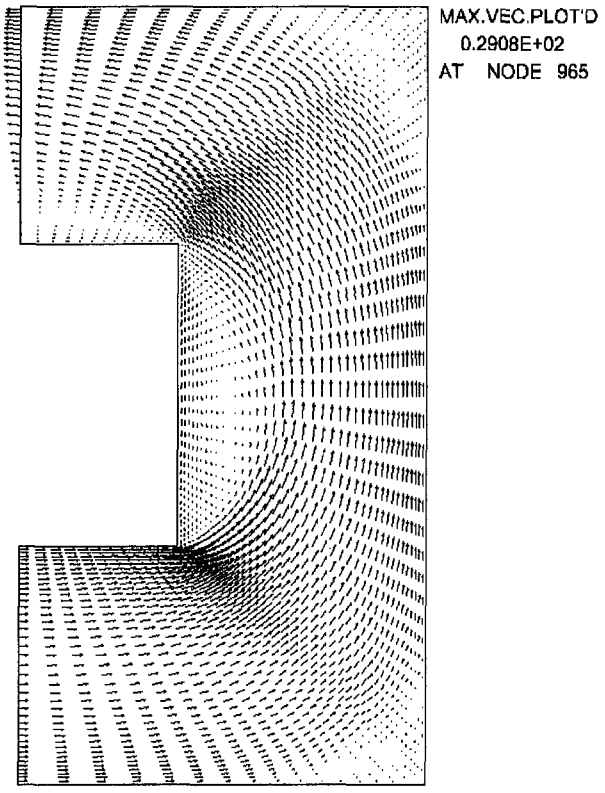

Fig. 2 Square bend: velocity vector plot

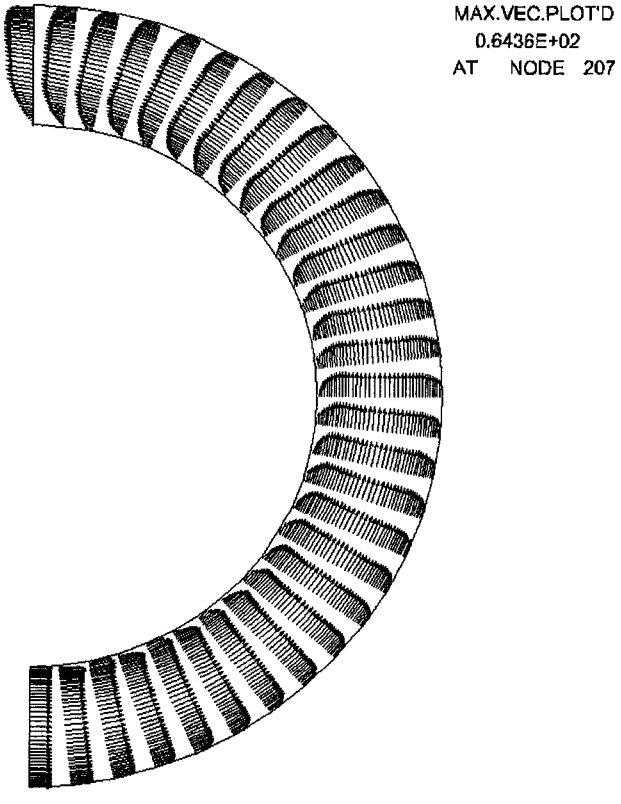

Fig. 3 180 deg bend: velocity vector plot

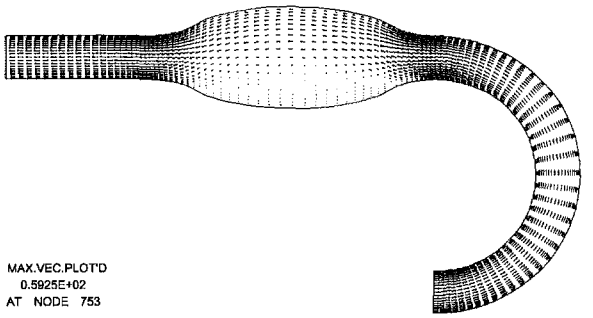

Fig. 4 Diffuser/contraction section, no screens: velocity vectors

$$\kappa = aU_\infty^2 \tag{10}$$

$$\epsilon = \rho c_\mu \frac{k^2}{R_\mu \mu} \tag{11}$$

where: $a = 0.001$ and $R_\mu = 10$ (FDI Inc., 1990). These values result in $k = 2.5$ and $\epsilon = 5.6$.

For all of the simulations reported a linear Stokes solution was used to set initial conditions for the velocity field. In the turbulent case, the initial conditions for kinetic energy and dissipation rate were set at 2.5 and 5.6, respectively, at all nodes.

4.2 Mesh Independence. For the early simulations, tests were performed to determine optimum mesh density. Up to four mesh gradings were tested to establish mesh independence for the sections simulated. For the more complex cases, incorporating guiding vanes or porous media mesh grading was determined from experience and with reference to previous work (Giliver et al., 1991). This approach resulted in 3104 elements for the square bend, 1200 elements for the 180 deg circular bend, 2240 elements for the diffuser/contraction/bend without diffuser screen or guiding vanes, and 8470 elements with diffuser screen and 10 guiding vanes, and 28800 brick elements for the 3D contraction/diffuser/45 deg bend simulations.

In all cases the mesh grading was finest at the boundaries. This permitted the higher velocity gradients, caused by boundary shear stress, to be modeled accurately. In the turbulent simulations a wall function boundary condition was applied to all surfaces. These near wall elements approximated the velocity variation in the viscous sublayer, reducing the need for extensive mesh refinement in this area. However, in order to obtain viable solutions it was necessary to position the near wall elements in the turbulent log-layer. Since the extent of the log-layer is not known apriori an iterative process was required to position these elements correctly. The near wall elements in this study were set between 3 and 5 mm from the solid boundaries.

5 Numerical Results

With reference to the vortex shedding experiment, 2-D laminar approximations were used for low values of the cylinder

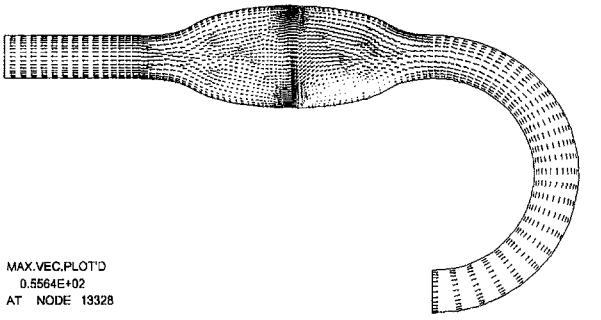

Fig. 5 Diffuser/contraction section, one screen: velocity vectors

Reynolds number (Re = 2×10^2), followed by turbulence models for Re = 10^4. For the simpler models a range of Reynolds numbers was investigated. The upper Reynolds number of 10,000 ensured that fully turbulent flow existed justifying the use of the time-averaged, steady flow approximation. Due to the problems associated with transitional flow behavior, no attempt was made to simulate this transition phase. However, it was felt that modeling the upper and lower Reynolds number ranges would provide sufficient information on how the tunnel would perform in real life. A final simulation was carried out of the diffuser/contraction section using a full 3-D turbulent model. These simulations were used for comparison purposes to validate the use of the 2-D model.

5.1 Square and 180 Deg Bend. In order to obtain a good understanding of how conventional tunnel components perform, simulations were first carried out of selected sections. Since these crude 2-D simulations were to serve simply as an aid for preliminary tunnel design, corner vanes and flow straighteners were omitted to cut computational time. The velocity vector plot from the turbulent model (Fig. 2) shows a progressive and smooth 180 deg change in flow direction. However, recirculation at the exit, corners, and vertical section suggested a new shape following the streamlines would reduce the overall volume of the bend. The outcome was a 180 deg curved bend (Fig. 3).

The velocity vector plot (Fig. 3) also revealed higher flow velocity at the exit than that obtained for the square bend, which in the conventional design embodies a settling chamber. The difference in flow velocity at the exit would have been even more pronounced had diffuser screens, corner vanes, and flow straighteners been included in simulation, since they would have countered the off-center shift in momentum. This suggested that a robust diffusion mechanism for the 180 deg circular bend was required to control the nonsymmetrical flow profile at the exit, and consequently reduce the flow velocity entering the diffuser section.

5.2 Diffuser/Contraction Section. As intimated earlier the contraction nozzle profile was based on two elliptical curves (Downie et al., 1984). However, there is little published on the subject of wind tunnel diffusers. Such diffusers are thought to have little influence on the flow within the test section because of the presence of a settling chamber upstream. Therefore, omission of the settling chamber to reduce the tunnel size places greater emphasis on the function of the diffuser section.

In our preliminary design the diffuser shape simply mirrored that of the contraction, and a 1 m length settling chamber was used to join the two. However, subsequent simulations with a diffuser screen in place of the settling chamber suggest that the latter could be easily discarded without detriment to flow quality. Progressive improvements of the cascaded diffuser/contraction sections were achieved by incrementally updating the geometry of the diffuser to match the streamlines of the flow, while ensuring satisfactory diffusion. A series of diffuser geometries and configurations was thus investigated.

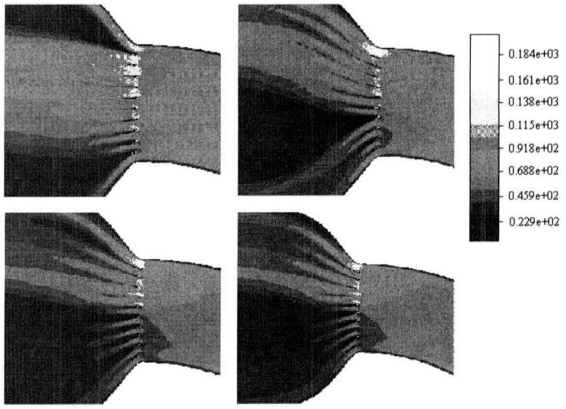

Fig. 7 Speed contour plots of various guiding vane settings

The first simulations using the cascaded diffuser/contraction (Fig. 4) showed the effect of nonuniform flow from the 180 deg circular bend on the flow in the test section for Re = 10,000. Clearly, as the flow velocity increases the lack of symmetry becomes more pronounced. From Re = 500 upwards the inflow jet from the bend is forced along the upper wall of the diffusing/contraction section. A large recirculation zone in the lower part of the section prevents the inflow from diffusing further. To rectify this problem the model was first extended to include a diffuser screen placed midway between the contraction and diffuser.

The velocity vector plot (Fig. 5) for Re = 10,000 confirmed that the diffuser screen would improve the velocity profile within the test section. The diffuser screen could be made more effective by reducing permeability, but at the expense of increasing the pressure drop (Lai et al., 1992). A larger pressure drop would require higher pump power output, and therefore screen permeability was not altered. As an alternative guiding vanes were utilized.

The next simulations established the optimum area ratio, diffuser profile, and most efficient means of diffusing the flow. The 180 deg bend was excluded from these simulations to reduce computational effort. Guiding vanes were used as a means of diffusing the flow over a short distance. These have the advantage over diffuser screens as they can achieve a relatively high diffusion without a significant increase in static pressure.

One of the first diffuser models incorporated four curved aerofoil blades set at angles of between 0 and 20 deg, with a screen included in the region between the diffuser and the contraction. Simulation of the four aerofoil blades, combined with a porous screen, required a finely graded mesh. Since this was computationally demanding, the Reynolds number was kept

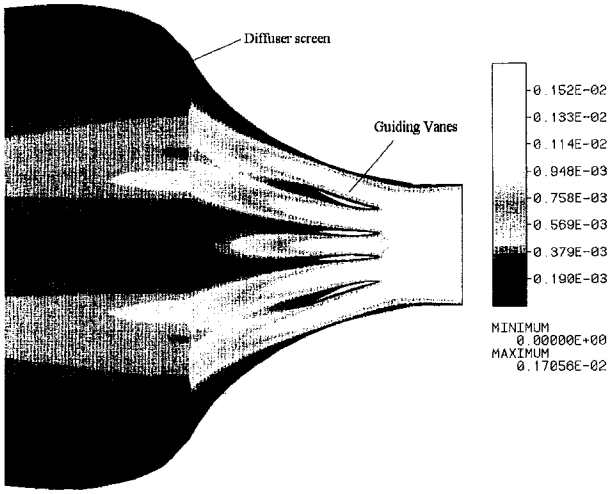

Fig. 6 Diffuser with guiding vanes and screen: speed contour plot

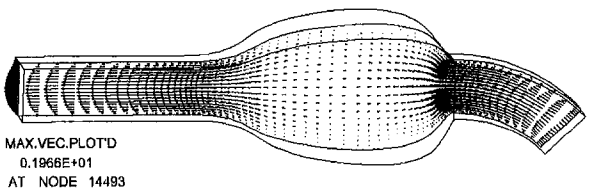

Fig. 8 3D velocity vector plot of final tunnel design

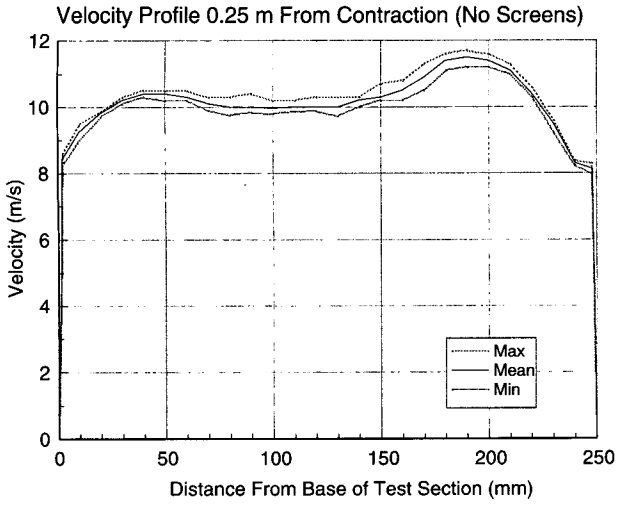

Fig. 9 Velocity profile, no screens

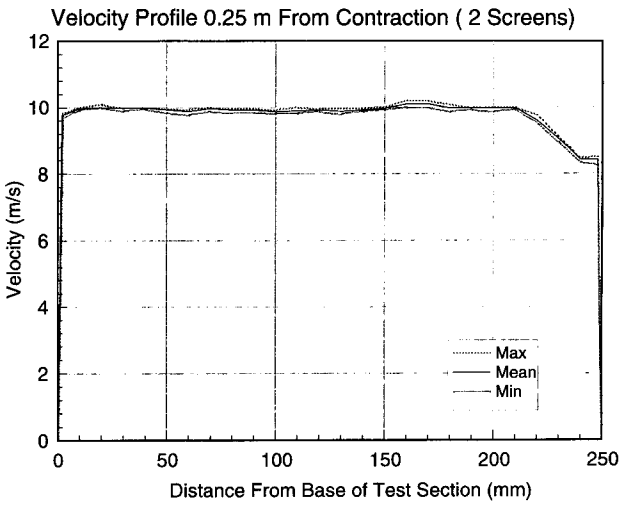

Fig. 11 Final tunnel velocity profile

low (Re $\leq$ 200). Even at this low Reynolds number the results showed the effectiveness of using guiding vanes as a means of diffusion (Fig. 6). However, guiding vanes of this size and shape were not readily available, and a standard two-way ventilation diffuser, comprising of 10 blades in either direction, was employed in later simulations.

Simulations were performed to determine the guiding vane setting for optimum diffusion over a short length. These confirmed the effectiveness of guiding vanes and highlighted the sensitivity of diffusion quality to the angle of the guiding vanes (Fig. 7), where a small change in angle of 3–4 deg had a dramatic effect on diffusion. This meant it was not possible to determine the exact settings of the guiding vanes numerically.

For completeness, a 3-D simulation of the diffuser, contraction, test section, and a quarter arc upstream bend was carried out. The Reynolds number was kept to a small value for reasons of economy. The velocity vectors obtained for Re = 200 (Fig. 8) compared favorably with earlier results and confirmed the validity of using the 2-D approximation.

A final 2-D simulation of the diffuser, contraction, test section, and a quarter arc upstream bend, was carried out. In this simulation, the diffuser screen, consisting of 2 mm diameter holes with 4 mm centers, and the 100 mm deep honeycomb flow straightener, consisting of 10 mm hexagons, were also included. The results are presented in the next section, in the form of an overall speed contour plot (Fig. 12) and a velocity profile at the outlet to the test section (Fig. 13). Although the simulation was for a higher velocity flow, good qualitative agreement with the experimental data was established.

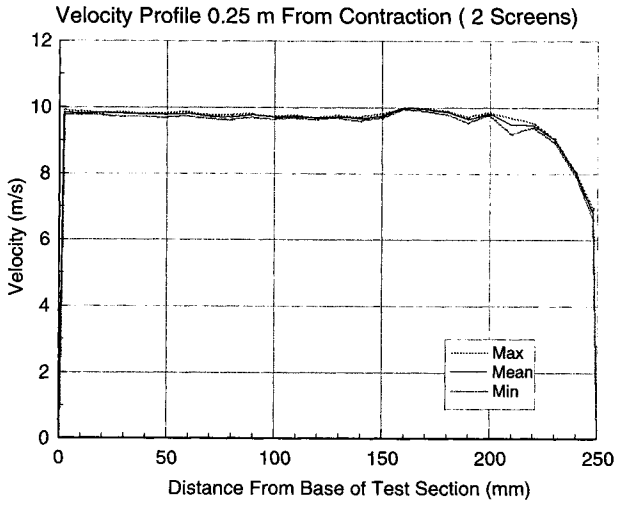

Fig. 10 Velocity profile, 2 screens

6 Experimental Validation and Testing

The tunnel was initially assembled to use air as working fluid, to facilitate adjustment of the guiding vanes. In order to obtain the optimum flow within the test section the guiding vanes were adjusted to yield a uniform flow profile at maximum flow velocity. Flow velocities were measured using a Dantec hot wire anemometer 200 mm distance from either end of the test section at intervals of 10 mm on the vertical symmetry plane. Screens were then inserted and flow profiles again measured. The qualitative observed effects of this were found to be in good overall agreement with the predictions obtained from our CFD simulation (Fig. 13).

The test section entrance flow profile, for an initial estimated guiding vane setting and no diffuser screens, is shown in Fig. 9. In this state, the average flow velocity was $\approx$10 m/s, the maximum variation in flow velocity, neglecting the boundary layer, was 1.53 m/s and the average velocity fluctuation 0.39 m/s.

With two screens present (Fig. 10), for the same diffuser setting, a more uniform flow profile was observed, demonstrating the effectiveness of the screens. In this case, the average flow velocity was $\approx$10 m/s, the maximum variation in flow velocity, ignoring boundary layer effects, was reduced to 0.26 m/s and the mean velocity fluctuations to 0.13 m/s.

The velocity profile for the final adjustment of guiding vane settings, with the honeycomb and two diffuser screens fitted,

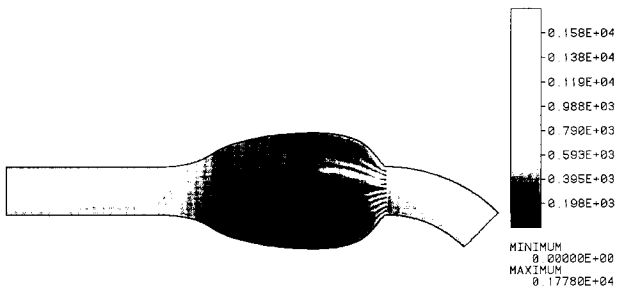

Fig. 12 Speed contour plot for final design

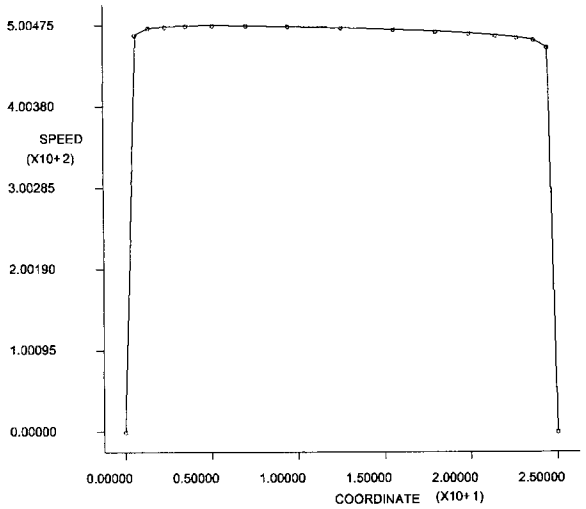

Fig. 13 Simulated test section velocity profile, with 2 screens

gave the maximum velocity variation of 2.3 percent and a mean fluctuation of 1.4 percent, of the mean velocity (Fig. 11).

Due to the imprecise nature of the guiding vanes and screens no attempt was made to match the magnitude of the computed velocity to that observed experimentally. However, the form of the simulated velocity profile (Fig. 13) compared favourably with that obtained experimentally (Fig. 11). The drop-off in flow velocity toward the top of the test section in the experimental profile was due to the presence of a small "lip" at the interface between the test section and contraction nozzle. This was due to fabrication error, and was easily corrected subsequently.

7 Discussion

The work presented demonstrates the feasibility of using CFD to examine ways of improving the design of a number of conventional tunnel components.

In the present case the modifications applied included a smooth 180 deg bends in place of the conventional 90 deg square bends and corner vanes, cascaded diffuser/contraction stages with no intermediate settling chamber, a single unit containing the screens and honeycomb placed between the diffuser and contraction, and guiding vanes at the diffuser inlet.

Based on the results of the investigation, the tunnel was constructed and commissioned in November, 1994. The main body of the tunnel was fabricated from 9 mm thick sheets of polypropylene, formed and welded to produce the appropriate sections. The exception to this was the tunnel contraction, which was built using 3 mm thick sheets of polypropylene reinforced with glass reinforced plastic.

The modular design permits sections to be replaced or updated as necessary, for example, allowing the water pump to be replaced by a fan when working with air. The components were bolted together via 12 mm thick polypropylene flanges reinforced with 12 mm thick polypropylene webs and sealed using 3 mm neoprene gaskets.

The entire assembly was mounted on a modular mild steel box section subframe, facilitating full access for the removal of any tunnel section. The test section itself, consisting of four 10 mm thick toughened float plate glass panels, was supported in a mild steel angle-iron frame and sealed with a silicon based sealant. Access to the test section was achieved by removing specially mounted side glass panels. Working drawings, showing the individual tunnel components, are included in Appendix A of the electronic version of the paper.

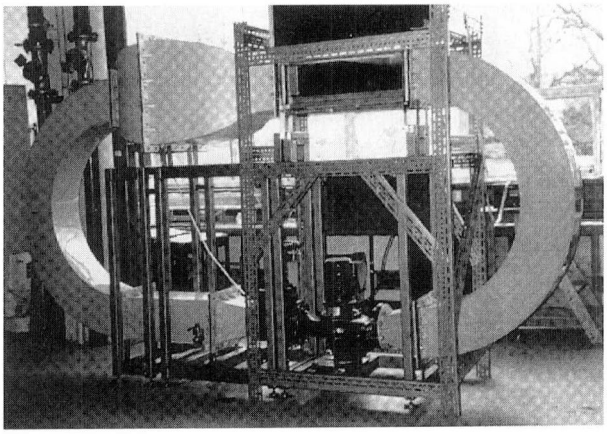

Plate 1 Photograph of the completed tunnel

The assembled tunnel was 4 m long, 2 m high and 1 m wide (Plate 1). It cost just over £4,000 Stirling to build (at 1994 prices), and offered a significant reduction in size and cost from the conventional design proposed by Mehta and Bradshaw (1979).

8 Conclusion

An important design criteria for the proposed wind/water tunnel design was to achieve the desired high level of performance within the limited budget available. The results confirm the validity of using an elliptical contraction profile, and assist in the design of the in-line diffuser. The effect of the screens was also simulated and the need for guidevanes, at higher Reynolds numbers, was established as being most effective over a short diffuser length.

The CFD simulation results presented show how a number of conventional tunnel components can be successfully modified, and that the modifications which we have proposed work well. These modifications include (*a*) smooth 180 deg bends in place of sharp 90 deg square bends with corner vanes, resulting in a smoother flow profile at the diffuser inlet; (*b*) cascaded diffuser/contraction with no intermediate settling chamber; (*c*) a single unit containing the screens and honeycomb placed between the diffuser and contraction, to provide easier access; and (*d*) the introduction of guiding vanes at the diffuser/contraction inlet, to diffuse the flow more effectively over a wide range of Reynolds numbers.

Our main objective was to develop a flexible tunnel design suitable for reproducing vortex shedding from a circular cylinder, and thereafter for use as a general purpose experimental facility. In this respect, the effort has been a success, and therefore worthwhile. For those involved in instability issues associated with bluff-body wakes and related phenomena, additional tests (and fine tuning) may need to be carried out to determine the spectral intensity and RMS value of the inflow turbulence intensity.

Several authors have in the past rightly warned against using CFD without the backup of experimental work. The simulations presented in this paper are largely based on the use of simplified 2-D models, but nevertheless effectively highlight the potential problem areas and provide valuable insight into how different components of the tunnel could affect the flow.

Acknowledgements

This work has been jointly funded by the Marine Technology Directorate (MTD) and Shell Expro U.K. (grant no. 190 201 BS99). The authors are indebted to The University of Aberdeen Computing Centre for their support in performing the simula-

tions, and also to Ms. E. Williams for proofreading the manuscript.

References

Albayrak, K., 1991. "Design Of Low-Speed Axisymmetric Wind Tunnel Contraction," *Journal of Wind Engineering and Industrial Aerodynamics,* Vol. 37, pp. 79–86.

Arakeri, V. H., Sharma, S. D., Mani, K., and Govinda Ram, H. S., 1988, "The High Speed Water Tunnel Facility At The Indian Institute Of Science," *Sädhanä,* Vol. 13(4), pp. 223–235.

Bear, J., 1988, *Dynamics Of Fluids In Porous Media,* Dover Publications.

Braun, M. J., Canacci, V. A., and Russell, L. M., 1992, "Full Field Flow Visualisation and Computer-Aided Velocity Measurements in a Bank of Cylinders in a Wind Tunnel," *Experiments in Fluids,* Vol. 13, pp. 117–127.

Downie, J., Jordinson, H. R., and Barnes, F. H., 1984, "On the Design of Three-Dimensional Wind Tunnel Contractions," *Aeronautical Journal,* Aug./Sept., pp. 287–295.

Durnet, C., 1994, *Conception Du Canal Hydraulique Polarographique,* Report from ENSIMEV, Universite Valenciennes et du Hainaut, Cambresis.

Eaton, B. E., 1987. "Analysis of Laminar Vortex Shedding Behind a Circular Cylinder by Computer-Aided Flow Visualisation," *Journal of Fluid Mechanics,* Vol. 180, pp. 117–145.

Engelman, M. S. and Jamnia, M., 1990, "Transient Flow Past a Cylinder: A Benchmark Solution," *International Journal for Numerical Methods in Fluids,* Vol. 11, pp. 985–1000.

FDI Inc, 1990, *Fidap Theoretical Manual,* Fluid Dynamics International Inc. Evanston, IL, Update 5.0.

Gibbings, J. C., 1993, "Incompressible Flow In Contracting Ducts," *Aeronautical Journal.* Aug./Sept., pp. 230–246.

Giliver, R. C., Gartling, D. K., Engelman, M. S., and Haroutunian, V., 1991, "Navier-Stokes Simulations Of Flow Past Three-Dimensional Submarine Models," *Computer Methods in Applied Mechanics and Engineering,* Vol. 87, pp. 175–200.

Hughes, W. F., 1979, *An Introduction To Viscous Flows,* Carnegie-Mellon University.

Ito, H. R., Koayashi, R., and Kohama, Y., 1992, "The Low-Turbulence Wind Tunnel at Tohoku University," *Aeronautical Journal,* Apr., pp. 141–151.

Kerres, W., and Grönig, H., 1990, "Instationäre Umströmung Von Profilen In Einem Flüssigigkeits-Ludwieg-Kanal," *Z. Flugwiss. Weltraumforsch.* Vol. 14, pp. 290–300.

Lai, M. C., Lee, T., Kim, J. Y., Cheng, C. Y., and Chui, G., 1992, "Numerical and Experimental Characterisations of Automotive Catalytic Converter Internal Flows," *Journal of Fluids and Structures,* Vol. 6(4), pp. 451–470.

Lam, K., and Pomfret, M. J., 1984, "Design and Performance of a Low Speed Wind Tunnel," *International Journal of Mechanical Engineering Education,* Vol. 13(3), pp. 161–172.

Lagarde de, B., 1984, "A Water Tunnel for Aerodynamical Studies," *Journal of Wind Engineering and Industrial Aerodynamics,* Vol. 16, pp. 301–314.

Massey, B. S., 1989, *Mechanics of Fluids,* T. J. Press Ltd, 6th Ed.

Mehta, R. D., and Bradshaw, P., 1979, "Technical Notes—Design Rules for Small Low Speed Wind Tunnels," *Aeronautical Journal,* Nov., pp. 443–449.

Morel, T., 1975, "Comprehensive Design of Axisymmetric Wind Tunnel Contractions," ASME JOURNAL OF FLUIDS ENGINEERING, Vol. 97, pp. 225–233.

Smith, B. E., Zell, P. T. and Shinoda, P. M., 1990, "Comparison of Model- and Full-Scale Wind Tunnel Performance," *Journal of Aircraft,* Vol. 27(3), pp. 232–238.

Su, Y., 1991, "Flow Analysis and Design of Three-Dimensional Wind Tunnel Contractions," *AIAA Journal,* Vol. 29(11), pp. 1912–1920.

Unal, M. F. and Rockwell, D., 1988, "On Vortex Formation from a Cylinder, Part 1, The Initial Instability," *Journal of Fluid Mechanics,* Vol. 190, pp. 491–512.

Simulation of the Piston Driven Flow Inside a Cylinder With an Eccentric Port

Adrin Gharakhani
Research Scientist.

Ahmed F. Ghoniem
Professor.

Department of Mechanical Engineering,
Massachusetts Institute of Technology,
Cambridge, MA 02139

A grid-free Lagrangian approach is applied to simulate the high Reynolds number unsteady flow inside a three-dimensional domain with moving boundaries. For this purpose, the Navier-Stokes equations are expressed in terms of the vorticity transport formulation. The convection and stretch of vorticity are obtained using the Lagrangian vortex method, while diffusion is approximated by the random walk method. The boundary-element method is used to solve a potential flow problem formulated to impose the normal flux condition on the boundary of the domain. The no-slip condition is satisfied by a vortex tile generation mechanism at the solid boundary, which takes into account the time-varying boundary surfaces due to, e.g., a moving piston. The approach is entirely grid-free within the fluid domain, requiring only meshing of the surface boundary, and virtually free of numerical diffusion. The method is applied to study the evolution of the complex vortical structure forming inside the time-varying semi-confined geometry of a cylinder equipped with an eccentric inlet port and a harmonically driven piston. Results show that vortical structures resembling those observed experimentally in similar configurations dominate this unsteady flow. The roll-up of the incoming jet is responsible for the formation of eddies whose axes are nearly parallel to the cylinder axis. These eddies retain their coherence for most of the stroke length. Instabilities resembling conventional vortex ring azimuthal modes are found to be responsible for the breakup of these toroidal eddies near the end of the piston motion. The nondiffusive nature of the numerical approach allows the prediction of these essentially inviscid phenomena without resorting to a turbulence model or the need for extremely fine, adaptive volumetric meshes.

Introduction

Over the past decade, the literature of internal combustion engines has seen a steady growth in the application of computational fluid dynamics to predict their characteristic flows over the entire engine cycle. The range of applications has varied from the idealized two-dimensional/axisymmetric flow in port-cylinder configurations (Cloutman et al., 1981; Gosman et al., 1978, 1980; Martins and Ghoniem, 1991; Morse et al., 1980) with and without a poppet valve, to the more realistic three-dimensional flow in the intake port and the engine cylinder, including moving valves (Errera, 1987; Khalighi, 1995; Naitoh et al., 1990; Taghavi and Dupont, 1988). Most solution methods have been based on the structured control-volume derivation with a body-fitted coordinate system, although finite element methods have also been utilized. These are Eulerian, grid-based methods which require careful volumetric meshing of the complex domain inside the engine, and incorporate turbulence closure models into the ensemble averaged equations. Although the solutions obtained have been very useful, there is still a need for more advanced approaches which can overcome some of the difficulties encountered in these methods.

The accurate, efficient, and automatic meshing of the complicated unsteady three-dimensional domain of an engine is a serious concern in grid-based methods. The mesh generation algorithm must consider a wide spectrum of length scales, ranging from the valve lift to the cylinder diameter and stroke length, and the complexity of the concomitant intersecting volumes. It should also be capable of capturing the sharp velocity gradients across thin jets, the multiple recirculation zones that evolve in time, and the large-scale turbulent structures that form due to separating, swirling, and tumbling flows. A direct consequence of the inappropriate meshing of the domain is the introduction of false diffusion—a numerically induced dissipation term—into the discrete equations, which leads to the formation of weaker eddies and the faster decay of vortical structures. To reduce numerical diffusion, one can increase the mesh resolution and use mesh adaptation, which are costly, or streamline the grid along the local flow direction. This, however, may lead to degenerate meshes and severe numerical problems.

The application of heuristic closure models to predict the turbulent flow in engines is another cause for concern in nonreacting, and especially in reacting flows. In most of these models, turbulence in the averaged equations is assumed to be nearly homogeneous, and the empirical constants utilized in the closure terms may discount the possible coexistence of multiple flow regimes within the engine and ignore the effects of confinement, the severe curvature of the streamlines, and the global and local unsteadiness caused by boundary conditions and flow instabilities, respectively—all of which limit the accuracy of the predictions. In addition, since traditional computational methods maintain a degree of false diffusion, it is often difficult to assess the accuracy of the turbulence models with certainty. Perhaps the most critical disadvantage of turbulence modeling is that information about the field is presupposed and supplied to the equations, rather than retrieved from them.

Experimental and numerical studies of engine-like flows, prominently characterized by a port, a cylinder and a driven piston, indicate that the most interesting feature of these time evolving fields is the formation, growth and eventual breakup of vortex structures. The sudden expansion of the intake port into the cylinder, the orientation of the intake jet with respect to the cylinder axis, the impact of the jet onto the moving piston face, and the presence of corners between the cylinder head,

Contributed by the Fluids Engineering Division for publication in the JOURNAL OF FLUIDS ENGINEERING. Manuscript received by the Fluids Engineering Division February 3, 1997; revised manuscript received November 11, 1997. Associate Technical Editor: M. N. Dhaubhadel.

the piston face, and the cylinder wall, all lead to the roll-up of the strongly sheared fluid to form "coherent eddies" of different forms and sizes. The dynamics of these eddies, including their formation, mutual interactions and eventual breakup—as determined by the operating conditions—are expected to govern the turbulent state of the engine flow.

The Lagrangian vortex method offers an attractive alternative to the finite-volume approaches for simulating flows which are expected to be dominated by unsteady, large-scale vortical structures. The method is grid free. It is self-adaptive and is capable of dynamically concentrating the computational elements in regions with significant velocity gradients, such as in shear layers, jets, and recirculation zones. Furthermore, due to the Lagrangian nature of the method, numerical diffusion is minimized, making the scheme an excellent tool for analyzing flows at high Reynolds numbers.

To take advantage of the properties of vortex methods in examining engine-like flows, we recently developed a three-dimensional random vortex-boundary element method for the simulation of the unsteady flow in geometries with moving boundaries. At present, the boundary surface is idealized by a union of planar rectangular elements, analogous to a staircase discretization in two dimensions. The extension to the more general quadrilateral elements will be presented in future publications. The vortex-boundary element method has been used successfully to simulate the unsteady wake behind a cube due to an impulsively started flow (Gharakhani and Ghoniem, 1996a). A massively parallel code has also been developed to accelerate the solution (Gharakhani and Ghoniem, 1996b). The details of the formulation and implementation of the method, and a parametric test of its accuracy were given by Gharakhani and Ghoniem (1997b).

In this paper, we present a simulation of the flow inside a cylinder connected to an eccentric port, driven by the harmonic motion of a piston. The objectives of this study are (1) to demonstrate the feasibility and potential advantages of applying our method to the prediction of engine flows, (2) to verify that the code produces a qualitatively reasonable portrait of the flow, and (3) to examine the creation and growth of large unsteady vortex structures in the field.

Formulation

The equations of motion of an incompressible flow within a three-dimensional domain, D, and with boundary surfaces, ∂D, are expressed by the vorticity transport form of the Navier-Stokes equations:

$$\frac{\partial \boldsymbol{\omega}}{\partial t} + \mathbf{u}.\nabla\boldsymbol{\omega} = \boldsymbol{\omega}.\nabla\mathbf{u} + \frac{1}{\mathrm{Re}}\nabla^2\boldsymbol{\omega} \quad \mathbf{x} \in D \tag{1a}$$

$$\nabla.\mathbf{u} = 0 \quad \mathbf{x} \in D \tag{1b}$$

$$\boldsymbol{\omega}(\mathbf{x}, t) = \nabla\wedge\mathbf{u} \quad \mathbf{x} \in D \tag{1c}$$

$$\mathbf{u}(\mathbf{x}, t) = (\mathbf{u}.\boldsymbol{\tau}, \mathbf{u}.\boldsymbol{\rho}, \mathbf{u}.\mathbf{n}) \quad \mathbf{x} \in \partial D \tag{1d}$$

$$\mathbf{u}(\mathbf{x}, t = 0) = \mathbf{u}_o \quad \mathbf{x} \in D \tag{1e}$$

where $\mathbf{x} = (x, y, z)$ is the position in the Cartesian coordinates normalized by a reference length, L; $\mathbf{u}(\mathbf{x}, t) = (u, v, w)$ is the velocity normalized by a characteristic speed, U; t is the time normalized by L/U; $\mathrm{Re} = UL/\nu$ is the Reynolds number and ν is the kinematic viscosity. $\boldsymbol{\omega}(\mathbf{x}, t) = (\omega_x, \omega_y, \omega_z)$ is the vorticity vector and $\wedge$ denotes the cross-product. At the boundary surfaces, velocity is expressed in terms of the local orthogonal coordinate system, $\boldsymbol{\tau}$-$\boldsymbol{\rho}$-$\mathbf{n}$, where $\mathbf{n} = (n_x, n_y, n_z)$ is the unit outward normal, and $\boldsymbol{\tau} = (\tau_x, \tau_y, \tau_z)$ and $\boldsymbol{\rho} = (\rho_x, \rho_y, \rho_z)$ are the unit tangents to the boundary.

We begin the solution by discretizing the vorticity using a collection of N_V vortex elements, each centered at $\mathbf{x}_j$, with volume ΔV_j and vorticity vector $\boldsymbol{\omega}_j$:

$$\boldsymbol{\omega}(\mathbf{x}, t) = \sum_{j=1}^{N_V} \tilde{\boldsymbol{\Gamma}}_j(t) g_\sigma(\mathbf{x} - \mathbf{x}_j) \tag{2}$$

where $\tilde{\boldsymbol{\Gamma}}_j(t) = \boldsymbol{\omega}_j(t)\Delta V_j$ is the volumetric vorticity, and $g_\sigma(\mathbf{x}) = g(|\mathbf{x}|/\sigma)/\sigma^3$ is a spherical core function with radius σ. We use the second order core function $g(\mathbf{x}) = (3/4\pi)[1 - \tanh^2(|\mathbf{x}|^3)]$, selected from a list of functions given by Beale and Majda (1985). The velocity is decomposed into potential and vortical components, governed by the kinematic relationships (1b) and (1c), respectively. The vortical component is evaluated using the Biot-Savart law, expressing the velocity as the sum of the velocity induced by all vortex elements. The potential component is obtained from the solution of a three-dimensional Neumann problem, used to impose the normal flux boundary condition. The boundary-element method is implemented to solve the Neumann problem, as well as to evaluate the potential velocity and its gradients at the vortex elements, without having to discretize the domain interior (Gharakhani and Ghoniem, 1997a). In this paper, the boundary potential and its normal flux are assumed to vary linearly across planar rectangular boundary elements (Gharakhani and Ghoniem, 1996c).

Within a thin layer, D_b, adjacent to the walls, away from sharp corners, the velocity gradient normal to the boundary is expected to dominate the gradients in the parallel direction. This leads to a local wall-boundary-layer approximation of Eqs. (1) (Chorin, 1980; Fishelov, 1990; Gharakhani and Ghoniem, 1997b):

$$\frac{\partial \boldsymbol{\omega}}{\partial t} + \mathbf{u}.\nabla\boldsymbol{\omega} = \frac{1}{\mathrm{Re}}\frac{\partial^2\boldsymbol{\omega}}{\partial z^2} \quad \mathbf{x} \in D_b \tag{3a}$$

$$\nabla.\mathbf{u} = 0 \quad \mathbf{x} \in D_b \tag{3b}$$

$$\boldsymbol{\omega}(\mathbf{x}, t) \cong (-\partial v/\partial z, \partial u/\partial z, 0) \quad \mathbf{x} \in D_b \tag{3c}$$

$$\mathbf{u}(\mathbf{x}, t = 0) = \mathbf{u}_o \quad \mathbf{x} \in D_b \tag{3d}$$

$$\mathbf{u}(x, y, z = 0, t) = (0, 0, 0),$$

$$\mathbf{u}(x, y, z = b, t) = (U_\infty, V_\infty, 0) \tag{3e}$$

where all variables are defined with respect to the local coordinate system, z is selected normal to the wall and into the domain interior, and $z = 0$ represents the wall surface. $(U_\infty, V_\infty, 0)$ is the velocity at the edge of the numerical boundary layer whose thickness is $b = \mathrm{BLTC}\sqrt{2\Delta t/\mathrm{Re}}$: Δt is the timestep, and $1.0 \leq \mathrm{BLTC} \leq 3.0$ (Fishelov, 1990; Puckett, 1989). The vorticity field within the thin layer is discretized using a set of infinitesimally thin rectangular vortex tiles; each centered at $\mathbf{x}_i$, with sides $h^t_{x_i}$ and $h^t_{y_i}$, and with surface vorticity $\tilde{\boldsymbol{\gamma}}(\mathbf{x}_i, t)$. The tangential components of the velocity at the tiles are evaluated by integrating Eq. (3c) directly, while the normal component is obtained using Eq. (3b).

During a typical timestep, the computations proceed as follows: The velocity and its gradients are evaluated by summing over the contributions of all the vortex and boundary elements. The convection of vorticity is performed by displacing the vortex elements along their Lagrangian trajectory. Diffusion is simulated by the random walk method. The elemental vorticity vectors are updated to account for stretch. An element leaving the domain or jumping into D_b is eliminated. The Lagrangian convection of the vortex tiles takes place concurrently with that of the vortex elements. The motion of the vortex elements and tiles induces a tangential velocity jump at the walls. This jump corresponds to the amount of vorticity that must be generated to satisfy the no-slip condition. Therefore, new vortex tiles are created on the solid walls with surface vorticity $\bar{\boldsymbol{\gamma}}(x, y, 0, t)$ equal to the velocity jump. Next, all tiles—old and new—are allowed to take a random walk in the direction normal to the wall. Tiles that jump below the wall are reflected back into the field (Puckett, 1989). Tiles jumping into the flow interior are

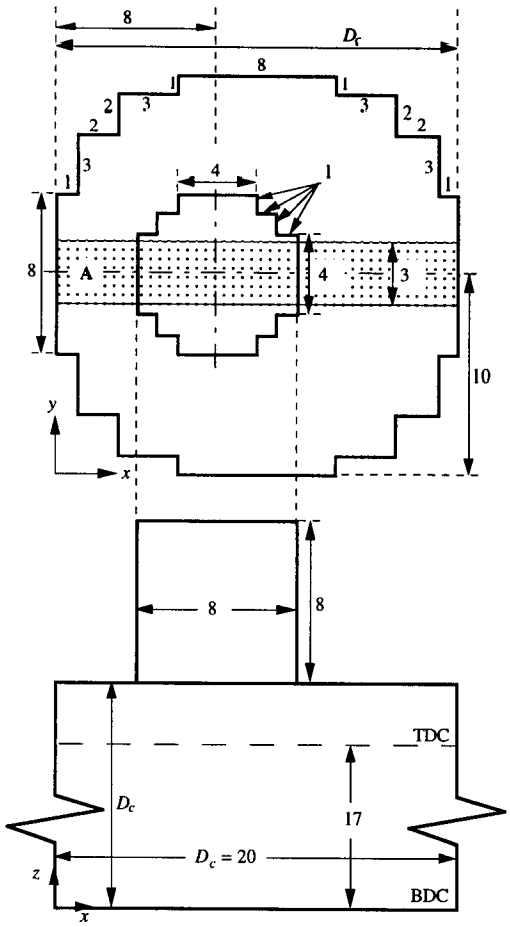

Fig. 1 Schematic diagram of the port-cylinder configuration. Integers refer to units of length 0.05.

converted into vortex elements with volumetric vorticity $\tilde{\Gamma}(\mathbf{x}, t) = \tilde{\gamma}(\mathbf{x}, t)h_x^t h_y^t$ and core radius $\sigma = \max(h_x^t, h_y^t)$. Note that, to maintain a fine discretization of the flow in the direction normal to the wall, a newly created tile may be split into $N_S = (|\bar{\gamma}(x, y, 0, t)|/\gamma_{\max} + 0.5)$ tiles with surface vorticity $\tilde{\gamma}(x, y, 0, t) = \bar{\gamma}(x, y, 0, t)/N_S$ (Ghoniem and Gagnon, 1987; Fishelov, 1990; Puckett, 1989). $\gamma_{\max}$ is a user-specified maximum surface vorticity. Finally, the boundary element solution of the Neumann problem is performed to obtain the new values of the boundary sources. See Gharakhani and Ghoniem (1997b) for the details of the vortex-boundary element method, as well as a parametric investigation of its accuracy using simple flows with known analytical, numerical or experimental data.

Results

Results from the simulation of the intake process inside an idealized engine cylinder with an off-centered port and a moving piston are presented next. The circular cross-sections of the port and the cylinder were represented by a staircase discretization, as depicted by the schematic diagram in Fig. 1.

The flow was generated by the harmonic displacement of the piston starting from rest at the top dead center (TDC) and ending at rest at the bottom dead center (BDC) positions. The uniform flow at the inlet was imposed by simply assigning the no-flux boundary condition to the remaining boundary surfaces and satisfying the continuity requirement. The no-slip boundary condition was applied to all solid boundaries. All dimensions were normalized by the cylinder diameter, D_c, and their values assigned, as shown in Fig. 1. The velocity was normalized by the maximum piston speed, V_m, at 90 deg crank angle after TDC (ATC). The Reynolds number based on D_c and V_m was set at 350. The induction process was discretized using 200 equal timesteps corresponding to a 0.9 deg crank angle. Other parameters of importance were set as follows: $\gamma_{\max} = 0.5$ and BLTC = 1.5.

A time-varying number of boundary elements was used to discretize the cylinder wall, whose length changes due to the piston motion. The criterion was to assign a maximum number of boundary elements, $N_{\max}$, to discretize the maximum cylinder length, $L_{\max}$, at BDC. The instantaneous number of elements, N, was obtained using the relation $N = \max(1, N_{\max}L_c/L_{\max} + 0.5)$, where L_c is the instantaneous length of the cylinder. The same procedure was repeated for the vortex tiles. In addition to saving computational time, this approach maintains a nominal elemental mesh size in the order of $L_{\max}/N_{\max}$. In contrast, selecting a fixed value for N would yield extremely thin elements at the beginning of the computation and would generate inaccurate solutions. The boundary element and tile sizes were set at 0.05 and 0.1, respectively, for all stationary surfaces. These values were also assigned as the maximum mesh size for the cylinder walls. The number of boundary elements used to discretize the domain ranged from 1176 at TDC to 2536 at BDC. The wall discretization for vorticity generation required 356 and 740 tiles, respectively. The number of vortex elements in the interior reached 9444 at the end of the simulation. Our previous studies of channel flows and the separating flow around a cube indicate that at this Reynolds number, the numerical resolution is sufficient to capture the flow structure accurately.

Figure 2 depicts the side view of the position and velocity of the vortex elements within a volumetric slice of 0.15 thickness, positioned symmetrically with respect to the plane of symmetry of the engine—region A in Fig. 1. The velocity vectors are represented by fixed-length sticks whose origins are positioned at the vortex element locations and depicted as solid circles. The colors indicate the magnitude of the velocity vectors normalized by the instantaneous maximum speed in the field.

The plots show that throughout the entire stroke, the chamber is continuously supplied with vorticity generated at the intake port walls, where the velocity is at a maximum. At $t = 0$, the piston starts from rest at TDC, establishing an interior potential flow with wall-bounded vortex sheets in the computational domain. The continuity constraint sets the area-averaged velocity in the port at 6.25 times the piston speed. By 9.3 deg crank angle, the area-averaged velocity in the port is already higher than the peak piston speed at 90 deg crank angle. At this moment, the piston has moved away from TDC by less than 0.007. Therefore, the flow dynamics inside the chamber are influenced by the intake port jet, instantly, and the jet issuing from the intake port, rather than the cylinder wall boundary layer, is the more significant source of vorticity. For this reason, Re = 875, based on the port diameter and its peak speed, may be a more appropriate measure of the flow characteristics, especially as it relates to the formation and growth of eddies in the chamber.

The envelope of the vortex elements in the port depicts the development of the familiar boundary layer on its walls. Note that as the piston accelerates from TDC to its peak speed at 90 deg ATC and decelerates thereafter to rest at BDC, the boundary layer thickness on the intake port walls experiences a commensurate decrease and increase, respectively. This is expected, because the harmonic motion of the piston changes the effective Reynolds number in the port as a function of the crank angle. Also notice that the boundary layer does not reach the port centerline, leaving a wide potential core which extends into the cylinder. A longer port and/or a smaller port diameter would be necessary to obtain a fully developed profile at the cylinder inlet. Nevertheless, results from the present computation compare quite favorably with those from the 2-D vortex simulation of an analog problem, using a smaller port diameter and a fully developed inlet velocity profile (Martins and Ghoniem, 1991).

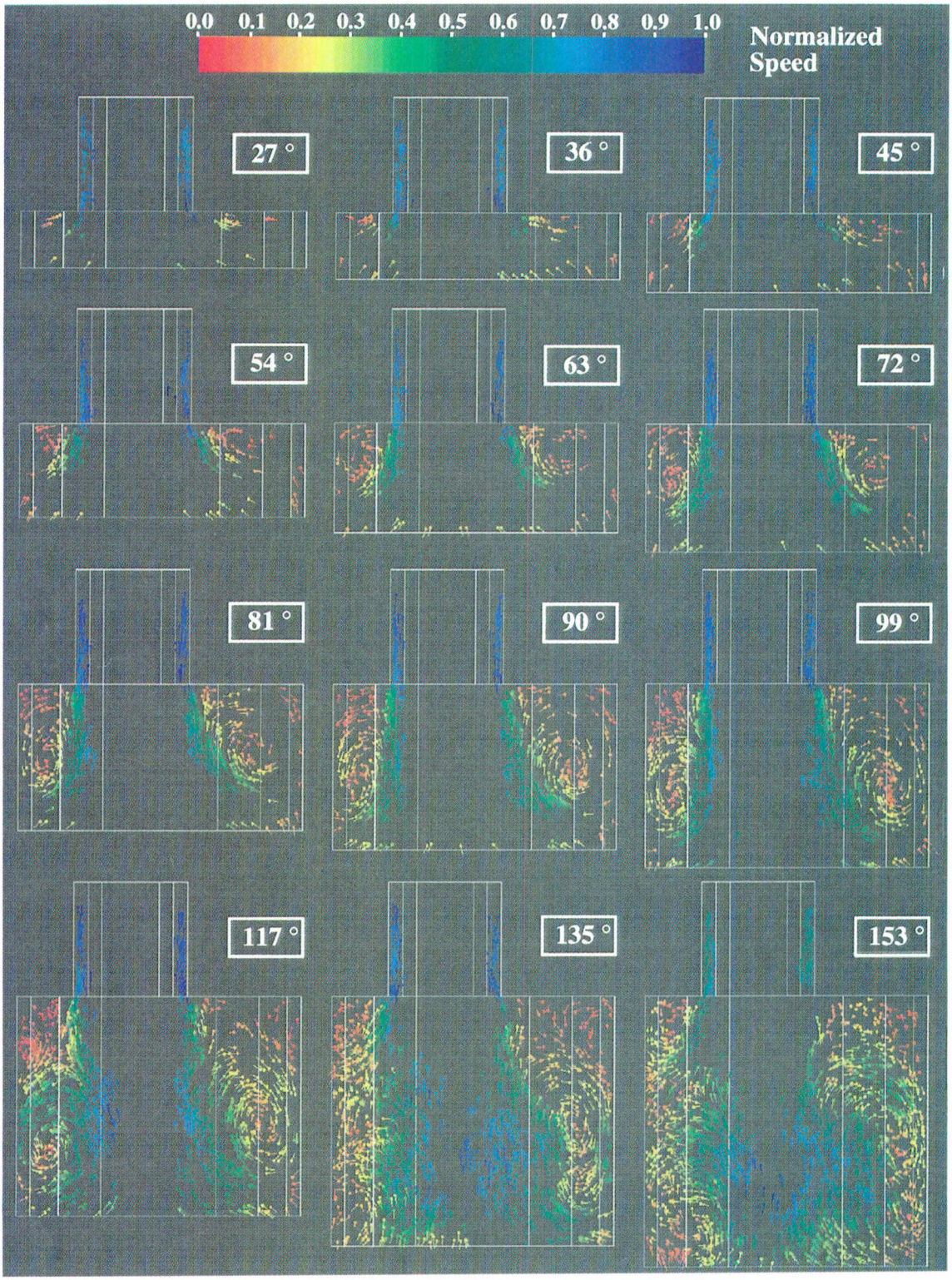

Fig. 2 Vortex element trajectories within volume A of Fig. 1. Velocity vectors are fixed in length. Normalization in each time frame is based on the instantaneous maximum speed in the field.

In contrast to the flow in the port, where a boundary layer develops quickly, the flow in the chamber remains essentially potential until 30 deg crank angle. This is evident from the absence of a sizable number of vortex elements inside the chamber. In particular, there is negligible vorticity generation on the cylinder walls since the velocity there is rather small. Furthermore, during this period, the trajectory of the vortices at the chamber top, which originate from the port, follow the boundary contour along lines similar to streamlines encountered in potential flow.

During intake, a circular jet issues from the port into the cylinder and separates at the cylinder head. Inside the cylinder, the jet rolls up into a donut-shaped toroidal eddy. The formation of this vortex torus near the cylinder head, and at a very early stage in the process, confirms that the intake jet is the primary mechanism responsible for generating the torus and that the

cylinder walls and the piston act more as confining media. The cross-section of the torus is depicted in Fig. 2 as two distinct eddies on the two sides of the port. The sense of rotation of the eddies is consistent with the direction of the jet flow, and the velocity vectors of the elements inside the torus cross-section indicate approximately a solid-body rotation type flow there. At the early stages of the flow, up to around 60 deg crank angle, the curvature and orientation of the shear layers on the left and right sides of the port are determined by the piston position, or the crank angle, and the relative position of the port with respect to the cylinder. This can be verified by recognizing that the shear layer on each side of the port is streamlined such that a curve through it extrapolates out to the intersection of the cylinder wall and the piston.

As the piston proceeds toward BDC, the toroidal eddy convects slowly away from the cylinder head, and grows by entraining most of the incoming jet fluid and some of the fluid which is already in the cylinder. Up to 63 deg crank angle, the left and right cross-sections of the toroidal eddy grow at an equal rate, maintaining near symmetry. However, this symmetry is lost beyond 63 deg as the left side of the core of the torus touches the wall and continues to grow *along* the cylinder, occupying the volume between the cylinder head and the piston. The right side of the eddy continues its radial growth to an effective diameter that is equal to the distance between the port and the cylinder wall on the right (at approximately 81 deg). The coherence of the toroidal vortical structure is preserved until 90 deg ATC.

In addition to the primary vortex torus, a weak counter-rotating toroidal vortex develops at the corner between the cylinder head and its walls at approximately 72 deg. This torus stays at the corner and remains weak. Furthermore, a small secondary torus starts to develop at 99 deg crank angle due to the jet separation at the chamber top. In contrast to the primary torus, the core of this torus is azimuthally non-uniform from inception, and its left side appears to be larger than the one on the right. The average core size is equivalent to the initial clearance height—the distance between the piston at TDC and the cylinder top.

In spite of the observed symmetry between the left and right sides of the primary eddy during its initial stages (up to 63 deg), the line passing through the eddy centers is slightly slanted with respect to the horizontal due to the off-center location of the port. An azimuthally uniform torus is initially created around the jet near the cylinder head, due to the jet separation into the cylinder. As the flow progresses, the torus rolls forward in the jet direction and expands out radially, while it enlarges its core size as a result of further entrainment of the jet and the chamber fluid. Prior to its first contact with the cylinder side walls at approximately 63 deg, during which the wall effects are negligible, the torus behaves strikingly similar to a vortex ring moving in an unbounded domain. Beyond 90 deg ATC, and as will be confirmed by the plots of the iso-surfaces of the magnitude of the vorticity, this vortex structure loses its coherence and starts to break into a number of smaller structures. The breakup appears to occur first around the azimuth of the torus, leading to the formation of a number of vortices whose primary direction is along the cylinder axis. In the following, we explain this transition using the dynamics of vortex rings.

As mentioned earlier, the vortical structure forming near the cylinder head (up to 90 deg) strongly resembles a vortex ring moving in free space (see also Fig. 4). The dynamics of the latter have been analyzed extensively (Saffman, 1978; Widnall et al., 1974), as well as investigated experimentally (Maxworthy, 1977; Sullivan et al., 1973) and computationally (Knio and Ghoniem, 1988) in free space and in wall confined flows. In a parametric study by Knio and Ghoniem (1988), vortex rings were excited radially by a sinusoidal perturbation using an integer number of waves in the azimuthal direction. The computations predicted the development and growth of streamwise vortices around the azimuth when the ring was perturbed at the most unstable wave length or at higher harmonics. The unstable modes were shown to depend on the ring properties. More specifically, the most unstable wavenumbers were found to be proportional to the ratio of the ring radius to the core size. In long time computations, these perturbations grew and led to the break up of the ring. Outside a narrow band around the most unstable wavenumbers, the rings were shown to oscillate stably. Even when perturbed at wavenumbers higher than the most unstable value, the rings eventually break down at wavenumbers close to the most unstable ones. In the present computation, the circular cross section of the port is represented by 20 unequal staircase segments, as depicted in Fig. 1; i.e., the flow is perturbed by noise with wavenumbers spanning the range of 1–20 and their higher harmonics. As a result, small radial perturbations are imparted continuously around the azimuth of the primary torus. The growth of these perturbations, via the mechanism mentioned above, leads to the development of streamwise vortices accompanied by mild oscillations. Eventually, as the waves grow further, the breakup is observed (see Fig. 4, at 153 deg). While the origin of the initial perturbation in our simulation is numerical, one expects to encounter similar perturbations in laboratory flows due to noise, vibrations, etc., that would lead to a similar break up of the vortex. We note that the growing mode wavenumber is much smaller than 20, i.e., the numerical perturbation excites a "natural" mode, which is consistent with the results summarized in the preceding statements.

In a related experimental study, Ekchian and Hoult (1979) showed that the vortex ring breakup in an axisymmetric engine model with a poppet valve agrees with the prediction of the linear theory of the inviscid instability of ring vortices in terms of the relationship between the number of unstable modes and the ring properties. While the case we simulate lacks a valve, and as such cannot be compared directly with the experimental study, both cases show the significance of the role of vortex ring instability in the breakup of the dominant flow structure and the generation of small scales at the later stages. The experimental and numerical studies confirm that, despite the relatively low Reynolds number of the flow, inviscid dynamics play an important role in this problem. Consequently, nondiffusive schemes are necessary for such simulations.

Figure 3 depicts the perspective view of the location of the vortex elements generated at the piston face, due to the interaction of the latter with the intake jet. The fixed length vectors attached to the elements represent the vorticity direction, and the color shows the magnitude normalized by the instantaneous maximum vorticity. The jet at the exit of the intake port is 6.25 times faster than the moving piston. Consequently, it impinges upon the piston face and disperses radially outward, generating circular vortex rings whose axes are normal to the piston face. The direction of vorticity in these rings is opposite the direction of the toroidal vortex in the cylinder. The inner most circular area directly below the port is devoid of vortex elements due to the vanishingly small jet velocity there.

The accelerated motion of the piston toward 90 deg crank angle is accompanied by an increase in the jet speed as it impinges on the piston, leading to an increase in the radial velocity of the rings generated on the piston. This, combined with the fact that the outermost rings—being closer to the chamber walls—are relatively slower than the inner rings, leads to the formation of a well-defined closely packed vortex torus which is nearly symmetric with respect to the plane of symmetry of the cylinder. As the vortex torus expands radially outward, it encounters perturbations generated by the velocity induced near the walls. As mentioned before, the source of these perturbations is the wall discretization. As a result, a strong waviness appears around the periphery of the torus, near the walls, which again leads to the growth of lobes. These lobes correspond to vortex structures whose axes are aligned in the direction of the cylinder axis. However, the relative magnitudes of these vortices are

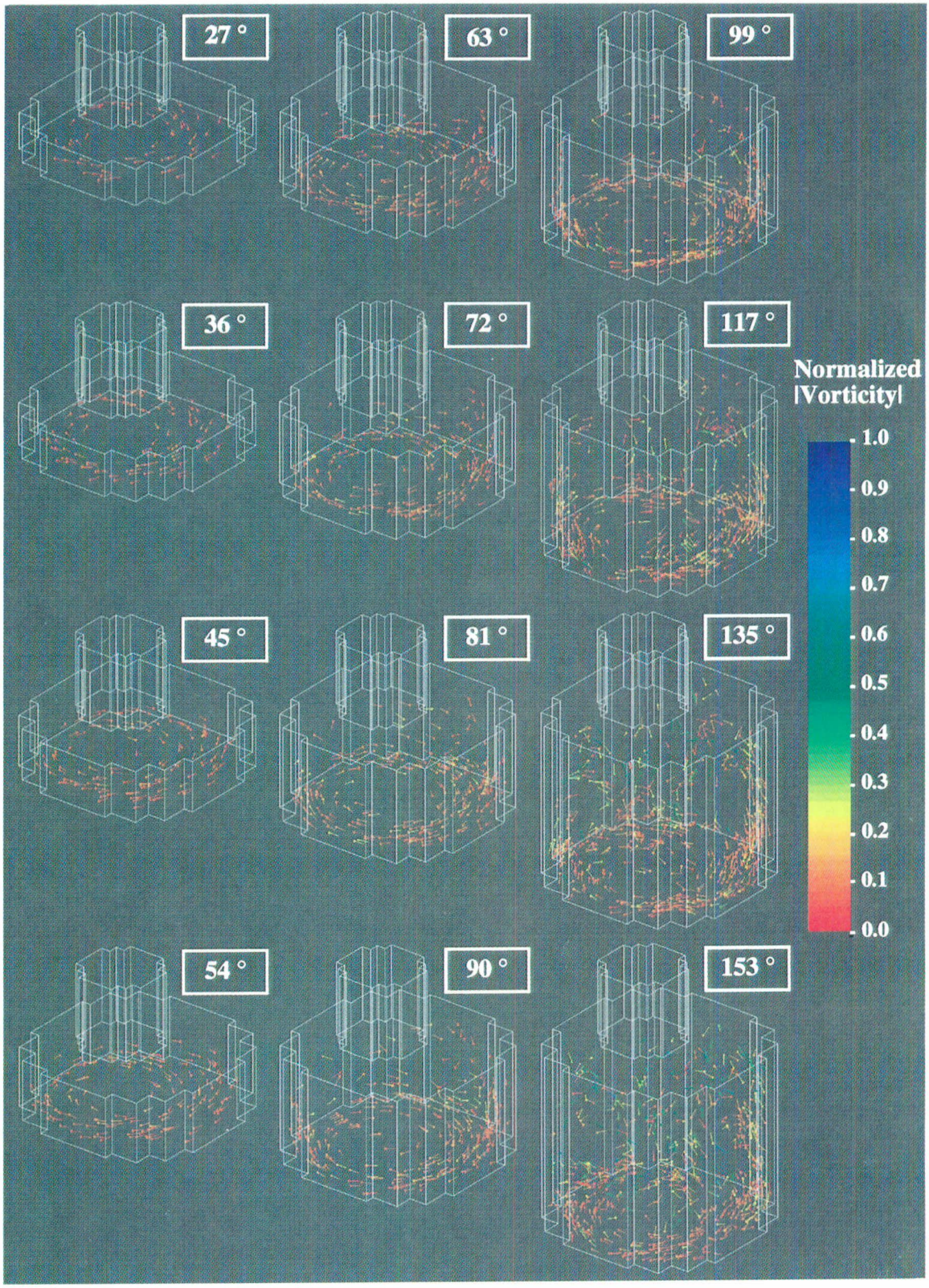

Fig. 3 Perspective view of vortex elements generated on the piston. Vorticity vectors normalized by the instantaneous maximum vorticity in the field.

small compared to the ones generated in the chamber due to the jet separation.

Figure 4 depicts the evolution of $|\boldsymbol{\omega}|^2 = 0.2$ surfaces, where $\boldsymbol{\omega}$ is the local vorticity normalized by the instantaneous maximum value in the field. The local value of the vorticity was evaluated on a uniform grid, divergence free, using its definition as the curl of the velocity. $|\boldsymbol{\omega}|^2$ corresponds to the enstrophy, which can also be taken as a measure of the energy dissipation rate per unit volume, and can be used to detect regions of strong shear, fast dissipation and mixing rates. During the early stages

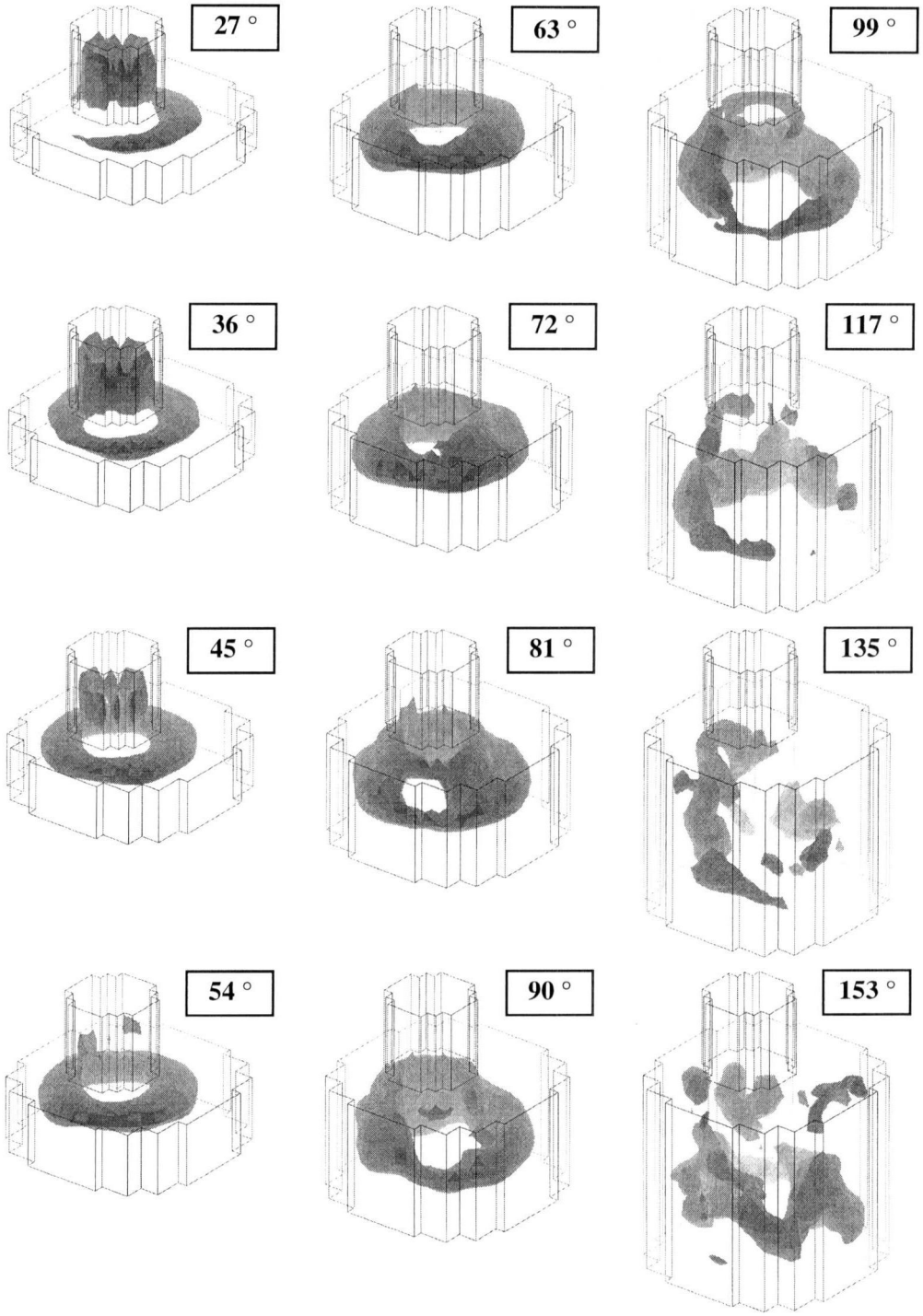

Fig. 4 Iso-surfaces of $\omega.\omega = 0.2$. ω is vorticity normalized by the instantaneous maximum field vorticity.

of the intake process, before 45 deg crank angle, the boundary layer in the intake port contributes substantially to the vorticity, hence the energy dissipation, within the cylinder. The figure confirms the earlier suggestion that the flow in the cylinder is essentially potential during this stage, and that the jet from the port is the only significant source of vorticity or shear. The development and roll up of the donut shaped vortex torus due to the sudden expansion of the jet in the cylinder are prominently displayed in the figure. The iso-surface evolves from a cylindrical shape inside the port into a donut shape in the cylinder. The latter is clearly the structure which stores most of the incoming shear/vorticity/rotational energy. A mild waviness can be seen on the iso-surface, for up to 72 deg crank angle. The perturbations associated with these waves grow and lead to the break up of the torus in the later stages. Also note that beyond 81 deg crank angle, the eventual formation of the secondary vortex near the cylinder head, and around the port, begins to contribute to the total dissipation.

Conclusions

The three-dimensional random vortex-boundary element method was applied to simulate the intake flow inside a cylinder

fitted with an eccentric port at one end and a harmonically driven piston at the other. The Reynolds number based on the piston diameter and its maximum speed was set at 350. Results show that the flow inside the cylinder is dominated by a set of evolving toroidal vortical structures generated primarily due to the separation of the jet issuing from the intake port, at the cylinder head. Thus, the boundary layer in the port is the major source of vorticity in the cylinder, at least during the early stages of the intake process. The largest, or primary, eddy continues to entrain the jet and grows to fill a significant portion of the cylinder near BDC. In addition, a secondary vortex torus forms later, which maintains a nominal core size in the order of the initial clearance height in the cylinder. A counter-rotating torus is also evident at the top corner of the chamber, which remains weak but stable. The structure of the primary torus remains coherent until 90 deg crank angle. Beyond this stage, the growth of small perturbations around the azimuth of the eddy, via a mechanism resembling the azimuthal instability mechanism of vortex rings, leads to the eventual break-up of the eddy and the formation of vorticity in the direction of the cylinder axis. Similar oscillations are observed around the azimuth of the piston-generated eddy.

The results demonstrated that, without resorting to a turbulence closure model or special manipulation of the "numerical grid," the method is capable of capturing the intricate dynamics of the vortical structures that form inside the cylinder. Even at the relatively low Reynolds number of the simulation, the dynamics of the vortical structures were shown to be related to essentially inviscid instability mechanisms, again demonstrating the near absence of artificial dissipation in the vortex method. While experimental studies on this and similar flows are rather scarce, there is a good qualitative agreement between available results and our observations. We are currently perusing one effort of acquiring such experimental data via collaboration with other groups, while extending our method to allow for the simulation of more complex configurations.

Acknowledgments

This project was funded by FORD Motor Company and Gas Research Institute. The numerical experiments were performed on the Cray C90 at the Pittsburgh Supercomputing Center.

References

Beale, J. T., and Majda, A., 1985, "High Order Vortex Methods with Explicit Velocity Kernels," *Journal of Computational Physics,* Vol. 58, pp. 188–208.

Chorin, A. J., 1980, "Vortex Models and Boundary Layer Instability," *SIAM Journal on Scientific and Statistical Computing,* Vol. 1, No. 1, pp. 1–21.

Cloutman, L. D., Dukowicz, J. K., and Ramshaw, J. D., 1981, "Numerical Simulation of Reactive Flow In Internal Combustion Engines," *Proceedings of the Seventh International Conference on Numerical Methods in Fluid Dynamics,* pp. 119–124.

Ekchian, A., and Hoult, D. P., 1979, "Flow Visualization Study of the Intake Process of An Internal Combustion Engine," SAE Technical Paper No. 790095, pp. 383–400.

Errera, M. P., 1987, "Numerical Prediction of Fluid Motion in the Induction System and the Cylinder in Reciprocating Engines," SAE Technical Paper No. 870594, pp. 1–11.

Fishelov, D., 1990, "Vortex Methods for Slightly Viscous Three-Dimensional Flow," *SIAM Journal on Scientific and Statistical Computing,* Vol. 11, No. 3, pp. 399–424.

Gharakhani, A., and Ghoniem, A. F., 1996a, "Vortex Simulation of the Three-Dimensional Wake Behind A Cube," AIAA-96-0170, 34th Aerospace Sciences Meeting, p. 22, Reno, NV.

Gharakhani, A., and Ghoniem, A. F., 1996b, "Massively Parallel Implementation of A 3D Vortex-Boundary-Element Method," *Proceedings of the Second International Workshop on Vortex Flows and Related Numerical Methods,* Montreal, Canada, 1995; ESAIM: http://www.emath.fr/proc/Vol.1/, Vol. 1, pp. 213–223.

Gharakhani, A., and Ghoniem, A. F., 1996c, "3D Vortex Simulation of Intake Flow In An Off-Centered Port and Cylinder with A Moving Piston," *Proceedings of the 1996 ASME Fluids Engineering Division Summer Meeting,* FED-Vol. 238, Vol. 3, pp. 13–24, San Diego, CA.

Gharakhani, A., and Ghoniem, A. F., 1997a, "BEM Solution of the 3D Internal Neumann Problem and A Regularized Formulation for the Potential Velocity Gradients," *International Journal for Numerical Methods in Fluids,* Vol. 24, No. 1, pp. 81–100.

Gharakhani, A., and Ghoniem, A. F., 1997b, "Three-Dimensional Vortex Simulation Of Time Dependent Incompressible Internal Viscous Flows," *Journal of Computational Physics,* Vol. 134, pp. 75–95.

Ghoniem, A. F., and Gagnon, Y., 1987, "Vortex Simulation of Laminar Recirculating Flow," *Journal of Computational Physics,* Vol. 68, No. 2, pp. 346–377.

Gosman, A. D., Meling, A., Watkins, A. P., and Whitelaw, J. H., 1978, "Axisymmetric Flow in a Motored Reciprocating Engine," *Proc. Instn. Mech. Engrs.,* Vol. 192, pp. 213–223.

Gosman, A. D., Johns, R. J. R., and Watkins, A. P., 1980, "Development of Prediction Methods for In-Cylinder Process in Reciprocating Engines," Mattavi, J. N. and Amann, C. A., eds., *Combustion Modeling in Reciprocating Engines,* Plenum, New York, pp. 69–129.

Khalighi, B., 1995, "Multidimensional In-Cylinder Flow Calculations and Flow Visualization in a Motored Engine," *ASME Journal of Fluids Engineering,* Vol. 117, No. 2, pp. 282–288.

Knio, O. M., and Ghoniem, A. F., 1988, "On the Formation of Streamwise Vorticity In Turbulent Shear Flows," AIAA-88-0728, 26th Aerospace Sciences Meeting, p. 17, Reno, NV.

Martins, L.-F., and Ghoniem, A. F., 1991, "Vortex Simulation of the Intake Flow in A Planar Piston-Chamber Device," *International Journal for Numerical Methods in Fluids,* Vol. 12, pp. 237–260.

Maxworthy, T., 1977, "Some Experimental Studies of Vortex Rings," *Journal of Fluid Mechanics,* Vol. 81, No. 3, pp. 465–495.

Morse, A., Whitelaw, J. H., and Yianneskis, M., 1980, "The Influence of Swirl on the Flow Characteristics of A Reciprocating Piston-Cylinder Assembly," *ASME Journal of Fluids Engineering,* Vol. 102, No. 4, pp. 478–480.

Naitoh, K., Fujii, H., Urushihara, T., Takagi, Y., and Kuwahara, K., 1990, "Numerical Simulation of the Detailed Flow In Engine Ports and Cylinders," SAE Technical Paper No. 900256, pp. 1–18.

Puckett, E. G., 1989, "A Study of the Vortex Sheet Method and Its Rate of Convergence," *SIAM Journal on Scientific and Statistical Computing,* Vol. 10, No. 2, pp. 298–327.

Saffman, P. G., 1978, "The Number of Waves On Unstable Vortex Rings," *Journal of Fluid Mechanics,* Vol. 84, No. 4, pp. 625–639.

Sullivan, J. P., Widnall, S. E., and Ezekiel, S. 1973, "A Study of Vortex Rings Using A Laser-Doppler Velocimeter," *AIAA Journal,* Vol. 11, No. 10, pp. 1384–1389.

Taghavi, R., and Dupont, A., 1988, "Multidimensional Flow Simulation in An Inlet Port/Combustion Chamber Assembly Featuring A Moving Valve," *ASME Internal Combustion Div.,* ICE Vol. 6, pp. 9–15.

Widnall, S. E., Bliss, D. B., and Tsai, C-Y., 1974, "The Instability of Short Waves on A Vortex Ring," *Journal of Fluid Mechanics,* Vol. 66, pp. 35–47.

Kiyoshi Minemura
Professor,
Graduate School of Human Informatics.

Tomomi Uchiyama
Associate Professor.

School of Informatics and Sciences,
Nagoya University,
Furo-cho, Chikusa-ku,
Nagoya 464-8601, Japan

Shinji Shoda
Leader.

Kazuyuki Egashira
Engineer.

Technical Research Center,
Japan National Oil Corporation,
Hamada, Mihama-ku,
Chiba 261-0025, Japan

Prediction of Air-Water Two-Phase Flow Performance of a Centrifugal Pump Based on One-Dimensional Two-Fluid Model

To predict the performance of centrifugal pumps under air-water two-phase flow conditions, a consistent one-dimensional two-fluid model with fluid viscosity and air-phase compressibility in a rotating impeller is proposed by considering energy changes in the transitional flow from the rotating impeller to the stationary volute casing. The two-fluid model is numerically solved for the case of a radial-flow pump after various constitutive equations are applied. The head and shaft power predicted are found to agree well with the measured values within ±20 percent of the rated flow capacity.

Introduction

It is important to know and improve the characteristics of centrifugal pumps operating under gas-liquid two-phase flow conditions in relation to the safety analysis of nuclear reactors. For prediction of the two-phase flow performance, the methods based on head-loss ratio (Mikielewicz et al., 1978, Minemura et al., 1985), homologous curve method (Nilsson, 1977), or polar homologous curve method (Minato, 1988a) are available, after correlating such parameters with the data experimentally obtained. It is, however, desirable to establish a numerical method by which the effects of the design parameters of a pump on its two-phase flow performance can be individually investigated, especially in relation to the development of off-shore oil fields (De Donno, 1985).

Regarding numerical prediction methods, Furuya (1985) has proposed a one-dimensional, incompressible two-fluid model. This model has been extended to a condensable two-fluid model (Furuya and Maekawa, 1987), which is successively employed in the studies by Calvin et al. (1992) and Noghrehkar et al. (1995). There is also a two-dimensional singularity method by Nishiyama et al. (1989) and a three-dimensional method using a quasi-harmonic equation based on a bubbly flow model by Minemura and Uchiyama (1993, 1994a). However, all these methods are obtained by assuming the fluid is inviscid, so that the pump head obtained is theoretical one, and does not include hydraulic losses. On the other hand, Minato (1988b) proposed a simple method to solve the momentum equations of both phases without respect of the changes in void fraction and pressure gradient within the impeller. Fujie (1985) has solved the one-dimensional momentum equations for both phases using a friction loss coefficient obtained when the hydraulic torque becomes zero and taking the effect of the transitional flow from the impeller to the stationary volute casing into account. But the handling of the constitutive equations of the two-fluid model is quite different from others and consideration to the velocity triangle at the impeller exit is not so consistent. The one-dimensional momentum equations are also solved by Van Den Hove and Geffrage (1992), though they ignored the significant effect of the slip velocity due to finite number of the impeller blades.

To grasp analytically the characteristics of two-phase flow pumps and to make it possible to improve their performance, this paper describes a consistent one-dimensional model, with fluid viscosity and gas-phase compressibility, by extending Furuya's two-fluid model (1985), and related energy changes in the transitional flow from the rotating impeller to the stationary volute casing. This model is also applied to solve the two-phase flow performance of a radial-flow pump having a low specific speed, and confirmed with the experimental data (Minemura et al., 1985), after investigating the applicability of various and representative constitutive equations for pipe flow.

Mathematical Foundations

Assumptions. Supposing that the friction loss of the flow in the stationary passages upstream and downstream of a rotating impeller is representatively presented by the friction loss within the impeller and that the flow behavior is fundamentally one-dimensional, the basic equations for the gas-liquid two-phase flow in the impeller are derived with the following assumptions:

(1) The impeller rotates with a constant velocity, and both phase flows are steady in the rotating frame of reference.
(2) Both phase flows have the same one-dimensional streamlines, and the slip velocity between the phases takes place only in the direction of the streamline.
(3) Both phase pressures are the same on each sectional area.
(4) The gas phase is a perfect gas and changes adiabatically, while the liquid phase is incompressible.
(5) Neither mass nor heat transfer takes place between the phases.
(6) The flow upstream of the impeller does not acquire prerotation.

Contributed by the Fluids Engineering Division for publication in the JOURNAL OF FLUIDS ENGINEERING. Manuscript received by the Fluids Engineering Division April 1, 1997; revised manuscript received January 20, 1998. Associate Technical Editor: B. Schiavello.

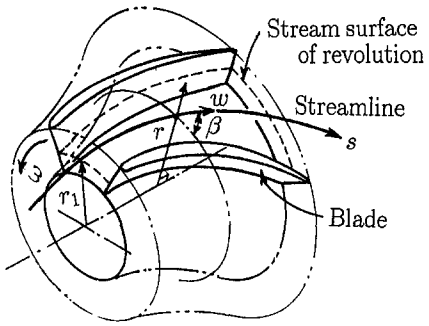

Fig. 1 One-dimensional conduit and coordinate system

(7) The effect of gravity can be ignored due to higher rotation speed.

Basic Equations of Flow in Impeller. The two-phase flow in the rotating impeller can be represented by a one-dimensional conduit along a streamline s, as shown in Fig. 1. Based on a two-fluid model, the equations of conservation of mass for each phase can be written as

$$(d\dot{m}_g/ds) = d/ds(\alpha\rho_g w_g A \sin\beta) = 0, \quad (1)$$

$$(d\dot{m}_l/ds) = d/ds[(1-\alpha)\rho_l w_l A \sin\beta] = 0. \quad (2)$$

The equations of conservation of momentum for each phase can be expressed by

$$\alpha\rho_g w_g(\partial w_g/\partial s) = -\alpha(\partial p/\partial s) - F_{w,g} + \alpha\rho_g r\omega^2(\partial r/\partial s) + F_i + F_v, \quad (3)$$

$$(1-\alpha)\rho_l w_l(\partial w_l/\partial s) = -(1-\alpha)(\partial p/\partial s) - F_{w,l} + (1-\alpha)\rho_l r w^2(\partial r/\partial s) - F_i - F_v. \quad (4)$$

By summing up (3) and (4), the equation of conservation of momentum for both phases is thus given by

Table 1 Interfacial friction coefficient

No.	Constitutive equations	References
a1	$C_D = \max[(24/Re)(1 + 0.15Re^{0.687}), (8/3)E_0/(E_0 + 4)]/\sqrt{1-\alpha}$ $Re = 2R_b\lvert\omega_g - \omega_l\rvert/\nu_l$, $E_0 = g(\rho_l - \rho_g)(2R_b)^2/\sigma$	Tomiyama et al. (1995)
a2	$C_D/R_b = 340.2$ [m^{-1}] ($R_b = 1.59$ mm)	Hench–Johnston (1972)
a3	$\frac{C_D}{R_b} = \frac{8}{3}\frac{(1-\alpha)(\rho_l - \rho_g)g}{\rho_l\lvert V_{Gj}\rvert^2}$ $V_{Gj} = \begin{cases} (1-\alpha)^{1.5}V^*_{Gja} \\ \quad \ldots \text{for bubble flow} \\ V^*_{Gja} \ldots \text{for churn flow} \end{cases}$ $V^*_{Gja} = \sqrt{2}\{\sigma(\rho_l - \rho_g)g/\rho_l^2\}^{1/4}$	RELAP5/MOD2 (1985)
a4	$C_D/R_b = 109.8(1-\alpha)^3$ [m^{-1}] ... for churn flow	Zuber–Hench (1962)

(ν: kinematic viscosity, σ: surface tension).

$$\alpha\rho_g w_g\frac{\partial w_g}{\partial s} + (1-\alpha)\rho_l w_l\frac{\partial w_l}{\partial s} = -\frac{\partial p}{\partial s} - (F_{w,g} + F_{w,l}) + [\alpha\rho_g + (1-\alpha)\rho_l]r\omega^2\frac{\partial r}{\partial s}. \quad (5)$$

The equation of state for the gas phase can be written as

$$p/\rho_g^\kappa = \text{const} \quad (6)$$

where κ is the isentropic exponent ($\kappa = 1.4$).

Constitutive Equations. The interfacial friction force F_i can be expressed as

$$F_i = \alpha\rho_l(3/8)(C_D/R_b)(w_l - w_g)\lvert w_l - w_g\rvert, \quad (7)$$

where the drag coefficient divided by the bubble radius, C_D/R_b, depends on the flow regime, and its representative values for bubbly flow and churn-turbulent flow regimes are listed in Table 1.

Nomenclature

A = crossflow area on a circumferential surface or sectional area of pipe
c = absolute flow velocity
C_D = drag coefficient of bubble
C_f = friction factor
C_V = virtual mass coefficient of bubble
D_h = hydraulic diameter of flow channel
F_i = interfacial friction force per unit volume
F_v = virtual mass force per unit volume
F_w = wall friction force per unit volume
g = gravitational acceleration
H = head
h = loss of head
L = shaft power
$\dot{m}$ = mass flow rate
p = static pressure
p_f = friction pressure loss
R_l, R_f = pressure loss multiplier
R_b = radius of bubble
r = radial coordinate
s = coordinate along streamline
u = peripheral velocity of impeller
w = relative flow velocity
x = quality = $\dot{m}_g/\dot{m}_{tp}$
α = void fraction
β = angle between relative flow velocity and circumferential direction
ϵ_r = dimensionless radius = $(r - r_1)/(r_2 - r_1)$
η = pump efficiency
μ = power coefficient = $L/(\rho_l A_2 u_2^3/g)$
ρ = density
ϕ = flow coefficient = $\dot{m}_l/(\rho_l A_2 u_2)$
ψ = head coefficient = $H/(u_2^2/g)$
$\Delta\psi_r$ = dimensionless pressure rise from pump inlet = $(p - p_s)/(\rho_l u_2^2)$
ω = angular velocity of impeller

Subscript

0 = liquid single phase flow condition
1 = just after impeller inlet
2 = just before impeller exit
3 = just after impeller exit
4 = just after flow-area expansion
5 = just after flow homogeneity
6 = just after volute (or diffuser) inlet
d = pump exit
g = gas phase
l = liquid phase
m = meridional component
n = best efficiency point
s = pump inlet
tp = gas-liquid two-phase flow condition
u = tangential component

Table 2 Virtual mass coefficient

No.	Constitutive equations	References
b1	$C_V = 0.5$ $\omega_1^* = \omega_l,\ \omega_2^* = \omega_g$	nonobjective form
b2	$C_V = 0.5 C_{Vm}(\rho_{tp}/\rho_l)$, $C_{Vm} = \begin{cases} (1 + 2\alpha) \ldots \text{for } \alpha \le 0.5 \\ (1 - \alpha)(3 - 2\alpha)/\alpha \\ \quad \ldots \text{for } \alpha > 0.5 \end{cases}$	RELAP5/MOD2 (1985)
b3	$C_V = 0.5$ $\omega_1^* = 2\omega_g - \omega_l,\ \omega_2^* = \omega_g$	Drew and Lahey (1987)

The force acting on the virtual mass of bubbles, F_v, can be given by the following form,

$$F_v = \alpha\rho_l C_V[w_1^*(\partial w_l/\partial s) - w_2^*(\partial w_g/\partial s)], \quad (8)$$

where the virtual mass coefficient C_V and the representative velocities w_1^* and w_2^* are generally evaluated with the relations listed in Table 2.

The wall friction force, F_w, can be expressed by

$$F_{w,g} = \alpha(\partial p_f/\partial s), \quad F_{w,l} = (1 - \alpha)(\partial p_f/\partial s), \quad (9)$$

in which the loss of pressure due to wall friction, p_f, is considered to be given by

$$\partial p_f/\partial s = R_f(\partial p_{f,0}/\partial s) = -R_f(C_f/D_h)\rho_l w_0^2, \quad (10)$$

that is, the whole loss of friction pressure, $\Delta p_f \{=\int (\partial p_f/\partial s)ds\}$, is considered to be given by multiplying the $\Delta p_{f,0}$ value by the multiplier R_f, where $\Delta p_{f,0}$ is the loss when only the liquid phase of the mixture flows in the conduit and $w_0 = \dot{m}_l/\rho_l A \sin\beta$. It is also supposed that the multiplier R_f for pipe flows, as listed in Table 3, is applicable to this case. Change of void fraction in the direction of a streamline is much greater in pumps rather than in pipe flows, and R_f is thus supposed in this study as a function of position s, that is, it changes according to local void fraction α or two-phase flow parameter X. For single-phase flow conditions, the $\Delta p_{f,0}$ value can be evaluated from (10) with $R_f = 1$ by integrating it from the impeller inlet to the outlet. Once the $\Delta p_{f,0}$ value is given, the distribution of p_f along the streamline for two-phase flow conditions can then be evaluated.

The whole pressure loss in the pump Δp consists of the pressure losses due to wall friction Δp_f and shock Δp_{shock}, that is,

$$\Delta p = \Delta p_f + \Delta p_{\text{shock}}. \quad (11)$$

Supposing that the shock loss in single-phase flow condition is estimated with Pfleiderer and Perterman's formula (1986) and that Chisholm and Sutherland's two-phase pressure-loss multiplier (1969) is applicable to the shock loss in two-phase flows, just the same as the loss in pipelines with valves, the value of Δp_{shock} for the two-phase flow is then evaluated with the multiplier R_f and flow rate ϕ $(=\dot{m}_l/\rho_l A_2 u_2)$ as,

$$\Delta p_{\text{shock}} = \frac{1}{2} R_f \zeta_{sh}\rho_l(\phi_n - \phi)^2\left[u_1^2 + \left(\frac{u_2}{1 + p_p}\frac{r_2}{r_4}\right)^2\right], \quad (12)$$

where ζ_{sh}, ϕ_n and p_p are pressure-loss coefficient, flow rate at the best efficiency point and Pfleiderer's head-reduction factor, respectively. The inlet radius of the vaned diffuser, r_4, is approximately replaced by the radius of the tongue when the pump has volute. It is also considered that the overall shock loss is shared between the impeller inlet $\Delta p_{\text{shock},s}$ $(=p_s - p_1)$ and outlet $\Delta p_{\text{shock},d}$ $(=p_5 - p_6)$ by the rates of the first and second term in the bracket of Eq. (12).

The pressure losses for single-phase flows, $\Delta p_{f,0}$ and $\Delta p_{\text{shock},0}$, can be evaluated as a function of ϕ when the theoretical and actual pump heads are known. In this case it should be noticed that the flow rate through the impeller is greater than the discharge flow rate by volumetric efficiency corresponding to the leakage flow.

Velocity Triangle at Impeller Exit and Related Losses. For the transitional flow from the rotating frame to the stationary frame of reference at the impeller exit, it should be considered that the two-phase mixture successively meets with deflection of the flow angle due to a finite number of impeller blades, the rapid expansion of the flow passage and flow homogenization due to phase mixing, and then flows into the volute casing, just the same as the processes considered by Fujie (1985), though the relations between the absolute and relative two-phase flow have not completely and clearly been defined. By assuming that such a process takes place successively at the almost same position and that the void fraction thus remains unaltered, the changes described in the following are based on the velocity triangle illustrated in Fig. 2, where the flow states ②, ③, . . . , are designated by the suffixes 2, 3, ...

(1) Deflection of Flow Angle. Although the gas and liquid phases at the impeller exit flow with the same angle β_2 and with different velocities, $w_{2,g}$ and $w_{2,l}$, respectively (state ②: blade direction), their velocities increase to $w_{3,g}$ and $w_{3,l}$, respectively, with angle β_3 due to so-called slip, i.e., effect of a finite number of impeller blades (state ③: actual flow direction with slip).

The slip factor for single-phase flow in pumps is commonly considered to be in first approximation independent of discharge flow rate or fluid density. It is thus supposed in this study that such relations are also applicable to the two-phase flow conditions and that the slip factor k is given by Wiesner's experimental formula, i.e., $k = \sqrt{\sin\beta_2}/z^{0.7}$, where z is the number of impeller blades and β_2 the blade exit angle. It is also assumed that the difference between the tangential components of the mean flow velocity, $\overline{w_{2,tp}}$ $\{=\alpha_2 w_{2,g} + (1 - \alpha_2)w_{2,l}\}$ and $\overline{w_{3,tp}}$ $\{=\alpha_2 w_{3,g} + (1 - \alpha_2)w_{3,l}\}$, obtained from the viewpoint of mass conservation, is equal to slip velocity ku_2. Since the radial velocity components do not alter, the angle β_3 can be given by

$$\beta_3 = \arctan[\overline{w_{2,tp}}\sin\beta_2/(ku_2 + \overline{w_{2,tp}}\cos\beta_2)]. \quad (13)$$

In single-phase flow condition, subtraction of the slip velocity head from the theoretical pump head for an infinite number of blades, $(u_2 c_{u2}/g)$, yields the pump head for a finite number of blades, $\{u_2(c_{u2} - ku_2)/g\}$. Therefore, we have the following relation for the head of the fluid at the impeller exit,

$$(p_2/\rho_l g + c_2^2/2g) - ku_2^2/g = (p_3/\rho_l g + c_3^2/2g). \quad (14)$$

By substituting the identical equations determined from the exit velocity triangle $(c_2^2 = w_2^2 - u_2^2 + 2u_2 c_{u2},\ c_3^2 = w_3^2 - u_2^2 + 2u_2 c_{u3})$ into the above equation and paying attention to the relation of $c_{u2} - c_{u3} = ku_2$, it is found that the velocity increase

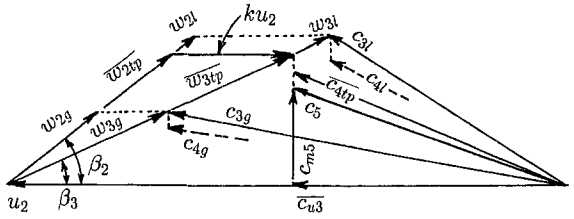

Fig. 2 Velocity triangle at impeller exit

from w_2 to w_3 due to the slip brings about the pressure difference $(p_2 - p_3)$, as evaluated by

$$(p_2 - p_3)/\rho_l g = (w_3^2 - w_2^2)/2g. \quad (15)$$

In the two-phase flow condition, the pressure p_3 is thus given with the increases in velocity head for each phase, Δw_g^2 $(=w_{3,g}^2 - w_{2,g}^2)$ and Δw_l^2 $(=w_{3,l}^2 - w_{2,l}^2)$, by the following equation (Fujie, 1985),

$$(p_2 - p_3)/g\rho_{tp,2} = x\Delta w_g^2/2g + (1 - x)\Delta w_l^2/2g \equiv \Delta h_{\text{slip}}. \quad (16)$$

The averaged density of the mixture ρ_{tp} for the flow with a relative velocity between the phases, yields the homogeneous density defined from the mass conservation, as

$$\rho_{tp} = [\alpha\rho_g w_g + (1 - \alpha)\rho_l w_l]/[\alpha w_g + (1 - \alpha)w_l], \quad (17)$$

while, from the momentum conservation, the momentum density is also defined as

$$\rho_{tp} = [\alpha\rho_g w_g + (1 - \alpha)\rho_l w_l]/[x w_g + (1 - x)w_l]. \quad (18)$$

As these definitions alter the results, their availability will be discussed later.

(2) Rapid Expansion of Flow Area. The absolute flow velocities of the gas and liquid phases just before the impeller exit, $c_{3,g}$ and $c_{3,l}$, respectively, have quite different flow directions. At the exit, both phases encounter rapid expansion of the flow passage corresponding to the blade thickness and reduce their velocities to $c_{4,g}$ and $c_{4,l}$ (state ④). If it is assumed that both radial velocity components are reduced by area ratio and that both tangential velocity components remain unaltered, the reduced velocities, $c_{4,g}$ and $c_{4,l}$, can then be evaluated.

Owing to the loss caused by this rapid expansion of flow area, pressure p_3 is reduced to p_4. If it is assumed that the averaged flow velocity just before the exit, $\overline{c_{3,tp}}$, is determined with the radial component from the viewpoint of mass conservation, $\overline{c_{m3}}$ $\{=\alpha_3 c_{m3,g} + (1 - \alpha_3)c_{m3,l}\}$, and with the tangential component from the viewpoint of angular-momentum conservation, $\overline{c_{u3}}$ $\{=xc_{u3,g} + (1 - x)c_{u3,l}\}$, and that the loss is evaluated with the same relation as that for rapid expanded pipe flow, the loss is expressed as a function of the hydraulic diameters of the flow area at the exit, as D_{h2}, D_{h4}, using the multiplier R_f (Chisholm and Sutherland, 1969), as follows;

$$(p_3 - p_4)/g\rho_{tp,2} = R_f\zeta_{\text{exp}}(\rho_l/\rho_{tp,2})(c_{3,l0}^2/2g) \equiv \Delta h_{\text{exp}}, \quad (19)$$

where $\zeta_{\text{exp}} = [1 - (D_{h2}/D_{h4})^2]^2$ and $c_{3,l0} = \dot{m}_l/\rho_l A_2 \sin \times [\arctan(\overline{c_{m3}}/\overline{c_{u3}})]$.

(3) Flow Homogenization Due to Phase Mixing. Let the mixture flowing out of the impeller mix into a homogeneous flow with the identical velocity just after the exit (state ⑤). This homogeneous velocity c_5 is evaluated with the homogeneous radial flow velocity c_{m5} $(=\dot{m}_{tp}/\rho_{tp,5}A_5)$ and with the tangential flow velocity $\overline{c_{u3}}$ from the standpoint of angular-momentum conservation. The exit void fractions obtained with the calculation for the churn-turbulent flow regime, α_2, become much higher than the value at the pump inlet, α_s. From the flow observations of the breakdown condition (Murakami and Minemura, 1974, Furukawa et al., 1990), however, predominant agglomeration of bubbles is confined within an area from the halfway to its short extension of every impeller passages into the volute casing. Except for these region, finer bubbly flow is observed even in the volute casing, in which the void fraction appears to nearly equal the same value as α_s, much less than that in the predominant region of bubbles. Hence, the void fraction of the homogeneous flow, α_5, is obtained by assuming that the number density of bubbles $[=\alpha/(4\pi R_b^3/3)]$ remains unaltered with that in the pump inlet. The averaged density of the mixture, $\rho_{tp,5}$, can then be obtained by iterative calculations according to the pressure drop.

Since the momentum reduction in the direction of flow, due to this flow change, yields the pressure drop $(p_4 - p_5)$, as done by Fujie (1985), we have

$$A_4(p_4 - p_5) = (\dot{m}_g c_{m4,g} + \dot{m}_l c_{m4,l}) - \dot{m}_{tp} c_{m5} \quad (20)$$

The head loss due to the mixing is thus given as,

$$\Delta h_{\text{mix}} = (p_4 - p_5)/g\rho_{tp,2}. \quad (21)$$

(4) Flow Change in Volute Casing. Since the friction loss in the volute casing has been assumed that it is combined with the loss within the impeller as Δp_f, the following relation does hold between the position just after the homogenized flow section ⑤ and the pump exit ⓓ.

$$p_d/g\rho_{tp,d} + c_d^2/2g = (p_5 - \Delta p_{\text{shock},d})/g\rho_{tp,5} + c_5^2/2g. \quad (22)$$

Pump Head. The head of the pump operating under air-water two-phase flow conditions, H_{tp}, can be defined by the sum of the energies per unit mass increased by the pump in each phase. Denoting the heads for the gas and liquid phases as H_g and H_l, respectively, H_{tp} is thus given by

$$\dot{m}_{tp}H_{tp} = \dot{m}_l H_l + \dot{m}_g H_g. \quad (23)$$

Since $\dot{m}_{tp} = \dot{m}_l + \dot{m}_g$, it can be rewritten using quality x as

$$H_{tp} = (1 - x)H_l + xH_g. \quad (24)$$

The mixture downstream of the impeller has been supposed to be homogeneous and have the same velocity without slip between the phases. Thus, the head for each phase is expressed as

$$H_l = (p_d - p_s)/\rho_l g + (c_d^2 - c_{s,l}^2)/2g,$$
$$H_g = \int_{p_s}^{p_d}(1/\rho_g g)dp + (c_d^2 - c_{s,g}^2)/2g, \quad (25)$$

where H_g can be evaluated by assuming an adiabatic change based on assumption (4).

Shaft Power and Efficiency. If it is assumed that the power loss due to bearings and disk friction L_f remains unaltered in the two-phase flow conditions as well, the shaft power to pump up the mixture, L_{tp}, is given, with assumption (6) for the angular-momentum balance, as

$$L_{tp} = \dot{m}_{tp}u_2\overline{c_{u3}} + L_f. \quad (26)$$

The pump efficiency η_{tp} can then be expressed by

$$\eta_{tp} = g\dot{m}_{tp}H_{tp}/L_{tp}. \quad (27)$$

Numerical Procedure and Analytical Terms

Numerical Procedure. By eliminating the pressure-gradient term from Eqs. (3) and (4) and using Eqs. (1) and (2), it reduces to the following equation after arranging,

$$(C_a + C_b)(d\alpha/ds) = \alpha(1 - \alpha)(\rho_l - \rho_g)r\omega^2(\partial r/\partial s) - (\alpha C_b/\rho_g)(\partial\rho_g/\partial s) + [(1 - \alpha)C_a - \alpha C_b] \times (1/A \sin\beta)(\partial A \sin\beta)/(\partial s) - F_i, \quad (28)$$

where C_a and C_b are given as a function of representative velocities w_1^* and w_2^*, respectively, listed in Table 2 as,

$$C_a = \{\alpha + C_V[\alpha/(1 - \alpha)](w_1^*/w_l)\}\rho_l w_l^2,$$
$$C_b = [(1 - \alpha)(\rho_g/\rho_l) + C_V(w_2^*/w_g)]\rho_l w_g^2. \quad (29)$$

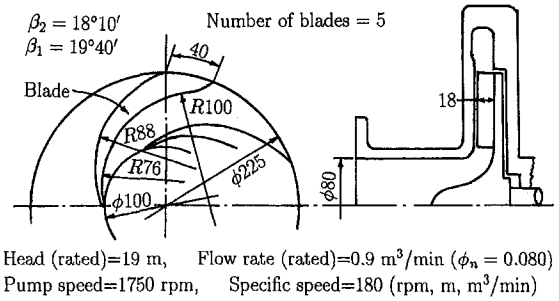

Fig. 3 Shape, dimensions and specifications of the centrifugal pump employed

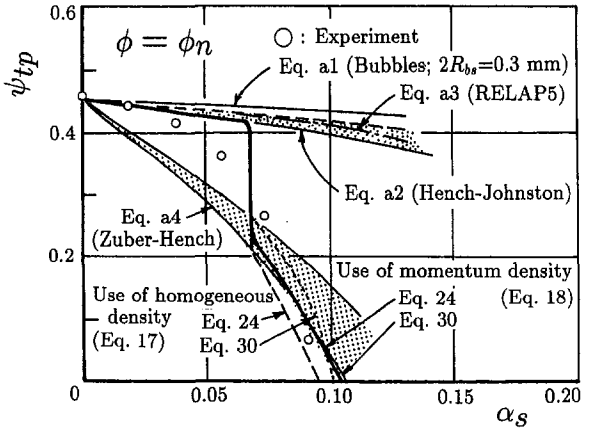

Fig. 4 Effects of interfacial and wall friction losses on pump head ψ_{tp}

For the one-dimensional conduit between the impeller, Eq. (28) is iteratively solved as follows:

(i) After assigning the values of ρ_g and R_b at the impeller inlet to every node, Eq. (28) is integrated to obtain distribution of α.

(ii) The velocities, w_g and w_l, are evaluated using Eqs. (1) and (2) with the α value obtained.

(iii) Pressure p is determined by substituting the values obtained, α, w_g, w_l, into Eq. (5), after the values of R_f and R_I are evaluated by the constitutive equations, $\partial p_{f,0}/ds$ by the measured values of $\Delta p_{f,0}$ and w_0 by Eq. (2) with $\alpha = 0$.

(iv) Revised values of ρ_g and R_b are calculated using the p value obtained.

(v) Revised value of α is obtained by substituting ρ_g and R_b into Eq. (28). Until the values of ρ_g and R_b are converged in the whole flow field, the calculation from steps (ii) to (v) are repeated.

After completing the calculations, the energy changes at the impeller exit are determined, as described in section for the velocity triangle, to yield the pump head with Eq. (24).

Analytical Terms. The described model is now applied to a special case of a radial-flow impeller pump of low specific speed (Minemura et al., 1985). The pump shape, dimensions and specification are shown in Fig. 3. The impeller is supposed to rotate with the rated speed 1750 rpm, and the air-water mixture to flow into the impeller without prerotation and without slip velocity between the phases at the impeller inlet. The angle of the streamline, β, is considered to be coincident with the angle of camber line of the impeller blade, and the values of the angle β and area A at every node are interpolated using a third-order spline-fit curve based on the measured values at several points. In this case, the inlet flow without prerotation yields an inlet flow angle different from the entrance blade angle determined from the blade geometry. To evaluate suitable, one-dimensional flow velocities from Eqs. (1) and (2), thus, the entrance blade angle is modified so as to meet the flow angle, since the effect of the difference between the blade and the flow inlet angle is already considered separately as the shock loss with Eq. (12). In the calculation, the inlet void fraction, α_s, is successively increased with the mass flow rate of the mixture constant to obtain two-phase-flow pump performance, in which the volumetric efficiency is supposed to remain unaltered. The volumetric efficiency varies due to the change in ϕ, but its variation is only a small when α_s is increased with ϕ constant (Murakami and Minemura, 1974). The bubble diameter at the pump inlet is estimated by an experimental formula (Minemura et al., 1985) considering the rotational speed of the impeller as $2R_b = 0.3$ mm. At the calculated conditions, no cavitation occurred in the experiment as well, and its suction pressure is 54 kPa at the rated flow rate.

Numerical Results and Discussions

Change of Energy at Impeller Exit. Predicted dimensionless pump head ψ_{tp} decreases at first gradually with an increase of inlet void fraction α_s, and then breaks down at $\alpha_s \approx 0.067$, before it degrades again gradually, as indicated with a thick solid line shown in Fig. 4, in which α_s is increased at the rated flow rate $\phi_n = 0.08$ with its mass flow rate unaltered [interfacial friction coefficient uses Eqs. ($a2$) and ($a4$) in Table 1, virtual mass coefficient Eq. ($b3$) in Table 2, and wall-friction multiplier Eq. ($c22$) in Table 3]. The results are seen to agree well with the experiment previously done by Minemura et al. (1985), indicated by the symbol ○. The agreement for the range of $0.04 < \alpha_s < 0.075$, however, is relatively poor. This is attributable to the fact that the three-dimensional effects of the flow within the impeller becomes dominant due to the occurrence of the local agglomeration of bubbles (Murakami and Minemura, 1974).

The pump head is defined with many assumptions for the transitional flow from the rotating frame to stationary frame of reference as described for Fig. 2. To check the validity of these assumptions, separate definitions of the pump are available: When the tangential component of absolute flow velocity at the impeller exit, c_{u3}, is known, theoretical pump head can be obtained as H_{th} $\{=u_2 c_{u3}/g\}$ for the inlet flow without prerotation. From this head, the subtractions of friction loss, Δh_f $\{= -\int (1/g\rho_{tp})(\partial p_f/\partial s)ds\}$, shock loss, Δh_{shock} $\{=\Delta p_{\text{shock}}/g\rho_{tp}\}$, rapid-expansion loss Δh_{exp}, and mixing loss Δh_{mix} yield the pump head in two-phase flow conditions, that is,

$$H_{tp} = u_2\overline{c_{u3}}/g - \Delta h_f - \Delta h_{\text{shock}} - \Delta h_{\text{exp}} - \Delta h_{\text{mix}}. \quad (30)$$

The head ψ_{tp}, dimensionless value of H_{tp} evaluated from Eq. (30), is superimposed by a thin solid line in Fig. 4 and is seen to agree well with the head calculated by Eq. (24) except for the region of considerably small value of ψ_{tp}, $\psi_{tp} < 0.05$, showing the validity of the assumptions made. In these calculations, the momentum density by Eq. (18) for the mean density of the mixture is used. When using the homogeneous density by Eq.

Table 3 Wall friction coefficient

No.	Constitutive equations	References
c1	$R_f = 1 + 21/X + 1/X^2$ $X = \{(1-x)/x\}\sqrt{\omega_l/\omega_g}$	Chisholm and Sutherland (1969)
c2	$R_f = (1-\alpha)^{-z}$	Akagawa (1974)
c21	$z = 1.5$	
c22	$z = 1.975 - 0.01006p$ (p: MPa)	

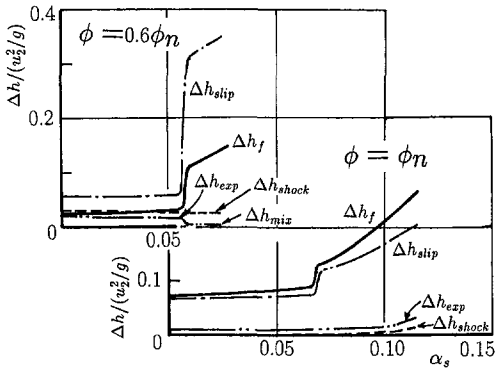

Fig. 5 Relationship between losses and inlet void fraction α_s

(17), however, it gives much different heads in the breakdown condition as shown by broken lines in Fig. 4. The difference of the density affects mainly the evaluation of Δh_f. Since, in such a breakdown condition, slip velocity between the phases becomes much greater as described later, it is found that the momentum density employed generally for separate flow model is more favorable to this case.

Dimensionless head losses of Δh_f, Δh_{shock}, Δh_{exp}, Δh_{mix} besides Δh_{slip} are changed according to inlet void fraction α_s, as shown in Fig. 5. The lower part of Fig. 5 shows the results for the rated flow rate, corresponding to Fig. 4. The head of friction loss, Δh_f, is the maximum among the losses and remarkably increases in the breakdown condition. The value of Δh_{slip} is large, too, and its increasing rate in $\alpha_s > 0.065$ is large as well. The greater value of Δh_{slip} in the breakdown condition is brought about by the greater increase in the relative flow velocity owing to the higher mean flow velocity, that is, the void fraction at the impeller exit region is so large that the liquid phase velocity is much greater than the gas phase velocity. The mixing loss, Δh_{mix}, is substantially zero, and the values of Δh_{exp} and Δh_{shock} are rather small.

The upper part of Fig. 5 shows the results for a lower flow rate of $\phi = 0.6\phi_n$. Owing to the smaller flow rate, the shock loss Δh_{shock} at $\alpha_s = 0$ is greater and Δh_f is smaller than those for ϕ_n, and their increasing rates due to α_s are smaller at $\phi = 0.6\phi_n$ than at $\phi = \phi_n$.

Effects of Constitutive Equations. By exchanging four kinds of the interfacial friction coefficients listed in Table 1, the heads obtained, ψ_{tp}, are superimposed in Fig. 4. The reduction of the heads becomes greater in the order of the drag coefficient for bubbles (a1), formula converted from drift flux model (a3), Hench-Johnston's formula (a2). Additionally, Zuber-Hench's formula for churn-turbulent flow (a4) yields considerably smaller head. From comparison with the experiment, Eqs. ($a2$) and ($a4$) are adopted in this study for the bubbly flow and churn-turbulent flow regimes, respectively. In this case, it is considered that the transition from the bubbly flow to churn-turbulent flow regime occurs in the range of $0.08 < \alpha < 0.14$ and that C_D value changes linearly within this range, the same as Furuya (1985). Since the transition is also connected with that for virtual mass coefficient, its effect is later discussed together.

Usage of the friction loss multiplier by Chisholm's formula (c1) or Akagawa's formula (c21), listed in Table 3, gives nearly the same head, but the use of formula (c22), expressing Martinelli and Nelson's experimental results under various pressure conditions, yields greater reduction of the head. This difference in head by (c1) and (c22) is denoted with shading in Fig. 4. For better agreement with the experiment, the formula (c22) is thus employed in the following.

By exchanging the virtual mass terms listed in Table 2, the resultant heads are compared in Fig. 6. Since the virtual mass is originated from transitional movement of a spherical particle, its coefficient C_V is generally supposed to need some modification except for the bubbly flow regime. In the following, four types of changes in the C_V value are investigated by considering that the transition takes place between the local void fractions of $\alpha_{cr,1}$ and $\alpha_{cr,2}$ as shown in an inset in Fig. 6: Type A is a linear reduction of C_V, type B a step reduction of C_V at $\alpha_{cr,2}$, and type C a constant value of C_V. Since the C_V value in RELAP code increases linearly in the range of $\alpha \leq 0.5$ and decreases in a quadratical curve in $\alpha > 0.5$, its modification, type D, is investigated as well, in which the C_V value takes the same maximum value with RELAP code at $\alpha_{cr,2}$. For all types, the critical values of $\alpha_{cr,1}$ and $\alpha_{cr,2}$ are taken so as to agree well with the experiment as 0.08 and 0.14, respectively.

When formula (b1), traditionally used for the virtual mass term is employed, the resultant head varies greatly depending on the type, that is, types B and C give the breakdown at $\alpha_s \approx 0.063$ though type A yields it at $\alpha_s = 0.125$. Formula (b3) (with $\lambda = 2$ in its original equation), which is given based on the consideration of frame indifference by Drew, yields a similar change of head irrespective of types. The value at breakdown is almost the same for types B and C; it is greater than A, and the reduction rate of the head in the breakdown condition increases in the order of C, B, A. RELAP type formula (b2), considering the frame indifference, yields a greater value of α_s for the breakdown than that by (b3), but the change is almost identical. From these results, formula (b3) with type A is adopted in this study by considering the frame indifference and common treatment for the C_V and C_D values in the transition region.

The transition region from bubbly flow to churn-turbulent flow regime is taken to be $0.03 \leq \alpha \leq 0.4$ for mixed-flow pumps by Furuya (1985) on his one-dimensional inviscid analysis. In the three-dimensional and inviscid bubbly flow model with fixed cavity (air-filled hollow) for this pump by Minemura and Uchiyama (1994a), the critical value of void fraction, at which the bubbles begin to coalesce and adhere to the neighboring wall, is assumed to be 0.2. Also it indicates that there is a starting of the cavity at $\alpha_s = 0.05$ and explosive expansion as to fill up the flow section at $\alpha_s = 0.0755$. This α_s value is in good agreement with the measured value for the breakdown. In their separate calculation (Minemura and Uchiyama, 1994b) based on a one-dimensional inviscid model, the transition region of $0.08 \leq \alpha \leq 0.1$ is employed to agree well with the experiment. As with these, the transition region varies depending on the kinds of analysis. In this study, therefore, the effect of variation in $\alpha_{cr,1}$ by only varying it (i.e., 0.06, 0.08, 0.10, and 0.12) is investigated with the $\alpha_{cr,2}$ value unaltered as $\alpha_{cr,2} = 0.14$. The results obtained are superimposed in Fig. 6, in which the α_s value at the breakdown is seen to be increased with the increase in $\alpha_{cr,1}$. The range between its maximum and minimum values

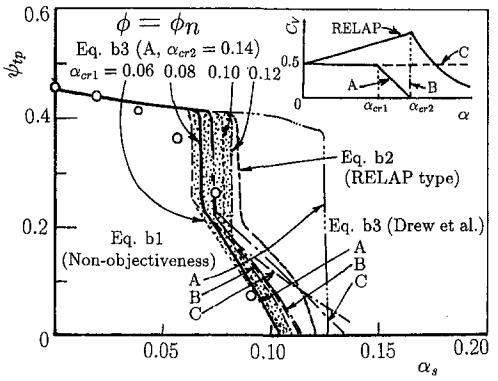

Fig. 6 Effects of virtual mass term and transit region of flow on pump head ψ_{tp}

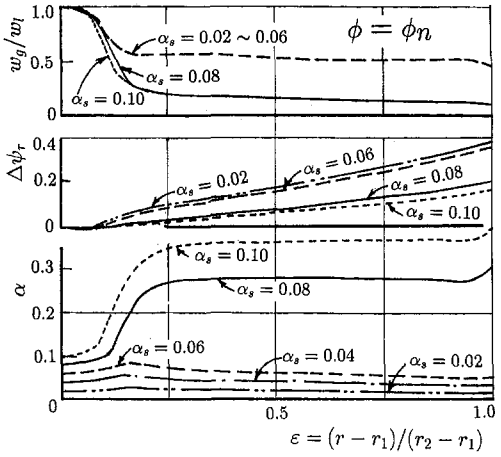

Fig. 7 Predicted radial distributions of void fraction α, pressure rise $\Delta\psi_r$ and slip ratio w_g/w_l

is denoted by shading, showing little difference of ψ_{tp} within the breakdown conditions irrespective of different values of $\alpha_{cr,1}$. From this comparison with the experiment, the transition region is taken to be $0.08 \leq \alpha \leq 0.14$ in the following. By using this value, it will be shown that the pump head is almost entirely predictable for different flow capacity.

Changes in Void Fraction, Pressure Rise and Slip Ratio in Impeller. Radial distributions of the void fraction calculated α are plotted in the lower part of Fig. 7, when inlet void fraction α_s is increased at the rated flow capacity. In smaller values of α_s as $\alpha_s \leq 0.06$, α tends to increase a little in the inlet region of $\epsilon_r \leq 0.15$ and then decrease gradually toward the exit. In greater values of α_s as $\alpha_s > 0.08$, α increases rapidly at $\epsilon_r \approx 0.12$, showing the change of flow regime from bubbly flow to churn-turbulent flow. The void fraction α also reaches its maximum at the exit, producing a greater value than three-times the inlet value. Such a relation is similar to the results calculated by Furuya's inviscid model (1985) though the rapid increase of α occurs at $\epsilon_r = 0.6$.

The middle part of Fig. 7 shows the pressure rise from the pump inlet, $\Delta\psi_r$. The $\Delta\psi_r$ value is increased linearly, and its increasing rate is quite similar to the others in the same flow regime, though the rate is decreased in the churn-turbulent flow.

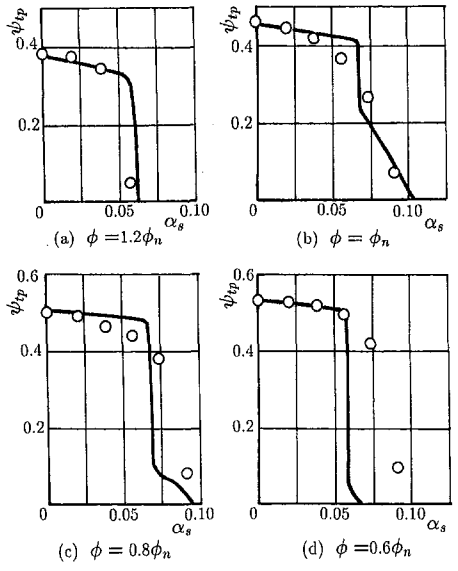

Fig. 8 Effect of flow capacity on pump head ψ_{tp}: predictions (lines) versus test (symbols)

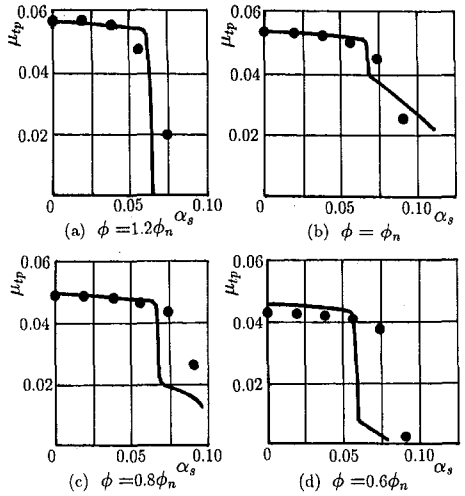

Fig. 9 Effect of flow capacity on shaft power μ_{tp}: predictions (lines) versus test (symbols)

The upper part of Fig. 7 shows the velocity ratio of the gas phase to the liquid phase, w_g/w_l. When $\alpha_s \leq 0.06$, w_g/w_l is decreased rapidly just after the inlet, and it takes a nearly constant value as $0.5 \sim 0.6$ in the region of $\epsilon_r \geq 0.25$. For the churn-turbulent flow regime, it takes a smaller value as $w_g/w_l \approx 0.15 \sim 0.20$ and tends to decrease monotonously toward the exit.

Effect of Flow Capacity. For the flow rates ϕ of 1.2, 0.8 and 0.6 times the rated flow capacity ϕ_n, the pump head predicted ψ_{tp} is plotted as the change due to α_s in Fig. 8. The change in the head as predicted for every capacity is seen to agree well with the experiment. Deficiency of the agreement in the low flow rate ($\phi = 0.06\phi_n$) may be caused by the simplifications using the one-dimensional assumption and zero values of pressure loss in the volute casing and leakage-flow loss through the running clearance of the open-impeller blades.

Figure 9 shows the relationship between predicted shaft power μ_{tp} and α_s. It can be seen that the calculated values agree well with the experiment within ±20 percent of the rated flow capacity ϕ_n.

Conclusions

By investigating the solution with a one-dimensional compressible and viscid two-fluid model for gas-liquid two-phase flow in a centrifugal pump, and energy changes in the transitional flows from the rotating frame to the stationary frame of reference, a special case of a radial-flow pump is numerically solved. By applying the constitutive equations for pipe flow in this case, Hench-Johnston's and Zuber-Hench's interfacial friction coefficients, Drew's virtual mass term, and Akagawa's friction loss multiplier are successfully adopted in such a way that the transition from the bubbly flow to churn-turbulent flow regime takes place in $\alpha_{cr,1} \leq \alpha \leq \alpha_{cr,2}$, in which the interfacial and virtual mass coefficients are supposed to change linearly. By using these relations, the resultant changes in pump head and shaft power due to the inlet void fraction are found to be fairly well predicted for the range of ±20 percent of the rated flow rate. Since the assumptions employed are approximately valid even for mixed-flow pumps with a moderate specific-speed, the described model is applicable to such pumps with somewhat modification to $\alpha_{cr,1}$ and $\alpha_{cr,2}$ values except for the low-flow-rate region, in which an excessive loss is caused by recirculating flow before or/and after the impeller.

References

Akagawa, K., 1974, *Gas/Liquid Two-Phase Flows* (in Japanese), Korona, Japan.

Calvin, E. S., et al., 1992, "Incorporation and Evaluation of a Generalized Two-Phase Degradation Model For Centrifugal Pumps in the RELAP5 Code," *Proceedings 5th International Topical Meeting on Reactor Thermal Hydraulics,* pp. 308–313.

Chisholm, D. and Sutherland, L. A., 1969, "Prediction of Pressure Changes in Pipeline Systems During Two-Phase Flow," *Institution of Mechanical Engineers/ Institution of Chemical Engineers Joint Symposium on Fluid Mechanics and Measurements in Two-Phase Systems.* Paper No. 4.

De Donno, S., et al., 1985, "The S.B.S. Project—Development of a Subsea Booster System for the Exploitation of Deep Water Oil Fields," *Proceedings 5th Deep Offshore Technology,* pp. B2-d49–d69.

Drew, D. & Lahey, R. T., 1987, "The Virtual Mass and Lift Force on a Sphere in Rotating and Straining Inviscid Flow," *International Journal of Multiphase Flow,* Vol. 13, No. 1, pp. 113–120.

Fujie, H., 1985, "A Study on Performance of Centrifugal Pumps Driven in Two-Phase Flow" (in Japanese), *Transaction of JSME,* Vol. 51, No. 471, pp. 3754–3759.

Furukawa, A., et al., 1990, "Some Experiments on Improving the Liquid/Gas Two-Phase Flow Performance of a Centrifugal Pump" (in Japanese), *Technical Report of Kyusyu University,* Vol. 63, No. 5, pp. 535–542.

Furuya, O., 1985, "An Analytical Model for Prediction of Two-Phase (Noncondensable) Flow Pump Performance," ASME JOURNAL OF FLUIDS ENGINEERING, Vol. 107, No. 1, pp. 139–147.

Furuya, O. and Maekawa, S., 1987, "An Analytical Model for Pump Performance in Condensable Two-Phase Flows," EPRI NP-5529M.

Hench, J. E. and Johnston, J. P., 1972, "Two-Dimensional Diffuser Performance with Subsonic, Two-Phase, Air-Water Flow," ASME *Journal of Basic Engineering,* Vol. 94, No. 1, pp. 105–121.

Mikielewicz, J., et al., 1978, "A Method for Correlating the Characteristics of Centrifugal Pumps in Two-Phase Flow," ASME JOURNAL OF FLUIDS ENGINEERING, Vol. 100, No. 4, pp. 395–409.

Minato, A., and Tominaga, K., 1988a, "Experiments of Steady State Heat and Torque of Centrifugal Pumps in Two-Phase Flow" (in Japanese), *Journal of Atomic Energy Society of Japan,* Vol. 30, No. 3, pp. 247–256.

Minato, A., 1988b, "Analysis of Head and Torque of Centrifugal Pumps in Two-Phase Flow (in Japanese), *Journal of Atomic Energy Society of Japan,* Vol. 30, No. 7, pp. 633–642.

Minemura, K., et al., 1985, "Characteristics of Centrifugal Pumps Handling Air-Water Mixtures and Size of Air Bubbles in Pump Impellers," *Bulletin of JSME,* Vol. 28, No. 244, pp. 2310–2318.

Minemura, K., and Uchiyama, T., 1993, "Three-Dimensional Calculation of Air-Water Two-Phase Flow in Centrifugal Pump Impeller Based on a Bubbly Flow Model," ASME JOURNAL OF FLUIDS ENGINEERING, Vol. 115, No. 4, pp. 766–771.

Minemura, K. and Uchiyama T., 1994a, "Three-Dimensional Calculation of Air-Water Two-Phase Flow in a Centrifugal Pump Based on a Bubbly Flow Model with Fixed Cavity," *JSME International Journal,* Series B, Vol. 37, No. 4, pp. 726–735.

Minemura, K. and Uchiyama, T., 1994b, "Numerical Prediction of Two-Phase-Flow Pump Performance by a Bubbly Flow Model with Fixed Cavity," *Proc. German-Japanese Symposium on Multi-Phase Flow,* KfK-5389, pp. 403–417.

Murakami, M. and Minemura, K., 1974, "Effects of Entrained Air on the Performance of a Centrifugal Pump (1st Report, Performance and Flow Conditions)," *Bulletin of JSME,* Vol. 17, No. 110, pp. 1047–1055.

Nilsson, K. A., 1977, "LWR Recirculation Pump Performance under Two-Phase Flow Conditions," *Proceedings Cavitation & Polyphase Flow Forum,* ASME, pp. 39–45.

Nishiyama, H. et al., 1989, "Flow Analysis of a Centrifugal Impeller in Bubbly Water Using Field Singularity Method," *Proc. 10th Australasian Fluid Mechanics Conference,* pp. 14.37–40.

Noghrehkar, G. R., et al., 1995, "Investigation of Centrifugal Pump Performance under Two-Phase Flow Conditions," ASME JOURNAL OF FLUIDS ENGINEERING, Vol. 117, No. 1, pp. 129–137.

Pfleiderer, C. and Peterman, H., 1986, *Strömungsmaschinen,* Springer-Verlag, p. 225.

RELAP5/MOD2 Code Mannual, 1985, NUREG/CR-4312, EGG-2396.

Tomiyama, A., et al., 1995, "Drag Coefficients of Bubbles (1st Report, Drag Coefficients of a Single Bubble in a Stagnant Liquid)" (in Japanese), *Transactions of JSME,* Vol. 61, No. 587, Series B, pp. 2357–2364.

Van Den Hove, P., and Geffraye, G., 1992, The CATHARE Code One-Dimensional Pump Model," *Proceedings 5th International Topical Meeting on Reactor Thermal Hydraulics,* pp. 1129–1137.

Zuber, N. and Hench, J. E., 1962, "Steady State and Transient Void Fraction of Bubbling Systems and Their Operating Limits. (Part I, Steady State Operation)," GE Rep. No. 62GL100.

A New Approach to Evaluate the Cavitation Erosion Power

Regiane Fortes Patella
Assistant Professor.

Jean-Luc Reboud
Research Engineer and Associate Professor.

Laboratoire des Ecoulements
Géophysiques et Industriels,
Institut de Mécanique de Grenoble,
BP 53, 38041 Grenoble, Cédex 9, France

The dynamic response of various materials exposed to liquid jet and pressure wave impacts was simulated making use of an elastoplastic solid model. Numerical pit profiles were compared to experimental ones produced in test materials by the cavitation of water, mercury, or sodium. It was found that a high pressure wave emission was the main factor contributing to the observed cavitation damage. A parametric study concerning the pressure wave phenomenon was proposed and some similarity laws were obtained. By using these laws, the corresponding impact hydrodynamic parameters can be deduced from the pit geometric characteristics and the material properties. Based on that study, histograms concerning impact hydrodynamic parameters were plotted as a function of impact number and/or pit eroded volume. The influence of the mean flow velocity, the geometric scale, the fluid characteristics, and the material properties on the flow aggressivity could be evaluated during the cavitation incubation period.

I Introduction

Cavitation is a phenomenon of great importance for the operation and reliability of hydraulic machinery. Especially, the risk of severe erosion of material from the inner surfaces in contact with the cavitating flow restricts the allowable operating conditions. Machinery manufacturers and users therefore need more knowledge on the physical effects causing cavitation erosion to determine the correct setting of operation limits with respect to cavitation, and to choose the appropriate construction materials and estimate their working life under given cavitation conditions.

In this context, Knapp (1955) proposed to use the material as a sensor to evaluate the cavitation erosion power of the flows. This idea is the basis of several experimental and theoretical works concerning prediction methods for cavitation damage (Hammit, 1979; Stinebring et al., 1980; Lecoffre et al., 1985; Kato et al., 1989; Avellan et al., 1991).

Based on this, the present study concerns the physical and numerical modeling of the impacts acting on a solid surface and the local plastic deformation caused on the material surface by imploding vapor structures. By comparing the solid surface deformations obtained numerically and experimentally, some local aspects of the hydrodynamic nature of the phenomenon responsible for cavitation erosion can be discerned.

In previous works (Reboud et al., 1991; Fortes-Patella and Reboud, 1993), the deformation of several materials exposed to jet impact or pressure wave emission was modeled making use of the SOLID numerical code. The resulting pit profiles were compared to several experimental indentations produced on different test materials by single spark-generated vapor bubbles or by cavitating flows in butterfly valves and Venturi apparatus. These comparisons and the analyses of the pit shapes indicated that a pressure wave emission within the liquid seems to be the main mechanism contributing to cavitation erosion. The emission of the pressure wave could be generated by spherical bubble and vortex collapses (as observed by Vogel et al., 1989; van der Meulen and van Renesse, 1993) as well as by microjet formation (Philipp et al., 1995).

To gain further knowledge concerning the pressure wave phenomenon and its interaction with a solid wall, a two-dimensional axisymmetric numerical simulation of the compressible fluid behavior was performed. By associating this FLUID model with the SOLID code it was possible to build a coupled fluid-structure model in the cavitation erosion field.

Another application of our study is related to the evaluation of cavitation aggressivity. Based on the numerical modeling, we developed and tested some programs:

(a) to determine flow aggressivity quantitatively by evaluating material surface damage,
(b) to study certain parameters and scaling laws that influence the cavitation erosion phenomenon.

This paper presents results obtained from an analysis of the influence of mean flow velocity, geometric scale, fluid properties, and solid characteristics on the cavitation erosion phenomenon.

II Numerical Models

II.1 SOLID Code. This study is based on a finite-element numerical code for calculating the plastic deformation of materials (Reboud and Guelin, 1988). The numerical model simulates the impact response of an elastoplastic medium subjected to different types of dynamic loading such as microjet or spherical overpressure wave impacts. The code involves a Lagrangian formulation and provides the complete transient evolution of strain, stress, and energy fields within the material and mainly the permanent surface deformation ("pits") resulting from axisymmetric high pressure impacts.

The material's behavior is described by four independent factors: Young's modulus E, Poisson's ratio ν, celerity of the longitudinal wave C_L (involving E, ν, and the material density), and a yield limit for the simple shear stress S_0. The model considers the classical laws of continuum mechanics (mass conservation; fundamental law of the dynamics) associated with a constitutive equation for the material which describes the elastoplastic hysteresis (Pegon and Guelin, 1987) (Fig. 1). This equation relates the stress rate to the metric, strain rate, and stress tensors. It is tangential to the elastic case for small stresses and tends asymptotically towards the pure plastic behavior described by the Von Mises criterion ($\mathrm{II}_\sigma = S_0^2$). Unloading and hysteresis cycles are taken into account by introducing the discrete memory concept. It is important to note that the code takes into account neither the mass loss nor the material fracture phenomena, and it can describe only the initial or incubation stage of cavitation erosion.

Contributed by the Fluids Engineering Division for publication in the JOURNAL OF FLUIDS ENGINEERING. Manuscript received by the Fluids Engineering Division July 17, 1995; revised manuscript received January 12, 1998. Associate Technical Editor: J. Katz.

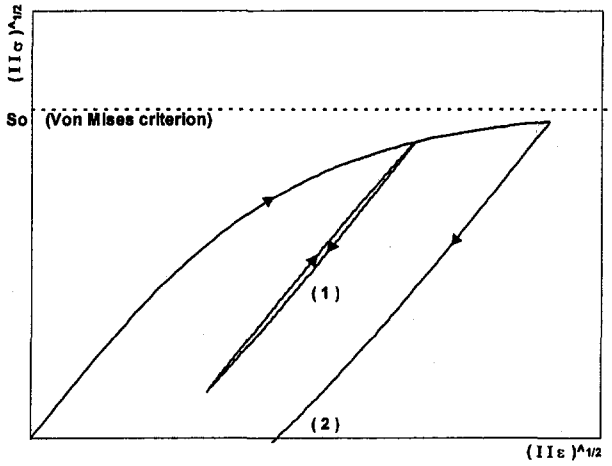

Fig. 1 Elastoplastic constitutive equation: example of a stress-strain diagram describing a complex loading-unloading cycle applied on solid surface. It can be seen the hysteresis cycle (1) and the permanent strain (2).

II.2 FLUID Model. Experimental and theoretical works, reported for example in Jones and Edwards (1960) and Fujikawa and Akamatsu (1980), indicated that bubble collapse is followed by the emission of an overpressure wave whose amplitude can exceed 1 GPa. To model the emission and propagation of a spherical pressure wave within the water, a two-dimensional axisymmetric numerical code was developed. The model uses an explicit finite-volume scheme (the Godunov numerical method) (Hirsch, 1990) to solve the unsteady Euler equations in cylindrical coordinates:

$$\frac{\partial U}{\partial t} + \frac{\partial F_1}{\partial r} + \frac{\partial F_2}{\partial z} + Q = 0$$

where

$$U = \begin{pmatrix} \rho \\ \rho Vr \\ \rho Vz \end{pmatrix} \; ; \quad F_1 = \begin{pmatrix} \rho Vr \\ p + \rho Vr^2 \\ \rho VrVz \end{pmatrix}$$

$$F_2 = \begin{pmatrix} \rho Vz \\ \rho VrVz \\ p + \rho Vz^2 \end{pmatrix} \; ; \quad Q = \begin{pmatrix} \rho Vr/r \\ \rho Vr^2/r \\ \rho VrVz/r \end{pmatrix}$$

V_r is the radial component of the velocity and V_z is the normal component of the velocity.

The code takes into account the hypothesis of compressible, monophase, and nonviscous fluid, and it includes a barotropic empirical state equation for the liquid (Knapp et al., 1970):

$$\frac{p + B}{P_\infty + B} = \left(\frac{\rho}{\rho_\infty}\right)^n$$

where $B = 3.10^8$ Pa and $n = 7$ for water. It applies a Roe solver developed by Chevrier (1990) to calculate the Riemann problem and the Thompson method (1987, 1990) to treat boundary conditions.

A description of the Fluid code is given in Fortes-Patella (1994).

II.3 Fluid-Structure Code Coupling. It is important to study the interaction between the fluid and the neighboring structures when performing comprehensive analyses of the cavitation erosion phenomenon. In this context, Zhang et al. (1993) and Miligan et al. (1993) use a fluid BEM code coupled with a structural FEM code to study the collapse of a cavitation bubble near a rigid and a compliant wall, respectively. These studies indicated a significant change in bubble behavior and the pressure field applied on the solid wall. Reference may also be made to the work of Curnier and Ridah (1987) concerning liquid microjet impact on an elastic-plastic solid and the study of Rosemblatt et al. (1979), which simulated the impact of water drops at different velocities on a plastic surface.

In this study, the numerical codes presented above, concerning the elastoplastic deformation of the material and wave propagation in the liquid, were coupled by an iterative solution to model the effects of the fluid-structure interaction. Calculations are performed at each time step in both the fluid and the solid. The common boundaries between solid and fluid have the same discretization. The mesh used for fluid calculation is assumed to be immobile while the displacement of the solid mesh is calculated by the structure code and represents the indentation profile.

At each time step, pressures calculated by the FLUID model are passed to the SOLID code and used to generate loads along the material surface. The SOLID code then calculates the displacement and velocity of each node of the structure. The radial and normal velocities obtained at the solid boundary are used by the FLUID code as new boundary conditions for the next time step.

It is worth noting that the coupled code takes into account a geometric approximation by considering a fixed mesh for the FLUID model and a movable one for the SOLID code.

Both codes consider symmetry conditions along the axis of revolution. The emission of the pressure wave is "artificially" imposed at a distance "L" to the solid wall, on the axis of the

Nomenclature

Solid

C_L = celerity of longitudinal waves (m/s)
E = Young's modulus (N/m^2)
h = pit depth (m)
$h_{\lim}$ = minimal depth of the analyzed pits (m)
II_σ, II_ϵ = second invariant of the deviatoric part of the stress tensor σ or strain tensor ϵ (N/m^2)
$R_{10\%}$ = pit radius at 10% of h (m)
S_0 = yield limit for simple shear stress (N/m^2)
ν = Poisson's ratio

Liquid

f = bubble production rate (s^{-1})
p = static pressure (N/m^2)
S = Strouhal number = $f\phi/v$
v = flow velocity (m/s)
ϕ_{throat} = Venturi diameter (m)
λ = geometric scale ratio = $\phi_{(1)}/\phi_{(1/3)}$
ρ = fluid density (kg/m^3)
σ = cavitation number
$\sigma = (P_{\text{downstream}} - P_{\text{vapor}})/P_{\text{upstream}}$

Pressure Wave Emission

C_{liq} = celerity of pressure wave (m/s)
dt = wave passage time (s)
L = distance emission center—solid boundary (m)
P = peak pressure applied on solid surface (N/m^2)
P_m = maximum emission overpressure (N/m^2)
P_∞ = initial fluid pressure (N/m^2)
r = radial distance from wave emission center (m)
ρ_∞ = initial fluid density (kg/m^3)

Histograms

N_d = pit number rate (pits/cm^2/s)
V_d = volumetric damage rate (μm^3/cm^2/s)

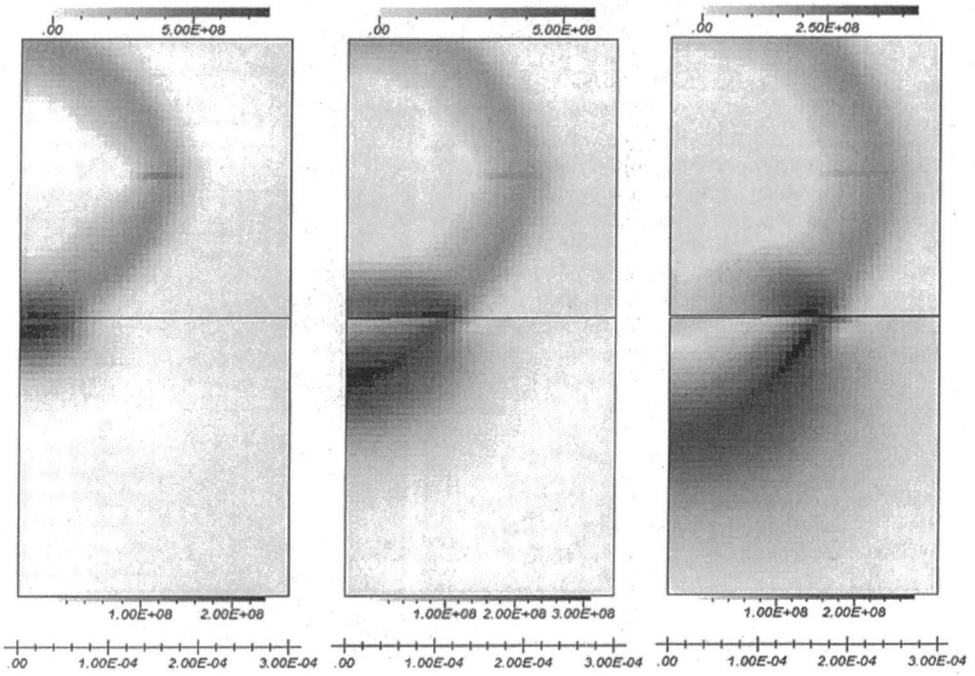

Fig. 2 Coupled Fluid-Structure code: this figure illustrates the pressure field in the water (above) and the stress field II_σ (second invariant of the deviatoric part of the stress tensor) in the material (below) at three different times. Results are given in N/m^2. The coordinates are cylindrical axisymmetric and only one meridian half-plane is presented.

liquid domain. The pressure distribution applied to simulate the wave emission follows a Gaussian law and it is taken as:

$$p(t) = P_\infty + f_{\text{gauss}}(dt) \cdot P_m$$

where "P_m" is the maximum emission overpressure, "P_∞" the initial pressure within the stagnant fluid, and "dt" is the wave passage time. To avoid the existence of a singular point at the wave emission center, this pressure distribution is imposed on three different points located at the domain center.

Moreover, the other boundaries are considered to be nonreflecting with respect to the pressure wave in the liquid and the longitudinal and transversal stress waves in the solid.

For instance, Fig. 2 presents results concerning the modeling of the impact of a pressure wave emitted in water on a 316L stainless-steel solid surface. The hydrodynamic parameters used in the calculation are: $P_m = 3$ GPa; $P_\infty = 0.1$ MPa; $dt = 0.1$ μs; $L = 0.15$ mm; resulting maximum pressure applied on the solid surface is $P \sim 1$ GPa.

The figure illustrates, in axisymmetric cylindrical coordinates, the pressure field in the liquid (above) and the strain fields in the solid (below) at three different times. The emission of the pressure wave, which propagates within the water and hits the solid surface, can be observed. The response of the material to the wave impact is also given and it can be seen that the longitudinal wave celerity within the solid is approximately four times the wave celerity in the liquid ($C_L = 5830$ m/s; $C_{\text{liq}} \sim 1500$ m/s).

According to the FLUID model, the speed of propagation depends on the pressure, and the wave shape varies significantly over the propagation distance at high pressure amplitudes. Moreover, also at high pressure, the dependence of pressure amplitude on radial distance deviates from the inverse proportional relation $p \sim r^{-1}$ (given by Fujikawa and Akamatsu, 1980) and tends toward $p \sim r^{-1.5}$ (Fig. 3).

The calculations concerning fluid/structure interaction indicated a weak effect of wall displacement on the propagation and reflection of the pressure wave. Therefrom, a simplified theoretical model was used to evaluate the loading applied on the solid surface during the pressure wave impact.

II.4 Simplified Pressure Wave Model. In the theoretical modeling of the pressure wave impact a spherical pressure wave was considered, characterized by four hydrodynamic parameters: the peak pressure applied on the solid surface "P"; the

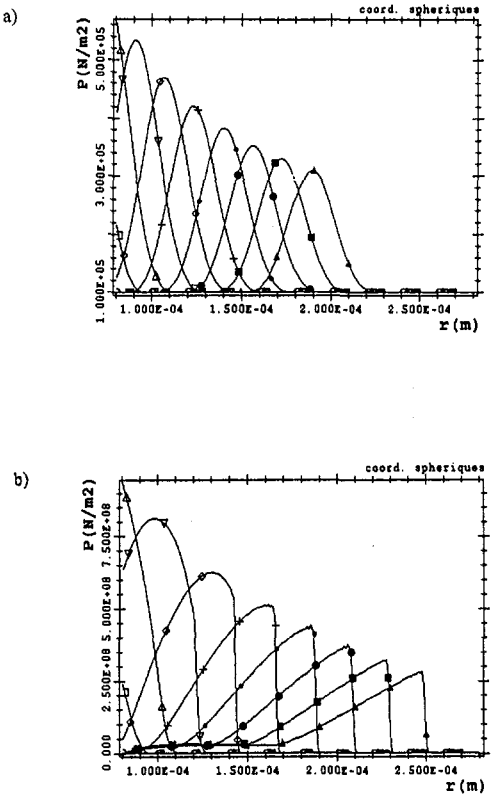

Fig. 3 Pressure wave simulation: pressure distribution in liquid at different times for (*a*) $P_m = 0.5$ MPa ($P \sim r^{-1}$; $C_{\text{liq}} \sim 1400$ m/s) and (*b*) $P_m = 0.5$ GPa ($P \sim r^{-1.5}$; $C_{\text{liq}} \sim 1600$ m/s)

wave passage time "dt"; the distance "L" between the solid surface and the wave emission center, which represents the impact size; and the wave propagation celerity "C_{liq}," which is considered constant, about the sound velocity in the liquid (Fig. 4).

According to Fujikawa and Akamatsu (1980), the wave amplitude is assumed to be inversely proportional to the distance "r" to the emission center. Moreover, based on the conservation of wave energy, the wave passage time "dt" is considered constant. During this time, the pressure distribution follows a Gaussian law. The resulting time-dependent stresses applied on a neighboring solid surface during wave impact were deduced by this theoretical model and were used by the SOLID code as the boundary conditions at the wetted surface of the structure. The transient pressure distribution applied on solid surface is given by:

$$p(r, t) = P \cdot f_{\text{gauss}}(r/L, t/dt)$$

where P is the peak pressure applied on material surface (Fig. 4).

This simplified model is the basis of the following studies concerning the analysis of pit profiles and the evaluation of cavitation aggressivity.

III Analysis of Erosion Pit Profiles

The first application of the numerical model was to analyze the shape of the pits produced by cavitation erosion during the incubation period. By using the numerical code, the response of several materials exposed to pressure wave emission was modeled and the resulting pit profiles were compared to the experimental ones.

The first aim of these analyses is to discern the hydrodynamic characteristics of the mechanism responsible for material damage. The main objective was to deduce the amplitude of the pressure applied on the solid surface and, thus, the pressure emitted by the cavitating structures by comparing the numerical and experimental results.

III.1 Experimental Studies. This involved analyzing several experimental results obtained in different research laboratories:

(a) In our initial study (Reboud et al., 1991), we analyzed pit profiles produced in test materials (copper 99.99%; aluminum) by single spark-generated vapor bubbles in pure water under stagnant conditions. Experiments were performed by EdF (Electricité de France) and ENSTA (Ecole Nationale Supérieure des Techniques Avancées) in a pressurized tank (Dorey and Nienaltowska, 1988);

(b) Fortes Patella and Reboud (1992) performed another sequence of numerical simulations of cavitation erosion pits observed experimentally on 8″ and 3″ butterfly valves (Dorey et al., 1991). Cavitation erosion of 316L polished stainless-steel samples was evaluated for different water flow velocities [$\sigma = 0.27$];

(c) CETIM (Centre Technique des Industries Mécaniques) performed experiments using a Venturi type apparatus. Several materials (some stainless steels and cupro-aluminum) were tested under different water cavitation conditions [$\sigma = 0.64$; $20 \leq v \leq 70$ m/s]. The first numerical analyses concerning these experiments were presented in Fortes-Patella and Reboud (1993) and Reboud et al. (1994).

(d) EdF used the same Venturi type duct geometry to study the cavitation erosion caused by sodium flows (400°C) (Dorey and Rascalou, 1992). The flow velocities vary between 25 m/s and 40 m/s, and the target material considered is 316L stainless steel;

(e) Two similar Venturi sections (scale $\phi^{1}_{\text{throat}} = 40$ mm and $\phi^{1/3}_{\text{throat}} = 13.3$ mm) were also used by the Institute of Mechanics of Grenoble (LEGI) to study the erosion of 316L stain-

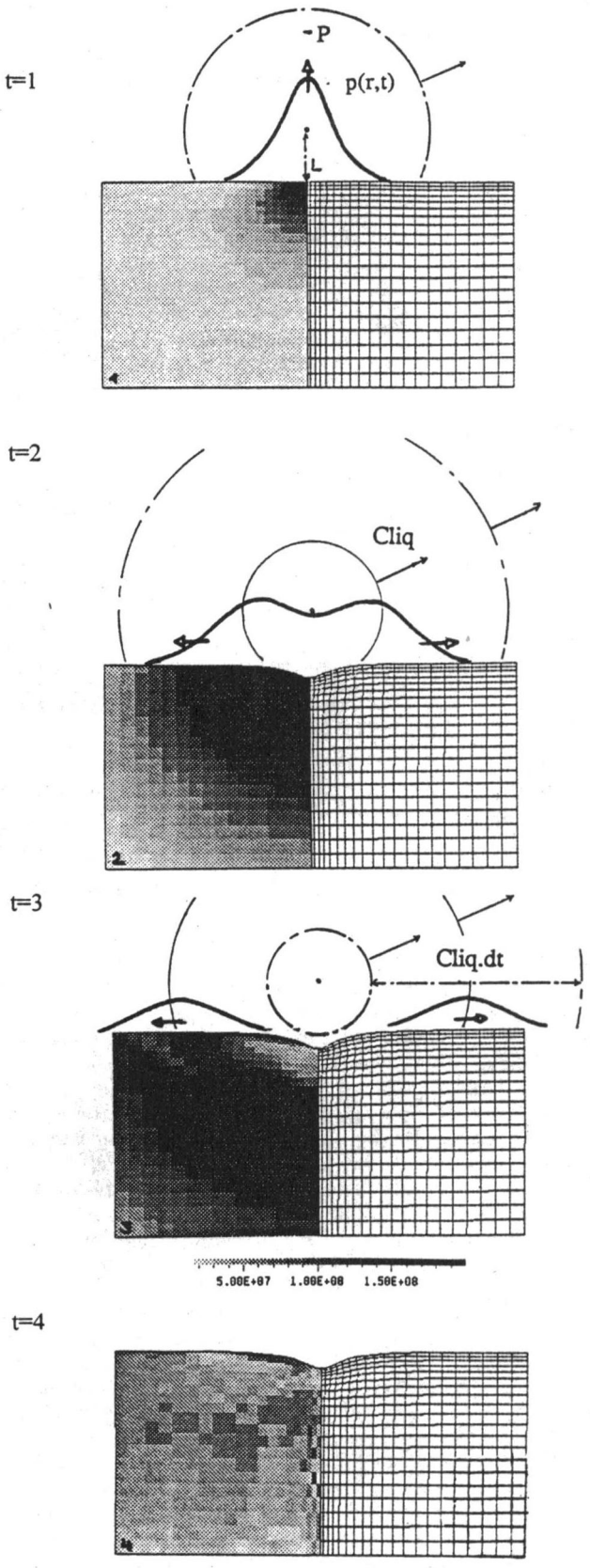

Fig. 4 Transient evolution of the solid state during the impact of a spherical pressure wave: these figures illustrate the load applied on the wetted surface of the solid, the resulting solid deformation, and (at left) the transient evolution of the stress field II_σ in the material at different times. The last figure ($t = 4$) shows the permanent surface deformation and the associated residual stress field in the solid. The coordinates are cylindrical axisymmetric.

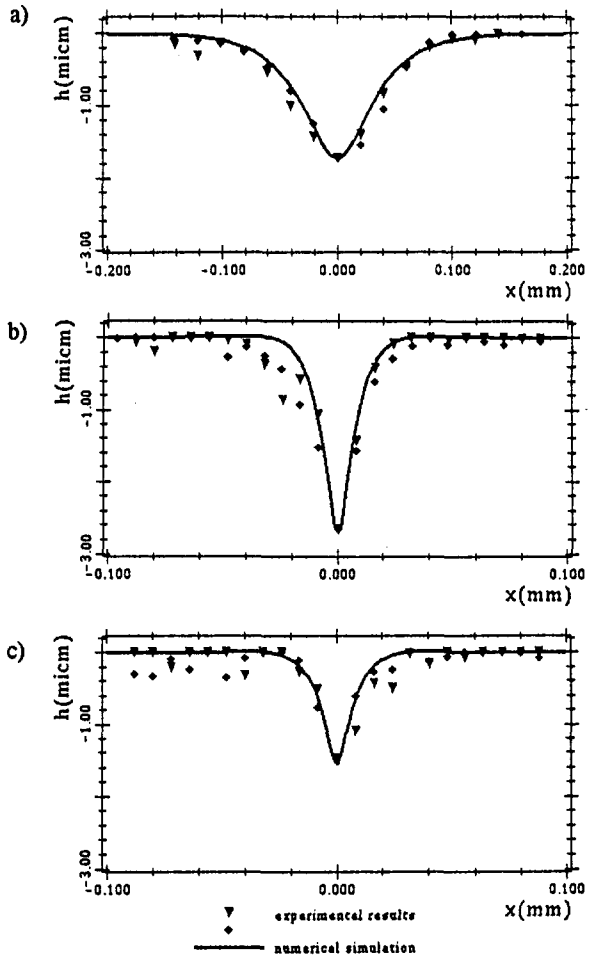

Fig. 5 Comparison between modeled pit profiles and experimental ones observed in 316L stainless-steel samples eroded in a Venturi type duct by the cavitation of (*a*) water (v = 40 m/s; P = 2.4 GPa; L = 33 μm; dt = 0.24 μs), (*b*) mercury (v = 6 m/s; P = 4.3 GPa; L = 7.5 μm; dt = 0.06 μs), and (c) sodium (v = 38 m/s; P = 4.2 GPa; L = 7 μm; dt = 0.03 μs)

less steel caused by mercury cavitation [v = 6 m/s; σ = 0.64] (Franc et al., 1992).

Its worth noting that the experimental tunnels are equipped with pressure transducers for the measurement of pressures upstream and downstream of the test sections. The cavitation number σ can be determined and was kept constant during experiments. Concerning the EdF water experiments, the upstream pressure can reach 16 bar. Water is demineralized and deaerated. The air content is controlled with an oxygenmeter and the oxygen rate is maintained under 3 ppm. For the CETIM test rig, the oxygen rate is 10 ppm (saturated water).

The erosion of the sample surfaces was measured by a UBM16 laser profilometer device (EdF and IMG test samples) or by making use of a three-dimensional roughness meter (CETIM experiments). Surface state measurement consists in determining the pit profiles observed on the eroded sample and in evaluating their geometric characteristics, i.e., the depth "h", the radius "$R_{10\%}$" and the volume of each indentation (Fig. 5). According to the manufacturer of the laser profilometer, the accuracy for depth measurements "h" is 0.06 μm. Pit radius measurements are made with a 1 μm resolution. The roughness meter is less accurate and the resolution for pit radius measurements is about 20 μm.

Using the numerical code described above, impact hydrodynamic properties were found by trial and error to obtain modeled pit profiles similar to the experimental ones. In this context,

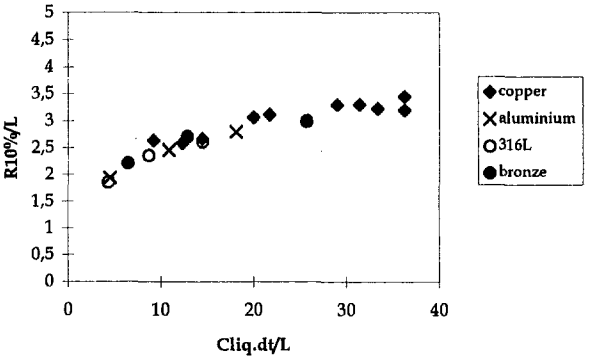

Fig. 6 Illustration of the ratio $R_{10\%}/L$ as a function of the number ($C_{liq} \cdot dt/L$) for different materials (results obtained from numerical simulations)

two kinds of dynamic loading acting on the solid surface were simulated: the impingement of a microjet (Reboud et al., 1991) and the impact of a pressure wave.

According to our analyses, indentations are generally axisymmetric and the best agreement between experimental and numerical pit shapes is obtained by pressure wave simulation. Figure 5 illustrates, for example, some comparisons between numerical pit profiles and experimental ones observed on 316L stainless-steel samples eroded in the Venturi apparatus by the cavitation of water (v = 40 m/s), mercury (v = 6 m/s), and sodium (v = 38 m/s). To model pit profiles, successive simulations for different wave passage times "dt", distances "L" and pressure amplitude "P" were performed in order to obtain the best fit with experimental data. In compliance with the duration of pressure pulses on solid boundaries estimated in several studies (Fujikawa and Akamatsu, 1980; Vogel et al., 1989), the numerical simulations consider wave passage times varying from 10 ns to 5 μs and peak pressure "P" about 1 to 5 GPa. In all of the cases analyzed, the numerical simulations agree well with experimental measurements and this indicates that the pressure wave emission associated with the collapses of vapor volumes seems to be the phenomenon responsible for the damage observed.

III.2 Similarity Laws. Considering the results obtained by analysis of erosion pit profiles, a dimensional and parametric study of the pressure wave phenomenon was performed. The purpose of this study was to use numerical calculations to evaluate the influence of material properties (S_0, C_L, E, and ν) and pressure wave characteristics (P, L, dt, and C_{liq}) on pit geometry (described by h and $R_{10\%}$).

Based on numerical calculations, dimensional analysis of the pressure wave phenomenon led to the following relationships:

(a) the first one indicates that the ratio $R_{10\%}/L$ is not a function of material's characteristics and of pressure "P". To a good approximation, the ratio $R_{10\%}/L$ is only function of the number $C_{liq} \cdot dt/L$ (Fig. 6):

$$\frac{R_{10\%}}{L} = f_1\left(\frac{C_{liq}}{L}\,dt\right)$$

(b) the second relationship is:

$$\frac{h}{L} = \left(\frac{P}{S_0}\right)^n \frac{S_0}{E} A^{1-n}$$

where

$$A = f_2\left(\frac{C_L}{L}\,dt,\ \nu\right) \quad \text{and} \quad n = f_3\left(\frac{C_{liq}}{L}\,dt,\ \frac{C_L}{L}\,dt\right).$$

The functions f_1, f_2, and f_3 (Figs. 6 and 7) were determined

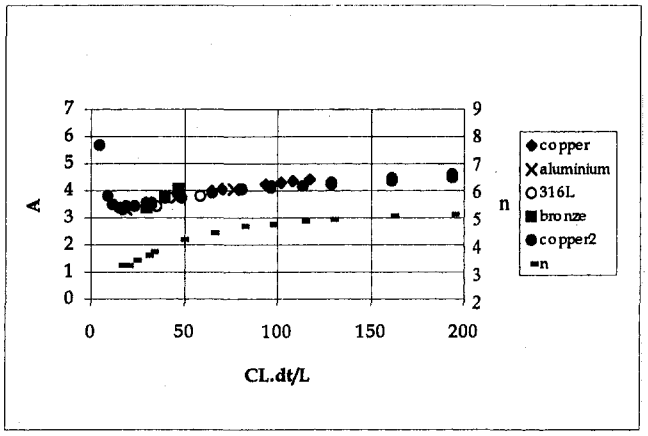

Fig. 7 The dimensionless number *A* as a function of the parameter ($C_L \cdot dt/L$) for different materials, and an example of "*n*" distribution for $C_L/C_{liq} = 4$ (results obtained by numerical simulation)

from numerical simulations concerning several materials and different wave characteristics.

Summarizing, these similarity laws relate the impact hydrodynamic conditions to the geometry of the pit profiles. For a given material:

$$L = g_1(R_{10\%}, dt, C_{liq})$$

$$P = g_2(h, C_{liq}, R_{10\%}, dt)$$

where only the function "g_2" depends on the material's static characteristics. These laws allow the impact values "P" and "L" to be deduced from the pit characteristics "h" and "$R_{10\%}$" for a given wave passage time "dt". It is worth saying that the pair (P, L) is unique for each pit (characterized by h, $R_{10\%}$) for a given material and wave passage time.

These relationships were fully tested by the authors (Fortes Patella, 1994) and were used by Bourdon et al. (1996) to transpose the cavitation erosion rate on Francis turbines from model to prototype. Pereira et al. (1995) also applied this method to perform a statistical analysis of transient cavities based on pitting measurements.

Application of the results and laws found therefrom proved to be useful for qualitative analysis of cavitation phenomena and their aggressivity.

At present, certain parameters taken into account in this study are not well determined. Indeed, there are many uncertainties concerning the order of magnitude of the wave passage time, which can vary from 10 ns to 5 μs (Fujikawa and Akamatsu, 1980; Vogel et al., 1989). To evaluate the wave passage time "dt" several hypotheses reported in Fortes Patella and Reboud (1992) were tested. The results presented in this paper are obtained by considering the dimensionless number $C_{liq} \cdot dt/L \sim$ constant.

To simulate solid plastic deformation, the numerical code uses material static properties, and to estimate uncertainties for calculated pressure amplitudes more information is needed concerning the mechanical behavior of materials at very high strain rates and their dynamic properties.

Therefore, the aim of the following part of this paper is to propose a qualitative analysis of the influence of material properties, fluid characteristics, geometric scale, and flow velocity on cavitation aggressivity.

IV Hydrodynamic Cavitation Intensity

IV.1 Histograms of Aggressivity. Prediction of cavitation erosion was the subject of various studies leading to the development of several models and hypotheses regarding the influence of material properties, flow velocity, fluid characteristics, and geometric scale (Lecoffre, 1995). Recently, Kato et al. (1995) proposed a quantitative erosion prediction scenario based on the value of impact forces and pressure spectra observed on a solid surface submitted to cavitation structure collapse. They predict pressure distribution on a solid surface by using analytical and empirical equations concerning a partially cavitating hydrofoil. The mass loss phenomenon is also studied in detail by Franc et al. (1994) who predicts removal of material from pressure pulse measurements by introducing metallurgical parameters.

In this context, based on the pressure calculated by numerical simulation, this paper proposes a new approach for evaluating cavitation erosion power by making use of "3D" pressure pulse histograms.

These analyses are based on the experimental results (in the form of pitted specimens) supplied by EdF, CETIM, and IMG-LEGI, that are described above. A special software was developed to scan the surface of the pitted samples. This code gives the location and size (depth, diameter, volume) of each individual pit and also the hydrodynamic parameters of the impact (P, dt, and L) which generated the pit. The hydrodynamic characteristics are deduced from pit geometry by making use of the similarity laws presented above (Section III.2).

These results are used to produce pit histograms for various pitted specimens tested under different hydrodynamic conditions. The histograms show the number of pits (or the eroded volume) as a percentage of the total number (or the total eroded volume) classified according either to the pit depth and pit radius or to the peak amplitude of the corresponding pressure wave and the distance of its center from the wall (Fig. 8). In this paper only the (P, L) histograms are presented. The corresponding ($R_{10\%}$, h) histograms are reported in Fortes Patella (1994).

To plot these histograms, only indentations whose depths are greater than a minimum value "h_{lim}" are considered. These are defined for each case as a function of the material and state of the analyzed sample surface (to count isolated indentations). For low values of "P" and "L", the resulting pits are too small and are not taken into account by the histograms. This cut-off problem leads to an "artificial" decrease in the number of pit at small distances "L" and pressure "P". This tendency can be noticed on all the histograms analyzed. Belahadji et al. (1992) also pointed out the cut-off problem met during their experimental investigation of cavitation erosion pits. At the present time, a statistical study of 3D histogram behavior is being performed in order to try to overcome the effect of the cut-off problem.

IV.2 Effect of Material Properties. In previous studies (Fortes Patella and Reboud, 1993; Reboud et al., 1994) we analyzed the influence of material properties on cavitation aggressivity. Based on the experimental results concerning three different materials (316L, U50 and CuAl) submitted to the same cavitating water flow in a Venturi at $v = 40$ m/s, various histograms were plotted considering impact hydrodynamic properties and pit geometry. Figure 9 and Table 1 summarize the results obtained. Different "h_{lim}" values were considered in order to obtain similar pit number rates "Nd" (i.e., the ratio between number of pits, analyzed eroded surface, and test duration) for all the materials analyzed ($Nd \sim 0, 4$ pits/cm^2/s).

In spite of the different material characteristics, the hydrodynamic histograms ($P \times L$) obtained in all the analyzed cases were similar, i.e., the range of pressure amplitudes P and distances L deduced from pit geometries were the same for different materials ($P \sim 2$ GPa; $L \sim 10$ μm). In this way, according to our numerical and experimental studies, the hydrodynamic characteristics (P, L) of the cavitation erosion phenomenon seem not to depend on the solid properties. Therefore, this method of analysis can be used to predict, from tests concerning

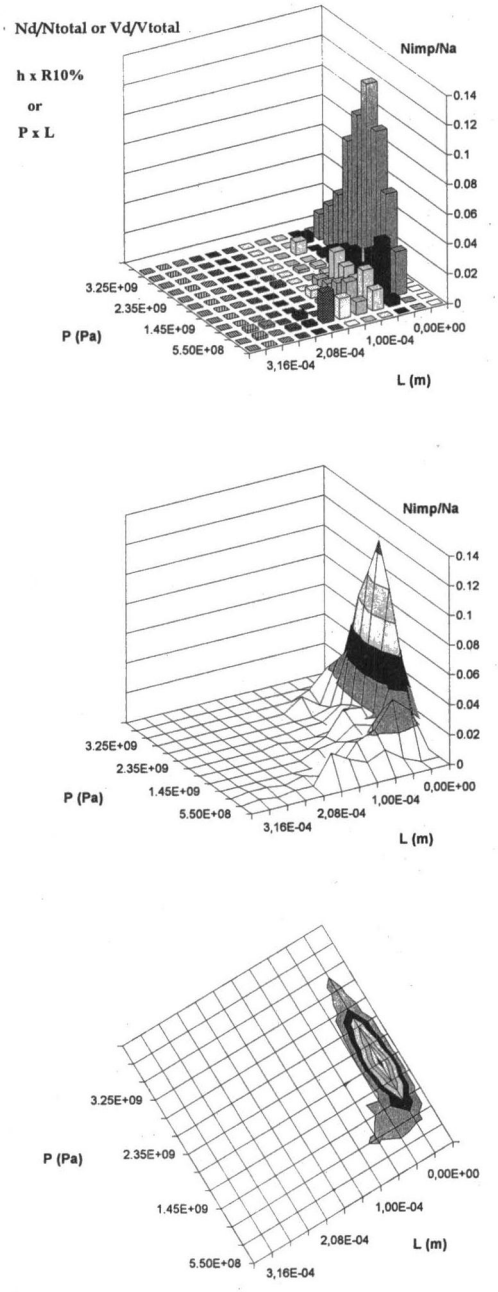

Fig. 8 Three views of a "3D" histogram. This illustrates the ratio between the number of pits for each class of "*P*" and "*L*" (total number of class = 12 × 12), and the total number of pits.

a reference material, the damage to other materials exposed to similar cavitation conditions:

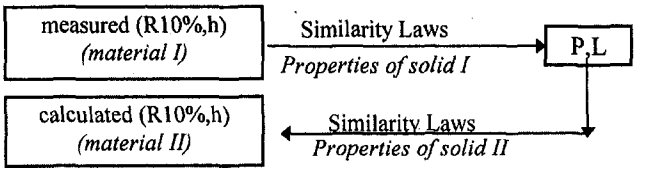

IV.3 Geometric Scale Effect. Length scale effects on cavitation erosion were studied by Kato (1975) who proposed scaling laws based on the concept of mean depth penetration rate. More recently, Franc et al. (1992) also studied the scale effects on two cavitating Venturis of different sizes in a mercury tunnel.

a)Nd=0.38 pits/cm^2/s; Vd=4843 μm^3/cm^2/s; h_{lim}= 0.2μm

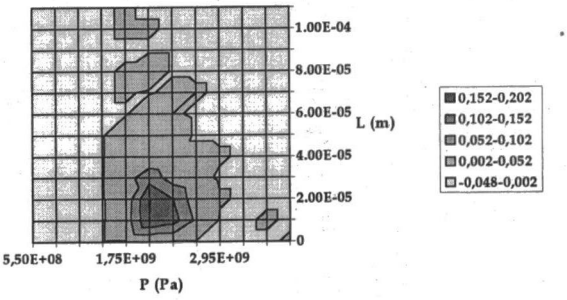

b) Nd=0.36 pits/cm^2/s; Vd =2079 μm^3/cm^2/s; h_{lim} = 0.25μm

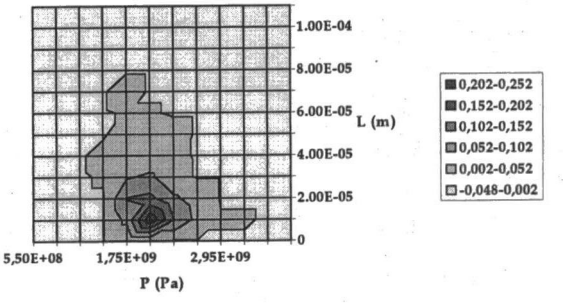

c) Nd = 0.49 pits/cm^2/s; Vd =1525 μm^3/cm^2/s; h_{lim}=0.07 μm

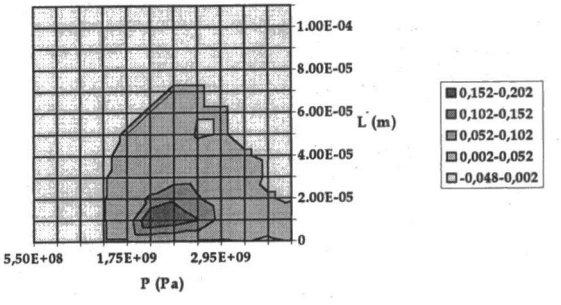

Fig. 9 Pit number (*P*, *L*) histograms—erosion caused by water cavitation (*v* = 40 m/s) in a Venturi duct: (*a*) 316L stainless steel, (*b*) Cupro-aluminium (CuAL), and (*c*) U50 stainless-steel sample

Table 1 Material's static properties taken into account by numerical calculations

	316L	U50	CuAl
S_0 (MPa)	398	566	389
E (GPa)	200	200	150
C_L (m/s)	5830	5830	4838

On the basis of some experimental results concerning similar Venturi type ducts (scales 1 and $\frac{1}{3}$; λ = 3), the influence of the geometric scale on mercury cavitation aggressivity was analyzed.

a) Nd = 1.9 pits/cm^2/s; Vd = 13 μm^3/mm^2/s; h_{lim} = 0.5 μm

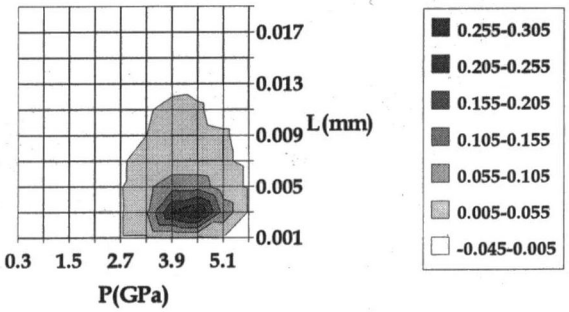

b) Nd = 0.1 pits/cm^2/s; Vd = 12 μm^3/mm^2/s; h_{lim} = 1.5 μm

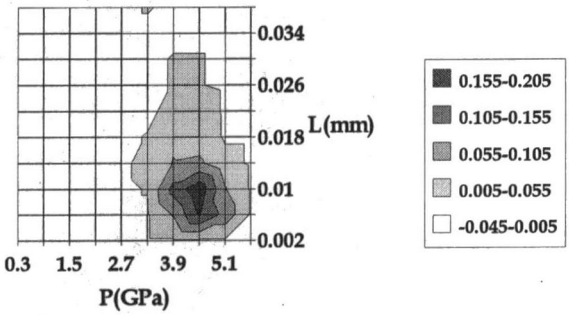

Fig. 10 Pit number (*P*, *L*) histograms—316L stainless-steel erosion caused by mercury cavitation (*v* = 6 m/s) in two Venturi ducts: (*a*) scale $\frac{1}{3}$ and (*b*) scale 1

Figure 10 summarizes certain results concerning the main erosion areas in each Venturi section for identical exposure times. From the analysis it appears that:

- The pit number rate "*Nd*" (i.e., the ratio between number of pits, analyzed eroded surface, and test duration) is higher for the small test section: $Nd_1/Nd_{1/3} \sim 1/\lambda^{2.7}$. This result agrees with the scaling laws proposed by Lecoffre (1995). Indeed, according to the Strouhal similarity law, the bubble production rate "*f*" should vary as $1/\lambda$. Hence, because of the λ^2-similarity in areas, pit density should vary as $1/\lambda^3$. Moreover, the theory forecasts the equality of the volumetric damage rates "*Vd*" (i.e., the ratio between deformed volume, the analyzed eroded surface and the test duration) which is well corroborated by our analyses.
- On average, the maximum pressure "*P*" applied to the solid surface is the same in both Venturis ($P \sim 4.5$ GPa) and the distance "*L*" is smaller for the small test section ($L_1 \sim 3 \cdot L_{1/3}$). Due to the increase in pressure amplitude with the distance of the emission center, these results indicate that the energy emitted during vapor volume collapse is greater for the large test section.

More experimental studies are required to verify and improve this initial analysis concerning the scale effect.

a) v = 40m/s; Nd = 0.28 pits/cm^2/s; Vd = 3321 μm^3/cm^2/s

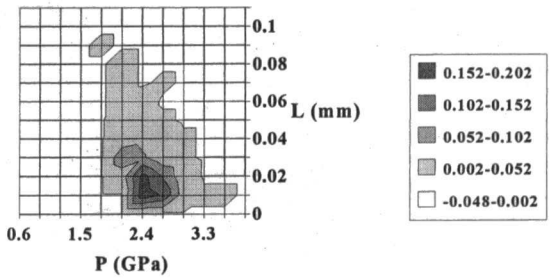

b) v = 6 m/s; Nd = 0.23 pits/cm^2/s; Vd = 1546 μm^3/cm^2/s

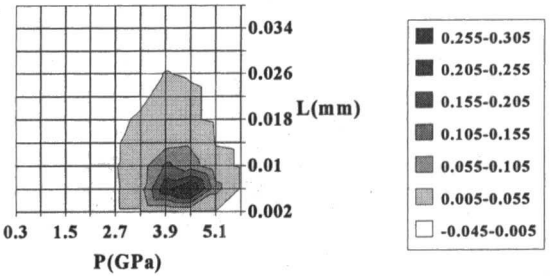

c) v = 28.5 m/s; Nd = 0.5 pits/cm^2/s; Vd = 956 μm^3/cm^2/s

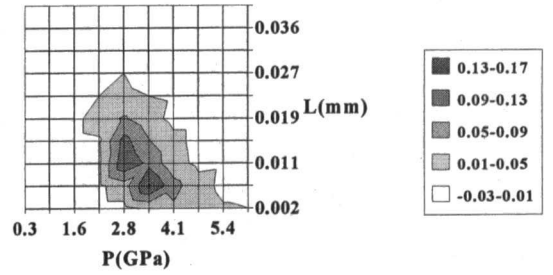

Fig. 11 Pit number histograms (316L SS) concerning Venturi tests in (*a*) water (C_{liq} = 1450 m/s, h_{lim} = 0.5 μm), (*b*) mercury (C_{liq} = 1450 m/s, h_{lim} = 1 μm), and (*c*) sodium (C_{liq} = 2365 m/s, h_{lim} = 0.75 μm) flows.

IV.4 Influence of Fluid Characteristics. In addition to geometric scale effects, changes in flow velocity and in fluid are also of great practical importance. The present section presents some comments on the domain of fluid influence on cavitation erosion. By comparing the results concerning mercury, water, and sodium tests in the same Venturi geometry, a qualitative analysis could be performed concerning the influence of liquid properties on cavitation erosion power.

Figure 11 illustrates, for example, the pit number histograms concerning flow velocities of 40 m/s in water, 6 m/s in mercury and 28.5 m/s in sodium. Furthermore, the peak wall pressure seems to be twice as high in mercury compared to water and the distance of the center of the pressure wave seems to be approximately one half. The same ratios are close to 1.5 and $\frac{1}{1.5}$ for the comparison between sodium and water. Indeed, pits due to water cavitation are generally wider but not as deep as ones observed during mercury and sodium cavitation.

a) Pit number (P,L) histogram

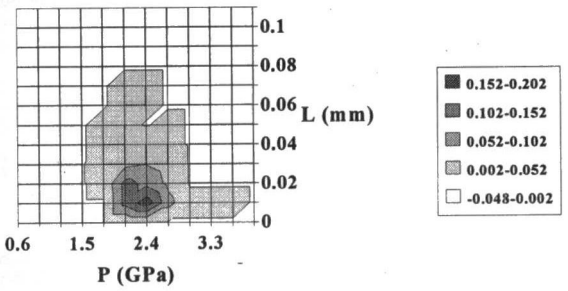

b) Pit eroded volume (P,L) histogram

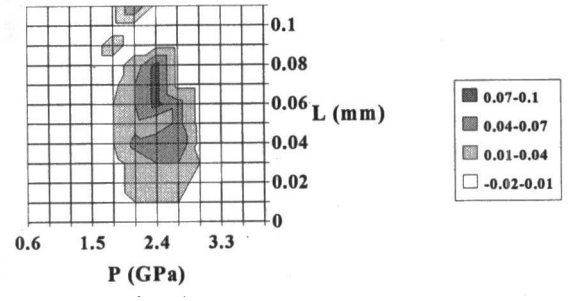

Fig. 12 Histograms concerning 316L stainless-steel erosion due to water cavitation in a Venturi duct at v = 55 m/s; Nd = 1.49 pits/cm^2/s; Vd = 17830 μm^3/cm^2/s

a) v = 28m/s , Nd = 0.08 pits/cm^2/s , Vd = 222 μm^3/cm^2/s

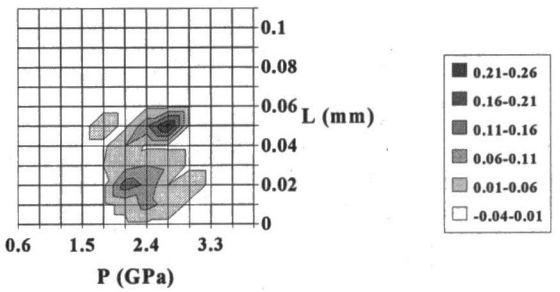

b) v = 40 m/s , Nd = 0.4 pits/cm^2/s , Vd = 4177 μm^3/cm^2/s

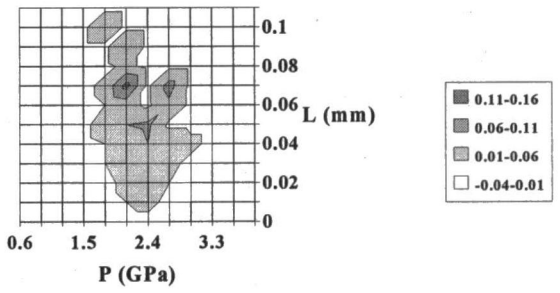

Fig. 13 Pit eroded volume (P, L) histograms concerning 316L stainless-steel erosion due to water cavitation in a Venturi type duct (h_{lim} = 0.1 μm)

Because of the difference in flow velocity the similarity conditions are not respected and this analysis remains illustrative of the application of our prediction method.

IV.5 Effect of Flow Velocity. The effect of flow velocity on pitting rate was examined first by Stinebring et al. (1980) in the case of aluminum eroded by water cavitation. In previous works (Fortes-Patella and Reboud, 1993; Reboud et al., 1994), the influence of flow velocity on cavitation aggressivity was evaluated by analyzing some pit number histograms concerning the erosion of 316L stainless steel caused by water cavitation in a Venturi type apparatus at different flow velocities ($20 \leq v \leq 70$ m/s). From this analysis it appears that the maximum relative quantity of pits always occurs for a same class of pits ($P \sim 2.5$ GPa; $L \sim 10$ μm, $R_{10\%} \sim 45$ μm; $h \sim 0.5$ μm), independently of the flow velocity (Figs. 12 and 13). This result indicates that the peak pressure applied on the solid wall seems not to be proportional either to ρv^2 or to $\rho C_{liq} v$ as could be assumed by the water hammer theory. In further work, based on experimental results, we will improve the physical analysis in order to relate the flow pressure gradient (and, consequently, the flow velocity) with the peak pressure applied on the material.

For all the material tested, the pitting rate increases approximately as $Nd \sim v^5$, which agrees with the classical power laws reported in Stinebring et al. (1980) and Kato et al. (1989). So, an increase in flow velocity seems to arise merely the number, but almost not the depth of the resulting pits.

To extend this study, the corresponding pit volume histograms were plotted. Figure 12 illustrates, for example, both pit number and pit volume histograms concerning water flow velocity v = 55 m/s. The representation of pit volume increases the weight given to impacts corresponding to large distance values L. In spite of the small number of large pits (created by the pressure waves emitted far from the solid surface), they provide the most significant deformed volume.

By analyzing the eroded pit volume histograms obtained for different flow velocities, it can be seen that the total deformed volume rises approximately as $Vd \sim v^7$, which can be explained by the increase in the number of wide pits with flow velocity. Figure 13 illustrates the results concerning two different flow velocities v = 28 m/s and v = 40 m/s.

Conclusion

- According to this local study of the cavitation erosion phenomenon, especially the analysis of indentation shapes, pressure wave impact seems to be the mechanism responsible for the damage observed on various material samples submitted to different cavitation conditions.
- A coupled fluid/structure code was developed and a first analysis of the interaction between pressure wave propagation and impact response of the solid was proposed.
- By using a simplified model of the pressure wave phenomenon, it was possible to deduce similarity laws which relate, for a given material, the impact hydrodynamic characteristics (P, L) to the geometry of the pit profiles ($R_{10\%}$, h). These laws are the basis of a new method to evaluate hydrodynamic cavitation intensity by analyzing aggressivity histograms.
- The analyses of different eroded material samples exposed to cavitating flows indicated that flow aggressivity does not depend on the characteristics of the solid. Therefore, pressure pulse histograms might be used, associated with metallurgi-

cal fracture criteria, to predict the erosion rate of several materials submitted to the same cavitation conditions.

- Evaluation of the geometric scale effect indicates that pit density "Nd" varies as $1/\lambda^3$. This result agrees with the theory proposed before by Lecoffre et al. (1985).
- The first analyses concerning specimens eroded by the cavitation of different fluids indicated a significant influence of the fluid characteristics on cavitation aggressivity. Further experimental analyses are necessary to extend this initial study.
- Some pit volume histograms concerning different flow velocities were presented. They are relevant because deformed volume is directly related to the amount of energy necessary to erode the material surface. They pointed out the important role of the wider pits on the total eroded volume.
- A qualitative study of the cavitation erosion power was proposed. Further work, requiring more experimental data, is in progress to improve the statistical and quantitative analysis of the cavitation erosion phenomenon.

Acknowledgments

This research was supported by EdF-"Electricité de France," and by a doctoral grant from the "Conselho Nacional de Desenvolvimento Cientifico e Tecnologico," Brazil. The authors wish to express their gratitude to EdF, to CETIM-"Centre Technique des Industries Mécaniques," France, and to IMG Cavitation Group which supplied the experimental results.

References

Avellan, F., Dupont, Ph., and Farhat M., 1991, "Cavitation Erosion Power," *Cavitation '91,* ASME FED Vol. 116, Portland, pp. 135–140.

Belahadji, B., Franc, J. P., and Michel, J. M., 1991, "A Statistical Analysis of Cavitation Erosion Pits," ASME JOURNAL OF FLUIDS ENGINEERING, Vol. 113, pp. 700–706.

Bourdon, P., Farhat, M., Simoneau, R., Pereira, F., Dupont, P., Avellan, F., and Dorey, J. M., 1996, "Cavitation Erosion Prediction on Francis Turbines—Part 1: Measurements on the Prototype," *Proc. IARH,* Valence, E. Cabrera et al., eds, Hydraulic Machinery and Cavitation, pp. 534–543.

Chévrier, P., 1990, "Simulation Numérique de l'Interaction Arc Electrique—Ecoulements Gazeux dans les Disjoncteurs Moyenne et Haute Tension," Doctoral Thesis, Institut National Polytechnique de Grenoble, France.

Curnier, A., and Ridah, S., 1987, "Impact of a Liquid Micro-Jet on a Elastic-Plastic Solid Surface," *Proc. 7th Int. Conf. on Erosion by Liquid and Solid Impact,* Cambridge, pp. 2.1–2.10.

Dorey, J. M., and Nienaltowska, E., 1988, "Empreintes dues à l'Implosion de Bulles Isolées: Etude Paramétrique Expérimentale," *La Houille Blanche n°7/8.*

Dorey, J. M., Le, Q., and Tura, F., 1991, "A New Test Procedure Using Plant and Polished Samples to Quantify Cavitation Aggressivity on Industrial Components," *Cavitation '91,* ASME FED Vol. 116, Portland, pp. 141–147.

Dorey, J. M., and Rascalou, 1992, "Similitude en Erosion de Cavitation: Essais sur une Roue de Pompe en Eau et en Sodium," *La Houille Blanche n°7/8.*

Fortes-Patella, R., and Reboud, J. L., 1992, "Analysis of Cavitation Erosion by Numerical Simulation of Solid Damage," *Proceedings of the 16th Symposium of the IARH,* Sao Paulo, Brazil.

Fortes-Patella, R., and Reboud, J. L., 1993, "Numerical Analysis for Evaluating Cavitation Erosion Phenomenon," *Cavitation & Multiphase Flow Forum,* ASME FED Vol. 153, Washington, pp. 105–110.

Fortes-Patella, R., 1994, "Analyse de l'Erosion de Cavitation par Simulations Numériques d'Impacts," Doctoral Thesis, Institut National Polytechnique de Grenoble, France.

Franc, J. P., Michel, J. M., and Nguyen-Trong, H., 1992, "An Experimental Investigation of Scale Effects in Cavitation Erosion," *Proceedings of 2nd Conference on Cavitation, IMechE,* Edinburgh, pp. 111–119.

Franc, J. P., Michel, J. M., Nguyen-Trong, H., and Karimi, A., 1994, "From Pressure Pulses Measurements to Mass Loss Prediction: The Analysis of a Method," *Proc. 2nd Int. Symp. on Cavitation,* Tokyo, pp. 231–236.

Fujikawa, S., and Akamatsu, T., 1980, "Effects of Non-Equilibrium Condensation of Vapor on the Pressure Wave Produced by Collapse of a Bubble in Liquid," *Journal of Fluid Mechanics,* Vol. 97-3, pp. 481–512.

Hammit, F. G., 1979, "Cavitation Erosion: the State of the Art and Predicting Capability," *Applied Mechanics Reviews,* Vol. 32-6, pp. 665–675.

Hirsch, 1990, *Numerical Computation of Internal and External Flows, Vol II: Computational Methods for Inviscid and Viscous Flows,* Wiley, New York, NY.

Jones, I. R., and Edwards, D. H., 1960, "An Experimental Study on the Forces Generated by Collapse of Transient Cavities in Water," *Journal of Fluid Mechanics,* Vol. 7, pp. 596–609.

Kato, H., 1975, "A Consideration on Scaling Laws of Cavitation Erosion," *International Shipbuilding Progress,* Vol. 22, No. 253, pp. 305–327.

Kato, H., Ye, Y. P., and Maeda, M., 1989, "Cavitation Erosion and Noise Study on a Foil Section," *Int. Symp. on Cavitation Noise and Erosion in Fluid Systems,* ASME FED Vol. 88, San Fransisco, pp. 79–88.

Kato, H., Konno, A., Maeda, M., and Yamaguchi, H., 1995, "Possibility of Quantitative Prediction of Cavitation Erosion Without Model Test," *Proceedings of Int. Symp. on Cavitation, CAV'95,* Deauville, pp. 289–296.

Knapp, R. T., 1955, "Recent Investigations of the Mechanics of Cavitation and Cavitation Damage," *Trans. ASME,* Vol. 75, pp. 1045–1054.

Knapp, R. T., Daily, J. T., and Hammit, F. G., 1970, *Cavitation,* McGraw Hill, New York, NY.

Lecoffre, Y., Marcoz, J., Franc, J. P., and Michel, J. M., 1985, "Tentative Procedure for Scaling Cavitation Damage," ASME *Inter. Symp. on Cavitation in Hydraulic Structure and Turbomachinery,* Albuquerque.

Lecoffre, Y., 1995, "Cavitation Erosion, Hydrodynamics Scaling Laws, Practical Method of Long Term Damage Prediction," *Proceedings of Int. Symp. on Cavitation, CAV'95,* Deauville, pp. 249–256.

Milligan, C. D., Duncan, J. H., and Zhang, S., 1993, "Numerical Simulations of Experiments on the Interaction of a Cavitation Bubbler and a Compliant Wall," *Cavitation and Multiphase Flow Forum,* Washington, ASME FED Vol. 153, pp. 137–142.

Pegon, P., and Guelin, P., 1987, "On Thermomechanical Zaremba Schemes of Hysteresis," *Res. Mechanica,* Vol. 21, pp. 21–34.

Pereira, F., Avellan, F., and Dorey, J. M., 1995, "Cavitation Erosion: Statistical Analysis of Transient Cavities," *Proceedings of Int. Symp. on Cavitation, CAV'95,* Deauville, pp. 257–264.

Philipp, A., Ohl, C. D., and Lauterborn, W., 1995, "Single Bubble Erosion on a Solid Surface," *Proceedings of Int. Symp. on Cavitation-CAV'95,* Deauville, pp. 297–303.

Reboud, J. L., and Guelin, P., 1988, "Impact Response of an Elasto-plastic Medium," *Mech. Research Communications,* Vol. 4.

Reboud, J. L., Fortes-Patella, R., and Dorey, J. M., 1991, "Simulation of Cavitation Impact Damage on an Elastoplastic Solid," *Cavitation and Multiphase Flow Forum,* ASME FED Vol. 109, Portland, pp. 187–191.

Reboud, J. L., Fortes-Patella, R., Le Fur, B., and David, J. F., 1994, "Experimental Investigations and Numerical Analyses on Cavitation Erosion," *Proceedings of 2nd Int. Symp. on Cavitation,* Tokyo, pp. 191–196.

Rosemblatt, M., Ito, Y. M., and Eggum, G. E., 1979, "Analysis of Brittle Target Fracture from a Subsonic Water Drop Impact," *Erosion: Prevention and Useful Applications,* ASTM STP 664, W. F. Adler, ed., pp. 227–254.

Stinebring, D. R., William Holl, J., and Arndt, R. E., 1980, "Two Aspects of Cavitation Damage in the Incubation Zone: Scaling by Energy Considerations and Leading Edge Damage," ASME JOURNAL OF FLUIDS ENGINEERING, Vol. 102, pp. 481–485.

Thompson, K. W., 1987, "Time Dependent Boundary Conditions for Hyperbolic Systems I," *Journal of Computational Physics,* Vol. 68, pp. 1–24.

Thompson, K. W., 1990, "Time Dependent Boundary Conditions for Hyperbolic Systems II," *Journal of Computational Physics,* Vol. 89, pp. 439–461.

van der Meulen, J. H. J., and van Renesse, R. L., 1993, "The Collapse of Laser-Induced Bubbles Near a Solid Boundary and the Generation of Pressure Pulses," *Cavitation and Multiphase Flow Forum,* Washington, ASME FED Vol. 153, pp. 127–132.

Vogel, A., Lauterborn, W., Timm, R., 1989, "Optical and Acoustic Investigations of the Dynamics of Laser-Produced Cavitation Bubbles Near a Solid Boundary," *Journal of Fluid Mechanics,* Vol. 206, pp. 299–338.

Zhang, S., Duncan, J. H., and Chahine, G. L., 1993, "The Final Stage of the Collapse of a Cavitation Bubble Near a Rigid Wall," *Journal of Fluid Mechanics,* Vol. 257, pp. 147–181.

Numerical Study of the Steady-State Tip Vortex Flow Over a Finite-Span Hydrofoil

Chao-Tsung Hsiao
Research Assistant.

Laura L. Pauley
Associate Professor.

Department of Mechanical Engineering,
Penn State University,
University Park, PA 16802

The flow over a finite-span hydrofoil creating a tip vortex was numerically studied by computing the full Navier-Stokes equations. A good agreement in pressure distribution and oil flow pattern was achieved between the numerical solution and available experimental data. The steady-state roll-up process of the tip vortex was described in detail from the numerical results. The effect of the angle of attack, the Reynolds number, and the hydrofoil planform on the tip vortex was investigated. The axial and tangential velocities within the tip-vortex core in the near-field wake region were greatly influenced by the angle of attack. A jet-like profile in the axial velocity was found within the tip-vortex core at high angle of attack, while a wake-like profile in the axial velocity was found at low angle of attack. Increasing the Reynolds number was found to increase the maximum axial velocity, but only had a slight impact on the tangential velocity. Finally, a swept hydrofoil planform was found to attenuate the strength of the tip vortex due to the low-momentum boundary layer traveling into the tip vortex on the suction side.

1 Introduction

It is well known from classical wing theory that a tip vortex is generated for all finite-span lifting surfaces. The tip-vortex flow is a very complicated three-dimensional viscous flow phenomenon. The details of the flow in the tip region can have a major effect on the performance of lifting surfaces in both aerodynamic and hydrodynamic applications. For example, tip vortex cavitation is of major concern for marine propellers since it is an important source of noise. In order to avoid or control tip vortex cavitation, the underlying flow physics, especially the pressure field, needs to be fully understood.

Since the tip vortex is often considered detrimental, extensive studies have been conducted to understand the formation process of the tip vortex in order to alleviate, if not eliminate, the effects of the tip vortex. In early years, most studies which have focused on the tip vortex problem have been either experimental or analytical efforts. Analytical studies are confined primarily to inviscid tip-vortex roll-up or viscous decay of an isolated vortex. Although the experimental studies have extensively explored many aspects of the tip-vortex flow, some physical measurements such as the pressure field in the tip-vortex core are incomplete. Therefore, a numerical study can serve as a good supplement to experiments in complex flows. Numerical solution of the Navier-Stokes equations was not extensively utilized in early years, especially for hydrodynamic applications, due to the limitations of computational resources. In recent years, however, numerical simulation has been more frequently applied.

Early numerical simulations usually made assumptions to simplify the Navier-Stokes equations to the Parabolized Navier-Stokes equations (PNS) (Shamroth and Briley, 1979 and Tsai et al., 1988) or the Thin-Layer Navier-Stokes equations (TLNS) (Mansour, 1984, Srinivasan et al., 1988). However, for separated flows with large secondary velocities such as lift-off of the tip vortex, the streamwise diffusion effect neglected by both PNS and TLNS is significant. Previous studies using PNS or TLNS were unable to determine the tip-vortex formation adequately. Recently, Dacles-Mariani et al. (1993) carried out a full Navier-Stokes simulation with the one-equation Baldwin-Barth turbulence model (1990) and applied the inflow and outflow boundary conditions from the experimental data. The particular tip-vortex studies were conducted on a rectangular planform with a NACA0012 cross section at a chord Reynolds number of 4.6 million. Although they showed an improvement over numerical results obtained by previous researchers, the tip-vortex strength was still underpredicted. The less than perfect agreement between computations and experiments was attributed to the insufficient grid density near the tip vortex and the transition/turbulence modeling.

The goal of the present study is to advance the understanding of tip-vortex formation, especially in the near-field wake region. To achieve this goal, a three-dimensional incompressible Navier-Stokes flow solver, INS3D-UP, developed by Rogers et al. (1991) is applied in the current study. In order to obtain an appropriate grid distribution and sufficient grid density for the near-field wake region and the tip-vortex core, a combination of algebraic and elliptic grid generation techniques is implemented.

2 Numerical Implementation

2.1 Geometry and Grid Generation. The current study considers a uniform flow past a rectangular hydrofoil having a NACA0015 airfoil cross section with a round tip and an aspect ratio Ar equal to 3.0 (based on semi-span) without twist or taper. The edge shape of the round tip is formed by rotation of the hydrofoil section about its camber line based on the local thickness.

From previous numerical studies, it is known that a sufficiently dense grid must exist near the tip-vortex core and the hydrofoil surface in order to adequately resolve the tip vortex and predict boundary-layer effects. Although a conventional elliptic grid generation technique (Sorenson, 1989) can be used to create a smooth grid, it is rather difficult to specify the clustering of the grid inside the computational domain. Conversely, algebraic grid generation techniques can easily create the desired grid distribution, but this grid is usually not smooth. A combination of algebraic and elliptic grid generation techniques is therefore implemented. This grid generation scheme is ac-

Contributed by the Fluids Engineering Division for publication in the JOURNAL OF FLUIDS ENGINEERING. Manuscript received by the Fluids Engineering Division February 19, 1996; revised manuscript received January 26, 1998. Associate Technical Editor: M. S. Triantafyllou.

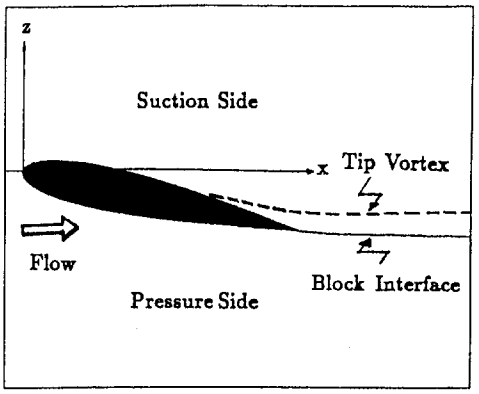

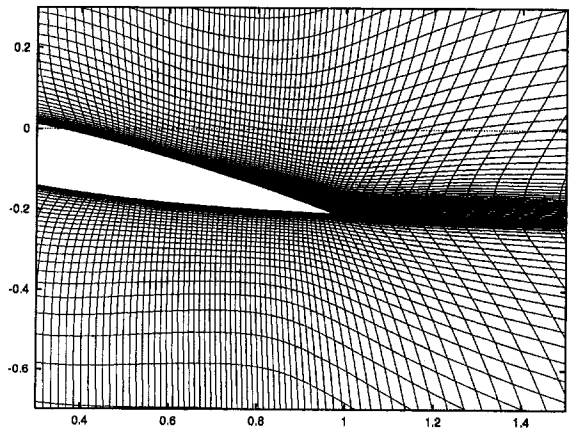

Fig. 1 The grid clustering in the $x - z$ plane used to capture the tip vortex trajectory

complished by generating the initial grid distribution with an algebraic method and applying the elliptic routine to smooth out the grid.

In order to easily control the computational domain and grid distribution on both pressure and suction sides independently, an H-H grid topology with two blocks (one for the pressure side and one for the suction side) is applied in the three-dimensional computational domain. Since the tip vortex always sheds from the suction side of a finite-span hydrofoil and approaches asymptotically to the angle of attack, additional grid clustering can be added on the suction side to capture the tip vortex without adding the same number of grid points on the pressure side. Therefore, in addition to generating the grid clustering near the tip in the spanwise direction, the grid clustering is also arranged to capture the tip vortex trajectory as shown in Figs. 1 and 2. Another benefit of using the block structure is that one can reduce the amount of computer memory required by the flow solver as the data from only one block needs to be present in memory at once; the other block can be buffered out of memory.

2.2 Numerical Method. The three-dimensional incompressible Navier-Stokes flow solver, INS3D-UP, developed by Rogers et al. (1991) is based on the artificial-compressibility method. In the artificial-compressibility method, a time derivative of pressure is added to the continuity equation to couple it with the momentum equations. As a consequence, a hyperbolic system of equations is formed and can be solved using a time-marching scheme. This method can be marched in pseudo-time to reach a steady-state solution. To obtain a time-dependent solution, a sub-iterative procedure for pseudo-time needs to be performed in each physical time step such that the continuity equation is satisfied. The spatial differencing of the convective terms uses a fifth-order accurate flux-difference splitting based on Roe's method (1981). A second-order central differencing is used for the viscous terms. The resulting system of algebraic equations is solved by a Gauss-Seidel line-relaxation method in which several line-relaxation sweeps through the computational domain are performed before the solution is updated at the new pseudo-time step.

The INS3D-UP code is accompanied by the Baldwin-Barth one-equation turbulence model (Baldwin and Barth, 1990) which is derived from a simplified form of the standard $k - \epsilon$ equation. This model is not only simpler than the two-equation model, but also eliminates the need to define the turbulent mixing length, which is required in Baldwin-Lomax algebraic model.

2.3 Boundary Conditions. Since the multiblock scheme is used in the present study, there are two types of boundaries where conditions have to be specified: 1) the physical boundaries, such as inflow, outflow, far field, and solid surfaces; and 2) the block-interface boundaries across which all flow quantities must be continuous. In order to allow the use of large pseudo-time steps, implicit boundary conditions need to be applied at all of the boundaries.

For the physical boundaries, freestream velocity and pressure are specified at the far-field boundary and the inflow boundary while the first-order extrapolation for all variables is used at the outflow boundary. On the solid hydrofoil surface, no-slip flow and zero normal pressure gradient conditions are used and at the root boundary, a symmetry condition is specified.

The convergence rate and stability of the implicit scheme can be severely limited by an explicit boundary condition at the interface between blocks in a multiblock scheme. An explicit boundary condition is applied if the block-interface boundaries

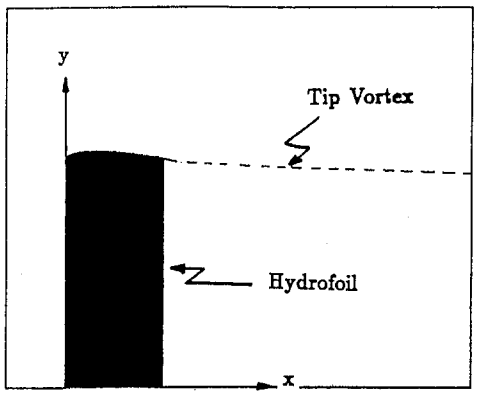

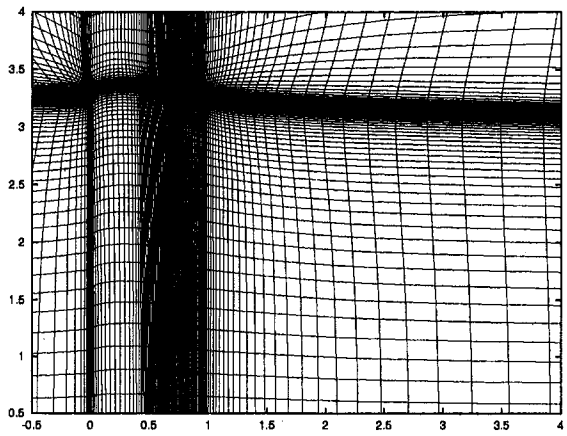

Fig. 2 The grid clustering in the $x - y$ plane used to capture the tip vortex trajectory

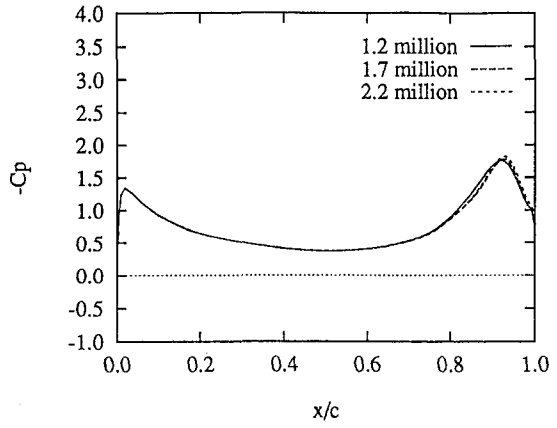

Fig. 3 Comparison of the chordwise pressure distribution at $y/c = 2.98$ for different density grids

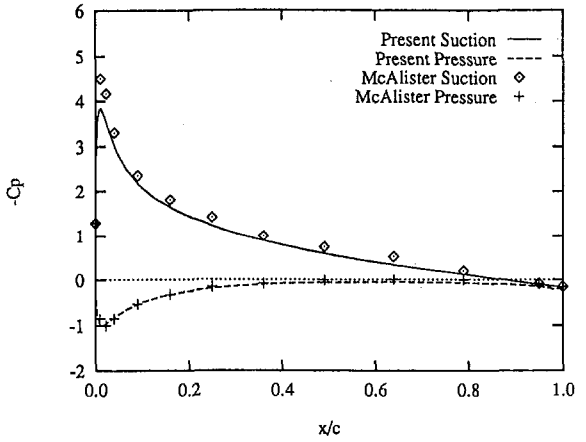

Fig. 4 The chordwise pressure distribution on the hydrofoil surface at spanwise stations ($y/c = 1.62$) away from the tip for $\alpha = 12$ deg and $Re = 1.5 \times 10^6$

are updated after all blocks are calculated by an implicit solver. For the current Gauss-Seidel line-relaxation method, several sweeps need to be performed for each block before the solution is updated. Therefore, a semi-implicit method of passing the boundary conditions between blocks can be easily accomplished by updating the velocities and pressure at the block-interface after each sweep of a block. The next sweep through the other block would utilize the updated values at the common block interface.

3 Results and Discussion

As a base case, a computation is conducted at Reynolds number $Re = 1.5 \times 10^6$ (based on the chord length and the freestream velocity) and angle of attack $\alpha = 12$ deg for a rectangular hydrofoil with a NACA 0015 cross section and a round tip. Before comparing the results with the available experimental data to validate the current numerical scheme, several numerical experiments were performed to assess the influence of the computational domain and the grid density. After validation, the steady-state roll-up process of the tip vortex is described in detail. Finally, the effect of the Reynolds number, the angle of attack, and the hydrofoil planform on the tip vortex are addressed.

3.1 Assessment of Critical Numerical Aspects. Since the flow field around the hydrofoil is considered as an external flow in the present study, the outer boundaries can not be placed too close to the solid surface. Otherwise, the freestream boundary approximation will break down and result in an over-constraint of the flow. Two different computational domains, with two different far-field boundaries locations (at 6 and 10 chord lengths), were tested. The grid density for these two computational domains was the same near the hydrofoil and grid points were added in the extended portion of the larger computational domain. No significant difference (less than 0.1%) was found from comparison of the two flow fields. Therefore, all results shown in the present study are obtained from the smaller computational domain.

The primary grid used in the present study has total 1.2 million grid points including $135 \times 91 \times 61$ for suction side and $135 \times 91 \times 41$ for pressure side in the streamwise, spanwise, and normal direction, respectively. In the primary grid, 81 of the 135 streamwise grid points and 61 of the 91 spanwise grid points are used on the hydrofoil. The first grid spacing on the hydrofoil surface is specified as 1×10^{-5}. The tip-vortex core includes at least 17 grid points in the crosswise direction and 28 grid points in the spanwise direction. It is computationally prohibitive to perform a grid independence study by doubling grid points in each direction for a complex three-dimensional flow. Instead of doubling grid points, two different cases with higher local density near the hydrofoil tip and tip-vortex core were tested and compared with the primary grid. The surface pressure distributions close to the tip obtained from 1.7 and 2.2 million grid points are shown in Fig. 3 and compared with the primary grid. Increasing grid density to 1.7 and 2.2 million grid points was found to increase the pressure difference at the trailing-edge peak by 1 and 2 percent, respectively.

3.2 Validation of the Numerical Results. The steady-state numerical solution is compared to the experimental data of McAlister and Takahashi (1991). For this comparison, several computations were conducted with the aspect ratio of 3.3 used by McAlister and Takahashi. Figures 4 and 5 show the surface pressure distribution at two different spanwise stations, away from and close to the tip. Comparison with the experimental data at the station away from the tip shows that the current suction side pressure coefficient is slightly lower than McAlister and Takahashi's experimental data. It is important to note that wall corrections to the experimental data were not made in McAlister and Takahashi's study. Since the experiment was conducted for a finite-span wing with chord length of 1.7 ft in a 7- by 10-foot subsonic wind tunnel, the wall blockage effect is expected to lead to a slightly larger negative pressure coefficient, $-C_p$. Although there are some differences for the station close to the tip, comparison in Fig. 5 indicates that the vortex-induced peak is captured well by the computation.

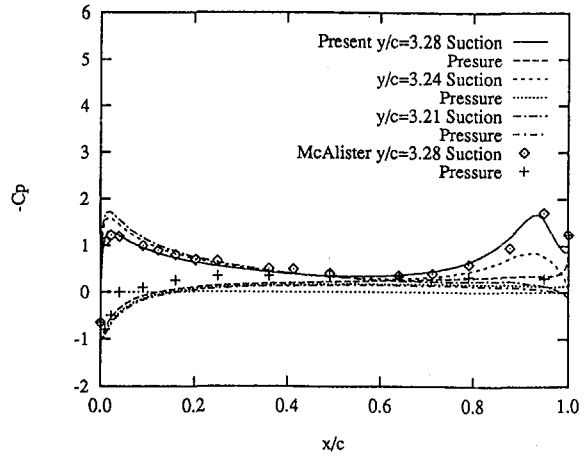

Fig. 5 The chordwise pressure distribution on the hydrofoil surface close to the tip

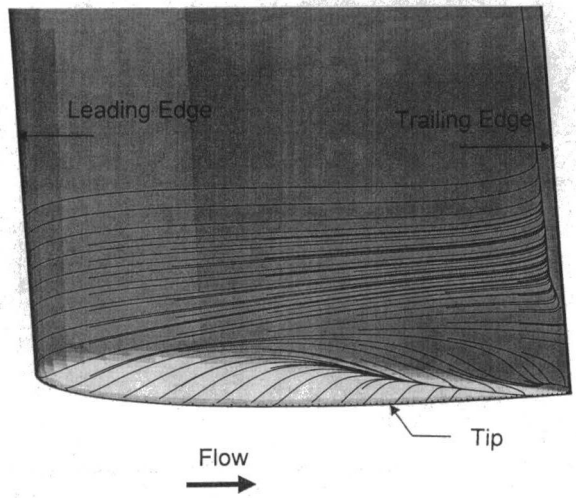

Fig. 6(*a*)

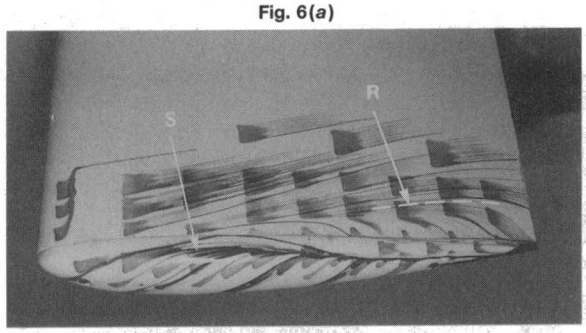

a) ROUND TIP-EXPERIMENT

Fig. 6(*b*)

Fig. 6 The surface "oil flow" pattern near the tip region (a) the computed result (b) the experimental results (Srinivasan et al., 1988) for α = 12 deg and Re = 1.5 × 10^6

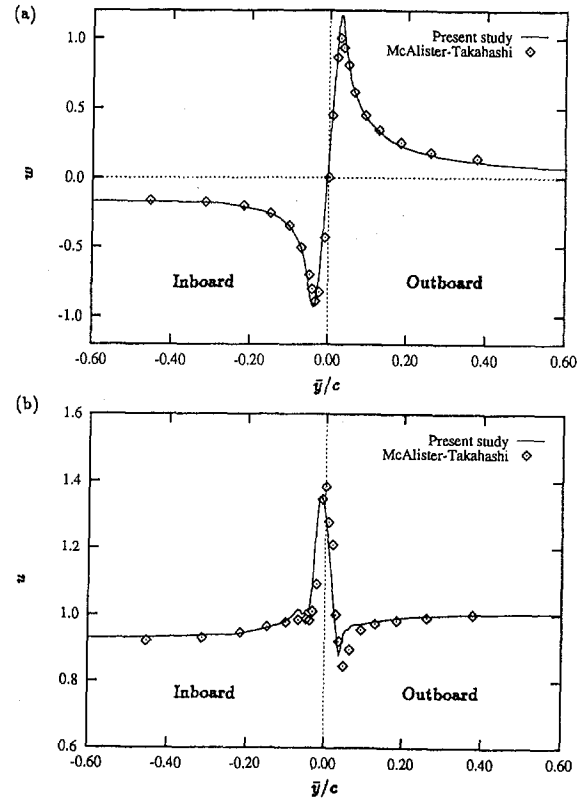

Fig. 7 Comparison of the vertical and axial velocity components across the tip-vortex core in inboard-outboard direction at x/c = 1.1 for α = 12 deg and Re = 1.5 × 10^6

The influence of the tip vortex on the chordwise pressure distribution near the tip region is also shown in Fig. 5. In addition to the leading-edge suction peak, a second suction peak that appears in the tip region can be observed. This additional suction peak is associated with the tip vortex that forms on the suction side. The region influenced by the tip vortex can also be shown from the details of the surface "oil flow" pattern shown in Fig. 6. Comparison between the experimental surface oil flow (Srinivasan et al., 1988) and the computed result shows a good agreement on the suction side near the tip. The major and secondary separation lines (convergent lines) and reattachment line (divergent line) observed in the experiment are well predicted.

Further quantitative comparison with McAlister and Takahashi's experimental data is made for the velocity field around the tip-vortex core. A new coordinate ($\bar{y}$, $\bar{z}$), aligned in the directions of y and z but with its origin located on the tip-vortex core, is defined for plotting the velocity field around the tip-vortex core. The tip-vortex core is defined as the location of the minimum pressure coefficient at the local $y - z$ plane. From Fig. 7 it is observed that the vertical w (z component) and axial u (x component) velocities of the tip-vortex core in the inboard-outboard direction are well predicted in the present study within the near-field wake region. In Fig. 8, however, the flow field far downstream shows an over-diffusive error within the tip-vortex core. The vertical velocity is much smaller and the tip-vortex core is much larger than the experimental data. In addition, the axial velocity within the tip-vortex core displays a deficit instead of the excess obtained experimentally. Further

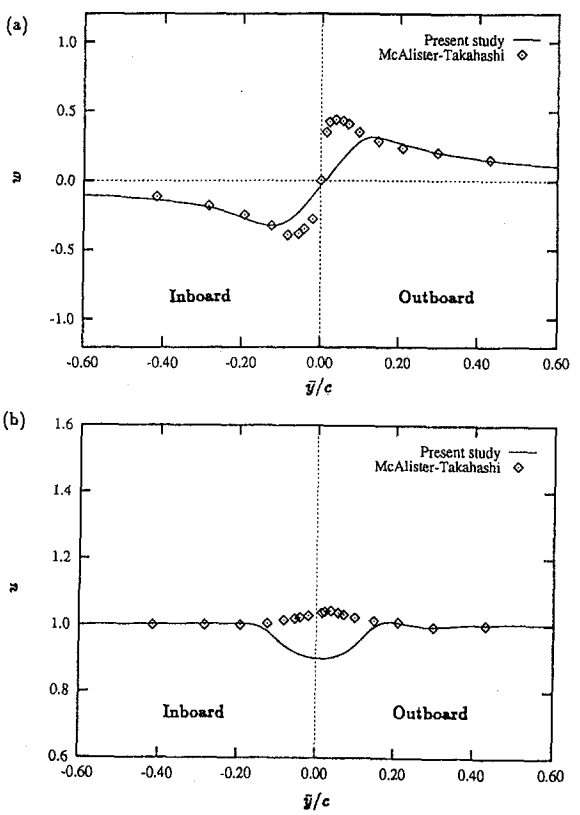

Fig. 8 Comparison of the vertical and axial velocity components across the tip-vortex core in the inboard-outboard direction at x/c = 5 for α = 12 deg and Re = 1.5 × 10^6

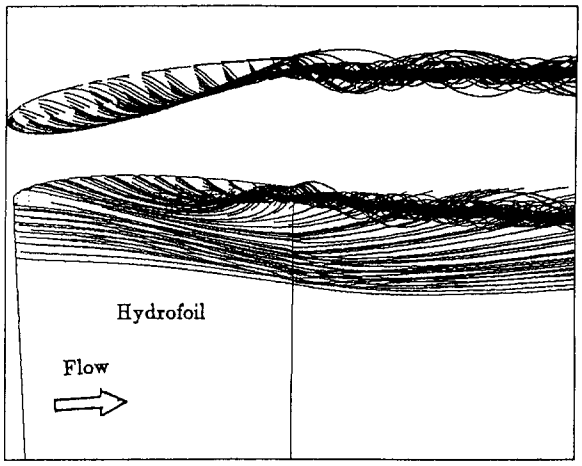

Fig. 9 Particle traces of the tip vortex on $x - y$ plane and on $x - z$ plane for $\alpha = 12$ deg and Re $= 1.5 \times 10^6$

mesh refinement on the tip-vortex core was tested, but no significant improvement was found.

It is known that the flow is dominated by the pressure gradient between the pressure and the suction sides near the hydrofoil tip. From the momentum equations, one can see that the viscous terms will have only a secondary effect on the tip-vortex flow. However, as the tip vortex continues downstream and away from the hydrofoil, the pressure gradient is not dominant and the viscous terms will play an important role. Since all the eddy viscosity models, including the Baldwin-Barth model, use the Boussinesq approximation for the Reynolds stress and incorporate it into the viscous terms, an inappropriate turbulence model will cause an error in the viscous dissipation. This also explains why a good agreement with the experimental data can be obtained in the very near-field wake region although the present turbulence model cannot adequately model the tip-vortex turbulence. Therefore, we attribute the over-diffusive error and excessive dissipation to the turbulence model used in the current study. Higher order turbulence modeling such as the $k - \epsilon$ two-equation model is not expected to significantly improve the results since the turbulence around a tip vortex is thought to be highly nonisotropic.

3.3 The Origin of the Tip Vortex. In the present numerical study the tip vortex can be visualized by creating particle traces near the tip region. The formation and lift-off of the tip vortex for Re $= 1.5 \times 10^6$, $\alpha = 12$ deg, and Ar $= 3.0$ are shown in Fig. 9 as the traces of unrestricted fluid particles released at several locations. It is seen that the roll-up process of the tip vortex consists of the braiding of fluid particle traces released from both suction and pressure sides of the hydrofoil surface. The fluid particles released on the pressure side smoothly cross over the hydrofoil tip and braid with the particles released on the suction side. This tightly braided ribbon of fluid particles defines a tip vortex that is distinct from the rest of the wake vortex sheet. While the braiding process is still in progress, the vortex lifts off the surface and, as it rolls up, it also starts rolling inboard of the hydrofoil tip. Further downstream of the hydrofoil, it continues to roll inboard and stays distinctly above the shed wake vortex sheet.

Another way to illustrate the roll-up process is to show the contour of streamwise vorticity (x component) at different streamwise locations as seen in Fig. 10. The secondary flow at the cross flow plane must satisfy the no-slip condition at the hydrofoil surface. This no-slip condition generates positive vorticity on both the pressure- and suction-side surfaces as shown in Fig. 10(a) (solid lines for positive values and dotted line for negative values). Further downstream, the cross flow separates from the hydrofoil surface and starts to roll up. A clockwise vortex motion above the suction side is established which changes the direction of the cross flow to outward at the hydrofoil surface. This vortex will finally lift off the hydrofoil surface

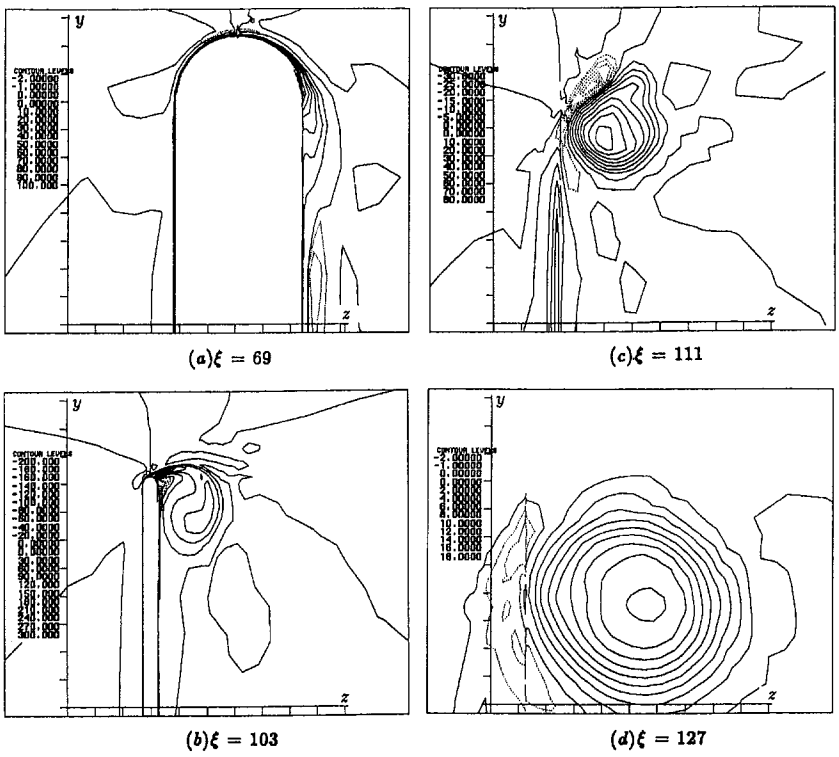

Fig. 10 The contour projection of streamwise vorticity on the $z - y$ plane at different streamwise locations for $\alpha = 12$ deg and Re $= 1.5 \times 10^6$. (The flow direction is into the figure.)

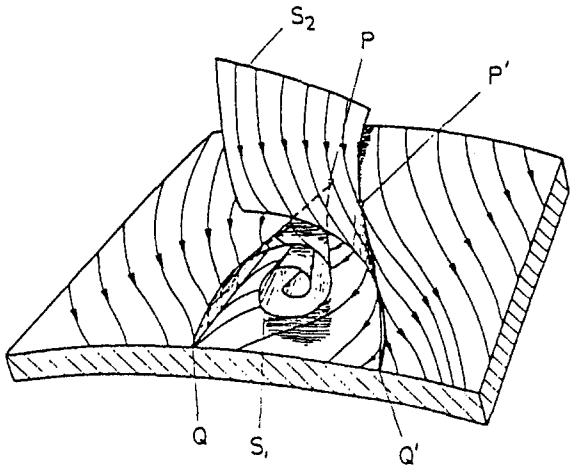

Fig. 11 Sketch of vortex rollup showing an open negative and an open positive stream-surface bifurcation (Hornung and Perry, 1984)

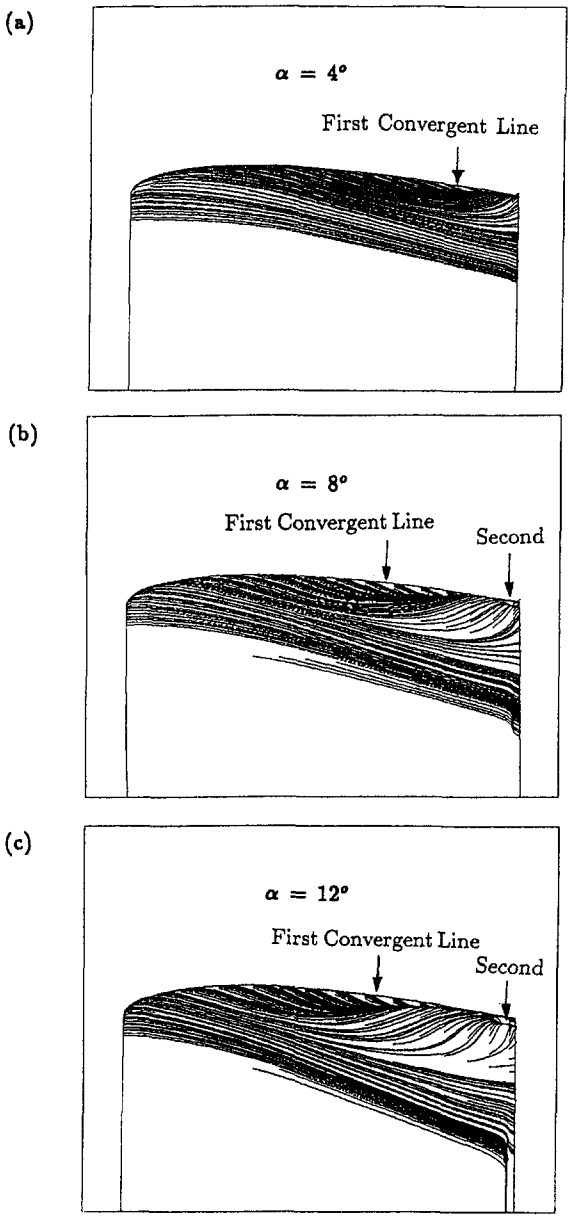

Fig. 12 Comparison of the surface "oil flow" for α = 4, 8, and 12 deg

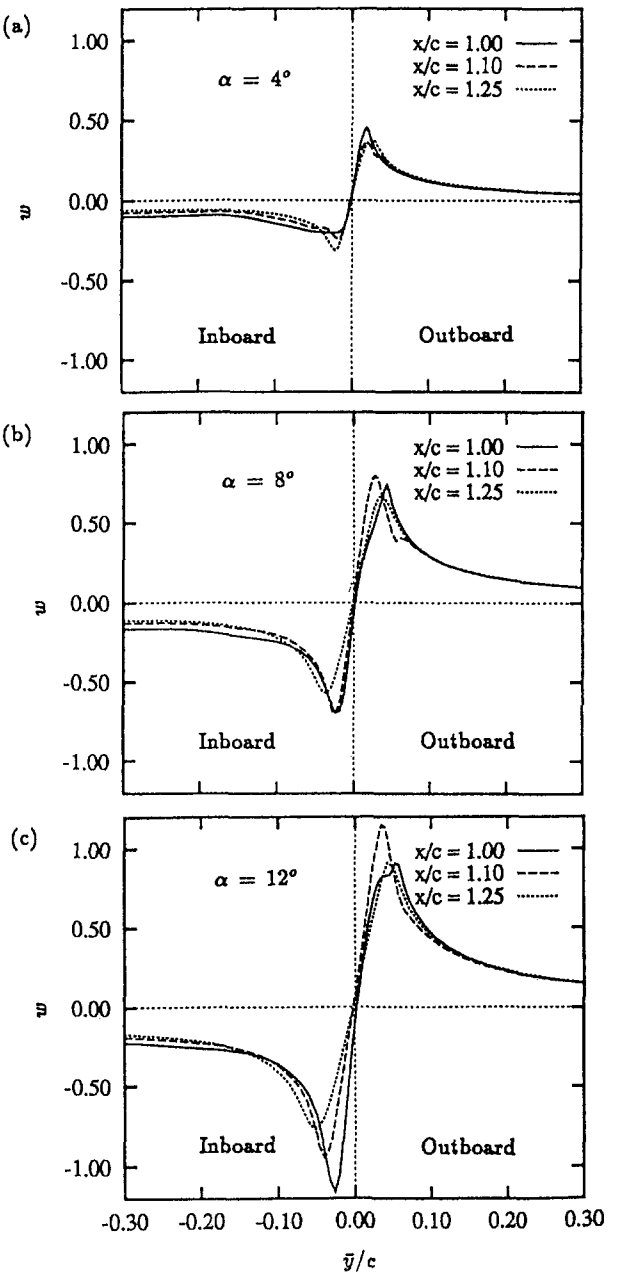

Fig. 13 Comparison of vertical velocity across the tip-vortex core in inboard-outboard direction at x/c = 1.0, 1.1, 1.25 for α = 4, 8, and 12 deg and Re = 1.5 × 10^6

as shown in Fig. 10(b). The outward cross flow combined with the no-slip condition results in negative vorticity along the suction side in the immediate vicinity of the hydrofoil. This negative vorticity (secondary vortex) will interfere with the structure of the main vortex and finally merge into the main vortex when the flow passes over the whole hydrofoil as shown in Fig. 10(c). The tip vortex will form a completely circular path after the interference of the negative vorticity disappears as shown in Fig. 10(d). It is important to note that the vortex roll-up process may be different for different tip shapes. In the experimental study of McInerny et al. (1990), a secondary tip vortex was found to emanate from the tip face for a blunt-tipped airfoil. This secondary tip vortex was formed due to the separation of the cross flow passing over the sharp edge and not induced by the main tip vortex. In this case, the secondary tip vortex rotated in the same direction as the main vortex. At higher angle of attack, however, both the main and secondary

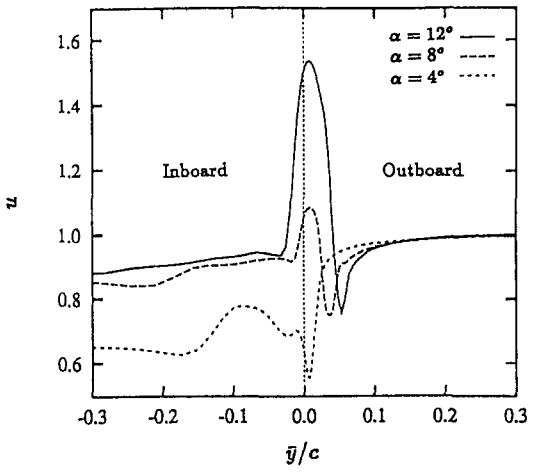

Fig. 14 Comparison of axial velocity across the tip-vortex core in inboard-outboard direction at x/c = 1.0 for α = 4, 8, and 12 deg and Re = 1.5 × 10⁶

tip vortex will induce subset vortices and result in a very complicated multiple-vortices roll-up process as shown in the flow visualization study of Thompson (1983).

The detailed initial roll-up process for the present case can be well described from the topology of three-dimensional separated flows. According to the definition of Wang (1976), this initial roll-up phenomenon of the tip vortex can be classified as an "open" (vs "closed") separation, i.e., flow upstream can access the separation region. From the surface "oil flow" pattern in the hydrofoil tip region, the tip vortex roll-up also satisfies the definition of "local" (vs "global") separation described by Tobak and Peake (1982), i.e., the line of separation starts from a noncritical point. While there are still disputes about the definition of open or local separation (Wang, 1983), the streamsurface bifurcation was introduced by Hornung and Perry (1984) to define the different types of separated flows. According to their definition the tip vortex roll-up is a type of slightly asymmetric open negative streamsurface bifurcation. In the asymmetric open negative streamsurface bifurcation, a free vortex sheet begins to roll-up from its free edge in a direction given by the component of vorticity in the streamline direction on the sheet. The streamwise vorticity gathers into a vortex, which induces a velocity away from the wall on one of its flanks and a velocity towards the wall on the other. The latter effect necessitates the presence of a positive streamsurface bifurcation beside a negative one. Hornung and Perry illustrated this type of vortex roll-up in a perspective view looking upstream, shown

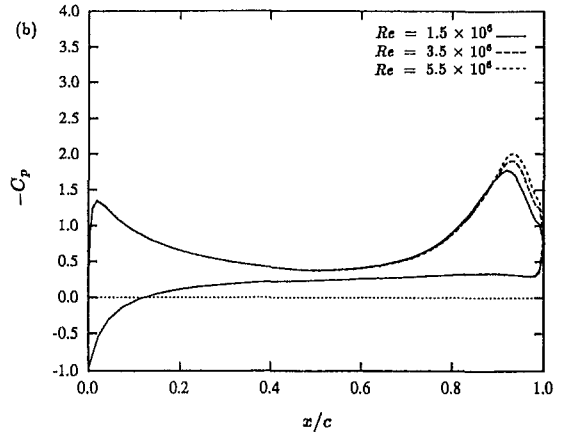

Fig. 15 Comparison of the surface pressure distribution at y/c = 2.98 for Re = 1.5 × 10⁶, 3.5 × 10⁶, and 5.5 × 10⁶ at α = 12 deg

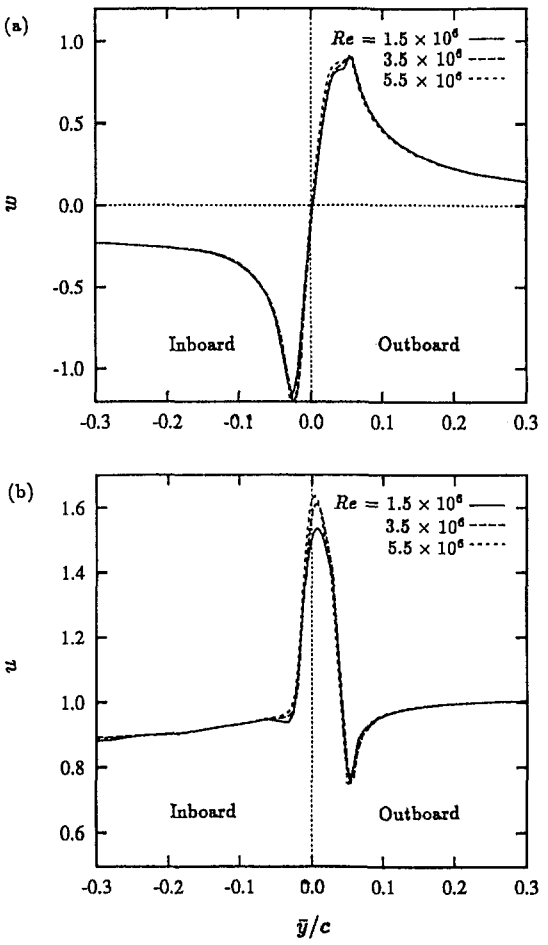

Fig. 16 Comparison of the vertical and axial velocities across the tip-vortex core in inboard-outboard direction at x/c = 1.0 for Re = 1.5 × 10⁶, 3.5 × 10⁶, and 5.5 × 10⁶ at α = 12 deg

in Fig. 11. The free sheet S_1 of the open negative bifurcation issues from the open negative bifurcation line PQ and induces the positive streamsurface bifurcation S_2 along the open positive bifurcation line $P'Q'$. The negative bifurcation and the positive bifurcation lines are related to the convergent and divergent lines, respectively, in the surface oil flow.

3.4 Angle of Attack Effect. Three different angles of attack, α = 4, 8, and 12 deg are studied to investigate the effect on the tip-vortex flow at a fixed Reynolds number Re = 1.5 × 10⁶. Figure 12 shows the surface oil flow for these three angles of attack investigated. It is found that as the angle of attack is increased, the roll-up location of the tip vortex moves further upstream. As described in Section 3.3, a secondary vortex will be induced by the main vortex. In Fig. 12, the surface oil flow for higher angles of attack at α = 8 and 12 deg shows a second convergent line near the trailing edge. This second convergent line is referred to as the second open negative bifurcation line formed by the secondary vortex. Although the second convergent line is not found at α = 4 deg, a negative streamwise vorticity is still generated due to the induced flow beneath the major vortex.

Figure 13 shows the vertical velocity of the tip-vortex core in the inboard-outboard direction at three downstream locations. The negative streamwise vorticity carried outboard by the induced flow beneath the tip vortex interacts with the major vortex and causes a "kink" in the outboard vertical velocity. Downstream this kink smooths as the secondary vortex merges with the primary vortex. At α = 4 deg, the inboard vertical tip-vortex velocity also contains a kink due to the hydrofoil wake. Due to

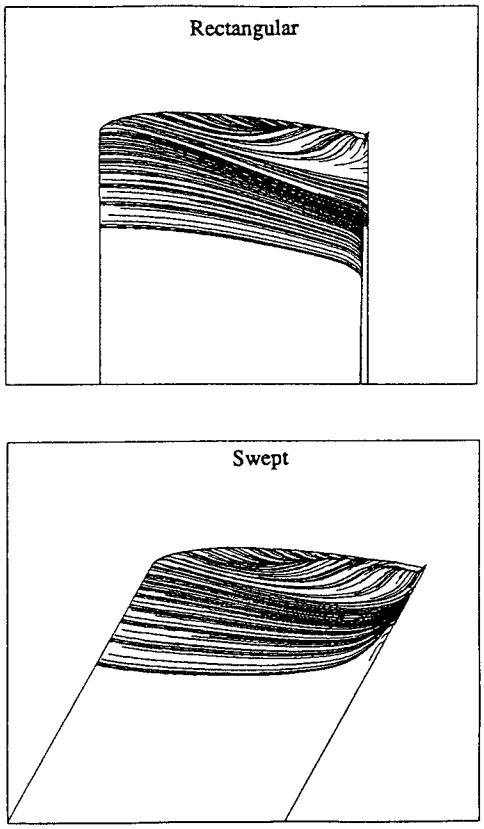

Fig. 17 Comparison of the surface "oil flow" for the rectangular and swept hydrofoil at Re = 1.5 × 10^6 and α = 12 deg

the interaction between the primary and secondary vortices, the tangential velocity profile of the tip vortex will be strongly asymmetric in the near-field region. This strongly asymmetric profile also implies that the Rankine vortex will not be a realistic model for the tip vortex in this region. In the analytical study of Hsu (1991), the calculated values of cavitation inception number were shown to be generally two orders of magnitude larger than commonly observed when the Rankine vortex was used to model the tip vortex. From Fig. 13, it is also found that the vortex core size increases with angle of attack. This is consistent with the experimental observation of Liang and Ramaprian (1991).

The effect of the angle of attack on the axial velocity of the tip-vortex core is shown in Fig. 14 in the inboard-outboard direction at one downstream location. The axial-flow pattern is found to be highly influenced by the angle of attack. An excess in the axial flow is found within the tip-vortex core at higher angle of attack while a deficit in the axial flow occurs at lower angle of attack. Since the vortex forms further upstream at higher angle of attack, a larger pressure gradient will convey more fluid from the pressure side to the suction side which will significantly increase the velocity, both tangential and axial components, within the tip-vortex core.

3.5 Reynolds Number Effect. To study the effect of the Reynolds number on the tip vortex, computations at Re = 1.5 × 10^6, 3.5 × 10^6, and 5.5 × 10^6 are conducted for α = 12 deg. From previous two-dimensional airfoil studies, it is known that increasing the Reynolds number will not alter the lift coefficient of the airfoil when the boundary layer remains attached, although it will decrease the boundary-layer thickness. The present results show that as the Reynolds number is increased, the pressure distribution is only influenced in the tip region where the second suction peak appears. Figure 15 shows that a higher Reynolds number leads to a higher second suction peak corresponding to an increased strength of the tip vortex. The effect of increasing the Reynolds number on the tip-vortex core can also be found from the velocity field. Figure 16 shows that increasing the Reynolds number increases the maximum axial velocity but has a minor impact on the vertical velocity. The vortex core size is found to decrease when the Reynolds number increases. This is also consistent with the experimental observation of Francis and Katz (1988).

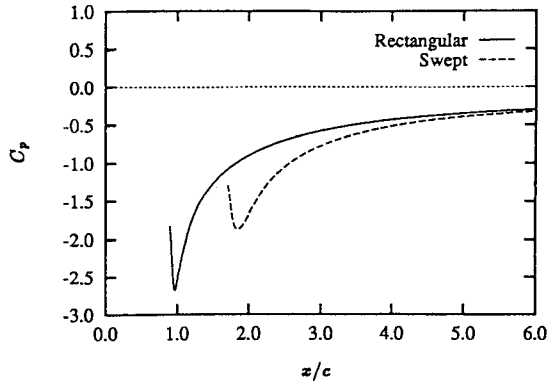

Fig. 18 Comparison of the pressure coefficient along the tip-vortex core for the rectangular and swept hydrofoil at Re = 1.5 × 10^6 and α = 12 deg

3.6 Hydrofoil Planform Effect. To study the influence of planform geometry, a hydrofoil with a 30 deg swept angle is considered and results compared to those from the rectangular hydrofoil. Computations are conducted at Re = 1.5 × 10^6 and α = 12 deg for both geometries. Both rectangular and swept hydrofoil studies presented here have an aspect ratio Ar = 1.5. This is different than the aspect ratio used for the computations reported in the previous sections (Ar = 3).

It is expected that the swept hydrofoil will induce a spanwise secondary flow toward the tip on both pressure and suction sides due to the spanwise pressure gradient. Figure 17 shows the comparison of the surface oil flow between the swept and the rectangular hydrofoils. It is seen that the tip vortex forms further upstream and induces a secondary vortex earlier in the swept hydrofoil. In contrast to the rectangular hydrofoil, the boundary-layer flow on the suction side for the swept hydrofoil also travels toward the tip region near the trailing edge. By comparing the pressure coefficient along the tip-vortex core shown in Fig. 18, it is found that the strength of the tip vortex of the swept hydrofoil is weaker than that of the rectangular hydrofoil. It should be noted that the tip trailing edge is at x/c

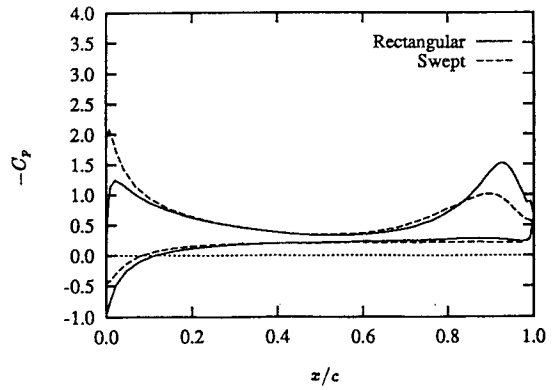

Fig. 19 Comparison of the surface pressure distribution for the rectangular and swept hydrofoil at y/c = 1.48 for Re = 1.5 × 10^6 and α = 12 deg

= 0.978 for the rectangular hydrofoil and x/c = 1.844 for the swept hydrofoil.

From the pressure distribution near the tip region on both pressure and suction sides shown in Fig. 19, one can find that the swept hydrofoil has a higher pressure gradient between the pressure side and the suction side near the leading edge. This larger pressure gradient, therefore, drives a stronger flow across the tip from the pressure side to the suction side and leads to an earlier vortex roll-up. As the flow travels further downstream, however, the low-momentum boundary-layer flow on the suction side will enter the tip vortex and attenuate the strength of the tip vortex.

4 Conclusions

The present study applied full Navier-Stokes computations with the Baldwin-Barth one-equation turbulence model and an H-H type grid to study the finite-span hydrofoil flow. Comparison with the available experimental data showed that the present results favorably predicted the tip-vortex flow on the hydrofoil and near-field wake region. However, over-diffusive error and excessive dissipation were found downstream in the tip vortex. Due to highly nonisotropic turbulence around the tip vortex, current eddy viscosity models were not able to accurately model this free shear layer turbulence. Nonisotropic turbulence models such as a Reynolds-stress model or Large Eddy Simulation may be required to resolve accurately the tip vortex downstream.

The roll-up process of the tip vortex was studied from the numerical results. The initial roll-up process of the tip vortex was well described from the topology of three-dimensional separated flow introduced by Hornung and Perry (1984).

In the present study, multiple vortex roll-up was observed at higher angle of attack. A secondary vortex was induced by the major vortex when the major vortex rolled up and lifted off the hydrofoil surface. From comparison of results at three different angles of attack, it was found that the profile of the axial velocity in the tip-vortex core was greatly influenced by the angle of attack. In the near-field wake region, a jet-like profile in the axial velocity within the tip-vortex core was found at high angle of attack while a wake-like profile in the axial velocity was found at low angle of attack.

From the comparison at two different Reynolds numbers, it was found that increasing Reynolds number increased the maximum axial velocity, but only slightly altered the vertical velocity of the tip vortex in the near-field wake region. The strength of the tip vortex was also enhanced by increasing Reynolds number.

A swept hydrofoil planform was considered to study its effect on the tip vortex. The swept hydrofoil induced a spanwise flow toward the tip on both pressure and suction sides. As the low-momentum boundary layer on the suction side was carried into the tip vortex, the strength of the tip vortex was attenuated.

Acknowledgments

This research has been supported by the Office of Naval Research under contract N00014-90-J-1169 monitored by Dr. Edwin P. Rood. Computational facilities were provided by the NAVOCEANO Supercomputer Center and the CEWES High Performance Computing Center. These contributions are gratefully acknowledged.

References

Baldwin, B. S., and Barth, T. J., 1990, "A One-Equation Turbulence Transport Model for High Reynolds Number Wall-Bounded Flows," NASA TM 102847.

Dacles-Mariani, J., Rogers, S. E., Kwak, D., Zilliac, G., and Chow, J., 1993, "A Computational Study of Wingtip Vortex Flowfield," AIAA Paper 93-3010.

Francis, T. B., and Katz, J., 1988, "Observations on the Development of a Tip Vortex on a Rectangular Hydrofoil," ASME JOURNAL OF FLUIDS ENGINEERING, Vol. 110, pp. 208–215.

Hsu, C. C., 1991, "Studies of Scaling of Tip Vortex Cavitation Inception on Marine Lifting Surfaces," ASME JOURNAL OF FLUIDS ENGINEERING, Vol. 113, pp. 504–508.

Liang, X., and Ramaprian, B. R., 1991, "Visualization of the Wing-Tip Vortex in Temporal and Spatial Pressure Gradients," ASME JOURNAL OF FLUIDS ENGINEERING, Vol. 113, pp. 511–515.

Mansour, N. N., 1984, "Numerical Simulation of the Tip Vortex of a Low-Aspect Ratio Wing at Transonic Speeds," AIAA Paper 84–522.

McAlister, K. W., and Takahashi, R. K., 1991, "NACA0015 Wing Pressure and Trailing Vortex Measurements," NASA Technical Paper 3151.

McInerny, S. A., Meecham, W. C., and Soderman, P. T., 1990, "Pressure Fluctuations in the Tip Region of a Blunt-tipped Airfoil," *AIAA Journal,* Vol. 28, pp. 6–13.

Hornung, H. G., and Perry, A. E., 1984, "Some Aspects of Three-Dimensional Separation, Part I: Streamsurface Bifurcations," *Zeitschrift fuŕ Flugwissenschaften und Weltraumforschung,* Vol. 8, pp. 77–87.

Roe, P. L., 1981, "Approximate Riemann Solvers, Parameter Vectors, and Difference Schemes," *Journal of Computational Physics,* Vol. 43, pp. 357–372.

Rogers, S. E., Kwak, D., and Kiris, C., 1991, "Steady and Unsteady Solutions of the Incompressible Navier-Stokes Equations," *AIAA Journal,* Vol. 29, No. 4, pp. 603–610.

Shamroth, S. J., and Briley, W. R., 1979, "A Viscous Flow Analysis of the Tip Vortex Generation Process," AIAA Paper 79–1546.

Sorenson, R. L., 1989, "The 3DGRAPE Book: Theory, Users' Manual Examples," NASA TM 102224.

Srinivasan, G. R., McCroskey, M. J., Baeder, J. D., and Edwards, T. A., 1988, "Numerical Simulation of Tip Vortices of Wings in Subsonic and Transonic Flows," *AIAA Journal,* Vol. 26, No. 10, pp. 1153–1162.

Thompson, D. H., 1983, "A Flow Visualization Study of Tip Vortex Formation," Aeronautical Research Laboratories, Melbourne, Australia, ARL-AERO-NOTE-421, Aerodynamics Note 421.

Tobak, M., and Peake, D. J., 1982, "Topology of Three-Dimensional Flow Separations," *Annual Review of Fluid Mechanics,* Vol. 14, pp. 61–85.

Tsai, T. M., de Jong, F. J., and Levy, R., 1988, "Computation of the Tip Vortex Flowfield for Advanced Aircraft Propellers," NASA CR-182179.

Wang, K. C., 1983, "On the Disputes About Open Separation," AIAA Paper 83–0296.

Wang, K. C., 1976, "Boundary-Layer Separation in Three Dimensions," Review in Viscous Flow, *Proceedings of the Lockheed-Georgia Company Viscous Flow Symposium,* Marietta, GA. pp. 341–414.

Prediction of Solid/Free-Surface Juncture Boundary Layer and Wake of a Surface-Piercing Flat Plate at Low Froude Number

Madhu Sreedhar
Research Associate.

Fred Stern
Professor and Research Engineer.

Institute of Hydraulic Research,
University of Iowa,
Iowa City, IA 52242-1585

Results are reported of a RANS simulation investigation on the prediction of turbulence-driven secondary flows at the free-surface juncture of a surface-piercing flat plate at low Froude numbers. The turbulence model combines a nonlinear eddy viscosity model and a modified version of a free-surface correction formula. The different elements of the model are combined and the model constants calibrated based on the premises that the anisotropy of the normal stresses is mainly responsible for the dynamics of the flow in the juncture region, and an accurate modeling of the normal-stress anisotropy as obtained from the data is a primary requirement for the successful prediction of the overall flow field. The predicted mean velocity, streamwise vorticity, turbulent kinetic energy, and other quantities at the juncture are then compared with data and analyzed with regard to findings of related studies. In agreement with the experimental observations, the simulated flow at large depths was essentially two-dimensional and displayed all the major features of zero pressure gradient boundary layer and wake, including the anisotropy of normal stresses in the near-wall region. In the boundary-layer free-surface juncture region, the major features of interest that were predicted include the generation of secondary flows and the thickening of the boundary layer near the free surface. In the wake free-surface juncture region, even though secondary flows and a thickening of the wake width near the free surface were predicted in accordance with the experimental observations, the overall comparison with the experiment was not as satisfactory as the boundary-layer juncture. This is partly due to the lack of a strong coherent flow structure in the wake juncture and the presence of possible wave effects in the wake in the experiments. An examination of the terms in the Reynolds-averaged streamwise vorticity equation reconfirmed the importance of the anisotropy of the normal Reynolds stresses in the production of streamwise vorticity. The free-surface wave elevations were negligible for the present model problem for the nonzero Froude number studied. Finally, concluding remarks are presented with regards to extensions for practical geometries such as surface ship flows.

1 Introduction

Turbulence modeling for developing solid/free-surface juncture flow has received limited attention in comparison to fully developed flow such as open-channel flow. An example of developing juncture flow of particular interest is the boundary layer developing around a surface ship. One underlying difference between fully developed and developing juncture flows is that in the former the entire domain is turbulent whereas in the latter the turbulence is confined to the boundary layer. Important features to be modeled for both cases include turbulence-induced secondary flows (Prandtl's second kind) and free-surface effects on turbulence. Additional features to be considered for surface ships and other complex geometries include pressure-gradient, curvature, separation, and Reynolds-number effects. Another important factor, which can play a dominating role, is free-surface waves and accompanying pressure-gradient effects at nonzero Froude numbers. Also of interest is the development of the wake shed by surface-piercing bodies. Of particular concern is the prediction of the wake spreading near the free surface and bubble distributions (Paterson et al., 1996).

The eddy-viscosity based linear models cannot predict the turbulence anisotropy and the effects of free surface. Considering the increased computational complexity of second-order closures and their inconsistent performance, it is desirable to develop simpler turbulence models which can account for the turbulence anisotropy and other free-surface effects. Algebraic-stress models and nonlinear eddy-viscosity models retain some of the attractive features of the second-order closures yet require only marginal increments in computational resources in comparison to linear two-equation models.

The objective of the present study is to test the performance of a turbulence model obtained by combining a nonlinear explicit eddy viscosity model with a free-surface correction term for the prediction of turbulence-driven secondary flows and other experimentally observed features in the developing solid/free-surface juncture boundary layer and wake of a surface-piercing body. The different elements of the model were combined and the constants calibrated based on the premises that the anisotropy of the normal stresses is mainly responsible for the dynamics of the flow in the juncture region and an accurate distribution of the normal-stress anisotropy is a primary requirement for the successful prediction of the overall flow field. The present investigation is limited to a model problem of a surface-piercing flat plate at low Froude numbers where free-surface wave effects, even though present, are not very significant.

Background information on the present problem is presented next followed by sections on computational approach and parameters, uncertainty analysis, and description and analysis of results. Finally, concluding remarks are made.

Contributed by the Fluids Engineering Division for publication in the JOURNAL OF FLUIDS ENGINEERING. Manuscript received by the Fluids Engineering Division April 7, 1996; revised manuscript received January 29, 1998. Associate Technical Editor: C. L. Merkle.

2 Background

The effect of free surface on turbulence is similar to that of the wall in some respects, especially in the behavior of normal Reynolds stresses. The turbulent eddies are flattened as they approach the surface with the surface-normal fluctuations suppressed and the other two components of velocity fluctuations gaining energy. While the anisotropic behavior of turbulence is common to near-wall turbulence, unlike the wall region, there is negligible shear and turbulent production near the free surface. This anisotropy of normal stresses is generally known to be the cause of origin of secondary flows near solid-solid and solid/free-surface junctures.

In the remainder of this section, the current status of experimental and numerical studies, and turbulence modeling issues pertaining to free-surface effects and secondary flow generation which are of relevance to the current study are presented.

Experimental Studies. The experimental studies on surface-piercing flat plate include the measurements of Longo, Huang and Stern (1998), henceforth LH&S, Grega et al. (1995), and Logory et al. (1996). While the investigation of Grega et al. (1995) is for the boundary layer and Logory et al. (1996) for the wake, LH&S report measurements of both boundary layer and wake. Their investigation represents the most complete one in terms of measurement and analysis of Reynolds-averaged quantities and also includes an appropriate uncertainty analysis. This data set is the benchmark data for the present numerical simulation. Henceforth, unless otherwise stated, any mention to data refers to LH&S.

The main features of the flow reported by LH&S include the thickening of the boundary layer and wake near the free surface and the existence of two regions of high streamwise vorticity of opposite sign near the juncture region with the inner region corresponding to a counter-clockwise vortical motion. The underlying flow (flow at large depths) was essentially two dimensional and followed the established trends for 2-D canonical flat-plate boundary layer and wake flow. The results from the other two studies (Grega et al., 1995 and Logory et al., 1996) are similar and consistent with LH&S providing cross validation. In those two studies, however, a greater emphasis is put on coherent structures than Reynolds-averaged quantities.

A related problem is the submerged jet (e.g., Swean et al., 1991a; Anthony and Willmarth, 1992; Walker et al., 1995) where the jet develops parallel and close to the free surface. Certain aspects of the flow show similarity to solid/free-surface juncture flows including the anisotropic nature of turbulent stresses, the generation of the turbulence-driven secondary flows and the subsequent thickening of the jet width near the free surface.

Numerical Studies. In most of the numerical studies on solid/free-surface juncture flows reported to date the free surface is approximated as a rigid shear-free surface, also termed as a rigid lid. These investigations include a DNS study by Leighton et al. (1994) and an LES investigation by Sreedhar and Stern (1998). The initial conditions for these two studies were obtained from temporally developing channel and boundary layer simulations, respectively. Even though the initial conditions, domain size, and the setup of these studies were dissimilar, both studies showed similar features including the presence of a counter clockwise vortex near the juncture region. The assumptions and approximations used in these studies, however, preclude a direct comparison with the data. Related studies include a DNS of a submerged jet by Mangiavacchi et al. (1994). Since DNS and LES studies are limited to low-to-moderate Reynolds numbers, RANS computations remain the only viable tool for practical engineering calculations of free-surface flows, one of the critical pacing items being the turbulence modeling.

RANS Studies and Turbulence-Modeling Issues. The turbulence modeling of free-surface flows has received fair attention in recent times. Some of the model problems investigated include open-channel flow (Naot and Rodi, 1982; Celik and Rodi, 1984; Gibson and Rodi, 1989; Swean et al., 1991b; Naot et al., 1993) and submerged jet flow (Miner et al., 1993 and Walker and Chen, 1994). Among these, the RANS computations of the solid/free-surface juncture are limited to open channel flows (Naot and Rodi, 1982 and Naot et al., 1993), whereas developing solid/free-surface juncture flows have received practically no attention until now. In open channel flows the turbulence is generated at the channel beds as well as the side walls and the strength and nature of secondary flows are dependent on the aspect ratio of the channel. For developing juncture flows, the turbulence production is confined to the boundary layer and a pertinent length scale is the boundary-layer thickness. While the standard two equation and lower level linear models based on Boussinesq eddy-viscosity hypothesis fail to predict the anisotropy of normal Reynolds stresses, models based on second-moment closures and other nonlinear constitutive stress-strain relationships can account for these features. The failure of standard linear models is due to their inability to properly account for the pressure-strain correlation term.

While full second-order closures can account for more physics, algebraic-stress models derived from the full Reynolds-stress transport equations appear to be an attractive alternative with regard to computational requirements and predictive capabilities. Naot and Rodi (1982) predicted secondary flows in open channels using a version of the algebraic-stress model derived based on the work of Launder et al. (1975). The transport equations for the Reynolds stresses were reduced to a set of algebraic equations for the individual stresses. The near-wall regions in their study were accounted for by a wall-function approach. Other applications of algebraic-stress models to free-surface turbulence (not necessarily involving solid/free-surface junctures) include the open channel studies of Celik and Rodi (1984), Naot et al. (1993), Swean et al. (1991b), and submerged jet studies of Miner et al. (1993) and Walker and Chen (1994). The application of algebraic stress models reported in the above studies mainly differs from one another in the treatment of the pressure-strain correlation and the treatment of the dissipation rate near the free surface. In general, even though these models are considerably less expensive than full Reynolds-stress closures, they are also not immune from poor convergence and stability problems as pointed out by Demuren (1991).

The influence of free-surface effects in the previously mentioned studies were incorporated into the pressure-strain correlation terms. One commonly used form of correction is due to Shir (1973). A similar free-surface correction term is used in the present study and details are given later.

Apart from algebraic stress models discussed above, there are explicit models with nonlinear stress-strain relationships (Gatski and Speziale, 1993; Myong and Kassagi, 1990) which are capable of predicting anisotropy of normal stresses under unidirectional mean strain. Several such models are listed in Wilcox (1993). Like the implicit algebraic-stress models, these models are strictly valid only for equilibrium flows. These models are inexpensive to use compared to implicit algebraic stress models and predict more turbulence features than linear models. The main disadvantage of these models is that most of them are not designed to satisfy all the criteria which assure consistency with the exact Navier-Stokes equations including the realizability and general frame invariance. An exception to the above is the model due to Gatski and Speziale (1993). The application of this model to flat plate boundary layer flow has yielded good results except near the wall where the turbulence intensities and kinetic energy were under predicted (Speziale and Abid, 1995).

Another issue that needs to be addressed is the boundary conditions on k and ϵ. Previous open channel studies have used a symmetry condition for k and prescribed a finite value for ϵ at the free surface. The prescribed value for ϵ is dependent on the free-surface kinetic energy and the distance from a virtual origin above the free surface (Naot and Rodi, 1982). Nezu and Nakagawa (1987) applied the boundary correction on k rather than on ϵ. The k obtained from the symmetry condition was multiplied by a free-surface factor which essentially had the same effect as prescribing a higher value for ϵ at the free surface. Gibson and Rodi (1989) showed that with symmetric boundary conditions for both quantities, reasonable results can be obtained.

3 Approach

The RANS method of Tahara and Stern (1996) developed for surface ships is extended to include nonlinear eddy-viscosity turbulence models in addition to the zero-equation Baldwin-Lomax (Baldwin and Lomax, 1978) model. In what follows, the major features of the numerical method are presented followed by details of the improvements to the turbulence modeling capabilities.

Computational Method. The numerical scheme uses finite-analytic spatial discretization. First and second-order backward differencing temporal discretization is used for steady and unsteady flows, respectively. For steady flow, subiteration convergence is not required and time serves as an iteration parameter. The pressure equation is derived from a discretized form of the continuity equation and solved using second-order-central finite differences. The overall solution procedure is based on the two step pressure-implicit-split-operator (PISO) algorithm. Body-fitted/free-surface conforming grids are used with exact nonlinear kinematic and approximate dynamic free-surface boundary conditions. For the zero-Froude number case, the free-surface boundary is treated as a rigid lid, details of which are given later.

Turbulence Model. The turbulence model makes use of a near-wall model, which can predict the anisotropy of the normal stresses, and a free-surface correction term. The free-surface correction term damps the surface-normal component of the Reynolds-stress tensor and redistributes the energy among the other two components thus enhancing the anisotropy of the normal stresses near the free surface. In implicit models (Naot and Rodi, 1982), the free-surface correction appears as a sink term in the algebraic equation for the surface-normal component of the normal stresses and as source terms in the other two components. In the present application, the free-surface correction is applied in an explicit manner, as shown in Eq. (1). The model for the Reynolds stress tensor τ_{ij} for the juncture flow is

$$\tau_{ij} = (1 - \Delta)T_{ij} \tag{1}$$

where T_{ij} is the eddy-viscosity model capable of predicting the anisotropy of normal stresses and Δ is the free-surface correction operator. Away from the free surface, the correction term becomes negligible so that $\tau_{ij} = T_{ij}$. As mentioned earlier, the different components of the model are combined so that the distribution of the anisotropy of the normal stresses in the juncture region matches the data. The exact expressions of T_{ij} and Δ used in this investigation are given in the next two sections.

Near-Wall Model: The need to predict the anisotropy of normal stresses precludes the application of zero-equation or linear two-equation models. The explicit nonlinear eddy-viscosity model due to Myong and Kassagi (1990), henceforth M&K, gives satisfactory results throughout the boundary layer, particularly the anisotropic behavior of the normal stresses. This model is used in the present study and is reproduced below from M&K.

$$T_{ij} = \frac{2}{3}k\delta_{ij} - \nu_t\left(\frac{\partial u_i}{\partial x_j} + \frac{\partial u_j}{\partial x_i}\right) + \frac{k}{\epsilon}\nu_t \sum_{\beta=1}^{3} C_\beta\left(S_{\beta_{ij}} - \frac{1}{3}S_{\beta_{ij}}\delta_{ij}\right) + \frac{2}{3}\nu\frac{k}{\epsilon}\left(\frac{\partial\sqrt{k}}{\partial x_n}\right)^2 W_{ij}(n, m) \tag{2}$$

where W_{ij} and $S_{\beta ij}$ are given by

$$S_{1ij} = \frac{\partial u_i}{\partial x_m}\frac{\partial u_j}{\partial x_m}$$

$$S_{2ij} = \frac{1}{2}\left(\frac{\partial u_m}{\partial x_i}\frac{\partial u_j}{\partial x_m} + \frac{\partial u_m}{\partial x_j}\frac{\partial u_i}{\partial x_m}\right)$$

$$S_{3ij} = \frac{\partial u_m}{\partial x_i}\frac{\partial u_m}{\partial x_j}$$

$$W_{ij}(n, m) = -\delta_{ij} - \delta_{in}\delta_{jn} + 4\delta_{im}\delta_{jm}$$

The indices n and m in the above expression denote the wall-normal and streamwise directions and summation convention is not applied to them. The eddy viscosity ν_t, k, and ϵ are obtained similar to the linear k-ϵ model and are obtained from the two-layer formulation due to Chen and Patel (1988). The constants in Eq. (2) are $C_1 = 0.8$, $C_2 = 0.45$ and $C_3 = -0.15$ following M&K. The first two terms in Eq. (2) are common to the linear k-ϵ model whereas the third and the fourth terms are nonlinear in nature and contribute to the anisotropic character of the normal stresses. The third term is derived from the interrelationship between the production and dissipation terms in the k equation and is effective in the entire flow field except the immediate vicinity of the wall. The fourth term is derived from the balance of diffusion and dissipation terms and influences the wall-limiting behavior of the normal stresses. It may be noted that the third term contains the eddy viscosity whereas the fourth term the molecular viscosity.

One drawback of the model is the lack of satisfaction of the general frame invariance condition for the fourth term, which precludes its application to flows with regions of two-dimensional turbulence unless modified by correction terms/damping functions. In the present study, in the regions upstream and downstream of the plate, the third and fourth terms in Eq. (2) were deactivated since they are designed strictly for near-wall flows. The deactivation is enforced by multiplying the nonlinear terms in Eq. (2) with a hyperbolic tangent function which vanished upstream and downstream of the plate. The nonlinear model of Gatski and Speziale (1993) does not have these drawbacks because of its rigor and generality and tests with it are still in progress.

Free-Surface Correction: The free-surface correction term used in this study is based on the one developed by Shir (1973) and modified for the present explicit model. The primary effect of free-surface correction is the partition of normal stresses where the surface parallel fluctuations gain energy at the expense of surface normal components. The free-surface operator defined in Eq. (1) is given as

$$\Delta T_{ij} = C_s(T_{km}n_k n_m\delta_{ij} - \tfrac{3}{2}T_{ki}n_k n_j - \tfrac{3}{2}T_{kj}n_k n_i)f(y, z) \tag{3}$$

Here C_S is a constant which controls the free-surface correction and n_m is the normal to the free surface. The function $f(y, z)$ controls the overall distribution of the normal-stress anisotropy in the streamwise-normal plane and is a key element of the model. Here Y and Z axes are normal to the solid wall and the free surface, respectively. The function f is problem specific. In free-shear flows, such as a submerged jet, it controls the depth to which the free-surface correction is applied and provides a gradual transition between the deep and the free surface with

its value ranging from zero in the deep to one at the free surface. In such cases, the function is dependent only on the Z coordinate (e.g., Miner et al., 1993). In the present application, it also accommodates the effect of the solid-wall so that the free-surface correction slowly decreases toward the solid wall and vanishes at the wall. Hence the dependence on both Y and Z coordinates. The function f used in the present investigation is given below.

$$f(y, z) = \left[\max\left(1, C_y \frac{y}{\delta}\right)\right]\left[1 - \max\left(1, C_z \frac{z}{\delta}\right)\right] \quad (4)$$

For this flow field, the boundary-layer thickness (δ) at the deep was selected as a suitable length scale. For surface ships, the boundary layer thickness at the mid-girth could be a suitable candidate for the length scale. It should be kept in mind that neither the length scale nor the form of the function is unique. Other length scales and functions may be adopted provided they give the correct distribution of anisotropy of the normal stresses. The function $f(y, z)$ given above is linear in both y and z and approaches unity near the free surface and vanishes away from the free surface so that the correction is effective only near the free surface. The ratio of constants C_Y and C_Z controls the extent of the influence of the solid wall in comparison to the effect of the free surface. Calibration studies were conducted by obtaining solutions for ratios ranging from (1, 2) to (1, 5). A ratio of (1, 4) was selected such that the predicted distribution of the anisotropy of the normal stresses ($v^2 - w^2$) best matched the experimentally observed distribution of LH&S. As mentioned earlier, the constant C_S controls the magnitude of the free-surface correction which in turn controls the strength of the secondary flows. Low values of C_S produces no free-surface correction whereas values higher than 0.5 can give rise to negative normal stresses at the free surface in the present explicit model. A value of 0.5 was used in the study which is close to the value adopted in the implicit version of the model (Celik and Rodi, 1984 and Miner et al., 1993).

4 Computational Parameters, Domain, and Boundary Conditions

The reference length (L) and velocity (Uo) are the plate (streamwise) length and the free-stream velocity. The computational parameters were selected to match the conditions of the data which were at a Froude number of 0.13. The Re_L for the data is 5.3E+05. Since Re_L is relatively small, the boundary layer was tripped near the leading edge to ensure that the flow is fully turbulent within a short distance from the leading edge. The boundary-layer measurements were obtained at $X = 0.5$ L where Re_θ was measured to be about 1160. The wake measurements were obtained at $X = 1.25$ L ($X/\theta = 30$). At both stations, measurements were taken at several depths. A detailed comparison of the deep flow measurements with several classic flat plate and wake data are provided in LH&S.

For the computations, no attempt was made to simulate the laminar and transitional region near the leading edge in the experiment. Reynolds number based on L and Uo was chosen to be 1.06E+06 so that Re_θ approaches the experimental value of 1160 at the mid-plate. No further effort was made to match x/θ in the wake. The simulated X/θ at $X = 1.25$ L in the near wake was obtained to be about 50.

Solutions were obtained for Froude numbers 0.0, 0.13, and 0.41 to study the free-surface wave prediction. However, detailed interrogation on the juncture vortices were limited to the low Froude number runs in the present investigation due to the fact that the data of LH&S are at Fr = 0.13.

The domain extends from $-L$ to $2L$ in the streamwise (X) direction and 0 to $L/2$ in the wall-normal (Y) direction. In the free-surface normal (Z) direction, domain size was selected based on the experimental observations that at a depth of $L/25$ the solution was almost two-dimensional with no significant free-surface effects. The deepest measurement points are at a depth of $Z = -L/8$. In the present numerical investigation, domain sizes of $L/8$, $L/4$, and $L/2$ gave similar results in the deep. The leading edge corresponds to $X = 0$. The simulations were obtained on three different grids: ($49 \times 25 \times 21$), ($73 \times 37 \times 31$) and ($97 \times 49 \times 41$). The corresponding $y^+_{\min}$ values were 0.2, 0.3 and 0.4 at $X = 0.5$ L. For zero Froude number simulations, identical mesh stretching is used in the free-surface normal direction such that $z^+_{\min}$ values at the free surface were 0.2, 0.3 and 0.4 for the three grids. For non-zero Froude number simulations, a similar grid study was not performed. The grid requirement, especially near and at the free-surface are dictated by the free-surface update algorithm. Most of the runs were performed on the finest grid ($97 \times 49 \times 41$) with a relaxed stretching ($z^+_{\min}$ about 3) and an increased domain size ($L/2$) in the free-surface normal direction. In addition to the 3-D juncture flow simulations, a 2-D investigation of flat plate boundary layer and wake was also conducted using three different turbulence models. The turbulence models used were the zero equation Baldwin Lomax (1978), henceforth B&L, linear two-equation k-ϵ model due to Chen and Patel (1988), henceforth C&P and the M&K model. The grids used in the 2-D study are identical to those used in the 3-D juncture flow study in the XY plane. Details of grid and convergence tests are discussed in the next section.

Free-stream values were prescribed at the inlet. The inlet values for k and ϵ were prescribed at 1.0E−10 and 1.0E−06 and the near-wall values are obtained from C&P. Zero gradient conditions are applied at the far field and the exit. Symmetry conditions are applied along the centerplane upstream and downstream of the plate and no-slip is applied on the plate. At the free-surface, for the zero Froude number a rigid-lid boundary is applied: zero normal velocity and zero-gradient for all other variables. For nonzero Froude number, the free-surface elevation is obtained by satisfying the kinematic condition. The dynamic boundary condition was approximated with zero gradient condition applied for the velocity components and the pressure boundary conditions obtained as a function of free-surface elevation and the Froude number. The complete derivation of the free-surface update algorithm and boundary conditions are given in Stern et al. (1996). For both zero and nonzero Froude numbers, a zero-gradient boundary condition is used for k at the free surface. For ϵ, a few different boundary treatments were tried, but it was found that no significant improvements could be gained over the zero-gradient condition.

5 Uncertainty Analysis

Uncertainty analysis for the present investigation was performed following ASME editorial policy statements and guidelines. Stern et al. (1996) grouped the procedures into three categories: documentation, verification and validation. The documentation, verification and validation of the code for surface ships are reported in Tahara and Stern (1996) and Stern et al. (1996). Issues regarding turbulence modeling for the present model problem were investigated during the present study. Documentation regarding turbulence modeling is provided in this paper; verification and validation are performed following Stern et al. (1996) and Coleman and Stern (1997).

The grids used in this study are selected based on preliminary investigative runs. For the flat-plate boundary-layer and wake flow, the important parameters identified for verification and validation include the distribution of mean streamwise velocity and turbulent kinetic energy, total drag on the plate, momentum thickness, upstream and wake centerline velocity and pressure. For the 3-D juncture flows, additional parameters selected include the strength of the secondary vortical regions. In the present study, for both 2-D and 3-D studies, the iterative convergence was obtained such that the residuals were at least 1E−05

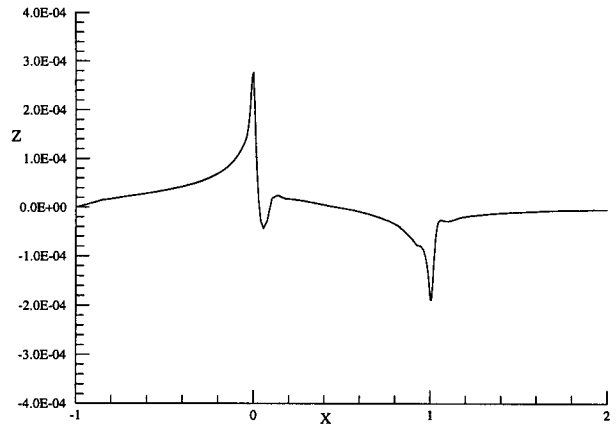

Fig. 1 Free-surface elevation at $Y = 0$, Fr = 0.13

or less. The grid convergence ratios were all less than a few percent. Regarding artificial dissipation, explicit dissipation was added to the free-surface solver (see Stern et al., 1996 for details) for the nonzero Froude number run in addition to the implicit dissipation associated with the finite analytic method for the RANS solver. No order of accuracy study was performed for this study.

As mentioned previously, the validation of the 2-D data with regards to comparison of the turbulence models were performed following Coleman and Stern (1997) and used as an example therein. The overall conclusion was that the mean flow and turbulent quantities are reasonably predicted by all the three models (B&L, C&P and M&K). Details are given in Coleman and Stern (1997). In the 3-D juncture flows, the flow at sufficient depths was essentially 2-D and identical to the results of the 2-D simulations. A brief discussion and a few typical figures comparing the 2-D results at large depths for the M&K model with the data are shown in the results section.

With regards to the 3-D juncture flow results, since the distribution of anisotropy of the normal stresses obtained from the data was used to calibrate the model, the term validation does not apply to that quantity. The comparison of other quantities for the 3-D juncture flow simulations against data are presented and discussed in the results section.

6 Results

The underlying (deep) flow solution is discussed first followed by the 3-D juncture flow results. The results are presented mainly with regard to the mean velocity, turbulent kinetic energy, streamwise vorticity and turbulent-stress anisotropy. The features of the data are described first for each of the quantities and then the simulation results are discussed bringing out the similarities and differences with the data. Unless otherwise stated all the results shown are for the M&K model.

With regards to the free-surface wave effects, even though the wave patterns for the present model problem of a surface-piercing flat plate are similar to a surface ship, the free-surface wave elevations are very small to be accurately measured with the available equipment. The maximum free-surface wave elevation is negligible and at least two orders of magnitude smaller than the boundary-layer thickness of the underlying flow with no waves predicted in the downstream wake region. The wave profile on the body for Fr = 0.13 is shown in Fig. 1. This profile is similar to that observed in the experiment and the wave patterns are consistent with those predicted for surface-piercing bodies. With regards to the present interest, the Fr = 0, where the boundary is treated as a rigid lid, and Fr = 0.13 solutions were identical, i.e., the waves had no effect on the solution, at least at the locations ($X = 0.5$ L and 1.25 L) where the data is interrogated in a detailed fashion. Hence the Fr = 0 solutions are presented hereafter. An outstanding issue, however, is the failure to predict the wave effects that are present in the data in the wake region downstream of the plate. These may be due to the detailed trailing-edge geometry and surface-tension effects which were not included in the computations.

Underlying Flow (Deep Flow). The solutions and data are compared at large depths ($Z = 0.125$ L). The skin friction coefficient and the wake-deficit are shown in Fig. 2 along with the mean streamwise velocity in the familiar wall coordinates. The solutions show reasonable agreement with the data. The other two velocity components (V and W) in the data are very small (around one percent Ue) with V and W showing outward and downward flow, respectively. The simulations also predict very small values for V (outward) and near zero values for W. The turbulent kinetic energy is also reasonably predicted.

Of critical concern is the prediction of the normal stresses. The normal turbulent intensities in the boundary layer are shown in Fig. 3. Also shown are the data, LES (Sreedhar and Stern, 1998), DNS (Rai and Moin, 1993), and the C&P results. The LES and DNS results are included to show the near-wall behavior. The M&K results are discussed first. The streamwise turbulence intensity is under predicted. The v^2 shows better agreement in the outer part of the boundary layer whereas it is over predicted in the inner part. The agreement of w^2 appears to be the best. As expected, the C&P model predicted isotropic normal stresses. More discussions on the normal Reynolds stresses with regard to the anisotropy term $v^2 - w^2$ are given in later sections. The predicted shear stress uv showed good agreement with the data whereas the other two shear-stress components were very small as per the data.

Boundary-Layer Juncture. The normal stress anisotropy is shown in Fig. 4. Recall that the distribution of the anisotropy of the normal stresses was used to construct the damping function in the free-surface correction term. The data show very high negative values near the plate and high positive values near the free surface with the two regions meeting near the juncture region at almost 45 deg angle. While the overall distribution of the anisotropy term in the simulated flow field is similar (this is expected since the model was calibrated based on this aspect of the data), there are some differences also, especially very close to the vertex in the juncture region.

Figure 5 shows the vorticity field and cross-plane velocity vectors. The data show counter-clockwise vorticity in the inner region and clockwise vorticity in the outer region very close to

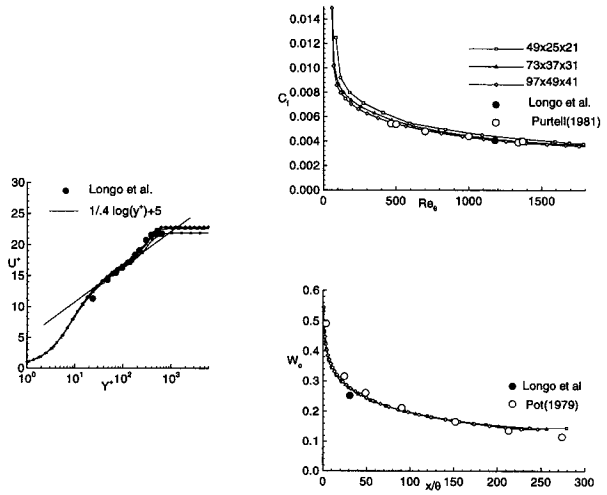

Fig. 2 Myong and Kassagi model deep solution, Mean streamwise velocity (left), skin friction (top right) and wake deficit (bottom right)

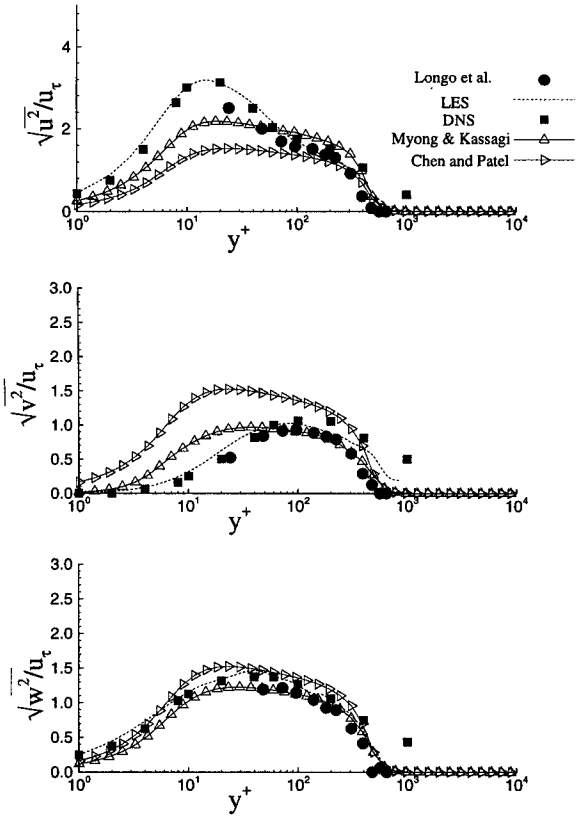

Fig. 3 Turbulence intensities, LES (Sreedhar and Stern, 1998, $Re_\theta = 1150$), DNS (Rai and Moin, 1993, $Re_\theta = 1350$), Data and RANS are at $Re_\theta = 1160$

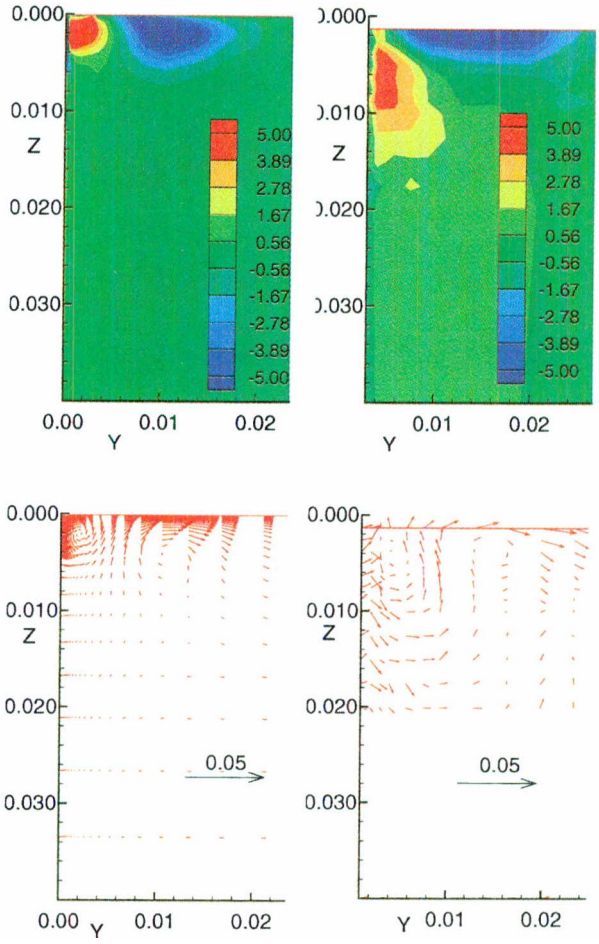

Fig. 5 Boundary layer juncture ($X = 0.5$), streamwise vorticity (top), *VW* vectors (bottom), data on the right

the free surface. The perturbation velocity vectors are shown for the data (i.e., the mean velocities minus its counterparts in the deep) to better see the secondary flow regions. Compared to the data, the inner vortical region in the simulations has a much tighter vortical core and is closer to the free surface. The outer vortical region is positioned similar to the data.

Figure 6 shows the streamwise-velocity and kinetic-energy contours. The data show a decrease in the boundary-layer thickness followed by an increase as the free surface is approached. The simulations predict similar results even though the initial decrease in the thickness is not as strong as the data. With regards to the kinetic energy contours, the data show a decrease and an increase as the free surface is approached which is analogous to the behavior of the mean streamwise-velocity contours. The increase in kinetic energy extends over a large portion of the boundary-layer thickness. The simulation on the other hand shows a decrease in kinetic energy near the free surface over a major portion of the boundary-layer thickness. The kinetic energy increases are seen only at the outer edge of the boundary layer.

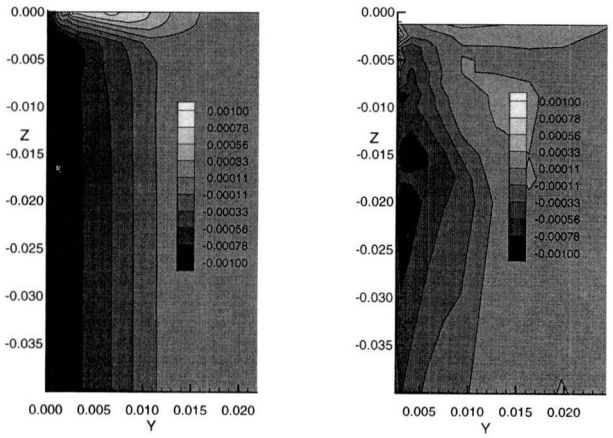

Fig. 4 Anisotropy term $v^2 - w^2$ at $X = 0.5$, data on the right

Wake Juncture. The flow in the wake-juncture region is not fully understood in comparison to the boundary-layer juncture. Data show a thin layer near the free surface where the anisotropy of the normal stresses ($v^2 - w^2$) is positive. Beneath that layer, the values are mainly negative. Even though, the present model also predicts a pattern with a region of positive values near the free surface and a mainly negative region beneath the agreement is rough.

With regard to secondary flows and the vorticity distribution, certain similarities are present, but the secondary flows are not as coherent and strong as the boundary-layer juncture. This can be seen in Fig. 7 which shows the streamwise vorticity and velocity vectors. The data show a region of high clockwise-oriented vorticity near the free surface in the outer edge of the wake. In the inner region, a region of counter-clockwise-oriented vorticity is seen even though not very coherent or well defined. The predictions, on the other hand, show somewhat similar pattern except that the outer vortical region extends deeper and is less wide, and the inner vortical region is better defined and circular in shape. Figure 8 shows the mean velocity and kinetic energy distribution. The spreading of the wake near the free surface is observable. The large increases in the kinetic energy at the free surface are due to the free-surface wave

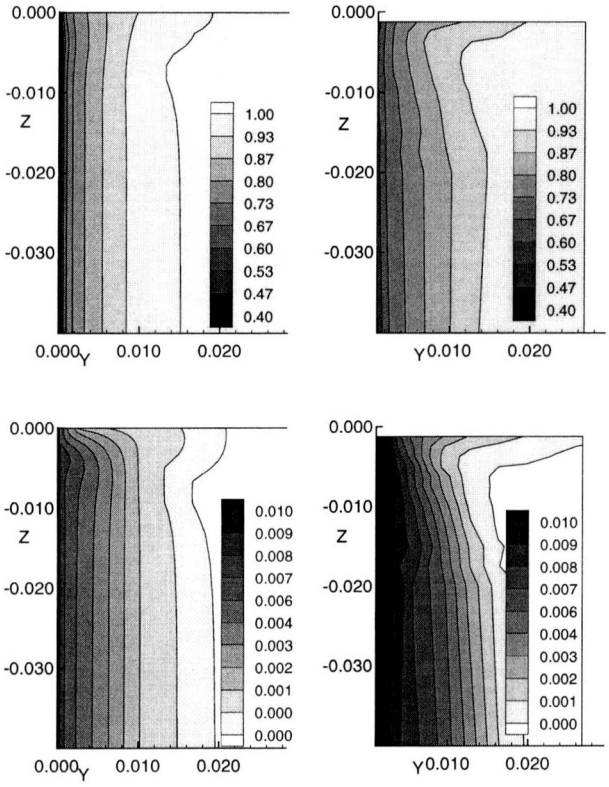

Fig. 6 Boundary layer juncture (X = 0.5), streamwise velocity (top), kinetic energy (bottom), data on the right

effects. With regards to the simulation, the spreading of the wake is seen near the free surface. However, it is not as extensive as the data. The kinetic energy shows qualitative agreement with the data only in the inner portion of the wake. The disagreement in the outer portion of the wake may be due to the wave effects present in the data.

The simulations obtained without the surface-correction term (in Eq. (1)) in the wake region predicted a weaker inner vortex near the symmetry plane. However, other features including the thickening of the wake near the free-surface region remained almost unaffected at X = 1.25 L.

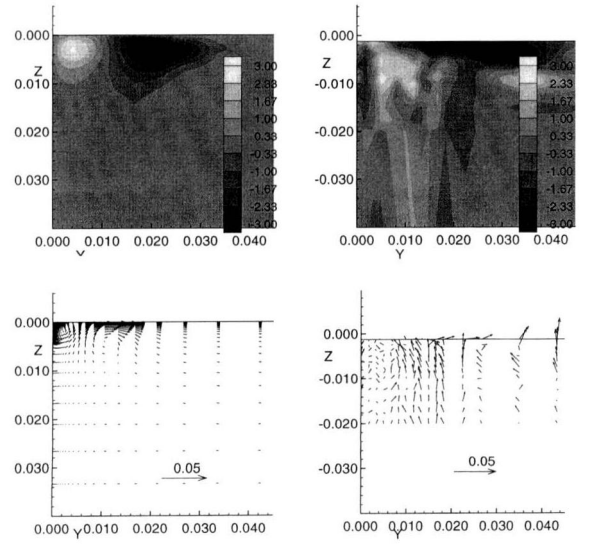

Fig. 7 Wake juncture (X = 1.25), streamwise vorticity (top), *VW* vectors (bottom), data on the right

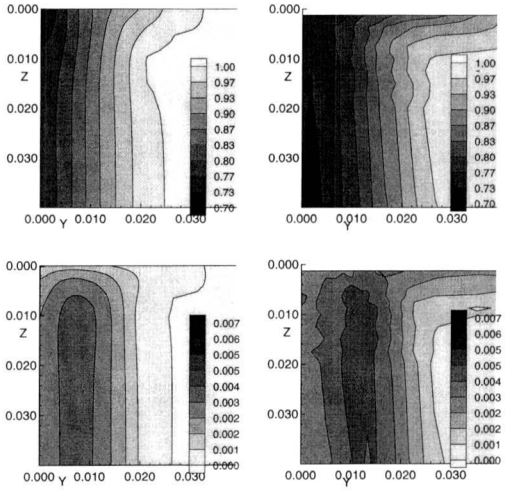

Fig. 8 Wake juncture (X = 1.25), streamwise velocity (top), kinetic energy (bottom), data on the right

Intermediate Wake Region. The exit boundary of the present simulation corresponds to x/θ of around 250 which is in the intermediate wake region ($25 < x/\theta < 350$). The present simulation displayed good agreement with the two-D data of Pot (1979) with regards to the wake half width and wake centerline velocity. The asymptotic half-power laws are generally not applicable until the far wake ($X/\theta > 350$) and hence not valid here. However, it is well known that the present k-ϵ model without modifications can not correctly predict the asymptotic growth and decay rates in the far wake.

The plots of streamwise mean velocity at various cross sections indicate a simultaneous growth of the wake in the deep and near the free surface. Even though the streamwise vorticity on the other hand showed a decaying trend downstream, the thickening of the wake near the free surface was clearly sustained at all the cross sections. On the other hand, the simulations obtained without the free-surface-correction term in the wake region (i.e., $C_S = 0$ in the wake) showed a decrease in the extent of the free-surface thickening in the downstream cross sections very close to the exit plane at X = 2 L.

7 Analysis and Comparison With Related Studies

An analysis is made of the physical mechanism for the streamwise vortices and of the free-surface effects on the Reynolds stresses and compared with the findings of related studies.

Physical Mechanism for the Secondary Flows. The Reynolds-averaged streamwise-vorticity transport equation is given below.

$$\frac{D\omega_x}{Dt} = \omega \cdot \nabla U + \frac{1}{\mathrm{Re}} \nabla^2 \omega_x + \frac{\partial}{\partial x}\left(\frac{\partial uv}{\partial z} - \frac{\partial uw}{\partial y}\right) + \frac{\partial^2}{\partial y \partial z}(v^2 - w^2) + \left(\frac{\partial^2}{\partial z^2} - \frac{\partial^2}{\partial y^2}\right) vw \quad (5)$$

LH&S label the terms from left to right as A to F. Based on their analysis and other previous studies for closed and open channel flows, it has been concluded that the last two terms, i.e., terms E and F are the dominant terms. Moreover, E and F have opposite signs with E acting like a source term and F like a damping term and it is their difference that generates the secondary flows. A term by term examination of Eq. (5) using the present model and simulation results at X = 0.5 reconfirmed the above conclusions regarding the role of the anisotropy term $v^2 - w^2$ (shown in Fig. 4) in the generation of secondary flows.

LH&S obtained a scaling relation for the normalized anisotropy term based on its maximum value and the distance along the intercept from the boundary to the location where the term attains zero value (see LH&S for details). The LES study of Sreedhar and Stern (1998) also displayed similar trends. The present simulation results (not shown here) indicated only a rough qualitative similarity. A curve fit to the data based on the scaling relation and the reconstruction of the Term E showed that the regions of high vorticity correlated with the high values of Term E. This was predicted by the present results. The detailed patterns of the reconstructed contours of term E also indicated blending regions of opposite signs between the regions of high values near the plate and the free surface. This was also roughly predicted by the present scheme. While the present study and the data showed two vortical regions of opposite signs, the LES (Sreedhar and Stern, 1998) and a related DNS study (Leighton et al., 1994) predicted only one cross plane vortical region near the solid/rigid-lid juncture. With regards to submerged jets, even though cross plane vortices have been predicted near the free surface in a DNS study (Mangiavaachi et al., 1994), detailed analysis is lacking.

The thickening of the boundary layer predicted by the present model near a rigid-lid boundary was observed by Sreedhar and Stern (1998) in their LES study. The thickening of the wake near the free surface behind a surface-piercing flat-plate has been experimentally observed by Logory et al. (1996). A similar thickening of the jet width is observed in submerged-jet studies. Walker (1997), in his analysis of submerged jets, labels this phenomenon as surface current and relates its origin to the anisotropy the normal stresses near the free surface.

With regards to the wake-juncture region, at $X = 1.25$ L, the terms E and F in the streamwise vorticity transport equation were not as dominant as they were on the plate. Moreover, in contrast to the plate region, the convection term appears to be equally significant as the terms E and F. As we proceed further downstream, near the exit plane at $X = 2$ L, the convection term becomes the dominant term indicating that most of the streamwise vorticity present in the wake region is not generated in the wake region, instead, it is either convected downstream from the plate or is generated as a result of the transported anisotropic distribution of the normal stresses from the plate. This explains the relatively large values of terms E and F in the near wake region before diffusing away as they are convected further downstream. Even though the strength of the secondary vortices weakened, the free-surface wake spreading continues as the deep-wake width grows downstream.

Free-Surface Effects on Turbulence. The present simulation predicts a decrease in kinetic energy as the free surface is approached in the major portion of the boundary layer and the increase in kinetic energy is only in the outer edge of the boundary layer. However, the data and LES show increases in kinetic energy near the free-surface/rigid-lid boundary over a substantial portion of the boundary layer. Kinetic-energy increases are also observed in open-channel flow and submerged-tip-vortex data, whereas the submerged-jet data indicate nearly constant values. A DNS of an initially homogeneous turbulent field (Walker et al., 1996) subjected to a rigid-lid boundary indicated an increase in kinetic energy. This increase in kinetic energy is shown to be due to a decrease in dissipation near the rigid-lid boundary. This is in contrast to the assumptions made in previous RANS simulations (e.g., Celik and Rodi, 1984) where the dissipation at the free surface is prescribed at a higher value. This is an area that requires further investigation.

The anisotropy tensor (a_{ij}) and its invariants ($A_2 = a_{ij}a_{ij}$ and $A_3 = a_{ij}a_{jk}a_{ki}$) computed from the Reynolds stresses is a measure of the level of anisotropy. Shown in Fig. 9 is the comparison of the normal components of the anisotropy stress tensor with the data and other related studies. A similar plot of the invariants of the anisotropy tensor (not shown here) also displayed general

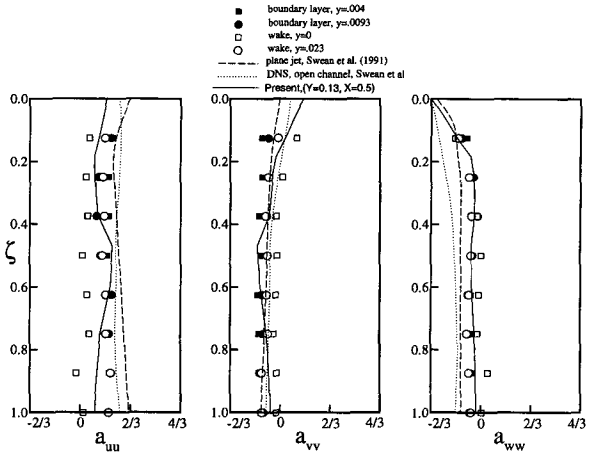

Fig. 9 Anisotropy tensor components, symbols indicate data (Longo et al., 1998), $z = z/\delta$ for data and present RANS, z normalized by channel depth and jet axis in the other two studies

agreement with the data of LH&S and submerged-jet and open-channel flow studies with regard to their distribution and the limiting behavior.

8 Conclusions and Future Work

A nonlinear eddy-viscosity near-wall model combined with a free-surface correction term is tested for solid/free-surface boundary-layer and wake juncture flows of a surface-piercing flat plate at low Froude numbers. The different elements of the model are combined and the model constants calibrated based on the premises that the anisotropy of the normal stresses is mainly responsible for the dynamics of the flow in the juncture region and an accurate distribution of the normal-stress anisotropy is a primary requirement for the successful prediction of the overall flow field.

The solution at large depths displays the characteristic behavior of two-dimensional canonical flat-plate boundary-layer and wake flow including the anisotropy of normal stresses in the near-wall region. The damping effect of the free-surface correction term alters the distribution of the anisotropy of the normal stresses and sets up secondary flows. The secondary flows transport low mean velocity and high turbulence to the outer edge of the boundary layer thus effecting a thickening of the boundary layer near the free surface. A similar thickening was observed for the near wake also. However, the flow in the wake-juncture region is not as well understood as that in the boundary-layer juncture. While certain similarities are present, the secondary flows are not as coherent and strong as the boundary-layer juncture. The effect of free-surface waves on the overall solution was found to be negligible for the low Froude number range of the present investigation. An examination of the terms in the turbulent streamwise-vorticity transport equation reconfirmed the importance of the anisotropy of the normal Reynolds stresses in the production of streamwise vorticity. Free-surface effects on Reynolds stresses were analyzed with regard to the anisotropy tensor and its invariants. The overall near-surface behavior of these quantities is consistent with the data and other related studies.

While the turbulence model used in this study was successful in predicting most of the major features of interest for the model problem investigated notably for the boundary-layer juncture, there are still several issues that need to addressed especially for the wake-juncture. Because the present model problem had negligible free-surface wave and geometry effects, the present study must be regarded as a building block and future work must include the testing for wave-induced pressure-gradient effects (i.e., flat plate with Stokes waves for which extensive data

is available) and for combined wave and geometry effects (i.e., for practical ship forms including combatants). The extension of the model for surface ships involves the development of a more generalized form of the damping function for the free-surface correction term. Also of interest for future work are refinements for improved resolution, extension of domain to include the far-wake region, investigation of k and ϵ boundary conditions near the free surface, extensions for more general near-wall models such as the Gatski and Speziale (1993) model along with implicit algebraic and full Reynolds stress models.

Acknowledgments

This work is supported by the Office of Naval Research under Grant No. N0014-96-1-0018 under the administration of Dr. E. P. Rood. We also acknowledge the support of supercomputers at the NAVO Oceanographic Office.

References

Anthony, D. G., and Willmarth, W. W., 1992, "Turbulence Measurements in a Round Jet Beneath a Free Surface," *Journal of Fluid Mechanics,* Vol. 243, pp. 699–720.

Baldwin, B. S., and Lomax, H., 1978, "Thin Layer Approximation and Algebraic Model for Separated Turbulent Flows," *AIAA* 78–257.

Celik, I., and Rodi, W., 1984, "Simulation of Free-Surface Effects in Turbulent Channel Flow," *Physicochemical Hydrodynamics,* Vol. 5, pp. 217–226.

Chen, H. C., and Patel, V. C., 1988, "Near-Wall Turbulence Models for Complex Flows Including Separation," *AIAA Journal,* Vol. 26, No. 6, pp. 641–648.

Coleman, H., and Stern, F., 1997, "Uncertainties and CFD Code Validation," to appear in ASME JOURNAL OF FLUIDS ENGINEERING.

Demuren, A. O., 1991, "Calculation of Turbulence-Driven Secondary Motion in Ducts with Arbitrary Cross Section," *AIAA Journal,* Vol. 29, No. 4, pp. 531–537.

Gatski, T. B., and Speziale, C. G., 1993, "On Explicit Algebraic Stress Models for Complex Turbulent Flows," *Journal of Fluid Mechanics,* Vol. 254, pp. 59–78.

Grega, L. M., Wei, T., Leighton, R. I., and Neeves, J. C., 1995, "Turbulent Mixed-Boundary Flow in a Corner Formed by a Solid Wall and a Free Surface," *Journal of Fluid Mechanics,* Vol. 294, pp. 17–46.

Gibson, M. M., and Rodi, W., 1989, "Simulation of Free-Surface Effects on Turbulence with a Reynolds Stress Model," ASCE *Journal of Hydraulic Research,* Vol. 27, No. 2, pp. 233–244.

Launder, B. E., Reece, G. J., and Rodi, W., 1975, "Progress in the Development of a Reynolds-Stress Turbulence Closure," *Journal of Fluid Mechanics,* Vol. 68, pp. 537–566.

Longo, J., Huang, H. P., and Stern, F., 1998, "Solid/Free-Surface Juncture Boundary Layer and Wake," to appear in *Experiments in Fluids.*

Logory, L. M., Hirsa, A., and Anthony, D. G., 1996, "Interaction of Wake Turbulence with a Free Surface," *Physics of Fluids,* Vol. 8, No. 3, pp. 805–815.

Leighton, R., Wei, T., and Neves, J. C., 1994, "The Secondary Flow of the Mixed Boundary-Layer Corner Flow," *Free Surface Turbulence,* FED Vol. 181, ASME Fluid Dynamics Conference, pp. 15–24.

Mangiavacchi, Gudlapalli, R., and Akhavan, R., 1994, "Dynamics of a Turbulent Jet Interacting with a Free Surface," *Free Surface Turbulence,* FED Vol. 181, ASME Fluid Dynamics Conference, pp. 69–76.

Miner, E. W., Stewart, M. B., and Swean, T. F., 1993, "Modeling and Computation of Turbulent Free-Surface Jets," *AIAA* 93-0201.

Myong, H. K., and Kassagi, N., 1990, "Prediction of Anisotropy of the Near-Wall Turbulence with an Anisotropic Low-Reynolds-Number k-e Turbulence Model," ASME JOURNAL OF FLUIDS ENGINEERING, Vol. 112, No. 12, pp. 521–524.

Naot, D., and Rodi, W., 1982, "Calculation of Secondary Currents in Channel Flows," ASCE *Journal of Hydraulics,* Vol. 108, pp. 949–968.

Naot, D., and Nezu, I., and Nakagawa, H., 1993, "Hydrodynamic Behavior of Compound Rectangular Open Channels," ASCE *Journal of Hydraulic Engineering,* Vol. 119, No. 3, pp. 390–408.

Nezu, I., and Nakagawa, H., 1987, "Numerical Calculation of Turbulent Open-Channel Flows in Consideration of Free-Surface Effect," Memoirs, Faculty. of Eng., Kyoto University, 49, No. 2.

Paterson, E. G., Hyman, M. C., Stern, F., Carrica, P. A., Bonetto, F., Drew, D., and Lahey, R. T., 1996, "Near- and Far-Field CFD for Naval Combatants Including Thermal Stratification and Two-Fluid Modeling," *Proceedings of the 21st ONR Symp. on Naval Hydrodynamic,* Trondheim, Norway.

Pot, P. J., 1979, "Measurements in a 2-D Wake and in a 2-D Wake Merging into a Boundary Layer," Data Report, NLR TR-79063 U, The Netherlands.

Purtell, L. P., Klebanoff, P. S., and Buckley, F. T., 1981, "Turbulent Boundary Layer at Low Reynolds Number," Vol. 24, No. 5, pp. 802–811.

Rai, M. M., and Moin, P., 1993, "Direct Numerical Simulation of Transition and Turbulence in a Spatially-Evolving Compressible Boundary Layer," *Journal of Computational Physics,* Vol. 109, pp. 169–192.

Shir, C. C., 1973, "A Preliminary Numerical Study of Atmospheric Turbulent Flows in the Idealized Planetary Boundary Layer," *Journal of Atmospheric Sciences,* Vol. 30, pp. 1327–1339.

Speziale, C. G., and Abid, R., 1995, "Near-Wall Integration of Reynolds-Stress Turbulence Closures with No Wall Damping," *AIAA Journal,* Vol. 33, No. 10, pp. 1974–1977.

Sreedhar, M., and Stern, F., 1998, "Large Eddy Simulation of Temporally Developing Juncture Flows," to appear in *International Journal of Numerical Methods in Fluids.*

Stern, F., Paterson, E., and Tahara, Y., 1996, "CFDSHIP-IOWA: Computational Fluid Dynamics Method for Surface-Ship Boundary Layers, Wakes, and Wave Fields," IIHR report No. 381, University of Iowa.

Swean, T. F., Ramberg, S. E., and Miner, E. W., 1991a, "Anisotropy in a Turbulent Jet Near a Free Surface," ASME JOURNAL OF FLUIDS ENGINEERING, Vol. 113, pp. 430–438.

Swean, T. F., Leighton, R. I., and Handler, R. A., 1991b, "Turbulence Modeling Near the Free Surface in an Open Channel Flow," *AIAA* 91-0613.

Tahara, Y., and Stern, F., 1996, "A Large-Domain Approach for Calculating Ship Boundary Layers and Wakes and Wave Fields for Non-Zero Froude Number," *Journal of Computational Physics,* Vol. 127, pp. 398–411.

Walker, D. T., and Chen, C. Y., 1994, "Evaluation of Algebraic Stress Modeling in Free-Surface Jet Flows," *Free Surface Turbulence,* ASME FED Vol. 181, pp. 83–95.

Walker, D. T., Chen, C. Y., and Willmarth, W. W., 1995, "Turbulent Structure in Free-Surface Jet Flows," *Journal of Fluid Mechanics,* Vol. 291, pp. 223–261.

Walker, D. T., Leighton, R. I., and Garza-Rios, L. O., 1996, "Shear Free Turbulence Near a Flat Free Surface," *Journal of Fluid Mechanics,* Vol. 320, pp. 19–51.

Walker, D. T., 1997, "On the Origin of the Surface Current in Turbulent Free-Surface Flows," Personal communication, Also to appear in *Journal of Fluid Mechanics.*

Wilcox, D. C., 1993, *Turbulence Modeling for CFD,* DCW Industries, La Jolla, CA.

First and Second-Order Accurate Schemes for Two-Fluid Models

Iztok Tiselj
Researcher.

Stojan Petelin
Professor.

"Jožef Stefan" Institute
Jamova 39, 1111 Ljubljana, Slovenia

The six-equation two-fluid model of two-phase flow taken from the RELAP5/MOD3 computer code has been used to simulate three simple transients: a two-phase shock tube problem, the Edwards Pipe experiment, and water hammer due to rapid valve closure. These transients can be characterized as fast transients, since their characteristic time-scales are determined by the sonic velocity. First and second-order accurate numerical methods have been applied both based on the well-known, Godunov-type numerical schemes. Regarding the uncertainty of the two-fluid models in today's large computer codes for the nuclear thermal-hydraulics, use of second-order schemes is not always justified. While this paper shows the obvious advantage of second-order schemes in the area of fast transients, first-order accurate schemes may still be sufficient for a wide range of two-phase flow transients where the convection terms play a minor role compared to the source terms.

Introduction

Safety analyses of nuclear reactors require computations of complex two-phase flows. One of the codes used for simulations of transients in the systems of the nuclear power plants is RELAP5 (Carlson et al., 1990). The numerical method used in RELAP5 is based upon a semi-implicit finite difference scheme with staggered grid and donor-cell discretization of the convective terms. The method is first-order accurate in time and space. The main advantages of such a scheme are robustness and efficiency while the weak side is its numerical dissipation, which tends to smear discontinuities on coarse grids. The basic partial differential equations are one-dimensional, contain first-order derivatives only and are of mixed hyperbolic-elliptic type, i.e. two of the six eigenvalues can have a small imaginary component (No, Kazimi, 1985). The RELAP5 equations, with the boundary and initial conditions, present an ill-posed problem. However, the discretized equations are not ill-posed (see Shieh et al., 1994 for details).

Simulations with the second-order scheme described in this paper require a hyperbolic set of equations. This was achieved with an improved form of the virtual mass term and a slight modification of the virtual mass coefficient in the momentum equations (Tiselj, Petelin, 1995). Correlations of bubbly and droplet regimes of two-phase flow were used as closure relations for interphase mass, momentum, and energy exchange.

Advantages of the second-order methods compared to the first-order schemes are well known: improved accuracy and shock capturing capability. However, the main question for the discussion in this paper is whether the second-order schemes are needed at all for the current two-fluid models with a relatively high uncertainty of the basic mathematical models.

Basic Equations

The basic equations taken from RELAP5 are mass, momentum, and energy balances for vapor and liquid (Carlson et al., 1990) without terms for wall-to-fluid heat transfer:

$$\frac{\partial(1-\alpha)\rho_f}{\partial t} + \frac{1}{A}\frac{\partial(1-\alpha)\rho_f v_f A}{\partial x} = -\Gamma_g, \quad (1)$$

$$\frac{\partial \alpha \rho_g}{\partial t} + \frac{1}{A}\frac{\partial \alpha \rho_g v_g A}{\partial x} = \Gamma_g, \quad (2)$$

$$(1-\alpha)\rho_f \frac{\partial v_f}{\partial t} + \frac{1}{2}(1-\alpha)\rho_f \frac{\partial v_f^2}{\partial x} = -(1-\alpha)\frac{\partial p}{\partial x} + (1-\alpha)\rho_f g \cos\theta - \frac{1}{2}(1-\alpha)\rho_f \frac{f_{wf}}{D}|v_f|v_f - \Gamma_g(v_{fi}-v_f) + \frac{C_D}{8}\rho_c a_{gf}|v_r|v_r + CVM, \quad (3)$$

$$\alpha\rho_g \frac{\partial v_g}{\partial t} + \frac{1}{2}\alpha\rho_g \frac{\partial v_g^2}{\partial x} = -\alpha\frac{\partial p}{\partial x} + \alpha\rho_g g\cos\theta - \frac{1}{2}\alpha\rho_g \frac{f_{wg}}{D} \times |v_g|v_g + \Gamma_g(v_{gi}-v_g) - \frac{C_D}{8}\rho_c a_{gf}|v_r|v_r - CVM, \quad (4)$$

$$\frac{\partial(1-\alpha)\rho_f u_f}{\partial t} + \frac{1}{A}\frac{\partial(1-\alpha)\rho_f u_f v_f A}{\partial x} = -p\frac{\partial(1-\alpha)}{\partial t} - \frac{p}{A}\frac{\partial(1-\alpha)v_f A}{\partial x} + Q_{if} - \Gamma_g h_f^* + \frac{1}{2}(1-\alpha)\rho_f \frac{f_{wf}}{D} v_f^2 |v_f|, \quad (5)$$

$$\frac{\partial \alpha\rho_g u_g}{\partial t} + \frac{1}{A}\frac{\partial \alpha\rho_g u_g v_g A}{\partial x} = -p\frac{\partial \alpha}{\partial t} - \frac{p}{A}\frac{\partial \alpha v_g A}{\partial x} + Q_{ig} + \Gamma_g h_g^* + \frac{1}{2}\alpha\rho_g \frac{f_{wg}}{D} v_g^2 |v_g|. \quad (6)$$

Two additional equations of state for each phase are needed to close the system of equations. The equation of state for phase k is

$$d\rho_k = \left(\frac{\partial \rho_k}{\partial p}\right)_{u_k} dp + \left(\frac{\partial \rho_k}{\partial u_k}\right)_p du_k. \quad (7)$$

Derivatives on the right-hand side of Eq. (7) are determined by the RELAP5 water property subroutines using pressure and specific internal energy as an input.

Constitutive equations for the wall friction (terms with f_{wf}, f_{wg}), interphase drag (terms with C_D) and the interphase exchange of mass and energy (terms with Γ_g, Q_{ig}, Q_{if}) were also taken from the RELAP5 code. We applied the correlations of the RELAP5 "high-mixing" flow regime map: bubbly flow correlations ($\alpha < 0.5$), droplet flow correlations ($\alpha > 0.95$), and interpolation for the intermediate vapor volume fractions

Contributed by the Fluids Engineering Division for publication in the JOURNAL OF FLUIDS ENGINEERING. Manuscript received by the Fluids Engineering Division February 14, 1997; revised manuscript received December 5, 1997. Associate Technical Editor: J. K. Eaton.

$(0.5 < \alpha < 0.95)$. With such a rough flow regime map better results are expected for well mixed flows with lower vapor volume fractions ($\alpha < 0.5$) and less reliable results for vapor volume fractions above 0.5, where the slug and annular flow regime correlations were omitted. Realistic results cannot be expected for the stratified two-phase flows.

The RELAP5 manual (Carlson et al., 1990) offers the following virtual mass term *CVM* in Eqs. (3) and (4):

$$CVM = C_{vm}\alpha(1-\alpha)\rho_m\left(\frac{\partial v_g}{\partial t} + v_f\frac{\partial v_g}{\partial x} - \frac{\partial v_f}{\partial t} - v_g\frac{\partial v_f}{\partial x}\right). \quad (8)$$

However, due to problems with the RELAP5 numerical scheme, *CVM* term is coded with the time derivative of the relative velocity only:

$$CVM = C_{vm}\alpha(1-\alpha)\rho_m\frac{\partial v_r}{\partial t}. \quad (9)$$

The virtual mass term (8) was used in our code since it improves the hyperbolicity of the equations.

Basic RELAP5 equations present an ill-posed problem (No, Kazimi, 1985) with complex eigenvalues of the Jacobian matrix (matrix **C** in Eq. (16)). With the virtual mass term (8) the equations are well-posed for vapour volume fractions lower than approximately 0.7. With a small modification of the virtual mass coefficient C_{vm} at higher vapor volume fractions ($\alpha > 0.5$) an additional improvement of the hyperbolicity of the equations has been achieved. With the virtual mass term (8), and virtual mass coefficient proposed by Tiselj and Petelin (1995), equations are well-posed, except for the extremely high relative interphase velocities (comparable to the sonic velocities).

Numerical Method

Our program used for solving RELAP5 equations was named 2F (Two-Fluid) and can solve hyperbolic equations. The numerical scheme applied is based on the Godunov method. Its behavior with the equations of the two-fluid models was analyzed by Tiselj and Petelin (1997).

The system of equations (1)–(6) can be written in the following nonconservative form which is suitable for the numerical solving:

$$\mathbf{A}\frac{\partial \boldsymbol{\psi}}{\partial t} + \mathbf{B}\frac{\partial \boldsymbol{\psi}}{\partial x} = \mathbf{S}, \quad (10)$$

where $\boldsymbol{\psi}$ represents the vector of the independent variables $\boldsymbol{\psi} = (p, \alpha, v_f, v_g, u_f, u_g)$, **A** and **B** are matrices of the system and **S** is a vector with nondifferential terms in the equations. The numerical scheme used in 2F code is a two-step scheme with operator splitting; i.e., convection and sources in Eq. (10) were treated separately:

$$\mathbf{A}\frac{\partial \boldsymbol{\psi}}{\partial t} + \mathbf{B}\frac{\partial \boldsymbol{\psi}}{\partial x} = 0, \quad (11)$$

$$\mathbf{A}\frac{d\boldsymbol{\psi}}{dt} = \mathbf{S}, \quad (12)$$

Second-order accuracy was achieved with Strang splitting (LeVeque, 1992). One time step includes the following three substeps (superscripts n, $n+1$ denote time levels—*, ** denote intermediate time levels):

(1)—integration of the sources—Eq. (12)—over one half of the time step:

$$\boldsymbol{\psi}_j^* = \boldsymbol{\psi}_j^n + \int_{t^n}^{t^n+\Delta t/2} \mathbf{A}^{-1}(\boldsymbol{\psi}_j)\mathbf{S}(\boldsymbol{\psi}_j(t))dt \quad (13)$$

(2)—convection—Eq. (11):

$$\boldsymbol{\psi}_j^{**} = \boldsymbol{\psi}_j^* - \Delta t\left((\mathbf{A}^{-1}\mathbf{B})^*\frac{\partial \boldsymbol{\psi}^*}{\partial x}\right)_j \quad (14)$$

(3)—integration of the sources—second half of the time step:

$$\boldsymbol{\psi}_j^{n+1} = \boldsymbol{\psi}_j^{**} + \int_{t^{**}}^{t^{**}+\Delta t/2} \mathbf{A}^{-1}(\boldsymbol{\psi}_j)\mathbf{S}(\boldsymbol{\psi}_j(t))dt \quad (15)$$

Each of the substeps is solved with the second-order accurate method.

Convection Terms

Equation (11) multiplied by $\mathbf{A}^{-1}$ from the left gives

$$\frac{\partial \boldsymbol{\psi}}{\partial t} + \mathbf{C}\frac{\partial \boldsymbol{\psi}}{\partial x} = 0. \quad (16)$$

$\mathbf{C} = \mathbf{A}^{-1}\mathbf{B}$ is the Jacobian matrix, which is diagonalized

$$\mathbf{C} = \mathbf{L}\boldsymbol{\Lambda}\mathbf{L}^{-1} \quad (17)$$

with the diagonal matrix of eigenvalues $\boldsymbol{\Lambda}$ and the matrix of eigenvectors **L** of the matrix **C**. Characteristic variables are introduced as

$$\delta\boldsymbol{\xi} = \mathbf{L}^{-1}\delta\boldsymbol{\psi}, \quad (18)$$

where $\delta\boldsymbol{\xi}$ represents an arbitrary variation: $\partial\boldsymbol{\xi}/\partial t$ or $\partial\boldsymbol{\xi}/\partial x$. The characteristic form of Eq. (16)

$$\frac{\partial \boldsymbol{\xi}}{\partial t} + \boldsymbol{\Lambda}\frac{\partial \boldsymbol{\xi}}{\partial x} = 0 \quad (19)$$

presents a basis for the second-order accurate numerical schemes.

Nomenclature

A = cross section (m^2)
a_{gf} = interphase surface area (m^2)
C_D = coef. of interphase friction
c_p = specific heat capacity at constant pressure (J/kg-K)
C_{vm} = virtual mass coef.
D = tube diameter (m)
f_w = wall drag coef.
g = acc. of gravity
h = specific enthalpy (J/kg)
p = pressure (Pa)
T = temperature (K)
u = specific internal energy (J/kg)
v = velocity (m/s)
α = vapor volume fraction
Γ = mass source (kg/m^3 s)
Q_i = heat exchange between phases (W/m^3)
ρ = density (kg/m^3)
$\boldsymbol{\Lambda}$, λ = matrix of the eigenvalues, eigenvalue

Subscripts

c = continuous phase
f = liquid
g = vapor
i = interphase surface
r = relative (velocity $v_r = v_g - v_f$)
m = mixture

Problems of the pure second-order accurate discretization—Lax-Wendroff for example—are oscillations which appear in the vicinity of the nonsmooth solutions. The problem is solved (Leveque, 1992) if a combination of the first and second-order accurate discretizations is used. Part of the second-order discretization is determined by the limiters, which "measure" the smoothness of the solutions. If the solutions are smooth, larger part of the second-order discretization is used, otherwise the larger part of the first-order discretization is used. An improved characteristic upwind discretization of the Eq. (19) was used as a first-order discretization (Hirsch, 1988).

Combination of the first and second-order accurate discretizations of Eq. (19) is (Tiselj, Petelin, 1997):

$$\frac{\boldsymbol{\xi}_j^{n+1} - \boldsymbol{\xi}_j^n}{\Delta t} + (\boldsymbol{\Lambda}^{++})_{j-1/2}^n \frac{\boldsymbol{\xi}_j^n - \boldsymbol{\xi}_{j-1}^n}{\Delta x} + (\boldsymbol{\Lambda}^{--})_{j+1/2}^n \frac{\boldsymbol{\xi}_{j+1}^n - \boldsymbol{\xi}_j^n}{\Delta x} = 0. \quad (20)$$

Elements of the diagonal matrices $\boldsymbol{\Lambda}^{++}$, $\boldsymbol{\Lambda}^{--}$ are calculated as:

$$\lambda_k^{++} = \max(0, \lambda_k) + \frac{\phi_k \lambda_k}{2}\left(\lambda_k \frac{\Delta t}{\Delta x} - \frac{\lambda_k}{|\lambda_k|}\right), \quad k = 1, 6, \quad (21)$$

$$\lambda_k^{--} = \min(0, \lambda_k) - \frac{\phi_k \lambda_k}{2}\left(\lambda_k \frac{\Delta t}{\Delta x} - \frac{\lambda_k}{|\lambda_k|}\right), \quad k = 1, 6. \quad (22)$$

The flux limiter ϕ_k is calculated using MINMOD formula (LeVeque, 1992):

$$\phi_k = \max(0, \min(1, \theta_k)), \quad k = 1, 6, \quad (23)$$

where θ_k measures the ratio of the left and the right gradients in the grid point $j + \frac{1}{2}$:

$$\theta_{k,j+1/2} = \frac{\xi_{k,j+1-m} - \xi_{k,j-m}}{\xi_{k,j+1} - \xi_{k,j}},$$

$$m = \frac{\lambda_{k,j+1/2}}{|\lambda_{k,j+1/2}|}, \quad k = 1, 6, \quad j = 1, N-1. \quad (24)$$

If Eq. (20) is transformed back into the basic variables, we obtain a difference scheme that is used in 2F code for the convective part of the Eq. (10):

$$\frac{\boldsymbol{\psi}_j^{n+1} - \boldsymbol{\psi}_j^n}{\Delta t} + \mathbf{C}_{j-1/2}^{++} \frac{\boldsymbol{\psi}_j^n - \boldsymbol{\psi}_{j-1}^n}{\Delta x} + \mathbf{C}_{j+1/2}^{--} \frac{\boldsymbol{\psi}_{j+1}^n - \boldsymbol{\psi}_j^n}{\Delta x} = 0, \quad (25)$$

with

$$\mathbf{C}_{j-1/2}^{++} = \mathbf{L}_{j-1/2} \boldsymbol{\Lambda}_{j-1/2}^{++} \mathbf{L}_{j-1/2}^{-1},$$
$$\mathbf{C}_{j+1/2}^{--} = \mathbf{L}_{j+1/2} \boldsymbol{\Lambda}_{j+1/2}^{--} \mathbf{L}_{j+1/2}^{-1}. \quad (26)$$

First-order accurate scheme (code named 2F-1) follows from the discretization (25) if the values of the limiters (23) are set to zero.

In 2F codes a simple average of the nonconservative variables was used for the evaluation of the Jacobian matrix at the point $j + \frac{1}{2}$:

$$\mathbf{C}_{j+1/2} = \mathbf{C}[(\boldsymbol{\psi}_j + \boldsymbol{\psi}_{j+1})/2] \quad (27)$$

A similar approach has been taken by Gallouet and Masella (1996), who showed that this type of averaging had given surprisingly good results for Euler equations. Toumi in his work (1995) attempted to evaluate the Roe approximate Riemann solver (Roe, 1981) for the six-equation Jacobian matrix $\mathbf{C}_{j+1/2}$ and proposed a complicated procedure for the evaluation of the Jacobian matrix between the grid points from the left and right states j and $j + 1$. However, due to the general uncertainty of the two-fluid equations, the justification of his approach is questionable.

The stability domain for the integration of the convective terms is limited by the CFL (Courant-Friedrichs-Levy) condition:

$$\Delta t \le \Delta x / \max(|\lambda_k|), \quad j = 1, 6. \quad (28)$$

Decomposition of the Jacobian matrix (17) has been performed with analytical approximations (Tiselj, Petelin, 1997) for moderate interphase relative velocities ($v_r < 20$ m/s), and numerically with the subroutines from the EISPACK library (Smith et al., 1976) for larger v_r. The 2F program is written only for problems with real eigenvalues of the Jacobian matrix. The calculation is interrupted if complex eigenvalues are found.

A specific problem of the application of the second-order accurate schemes in two-phase flow is degeneration of the eigenvectors as relative interphase velocity approaches zero. Only five linearly independent eigenvectors exist in that case. The problem is solved (Tiselj, Petelin, 1997), if a small artificial $|v_r| = 10^{-9}$ m/s is maintained.

Sources

Integration of the sources in Eqs. (13) and (15) is performed with the second-order Euler method. The form of the source term is very important for the behavior of the equations. Sources for the interphase exchange of mass, momentum, and energy in the system of equations for steam-water mixture are stiff, i.e., their characteristic time scale can be much lower that the time step of the CFL condition. The time step for the integration of the sources is thus not constant and is controlled by the relative change of the basic variables. The maximal relative change of the basic variables in one step of the integration is 0.001. Source terms describing interphase exchange are weak when the two-phase mixture is close to the thermal and mechanical equilibrium and the time step for their integration is equal to the convection time step Δt in that case. When the mixture is far from equilibrium, the source term integration time steps can be a few orders of magnitude shorter that Δt. A few hundred substeps are required to integrate the sources over a single convection time step Δt in such cases. Pember (1993) showed that such treatment of the stiff sources presents an acceptable approach when sources tend to establish an equilibrium solution (in the case of the Eqs. (1)–(6) mechanical equilibrium with $v_r = 0$ m/s and thermal equilibrium with $T_f = T_g$).

Why Use a Nonconservative Scheme?

The numerical scheme applied in the current 2F programs is nonconservative. There are several reasons for that choice:

—The continuity and energy equations can be written in the conservative form, while the fluxes for the momentum equations do not exist due to the pressure gradient terms and virtual mass terms. The momentum equations thus cannot be written in the conservative (flux) form.

—Oscillations appear in the vicinity of discontinuities, if complex systems of equations are solved with conservative variables (Tiselj, Petelin, 1997). Abgrall (1996) explained such oscillations for the four-equation model (two continuity, one momentum, and one energy equation). Oscillations do not depend on the numerical scheme accuracy and can be observed in the results of first and second-order schemes.

—New water properties subroutines would be required which would calculate two-phase properties (p, α, ρ_f, ρ_g) from the conservative variables ($(1-\alpha)\rho_f$, $\alpha\rho_g$, $(1-\alpha)\rho_f u_f$, $\alpha\rho_g u_g$).

According to the results presented in this paper, nonconservative variables present an acceptable approximation for fast transients

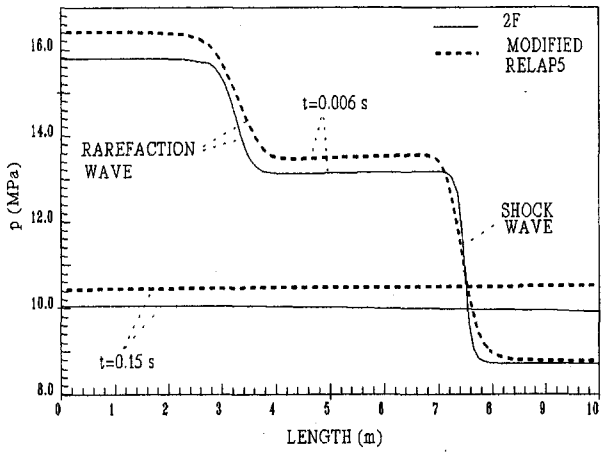

Fig. 1 Two-phase shock tube pressure

while for the long transients, where conservation of mass and energy is very important, this might be a serious drawback. In the presented calculations negligible fluctuations of the overall mass and energy have been observed despite the nonconservative scheme.

Shock Tube Problem Results

Toumi's (1995) two-phase shock tube problem is a Riemann problem for two-fluid models. An infinite tube is filled with two-phase water mixture with the left and right states defined as:

—left state: $\alpha = 0.25$, $p = 20$ MPa, $v_g = 0$ m/s, $v_f = 1$ m/s, $u_g = 2824$ kJ/kg, $u_f = 1311$ kJ/kg,
—right state: $\alpha = 0.1$, $p = 10$ MPa, $v_g = 0$ m/s, $v_f = 1$ m/s, $u_g = 2836$ kJ/kg, $u_f = 1330$ kJ/kg.

The membrane which separates left and right part of the tube at the position 5 m is removed at time zero. The RELAP5 code was modified for the shock tube simulation: only the "high-mixing" flow regime map has been applied and underrelaxation (time smoothing—Eq. (29)) of the interphase heat transfer coefficients and interphase drag coefficient was omitted. These modifications enabled direct comparison of the RELAP5 and 2F results, since the only difference in the mathematical models of the 2F and RELAP5 codes was a virtual mass term (Eq. (8) versus Eq. (9)).

Results are shown in Figs. 1 and 2, where the same grid (100 mesh points) and the same time step (0.00015 s) were used in both codes. Figure 1 shows the pressure profile at time 0.006 s, with a shock wave on the right and a rarefaction wave on the left, and at time 0.15 s, where pressure in the observed part of the tube is flat. Steeper waves are predicted by the 2F code while the RELAP5 waves are wider due to the numerical diffusion of the first order accurate scheme (Figs. 1, 2).

The pressure at time 0.15 s is lower than the pressure in the middle of the tube at time 0.006 s due to the initial thermal nonequilibrium between both phases which is gradually vanishing. Integration of the source terms is responsible for the slower approaching of the RELAP5 pressure to the equilibrium pressure (Fig. 1). RELAP5 is treating sources with the implicit integration with the convection time step, while the integration of the sources in the 2F code is more accurate due to the procedure with variable time steps. However, due to the source term integration, the 2F code is three to ten times slower than RELAP5. We have checked that in RELAP5 results calculated with a 1000 times shorter time step (1.5×10^{-7} s), mixture is approaching equilibrium with the same speed as in the 2F code.

A vapor volume fraction spike in Fig. 2 at the position 5 m and time 0 s appears as a result of the interaction of the shock and rarefaction waves and rapid vapour condensation immediately after the transient initiation. Due to the numerical diffusion, the spike is much weaker in the RELAP5 results.

Edwards Pipe Results

The Edwards pipe experiment (Edwards, O'Brien, 1970) is one of the basic benchmarks for the two-phase flow codes due to its simple geometry and the wide range of phenomena that it covers. The pipe of length 4 m was filled with liquid water at 7 MPa and 514 K and one end of the tube was suddenly ruptured. Pressures and vapor volume fractions were measured during the blowdown at a few points along the pipe. Important observed phenomena were: pressure rarefaction wave, flashing onset, critical two-phase flow, and vapor volume fraction wave.

The pressure rarefaction wave presented in Fig. 3 was predicted by the RELAP5, 2F-1 (first-order) and 2F (second-order) codes with the pipe divided into 100 volumes and the time step close to the CFL time step. As expected, the 2F rarefaction wave is the steepest. The 2F-1 wave is steeper than the RELAP5 wave due to the different numerical schemes: numerical diffusion in 2F-1 is the lowest at the CFL time step and is increasing, if the time step is decreased (characteristic of explicit schemes); the numerical diffusion of the acoustic waves in RELAP5 is decreasing with the decrease of the time step (characteristic of implicit schemes).

The pressure behind the measured rarefaction wave in Fig. 3 is approximately 0.4 MPa lower than the calculated pressures

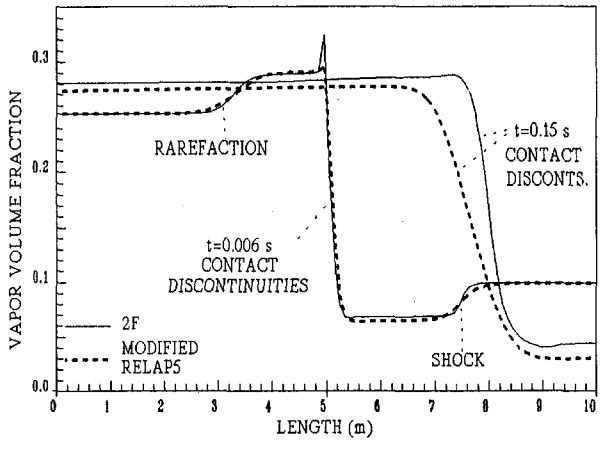

Fig. 2 Two-phase shock tube vapor volume fraction

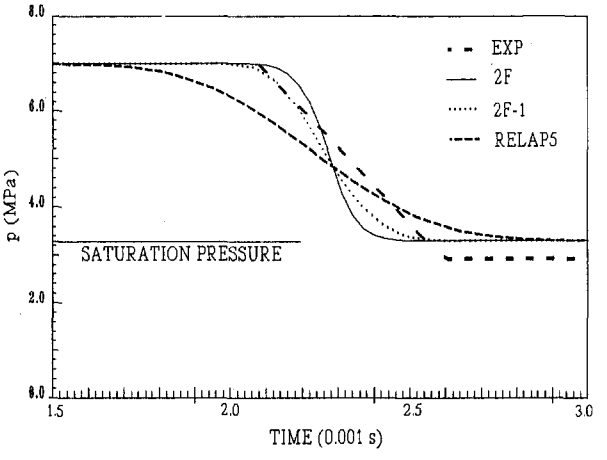

Fig. 3 Calculated and measured pressure history 1.46 m from the closed end of the pipe in the first 0.003s (100 volumes, $dt = 0.00003$ s)

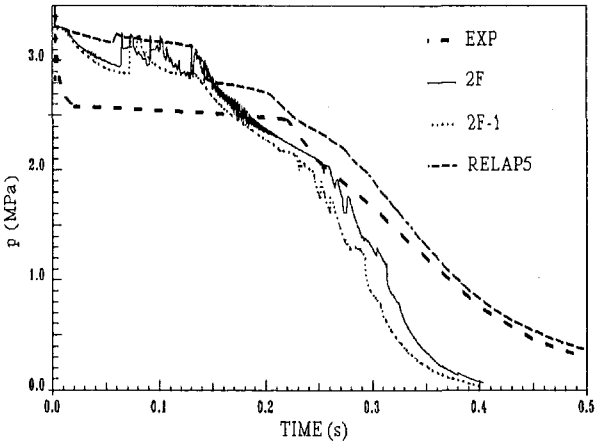

Fig. 4 Measured and calculated pressure history 1.46 m from the closed end of the pipe (100 volumes, *dt* = 0.00003 s)

which are equal to the saturation pressure. The RELAP5 model of interphase mass and heat transfer predicts a very quick establishment of the saturation conditions, while the measured pressure remains bellow saturation (Figs. 3 and 4).

The width of the measured rarefaction wave is relatively large due to the finite time interval needed for the initiation of the transient and is not a consequence of the diffusion (the same wave width is measured at the point near the break).

The main differences between RELAP5, 2F and measurements in Figs. 4 and 5, where a longer time scale is shown, are not a consequence of the numerical schemes of different orders of accuracy, but rather a consequence of the different source terms and different outflows through the rupture.

Although the main flow regime (bubbly flow) in the Edwards pipe experiment is the same in 2F and RELAP5 codes, differences appear at higher vapour volume fractions where slug and annular flow regime correlations are applied in RELAP5, while in 2F codes a less accurate interpolation between bubbly and droplet regimes is used (Žun et al., 1993). This is the reason for the faster pressure drop and faster vapor volume fraction rise in Figs. 4 and 5 after time 0.25 s.

Differences are also due to the RELAP5 special model for critical two-phase flow; RELAP5 calculates the critical flow through the rupture with a simplified model which is derived from simplified mathematical models and empirical correlations (Trapp, Ransom, 1982). The basic RELAP5 equations are not suitable for the critical flow modelling due to their ill-posedness and the weakness of the numerical scheme in the critical flow conditions (Petelin et al., 1994). The 2F code predicts the critical flow from the basic equations without any special model.

Difference which cannot be explained by any of the physical models is rapid increase of the measured vapor volume fraction at the beginning of the transient (Fig. 5). Analyses have shown that slightly higher initial temperature at the point of the measurement could possibly explain such behaviour.

The pressure oscillations calculated by the 2F codes in Fig. 4 at times 0.23 and later stem from the correlations for the interphase heat transfer in the source terms. The heat transfer coefficients are functions of the relative interphase velocity; at the points where v_r changes sign, large and rapid changes of the coefficients appear. The underrelaxation of the heat transfer coefficients is used in RELAP5 to prevent such oscillations:

$$H^n_{\text{used}} = (H^n_{\text{calculated}})^{1-\eta}(H^{n-1}_{\text{used}})^{\eta}, \quad 0 \le \eta < 1 \qquad (29)$$

where H_{used} presents gas or liquid heat transfer coefficient used in Eqs. (1)–(6) while $H_{\text{calculated}}$ presents gas or liquid heat transfer coefficient which follows from the correlations. The upper index n denotes the time step, while η presents the underrelaxation parameter, which is a function of Δt, Δx, and the physical parameters. An unpleasant side effect of the underrelaxation is, that RELAP5 results do not necessarily converge to the solutions of the Eqs. (1)–(6) as Δt and Δx tend to zero. Underrelaxation was, thus, not used in 2F and 2F-1 codes.

Water Hammer Due to the Valve Closure

The simple water hammer transient following the instantaneous closure of the valve presented in Fig. 6 (Simpson, 1989;

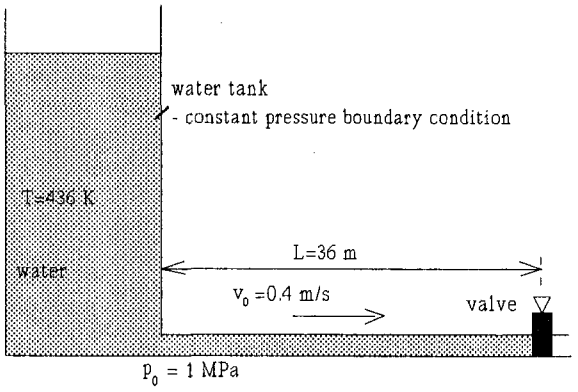

Fig. 6 Scheme of the experimental device with initial and boundary conditions

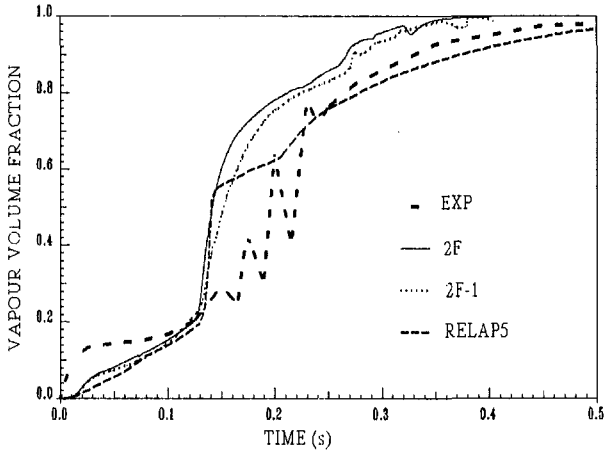

Fig. 5 Measured and calculated vapour volume fraction 1.46 m from the closed end of the pipe (100 volumes, *dt* = 0.00003 s)

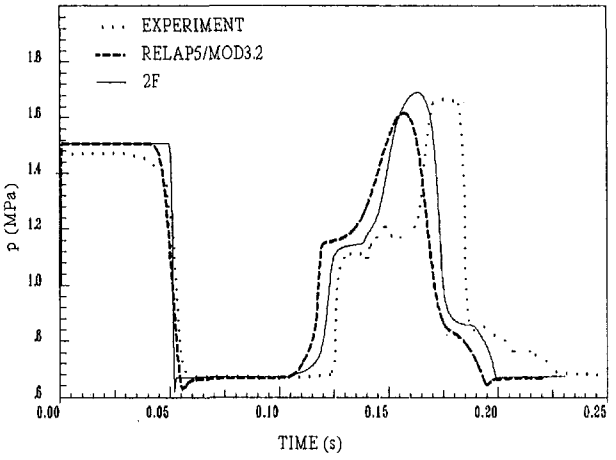

Fig. 7 Measured and calculated pressure history near the valve

Černe et al., 1996) is an example of a transient, where the advantage of second-order schemes is obvious. Important phenomena are pressure waves, flashing, and condensation of the steam near the valve.

Measurements and results of the different models are compared in Fig. 7 where the pressure history at the valve is shown. The valve is assumed to close instantaneously at time 0 seconds. At the moment of valve closure the pressure there would increase by an amount $\Delta p = \rho c v \approx 5$ bar. The pressure is maintained until the expansion wave from the free end arrives back after a time $2L/c \approx 0.05$ s and flashing appears. When the second expansion wave reflected from the tank reaches the valve two reflections appear: one from the vapor and the other one from the valve. Combination of both waves creates peak pressure which is higher than the initial pressure rise.

RELAP5 and 2F results are similar since both codes solve the same equations (only bubbly flow regime appears in the transient). However, steeper gradients and a higher peak pressure are predicted by 2F due to the better numerical scheme.

Conclusions

A second-order accurate scheme has been successfully applied to the two-fluid model of steam-water flow. The scheme shows obvious advantages in the area of the fast two-phase flow transients with acoustic waves—shock and rarefaction waves.

Simulations of the slow transients with characteristic time scale determined by the fluid velocity (as, for example, the second phase of the Edwards pipe experiment) show that the source terms are usually more important then the convection terms. The uncertainties of the source term correlations and special models (like critical flow model in RELAP5) in the current two-fluid models are often larger than errors due to the numerical diffusion. Application of the second-order schemes is thus questi-onable, and the first-order accurate schemes are sufficient for most of the slow transients. We believe that development of a code with a second-order accurate numerical scheme is meaning-less without parallel improvement of the mathematical models.

References

Abgrall, R., 1996, "How to Prevent Pressure Oscillations in Multicomponent Flow Calculations: A Quasi Conservative Approach," *Journal of Computational Physics,* Vol. 125, pp. 150–160.

Carlson, K. E., Riemke, R. A., Rouhani, S. Z., Shumway, R. W., and Weaver, W. L., 1990, *RELAP5/MOD3 Code Manual,* Vol. 1–7 NUREG/CR-5535, EG&G Idaho, Idaho Falls.

Černe, G., Tiselj, I., and Petelin, S., 1996, "Modeling of Water Hammer with Column Separation," *Transactions of the American Nuclear Society,* Vol. 75, pp. 387–388.

Edwards, A. R., and O'Brien F. P., 1970, "Studies of Phenomena Connected with the Depressurization of Water Reactors," *Journal of the British Nuclear Society,* Vol. 9, pp. 125–135.

Gallouet, T., and Masella, J. M., 1996, "A Rough Godunov Scheme," *C.R.A.S.,* Paris, Vol. 323/I, pp. 77–84.

Hirsch, C., 1988, *Numerical Computation of Internal and External Flows,* Vol. 1–2, Wiley.

LeVeque, R. J., 1992, "Numerical Methods for Conservation Laws," Lectures in Mathematics ETH Zurich, Birkhauser Verlag, Basel.

No, H. C., and Kazimi, M. S., 1985, "Effects of Virtual Mass on the Mathematical Characteristics and Numerical Stability of the Two-Fluid Model," *Nuclear Science and Engineering,* Vol. 89, pp. 197–206.

Pember, R. B., 1993, "Numerical Methods for Hyperbolic Conservation Laws with Stiff Relaxation I. Spurious Solutions," *SIAM Journal of Applied Mathematics,* Vol. 53, No. 5, pp. 1293–1330.

Petelin, S., Mavko, B., and Gortnar, O., 1994, "RELAP5 Critical Flow Model Assesment," Conference Proceedings on Thermal Reactor Safety Assesment, British Nuclear Energy Society, Manchester, pp. 125–129.

Roe, P. L., 1981, "Approximate Riemann Solvers, Parameter Vectors and Difference Schemes," *Journal of Computational Physics,* Vol. 43, pp. 357–372.

Shieh, L. A. S., Krishnamurty, R., and Ransom, V. H., 1994, "Stability, Accuracy, and Convergence of the Numerical Methods in RELAP5/MOD3," *Nuclear Science and Engineering,* Vol. 116, pp. 227–244.

Simpson, A. R., 1989, "Large Water-Hammer Pressures for Column Separation in Pipelines," *Journal of Hydraulic Engineering,* Vol. 117, No. 10, pp. 1310–1316.

Smith, B. T., et al., 1976, *Matrix Eigensystem Routines—EISPACK Guide,* 2nd Ed., Vol. 6 of Lecture Notes in Computer Science, Springer-Verlag.

Tiselj, I., and Petelin, S., 1995, "Second Order Numerical Method for Two-Fluid Model of Air-Water Flow," Nuclear Society of Slovenia Annual Meeting, pp. 348–355.

Tiselj, I., and Petelin, S., 1997, "Modelling of Two-Phase Flow with Second-Order Accurate Scheme," *Journal of Computational Physics,* Vol. 136, No. 2, pp. 503–521.

Toumi, I., 1995, "An Implicit Second Order Numerical Method for Two-Fluid Models," *Proceedings of ICONE3,* Kyoto.

Trapp, J. A., and Ransom, V. H., 1982, "A Choked-Flow Calculation Criterion for Nonhomogeneous, Nonequilibrium, Two-Phase Flow," *International Journal of Multiphase Flow,* Vol. 8, No. 6, pp. 669–681.

Žun, I., Kljenak, I., and Može, S., 1993, "Space-Time Evolution of the Nonhomogeneous Bubble Distribution in Upward Flow," *International Journal of Multiphase Flow,* Vol. 19, No. 1, 151–172.

Z. Bilicki
Professor.

D. Kardas
Research Associate.

Institute of Fluid-Flow Machinery,
Polish Academy of Sciences,
Gen. J. Fiszera 14,
80-952 Gdansk, Poland

E. E. Michaelides
Professor,
Department of Mechanical Engineering,
Tulane University, New Orleans, LA 70118

Relaxation Models for Wave Phenomena in Liquid-Vapor Bubble Flow in Channels

We examine wave characteristics of a liquid-vapor mixture in order to investigate certain features of the homogeneous relaxation model. The model is described by one-dimensional averaged mass, momentum, energy equations, and a rate equation. Since the homogeneous relaxation model delivers a qualitative incompatibility of numerical and experiment results of large wave propagation, it is extended so as to take into account the heat conduction in the liquid surrounding vapor bubbles. With this extension, the effects of spreading and damping of the waves in the numerical solutions are similar to those observed in the experiment. Thus, a new model is created, the homogeneous relaxation-diffusion model which contains two physical quantities—the relaxation time and macroscopic heat conduction coefficient. Both quantities are determined based on experimental data. It seems that the results obtained from the new model agree well qualitatively with the experiments.

1 Introduction

The propagation of perturbations in channels is one of the most important problems of two-phase flows. Therefore, to nobody's surprise, much effort and intellect has gone into this question. In the literature relevant to the topic, one can distinguish two approaches to wave propagation in the two-phase mixture. The first approach is based on mechanical interactions between the bubbles and the surrounding liquid usually expressed in terms of the well known Rayleigh equation. This method of theoretical investigations of wave aspects in two-phase flows was pursued by Szaniawski (1957), Campbell and Pitcher (1954), Batchelor (1969), and also by Russian scientists who achieved a significant progress in this area, namely, Nigmatulin (1991), Nakoryakov et al. (1988), and Nakoryakov et al. (1993). The second approach makes use of one-dimensional averaged conservation equations for each phase, in a way which is analogous to gas dynamics. This concept was implemented in the works of Konorski (1971), Ardron and Duffey (1978), Puzyrewski (1980), and Guha and Young (1990). The second approach seems to be simplified, compared to the first one, mainly due to the fact that it does not provide the description of local distribution of flow properties which determine the process of mass, momentum and energy transfer at the interfaces. Instead of searching for complex representation of the local field, some quantities which characterize the diffusion processes are introduced, including the relaxation time and macroscopic thermal conductivity. These quantities are functions of properties of the two-phase medium and do not remain constant.

The present paper deals with large perturbations in steam-water mixtures. To analyze the relevant phenomena, we have decided to use the second approach, as outlined in Ishii (1975). Bearing in mind the whole variety of models set forth by previous researchers, we have decided to use one of the simplest models of two-phase flow—the homogeneous relaxation model (HRM) which was described by Bilicki and Kestin (1990). The justification of this choice comes from our own experience of investigations performed to date. HRM is selected not only by its simplicity, but also by its reasonably good correlation with the experiments concerning the effects of choking and flashing in two-phase flows, see Bilicki et al. (1990). In the model it is assumed that the effects of vaporization and condensation are significant and more important than the mechanical effects. This assumption seems to be justified for the considered bubble flow of a small void fraction below $\varphi = 0.05$, as the interfacial slip is relatively small then and the relaxation times for the heat transfer processes at the interfaces are relatively large reaching 1 s. In this case the dissipation of thermal energy is considerably larger than that of mechanical energy, see Bilicki et al. (1996). With the help of HRM, Bilicki et al. (1990) explained the pressure distributions in a two-phase flow with superheated vapor. On the basis of this model, Downar-Zapolski (1992) showed that two-phase flow is choked at velocities smaller than the critical velocity which corresponds to the frozen velocity in HRM and the flow is pseudo-critical in a wide range of velocities. A relaxation model with dominant mechanical nonequilibrium was used by Lemonnier and Selmer-Olsen (1992) for the flow of a mixture of air and water. Their numerical results exhibit good agreement with experimental data. However, an analysis of large perturbations in the mixture of steam and water carried out by Bilicki and Kardas (1993) revealed that the relaxation model does not encompass an important flow feature, namely the effect of diffusion. They pointed out that the heat diffusion or fluid viscosity (affecting the vicinity of the interface) should be introduced into the governing equations of the model. The diffusion term was included in HRM by Kardas (1994); the model was transformed into a homogeneous relaxation-diffusion model (HRDM) to deliver more appropriate features of numerical solutions that agree better with the experimental data.

The aim of this work is to explore the potential of HRM and HRDM as a basis for the description of propagation of large disturbances in a channel filled with water and vapor bubbles. In the sections to follow we will describe briefly HRM, develop the idea of HRDM, and present the results of numerical calculations of propagation of pressure signals, compared with the available experimental data.

2 Homogeneous Relaxation Model

We begin our study by recapitulating the most important features of HRM (see Bilicki and Kestin, 1990). For simplicity, we restrict our presentation to a single space variable z and

Contributed by the Fluids Engineering Division for publication in the JOURNAL OF FLUIDS ENGINEERING. Manuscript received by the Fluids Engineering Division February 18, 1997; revised manuscript received August 27, 1997. Associate Technical Editor: S. Banerjee.

adiabatic flow. The model draws on three conservation equations of mass, momentum, and energy

$$\frac{\partial \rho}{\partial t} + \frac{1}{A}\frac{\partial \rho w A}{\partial z} = 0, \tag{1}$$

$$\rho \frac{\partial w}{\partial t} + \rho w \frac{\partial w}{\partial z} = -\frac{\partial P}{\partial z} - \tilde{\tau}_w + \rho g, \tag{2}$$

$$\frac{\partial \rho u}{\partial t} + \frac{1}{A}\frac{\partial \rho u w A}{\partial z} = -\frac{P}{A}\frac{\partial w A}{\partial z} + \tilde{\tau}_w w, \tag{3}$$

where ρ denotes the density, w is the velocity, P—pressure, u—specific internal energy, $\tilde{\tau}_w$—wall shear, A—cross-sectional area, g—acceleration of gravity. The set of Eqs. (1)–(3) is supplemented by one more differential equation. This equation describes the local and instantaneous rate at which the dryness fraction x tends to its local unconstrained-equilibrium value $\bar{x}(P, u)$

$$\frac{Dx}{Dt} = -\frac{x - \bar{x}}{\theta_x}, \tag{4}$$

where

$$\frac{D}{Dt} = \frac{\partial}{\partial t} + w\frac{\partial}{\partial z}.$$

Equation (4) introduces a finite relaxation time $\theta_x(P, u, x)$ into the system and as a result the dryness fraction x acquires the character of a dependent variable. It should be noted that in the light of the theory of thermodynamics of hidden or internal variables (see Lebon et al., 1992 or Bilicki and Michaelides, 1997), the dryness fraction is also an internal variable. By using Eq. (4), it is easy to write the rate of vapor generation as follows:

$$\Gamma_x = \frac{x - \bar{x}}{\theta_x}\rho. \tag{5}$$

It is assumed that the liquid is superheated while the vapor is in the state of equilibrium at the saturation temperature, so the density of the mixture is a function of three variables $\rho = \rho(P, u, x)$. This assumption seems to be acceptable because the experiments which we refer to were carried out at a small void fraction $\varphi = 0.01$. The above allows us to write the state equation in the following form:

$$\frac{1}{\rho} = v = xv_G^s(P) + (1 - x)v_L(P, u_L), \tag{6}$$

where

$$u_L = \frac{u - xu_G^s(P)}{1 - x}. \tag{7}$$

The thermodynamic property v_L is approximated by a function, which is obtained by means of the least square method applied to the available experimental data of the compressed liquid region. It is assumed that the essential form of the specific volume function v_L in the metastable region is the same as that in the compressed liquid (see Kardas and Bilicki, 1995).

The wall shear is evaluated from the following formula:

$$\tilde{\tau}_w = \frac{2f\rho w^2}{D}, \tag{8}$$

where f is the wall friction factor and D is the diameter of the channel.

From the point of view of "wave mechanics" this model is dispersive because the velocity of small disturbances depends on their frequency. Another feature of HRM is the presence of two characteristic limit velocities: the equilibrium velocity a_e, which refers to the velocity of infinitely long waves, and the frozen velocity a_f, which corresponds to the velocity of waves of infinite frequency.

The following initial and boundary conditions can be specified for the system of Eqs. (1)–(4).

(IC)

$$P(t = 0, z) = P_0, \quad w(t = 0, z) = 0,$$
$$u\rho(t = 0, z) = u\rho_0, \quad x(t = 0, z) = x_0, \tag{9}$$

and (BC),

$$P(t, z = 0) = P_a, \quad u\rho(t, z = 0) = u\rho_a,$$
$$x(t, z = 0) = x_a, \quad P(t, z = l) = P_b. \tag{10}$$

In the course of numerical calculations, the friction factor is assumed constant $f = 0.008$. The relaxation time θ is also chosen to be constant. The cross-sectional area A is a characteristic of the channel and in our calculations is assumed the same as in the experimental facility. The system of Eqs. (1)–(4) is closed and can be solved numerically.

3 Numerical Method

A finite difference scheme with fixed and staggered mesh points is used to solve the relaxation model (1)–(4) with initial and boundary conditions (9), (10). This numerical scheme was first employed by Ransom et al. (1983) in the code RELAP for

Nomenclature

A = cross sectional area
a, b, c, d = coefficients
f = friction factor
g = acceleration of gravity
h_{LG} = heat of evaporation
j_s = rate of entropy
l = channel length
N = bubble number
P = pressure
q = heat flux
r = bubble radius
s = entropy
t = time
$\hat{T}_{LG} = T_L - T_G^s$
u = specific internal energy
v = specific volume
w = bulk velocity
x = dryness fraction (actual)
$\bar{x}$ = equilibrium dryness fraction
z = coordinate along channel
δ_t = thermal boundary layer thickness
ϵ = void fraction
θ = relaxation time
ρ = density
τ_w = wall shear
Γ_G = volumetric vapor generation rate
$\hat{\lambda}$ = macroscopic heat conductivity
λ = heat conductivity
$\dot{\sigma}$ = entropy production
Θ = local superheating
Δt = time step
Δz = spatial mesh size

Subscripts

L = liquid
G = vapor
j = mesh points
a, b = boundary conditions
0 = initial conditions
μ = microscale
M = macroscale

Superscript

n = time level
s = saturation

modeling of the LWR system. The scheme is partially implicit so it does not require any iterative process. The dependent vector consists of 4 components $\sigma = \sigma(P, w, \rho u, x)$. The scalar quantities P, ρu, x are calculated at the cell centers, whereas the velocity w is evaluated at the cell boundaries. An advantage of the RELAP scheme is that the nonlinear system of partial differential equations is resolved into a system of linear algebraic equations for the pressure:

$$a^n P_{j-1}^{n+1} + b^n P_j^{n+1} + c^n P_{j+1}^{n+1} = d^n, \qquad (11)$$

where a^n, b^n, c^n, d^n are functions of the dependent vector at an nth instant of time. The unknown variables P_j form a tridiagonal matrix and are easy to solve. The remaining variables are calculated from other difference equations. The numerical scheme is first order in space and time. However, its accuracy is found to be satisfactory because of considerable diffusion in typical steam-liquid flows. It is worth noting that the diffusive and dispersive components which appear in the so-called modified equations affect the velocity of wave propagation. For more detailed comments on this question readers can refer to the work of Kardas (1994).

4 Comparison of Numerical Solutions With Experimental Data

Among the multitude of available experimental data, we found that the sets of data obtained by Nakaryakov et al. (1988) are the only well-reported and calibrated data which lend themselves to the verification of initial/boundary value problems for a model such as HRM. The experiments were carried out in a shock tube of diameter $D = 0.052$ m, filled with a mixture of water and vapor bubbles of a small void fraction. The evolution of pressure disturbances along the channel is shown in Fig. 1 by the solid lines. Initial pressure signals were generated at a station $z = 0$, while the evolution of disturbances was measured at stations $z = 0$, $z = 0.01$ m, $z = 0.11$ m, and $z = 0.485$ m from the inlet to the shock tube. The numerical calculations were performed based on HRM and compared with the experimental data. It was assumed that the space step $\Delta z = 0.01$ m, time step $\Delta t = 2 \cdot 10^{-4}$ s. These steps were carefully selected to ensure that the numerical velocity $\Delta z/\Delta t = 500$ m/s was several times larger than the frozen velocity in HRM. The value of the relaxation time was chosen so as to obtain the best possible agreement between the numerical and experimental results. This value was assumed $\theta = 0.4$ s. The comparison of numerical and experimental results is presented in Fig. 1. The dashed lines in Fig. 1 refer to numerical results obtained for $\Delta z = 0.01$ m. One can easily see that the numerical solutions diverge from the experimental data, especially at larger distances from the inlet. The most striking in the comparison is the difference in slopes of the obtained pressure signals. This gives rise to a conclusion that strong diffusion effects are not accounted for in the numerical solutions. Several attempts were made to improve the numerical solutions by changing the relaxation time θ and friction factor f. However, shorter relaxation times and larger friction factors resulted in a stronger wave decay but did not change the slopes of computational pressure signals. As expected, an increase in the space step up to $\Delta z = 0.1$ (the dash-and-dot lines in Fig. 1), leaving all remaining variables unchanged, brought conveniently the numerical solutions closer to the experimental results because of an increase in the numerical diffusion. The forefronts of the pressure signals marked by the dash-and-dot lines in Fig. 1 are far more decayed and spread than those of the previous case for $\Delta z = 0.01$ m indicated by the dashed lines. An explanation of this fact can be easily found by considering the modified equations, where it is clear that the numerical diffusion is proportional to Δz and Δt. Therefore, ironically the solutions of HRM with larger space and time steps yield more accurate results.

The above results confirm that the heat diffusion and viscosity are very important in the two-phase flow of a liquid and its vapor and cannot be neglected in any bona fide model. However, the viscosity or heat conductivity, when considered in their ordinary sense (in the molecular scale), have a minor influence on the solution of this problem. For this reason, they do not need to be taken explicitly into consideration. Our numerical calculations confirm that the heat conduction in one phase would exert a significant influence if the thermal conductivity was assumed to be by several orders of magnitude larger than its normal value. This leads to the conclusion that the diffusion terms have to be different from those of the classical fluid dynamics and heat transfer. The numerical results have also shown that wave damping and spreading is caused by heat and mass exchange between phases. Therefore, an additional second-order term, which takes into account the dissipation in the vicinity of the interface must be introduced into the model. At the same time the model will be extended by taking into account features from the mesoscopic level, e.g., from the vicinity of the interface.

5 The Homogeneous Relaxation-Diffusion Model (HRDM)

It is apparent from the numerical experiments with HRM that we need to introduce a second-order term to the relaxation Eq. (4) in order to account for thermal diffusion. The thermal diffusion takes place in the mesoscopic level in the vicinity of the interface and is due to a relatively steep temperature gradient in the superheated liquid (see Bilicki et al., 1996). In order to take into account this phenomenon, one can draw on the methods of extended thermodynamics, as postulated by Lebon et al. (1992) and internal variables, described by Kestin (1993), Bilicki (1994), and Bilicki and Michaelides (1997), where the internal variables, such as x, can be expressed in the form of a first-order differential equation (with time as an independent variable) with respect to the thermodynamic components of the state vector, such as P, u, their gradients, heat flux $\dot{q}$ and its divergence $\nabla \cdot \dot{q}$, for example

$$\dot{x} = \phi(x, P, u, \dot{q}, \nabla x, \nabla P, \nabla u, \nabla \cdot \dot{q}, \ldots). \qquad (12)$$

Most terms in Eq. (12) are neglected in HRM because the heat diffusion is not taken into account there and the above equation can be rewritten in a simpler form as $\dot{x} = \phi(x, \bar{x}(P, u), \theta_x(x, P, u), \nabla x)$.

In order to represent the heat diffusion in the model, one can supplement Eq. (4) with a term containing $\nabla \cdot \dot{q}$, which describes the thermal conduction resulting in the transfer of heat flux $\dot{q}$ between the superheated water and vapor bubbles. The new rate equation—a relaxation-diffusion equation reads

$$\frac{Dx}{Dt} = -\frac{x - \bar{x}}{\theta_x} + \frac{1}{\rho h_{LG}} \frac{\partial}{\partial z} \dot{q}. \qquad (13)$$

For the heat flux $\dot{q}$, which has to be expressed in terms of macroscopic parameters, averaged in the cross sectional area, we postulate the form

$$\dot{q} = -\tilde{\lambda} \nabla \hat{T}_{LG}, \qquad (14)$$

where $\hat{T}_{LG} = T_L - T_G^s$ denotes the liquid superheat and $\tilde{\lambda}$ represents the macroscopic thermal conductivity. The macroscopic thermal conductivity is not only the physical property of the liquid-vapor mixture but it also describes the heat transfer process on the mesoscopic level. The vapor or liquid generation Eq. (13) assumes the following form:

$$\Gamma_G = -\frac{x - \bar{x}}{\theta} \rho - \frac{1}{h_{LG}} \frac{\partial}{\partial z} \left(\tilde{\lambda} \frac{\partial \hat{T}_{LG}}{\partial z} \right). \qquad (15)$$

Basically, both processes of mass exchange, i.e. evaporation

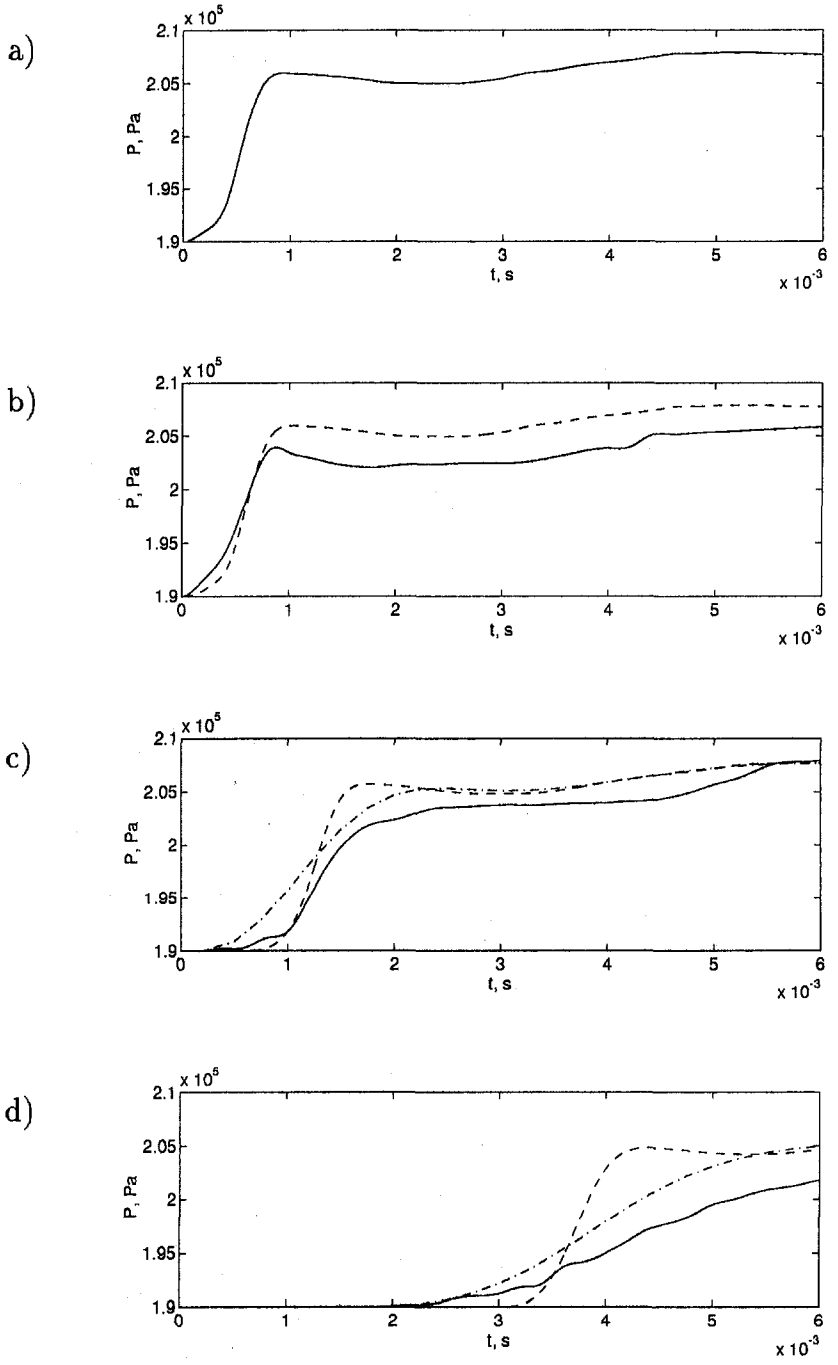

Fig. 1 The evolution of a step signal along the channel. The comparison of the experimental data for a water-vapor mixture (—) with the numerical solutions of HRM (θ = 0.4 s) for different space steps – Δz = 0.01 m(--) and Δz = 0.1 m (-···-). Points of recording for Δz = 0.01 m: (*a*) z = 0 m, (*b*) z = 0.01 m, (*c*) z = 0.11 m, (*d*) z = 0485 m and for Δz = 0.1 m: (*c*) z = 0.1 m, (*d*) z = 0.5 m.

and condensation, come into play when the temperature of the liquid is different from that of the vapor. When $\nabla \hat{T}_{LG} \neq 0$, the mass exchange takes place, partly due to the strong interaction between the phases, which is proportional to $(x - \bar{x})$, and partly due to the weaker effect of energy transfer. The latter is proportional to the heat flux gradient. In the case of $\nabla \hat{T}_{LG} = 0$ and $T_G \neq T_L$, the exchange takes place only because of the departure of the dryness fraction from its equilibrium value.

The homogeneous relaxation-diffusion model (HRDM) proposed here is composed of the usual conservation Eqs. (1)–(3) and Eq. (13). Since the relaxation-diffusion Eq. (13) is one-dimensional, the features of the two-phase system in the mesoscale have to be transferred onto the macroscopic scale by means of a substitute coefficient $\tilde{\lambda}$, which represents the macroscopic thermal conductivity. It is clear that θ and $\tilde{\lambda}$ are quantities external to the model and need to be determined from the experiments or analysis.

6 The Macroscopic Thermal Conductivity

In order to show the physical meaning of the coefficient $\tilde{\lambda}$ and how it is expressed in terms of properties of the two-phase bubble mixture at the mesoscale, we follow the analysis carried out by Kardas (1994). The analysis is based on the hypothesis

that the irreversibilities due to the process of thermal diffusion, when measured at the mesoscopic level by the entropy production, are the same as the irreversibilities at the macroscopic level modeled by the diffusion term in Eq. (13).

It is well known from thermodynamics (see Kestin, 1979) that the local entropy change due to a temperature field is:

$$\rho \frac{ds}{dt} = -\frac{\nabla \cdot \vec{q}}{T}. \tag{16}$$

The right-hand side of this equation can also be written as a sum of the rate of entropy $\vec{j}_s$ and the entropy production $\dot{\sigma}$ as follows:

$$\rho \frac{ds}{dt} = -\nabla \vec{j}_s + \dot{\sigma}, \tag{17}$$

where

$$\vec{j}_s = \frac{\vec{q}}{T}, \tag{18}$$

and

$$\dot{\sigma} = -\frac{\vec{q}}{T^2} \nabla T. \tag{19}$$

The heat flux can be described in terms of the temperature gradient from the Fourier law

$$q = -\lambda \nabla T. \tag{20}$$

For the calculation of the entropy production in a liquid-vapor mixture, we assume that there are significant temperature gradients inside the superheated liquid, while inside the vapor bubble the temperature field is uniform. This assumption, used extensively in the literature (see Bilicki et al., 1996, Michaelides and Feng, 1994) is supported by the small size of the bubbles. For the sake of simplicity, we also assume a linear distribution of temperature in the thin liquid thermal boundary layer δ_T. This assumption is justified by the calculated thickness of the thermal boundary layer, which is smaller than the radius of the bubbles. Hence, the gradient of the temperature field at the interface can be approximated by the following expression:

$$\nabla T_L = \frac{T_L - T_G^s}{\delta_T} \vec{r} = \frac{\Theta}{\delta_T} \vec{r}, \tag{21}$$

and the entropy production due to a single vapor bubble can be written as follows:

$$\dot{\sigma}_i = \frac{\lambda_L}{T_L^2} (\nabla T_L)^2 = \frac{\lambda_L}{T_L^2} \left(\frac{\Theta}{\delta_T} \right)^2. \tag{22}$$

Then, the entropy production can be expressed in terms of the void fraction of the mixture which for a group of N identical spherical bubbles of diameter r in a volume V can be found from the formula:

$$\epsilon = \frac{V''}{V} = \frac{\frac{4}{3}\pi r^3 N}{V}. \tag{23}$$

Thus, the entropy production in the entire volume V is:

$$\dot{\sigma} = \frac{\dot{\sigma}_i 4\pi r^2 \delta_T N}{V}, \tag{24}$$

and with the help of Eq. (19) can be transformed into the form:

$$\dot{\sigma} = 3\lambda_L \epsilon \frac{\frac{\Theta^2}{\delta_T r}}{T_L^2}. \tag{25}$$

Let us now compare the entropy production in the same volume V in the macroscale. In this scale there are two different average temperatures T_L and T_G and the entropy production is due to the temperature difference. Hence, the entropy production obtained from the relaxation-diffusion Eq. (15) of HRDM is as follows:

$$\dot{\sigma}_M = -\frac{\vec{q}}{\hat{T}_{LG}^2} \nabla \hat{T}_{LG} = \tilde{\lambda} \left(\frac{\nabla \hat{T}_{LG}}{\hat{T}_{LG}} \right)^2, \tag{26}$$

and is a result of the temperature gradient along the channel. Since an equal entropy production in the mesoscale and macroscale ($\dot{\sigma} = \sigma_M$) is postulated in our approach, the macroscopic coefficient of the thermal conductivity must be given by the following equation:

$$\tilde{\lambda} = \frac{3\lambda\epsilon\Theta^2 \hat{T}_{LG}^2}{r^2 T_L^2 (\nabla \hat{T}_{LG})^2} \left(\frac{r}{\delta_T} \right). \tag{27}$$

It should be pointed out that, unlike the usual thermal conductivity λ, the macroscopic conductivity $\tilde{\lambda}$ is not a thermodynamic property of the fluid. It is one of the characteristic parameters of the two phase mixture and depends on the flow characteristics as well as the thermodynamic properties of the two phases. This macroscopic, operative heat conductivity $\tilde{\lambda}$ is ill-defined when $\nabla T_{LG} = 0$, which can be seen from Eq. (27). However, in this case the second term in Eq. (13) vanishes, Eq. (13) reduces to Eq. (4), and therefore the quantity $\tilde{\lambda}$ loses its physical meaning. Due to the fact that the ratio $\tilde{\lambda}/\lambda$ is of the order of $10^3 - 10^6$, Eq. (27) can be modified and rewritten as follows

$$\frac{\tilde{\lambda}}{\lambda} = \left[1 + \frac{3\varphi\Theta^2 \hat{T}_{LG}^2}{r^2 T_L^2 (\nabla \hat{T}_{LG})^2} \left(\frac{r}{\delta_T} \right) \right]. \tag{28}$$

The macroscopic conductivity as well as the diffusion are very convenient quantities to describe the flow of a two-phase mixture in terms of a simple homogeneous model, which retains all the wave attributes of single-phase fluids. Thus, by using characteristic parameters, such as the macroscopic conductivity, we are able to use single-phase results for the wave propagation and apply them to the cases of more complex two-phase mixtures.

7 Results and Comparison With Experiments

The relaxation-diffusion model contains two unknown variables, which are essential for the calculations: the relaxation time θ and macroscopic coefficient of heat conduction $\tilde{\lambda}$. These two quantities characterize the wave properties of the two-phase system, such as damping of the signal amplitude and widening of the signal forefront. As already mentioned, θ and $\tilde{\lambda}$ may be evaluated in an analytical way (which makes the closure equations necessary) or from experimental data. In this paper we draw on the experiments in order to estimate the two parameters θ and $\tilde{\lambda}$.

By means of the trial and error method, we carefully select θ and $\tilde{\lambda}$ for the numerical calculations so as to reproduce best the experimental data. As far as θ, it is also possible to compare values we obtain from this model, with the values of the relaxation time previously obtained by means of HRM in Bilicki et al. (1990), Downar-Zapolski (1992), Bilicki et al. (1996), and Downar-Zapolski et al. (1996). In these studies it was observed that the relaxation time varies from 0.02 s to 1.0 s, under the assumption that the mass exchange due to the heat diffusion can be neglected.

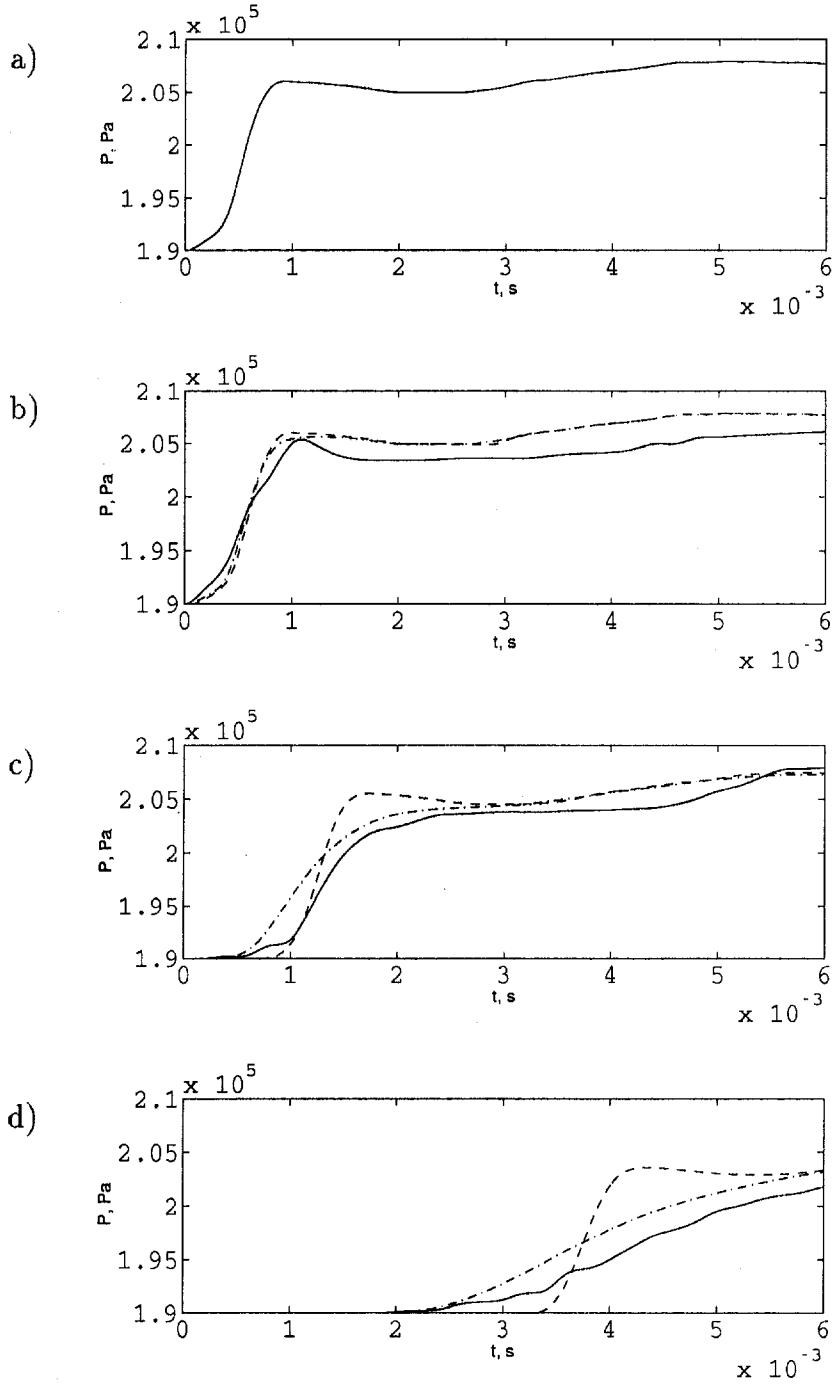

Fig. 2 The evolution of a step signal along the channel. The comparison of the experimental data for a water-vapor mixture (—) with the numerical solutions of HRDM for θ = 0.15 s, $\tilde{\lambda}$ = 6350 W/(mK) (-·-·-) and HRM for θ = 0.15 s (--). Points of recording (*a*) z = 0 m, (*b*) z = 0.01 m, (*c*) z = 0.11 m, (*d*) z = 0.485 m.

The macroscopic heat conduction $\tilde{\lambda}$ depends on the averaged characteristics of the mixture ∇T, T_L, T_G as well as on the mesoscopic variables, such as r, θ, and δ_t. Some difficulties in the calculations were encountered in the evaluation of the thermal boundary layer thickness because it is sensitive to initial conditions and superheating, and also because it apparently varies in the course of experiments. Nevertheless, after evaluating θ and $\tilde{\lambda}$, and fitting the numerical results to the experimental data, it became possible to make an estimate for the thermal boundary layer thickness δ_t. Although it is recognized that mesoscopic and macroscopic parameters vary during the signal propagation, because of lack of any pertinent data, it was assumed that both the relaxation time and the macroscopic heat transfer coefficient remain constant.

The first set of results illustrates the evolution of a pressure wave given as a step function in a two-phase water-steam mixture. During the experiment, pressure signals were recorded at distances z = 0.001 m, z = 0.11 m, and z = 0.485 m from the initial point of disturbance. The numerical results and experimental data are presented in Fig. 2. The solid lines correspond to the experimental data, the dash-and-dot lines are curves obtained from HRDM and the dashed lines refer to calculations obtained from HRM. The initial parameters used in the calculations were selected to match, as closely as possible, those of

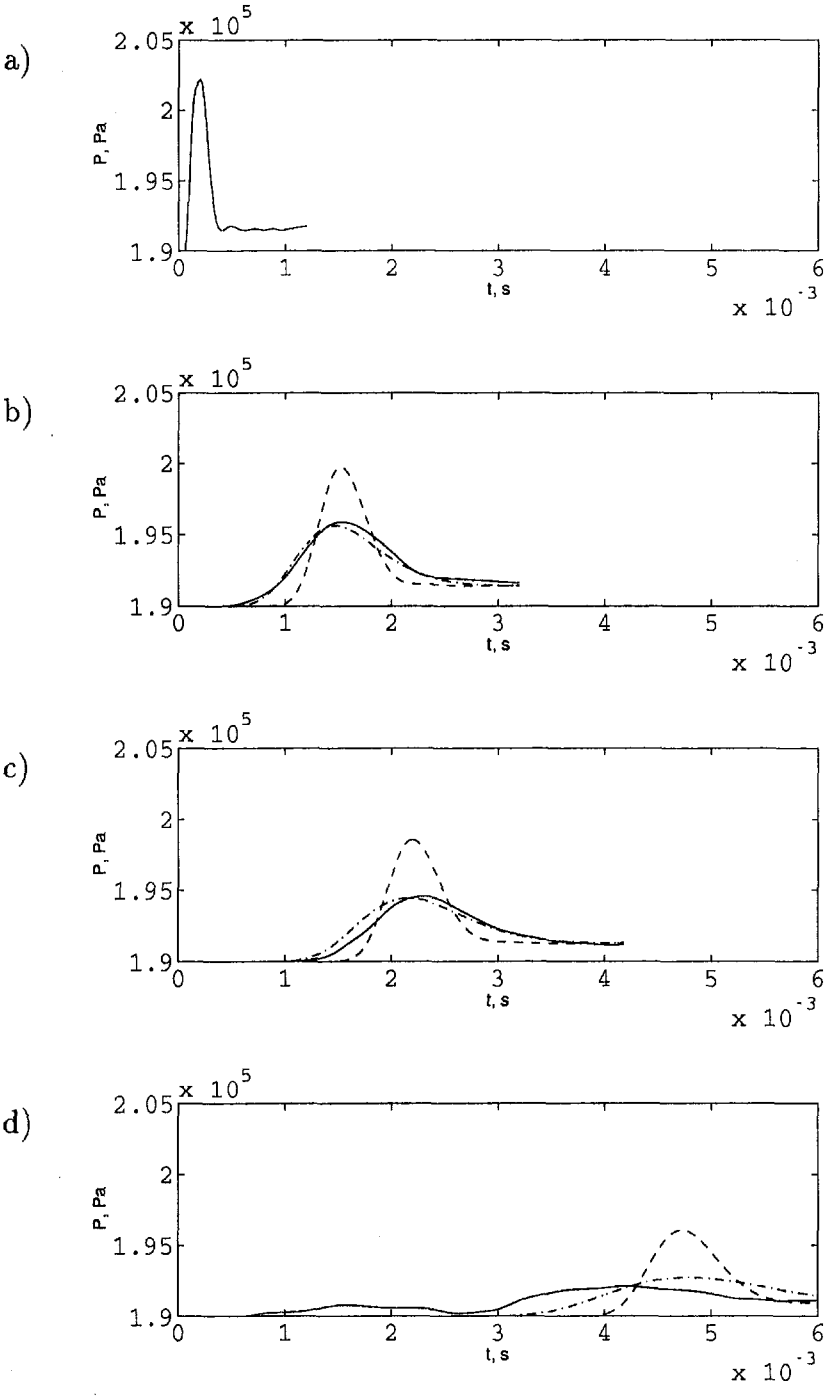

Fig. 3 The evolution of a pressure pulse along the channel. The comparison of the experimental data for a water-vapor mixture (—) with the numerical solutions of HRDM for θ = 0.7 s, $\tilde{\lambda}$ = 1800 W/(mK) (-·-·-) and HRM for θ = 0.7 s (--). Points of recording (*a*) z = 0 m, (*b*) z = 0.155 m, (*c*) z = 0.255 m, (*d*) z = 0.63 m.

the experiment. The initial void fraction was taken as $\epsilon_0 = 0.01$, the average radius of the bubbles $r_0 = 1.3$ mm, the initial pressure $P_0 = 0.19$ MPa, and the initial velocity $w_0 = 0$. The best numerical solution from HRDM was obtained for the relaxation time equal to $\theta = 0.15$ s and macroscopic conductivity $\tilde{\lambda} = 6350$ W/(mK). For this value of $\tilde{\lambda}$ the ratio of the bubble radius to the thermal boundary layer thickness is 5. The calculations were performed for the space step $\Delta z = 0.01$ m and $\Delta z/\Delta t = 500$ m/s. It is clear from Fig. 2 that all curves calculated with the help of HRDM bear qualitative resemblance to the experimental curves. The importance of the inclusion of the thermal diffusion process is easily seen in Figs. 2(*c*) and 2(*d*).

The second set of results refers to a single pulse in a steam-water mixture. In this case, the initial pressure impulse is depicted in Fig. 3(*a*). The evolution of the impulse was recorded at $z = 0.155$ m, $z = 0.255$ m, and $z = 0.63$ m. The solid lines correspond to the experimental pressure data, while the dash-and-dot lines refer to the numerical solutions obtained from HRDM. The calculations were carried out for the initial conditions which correspond exactly to the experimental conditions:

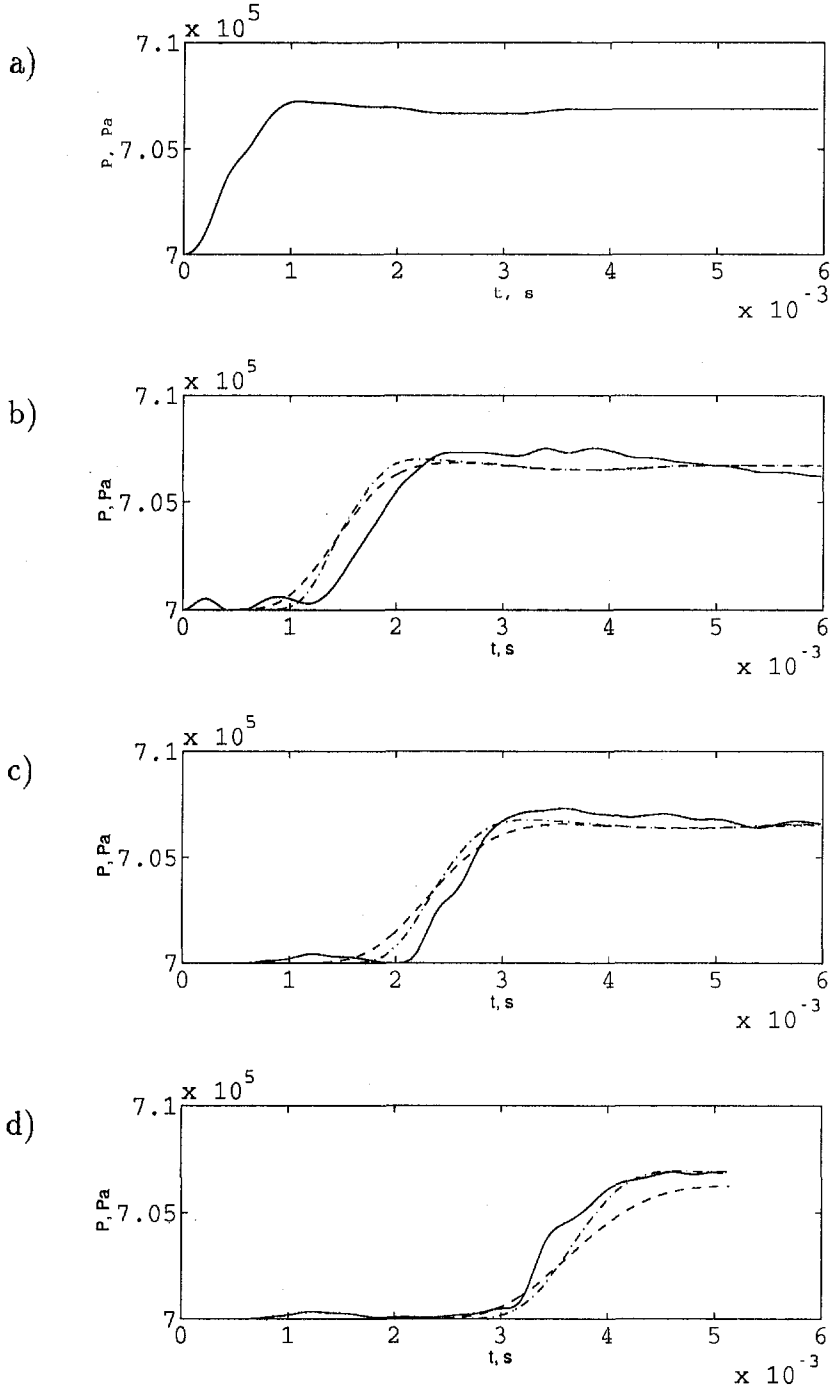

Fig. 4 The evolution of a step signal along the channel. The comparison of the experimental data for a liquid-vapor mixture of freon R-12 (—) with the numerical solutions of HRDM for freon and its vapor for θ = 1 s, $\tilde{\lambda}$ = 910 W/(mK) (-···) and HRDM as for a water-vapor mixture for θ = 1 s, $\tilde{\lambda}$ = 8350 W/(mK) (--). Points of recording (*a*) z = 0 m, (*b*) z = 0.29 m, (*c*) z = 0.54 m, (*d*) z = 0.915 m.

$\epsilon_0 = 0.01$, average bubble radius $r_0 = 1.3$ mm, initial pressure $P_0 = 0.19$ MPa and initial velocity $w_0 = 0$. The best agreement between the numerical solutions and experimental results was achieved for the relaxation time $\theta = 0.7$ s and macroscopic thermal conductivity coefficient $\tilde{\lambda} = 1800$ W/(mK). The ratio of the bubble radius to the thermal boundary layer was equal to $r/\delta_t = 4.6$. As in the previous case, it is easy to see the two effects of wave propagation in the two-phase mixture, that is the damping and dispersion. It is clear from the figures depicting the evolution of the pressure pulse that modelling the thermal diffusion has an important effect on the obtained numerical results.

It has been established that the relaxation times θ for the two cases described above in Figs. 2 and 3 substantially differ from each other taking values 0.15 s and 0.7 s, respectively, although both cases correspond to the water-steam mixture. It leads to the conclusion that θ is not only a function of the fluid properties but also depends on parameters such as the bubble radius, bubble distribution, initial water superheat resulting from the pressure pulse, as it is shown in Bilicki et al. (1996). The

calculations of the evolution of the pressure pulse also exhibit differences between the solutions of the relaxation and relaxation-diffusion models. The effect of damping is conspicuous in both models; however, HRDM demonstrates it in a more spectacular way. The spreading of the signal is better represented in the relaxation-diffusion model. The comparison of the solutions of these two models clearly shows that the difference is not only quantitative, but also qualitative in character.

Finally, the calculations were also performed for a two-phase mixture of freon R-12 and its vapor. The results are depicted in Fig. 4. The solid lines refer to the experimental results, while dash-and-dot lines correspond to the numerical solutions obtained from HRDM. The computations were carried out for the following parameters: $\theta = 1.0$ s, $\tilde{\lambda} = 910$ W/(mK), giving $r/\delta_t = 4.7$. For the sake of comparison, a numerical run for water was performed, denoted by the dashed lines in Fig. 4, for the same initial pressure, temperature, void fraction, bubble radius as for freon. For these parameters the macroscopic heat conduction coefficient $\tilde{\lambda}$ of water was found 9.2 times greater than that of freon. The solution for water was obtained for $\theta = 1.0$ s and $\tilde{\lambda} = 8350$ W/(mK). It is conspicuous from Fig. 4 that the wave propagation in freon is characterized by weaker diffusion effects than in water. This is due to the fact that $\tilde{\lambda}$ for freon is considerably smaller than for water. Therefore, one can say that the wave propagation in freon is more inertial than thermal.

It is apparent in the above three examples that HRDM describes very well the experimental runs of wave propagation with strong effects of thermal diffusion. This is an advantage of this model in comparison to HRM. In all these cases a sufficiently refined grid of $\Delta z = 0.01$ m, $\Delta z/\Delta t = 500$ m/s was selected so as to make sure that the influence of the numerical diffusion is negligibly small. The proposed method of using a macroscopic thermal conductivity determined from the entropy production yields results which agree well with the experimental data. At this stage, however, we do not claim that satisfactory agreement can be obtained for all experimental conditions.

8 Conclusions

The results of numerical calculations of wave propagation in two-phase flows performed with the help of HRM and HRDM have been compared with the experimental data. The evolution of a pressure signal in the situation dominated by the effects of interfacial heat and mass exchange, is characterized by the damping and spreading effects. The computations show that an ordinary relaxation model (HRM) does not describe quantitatively these phenomena, although the model sometimes reproduces their qualitative features. The relaxation model has been extended by the introduction of a heat diffusion term, which describes the rate of energy transfer. It is observed that the diffusion of the signal depends on the superheating of the liquid, the surface area of the vapor bubbles, the coefficient of heat transfer from the liquid to the vapor and also on the void fraction. With the introduction of the diffusion term, a qualitative agreement with the experimental data of wave propagation is always obtained. Sometimes (but not always) also quantitative coincidence of numerical and experimental results can be found. A further development of the relaxation-diffusion model requires the experimental determination of the mesoscale parameters. This is supposed to yield more reliable values for the macroscopic thermal conductivity and relaxation time.

Acknowledgment

This work was supported by the Polish State Committee for Scientific Research under grant no. 3 P404 030 06.

References

Ardron, K. H., and Duffey, R. D., 1978, "Acoustic Wave Propagation in a Flowing Liquid-Vapor Mixture," *International Journal of Multiphase Flow,* Vol. 4, pp. 303–322.

Batchelor, G. K., 1969, "Compression Waves in a Suspension of Gas Bubbles in Liquid," *Fluid Dynamics Transactions,* W. Fiszdon, P. Kucharczyk and W. J. Prosnak, eds., PWN Warszawa, Vol. 4, pp. 415–424.

Bilicki, Z., and Kestin, J., 1990, "Physical Aspects of the Relaxation Model in Two-Phase Flow," *Proceedings of Royal Society,* London, Series A 428, pp. 379–397.

Bilicki, Z., Kestin, J., and Pratt, M. M., 1990, "A Reinterpretation of the Results of the Moby Dick Experiments in Terms of the Nonequilibrium Model," ASME JOURNAL OF FLUIDS ENGINEERING, Vol. 112, pp. 212–217.

Bilicki, Z., and Kardas, D., 1993, "Numerical Solution of Transient and Non-equilibrium Two-Phase Liquid-Vapour Flow," *Transactions of Institute of Fluid-Flow Machinery,* Vol. 95, pp. 105–129.

Bilicki, Z., 1994, "Concept of Internal Variables in the Light of Contemporary Thermodynamics of Irreversible Processes and its Application in Two-Phase Flow" (in Polish), *Zeszyty Naukowe IMP PAN,* Vol. 421/94.

Bilicki, Z., Kwidzinski, R., and Mohammadein, S. A., 1996, "Evaluation of the Relaxation Time of Heat and Mass Exchange in the Liquid-Vapour Bubble Flow," *International Journal of Heat and Mass Transfer,* Vol. 39, pp. 753–759.

Bilicki, Z., and Michaelides, E. E., 1997, "Thermodynamic Nonequilibrium in Liquid-Vapour Flow," *Journal of Nonequilibrium Thermodynamics,* Vol. 22, 99–109.

Campbell, I. J. and Pitcher, A. S., 1954, "Flow of Air-Water Mixtures," *Symposium at Admiralty Research Laboratory,* Middlesex.

Downar-Zapolski, P., 1992, "An Influence of the Thermodynamic Disequilibrium on the Pseudo-Critical Flow of One-Component Two-Phase Mixture" (in Polish), Ph.D. thesis, Institute of Fluid-Flow Machinery, Polish Academy of Sciences, Gdansk.

Downar-Zapolski, P., Bilicki, Z. Bolle, L., and Franco, J., 1996, "The Nonequilibrium Relaxation Model for One-Dimensional Flashing Liquid Flow," *International Journal of Multiphase Flow,* Vol. 22, pp. 473–483.

Guha, A., and Young, J. B., 1990, "Stationary and Moving Normal Shock Waves in Wet Steam," *Adiabatic Waves in Liquid-Vapor Systems* G. E. A. Meier and P. A. Thompson, eds., Springer-Verlag, 159–170.

Ishii, M., 1975, *Thermo-Fluid Dynamics Theory of Two-Phase Flow,* Eyrolle, Paris.

Kardas, D., 1994, "Effect of the Dissipation Terms on Numerical Solutions of Non-Steady-State Two-Phase Flow" (in Polish), Ph.D. thesis, Institute of Fluid-Flow Machinery, Polish Academy of Sciences, Gdansk.

Kardas, D., and Bilicki, Z., 1995, "Approximation of the Thermodynamic Properties of Superheated Water and Subcooled Steam" (in Polish), *Zeszyty Naukowe IMP PAN,* Vol. 454/95.

Kestin, J., 1979, *A Course in Thermodynamics, Vol. I and Vol. II,* Hemisphere Publishing Corporation, New York.

Kestin, J., 1993, "Thermodynamics" (An essay), *Zagadnienia Maszyn Przeplywowych,* Gdansk, pp. 319–334.

Konorski, A., 1971, "Shock Waves in Wet Steam Flows," *Transactions of Institute of Fluid-Flow Machinery,* Vol. 57, pp. 101–110.

Lebon, G., Jou, D., and Casas-Vazquez, J., 1992, "Questions and Answers About a Thermodynamic Theory of Third Type," *Contemporary Physics,* Vol. 33, pp. 41–51.

Lemonnier, H., and Selmer-Olsen, S., 1992, "Experimental Investigations and Physical Modelling of Two-Phase Two Component Critical Flow in a Convergent Nozzle," *International Journal of Multiphase Flow,* Vol. 18, pp. 1–20.

Michaelides, E. E. and Feng, Z. G., 1994, "Heat Transfer from a Rigid Sphere in a Nonuniform Flow and Temperature Field," *International Journal of Heat and Mass Transfer,* Vol. 37, pp. 2069–2076.

Nakoryakov, V. E., Pokusaev, G. B., Shreiber, I. R., and Pribaturin, N. A., 1988, "The Wave Dynamics of Vapour-Liquid Medium," *International Journal of Multiphase Flow* Vol. 14, pp. 655–677.

Nakoryakov, V. E., Pokusaev, G. B., and Shreiber, I. R., 1993, *Wave Propagation in Gas-Liquid Media,* CRC Press.

Nigmatulin, R. I., 1991, *Dynamics of Multiphase Media, Vol. 1 and Vol. 2,* Hemisphere Publishing Corporation.

Puzyrewski, R., 1980, "Gasdynamics Effects due to Homogeneous Condensation of Vapours," *Heat and Mass Transfer in Multicomponent Gas-Liquid System,* Ossolineum.

Ransom, V. H., Wagner, R. J., and Trapp, J. A., 1983, "The RELAP 5 Two-Phase Fluid Model and Numerical Scheme for Economic LWR System Simulation," *Transient Two-Phase Flow,* M. S. Plesett, N. Zuber, and I. Catton, eds., Hemisphere Publishing Corporation, pp. 513–531.

Szaniawski, A., 1957, "Propagation of Small Disturbances in the Mixture of Liquid and Gas Bubbles" (in Polish), *Rozprawy Inzynierskie,* Vol. LXXI, p. 5.

Effect of Trailing Edge Suction on Coherent Structures in Near Wake

S. D. Sharma
Associate Professor.

R. K. Sahoo
Graduate Student.

Department of Aerospace Engineering,
Indian Institute of Technology,
Bombay, India

Experimental results, obtained from hot-wire measurements using a conditional sampling technique, demonstrate feasibility of controlling large-scale spanwise vortices (coherent structures) in the near wake region behind a rectangular base by means of suction through a slit at just one of the trailing edges. The suction thus employed, is found to influence the near wake topology with strong asymmetry and disturb the net vorticity balance. Moreover, a significant reduction in the base drag is achieved as a consequence of the trailing edge suction. The mechanism of the drag reduction is understood to lie in a marked change in the wake dynamics including attenuation in the size and strength of the coherent structures.

Introduction

Occurrence of large-scale organized vortical structures, also recognized as coherent structures, in free shear flows is known to cause certain detrimental as well as beneficial effects. The presence of coherent structures may therefore be desirable in some cases and undesirable in some other cases. While suppression of coherent structures is reported to alleviate engineering difficulties like high form drag, noise, and flow induced vibration (Armstrong et al., 1977; Crighton, 1981; Michalke, 1978; Sharma, 1988; Zdravkovich, 1981), their enhancement is found to yield appreciable gains in some applications such as reduction of wall shear stress, postponement of airfoil stall, and those related to the phenomena of transport and mixing in various engineering processes (Badri Narayanan, 1988; Fiedler, 1987; Peters and Williams, 1981). Considering such contrasting effects of the coherent structures in a variety of situations, significance of their appropriate manipulation to always derive favorable results in a particular application, cannot be over-emphasized. Various active and passive methods that can control the coherent structures in a range of shear flow through either boundary condition or initial condition or excitation have been discussed by Bridges et al. (1990) and Fiedler (1987).

The interaction between opposite shear layers in the base region of a two-dimensional bluff body plays a key role in the process of formation of vortices and their periodic shedding in the wake. Following the hypothesis proposed by Gerrard (1967) for mechanism of formation and shedding of vortices behind a bluff body, the present problem was formulated with a purpose to invent a simple technique of changing initial conditions of the flow over a plane blunt base and examine the effects on characteristics of the coherent structures in the near wake region. The main objective of the present work is to study experimentally the behavior of a two-dimensional bluff body wake wherein one of the two shear layers is removed. Realization of the concept of such a wake is attempted by employing suction of one of the boundary layers just before the separation point. Removal of one of the two shear layers was envisaged as an effective means of interference with the natural process of vortex shedding in the wake.

Experimental Methods

Figure 1 shows sectional view of the test model which is a 20 percent thick blunt trailing edge aerofoil having an elliptic forebody and parallel sided rear body. The model was made out of perspex with glossy finish and was machined hollow to make provision for the boundary layer suction through a 1 mm slit all along the trailing edge only on one side. As depicted by the model sectional details in the figure, the interior was shaped into a contraction such that it could also serve the purpose for tangential blowing in the form of a thin jet sheet. A fine phosphorus bronze screen was installed just before the contraction for spanwise uniformity of the flow through the model slit. For reference base pressure, a single pressure tap of about 0.5 mm diameter was provided in the middle of the model base.

Figure 2 shows a diagram of the experimental setup. A suction type, variable speed, low turbulence wind tunnel having a test section of 229 mm in width and 300 mm in height was used. A pressure drop across the tunnel contraction, registered through piezo-metric connection, gives the free-stream velocity. The maximum flow velocity that can be achieved in this tunnel is 24 m/s. The model was mounted spanning the test section walls at zero incidence with the slit side facing down. As depicted in Fig. 2, ducting for the flow through the model slit was connected to the suction-end of a variable speed centrifugal blower via a precalibrated orifice meter. The hot wire anemometer system comprised of two Sunshine Constant Temperature Anemometers (AMB-717), two types of DISA miniature hot wire probes (55P11 with normal wire and 55P12 with 45 deg slant wire) with 5μ tungsten wire spot welded on to the prongs, a DISA signal conditioner (55D26), a Sunshine digital dc voltmeter (AMM-717) and a two channel Gould 400 MHz storage oscilloscope. A normal hot wire probe with sensor aligned spanwise was permanently fixed from the test section ceiling behind the model and positioned at about 4h from the base and about 0.75h above the axis in the outer wake region. A two-component traverse with micro-processor controlled stepper motors was used to probe the flow in the streamwise vertical plane at midspan using hot wire probes of both the types—normal and slant. A spanwise gap of about 0.5h was kept between the fixed and the traversing hot wire probes. The fixed hot wire probe was used for reference signal, whereas, the traversing hot wire probe was mainly used to scan the base flow field.

Hot wire measurements in the near wake region were made in two parts, (*i*) time averaged and (*ii*) phase averaged using a conditional sampling technique. The conditional sampling technique employed was similar to that of Okude and Matsui (1990) using simultaneously two hot wire probes—one giving the sinusoidal reference signal and the other registering the velocity against time while being traversed across the entire wake width. It is essential that the reference signal from the

Contributed by the Fluids Engineering Division for publication in the JOURNAL OF FLUIDS ENGINEERING. Manuscript received by the Fluids Engineering Division April 17, 1997; revised manuscript received October 20, 1997. Associate Technical Editor: D. P. Telionis.

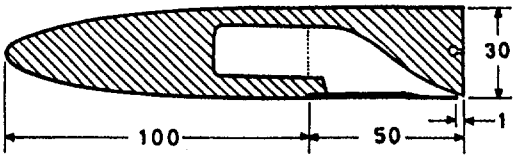

Fig. 1 Sectional details of test model

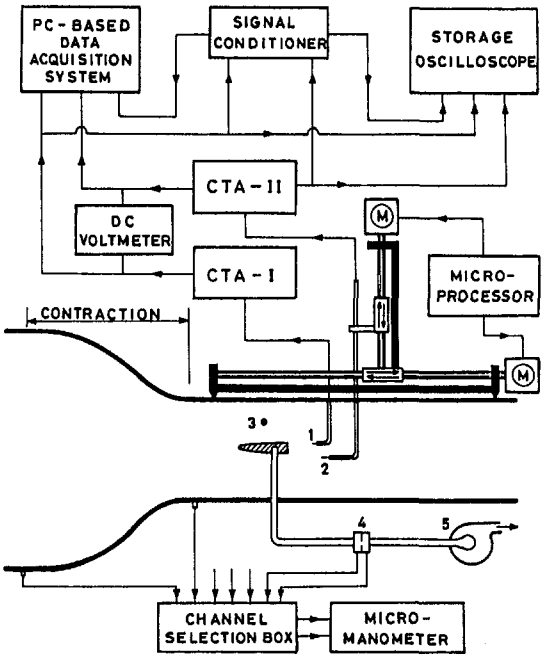

Fig. 2 Experimental apparatus. 1-fixed hot wire probe, 2-hot wire probe held in traverse, 3-location for reference velocity, 4-orifice meter, 5-blower, M-stepper motor.

fixed probe is regular and periodic to enable conditional sampling of the data from traversing probe. Each period was divided into 16 phases and to obtain a single point at each phase, 800 digitized samples of the data from each of the two probes were acquired by a computer based PCL 208 data acquisition system and stored for ensemble averaging.

When the centrifugal blower was not on and the tunnel was running, the orifice meter reading indicated the atmospheric air jetting through the model slit into the test section due to the pressure being lower inside the test section. Therefore, the model slit was closed with a thin adhesive tape when measurements were made without employing the suction. Switching on of the suction was observed to increase the free-stream velocity. Hence the tunnel speed was regulated along with the suction to

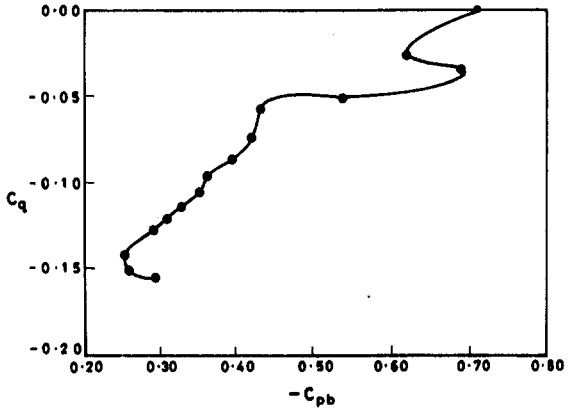

Fig. 3 Effect of suction on the model base pressure

maintain the selected free-stream velocity. Experiments were carried out at the Reynolds number of about 14000 based on the model base height of 30 mm and the free-stream velocity of 7 m/s. The wind tunnel free-stream turbulence level was 0.1 percent. The reading of the normal hot wire probe obtained at a mid-point in the gap between the tunnel ceiling and the model (shown as marked 3 in Fig. 2) was used as a reference velocity for the purpose of normalization.

The maximum experimental uncertainty involved in measurement of various quantities was ascertained as follows: mean velocity 2 percent, fluctuating velocity 5 percent, differential pressure 1 percent, and linear movement of the traverse 0.05 mm.

Results and Discussion

Figure 3 shows variation of the base pressure with suction of the boundary layer in the form of nondimensional coefficients. The indicated suction coefficient value, C_q, is obtained by normalizing the measured volumetric suction rate by the free-stream velocity and the model base area. Since the suction was employed only on one side, a nonuniformity was expected in the pressure distribution across the base height. Hence for an accurate determination of the base pressure, a pitot tube of 1 mm outer diameter was traversed with its tip touching to the model base and readings were taken at 10 equidistant points along the base height. However, no discernible variation was observed and the average value was found to compare well with the one registered by the single pressure tap provided in middle of the model base. A substantial rise in the base pressure is obtained with the activation of the boundary-layer control, but not steadily as in a narrow range of C_q between about -0.02 and -0.04 C_{pb} exhibits a reverse trend. Thereafter, C_{pb} continuously increases at varying rate, first rather steeply till C_q of about

Nomenclature

A = spectral amplitude in frequency spectrum plots, and area
a = lateral spacing of vortices
b = longitudinal spacing of vortices
C_{pb} = base pressure coefficient [$= 2(p_b - p_\infty)/\rho U_\infty^2$]
C_q = suction coefficient
d = width of suction slit in the model
h = model base height
p_b = base pressure
p_∞ = free-stream static pressure
P_n = dimensionless normal turbulence production
P_s = dimensionless shear turbulence production
P_t = dimensionless total turbulence production [$= P_n + P_s$]
S = strain [$= du/dy + dv/dx$]
t = time
u = streamwise mean velocity (along x-axis)
u' = streamwise fluctuating velocity
U = reference streamwise velocity
U_c = vortex convection velocity
U_∞ = free-stream velocity
v = transverse mean velocity (along y-axis)
v' = transverse fluctuating velocity
x, y = streamwise and transverse coordinates
Γ = circulation
ω = vorticity [$= dv/dx - du/dy$]
ρ = density of air
$\langle\ \rangle$ = phase average

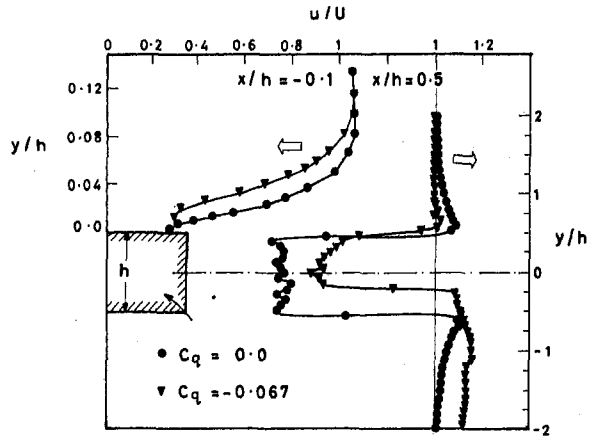

Fig. 4 Mean velocity profiles in the boundary layer near trailing edge on the nonsuction side and in the near wake region

-0.06 and later diminishingly to reach a local maximum of about -0.25 thereby resulting in 64 percent reduction of base drag. It may be worthwhile to point out here that during the base bleed experiments Bearman (1967) obtained an entirely opposite trend when a suction was employed—the base pressure was found to decrease steadily with increase in suction. In the present study, the base pressure was noted to be rather insensitive to the suction in a small range around $C_q = -0.067$ (see Fig. 3) and moreover, the wake traces on an oscilloscope still exhibited some periodicity. Therefore, it was decided to carry out the experiments with suction at $C_q = -0.067$.

Figure 4 shows the mean velocity profiles measured using the normal hot wire probe across the boundary layer at $x/h = -0.1$ before separation on the nonsuction side of the model and across the wake at $x/h = 0.5$ within the vortex formation region. The thickness of the boundary layer appears to be within about 0.1 h, which is in accordance with the value estimated assuming Blasius profile on a flat plate. Since a proper boundary-layer hot wire probe was not used, velocity profiles are seen to be inflexed due to the stem interference in the close proximity of the model surface. From the well-known correlation between the base pressure and the velocity at the separation, the boundary-layer edge velocity was expected to change with C_q. Surprisingly, no such feature is exhibited by the boundary-layer profile. Probably because the velocity gradient becomes increasingly steep as the trailing edge is approached, the expected high velocity associated with low base pressure would be registered in the plane of the model base. Nevertheless, the influence of suction is clearly seen from the velocity distribution. The suction apparently has a tendency to reduce the velocity close to the surface and to slightly increase the boundary layer thickness. This effect is seen to be translated in the wake as curtailment of velocity overshoot in the shear layer. Further, an effective decrease in the wake defect is consistent with the base drag reduction obtained due to the suction. An unusual increase in the velocity in the lower half region, particularly outside the wake, is induced by the suction. However, this was found to subside quickly downstream within $x/h = 5$ (Sahoo, 1996). Thus, it is surmized that the effect of the boundary-layer suction is not localized as it can alter the whole flow field around the model including the vorticity supply through the nonsuction side shear layer. From various time averaged measurements, Sahoo (1996) has noted effects of a gradual increase in the boundary-layer suction in terms of (*a*) shrinkage in the size of vortex formation region, (*b*) reduction in wake defect, (*c*) reduction in wake turbulence energy and Reynolds stresses, and (*d*) an asymmetry in the wake with its axis curving toward the opposite nonsuction side.

Figure 5 shows the frequency spectra obtained at various transverse positions at $x/h = 4$. An asymmetry in the wake is quite apparent from these plots. Figure 5(*a*), for no suction case, shows that similar spectral peaks occur when the hot wire is placed at two opposite equidistant points in the outer wake region, $y/h = \pm 1$. The spectral peak frequency of about 55 Hz corresponds to the primary frequency of vortex shedding in one of the rows. When placed in the center, $y/h = 0$, the hot wire becomes equally responsive to alternate vortices in the opposite rows and then the spectrum is expected to also register a secondary peak at twice the frequency. The figure indeed illustrates this fact. Figure 5(*b*) depicts a remarkable change in the frequency spectra when the boundary-layer suction is employed. Considering the frequency of the spectral peak, the wake axis appears to have deviated from the geometric axis to $y/h = 0.5$, which is in accordance with the locus of maximum wake defect, obtained from velocity profiles at various streamwise stations (not shown here). There is no noticeable change in the primary vortex shedding frequency. However, the spectral peak has now become broad with a significant attenuation.

Figures 6(*a*) and (*b*) show vector patterns of the mean velocity field relative to an observer moving along with the wake at the vortex convection velocity (celerity), respectively, for without and with the boundary-layer suction. These figures are obtained by deducting the vortex convection velocity from the phase averaged velocities measured across the wake at $x/h = 4$ by using conditional sampling technique. The average vortex convection velocity, measured over a cycle from $x/h = 4$, was found to be 0.713U without suction and 0.825U with suction. Although the shed vortices move with rapidly increasing speed in the near wake region, these values were assumed to be constant for convenience which is an accepted practice (Cantwell and Coles, 1983; Hussain and Hayakawa, 1987; Kiya and Matsumura, 1985). The velocity-vector patterns depicted here correspond to two cycles wherein the time scale on the x-axis has been converted into a notional length scale using the phase shift information. Using the vortex convection velocity and the shedding frequency, each cycle (longitudinal vortex spacing) is found to correspond to 2.88 h for $C_q = 0$ and to 3.2 h for $C_q = -0.067$.

Figure 6(*a*) clearly illustrates typical topological features of a plane bluff body wake. The centers with rotational fluid motion around them (vortical motion) and the saddle points with velocity vectors around them in a characteristic formation of converging and diverging separatrix are distinctly seen to exist. In velocity-vector pattern, both these points appear where the local velocity vectors are horizontal with their magnitude equal to the vortex convection velocity. In Fig. 6(*b*), with the boundary-layer suction, although the wake pattern appears to bear nearly similar features, the vortical structure is not as clear and moreover, it is rather difficult to detect the saddle points for they are not discernible. The illustrated shift of the vortical pattern toward the nonsuction side is in accordance with the asymmetry noted in Fig. 5.

Figure 7 shows contours of the nondimensionalized phase-averaged vorticity obtained from derivatives of the phase-averaged velocity components as given by

$$\frac{\langle\omega\rangle h}{U} = \frac{d(\langle v\rangle/U)}{d(x/h)} - \frac{d(\langle u\rangle/U)}{d(y/h)}. \qquad (1)$$

Contours of very low vorticity values are not included in this figure in order to avoid relatively noisy data near the outer edges of the vortices. As a result, a picture resembling the Karman vortex street has emerged with contra-rotating vortices in staggered arrangement indicating clockwise rotation with negative value of vorticity and anti-clockwise rotation with positive value of vorticity, which is reminiscent of the earlier results (Cantwell and Coles, 1983; Hussain and Hayakawa, 1987; Kiya and Matsumura, 1985 and 1988; Okude and Matsui, 1990; Zhou

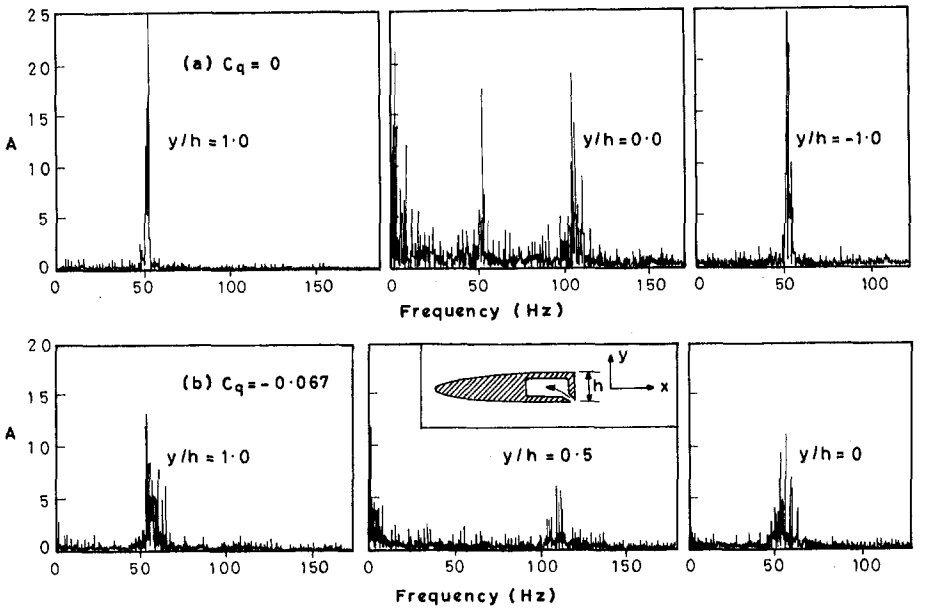

Fig. 5 Frequency spectra in a transverse plane at $x/h = 4$. (*a*) Without suction and (*b*) with suction.

and Antonia, 1993). The vorticity seems to concentrate around the centers that were seen in Fig. 6. Actually, the coordinates of the peak vorticity give more accurate location of the centers than the velocity-vector plots as the latter can be affected by the vortex convection velocity. The longitudinal (a/h) and lateral (b/h) spacings thus estimated are found to be 2.85 and 1.06 for $C_q = 0$, and 3.2 and 0.95 for $C_q = -0.067$. The resultant vortex spacing ratios (b/a) obtained from these values are 0.372 and 0.297, respectively. Further, a strong influence of the boundary-layer suction is evidently seen from the diminished vorticity and longitudinally elongated shape of the vortices. The saddle points in the figures are marked from the positions of the peak strain rate (not shown here) and the sense of separatrix is inferred from the velocity vector pattern shown in Fig. 6.

Figure 8 shows vorticity distribution along the two orthogonal axes passing through the centers of structures (vortices), re-

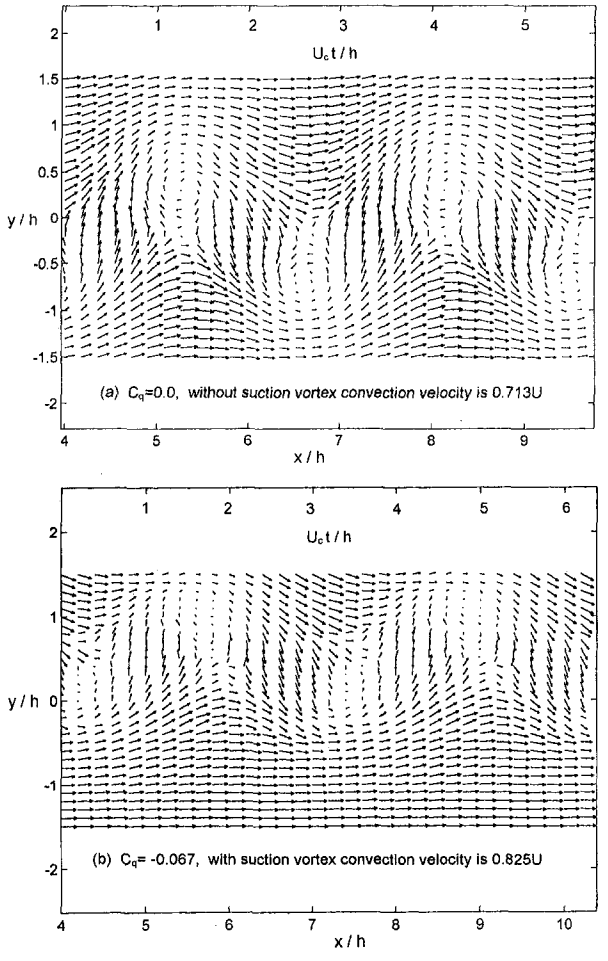

Fig. 6 Conditional velocity vector field as viewed in a moving frame of reference at $x/h = 4$ for two cycles

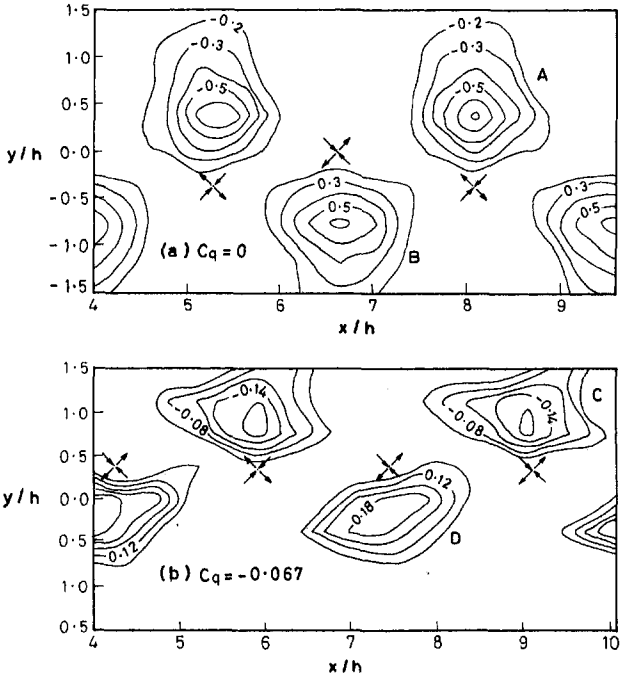

Fig. 7 Phase averaged vorticity contours obtained at $x/h = 4$ for two cycles. (*a*) Without suction and (*b*) with suction.

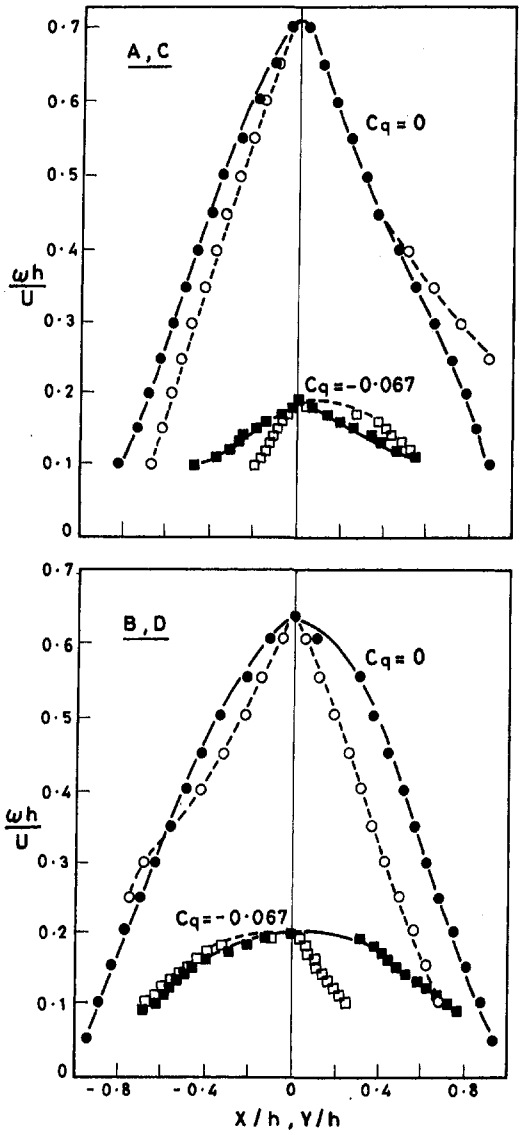

Fig. 8 Distribution of vorticity along longitudinal axis (filled symbols) and along transverse axis (empty symbols) passing through the centers of vortices designated by *A*, *B*, *C*, and *D* in Fig. 7

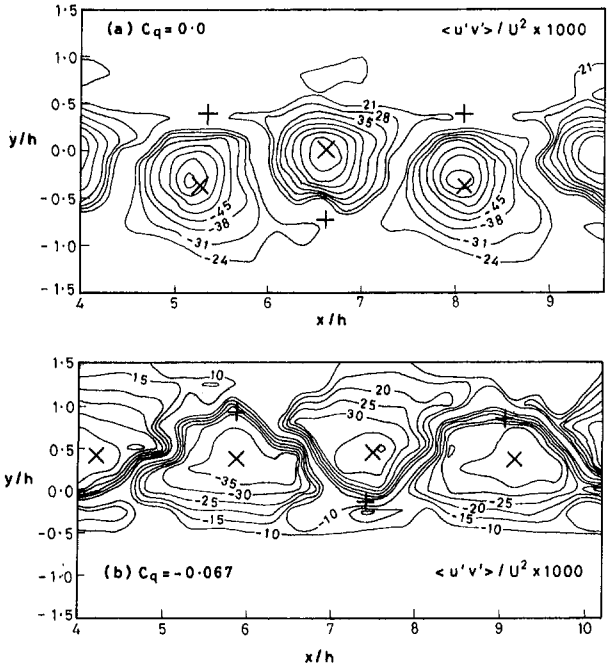

Fig. 9 Phase averaged Reynolds shear stress contours. (*a*) Without suction and (*b*) with suction.

spectively, in the upper and lower rows, designated by **A, B, C,** and **D** in Fig. 7. Here, zero on the x-axis corresponds to the center of the structure—a point of the peak vorticity. The vorticity distribution appears to be nearly symmetric about the center on the longitudinal axis. It is clear that the boundary layer suction greatly affects the vortex formation process and as a result a much weaker and smaller vortex is produced. However, what is interesting to note is that though vortex **C** is in the row of the nonsuction side, it is affected more than vortex **D**. In order to assess the vortex strength, circulation was estimated from the vorticity contour plots using the following expression,

$$\Gamma/Uh = \sum (\langle\omega\rangle h/U)(dA/h^2). \qquad (2)$$

The nondimensionalized circulation thus obtained in the case of no suction was found to be 2.315 for clockwise vortex **A** above the wake axis and 2.39 for anti-clockwise vortex **B** below the wake axis. Since the vorticity created on the surface of the body is sucked in, the net balance of vorticity is disturbed. Consequently, the corresponding values with the boundary-layer suction were found to be 0.657 and 0.898 for the clockwise and anti-clockwise vortices **C** and **D**, respectively, thereby indicating a significant inequality in the vortex strength across the wake axis. Recently, Hammond and Redekopp (1997) have numerically predicted such inequality emerging in an asymmetric wake behind a two-dimentional bluff body with a rectangular base. The asymmetry in the wake was generated by selection of a velocity difference between the two opposite shear layers. The inequality in the strength of vortices in opposite rows was found to strongly depend on the velocity difference. Their results have illustrated formation of stronger vortices from the shear layer with larger velocity as found experimentally in the present investigation. Considering the above estimated values of circulation, the suction is found to cause a remarkable attenuation in the vortex strength by about 72 percent in the upper row and about 62 percent in the lower row. The average of the two values then can be regarded as the effective attenuation in the vortex strength.

Figure 9 shows contour plots of the nondimensionalized phase-averaged Reynolds shear stress, $\langle u'v'\rangle/U^2$, due to random velocity fluctuations. The locations of critical points are marked with plus (+) for centers and with cross (×) for saddles. The Reynolds shear stress is concentrated around the saddle points which are characterized by the minimum in mean spanwise vorticity. Effect of the boundary-layer suction appears to truncate the shear stress peaks as can be seen from relatively large areas enclosed by the contours of the maximum shear stress values. This may be correlated with the indiscernible pattern of saddle points in Fig. 6(b). A close observation reveals that the contours are elongated in the probable direction of the diverging separatrix away from the wake axis. The Reynolds normal stresses, both longitudinal and transverse (not shown here), were found to have their maxima around the centers of vortices and due to the boundary-layer suction not only did the stress values drastically reduced, but they also became too insignificant to be registered in the lower half zone where suction was applied.

The total turbulence production is comprised of two components, the normal turbulence production and the shear turbulence production. Thus, the phase averaged total turbulence production $\langle P_t\rangle$ can be obtained from the summation of the phase averaged values of normal turbulence production $\langle P_n\rangle$ and the shear turbulence production $\langle P_s\rangle$ which are defined as,

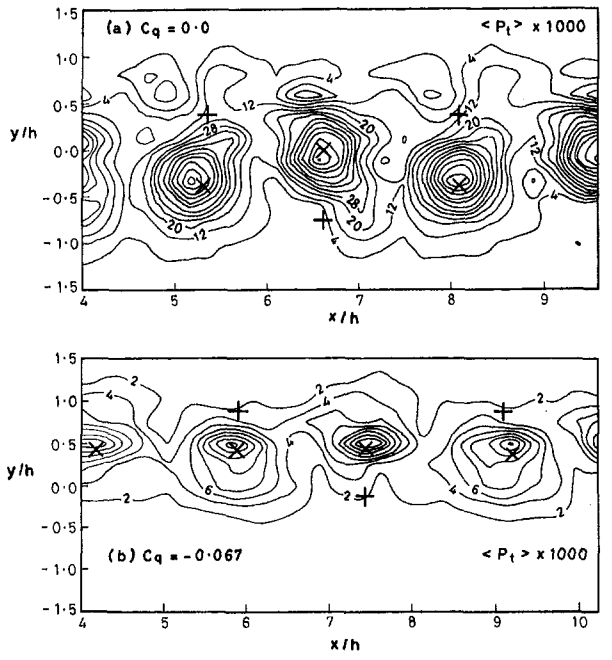

Fig. 10 Phase averaged total turbulence production contours. (*a*) Without suction and (*b*) with suction.

$$\langle P_n \rangle = \frac{\langle u'^2 \rangle}{U^2} \frac{d(\langle v \rangle / U)}{d(x/h)} + \frac{\langle v'^2 \rangle}{U^2} \frac{d(\langle u \rangle / U)}{d(y/h)} \tag{3}$$

$$\langle P_s \rangle = \frac{\langle u'v' \rangle}{U^2} \left[\frac{d(\langle v \rangle / U)}{d(x/h)} + \frac{d(\langle u \rangle / U)}{d(y/h)} \right] \tag{4}$$

Since the Reynolds shear stress and the strain both have the same sign and are localized with their maxima at around the saddle, from the above definition it is obvious that not only the peak of $\langle P_s \rangle$ would occur in that region but also its contours would always bear the positive sign. Despite the fact that the Reynolds normal stresses were found to concentrate in the centers, the peaks of $\langle P_n \rangle$ with opposite signs were located about the centers, flanking the vortices in the front (downstream side) with the negative sign and at the back with positive sign. When compared, the magnitudes of $\langle P_s \rangle$ were found to be much larger than those of $\langle P_n \rangle$ which is believed to be inherent of a plane turbulent wake for Hussain and Hayakawa (1987) have also reported the similar findings.

Figure 10 shows contour plots of the total turbulence production, $\langle P_t \rangle = \langle P_s \rangle + \langle P_n \rangle$. Although these have combined features of $\langle P_s \rangle$ and $\langle P_n \rangle$ contour plots (not shown here), owing to relatively small contribution from the normal turbulence production, the plots of the total turbulence production and those of the shear turbulence production were seen to have a good resemblance with comparable values. The quantity $\langle P_t \rangle$ has its peak in the saddle region with maximum values of 0.092 for $C_q = 0$ and 0.016 for $C_q = -0.067$. Such a marked drop of about 83 percent in the peak value of the total turbulence production shows a strong influence of the boundary layer suction. Cantwell and Coles (1983) and Hussain and Hayakawa (1987) have attributed the turbulent energy production to its strong coupling with the strain field associated with large scale vortices. Stretching of vortex along the diverging separatrix due to large strain field in the saddle region results in the turbulence production there. Here, it may be worth mentioning that of the total turbulence energy content in the near wake, contribution from the coherent structures form only about 25 percent (Fiedler, 1987).

Various nondimensionalized peak values of the phase averaged quantities measured in the present investigation are given in Table 1. Peak values of similar quantities are also included for comparison from other investigations on circular cylinder wake (Cantwell and Coles, 1983; Hussain and Hayakawa, 1987). However, it may be noted that these were obtained at different streamwise locations. As expected, the values are seen on a decline away from the base.

In general, collation of the data shown in the table suggests a good consistency among themselves. For example, a ratio of the shear turbulence production and the normal turbulence production, $\langle P_s \rangle / \langle P_n \rangle$, in the present investigation is 4 for $Cq = 0$ and that due to Hussain and Hayakawa (1987) is 3.3. A comparison of the peak phase averaged values of the Reynolds stresses with the corresponding maximum time averaged values at the same streamwise location (not shown here) further revealed a regular relationship between them. For example, the peak values of $\langle u'^2 \rangle$, $\langle v'^2 \rangle$ and $\langle u'v' \rangle$ were found to be, respectively, 1.5, 1.48, and 6 times greater than the maximum of u'^2, v'^2, and $u'v'$ in the plane at $x/h = 4$ for $C_q = 0$. The numerical figures similarly worked out from the values reported by Cantwell and Coles (1983) were 1.75, 1.72, and 3.95 at $x/h = 2.8$, and 1.67, 1.5, and 5 at $x/h = 4.9$, respectively. Hussain and Hayakawa (1987) have found the peak value of $\langle u'v' \rangle$ to be more than twice the maximum value of $u'v'$ at $x/h = 9.5$. Interestingly, the boundary-layer suction ($Cq = -0.067$) was found to affect the relative magnitudes of only normal stresses as the peak values of $\langle u'^2 \rangle$ and $\langle v'^2 \rangle$ are 0.18 and 0.21 times the maximum of u'^2 and v'^2 showing a completely opposite trend, whereas the peak value of $\langle u'v' \rangle$ is 4.3 times greater than the maximum of $u'v'$. Further, $\langle P_s \rangle / \langle P_n \rangle$ is 45, which is unusually high primarily because of drastic reduction in normal production term.

The comparisons of the plots of various phase-averaged quantities and their peak values obtained in the present investigation evidently reiterate the inference drawn by Cantwell and Coles (1983) and Hussain and Hayakawa (1987) in their investigations on coherent structures in a plane wake that the saddle is the most dominant topological feature coupled strongly with large strain field where the turbulence is produced by means of vortex stretching—the fluid advected to this field along the

Table 1 Peak values of nondimensionalized phase averaged properties

	Present results $x/h = 4$		Cantwell and Coles (1983)		Hussain and Hayakawa (1987)
Quantity	$Cq = 0$	$Cq = -0.067$	$x/h = 2.8$	$x/h = 4.9$	$x/h = 9.5$
Vorticity, $\langle \omega \rangle h/U$	0.7	0.2	1.69	1.3	1.09
Strain, $\langle S \rangle h/U$	1.2	0.34	0.9	0.49	0.514
Normal long. stress, $\langle u'^2 \rangle / U^2$	0.1	0.0026	0.11	0.0785	0.029
Normal tran. stress, $\langle v'^2 \rangle / U^2$	0.062	0.006	0.172	0.086	0.0256
Shear stress, $-\langle u'v' \rangle / U^2$	0.073	0.035	0.03	0.019	0.013
Shear turb. production, $\langle P_s \rangle$	0.096	0.018			0.00475
Normal turb. production, $\langle P_n \rangle$	0.024	0.0004			0.00145
Total turb. production, $\langle P_t \rangle$	0.092	0.016	0.032	0.012	0.0049

converging separatrix is stretched along the diverging separatrix.

Conclusion

The boundary-layer control by suction, employed only on one side of the model just before separation at the blunt trailing edge, has been found effective in suppression of the periodic vortex shedding—a novel technique of reducing the base drag, hitherto untried. The present results are found to reinforce the significance of the saddle zones and the associated strain field in production of the turbulence. Feeble stretching of vortices in weakened strain field due to the boundary-layer suction results in reduced turbulence production. Thus, it is concluded that the coherent structures and their dynamics in the wake of a bluff body can be manipulated by controlling the initial flow conditions.

Acknowledgment

The work was supported by the research grant received from the Aeronautics Research and Development Board, Ministry of Defence for the project Aero/RD-134/100/10/91-92/671. A major part of the project, carried out during 1992 and 1995, formed the Ph.D. work of the second author (RKS).

References

Badri Narayanan, M. A., 1988, "The Behaviour of Excited Plane Jets," *Developments in Fluid Mechanics and Space Technology,* R. Narasimha and A. P. J. Abdul Kalam, eds., Indian Academy of Sciences, Bangalore, pp. 129–141.

Bearman, P. W., 1967, "The Effect of Base Bleed on the Flow Behind a Two Dimensional Model with a Blunt Trailing Edge," *The Aeronautical Quarterly,* Vol. 18, pp. 207–224.

Cantwell, B. J., and Coles, D. E., 1983, "An Experimental Study of Entrainment and Transport in the Turbulent Near Wake of a Circular Cylinder," *Journal of Fluid Mechanics,* Vol. 136, pp. 321–374.

Fiedler, H. E., 1987, "Coherent Structures," *Advances in Turbulence,* G. Comte-Bellot and J. Mathieu, eds., Springer-Verlag, Berlin Heidelberg, pp. 320–336.

Gerrard, J. H., 1967, "The Mechanism of the Formation Region of Vortices Behind Bluff Bodies," *Journal of Fluid Mechanics,* Vol. 13, pp. 401–413.

Hammond, D. A., and Redekopp, L. G., 1997, "Global Dynamics of Symmetric and Asymmetric Wakes," *Journal of Fluid Mechanics,* Vol. 331, pp. 231–260.

Hussain, A. K. M. F., and Hayakawa, M., 1987, "Education of Large-Scale Organized Structures in a Turbulent Plane Wake," *Journal of Fluid Mechanics,* Vol. 180, pp. 193–229.

Kiya, M., and Matsumura, M., 1985, "Turbulence Structure in the Intermediate Wake of a Circular Cylinder," *Bull. JSME,* Vol. 28, pp. 2617–2624.

Kiya, M. and Matsumura, M., 1988, "Incoherent Turbulence Structure in the Near Wake of a Normal Plate," *Journal of Fluid Mechanics,* Vol. 190, pp. 343–356.

Okude, M., and Matsui, T., 1990, "Vorticity Distribution of Vortex Street in the Wake of a Circular Cylinder," *Trans. Japan Soc. Aero. Space Sci.,* Vol. 33, pp. 1–13.

Sahoo, R. K., 1996, "Plane Base Flow Structures of a Blunt Trailing Edge with Boundary Layer Control," Ph.D. thesis, Department of Aerospace Engineering., Indian Institute of Technology, Bombay.

Sharma, S. D., 1988, "Experimental Study of Low Speed Base Flows of Castellated Blunt Trailing Edge Aerofoils," Ph.D. thesis, Department of Aerospace Engineering., Indian Institute of Technology, Bombay.

Zdravkovich, M. M., 1981, "Review and Classification of Various Aerodynamic and Hydrodynamic Means for Suppressing Vortex Shedding," *Journal of Wind Engineering and Industrial Aerodynamics,* Vol. 7, pp. 145–189.

Zhou, Y., and Antonia, R. A., 1993, "A Study of Turbulent Vortices in the Near Wake of a Cylinder," *Journal of Fluid Mechanics,* Vol. 253, pp. 643–661.

A Simple Analytical Theory for Interpreting Measured Total Pressure in Multiphase Flows

Abhijit Guha[1]
Ph.D., Lecturer,
Whittle Laboratory,
University of Cambridge,
Madingley Road, Cambridge CB3 ODY, U.K.

This paper presents a simple, analytical theory for determining total pressure in multiphase flows, a subject of theoretical interest as well as of practical importance. It is shown here that the nonequilibrium processes occurring in the vicinity of a measuring device have a significant influence on the magnitude of flow velocity inferred from Pitot measurements. The present theory predicts that, depending on the size of the particles or droplets, the total pressure varies monotonically between the two limiting values: the frozen total pressure (when there is no interphase mass, momentum, and energy transfer in the decelerating flow toward the stagnation point) and the equilibrium total pressure (when the dispersed phase, either liquid droplets, or solid particles, is always at inertial and thermodynamic equilibrium with the continuous vapour phase). The presented analytical theory is a relation between nondimensional total pressure and Stokes number, representing particle size or inertia, and specifies the total pressure under different nonequilibrium conditions. One simple equation applies to diverse multiphase mixtures, solid particle laden gas as well as vapour-droplet mixtures, and at a wide range of flow conditions, both subsonic and supersonic. The associated issue of interpreting total temperature, and the relation between measured total pressure and entropy production in multiphase flows have been discussed at length by Guha (1998).

1 Introduction

Mixtures of gases laden with solid particles or mixtures of a vapor and liquid droplets occur frequently in many practical flow situations. Pitot measurements are often used for inferring velocity or loss (entropy generation) in multiphase mixtures. However, in single phase fluids, it is normally permissible to assume that the fluid is brought to rest at the mouth of the Pitot tube isentropically. Hence flow Mach number and entropy generation (in steady, adiabatic flow) are uniquely determined by the total pressure measured by a Pitot tube, together with an independent measurement of the static pressure. In supersonic flow in an ideal gas, application of Rankine-Hugoniot equations across the detached shock wave in front of a Pitot tube retains the utility of Pitot measurements for deducing flow Mach number and entropy generation. Pitot measurements in a multiphase mixture, however, require careful considerations (Guha, 1998).

The solid particles or the liquid droplets respond to changes in temperature, velocity, etc. of the gas phase through interphase exchanges of mass, momentum, and energy. These are essentially rate processes and hence significant departures from equilibrium can take place if the rate of change of external conditions, imposed by the deceleration in the stagnating flow, is comparable to the internal time scales. Thus, for example, if the size of the liquid droplets or the solid particles is very small, then inertial and thermodynamic equilibrium between the two phases are maintained always, and a Pitot tube would measure the equilibrium total pressure, p_{oe}. On the other hand, if the size of the droplets or the particles is very large, all interphase transfer processes remain essentially frozen. The Pitot tube records the pressure which it would have recorded if the vapour phase alone was brought to rest from the same velocity. The total pressure in this case is termed the frozen total pressure, p_{of}.

As an example, consider low-pressure wet steam with a typical wetness fraction of 10 percent and at a Mach number 1.5. Calculations show that $p_{of}/p_\infty = 3.3$ and $p_{oe}/p_\infty = 3.79$, where p_∞ is the static pressure. Therefore, in this particular example, the equilibrium total pressure is about 15 percent higher than the frozen total pressure.

The subject of interpretation of measured total pressure in two-phase mixtures has been considered by Taylor (1945), Dussourd and Shapiro (1958), Soo (1964), Rudinger (1964), and Crane and Moore (1972). None of these previous authors attempted any generalization for all flow conditions and different two-phase mixtures. For example, Crane and Moore considered Pitot measurements in wet steam at low subsonic velocities and concluded that the total pressure measured would lie between the frozen and the equilibrium value, and would virtually be independent of the droplet size. Soo, on the other hand, asserted that, for low mass fraction of the dispersed phase, a total head probe in a gas-particle flow would always measure the frozen total pressure.

However, as explained earlier, it is expected that for intermediate sizes of the droplets or particles, the pressure recorded by the probe would neither be the equilibrium nor the frozen value. The imposed deceleration in front of the Pitot tube would render the two-phase mixture into nonequilibrium situations, both inertially and thermodynamically. The deceleration process consequently ceases to be isentropic, as nonequilibrium exchanges of mass, momentum, and energy between the two phases create entropy. The degree of the nonequilibrium effects will depend on the droplet size, mass concentration, etc. or more precisely on the relaxation times of the system. Hence, relaxation gas dynamics has to be called for a solution of the problem. (For a lucid overview of the relaxation gas dynamics in vapor-droplet flow, one may refer to Guha, 1995.)

For a proper solution of the real flow field around the mouth of a Pitot tube, one therefore has to solve multidimensional (at least two dimensional axisymmetric) conservation equations with viscous, and thermal and inertial nonequilibrium effects. It is important to incorporate the inertial nonequilibrium effects, i.e., to allow a velocity slip between the two phases. It is so, not only

[1] Present Address: Aerospace Engineering Department, University of Bristol, University Walk, Bristol BS8 1TR, U.K.

Contributed by the Fluids Engineering Division for publication in the JOURNAL OF FLUIDS ENGINEERING. Manuscript received by the Fluids Engineering Division October 24, 1994; revised manuscript received February 9, 1998 (delayed due to editor's difficulties). Associate Technical Editor: D. E. Stock.

because the inertial effects are themselves significant but also because restraining the two phases to travel at the same velocity has serious implications for the thermal equilibration process. For example, a fluid particle moving along the stagnation streamline takes infinite time to reach the stagnation point. Therefore, in the absence of any velocity slip, the vapor-droplet mixture would have long enough time to come to thermal equilibrium, irrespective of the magnitude of the thermal relaxation time. In reality, however, large droplets may move without significant interphase mass and energy transfers and finally hit the back of the probe without influencing the pressure.

Most available computational schemes (explicit time-marching, e.g., Guha and Young, 1991; Young, 1992), however, neglect any velocity slip between the phases. In most situations with submicron size droplets, this is an acceptable assumption and saves computer time tremendously. (The relaxation time governing the velocity slip is very small and hence the computational time-step required for numerical simulation is small resulting in a large CPU time.) Even if all these effects are incorporated in the computer programs, it is quite likely that the numerical entropy generation would mask the entropy generation due to relaxation processes. Hence Guha (1998) presented a simple, quasi-one-dimensional model in which some plausible assumptions about the variation of the gas phase velocity were made. Step-by-step numerical integration of the conservation equations for a multiphase mixture, between a far-upstream point and the stagnation point, then determined the pressure that would have been recorded by a measuring device.

Guha (1998) considered a large number of two-phase mixtures, both gas-particle and vapour-droplet, at subsonic as well as supersonic velocities for many different sizes of the droplets (or particles). In the supersonic case a detached frozen shock wave stands in front of the Pitot tube. The relaxation mechanisms in a gas-particle mixture are different from those in a vapor-droplet flow. Despite all these complexities and differences, it was possible with proper nondimensionalization of flow parameters to adopt a *universal* plot, within acceptable tolerance, of nondimensional total pressure versus Stokes number (which is a nondimensional representation of particle inertia, Eq. (22)). The predicted total pressure correctly reduced to the frozen total pressure in the limit of large Stokes number (large particles) and to the equilibrium total pressure in the limit of small Stokes number (small particles). Maximum dependence of the total pressure on Stokes number was observed when the Stokes number was of the order unity.

Guha's (1998) calculations were, however, numerical in nature. In this paper, we develop an *analytical* theory for determining total pressure under nonequilibrium conditions, which is amenable to direct physical interpretation.

2 Conservation Equations

We consider a homogeneous, two-phase mixture consisting of a large number of small, spherical solid particles (or liquid droplets) dispersed in a continuous vapor phase. For simplicity, we assume that the particles (or droplets) are of the same size. Sufficient number density and uniform distribution of the particles (or droplets) make their interaction with the vapor describable by a continuous variation. We adopt the usual "two-fluid" model and view the particles (or droplets) as providing sources or sinks of mass, momentum, and energy for the vapor, each source term varying continuously in the x-direction.

The mass fraction of the dispersed phase, y, is given by

$$y = nm, \tag{1}$$

where there are n particles (or droplets), each of mass m, per unit mass of the mixture. The mass of an individual particle is connected to its radius, r, and the material density of the dispersed phase, ρ_d, via

$$m = 4/3\pi r^3 \rho_d. \tag{2}$$

If the vapor density is ρ_g, the mixture density ρ (neglecting the volume of the dispersed phase) is

$$\rho = \rho_g/(1 - y), \tag{3}$$

and the number of particles (or droplets) N per unit volume is given by:

$$N = \frac{n\rho_g}{(1 - y)}. \tag{4}$$

We assume that the vapor phase behaves as a perfect gas with constant isobaric specific heat capacity c_{pg}. Thus

$$p = \rho_g R T_g \tag{5}$$

and,

$$\frac{dh_g}{dx} = c_{pg}\frac{dT_g}{dx} \tag{6}$$

where R is the specific gas constant and T_g is the temperature of the vapor phase. For the dispersed phase,

$$\frac{dh_d}{dx} = c_d\frac{dT_d}{dx} \tag{7}$$

where h_d, T_d, and c_d are the specific enthalpy, temperature and the isobaric specific heat of the particles (or droplets).

Nomenclature

A = cross-sectional area of the stream-tube
a_e = equilibrium speed of sound
a_f = frozen speed of sound
c_d = isobaric specific heat of the dispersed phase
c_{pg} = isobaric specific heat of the gas phase
D = diameter of the Pitot tube
$\delta = \equiv c_d/c_{pg}$
γ = isentropic index of the gas phase
$\bar{\gamma}$ = isentropic index of a gas-particle mixture
h = enthalpy
Kn = Knudsen number
λ_g = thermal conductivity of the gas phase
m = mass of an individual particle (or droplet)
M_e = equilibrium Mach number
M_f = frozen Mach number
μ_g = dynamic viscosity of the gas phase
N = number of particles (or droplets) per unit volume
n = number of particles (or droplets) per unit mass of the mixture
p = pressure
p_o = total pressure
p_{oe} = equilibrium total pressure
p_{of} = frozen total pressure
Pr = Prandtl number of the gas phase
R = specific gas constant
ρ = density of the mixture
r = radius of a particle (or droplet)
ρ_d = material density of the dispersed phase
ρ_g = density of the gas phase
R_p = dimensionless total pressure
St = Stokes number
T = temperature
τ_I = inertial relaxation time
τ_T = thermal relaxation time
x = coordinate along the flow direction
y = mass fraction of the dispersed phase

Subscripts

∞ = unperturbed flow variables far upstream of the Pitot tube
g = gas phase
d = dispersed phase (particles or droplets)

The basic one-dimensional gasdynamic equations for steady, non-nucleating flow for a two-phase system can be written in the usual way (Guha, 1992):

Droplet number conservation:

$$\frac{d}{dx}(ANV_d) = 0 \tag{8}$$

Continuity:

$$\frac{d}{dx}(A\rho_g V_g) + \frac{d}{dx}(ANmV_d) = 0 \tag{9}$$

Momentum:

$$A\frac{dp}{dx} + \frac{d}{dx}(A\rho_g V_g^2) + \frac{d}{dx}(ANmV_d^2)) = 0 \tag{10}$$

Energy:

$$\frac{d}{dx}\left[\left(h_g + \frac{V_g^2}{2}\right)A\rho_g V_g\right] + \frac{d}{dx}\left[\left(h_d + \frac{V_d^2}{2}\right)ANmV_d\right] = 0 \tag{11}$$

where h is the specific enthalpy, V is the velocity, A is the flow area, and x is the distance along the flow direction. The subscript g denotes the vapor phase and subscript d refers to the dispersed phase. Equations (1)–(11) are valid for a solid particle laden gas as well as a vapor-droplet mixture.

Equations (1)–(11) have to be complemented with rate equations representing interphase transfer processes. For a solid-particle laden gas we need two equations representing the variation of particle velocity and temperature. These are given by (Guha 1998)

$$V_d\frac{dV_d}{dx} = \frac{V_g - V_d}{\tau_I}, \tag{12}$$

$$V_d\frac{dT_d}{dx} = \frac{T_g - T_d}{\tau_T}. \tag{13}$$

The inertial relaxation time τ_I and the thermal relaxation time τ_T are given by,

$$\tau_I = \frac{2r^2\rho_d}{9\mu_g}[1 + 4.5\ \mathrm{Kn}], \tag{14}$$

$$\tau_T = \frac{r^2\rho_d c_d}{3\lambda_g}\left(1 + \frac{4.5\ \mathrm{Kn}}{\mathrm{Pr}}\right), \tag{15}$$

where μ_g, λ_g, and Pr are the dynamic viscosity, thermal conductivity and the Prandtl number of the gas phase and Kn is the particle Knudsen number ($\mathrm{Kn} = l_g/2r$, where l_g is the molecular mean free path of the gas phase). Equation (13) needs to be replaced by a different equation in the case of vapour-droplet flow (Guha, 1998).

In a solid-particle-laden gas, there is no interphase mass transfer ($dm/dx = 0$). The mass conservation equation is, therefore, separately valid for each phase. Equations (1), (4), (8), and (9) can then be combined to give

$$\frac{Nm}{\rho_g}V_d = \frac{y_\infty}{1 - y_\infty}V_g, \tag{16}$$

where y_∞ is the mass fraction of the particles far upstream of the measuring device where the mixture is assumed to be at equilibrium. After some algebraic manipulation of Eqs. (1)–(11), the above momentum Eq. (10) can be expressed as:

$$\frac{1}{\rho_g}\frac{dp}{dx} + V_g\frac{dV_g}{dx} + \frac{NmV_d}{\rho_g}\frac{dV_d}{dx} = 0. \tag{17}$$

Equations (16) and (17) can be combined to give

$$\frac{1}{\rho_g}\frac{dp}{dx} + V_g\frac{dV_g}{dx} + \frac{y_\infty}{1 - y_\infty}V_g\frac{dV_d}{dx} = 0. \tag{18}$$

Equation (18) is exact. Note that, in flows with velocity slip between the phases, the value of $y/(1 - y)$ does not remain constant along a streamline even in the absence of any interphase mass transfer. Equation (18) shows the correct form of the droplet momentum term (the third term in the LHS of Eq. 18) which contains the product of the *gas phase velocity* and dV_d/dx. The coefficient $y_\infty/(1 - y_\infty)$ remains constant for a specific upstream condition.

3 Analytical Solution for Total Pressure Under Non-equilibrium Conditions

For a complete solution of Eqs. (8)–(11), one has to prescribe the variation of the area of the stream tube in front of the Pitot tube (Fig. 1). Since the area variation is not known, the variation of the gas phase velocity is assumed. The vapor velocity is assumed to vary exponentially from the Pitot mouth,

$$V_g = V_\infty[1 - \exp(x/kD)], \tag{19}$$

where V_∞ is the unperturbed velocity far upstream, D is the pitot diameter, and k is an empirical constant which may be determined experimentally. Equation (19) shows that as $x \to 0$, $V_g \to 0$; as $x \to -\infty$, $V_g \to V_\infty$. (It is found that the *nondimensional* curve representing the variation in total pressure, as shown later in Fig. 3, does not depend on the value of k. The parameter k is introduced in the theory to increase its flexibility to match with experiments. If no other data is available then use $k \sim 1$.)

For the sake of a simple theory, we linearize Eq. (12) so that an analytical solution can be formulated,

$$V_\infty\frac{dV_d}{dx} = \frac{V_g - V_d}{\tau_I}. \tag{20}$$

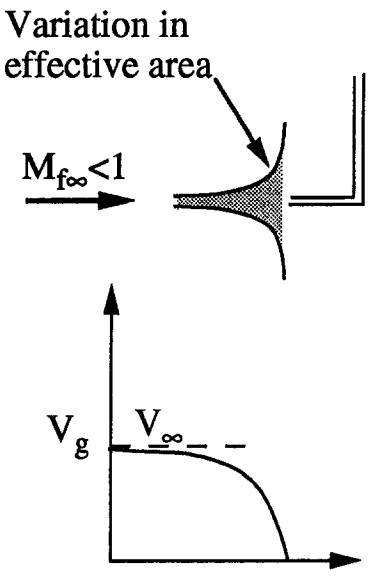

Fig. 1 Schematic flow structure in front of a Pitot tube and assumed variation in velocity of the gas phase

Equation (19) is substituted in Eq. (20) and the resulting equation is integrated subject to the boundary condition: at $x = -\infty$, $V_d = V_g = V_\infty$ to give

$$\frac{V_d}{V_\infty} = 1 - \frac{\exp(x/kD)}{1 + \mathrm{St}}, \tag{21}$$

where the dimensionless Stokes number, St, is defined by

$$\mathrm{St} = \frac{\tau_I V_\infty}{kD}. \tag{22}$$

The Stokes number, given by (22), is nothing but a Damkohler parameter signifying the importance of the relaxation processes.

It can be seen that Eq. (21) prescribes qualitatively correct variation of V_d in different limits. For example in the frozen limit, $\mathrm{St} \to \infty$, $V_d = V_\infty$ always. In the equilibrium limit, $\mathrm{St} \to 0$, $V_d = V_g$ always. Figure 2 shows the variation of V_d predicted by Eq. (21) for three different values of St.

Equations (19) and (21) can be substituted in Eq. (18), and the resulting equation can then be integrated between $x = -\infty$ and $x = 0$ in order to find the change in pressure as the gas is brought to rest by the Pitot tube. As a first approximation, we assume that the gas phase is effectively incompressible, so that we can use some average value for its density, ρ_g. (Later the effects of such approximation is studied.) In the frozen limit, $dV_d/dx \to 0$. Therefore, integrating Eq. (18) between $x = -\infty$ and $x = 0$ in the frozen limit, we obtain,

$$p_{of} - p_\infty = 1/2\ \rho_g V_\infty^2, \tag{23}$$

where, p_{of} is the frozen total pressure and p_∞ is the pressure far upstream.

In the equilibrium limit, $V_g = V_d$. Again, integrating Eq. (18) between $x = -\infty$ and $x = 0$ in the equilibrium limit, we obtain,

$$p_{oe} - p_\infty = 1/2\ \frac{\rho_g}{1 - y_\infty} V_\infty^2, \tag{24}$$

where p_{oe} is the equilibrium total pressure. Now we integrate Eq. (18) between $x = -\infty$ and $x = 0$ in the general nonequilibrium case with V_g and V_d given by Eqs. (19) and (21), respectively. The result is,

$$p_o - p_\infty = 1/2\ \rho_g V_\infty^2 \left(1 + \frac{y_\infty}{1 - y_\infty} \frac{1}{1 + \mathrm{St}}\right). \tag{25}$$

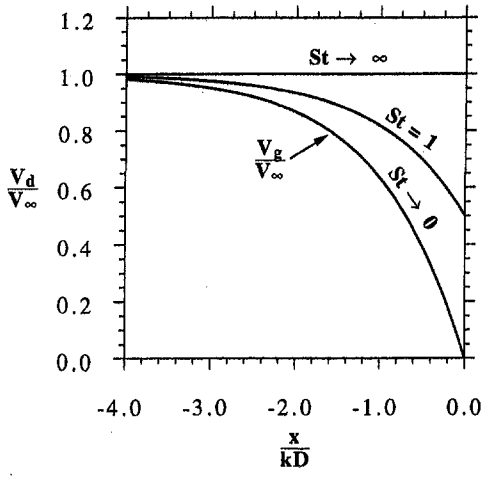

Fig. 2 Predicted variation in velocity of the particles (or droplets) in front of a Pitot tube as a function of Stokes number

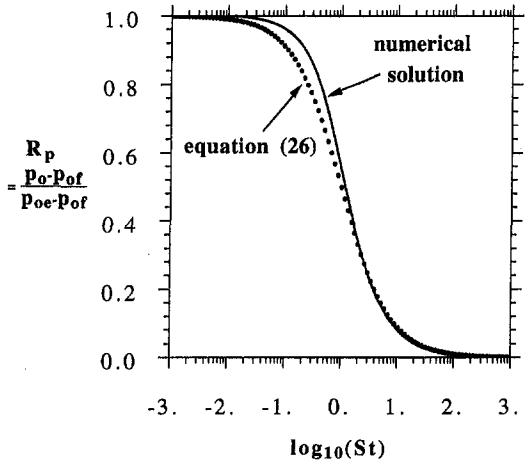

Fig. 3 Comparison of the analytical theory with numerical solutions for nondimensional total pressure. (For numerical solutions: $M_{f\infty} = 0.8$, $y_\infty = 0.1$, $\delta = 2.0$.)

Substituting Eqs. (23) and (24) in Eq. (25), one obtains,

$$R_p \equiv \frac{p_o - p_{of}}{p_{oe} - p_{of}} = \frac{1}{1 + \mathrm{St}}. \tag{26}$$

where R_p is the nondimensional total pressure. Although the analysis in this section assumed the gas phase density to remain constant at some average value, Eq. (26), because of the particular definition of R_p, compares very well with full numerical solution of Eqs. (8)–(13) even at very high subsonic velocity. Figure 3, for example, shows the comparison of Eq. (26) with an accurate numerical solution of Eqs. (8)–(13) at $M_{f\infty} = 0.8$, where $M_{f\infty}$ is the frozen Mach number far upstream. The numerical solution is obtained for air with solid particles ($\delta \equiv c_d/c_{pg} = 2.0$).

It should be noted that if the droplet momentum term in Eq. (17) were *approximated* by $[y_\infty/(1 - y_\infty)]\ V_d dV_d/dx$, then a similar analysis would have given

$$R_p \equiv \frac{p_o - p_{of}}{p_{oe} - p_{of}} = 1 - \left(\frac{\mathrm{St}}{1 + \mathrm{St}}\right)^2. \tag{27}$$

4 Analytical Theory Incorporating Density Changes of the Gas Phase and Thermal Nonequilibrium Effects

In this section, we introduce the effects of density change of the gas phase. For this, we rewrite Eq. (18) as

$$\frac{1}{p}\frac{dp}{dx} + \frac{V_g}{RT_g}\frac{dV_g}{dx} + \frac{y_\infty}{1 - y_\infty}\frac{V_g}{RT_g}\frac{dV_d}{dx} = 0. \tag{28}$$

Equation (28) can be integrated in the same manner as we integrated Eq. (18) in the previous section, if the additional variation in T_g is substituted in Eq. (28). In the frozen limit, the energy equation (11) shows that the temperature of the gas phase, T_{gf}, is given by

$$T_{gf} = (c_{pg}T_\infty + \tfrac{1}{2} V_\infty^2 - \tfrac{1}{2} V_g^2)/c_{pg}, \tag{29}$$

where, T_∞ is temperature at the far upstream. In the equilibrium limit, when the gas and the particles are always at thermal equilibrium, the temperature T_{ge} is again given by the energy equation,

$$T_{ge} = (\bar{c}T_\infty + \tfrac{1}{2} V_\infty^2 - \tfrac{1}{2} V_g^2)/\bar{c}, \tag{30}$$

where the mixture specific heat, $\bar{c}$, is given by

$$\bar{c} = (1 - y)c_{pg} + yc_d. \tag{31}$$

Since a complete solution of all the equations to determine T_g is not feasible in the present context of an analytical theory, we assume that, in analogy with Eq. (26), the temperature under nonequilibrium situations varies as

$$T_g = T_{gf} + \frac{T_{ge} - T_{gf}}{1 + \mathrm{St}}, \tag{32}$$

where T_{gf} and T_{ge} are given by Eqs. (29) and (30), respectively. Since V_g varies with x, Eq. (32) prescribes the variation of T_g with x. Equations (19), (21), and (32) can be substituted in Eq. (28) and the resulting equation integrated between $x = -\infty$ to $x = 0$. The result is

$$\frac{p_o}{p_\infty} = \left(1 + C\frac{V_\infty^2}{T_\infty}\right)^{(1+K)/(2RC)}, \tag{33}$$

where,

$$C = \frac{1}{2}\left[\frac{1}{c_{pg}} + \frac{1}{1 + \mathrm{St}}\left(\frac{1}{\bar{c}} - \frac{1}{c_{pg}}\right)\right], \tag{34}$$

and,

$$K = \frac{y_\infty}{1 - y_\infty}\frac{1}{1 + \mathrm{St}}. \tag{35}$$

Equation (33) reduces to exact solutions (Guha, 1998) in the limits of the frozen and equilibrium flow. In frozen flow, Eq. (33) reduces to

$$\frac{p_{of}}{p_\infty} = (1 + 0.5\,(\gamma - 1)\,M_{f\infty}^2)^{\gamma/(\gamma-1)}, \tag{36}$$

where, p_{of} is the frozen total pressure, γ is the isentropic exponent of the gas phase alone, and, the far upstream frozen Mach number, $M_{f\infty}$, is calculated from,

$$M_{f\infty} = \frac{V_\infty}{a_{f\infty}} = \frac{V_\infty}{\sqrt{\gamma RT_\infty}}. \tag{37}$$

In the equilibrium limit, Eq. (33) reduces to,

$$\frac{p_{oe}}{p_\infty} = (1 + 0.5\,(\bar{\gamma} - 1)\,M_{e\infty}^2)^{\bar{\gamma}/(\bar{\gamma}-1)}, \tag{38}$$

where, p_{oe} is the equilibrium total pressure, $\bar{\gamma}$ is the mixture isentropic exponent, and $M_{e\infty}$ is the equilibrium Mach number at far upstream. $\bar{\gamma}$ and $M_{e\infty}$ are given by

$$\bar{\gamma} = \frac{(1 - y)c_{pg} + yc_d}{(1 - y)(c_{pg} - R) + yc_d}, \tag{39}$$

$$M_{e\infty} = \frac{V_\infty}{a_{e\infty}} = \frac{V_\infty}{\sqrt{\bar{\gamma}(1 - y)RT_\infty}}. \tag{40}$$

The nondimensional total pressure R_p [$R_p \equiv (p_o - p_{of})/(p_{oe} - p_{of})$] can be calculated from Eqs. (33), (36), and (38) and plotted against Stokes number, St. The nature of the variation of R_p with St is, however, not immediately obvious from the complicated formulae. When the plot of R_p versus St obtained in this more rigorous way was compared with the prediction of Eq. (26), the results were almost identical at all Mach numbers and for different two-phase mixtures. Equation (26), although derived less rigorously, is simple, amenable to direct physical interpretation and gives almost exact answer. Equation (26) is, therefore, recommended for practical calculation methods. (The slight difference between Eq. (26) and the numerical solutions in Fig. 3 arises from the use of the linearized Eq. (20) in the derivation of Eq. 26.)

5 Conclusions

A simple, analytical theory is presented for calculation of the total pressure in two-phase flows. Equation (26) presented here is a very simple relation between the nondimensionalized total pressure, R_p, and Stokes number, St. The equation correctly reduces to the frozen total pressure in the limit of large St (large particles) and to the equilibrium total pressure in the limit of small St (small particles). Under nonequilibrium conditions for intermediate St, the prediction of this equation compares well with results from full numerical solution of the gas dynamic equations for multiphase mixtures.

Although Eq. (26) has been derived here by considering subsonic two-phase flow without any interphase mass transfer, it has been shown (Guha, 1998) that the same calibration curve of R_p versus St could be adopted with acceptable accuracy for diverse multiphase mixtures, vapor-droplet as well as solid particle laden gases, at a wide range of subsonic and supersonic Mach numbers. Equation (26) can, therefore, be used for inferring flow velocity from measured Pitot pressures in any multiphase mixture at a wide range of flow conditions. The associated problem of interpreting total temperature, analytical relations for determining p_{of} and p_{oe} in vapor-droplet mixtures, and, the relation between measured total pressure and entropy production in multiphase flow are discussed at length by Guha (1998).

Acknowledgment

The author is grateful to Gonville & Caius college, Cambridge, for electing him as a Research Fellow.

References

Crane, R. I., and Moore, M. J., 1972, "Interpretation of Pitot Pressure in Compressible Two-Phase Flow," *Journal of Mechanical Engineering Science,* Vol. 14, No. 2, pp. 128–133.

Dussourd, J. L., and Shapiro, A. H., 1958, "A Deceleration Probe for Measuring Stagnation Pressure and Velocity of a Particle-Laden Gas Stream," *Jet Propulsion,* Vol. 28, pp. 24–34.

Guha, A., and Young, J. B., 1991, "Time-Marching Prediction of Unsteady Condensation Phenomena Due to Supercritical Heat Addition," *Proc. Conf. Turbomachinery: Latest Developments in a Changing Scene,* London, IMechE, pp. 167–177.

Guha, A., 1992, "Structure of Partly Dispersed Normal Shock Waves in Vapour-Droplet Flows," *Physics Fluids A,* Vol. 4, No. 7, pp. 1566–1578.

Guha, A., 1995, "Two-Phase Flows with Phase Transition," *VKI Lecture Series,* 1995-06 (ISSN0377-8312), pp. 1–110, von Karman Institute for Fluid Dynamics.

Guha, A., 1998, "A Unified Theory for the Interpretation of Total Pressure and Temperature in Two-Phase Flows at Subsonic and Supersonic Speeds," *Proceedings of Royal Society,* Series A, Vol. 454, pp. 671–695.

Rudinger, G., 1964, Reply to comments by S. L. Soo, *Physics Fluids,* Vol. 7, pp. 1884–1885.

Soo, S. L., 1964, Comments on "Shock Relaxation in Flows carrying Particles," *Physics Fluids,* Vol. 7, pp. 1883–1884.

Taylor, G. I., 1945, Pitot pressures in moist air, reports and memoranda of the Aeronautical Research Council no. 2248.

Young, J. B., 1992, "Two-Dimensional, Nonequilibrium Wet Steam Calculations for Nozzles and Turbine Cascades," ASME *Journal of Turbomachinery,* Vol. 114, pp. 569–579.

R. Balachandar
Associate Professor,
Department of Civil Engineering,
University of Saskatchewan,
Saskatoon, Canada, S7N 5A9

S. R. Mulpuru
Research Scientist.

M. H. Ungurian
Technician.

Containment Analysis Branch,
Whiteshell Laboratories,
AECL, Pinawa,
Manitoba, Canada R0E 1L0

A Note on Particle Size Measurements in Two-Phase Flows

This paper discusses the use of a phase-Doppler anemometer to obtain the size and velocity characteristics of droplets formed and transported in a flashing water jet. In particular, the validation and calibration procedures adopted to ensure correct acquisition of experimental data are discussed in detail. The methodology involved in choosing the magnitudes of the various operating parameters of a phase-Doppler anemometer such as the intensity of the transmitting beams, signal-to-noise ratio, sample size, and sensitivity of the photomultiplier tubes are described. The droplet size and velocity distributions were acquired at two axial stations covering the width and height of the jet cross-section. Attempts were made to identify the proper scaling variables to develop suitable nondimensional parameters to characterize a flashing jet.

Introduction

Size and velocity of particles constituting sprays and jets are of interest to engineers in several fields. Especially of interest to design engineers, is the formation of sprays and jets by the mechanism of flashing. For example, during the event of a leak in a high-pressure piping system, the high-enthalpy liquid will undergo depressurization as it flows from the system to the surroundings. This may be an uncontrolled depressurization as in the case of a system rupture. The fluid flowing toward the leak experiences decompression to pressures below the saturation pressure and, at some lower pressure, the liquid begins to flash to vapor. The effluent jet consists of a two-phase mixture of the vapor and small droplets generated by flash boiling and aerodynamic fragmentation. With reference to the nuclear industry, there is the remote possibility of the presence of suspended or dissolved fission products in the high enthalpy fluid and during a loss-of-coolant-accident, the droplets formed can act as carriers of radioactivity. As a part of the nuclear reactor safety research program, data on size and velocity distribution of droplets generated by flashing are required to support safety and licensing calculations on the transport of fission products in the containment. The retention time of the particles in the containment atmosphere is expected to be drop size dependent. The phenomena of liquid jet breakup and aerosol formation during accidental release of pressurized toxic chemicals are also an issue of growing importance (Tilton and Farley, 1990).

The phenomenon of flashing is of interest to design engineers with reference to the operation of a throttle valve in pressure vessel dump operations, where the depressurization is controlled. Aerosols generated from spray cans by flashing have wide household utilization as insecticides, deodorants, etc. Furthermore, flash boiling atomization has applications in fuel-injection devices used to improve engine performance. Thus, there is a widespread interest in the study of the mechanics of flashing and study of droplet size distribution.

Attempts have been made to understand the physics of the flashing process (Appleton, 1984; Koestel et al., 1980; Oza, 1984; Sher and Elata, 1977; Wu and Chuang, 1984). Some attempts have also been made to measure the drop sizes in (super)heated water jets (Anderson et al., 1982; Anderson et al., 1984; Bates et al., 1986; Brown and York, 1962; Gooderum and Bushnell, 1969; Reitz, 1990). Many of the earlier reported drop size measurements, involved the use of photography or light-scattering techniques. With the advent of the phase-Doppler anemometer (PDA) some of the difficulties encountered in the earlier measurements have been effectively overcome (Bachalo and Houser, 1986; Durst, 1982; Tayali and Bates, 1990). However, the reliability and quality assurance of the data obtained using the various optical techniques have been under scrutiny. This paper discusses the methodology involved in choosing the magnitudes of the various parameters of the PDA such as laser power, signal-to-noise ratio, data rate, and sensitivity of the photodetector tubes in obtaining the experimental data in two-phase flows. The various calibration and validation procedures used are also reported. This study will also focus on the measurement of water droplet velocity and size as the effluent jet progresses into the containment. Radial distributions of mean velocity and particle size in a flashing jet are presented at two axial stations. The radial variation of velocity and particle size probability density functions is also discussed.

Experimental Setup

The experimental setup essentially consisted of a pressure vessel which was initially filled with water to about two thirds of its height and boiled at atmospheric pressure for approximately 15 min to liberate any dissolved gas in the supply system. A vent at the top of the vessel was closed and the vessel was gradually pressurized to the required value by filling in nitrogen gas from the top. The water was heated to the required temperature by means of a heating source inside the vessel. After the necessary test conditions were attained, the pipe connecting the pressure vessel to the nozzle arrangement was heated to the required value by means of electrical resistance tape heaters. This piping arrangement was well insulated to prevent any loss of heat along the flow line. The experimental facility was instrumented with pressure transducers and thermocouples at various locations. The data from these devices were recorded by interfacing with a computer.

As the hot water is depressurized through the nozzle arrangement (sudden contraction, diameter (D) = 0.061 cm, throat length (L) = 0.61 cm), a flashing jet is formed (Fig. 1). The jet consists of a two-phase mixture of steam and small water droplets and is characterized by the formation of a nearly hemispherical expansion followed by a linear spreading. Visually

Contributed by the Fluids Engineering Division for publication in the JOURNAL OF FLUIDS ENGINEERING. Manuscript received by the Fluids Engineering Division March 25, 1995; revised manuscript received February 9, 1998 (delayed due to editor's difficulties). Associate Technical Editor: D. E. Stock.

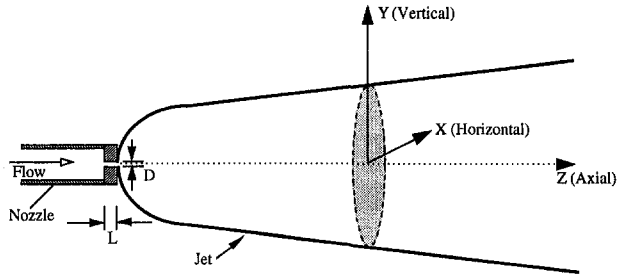

Fig. 1 Schematic of the coordinate system

comparing the present jet with the photographs of Oza (1984), one would conclude that the bulk of the atomization occurs external to the nozzle. However, a direct confirmation that no flashing has occurred inside the nozzle is not physically realizable owing to the small dimensions of the nozzle.

Figure 1 shows a simple schematic of the coordinate system adopted. Measurements were conducted at two stations along the jet axis (Z/D = 800 and 2400). At each station, data were acquired along both the X-axis (horizontal) and the Y-axis (vertical). At any point in the flow field of a flashing jet, the particle size and velocity are simultaneously measured using the phase-Doppler anemometer (Dantec Inc., Model 60X FiberFlow series). The present system uses a variable-power, water-cooled Argon-Ion laser (Liconix Inc.). A fiber-optic probe fitted with a lens of focal length 400 mm forms the transmitting optics. The optical parameters of the phase-Doppler anemometer system are indicated in Table 1. The transmitting and receiving optics are mounted on independent traversing mechanisms capable of repeatedly attaining the same location with an accuracy of ±0.5 mm. These traversing arrangements were stepper motor driven and controlled by a computer. The receiving optics has three photomultiplier (PM) tubes with built in preamplifiers to obtain and validate the phase information contained in the Doppler signals. Detailed descriptions of a typical PDA system and the signal processor used in the present study are available elsewhere and are avoided here for brevity (Saffman et al., 1987).

Size and Velocity Calibration

Prior to the commencement of the actual measurements using the PDA, both size and velocity calibrations were carried out to ensure proper measurement and validation of the procedures used. This required conducting measurements in previously well-established flow fields. To this end, measurements were conducted in the potential core of an axisymmetric air jet using an orifice arrangement (TSI flow calibrator, Model 1125).

For size calibration, monodisperse soda lime glass beads of three known size distributions (Duke Scientific Corporation, Mean diameter = 22.1 ± 1.5 μm, 58.9 ± 3.5 μm and 85.3 ± 4.3 μm) were chosen as the test particles. The test particles were injected uniformly into the TSI flow calibrator well ahead of the orifice mouth. The PDA operating parameters were set to match the conditions required for glass bead size measurements. Figure 2 shows the count-size histogram independently obtained for each set of monodisperse particles. The mean diameter calculated from each distribution validated the glass bead manufacturer's specification. Figure 2 also shows the count-size histogram obtained for a random mixture composed of the three sets of monodisperse particles. It can be noted from this figure that each one of the three sizes of monodisperse particles are individually identified in the histogram. Figure 2 attests to the fact that the PDA system responds truly not only to each one of the monodisperse particles but also to a range of particle sizes.

To carry out the velocity calibration, the jet flow was artificially seeded with water particles (<5.0 μm) generated by a custom made aerosol generator. The PDA system was used to measure the velocity in the potential core of the jet, and excellent agreement was found between the measured values and those calculated by the use of the pressure drop across the orifice.

Effect of Laser Power on Size Measurement

During preliminary tests, it was recognized that the intensity of the incident laser beam has an effect on the measurement of droplet size. To determine this effect, measurements were initially conducted in air jets seeded with monodisperse glass beads. Count-size histograms were obtained at various laser powers ranging from 0.1 to 3.5 W. These histograms were essentially the same at all powers with the exception that a very small fraction of the particles in the lower size range were not identified at the lowest laser power of 0.1 W. The mean diameters were also evaluated at various laser powers for each of the three different sets of monodisperse particles used. The particle sizes were validated over the entire range of laser power tested and was essentially independent of laser power. However, one should bear in mind that glass beads are monodisperse and are not indicative of the actual measuring conditions present in two-phase flashing jets.

To determine the effect of laser power on the size measurement in flashing jets, a series of tests were also carried out at a test pressure and temperature of 4 MPa and 230°C, respectively. Photomultiplier (PM) tubes with built in preamplifiers were adopted to increase the dynamic range of the size measurement.

Table 1 Optical parameters of the phase-Doppler anemometer

Transmitting optics	
Wavelength of the laser	514.5 nm
Diameter of the laser beam	1.35 mm
Focal length of the transmitting lens	400 mm
Beam separation	38 mm
Diameter of the measuring volume	195 μm
Length of the measuring volume	4.1 mm
Number of fringes	36
Fringe spacing	5.422 μm
Receiving optics	
Focal length of receiving lens	600 mm
Off axis angle	67 deg
Slit size (Spatial filter)	0.1 mm × 2 mm
Phase conversion factor (Refraction)	
Detector 1 – Detector 2	2.599 deg μm^{-1}
Detector 1 – Detector 3	1.299 deg μm^{-1}

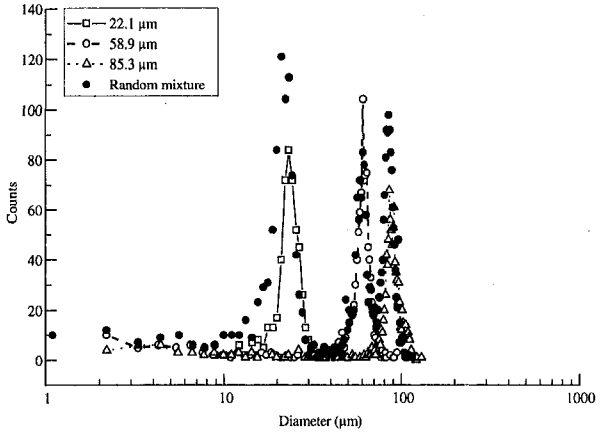

Fig. 2 Count-size histograms of glass beads

A brief remark about the light scattered by the particles is in order. For particle sizing systems with response curves increasing monotonically with particle size, a larger particle will scatter light of greater intensity than a smaller particle with the receiving optics set at the same scattering angle. For a given intensity of the transmitting beams, an increase in the high voltage (HV) gain of the photodetectors, result in the PM tubes becoming more sensitive to the light scattered from the smaller particles. Similarly, for a given setting of the high voltage gain, the scattered light intensity can be increased by increasing the light intensity of the transmitting beams. An indefinite increase in both the HV gain and transmitting light intensity (power of the laser source) is not possible due to various physical limitations. A suitable combination of these two factors is necessary to obtain accurate measurements in the minimum possible acquisition time. To this end, measurements were conducted at an axial location $Z/D = 800$. The laser power was varied from 0.5 W to 3.5 W while the HV gain was varied from 800 to 1200 V. The signal-to-noise-ratio (SNR) was held constant at 0 dB. The minimum sample size of the data acquired for each measurement was set at 3000 and all these data had to pass the validation criteria set by the SNR and the sphericity (deviation < 5 percent).

Figure 3 shows the variation of acceptance rate with PM tube HV gain and laser power at an axial location $Z/D = 800$. Here, acceptance rate is defined as the percentage of the acquired data that passes the validation criteria. One would be interested in obtaining data at as high an acceptance rate as possible. A lower acceptance rate signifies the rejection of a larger amount of data that is actually acquired and this would correspond to an increase in the acquisition time as the number of data points passing the validation criteria has been fixed at 3000 per measurement location. It can be noted from Fig. 3 that at lower values of HV, the acceptance rates are independent of laser power and are very close to 100 percent. However, at any given laser power, with increasing HV, the acceptance rate decreases. Typically, at a laser power of 3.5 W, the acceptance rates are of the order of 95 and 80 percent for a HV gain of 1000 and 1200, respectively. Furthermore, with increasing laser power, the acceptance rate decreases at any given HV. As seen from Fig. 3, at a HV gain of 1200 V, the acceptance rate drops from about 95 to 80 percent as the laser power is increased from 0.5 W to 3.5 W. Figure 3 also shows the variation of mean diameter with HV gain and laser power for the same set of data. At any given laser power, the mean diameter decreases with increasing HV gain. For a given HV gain, the mean diameter decreases with increasing laser power and at a laser power greater than 2.0 W the decrease is not significant. Furthermore, the values

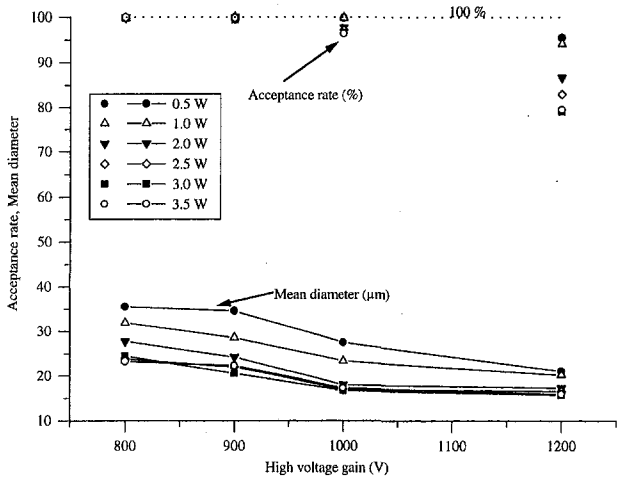

Fig. 3 Variation of acceptance rate and mean diameter with HV gain and laser power

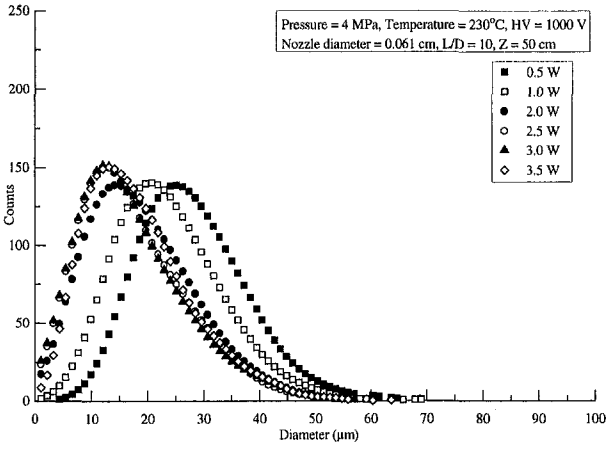

Fig. 4 Count-size histograms at various laser powers (Uncertainty in counts = ±5 percent, Uncertainty in diameter = ±3 percent)

of the mean diameter are fairly constant beyond a laser power of 2 W and a HV of 1000 V, i.e., any further increase in laser power or the value of HV gain does not result in a change in the mean diameter. Figure 3 indicates that a HV gain of 1000 V and a laser power of 2.5 W would be quite optimal to obtain data in flashing jets without a significant loss in acceptance rate.

Figure 4 shows the size-count distribution at an axial location $Z/D = 800$ at various laser powers. For purposes of clarity, the data shown here have been smoothed using a fast Fourier transform routine. There are significant differences between the distributions obtained at lower laser powers (<2 W) and those acquired at higher powers. In general, there is a shift in the distributions toward the smaller particles with increasing laser powers. This is a consequence of the smaller particles becoming more visible at higher laser powers, i.e., the light scattered by the smaller particles are of sufficient intensity to be recognized by the PM tubes. Both the lower and the upper tails of the distribution converge beyond a laser power of 2 W. From these distributions it is clear that conducting tests at a power of 2.5 W would essentially yield a similar distribution as at 3.5 W. From the information presented in Fig. 3, at a power of 3.0 W, the measurements would be acquired no faster than at 2.5 W as indicated by a lower acceptance rate. The same set of data follow a near linear variation when plotted on a log-probability paper in the form of cumulative volume distributions. This indicates that the data is fairly lognormal and compares favourably with previous size measurements conducted in sprays. Data similar to that shown in Fig. 4 were obtained at other axial locations and varying test pressures. These data sets qualitatively resemble the information presented at $Z/D = 800$.

It should be borne in mind that operating the PDA system at very high laser powers, significantly decreases the life of the laser tube. Operating the PM tube at high values of HV gain when the transmitting beam intensity is also high, significantly decreases its life. These factors, coupled with safety considerations (health, fire and invisible radiation), dictate the need to work at lower laser powers. However, the need to obtain accurate data in the lower range (<10 μm) necessitates the use of a laser power greater than 2 W. A value of 2.5 W for the laser power and a HV gain of 1000 V was adopted to conduct the subsequent measurements. These values are arrived at, based on the fact that there is no change in the value of the mean diameter and the volume median diameter with further increase in HV or laser power. Furthermore, at these settings, the acceptance rates are very high and the count-size distributions are essentially similar to those conducted at higher HV or higher laser power.

On initial inspection of Fig. 4, one would be tempted to conclude that a significant portion of the larger particles have

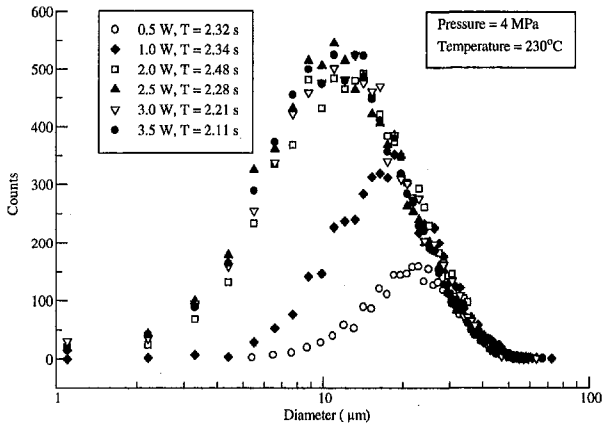

Fig. 5 Variation of count-size distribution with laser power for nearly equal acquisition time (Uncertainty in counts = ±5 percent, Uncertainty in diameter = ±3 percent)

not been accounted for at higher laser powers. The number of samples taken for each measurement has been fixed at 3000 and the acceptance rates are very close to 100 percent at all laser powers for the conditions indicated in Fig. 4. The time of acquisition is thus different for each measurement and decreases with increasing power. On observing the histograms obtained at each laser power for nearly equal acquisition times (Fig. 5), the results are clarified. One notes from this figure that the larger particles observed at a lower power of 0.5 W are continued to be measured at higher laser powers. With increasing laser powers, the upper tail of each one of the distributions merge with that obtained at 0.5 W. However, there is a significant increase in the number of smaller particles measured. With increasing laser power beyond 1.0 W, the distributions are essentially similar and the lower tails also converge. It is now clear that there may be a need to acquire data of a large enough sample size, without loosing information in the larger diameter range. Figure 6 shows the count-size distributions obtained at various sample sizes ranging from 3000 to 18,000. With increasing sample size the number of counts at any particular diameter increases. The inset in Fig. 6 shows the data replotted in a normalized fashion. It is clear from Fig. 6 that the data collapse on to a single curve and are thus independent of the sample size over the entire distribution reinforcing the fact that a sample size of 3000 is more than sufficient to obtain data in flashing jets.

In an earlier study, Bates et al. (1986), used a laser power of 25 mW to conduct size measurements in a flashing jet (Test conditions: 2.9 MPa, 150°C). Bates et al. (1986) obtained a volumetric mean size of 90 μm along the jet axis at a distance of 0.725 m from the mouth of the nozzle. This result compares favourably with the preliminary set of measurements conducted at lower laser powers. It is appropriate to point out that a portion of the smaller sized particles could have been invisible in their measurements. Furthermore, due to equipment limitations, Bates et al. (1986) were able to conduct measurements only at the outer region of the jet especially at higher temperatures. Measurements were conducted across the entire cross section including the central region of the jet in this study.

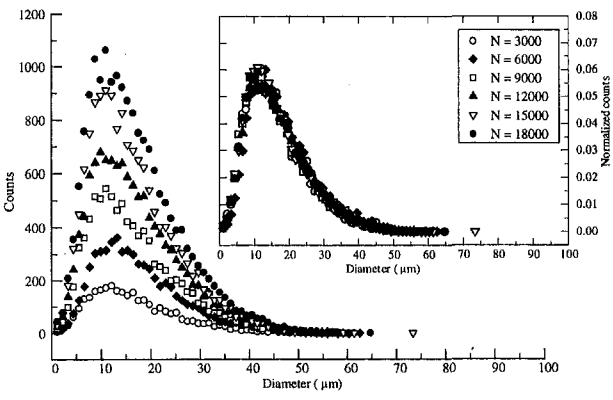

Fig. 6 Variation of count-size distribution with sample size at a laser power of 2.5 W and a PM tube sensitivity of 1000V. Inset: Normalized count-size histogram (Uncertainty in counts = ±5 percent, Uncertainty in diameter = ±3 percent)

Results

As indicated earlier, detailed measurements of velocity and size of the droplets were obtained at two locations in a flashing jet. The pressure and temperature just ahead of the nozzle were set at 4.0 MPa and 230°C, respectively.

Velocity Characteristics. Figure 7(*a*) shows the radial distribution of the particle mean velocity at the two axial stations measured along the *Y*-axis (solid symbols). In this figure, a positive value of *Y* indicates the top portion of the jet, whereas a negative value indicates the lower half of the jet. At each axial station, similar measurements were also conducted along the *X*-axis (open symbols). The half-width (δ) of the jet, denoted by the radial location where the velocity is one half of the centre-line velocity, was evaluated using the streamwise mean velocity distributions and used as the normalizing length scale. In Fig. 7(*a*), the mean velocity along the axis of the jet

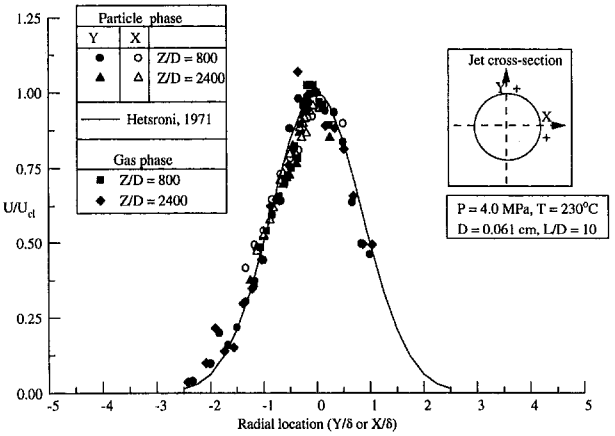

Fig. 7(*a*) Radial variation of normalized velocity at various axial stations (Uncertainty in velocity = ±2 percent, Uncertainty in location = ±5 percent)

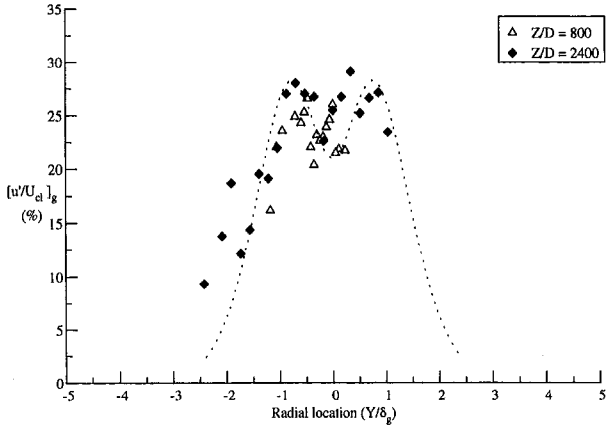

Fig. 7(*b*) Radial variation of turbulence intensity (Gas phase) (Typical uncertainty in turbulence intensity = ±2.5 percent, Uncertainty in location = ±5 percent)

(U_{cl}) was used as the normalizing velocity scale. The data fall on to a single curve, thereby bringing forth the inherent similarity of jets. The rate of growth of the jet resembles that obtained in a two-phase plane jet (Goldschmidt, 1966).

It has been suggested by several researchers (Hishida, 1990; Qui, 1991) that the smaller particles (<4 μm) in the flow are a good representation of the gas-phase velocity. Following this suggestion, the radial variation of mean gas-phase velocities at both the axial stations were evaluated and are shown in Fig. 7(a). This set of data also collapse on to a single curve indicating that the mean velocity profiles are similar. For qualitative comparison purposes, a typical velocity distribution obtained in a single phase flow (Hetsroni et al., 1971) is also shown in Fig. 7(a). It should be borne in mind that the water droplets are polydisperse in nature. For obvious reasons, the larger particles cannot be expected to faithfully follow the general flow. The larger water droplets being accelerated by gravity will tend to influence the jet characteristics and some of them could be visually seen to be dropping off the jet beyond Z/D = 1000. However, Fig. 7(a) shows that there is no significant mean slip between the gas-phase and the particle phase. Compared to previous measurements in free jets, it should be borne in mind that the present measurements are conducted at much larger distances from the nozzle and a fair equalization of momentum between the two-phases is expected to have occurred.

Figure 7(b) shows the radial variation of gas-phase turbulent intensity normalized by the centre-line mean gas-phase velocity. It is expected that particles less than 4 μm in diameter will be able to follow the fluid turbulent velocity fluctuations to a very large extent. This distribution resembles the variation noticed in earlier single and multi-phase turbulent jet studies (Hetsroni, 1971; Hishida, 1990). The near collapse of the data suggests a sense of similarity in the turbulent intensity data.

Figures 8(a) and 8(b) show the radial variation of the velocity probability density functions at the two axial stations, respectively. The data in each of the graphs in Figs. 8(a) and 8(b)

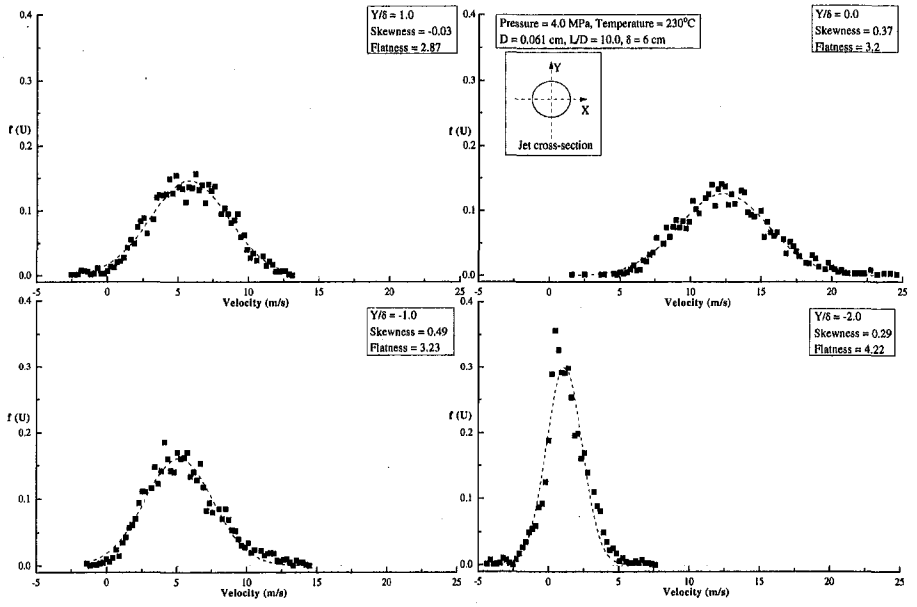

Fig. 8(a) Variation of velocity probability density functions along the radius at Z/D = 800. (Uncertainty in $f(U)$ = ±4 percent, Uncertainty in velocity = ±1 percent)

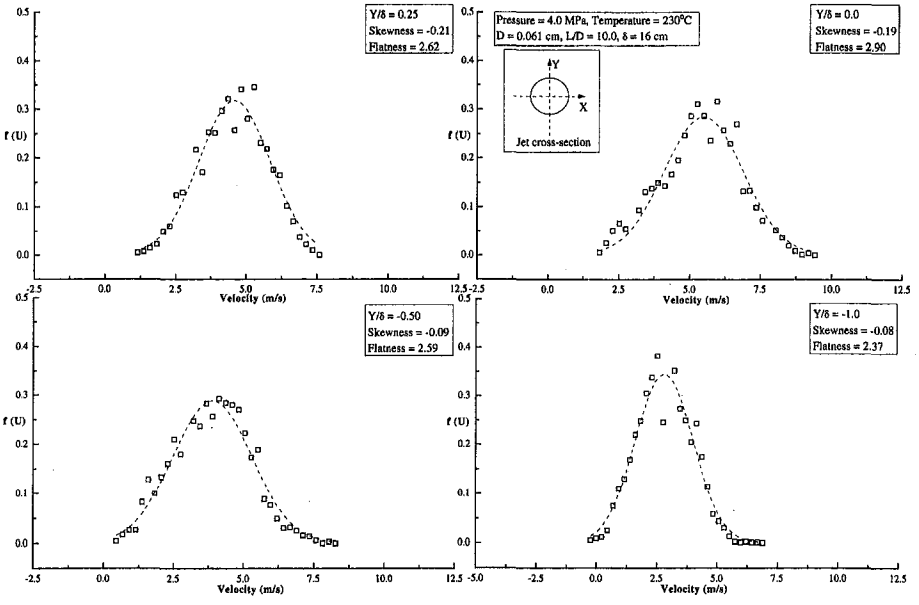

Fig. 8(b) Variation of velocity probability density functions along the radius at Z/D = 2400. (Uncertainty in $f(U)$ = ±4 percent, Uncertainty in velocity = ±1 percent)

are normalized such that the area under each distribution is unity, viz., $\int_o^\infty f(U)\,dU = 1$. Here, $f(U)$ is the frequency of occurrence of a velocity U. The probability density functions appear to follow a Gaussian curve as shown by the dashed lines. A similar observation has been noted in single phase flows (Hetsroni, 1971). However, the presence of the water droplets will affect the probability density functions. A closeness of fit test over the outer regions of the curve is provided by the flatness factor ($F = \sum_{i=1}^{N} (U_i - U_{\text{mean}})^4/\sigma^4 N$) of the distribution. Here, U_i is the velocity of the ith particle in the axial direction, U_{mean} is the mean velocity, N is the total number of particles forming the histogram and σ is the standard deviation of the velocity set under consideration. The theoretical value of F for a normal distribution is 3.0. Also noted in Figs. 8(a) and 8(b) are the experimental values of F. In the core region of the jet ($-1.0 < Y/\delta < 1.0$), the values of F ranged from 2.8 to 3.2 at $Z/D = 800$. This resembles the values obtained in single phase jets (Hetsroni, 1971). However, for locations beyond the half-width of the jet, the values of F increase. A similar observation was noted by Wygnanski et al. (1969) in single-phase free jets. A measure of the relative skewness ($S = \sum_{i=1}^{N} (U_i - U_{\text{mean}})^3/\sigma^3 N$) of the jet is indicated in Figs. 8(a) and 8(b). The theoretical value of S for a normal curve is zero. From the present results, one notes that the values of S are not significantly different from the normal distribution value.

Radial Distribution of Particle Size. Figure 9(a) shows the variation of the mean diameter along the radius at the two axial stations. At $Z/D = 800$, the droplets are larger along the mid portions of the jet. A similar observation was noted by Reitz (1990) at sections close to the nozzle. Using two different illumination techniques, Reitz (1990) was able to observe that the jet consists of two regions; a core region and a surrounding fine spray region. Reitz (1990) further speculates that the main jet has several sub jets whose breakup constitutes the smaller particles in the outer edges while longer wave length breakup (hence larger particles) contributes to the core region. This is reflected in the present measurements. However, in Fig. 9(a), one notes that the larger particles are found to occur below the axis of the jet and the size distributions along the Y-axis are clearly asymmetric. At any axial station, for symmetrical locations, the mean diameters are generally larger along the lower half of the jet ($Y < 0$). One would speculate that this is a consequence of gravitational settling and hence the asymmetry. However, it is interesting to note that along the jet axis, the value of the mean diameters decrease as one progresses from $Z/D = 800$ to $Z/D = 2400$. As indicated earlier, during visual observations, the particles could be seen physically dropping off after about $Z/D = 1000$.

It should be borne in mind that the particles crossing the measuring volume at a given measurement location are fairly polydisperse. The use of the count mean diameter does not in reality reflect the proper nature of the size distribution. Consequently, it is necessary to examine the entire size distribution and obtain a more meaningful representation of droplet size in flashing jets. Figure 9(b) shows the radial variation of the size probability density function at $Z/D = 800$. It is interesting to note that at a location $Y/\delta = 1.0$ (top portion of the jet), 50 percent of the particles measured are below 6.5 μm while 85 percent of the particles are below 20 μm. The range of particles seen at this location varies from about 1 to 60 μm. As one progresses toward the mid regions of the jet ($Y/\delta = 0.0$), the median droplet size increases. On converting the size data into particle volumes and by arranging the particles in ascending order of size, it was noted that 50 percent of the total volume was occupied by less than the last 5 percent of the particles while the first 50 percent of particles accounted for less than 5 percent of the total volume. Figure 9(c) shows the radial variation of the size probability density function at $Z/D = 2400$. At this axial station, for $Y/\delta = 1.0$, one notes by arranging the particles in ascending order of size, the first 50 percent of the particles occupy less than 1 percent of the total volume while 50 percent of the volume is contributed by less than 1 percent of the total number of particles. One notes that the vast majority of the particles are very small (<25 μm) while the size range is quite wide and a very small percentage of particles makes a much larger contribution to the total volume. A single representative diameter may not be sufficient to completely characterize particle size in flashing jets. These factors play a major role from an application point of view of the present study to the nuclear industry. The retention time of the particles in the containment atmosphere is expected to be drop size dependent and the larger particles have a greater tendency to gravitational settling. Data on both the smaller and the larger end of the histogram are required for modelling transport of water droplets in reactor containments. Aerosol mechanisms such as thermophoresis can affect primarily the smaller particles while gravity will influence mainly the larger particles. Radionuclides may be potentially suspended or dissolved in the primary heat transport coolant and characterizing the size of the water droplets formed during the blowdown phase of a loss-of-coolant-accident condition can have an important role in determining the potential radiation hazard to the public.

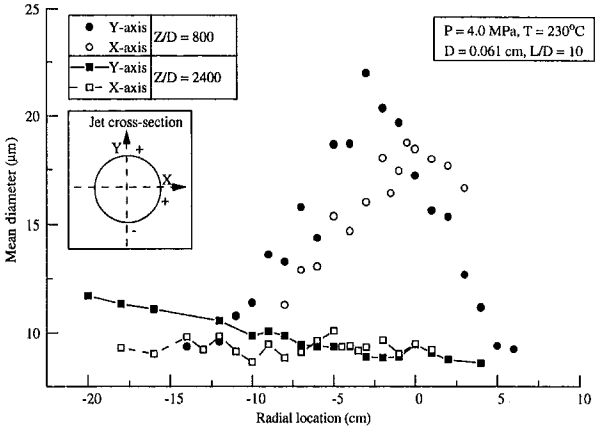

Fig. 9(a) Radial variation of mean diameter at Z/D = 800 and 2400. (Uncertainty in mean diameter = ±4 percent, Uncertainty in location = ±5 percent)

Experimental Uncertainty

The experimental uncertainties associated with the variables, evaluated at an odds of 20:1 (Moffat, 1988) are indicated in Table 2.

In the case of particle size measurement, the size distributions are essentially lognormal and the error estimates are largely dependent on the sampling size (N). A critical value of N is required to avoid a blow up in errors. This critical value of N is very sensitive to the width of the distribution and is proportional to the geometric standard deviation ($= (D_{84}/D_{16})^{1/2}$). Here, D_{16} and D_{84} represent the particle size corresponding to the 16th and 84th percentile of the cumulative volume distribution. Following Paine's (1993) analysis, a sampling size of 3000 was found to be quite adequate for the range of geometric standard deviations encountered.

Conclusions

In this study, details regarding the calibration and validation procedures related to the use of a phase-Doppler anemometer to measure size and velocity of droplets in flashing jets are discussed. The effect of the intensity of the laser source on the

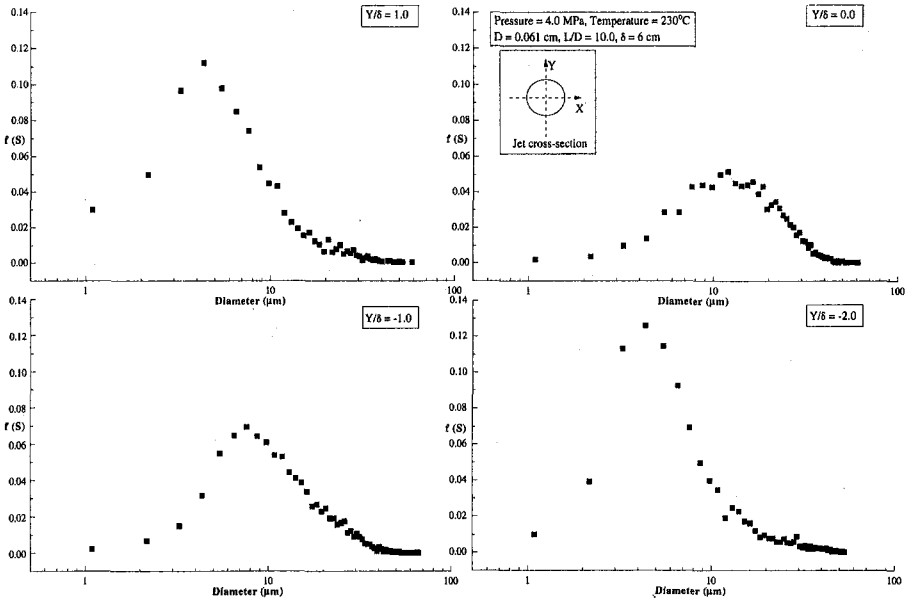

Fig. 9(*b*) Variation of size probability density functions along the radius at Z/D = 800 (Uncertainty in $f(S)$ = ±5 percent, Uncertainty in diameter = ±4 percent)

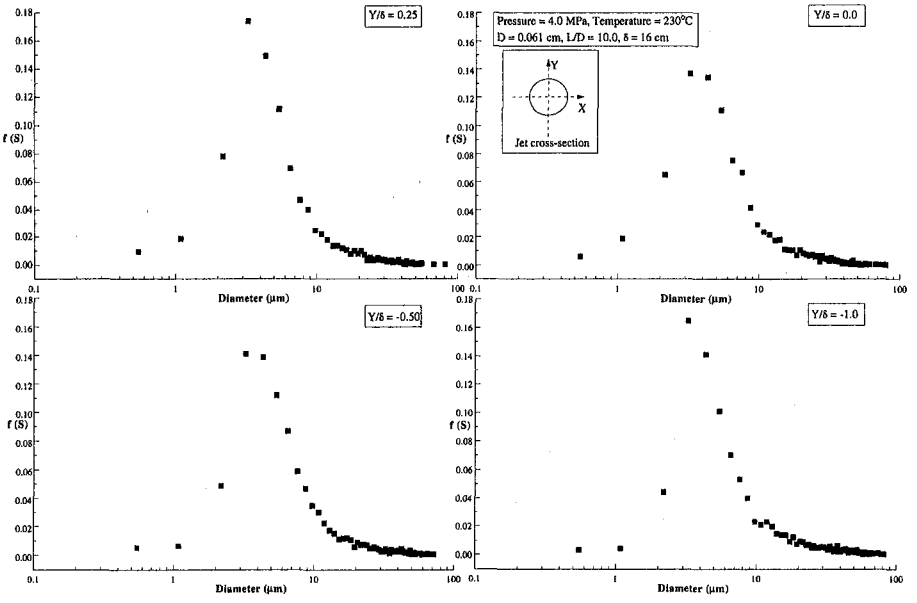

Fig. 9(*c*) Variation of size probability density functions along the radius at Z/D = 2400 (Uncertainty in $f(S)$ = ±5 percent, Uncertainty in diameter = ±4 percent)

water droplet size measurement is identified. Typical size and velocity distributions are reported at two axial stations. It is hoped that this will form the start of a good database useful for the analysis of the formation, transportation and deposition of aerosols generated by flashing under nuclear reactor accident conditions. The following observations can be drawn from the present set of results:

Table 2 Experimental uncertainty

Variable	Uncertainty
Velocity (U)	±1% (Typical)
Half width (d)	±5%
Mean diameter (D)	±4% (Typical)
VMD (D_{50})	±5%
Counts	±5%
Traversing location (X, Y, Z)	±5%

1. The phase-Doppler anemometer is a very useful tool to accurately measure particle size in sprays and jets. However, to ensure the correct measurement of particle size in the prevailing environment, the validation procedure should involve the identification of the minimum laser power for a given sensitivity of the photomultiplier tube. To use the PDA in flashing water jets, the recommended power of the transmitting laser beam is 2.5 W.

2. Visual observations indicate that for the given nozzle configuration and experimental conditions (pressure = 4.0 MPa, temperature = 230°C), the flashing jet initially expands in a near hemispherical fashion followed by a linear spreading. In the latter region, the radial distribution of the mean velocity exhibits a typical Gaussian distribution and this behaviour is similar to that noticed in single phase flows. Furthermore, the half-width of the jet indicates that the jet grows fairly linearly beyond the hemispherical expansion. Based on the velocity profiles, the half width of the jet appears to be the proper geometric normalizing variable. The mean velocity profiles indicate simi-

larity and the magnitude of the mean velocity decreases with increasing distance from the nozzle.

3. The radial distribution of particle size clearly indicates that the particles are highly polydisperse. To have a better description of the size distribution and provide the necessary data for modelling of droplet transport in reactor containments, a single value such as the count mean diameter is not sufficient. The influence of gravitational settling along the vertical downward direction is clearly noticed in the droplet size distribution.

Acknowledgment

This work was funded by the CANDU Owners Group (COG) consisting of Atomic Energy of Canada Limited, Ontario Hydro, New Brunswick Power and Hydro Quebec.

References

Appleton, P. R., 1984, "A Study of Axi-Symmetric Two-Phase Flashing Jets," Safety and Reliability Directorate, U.K. Atomic Energy Authority, SRD R 303.

Anderson, R. C., Reynolds, A. B., and Erdman, C. A., 1982, "Droplet Size Distributions from Flashing," *Transactions of the American Nuclear Society,* Vol. 43, pp. 786–787.

Anderson, R. C., Erdman, C. A., and Reynolds, A. B., 1984, "Droplet Size Distribution from Bulk Flashing," *Nuclear Science and Engineering,* Vol. 88, pp. 495–512.

Bachalo, W. D., and Houser, M. J., 1986, "An Instrument for Two-Component Velocity and Particle Size Measurement," *Third International Symposium on Applications of Laser Anemometry to Fluid Mechanics,* Lisbon, Portugal, Paper #18.3, pp. 1–6.

Bates, C. J., Hadded, O., and Yeoman, M. L., 1986, "High Pressure Steam/Water Jet Measurements Using a Portable Particle Sizing Laser Doppler System," AIAA-ASME 4th Fluid Mechanics, Plasma Dynamics and Lasers Conference, pp. 59–64.

Brown, R., and York, J. L., 1962, "Sprays Formed by Flashing Liquid Jets," *A.I.Ch.E. Journal,* Vol. 8, No. 2, pp. 149–153.

Durst, F., 1982, "Review-Combined Measurements of Particles Velocities, Size Distributions and Concentrations," ASME JOURNAL OF FLUIDS ENGINEERING, Vol. 104, pp. 284–296.

Goldschmidt, V., and Eskinazi, S., 1966, "Two-Phase Turbulent Flow in a Plane Jet," ASME JOURNAL OF APPLIED MECHANICS, Dec., pp. 735–747.

Gooderum, P. B., and Bushnell, D. M., 1969, "Measurement of Mean Drop Sizes for Sprays From Superheated Water Jets," *Engineering Notes, Journal of Spacecraft, 6,* No. 2, pp. 197–198.

Hetsroni, G., and Sokolov, M., 1971, "Distribution of Mass, Velocity and Intensity of Turbulence in a Two-Phase Turbulent Jet," ASME JOURNAL OF APPLIED MECHANICS, June, pp. 315–327.

Hishida, K., and Maeda, M., 1990, "Application of Laser/Phase Doppler Anemometer to Dispersed Two-Phase Jet Flow," *Particle and Particle Systems Characterization,* Vol. 7, No. 3, pp. 152–159.

Koestel, A., Gido, R. G., and Lamkin, D. E., 1980, "Drop-size Estimates for a Loss-of-Coolant-Accident," NUREG/CR-1607, Los Alamos Scientific Laboratory.

Moffat, R. J., 1988, "Describing the Uncertainties in Experimental Results," *Experimental Thermal and Fluid Science,* Vol. 1, pp. 3–17.

Oza, R. D., 1984, "On the Mechanism of Flashing Injection of Initially Subcooled Fuels," ASME JOURNAL OF FLUIDS ENGINEERING, Vol. 106, pp. 105–109.

Paine, A. J., 1993, "Error Estimates in the Sampling From Particle Size," *Particle and Particle Systems Characterization,* Vol. 10, No. 1, VCH Publishers Inc., pp. 26–32.

Qiu, H. H., Sommerfeld, M., and Durst, F., 1991, "High Resolution Data Processing for Phase-Doppler Measurements in a Complex Two-Phase Flow," *Meas. Sci. Technol.,* Vol. 2, pp. 455–463.

Reitz, R. D., 1990, "A Photographic Study of Flash-Boiling Atomization," *Aerosol Science and Technology,* Elsevier Sci. Publ. Co., 12, pp. 561–569.

Saffman, M., 1987, "Optical Particle Sizing Using the Phase of LDA Signal," Particle Dynamics, Dantec Information No. 5.

Sher, E., and Elata, C., 1977, "Spray Formation From Pressure Cans by Flashing," *Ind. Eng. Chem., Process Des. Dev.,* Vol. 16, No. 2, pp. 237–242.

Tayali, N. E., and Bates, C. J., 1990, "Particles Sizing Techniques in Multiphase Flows: A Review," *Flow. Meas. Instrum.,* Vol. 1, pp. 77–105.

Tilton, J. N., and Farley, C. W., 1990, "Predicting Liquid Jet Breakup and Aerosol Formation During the Accidental Release of Pressurized Hydrogen Flouride," *Plant/Operations Progress,* Vol. 9, No. 2, pp. 120–124.

Wu, J. M., and Chuang, C. F., 1984, "Consequence Analysis of a Steam Generator Tube Rupture Accident," *Nuclear Technology,* Vol. 67, pp. 381–406.

Journal of Fluids Engineering

Technical Briefs

Flow Characteristics of Splined Tipped Circular Jets

A. A. S. Arefin Kabir,[1] S. Dutta,[1] and M. A. Taher Ali[2]

Introduction

Experimental measurements for axial development of streamwise velocity distributions at the near field of a circular jet with splined nozzles are presented. Results include the axial distribution of mean flow and entrainment rates of a free jet with different exit conditions. Splined round jets reveal an interesting effect on jet spread and entrainment rates. Axial splines at the circumference of the jet nozzle enhance turbulence at the jet circumference boundary layer without significantly changing the nozzle core flow. The boundary layer at the jet nozzle exit, that is at the start of the free shear layer, increases in thickness due to the increase in turbulence mixing by splines. It is observed that the jet entrainment rate reduces by the addition of splines and therefore this method can be used as a passive control of jets.

The isothermal, incompressible, single phase free shear layer of a Newtonian fluid, such as a turbulent jet, is probably the simplest example of a turbulent shear flow and there have been many investigations to understand this flow structure. However, previous studies show that there are large discrepancies among measurements of jet mean characteristics such as the spread rate, similarity parameters, virtual and geometric origin locations, peak turbulence intensities, entrainment rates, etc. These discrepancies create conflicting interpretations of the flow physics and thus, originate confusion in the understanding of this simple flow. One of the basic properties of a jet is its entrainment and growth. The control of jet entrainment rate is of fundamental importance to many industrial applications. Nondimensional entrainment rate of a jet depends mostly on the inlet geometry, the nozzle exit Reynolds number, and upstream excitation of the jet.

There are several studies on axisymmetric laminar and turbulent jets. Crow and Champagne (1971) investigated the orderly structure in the initial region of a round turbulent jet. Like Kolpin (1964) they found a potential core spanning few hydraulic diameters distance from the nozzle exit. They found practically indistinguishable variation in centerline mean velocity and centerline turbulence intensity inside the potential core with a change in Reynolds number (62,000 to 124,000). The centerline mean velocity reduced gradually downstream of the potential core but the centerline turbulence intensity increased up to 8 to 9 diameters distance from the nozzle and then decreased. Bogulslawski and Popiel (1979) noticed similar centerline mean velocity profile in the flow structure of a free round turbulent jet for 51,000 and 125,000 Reynolds numbers.

Among other related studies, Hill (1972) measured the local entrainment in the initial region of a jet using the porous-wall technique. Hussain and Clark (1977) studied the upstream influence on the near field of a plane turbulent jet for different initial conditions and found that jet spread rate and centerline mean velocity decay, as well as the kinematic and geometric virtual origins depended on initial conditions. Later, Hussain and Zedan (1978a and 1978b) experimentally studied the effects of initial condition on an axisymmetric free shear layer. They varied the initial boundary layer thickness, momentum thickness, jet Reynolds number, and turbulence intensity. Their observation showed that the nondimensional jet spread rate, similarity parameter, and peak turbulence intensity in the self-preservation region were essentially independent of the jet Reynolds number, but dependent on the initial boundary layer and turbulence level. In another experimental work, Husain and Hussain (1979) experimented the influence of initial and boundary conditions in the near field of a 12.7 cm diameter circular jet at 2600 Reynolds number (based on nozzle diameter). They found almost no effect of the nozzle exit plate condition on the shear layer width, momentum thickness, and jet spread rate; however, all these parameters showed strong dependence on the nozzle exit turbulence intensity. Drubka and Nagib (1982) studied jet velocity and turbulence profiles with grid generated high turbulence in the core flow. The velocity spectrum in the streamwise direction was presented. More recent measurements and discussions on jets are given in Otugen et al. (1996).

The objective of this study is to experimentally investigate the near field flow development of an axisymmetric circular jet with different axial splines at the circumference of the jet nozzle. Essentially, the addition of splines creates an enhanced turbulent boundary layer at the nozzle exit. Previously published initial condition studies included laminar and turbulent boundary layers, enhanced turbulence in the core flow, boundary layer tripping etc., but not the role of axial splines on the jet flow.

Experimental Setup

The jet flow facility of the Bangladesh University of Engineering and Technology is used. The setup consists of a fan, flow controller, diffusers, two settling chambers and a nozzle. The overall length of the setup is 8.5 m. One 483 mm diameter

[1] Graduate Student and Assistant Professor, respectively, Department of Mechanical Engineering, University of South Carolina, Columbia SC 29208.

[2] Professor, Mechanical Engineering Department, Bangladesh University of Engineering and Technology, Dhaka-1000, Bangladesh.

Contributed by the Fluids Engineering Division of THE AMERICAN SOCIETY OF MECHANICAL ENGINEERS. Manuscript received by the Fluids Engineering Division July 29, 1996; revised manuscript received January 2, 1998. Associate Technical Editor: F. Giralt.

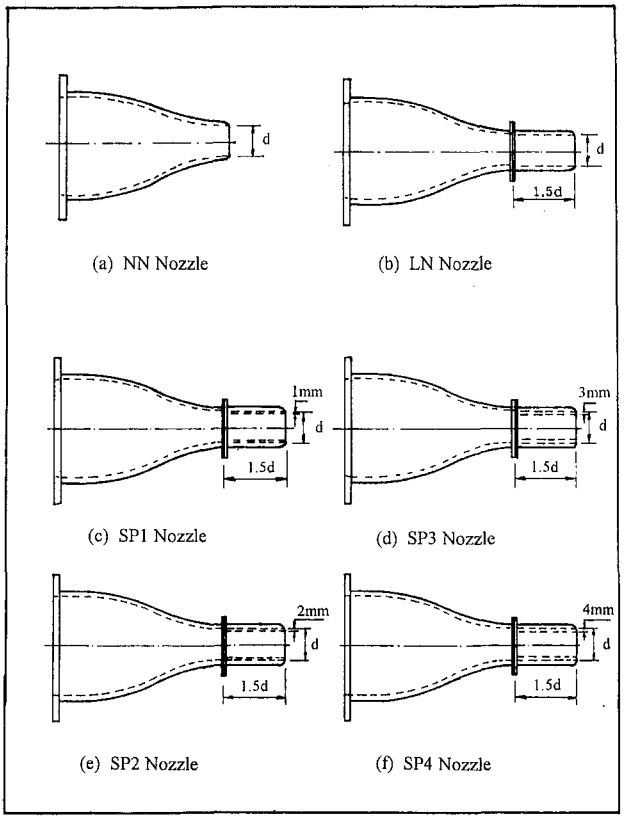

Fig. 1 Smooth and splined test nozzles and associated nomenclature

airfoil fan, capable of supplying 1600 cfm against 4.318 mm gage of water, with five different set speeds is used. A fan-speed control switch and a butterfly valve, placed at the upstream section of the fan unit control the air intake.

Turbulence and mean velocities are measured by a hot-wire anemometer and a pitot static tube respectively. Note that results based on mean velocity are presented here. The pitot tube and hot-wire probe are traversed in the air stream of the test facility with the help of a coordinate measuring device. Different nozzles used for this experiment are shown in Fig. 1. The NN nozzle has a cubic contour. The root circle diameter, d, of jet nozzles is 80 mm and maximum spline height is 4 mm. Equally spaced 60 triangular cross-section splines are machined in each splined nozzle. The splines are axially oriented (parallel to the flow) and are 1.5d in length. The jet Reynolds number is Re_d = 50,000 based on the nozzle exit centerline axial velocity, U_{ec}, and jet nozzle root diameter, d. The uncertainty in velocity is ±3.93 percent and that in Reynolds number is ± 6.3 percent.

Data Reduction

The local velocity, U, at different axial and radial positions is measured. The entrainment rate, e, is calculated from the velocity distribution as:

$$e = \frac{q}{q_e} - 1 \tag{1}$$

where the volumetric flow rate, q, is defined as:

$$q = 2\pi \int_{y=0}^{y=y_{max}} U \cdot y \, dy \tag{2}$$

In this equation, y_{max} is the location where the mean axial velocity is 10 percent of the local core axial velocity. At the nozzle exit, the volumetric flow rate, q_e, is given as:

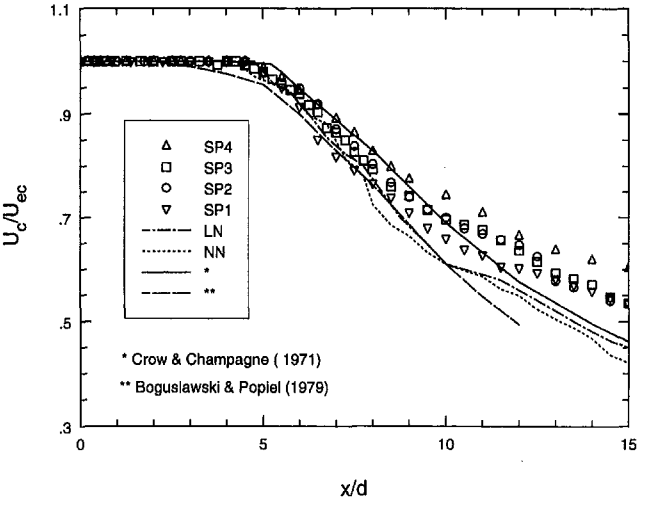

Fig. 2 Axial distribution of centerline mean velocity

$$q_e = 2\pi \int_{y=0}^{y=d/2} U \cdot y \, dy \tag{3}$$

Results and Discussion

Figure 2 shows the effect of splined tips on centerline mean velocity. Smooth nozzle results from Crow and Champagne (1971) and Boguslawski and Popiel (1979) are included for comparison. The regular decay of jet starts from x/d = 4.75 for all nozzles with almost no effect on the potential core due to splined tips. Data from Boguslawski and Popiel (1979) show a shorter potential core. Results show that the addition of splines helps the jet to sustain a longer distance and the centerline velocity for splined nozzles are higher than that for smooth jet at any axial location beyond the potential core.

The entrainment rates for different nozzles are shown in Fig. 3. Initially, near the nozzle exit, the spline height has small effect on the entrainment rate. After this region, the entrainment rate decreases with an increase in spline height. At x/d = 5, the entrainment rate decreases by 3.3, 9.09, 12.39, and 15.7 percent of the entrainment rate of LN nozzle for SP1, SP2, SP3, and SP4 nozzles, respectively. Entrainment rate decreases further along downstream locations with an increase in spline height. Experimental results of Boguslawski and Popiel (1979) are included for comparison. The reduction in entrainment with

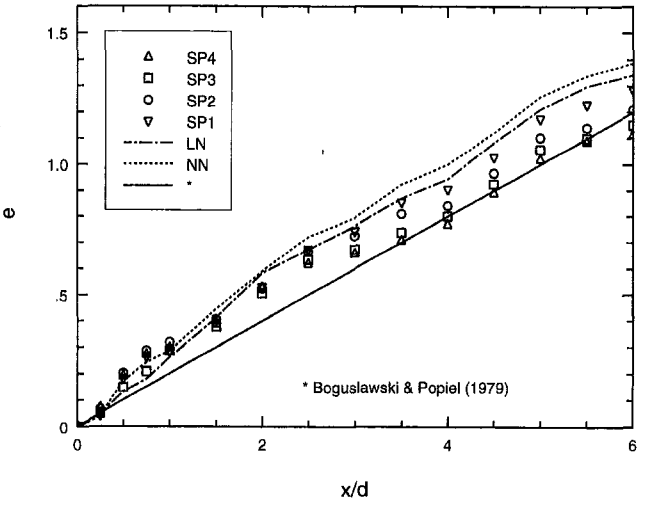

Fig. 3 Effect of splined tips on entrainment rate

an increase in the spline height can be explained from the nozzle exit velocity and turbulence conditions. The higher splines have a smoother velocity gradient at the jet boundary because of the turbulence enhancement by splines. In the free shear layer (jet boundary) the velocity gradient acts as the turbulence production term. The high turbulence caused by splines soon decays in the free jet and less turbulence is produced due to a smoother velocity gradient. Whereas, in smooth nozzles which have sharp velocity gradients at the nozzle exit, a gain in turbulence occurs due to the higher turbulence production rate. Therefore, downstream from the nozzle exit, smooth nozzles (NN and LN) have greater jet boundary turbulence fluctuations compared to those with splined nozzles. This higher turbulence mixing at the periphery of smooth nozzles increases entrainment rate and causes a faster decay of jet.

References

Boguslawski, L., and Popiel, C. O., 1979, "Flow Structure of the Free Round Turbulent Jet in the Initial Region," *Journal of Fluid Mechanics,* Vol. 90, Part 3, Feb., pp. 531–539.

Crow, S. C., and Champagne, F. H., 1971, "Orderly Structure in Jet Turbulence," *Journal of Fluid Mechanics,* Vol. 48, Part 3, Aug., pp. 547–591.

Drubka, R. E., and Nagib, H. M., 1982, "Turbulent Jets with Controlled Initial Conditions," *Structure of Complex Turbulent Flows,* IUTAM Symposium, Marseilles, France, Aug. 31–Sept. 3, Springer-Verlag.

Hill, B. J., 1972, "Measurement of Local Entrainment Rate in the Initial Region of Axisymmetric Turbulent Air Jets," *Journal of Fluid Mechanics,* Vol. 51, pp. 773–779.

Husain, Z. D., and Hussain, A. K. M. F., 1979, "Axisymmetric Mixing Layer: Influence of the Initial and Boundary Conditions," *AIAA Journal,* Vol. 17, No. 1, Jan., pp. 48–55.

Hussain, A. K. M. F., and Ray Clark, A., 1977, "Upstream Influence on the Near Field of a Plane Turbulent Jet," *The Physics of Fluids,* Vol. 20, No. 9, Sept., pp. 1416–1426.

Hussain, A. K. M. F., and Zedan, M. F., 1978a, "Effect of the Initial Condition on the Axisymmetric Free Shear Layer: Effects of the Initial Momentum Thickness," *The Physics of Fluids,* Vol. 21, No. 7, July, pp. 1100–1112.

Hussain, A. K. M. F., and Zedan, M. F., 1978b, "Effect of the Initial Condition on the Axisymmetric Free Shear Layer: Effect of the Initial Fluctuation Level," *The Physics of Fluids,* Vol. 21, No. 9, Sept., pp. 1475–1481.

Kolpin, M. A., 1964, "The Flow in the Mixing Region of a Jet," *Journal of Fluid Mechanics,* Vol. 18, Part 4, Apr., pp. 529–548.

Otugen, M. V., Girlea, F., and Sforza, P. M., 1996, "The Turbulent Incompressible Jet in a Curved Coflow," ASME JOURNAL OF FLUIDS ENGINEERING, Vol. 118, June, No. 2, pp. 300–306.

A Modified Borda-Carnot Relation for the Prediction of Maximum Recovery Pressure in Planar Sudden Expansions Flows

George Papadopoulos[1] and M. Volkan Ötügen[1]

1 Introduction

The passage of a fluid through a straight duct or pipe leads to pressure head losses resulting primarily from friction. When a sudden enlargement in cross-section is encountered additional losses occur, which are sometimes referred to as *shock* losses (see Idelchik, 1986). To determine these losses one uses the well known Borda-Carnot equation, which comes about from a simple momentum and energy balance consideration across the expansion (see Archer, 1913; Schutt, 1929). The equation states that the pressure coefficient of loss is only a function of the downstream-to-upstream area ratio ($\sigma = A_1/A_0$)

$$C_{p_{\text{loss}}} = \frac{p - p_{\text{ref}}}{\frac{1}{2}\rho U_0^2} = \left(1 - \frac{1}{\sigma}\right)^2 \tag{1}$$

where the static pressure at the plane of enlargement is used as the reference. Then, the actual pressure coefficient at maximum recovery is equal to the inviscid (ideal) recovery less the shock loss,

$$C_{p_{\text{BC}}} = \frac{2}{\sigma}\left(1 - \frac{1}{\sigma}\right). \tag{2}$$

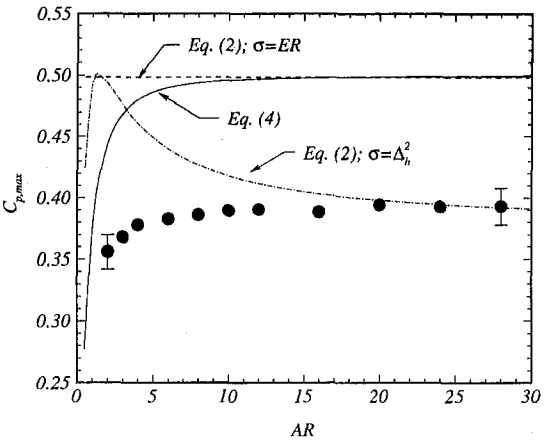

Fig. 1 Pressure coefficient values at maximum recovery versus AR for ER = 2 (symbols denote present experimental measurements)

For moderate to high Reynolds number incompressible flows (above 10,000 as indicated by Schutt, 1929), the Borda-Carnot relation yields good results. This has led to its acceptance for use in engineering applications involving axisymmetric, four-sided rectangular, as well as, two-dimensional (planar) expansions. For four-sided expansions the area ratio is formulated in terms of an equivalent circular area based on the hydraulic diameter. Detailed information on the pressure head loss or pressure coefficient at maximum recovery for such geometries is readily available in the handbooks of Idelchik (1986) and Miller (1990).

In a previous investigation, the authors reported on the effects of aspect ratio (step span-to-height ratio), AR, on the flow development in one-sided expansions (Papadopoulos and Ötügen, 1995). The study revealed decreasing centerplane maximum pressures downstream of the expansion for smaller AR, as the flow became progressively three-dimensional (Fig. 1). Since the Borda-Carnot relation expressed by Eq. (2) does not take into account the three-dimensional effects, it fails to predict $C_{p,\max}$ at small AR values, yielding a constant $C_{p,\max}$ for all AR. As will be shown later, even if an "effective" circular area ratio based on the upstream and downstream hydraulic diameters is used (in an attempt to capture the three-dimensional effects) Eq. (2) still fails, both quantitatively and in trend, to predict $C_{p,\max}$. In the present report, a modified Borda-Carnot relation is described that captures both the expansion ratio (downstream-to-upstream channel height, ER) and the aspect ratio effects for one- and two-sided sudden expansions within ducts.

[1] Research Scientist and Associate Professor, respectively, Mechanical and Aerospace Engineering, Polytechnic University, Six Metrotech Center, Brooklyn, NY 11201.

Dr. Papadopoulos is presently at NIST, B360/224, Gaithersburg, MD 20899.

Contributed by the Fluids Engineering Division of THE AMERICAN SOCIETY OF MECHANICAL ENGINEERS. Manuscript received by the Fluids Engineering Division March 10, 1997; revised manuscript received January 12, 1998. Associate Technical Editor: P. W. Bearman.

an increase in the spline height can be explained from the nozzle exit velocity and turbulence conditions. The higher splines have a smoother velocity gradient at the jet boundary because of the turbulence enhancement by splines. In the free shear layer (jet boundary) the velocity gradient acts as the turbulence production term. The high turbulence caused by splines soon decays in the free jet and less turbulence is produced due to a smoother velocity gradient. Whereas, in smooth nozzles which have sharp velocity gradients at the nozzle exit, a gain in turbulence occurs due to the higher turbulence production rate. Therefore, downstream from the nozzle exit, smooth nozzles (NN and LN) have greater jet boundary turbulence fluctuations compared to those with splined nozzles. This higher turbulence mixing at the periphery of smooth nozzles increases entrainment rate and causes a faster decay of jet.

References

Boguslawski, L., and Popiel, C. O., 1979, "Flow Structure of the Free Round Turbulent Jet in the Initial Region," *Journal of Fluid Mechanics,* Vol. 90, Part 3, Feb., pp. 531–539.

Crow, S. C., and Champagne, F. H., 1971, "Orderly Structure in Jet Turbulence," *Journal of Fluid Mechanics,* Vol. 48, Part 3, Aug., pp. 547–591.

Drubka, R. E., and Nagib, H. M., 1982, "Turbulent Jets with Controlled Initial Conditions," *Structure of Complex Turbulent Flows,* IUTAM Symposium, Marseilles, France, Aug. 31–Sept. 3, Springer-Verlag.

Hill, B. J., 1972, "Measurement of Local Entrainment Rate in the Initial Region of Axisymmetric Turbulent Air Jets," *Journal of Fluid Mechanics,* Vol. 51, pp. 773–779.

Husain, Z. D., and Hussain, A. K. M. F., 1979, "Axisymmetric Mixing Layer: Influence of the Initial and Boundary Conditions," *AIAA Journal,* Vol. 17, No. 1, Jan., pp. 48–55.

Hussain, A. K. M. F., and Ray Clark, A., 1977, "Upstream Influence on the Near Field of a Plane Turbulent Jet," *The Physics of Fluids,* Vol. 20, No. 9, Sept., pp. 1416–1426.

Hussain, A. K. M. F., and Zedan, M. F., 1978a, "Effect of the Initial Condition on the Axisymmetric Free Shear Layer: Effects of the Initial Momentum Thickness," *The Physics of Fluids,* Vol. 21, No. 7, July, pp. 1100–1112.

Hussain, A. K. M. F., and Zedan, M. F., 1978b, "Effect of the Initial Condition on the Axisymmetric Free Shear Layer: Effect of the Initial Fluctuation Level," *The Physics of Fluids,* Vol. 21, No. 9, Sept., pp. 1475–1481.

Kolpin, M. A., 1964, "The Flow in the Mixing Region of a Jet," *Journal of Fluid Mechanics,* Vol. 18, Part 4, Apr., pp. 529–548.

Otugen, M. V., Girlea, F., and Sforza, P. M., 1996, "The Turbulent Incompressible Jet in a Curved Coflow," ASME JOURNAL OF FLUIDS ENGINEERING, Vol. 118, June, No. 2, pp. 300–306.

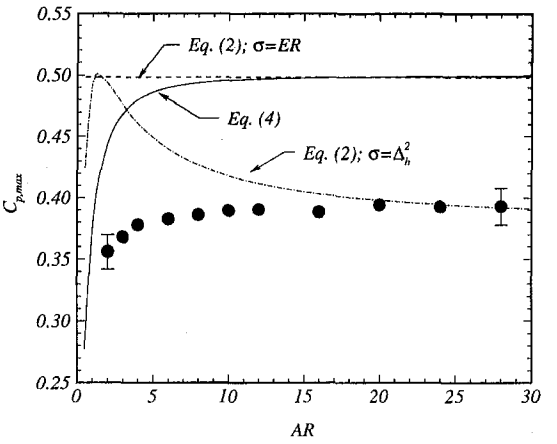

Fig. 1 Pressure coefficient values at maximum recovery versus AR for ER = 2 (symbols denote present experimental measurements)

A Modified Borda-Carnot Relation for the Prediction of Maximum Recovery Pressure in Planar Sudden Expansions Flows

George Papadopoulos[1] and M. Volkan Ötügen[1]

1 Introduction

The passage of a fluid through a straight duct or pipe leads to pressure head losses resulting primarily from friction. When a sudden enlargement in cross-section is encountered additional losses occur, which are sometimes referred to as *shock* losses (see Idelchik, 1986). To determine these losses one uses the well known Borda-Carnot equation, which comes about from a simple momentum and energy balance consideration across the expansion (see Archer, 1913; Schutt, 1929). The equation states that the pressure coefficient of loss is only a function of the downstream-to-upstream area ratio ($\sigma = A_1/A_0$)

$$C_{p_{\text{loss}}} = \frac{p - p_{\text{ref}}}{\frac{1}{2}\rho U_0^2} = \left(1 - \frac{1}{\sigma}\right)^2 \tag{1}$$

where the static pressure at the plane of enlargement is used as the reference. Then, the actual pressure coefficient at maximum recovery is equal to the inviscid (ideal) recovery less the shock loss,

$$C_{p_{\text{BC}}} = \frac{2}{\sigma}\left(1 - \frac{1}{\sigma}\right). \tag{2}$$

For moderate to high Reynolds number incompressible flows (above 10,000 as indicated by Schutt, 1929), the Borda-Carnot relation yields good results. This has led to its acceptance for use in engineering applications involving axisymmetric, four-sided rectangular, as well as, two-dimensional (planar) expansions. For four-sided expansions the area ratio is formulated in terms of an equivalent circular area based on the hydraulic diameter. Detailed information on the pressure head loss or pressure coefficient at maximum recovery for such geometries is readily available in the handbooks of Idelchik (1986) and Miller (1990).

In a previous investigation, the authors reported on the effects of aspect ratio (step span-to-height ratio), AR, on the flow development in one-sided expansions (Papadopoulos and Ötügen, 1995). The study revealed decreasing centerplane maximum pressures downstream of the expansion for smaller AR, as the flow became progressively three-dimensional (Fig. 1). Since the Borda-Carnot relation expressed by Eq. (2) does not take into account the three-dimensional effects, it fails to predict $C_{p,\max}$ at small AR values, yielding a constant $C_{p,\max}$ for all AR. As will be shown later, even if an "effective" circular area ratio based on the upstream and downstream hydraulic diameters is used (in an attempt to capture the three-dimensional effects) Eq. (2) still fails, both quantitatively and in trend, to predict $C_{p,\max}$. In the present report, a modified Borda-Carnot relation is described that captures both the expansion ratio (downstream-to-upstream channel height, ER) and the aspect ratio effects for one- and two-sided sudden expansions within ducts.

[1] Research Scientist and Associate Professor, respectively, Mechanical and Aerospace Engineering, Polytechnic University, Six Metrotech Center, Brooklyn, NY 11201.

Dr. Papadopoulos is presently at NIST, B360/224, Gaithersburg, MD 20899.

Contributed by the Fluids Engineering Division of THE AMERICAN SOCIETY OF MECHANICAL ENGINEERS. Manuscript received by the Fluids Engineering Division March 10, 1997; revised manuscript received January 12, 1998. Associate Technical Editor: P. W. Bearman.

Table 1 Details of experimental investigation: configuration and flow conditions

Step height (mm) h	Expansion ratio ER	Aspect ratio AR	Hydraulic diameter ratio Δ_h	Reynolds number $Re = U_0h/\nu$
34.9 ± 0.5	3.09 ± 0.13	7.28 ± 0.11	2.74 ± 0.12	20,400 ± 700
39.6 ± 0.5	4.30 ± 0.18	6.41 ± 0.09	3.74 ± 0.16	19,100 ± 600
40.3 ± 0.5	4.57 ± 0.19	6.30 ± 0.09	3.96 ± 0.17	19,000 ± 600
43.9 ± 0.5	6.70 ± 0.27	5.79 ± 0.07	5.74 ± 0.24	14,100 ± 400
46.9 ± 0.5	10.98 ± 0.44	5.42 ± 0.07	9.29 ± 0.39	8,300 ± 300

2 Experimental Setup and Methodology

Little information is available in the literature on wall pressure distributions for one-sided expansions with ER > 2, and most of the information that does exist is for ER ≈ 1, or "external" type of flows. Furthermore, limited information is available on AR effects on such flows outside of the experimental work of Papadopoulos and Ötügen (1995). In order to extend the range of previous measurements and to capture the combined effects of ER and AR, both the facility of Papadopoulos and Ötügen (1995) and a new facility was used for the present investigation.

The new one-sided expansion wind tunnel had a step height of $h = 34.9 \pm 0.5$ mm[2] in its unmodified form, a fixed step span of $S = 254 \pm 1.5$ mm, and a fixed downstream channel height of $Y_1 = 51.6 \pm 1.0$ mm. The test section was made of $\frac{1}{4}$-in. thick Plexiglas and had a streamwise length of 1.4 m. This duct expansion configuration yielded ER = 3.10 and AR = 7.27. Other configurations detailed in Table 1 were obtained by increasing the step height without modifying the downstream channel. This was accomplished by using specially formed sections that spanned the width of the test section and length of the step (260 mm), to increase the original step height. The leading edge of these sections was contoured to achieve smooth integration with the contraction section (4:1 minimum) of the settling chamber leading to the original step. A change in the step height yielded a variation in both the expansion and the aspect ratio since test section span and downstream height were kept fixed.

Wall pressure along the centerline of the step-wall was measured through taps using a set of variable reluctance pressure transducers, one measuring the local pressure, and another measuring a reference pressure from a tap located on the face of the step perpendicular to the bulk stream motion. A small-diameter pitot tube, placed along the centerplane near the end of the settling chamber contraction section, was used to determine the freestream velocity in the duct section upstream of the expansion. The Reynolds number is based on this velocity and the step height.

3 Results

The pressure distribution along the centerline of the step wall was measured and the maximum recovery pressure downstream of the expansion was subsequently determined. (The flow conditions for these measurements are summarized in Table 1.) $C_{p,\max}$ was determined by referencing the maximum pressure to the static pressure measured at the plane of the expansion, $x = 0$. Values of $C_{p,\max}$, along with others found in the literature, are shown in Fig. 2 plotted against the reciprocal of the hydraulic diameter ratio of the downstream to upstream duct sections. The hydraulic diameter ratio is defined as

$$\Delta_h = \frac{D_{h_1}}{D_{h_0}} = \mathrm{ER} \times \frac{n + \mathrm{AR}(\mathrm{ER} - 1)}{n \cdot \mathrm{ER} + \mathrm{AR}(\mathrm{ER} - 1)} \tag{3}$$

where $D_h = 4A/\Pi$, Π being the perimeter of the cross-section.

[2] Reported uncertainties are at 95 percent confidence.

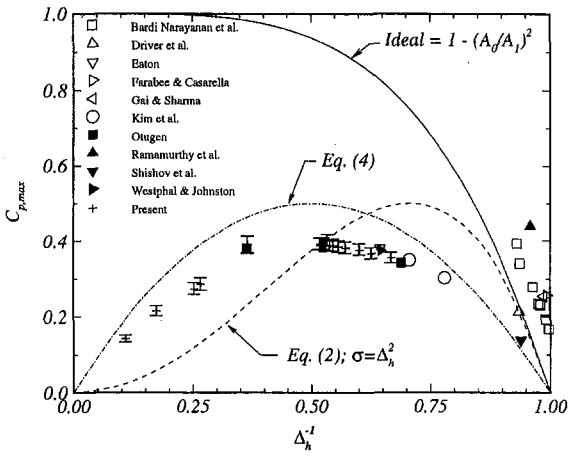

Fig. 2 Correlation of experimental maximum pressure coefficient values with theoretical predictions

For single-sided expansions (backward-facing step) $n = 1$, while for symmetric double-sided expansions $n = 2$.

The hydraulic diameter ratio is a function of both expansion and aspect ratios, and all possible geometric configurations fall in the range of $0 < \Delta_h^{-1} < 1$. Thus, it is an appropriate independent variable since it provides a full representation of the geometric expansion, while including the possible effects of AR. The maximum pressure coefficient predicted by Eq. (2) using the hydraulic diameter is also included in Fig. 2. Clearly, even this revised Borda-Carnot relation gives rather poor results completely missing the trend of the experimental data.

The cause behind the erroneous trend is easily discerned when one considers the value of the Borda-Carnot relation at the two-dimensional expansion limit (case when AR → ∞). When $\sigma = \Delta_h^2$ is substituted in Eq. (2) according to the reasoning above, as AR → ∞, then $\sigma \to \mathrm{ER}^2$. However, for an ideal two-dimensional expansion the pressure recovery must be proportional to the geometric area ratio, which is ER, since no side walls are present to contain the flow and introduce three-dimensional effects. This inconsistency at the limit points to the fact that in the case of one- and two-sided planar expansions the definition of a ratio to capture the full geometric effect of the sudden enlargement needs to be based on linear, and not squared, length scales. Thus, the obvious solution is to modify Eq. (2) by removing the area ratio and instead using the hydraulic diameter ratio. This yields

$$C_{p,\Delta} = \frac{2}{\Delta_h}\left(1 - \frac{1}{\Delta_h}\right) \tag{4}$$

which is no longer inconsistent at the limiting value of AR → ∞ and incorporates effects of both ER and AR. The resulting curve given by Eq. (4) is shown in Figs. 1 and 2 for comparison. Unlike Eq. (2), the modified relation correctly follows the trend of the experimental data. It yields a higher pressure coefficient at recovery, which is expected since it is based on an idealized flow expansion that neglects upstream and downstream velocity profile non-uniformities, and losses due to turbulence, secondary flow motion and viscous dissipation.

Kays (1950) modified the Borda-Carnot relation to include the effect of a nonuniform velocity distribution upstream and downstream of the expansion by introducing a velocity distribution coefficient, $K = (1/A)\int_A (u/U_{\mathrm{avg}})^2 dA$. Incorporating this coefficient in the present case yields,

$$C_{p,\Delta_{NU}} = \frac{2\varphi_0^2}{\Delta_h}\left(K_0 - \frac{K_1}{\Delta_h}\right) \tag{5}$$

where φ_0 corrects for having defined the pressure coefficient in

terms of the upstream freestream (maximum) velocity and not in terms of the upstream average velocity, $U_{0,\text{avg}}$, that appears in K. The velocity distribution coefficient for nominally two-dimensional flow in a duct (simplest case for which relative spanwise non-uniformity is negligible in comparison to transverse nonuniformity) can be reasonably approximated assuming a velocity profile in the boundary layer that is a second-order polynomial for the laminar case and a simple power law for the turbulent case. This gives

$$K = \frac{1 - \frac{14}{15}\frac{\delta}{Y}}{\left(1 - \frac{2}{3}\frac{\delta}{Y}\right)^2};$$

$$\varphi = \frac{U_{\text{avg}}}{U_{\max}} = 1 - \frac{2}{3}\frac{d}{Y} \quad \text{laminar boundary layer,}$$

$$\frac{u}{U_{\max}} = \frac{y}{\delta}\left(2 - \frac{y}{\delta}\right)$$

$$K = \frac{1 - \frac{4m}{2m+1}\frac{\delta}{Y}}{\left(1 - \frac{2m}{m+1}\frac{\delta}{Y}\right)^2};$$

$$\varphi = 1 - \frac{2m}{m+1}\frac{\delta}{Y} \quad \text{turbulent boundary layer,}$$

$$\frac{u}{U_{\max}} = \left(\frac{y}{\delta}\right)^m \quad (6)$$

where δ is the boundary layer thickness, y is the distance from the wall, and $m \approx 1/7$. The expressions in Eq. (6) may be used if a reasonable estimate of the boundary layer thickness upstream of the step and in the recovery region is only available. However, if detailed velocity profile data is available then accurate evaluation of the velocity distribution coefficients upstream and downstream of the expansion is possible, which will yield an improved estimate of $C_{p,\max}$. For example, Westphal and Johnston (1984) reported velocity profiles at $x/h = -0.75$ and $x/h = 20$ for a one-sided expansion having AR = 12 and ER = 1.667. Integrating these profiles to get φ_0, K_0 and K_1, and substituting into Eq. (5) yields $C_{p,\Delta_{NU}} = 0.38$. The value of $C_{p,\max}$ extracted from their data is 0.37. The authors also reported velocity profiles, along the centerplane for several AR cases (see Papadopoulos and Ötügen, 1995). Considering the case AR = 20, ER = 2, then using the profiles at $x/h = -0.5$ and $x/h = 12$ yields $C_{p,\Delta_{NU}} = 0.42$, which is a few percent different from the experimental value of $C_{p,\max} = 0.394 \pm 0.018$.

4 Conclusions

A modified Borda-Carnot relation that incorporates correctly effects of ER and AR for one- and two-sided planar sudden expansions within ducts was presented. It is common practice to represent the pressure head loss of a system in terms of a velocity head multiplied by a loss coefficient, K_e. For axisymmetric and four-sided expansions K_e is equal to the difference between the ideal recovery and that given by the Borda-Carnot relation, namely $K_e = (1 - (1/\sigma))^2$. From the results of the present study it is concluded that for one- and two-sided planar sudden expansions within ducts the expansion loss coefficient is

$$K_e = \left(1 - \frac{1}{\Delta_h}\right)^2 + \frac{1}{\Delta_h^2}\left(1 - \frac{1}{\Delta_h^2}\right). \quad (6)$$

Furthermore, for a one-sided expansion the engineering applicability of Eq. (6) may be improved by noticing that the experimental data presented in the paper show an actual maximum pressure coefficient that is about 20% less than the theoretical. Hence, a correction factor may be incorporated into Eq. (6),

$$K_e = 1 - \frac{1}{\Delta_h^4} + \frac{2\kappa}{\Delta_h}\left(1 - \frac{1}{\Delta_h}\right) \quad (7)$$

where $\kappa = 0.80 \pm 0.03$, obtained by considering all the data in Fig. 2 within the range of $\Delta_h^{-1} < 0.8$. Configurations outside of this range are nominally momentum driven rather than pressure driven, which would constitute them as being "external" rather than internal flows and hence not well predicted by the Borda-Carnot relation. To the authors' knowledge no experimental pressure data is available in the open literature to help determine a similar correction factor to two-sided expansions.

References

Archer, W. H., 1913, "Experimental Determination of Loss of Head due to Sudden Enlargement in Circular Pipes," *Transactions of the ASCE,* Vol. 76, pp. 999–1026.

Badri Narayanan, M. A., Khadgi, Y. N., and Viswanath, P. R., 1974, "Similarities in Pressure Distribution in Separated Flow behind Backward-Facing Steps," *Aeronautical Quarterly,* Vol. 25, pp. 305–312.

Driver, D. M., Lee Seegmiller, H., and Marvin, J. G., 1987, "Time-dependent Behavior of a Reattaching Shear Layer," *AIAA Journal,* Vol. 25, pp. 914–919.

Eaton, J. K., 1980, "Turbulent Flow Reattachment: An Experimental Study of the Flow and Structure behind a Backward-Facing Step," Ph.D. thesis, Stanford University, California.

Farabee, T. M., and Casarella, M. J., 1986, "Measurements of Fluctuating Wall Pressure for Separated/Reattached Boundary Layer Flows," ASME JOURNAL OF FLUIDS ENGINEERING, Vol. 108, pp. 301–307.

Gai, S. L., and Sharma, S. D., 1987, "Pressure Distributions behind a Rearward Facing Segmented Step," *Experiments in Fluids,* Vol. 5, pp. 154–158.

Idelchik, I. E., 1986, *Handbook of Hydraulic Resistance,* 2nd Ed., Hemisphere Publishing, New York, NY.

Kays, W. M., 1950, "Loss Coefficient for Abrupt Changes in Flow Cross Section with Low Reynolds Number Flow in Single and Multiple Tube Systems," *Trans. ASME,* Vol. 72, No. 8, pp. 1067–1074.

Kim, J., Kline, S. J., and Johnston, J. P., 1980, "Investigation of a Reattaching Turbulent Shear Layer: Flow over a Backward-Facing Step," ASME JOURNAL OF FLUIDS ENGINEERING, Vol. 102, pp. 302–308.

Miller, D. S., 1990, *Internal Flow Systems,* 2nd Ed., Gulf Publishing Co., Houston, Texas.

Ötügen, M. V., 1991, "Expansion Ratio Effects on the Separated Shear Layer and Reattachment Downstream of a Backward-Facing Step," *Experiments in Fluids,* Vol. 10, pp. 273–280.

Papadopoulos, G., and Ötügen, M. V., 1995, "Separating and Reattaching Flow Structure in a Suddenly Expanding Rectangular Duct," ASME JOURNAL OF FLUIDS ENGINEERING, Vol. 117, pp. 17–23.

Ramamurthy, A. S., Balchandar, R., and Govinda Ram, H. S., 1991, "Some Characteristics of Flow Past Backward Facing Steps Including Cavitation Effects," ASME JOURNAL OF FLUIDS ENGINEERING, Vol. 113, pp. 278–284.

Schutt, H. C., 1929, "Losses of Pressure Head due to Sudden Enlargement of Flow Cross-Section," *Trans. ASME,* Vol. 51, pp. 83–87.

Shishov, E. V., Roganov, P. S., Grabarnik, S. I., and Zabolotsky, V. P., 1988, "Heat Transfer in the Recirculating Region formed by a Backward-Facing Step," *International Journal of Heat and Mass Transfer,* Vol. 31, pp. 1557–1562.

Westphal, R. V., and Johnston, J. P., 1984, "Effect of Initial Conditions on Turbulent Reattachment Downstream of a Backward-Facing Step," *AIAA Journal,* Vol. 22, pp. 1727–1732.

A Note on the Characteristics of Droplet-Laden Jets

R. Balachandar[1]

Introduction

In the recent past there has been increased attention focused on turbulent jets laden with both solid particles and droplets (Balachandar, 1994; Barlow et al., 1990; Hardalupas et al., 1989; Longmire and Eaton, 1992). Several examples of such jets can be found in civil and mechanical engineering practice. Many of the reported studies have generally dealt with the far flow field at low loading ratios [$\phi < 1$, ϕ = particle mass flux/carrier gas mass flux]. As rightly pointed out by Crowe (1993), more information is required at the higher loading ratios. Gore and Crow (1989) have observed that the presence of the particulate phase could either increase or decrease the carrier phase turbulent intensity. Interestingly, Elghobashi and Truesdell (1993) note that many of the experimental data on particle-laden flows are valid only for the specific conditions of the experiment and cannot be generalized.

The present study deals with an air jet laden with water droplets at a fairly large mass loading ratio ($\phi \approx 5$). The flow Reynolds number is low when compared to previous studies and measurements are conducted in the near jet region.

Experimental Setup and Procedure

Figure 1 shows the jet configuration together with the arrangements for metering the air flow. Here, Z refers to the coordinate along the jet axis. The fluid supply was drawn from the compressed shop air and a pressure regulator kept this flow constant, independent of the fluctuations in the supply pressure. An independent water source was used to pump water at a predetermined rate into a blast atomizer to maintain a constant water level in the atomizer. The atomizer was followed by a 90 deg bend and a nozzle contraction. The length of the vertical portion of the 90 deg bend was such that the larger droplets would fall back into the atomizer. The diameter of the nozzle exit (D) was 3.6 mm. The nozzle was preceded by a smooth 30:1 contraction to minimize the turbulence level at the exit. The geometric mean diameter of the water droplets at the nozzle exit was 5.88 μm and the geometric standard deviation was 1.54 μm. About 82 percent of the particles were in the range 3 to 8 μm indicating a fairly narrow distribution. The repeatability of this distribution was verified several times to ensure the generation of a recurring droplet size histogram at the nozzle exit. The Reynolds number based on the nozzle exit bulk air flow and jet exit diameter was 2814. The initial ratio of water droplet mass flux to air mass flux was 4.9. The particle momentum relaxation time (τ_p) which characterizes the inertia of the particle is 0.13 ms. Using this, one can calculate an exit Stokes number $St_e = \tau_p/(D/U_o)$ (Longmire and Eaton, 1992). Here, U_o is the bulk air velocity at the nozzle exit. For the present experimental conditions, the value of the Stokes number is less than 1 indicating that the droplets are fully responsive.

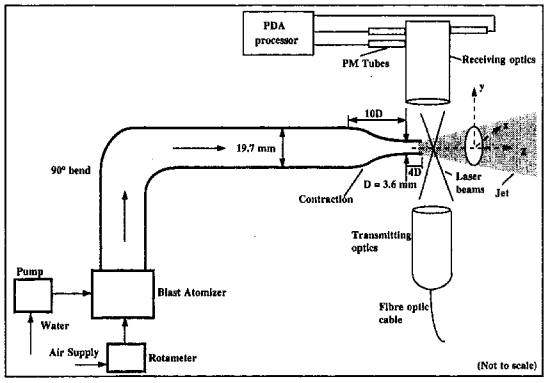

Fig. 1 Experimental setup

Details of the phase-Doppler anemometer (PDA) used and the relevant calibration procedures adopted are similar to that described in Balachandar et al. (1994). The transmitting and the receiving optics of the PDA are mounted on independent, computer controlled traversing mechanisms. This enabled the measurement of both size and velocity along the X direction in Fig. 1.

The variables of interest include the mean particle velocity (U), mean diameter (d_{mean}), particle rms velocity (u'), skewness ($S = \sum_{i=1}^{N} (u_i - U)^3/\sigma_u^3 N$), and flatness ($F = \sum_{i=1}^{N} (u_i - U)^4/\sigma_u^4 N$) of the particle velocities. Here, u_i refers to the velocity associated with a particular droplet of diameter d_i and N (=10,000) is the sample size. At any axial station, the value of U along the jet axis is indicated as U_a. A simple covariance correlation factor (ρ) describing the possible dependence of particle size on its velocity is also obtained at various locations in the jet. Here, ρ is defined as:

$$\rho = \frac{\frac{1}{N-1}\sum_{1}^{N}(u_i - U)(d_i - d_{\text{mean}})}{\sigma_u \sigma_d}$$

Here, σ_u is the velocity standard deviation and σ_d is the droplet size standard deviation. A measure of the strength of the linear association between the droplet diameter and droplet velocity is indicated by ρ. The values of ρ lie in the range -1 to 1. A strong positive correlation (smaller particles associated with lower velocities) is indicated by a value of ρ close to $+1$ while a strong negative correlation is indicated by a value of ρ close to -1 (larger particles associated with lower velocities or smaller particles associated with larger velocities). A value of $\rho = 0$ indicates that there is no correlation between droplet size and velocity.

Results

Figure 2 shows the variation of the longitudinal mean particle velocity at various axial stations. It is clear from Fig. 2 that the velocity distributions collapse fairly to a single line for $Z/D > 4.0$. This self-similar nature has been previously observed by numerous researchers (e.g., Wygnanski and Fiedler, 1969 and Hussein et al., 1994) and serves to confirm the quality of measurements in the present study. Compared to previous studies, the present data indicate that the self-similar nature is found to occur at smaller values of Z/D. Also shown in Fig. 2 are the results of Kumar et al. (1989) at $Z/D = 3.2$ (Reynolds number = 4716, volume fraction = 6.7).

An important aspect to note in the present study is that the normalized droplet mean velocities are higher than the single-phase flow values in the self-similar range (Fig. 3). The present set of data compare favorably with the results of Kumar et al.

[1] Associate Professor, Department of Civil Engineering, University of Saskatchewan, Saskatoon, Canada, S7N 5A9.

Contributed by the Fluids Engineering Division of THE AMERICAN SOCIETY OF MECHANICAL ENGINEERS. Manuscript received by the Fluids Engineering Division May 13, 1996; revised manuscript received January 13, 1998. Associate Technical Editor: J. K. Eaton.

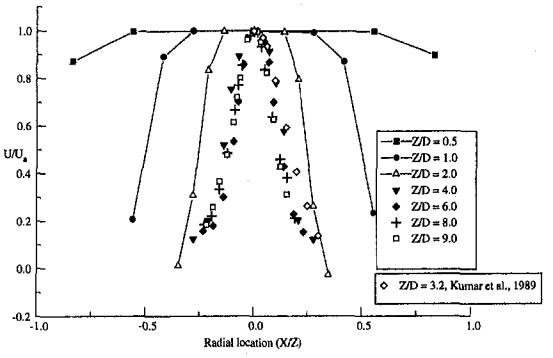

Fig. 2 Radial distribution of mean droplet velocity at various axial stations (Uncertainty in mean velocity = ±2.5 percent, Uncertainty in location = ±2.5 percent)

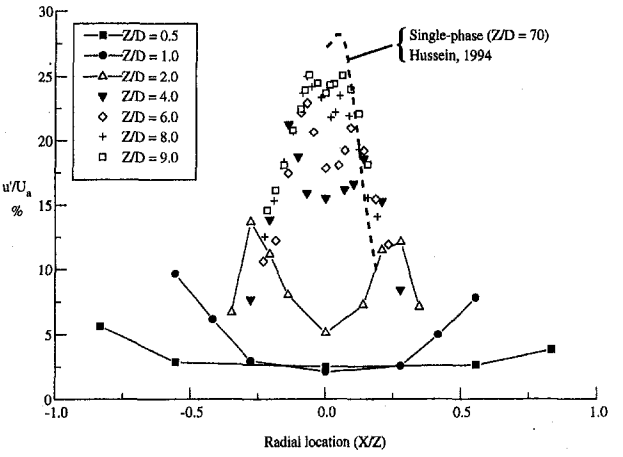

Fig. 4 Radial distribution of droplet rms. velocity at various axial stations (Uncertainty in typical rms. velocity = ±3 percent, Uncertainty in location = ±2.5 percent)

(1989). Moreover, the present results and that of Kumar et al. (1989) indicate that the rate expansion of the jet is higher than reported previously. Previous measurements (Popper et al., 1974; Hetsroni and Sokolov, 1971; Balachandar et al., 1996) in two-phase flow indicate that the droplet/particle velocities are consistently lower than the single-phase flow curve. In the present study, the value of the jet spreading coefficient is around 0.10. Hetsroni and Sokolov (1971) found a value of 0.071 for single-phase jets and values ranging from 0.057 to 0.069 for two-phase jets. Furthermore, the measurements of Hetsroni and Sokolov (1971) indicate that the spreading of the jet decreased with increasing droplet loading ratio. In the present study, this ratio is several folds higher than that of Hetsroni and Sokolov (1971) and the radial variation of the streamwise mean velocity does not conform to their results. It should be noted that the present tests and that of Kumar et al. were carried out at a lower Reynolds number. Under this circumstance, it can be expected that the buoyancy effects may dominate the fluid inertia and increase the jet width.

It should be remarked that higher-order velocity moments, such as, turbulence intensity, skewness, and flatness are useful continuum field concepts. In the present context, droplets are discrete entities. However, the higher order droplet velocity moments would provide useful flow descriptions and enable better comparison with other studies. With this prequalification, Fig. 4 shows the radial variation of the particle rms velocity at various axial stations. The presence of particles alter the turbulent structure of the flow field (Gore and Crow, 1989). For $Z/D > 4$, the data do not completely collapse on to a single curve. The single-phase results of Hussein et al. (1994) is also shown in the figure.

A measure of the relative skewness (S) of the velocity probability density function is shown in Fig. 5. Similar to single-phase flow observations of Wygnanski and Fiedler (1969), the values of S decrease from the jet periphery toward the center. From Fig. 5, one can note that, for $Z/D \leq 4.0$, the values of S increase with increasing Z/D. For greater Z/D, the radial distribution of S tend to collapse onto a single curve. Furthermore, in this range of Z/D, the values of S in the axial regions tend to a value of zero. This is the value expected for a Gaussian distribution. In general, a sensitive test of the closeness of fit over the outer parts of the probability density function is provided by the relative magnitude of the flatness of the distribution. Figure 6 shows the radial variation of the flatness factor (F) at various Z/D. There is a gradual decrease in F with increasing Z/D and once again for $Z/D > 4$, the data fall on a single curve. Thus, both the lower and higher order moments indicate similarity for $Z/D > 4$. The value of F obtained in the core regions of the jet resemble the values obtained in single-phase flows and tends to be close to the Gaussian distribution value of 3.0.

Figure 7 which shows the radial variation of the mean diameter at various axial stations. The first three axial stations ($Z/D \leq 2$) show no significant differences in the size distribution. However, beyond $Z/D = 2$, there is an increase in mean size with increasing Z/D. This may be a consequence of coalescence due to turbulence and/or due to droplet collisions. The increase in size may also be accounted for by the larger end of the size

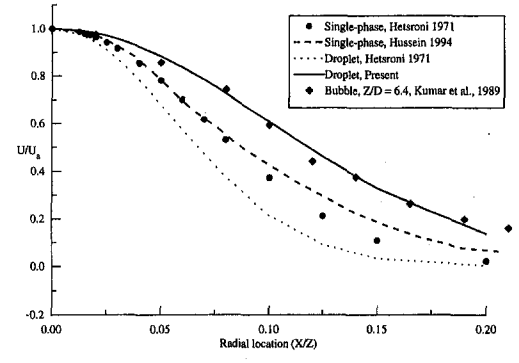

Fig. 3 Radial distribution of mean velocity in the self-similar region (Uncertainty in mean velocity = ±2.5 percent, Uncertainty in location = ±2.5 percent)

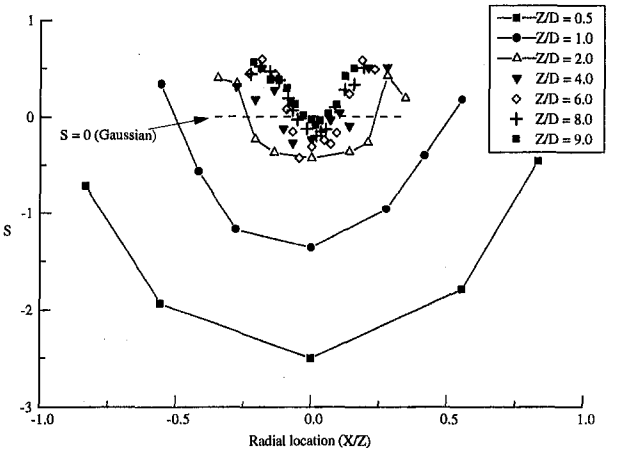

Fig. 5 Radial distribution of droplet velocity skewness at various axial stations (Uncertainty in a typical value of S = ±3 percent, Uncertainty in location = ±2.5 percent)

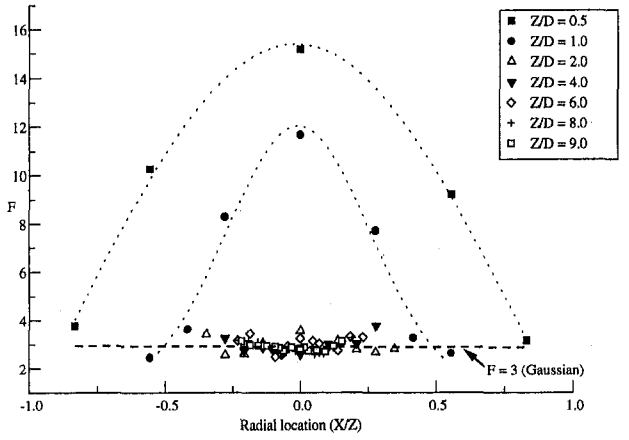

Fig. 6 Radial distribution of droplet velocity flatness factor at various axial stations (Uncertainty in F = ±5 percent, Uncertainty in location = ±2.5 percent)

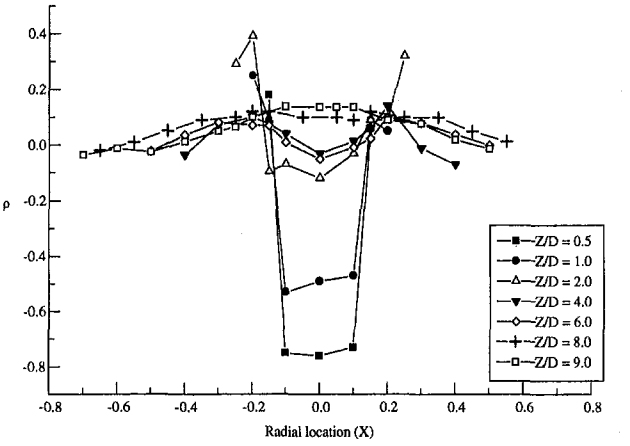

Fig. 8 Radial variation of covariance correlation factor at various axial stations (Uncertainty in ρ = ±5 percent, Uncertainty in location = ±2.5 percent)

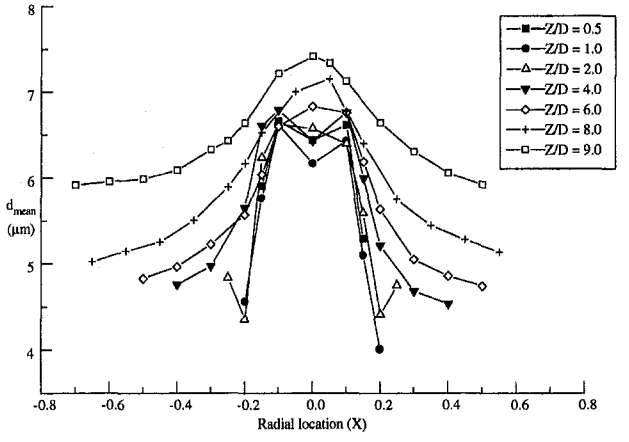

Fig. 7 Radial variation of mean diameter at various axial stations (Uncertainty in mean diameter = ±4 percent, Uncertainty in location = ±2.5 percent)

distribution retaining its momentum and passing the smaller droplets as Z/D increases.

It is expected that the variations in droplet velocity skewness and flatness noted earlier could be a consequence of size variations in the dispersed phase across the jet cross-section. In this regard, an understanding of the size-velocity dependence would be an useful aspect. Figure 8 shows the radial variation of ρ at the seven axial stations. In sections closer to the nozzle ($Z/D \leq 1$) and in the core regions of the jet, there is a strong negative linear correlation between size and velocity, reflecting the fact that the smaller particles tend to travel at higher velocities. As the fluid and the droplets traverse the nozzle contraction, the smaller particles respond faster and are accelerated with the flow while the larger particles lag behind resulting in a negative value of ρ. Figure 8 also indicates that in the sections closer to the nozzle and in the peripheral regions of the jet, there is a decrease in negative correlation and ρ tends towards zero. At these locations, from Fig. 7, one notes that the mean particle size decreases along the radius toward the outer edge. From these two figures, one can conclude that for $Z/D \leq 1$, in the peripheral regions, the particles are small and tend to travel with similar velocities. As one proceeds to larger values of Z/D up to 6, the values of ρ are increasing toward zero, i.e., with increasing Z/D, one would be tempted to conclude that there has been a fair equalization of momentum and all the particles are traveling at nearly the same velocity. Since the very small particles tend to travel at the same velocity as the larger particles, it may be fair to assume that the gas-phase velocity and the droplet velocity are nearly equal. Consequently, at larger distances from the jet exit, the distribution of the higher-order velocity moments resemble that noticed in single-phase flows. For $Z/D \geq 8$, Fig. 8 shows a slight positive correlation indicating that larger particles may be traveling with larger velocities. For a given data acquisition time, relatively more larger particles would be seen at these locations. Consequently, there would be an increase in the mean diameter as reflected in Fig. 7.

Conclusions

The air jet laden with water droplets at a large mass loading ratio is self-similar for axial distances greater than the potential core of the jet. However, the rate of spreading of the jet is higher than that noticed in both single-phase flow and some previous two-phase flow studies. The radial variation particle velocity skewness and flatness indicate that the similarity is valid at the higher order moments for $Z/D > 4.0$. There is an increase in droplet size with increasing distance from the nozzle for $Z/D > 4.0$. In the early regions of the jet, the water droplet size and velocity are strongly correlated, especially in the core regions. With increasing Z/D, there is a decrease in association between size and velocity.

References

Balachandar, R., Mulpuru, S., and Ungurian, M. H., 1994, "A Note on Particle Size Measurements in Two-Phase Flows," FED-Vol 180, *Experimental and Computational Aspects of Validation of Multiphase Flow* CFD Codes, ASME, pp. 107–117.

Balachandar, R., Mulpuru, S. and Ungurian, M. H., 1996, "A Study on the Transport of Dry Aerosols in Turbulent Jets," Under review for possible publication in the *Journal of Environmental Engineering,* ASCE.

Barlow, R. S., and Morrison, C. Q., 1990, "Two-Phase Velocity Measurements in Dense Particle Laden Jets," *Experiments in Fluids,* Vol. 9, pp. 93–104.

Crowe, C. T., 1993, "Basic Research in Fluid-Solid Multiphase Flows," Technical Forum, ASME JOURNAL OF FLUIDS ENGINEERING, Vol. 115, pp. 341–342.

Elghobashi, S. and Truesdell, G. C., 1993, "On the Two-Way Interaction Between Homogeneous Turbulence and Dispersed Solid Particles. I: Turbulence Modification," *Physics of Fluids,* Vol. 5, No. 7, pp. 1790–1801.

Gore, R. A., and Crowe, C. T., 1989, "Effect of Particle Size on Modulating Turbulence Intensity," *International Journal of Multiphase Flow,* Vol. 15, No. 2, pp. 279–285.

Hardalupas, Y., Taylor, A. M. P. K., and Whitelaw, J. H., 1989, "Velocity and Particle-Flux Characteristics of Turbulent Particle-Laden Jets," *Proceedings of the Royal Society,* Series A 426, pp. 31–78.

Hetsroni, G., and Sokolov, M., 1971, "Distribution of Mass, Velocity and Intensity of Turbulence in a Two-Phase Turbulent Jet," ASME *Journal of Applied Mechanics,* pp. 315–327.

Hussein, J. H., Capp, S. P., and George, W. K., 1994, "Velocity Measurements in a High-Reynolds-Number, Momentum Conserving, Axisymmetric, Turbulent Jet," *Journal of Fluid Mechanics,* Vol. 258, pp. 31–75.

Kumar, S., Nikitopoulos, D. N. and Michaelides, E. E., 1989, "Effect of Bubbles on the Turbulence Near the Exit of a Liquid Jet," *Experiments in Fluids,* Vol. 7, pp. 487–494.

Longmire, E. K., and Eaton, J. K., 1992, "Structure of Particle-Laden Round Jet," *Journal of Fluid Mechanics,* Vol. 236, pp. 217–257.

Popper, J., Abauf, N. and Hetsroni, G., 1974, "Velocity Measurements in a Two-Phase Turbulent Jet," *International Journal of Multiphase Flow,* 1, pp. 715–726.

Wygnanski, I. and Fiedler, H., 1969, "Some Measurements in the Self Preserving Jet," *Journal of Fluid Mechanics,* Vol. 38, Part 3, pp. 577–612.

An h-Adaptive Finite Element Model for Environmental Transport Prediction

D. B. Carrington[1] and D. W. Pepper[1]

Introduction

It is widely recognized that major pollution problems and potential hazardous consequences now exist worldwide. Such concerns have lead to increased efforts in pollution transport and diffusion modeling by many researchers (Pielke, 1984; Domenico and Schwartz, 1990).

A rapid, h-adaptive finite element model has been developed to calculate 2- and 3-D environmental fluid flow and species transport. The model runs on enhanced PCs, SGI workstations, and Cray class supercomputers.

The employment of adapting, unstructured meshes permits one to accurately solve large problems with a reduced number of nodal points. This is accomplished by concentrating (refining) nodes in those regions where most of the activity takes place, and unrefining in regions where solutions are smooth. However, the key to successful implementation of adaptive mesh techniques is in the choice of element type, handling of interface transitions, and rapid mesh refinement and unrefinement operations during the transient solution. Adaptive techniques are currently being used to simulate a wide range of complex flows, e.g., groundwater transport in porous media (Pepper and Stephenson, 1995), atmospheric transport over complex terrain (Pepper and Carrington, 1995), and compressible flows with shock capture (Devloo et al., 1988).

Finite Element Approach

Atmospheric Flow and Species Transport. The standard weak formulation of the Galerkin weighted residual method is used to discretize the atmospheric equations of motion and energy (Pepper, 1990).

Atmospheric turbulence is simplified by using the horizontal exchange coefficient developed by Smagorinsky et al. (1965). An explicit Euler scheme is used to advance the solution in time. Mass lumping is employed. In order to reduce numerical dispersion, a Petrov-Galerkin technique is used for the advection terms (Yu and Heinrich, 1986). The use of this weighting function selectively eliminates the dispersive computational noise associated with steep gradient resolution.

Groundwater Flow and Species Transport. The governing equations for groundwater flow and subsurface contaminant transport are well known (Domenico and Schwartz, 1990). The standard weak formulation of the Galerkin weighted residual method is used to discretize the governing equations for groundwater head and species transport (Pepper and Stephenson, 1995).

A Picard iteration is used to achieve convergence for pressure head for the unsaturated model. A Petrov-Galerkin scheme is also used to weight the advection terms, and an explicit forward-in-time Euler scheme used to advance the solution in time.

The *h*-Adaptation Method. Quadrilateral and hexahedral elements are used in the discretization of 2-D and 3-D domains respectively, even though they create virtual nodes when refined. These nodes must be tied back to the corner nodes, thus creating an element with extra node(s) on a face causing a serious mesh compatibility problem. This problem is usually handled with some elaborate bookkeeping. Although more computationally inhibiting as the number of nodes increases—especially when the problem is three-dimensional—element distortion is generally limited, and permits use of reduced integration. Rules regarding the refinement and unrefinement of elements and nodal connectivity are discussed in Pepper and Stephenson (1995).

Model Results

1) **Atmospheric Flow Over a Ridge.** Transient dispersion is simulated using mesh adaptation associated with the transport of contaminant from an elevated (z = 50 m), constant source (S = 100 gm/m^3-s) upwind of two ridges. A constant wind (u = 5 m/s) is assumed to flow into the problem domain from the left boundary. The vertical and lateral dimensions are 600 m and 2000 m, respectively; the height of the small ridge is 100 m while the larger ridge is 300 m. Figure 1(a, b) shows the final mesh and concentration pattern after 400 seconds. The original mesh consisted of 220 elements; the adapted mesh contained a total of 884 elements.

The concentration diffuses towards the surface between the ridges and continues to be transported horizontally over the surface of the higher ridge. Knowledge of where such regions occur is essentially unknown prior to obtaining a complete solution; this typically requires *global* remeshing of the problem

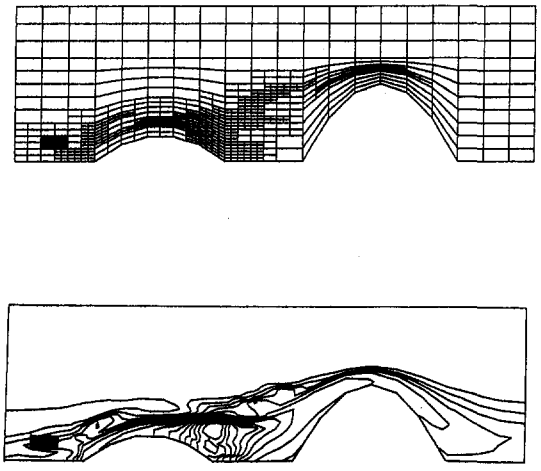

Fig. 1 Atmospheric transport from an elevated source. (*a*) Adapted mesh; (*b*) concentration transport

[1] Graduate Student and Professor and Chairman, respectively, Department of Mechanical Engineering, University of Nevada, Las Vegas, Las Vegas, NV 89154-4027. Professor Pepper is a Fellow ASME.

Contributed by the Fluids Engineering Division of THE AMERICAN SOCIETY OF MECHANICAL ENGINEERS. Manuscript received by the Fluids Engineering Division October 2, 1996; revised manuscript received March 3, 1998. Associate Technical Editor: P. W. Bearman.

Hussein, J. H., Capp, S. P., and George, W. K., 1994, "Velocity Measurements in a High-Reynolds-Number, Momentum Conserving, Axisymmetric, Turbulent Jet," *Journal of Fluid Mechanics,* Vol. 258, pp. 31–75.

Kumar, S., Nikitopoulos, D. N. and Michaelides, E. E., 1989, "Effect of Bubbles on the Turbulence Near the Exit of a Liquid Jet," *Experiments in Fluids,* Vol. 7, pp. 487–494.

Longmire, E. K., and Eaton, J. K., 1992, "Structure of Particle-Laden Round Jet," *Journal of Fluid Mechanics,* Vol. 236, pp. 217–257.

Popper, J., Abauf, N. and Hetsroni, G., 1974, "Velocity Measurements in a Two-Phase Turbulent Jet," *International Journal of Multiphase Flow,* 1, pp. 715–726.

Wygnanski, I. and Fiedler, H., 1969, "Some Measurements in the Self Preserving Jet," *Journal of Fluid Mechanics,* Vol. 38, Part 3, pp. 577–612.

An h-Adaptive Finite Element Model for Environmental Transport Prediction

D. B. Carrington[1] and D. W. Pepper[1]

Introduction

It is widely recognized that major pollution problems and potential hazardous consequences now exist worldwide. Such concerns have lead to increased efforts in pollution transport and diffusion modeling by many researchers (Pielke, 1984; Domenico and Schwartz, 1990).

A rapid, h-adaptive finite element model has been developed to calculate 2- and 3-D environmental fluid flow and species transport. The model runs on enhanced PCs, SGI workstations, and Cray class supercomputers.

The employment of adapting, unstructured meshes permits one to accurately solve large problems with a reduced number of nodal points. This is accomplished by concentrating (refining) nodes in those regions where most of the activity takes place, and unrefining in regions where solutions are smooth. However, the key to successful implementation of adaptive mesh techniques is in the choice of element type, handling of interface transitions, and rapid mesh refinement and unrefinement operations during the transient solution. Adaptive techniques are currently being used to simulate a wide range of complex flows, e.g., groundwater transport in porous media (Pepper and Stephenson, 1995), atmospheric transport over complex terrain (Pepper and Carrington, 1995), and compressible flows with shock capture (Devloo et al., 1988).

Finite Element Approach

Atmospheric Flow and Species Transport. The standard weak formulation of the Galerkin weighted residual method is used to discretize the atmospheric equations of motion and energy (Pepper, 1990).

Atmospheric turbulence is simplified by using the horizontal exchange coefficient developed by Smagorinsky et al. (1965). An explicit Euler scheme is used to advance the solution in time. Mass lumping is employed. In order to reduce numerical dispersion, a Petrov-Galerkin technique is used for the advection terms (Yu and Heinrich, 1986). The use of this weighting function selectively eliminates the dispersive computational noise associated with steep gradient resolution.

Groundwater Flow and Species Transport. The governing equations for groundwater flow and subsurface contaminant transport are well known (Domenico and Schwartz, 1990). The standard weak formulation of the Galerkin weighted residual method is used to discretize the governing equations for groundwater head and species transport (Pepper and Stephenson, 1995).

A Picard iteration is used to achieve convergence for pressure head for the unsaturated model. A Petrov-Galerkin scheme is also used to weight the advection terms, and an explicit forward-in-time Euler scheme used to advance the solution in time.

The *h*-Adaptation Method. Quadrilateral and hexahedral elements are used in the discretization of 2-D and 3-D domains respectively, even though they create virtual nodes when refined. These nodes must be tied back to the corner nodes, thus creating an element with extra node(s) on a face causing a serious mesh compatibility problem. This problem is usually handled with some elaborate bookkeeping. Although more computationally inhibiting as the number of nodes increases—especially when the problem is three-dimensional—element distortion is generally limited, and permits use of reduced integration. Rules regarding the refinement and unrefinement of elements and nodal connectivity are discussed in Pepper and Stephenson (1995).

Model Results

1) Atmospheric Flow Over a Ridge. Transient dispersion is simulated using mesh adaptation associated with the transport of contaminant from an elevated (z = 50 m), constant source (S = 100 gm/m^3-s) upwind of two ridges. A constant wind (u = 5 m/s) is assumed to flow into the problem domain from the left boundary. The vertical and lateral dimensions are 600 m and 2000 m, respectively; the height of the small ridge is 100 m while the larger ridge is 300 m. Figure 1(a, b) shows the final mesh and concentration pattern after 400 seconds. The original mesh consisted of 220 elements; the adapted mesh contained a total of 884 elements.

The concentration diffuses towards the surface between the ridges and continues to be transported horizontally over the surface of the higher ridge. Knowledge of where such regions occur is essentially unknown prior to obtaining a complete solution; this typically requires *global* remeshing of the problem

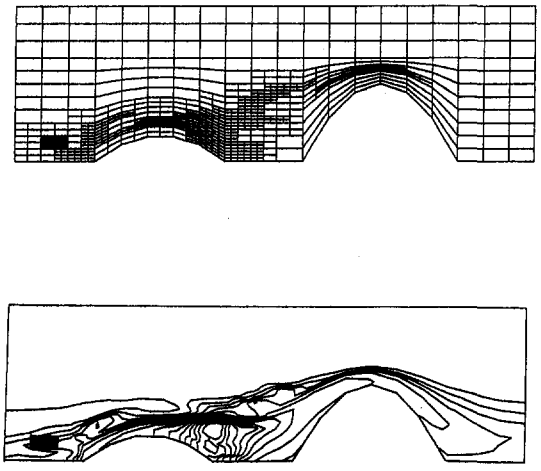

Fig. 1 Atmospheric transport from an elevated source. (*a*) Adapted mesh; (*b*) concentration transport

[1] Graduate Student and Professor and Chairman, respectively, Department of Mechanical Engineering, University of Nevada, Las Vegas, Las Vegas, NV 89154-4027. Professor Pepper is a Fellow ASME.

Contributed by the Fluids Engineering Division of THE AMERICAN SOCIETY OF MECHANICAL ENGINEERS. Manuscript received by the Fluids Engineering Division October 2, 1996; revised manuscript received March 3, 1998. Associate Technical Editor: P. W. Bearman.

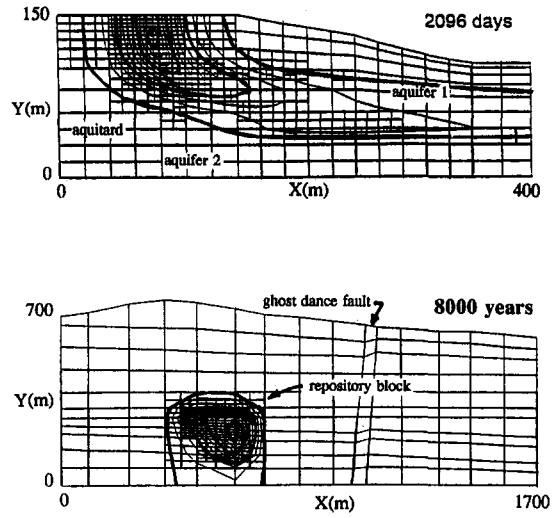

Fig. 2 Groundwater media and species transport (a) saturated media (Savannah river site); (b) unsaturated media (Yucca Mountain)

when using non-adapting finite element and finite difference methods.

2) Subsurface Transport of Toxic Material

(a) Saturated Case. Transient dispersion in saturated porous media is simulated using mesh adaptation for a buried leaking container (constant source). Figure 2(*a*) shows the final adapted mesh and concentration contours after 2096 days. The initial mesh contained 171 elements—which is coarse. Hydraulic conductivities typical of the strata found at the Savannah River Site were used (Pepper and Stephenson, 1995). In aquifer 1, $k_{xx} = 1.10$ (m/day), $k_{yy} = 6.0 \times 10^{-3}$; in the aquitard, $k_{xx} = 1.0 \times 10^{-7}$ and $k_{yy} = 6.0 \times 10^{-5}$. In aquifer 2, the conductivities are $k_{xx} = 1.20$ and $k_{yy} = 6.0 \times 10^{-5}$. Several adaptations have occurred during the transient solution of the contaminant transport. The final mesh contains 684 elements. The concentration has slowed its vertical descent and is being transported horizontally along the upper surface of the aquitard.

(b) Unsaturated Case. Groundwater flow and species transport within unsaturated porous media is calculated for a constant source in a representative cross-section of the proposed Yucca Mountain Repository for nuclear waste. Figure 2(*b*) shows the final adapted mesh and concentration contours after 8000 years. The initial mesh contained 165 elements. Conductivities typical of the strata found at Yucca Mountain were used, e.g., $k_{xx} = k_{yy} = 7.0 \times 10^{-4}$ (m/day). A constant infiltration rate of 0.1 mm/yr was assumed at the top boundary. After several adaptations, the final mesh contained 495 elements. Model results indicate that the concentration begins to reach the water table (bottom boundary) after approximately 8000 years.

Conclusions

The development and implementation of an h-adaptive algorithm with a general finite element solver has been achieved for predicting species transport and dispersion within complex problem geometries. Coupling h-adaptation with a Petrov-Galerkin finite element algorithm produces very accurate solutions while minimizing computer time and storage demands.

The finite element method, when coupled with h-adaptation, is well suited for calculating atmospheric and groundwater transport. Future research efforts will include the use of Delaunay triangulation (with the ability to produce hexahedrals), and h-p adaptation.

References

Devloo, P., Oden, J. T., and Pattani, P., 1988, "An h-p Adaptive Finite Element Method for the Numerical Simulation of Compressible Flow," *Computational Methods in Applied Mechanics and Engineering,* Vol. 70, pp. 203–235.

Domenico, P. A., and Schwartz, F. W., 1990, *Physical and Chemical Hydrogeology,* Wiley, New York.

Pepper, D. W., 1990, "A 3-D Numerical Model for Predicting Mesoscale Windfields over Vandenberg Air Force Base," *Final Report USAF/AFSC F04701-89-C-0051,* Advanced Projects Research, Inc., Moorpark, CA.

Pepper, D. W., and Carrington, D. B., 1995, "An h-Adaptive Finite Element Model for 3-D Atmospheric Transport Prediction," *3rd International Air Pollution Conference,* Porto Carras, Greece, Sept. 26–28.

Pepper, D. W., and Stephenson, D. E., 1995, "An Adaptive Finite Element Model for Calculating Subsurface Transport of Contaminant," *Ground Water,* Vol. 33, No. 3, pp. 486–496.

Pielke, R. A., 1984, *Mesoscale Meteorological Modeling,* Academic Press, Orlando, FL.

Smagorinsky, J., Manabe, S., and Holloway, J. L., 1965, "Numerical Results from a Nine-Level General Circulation Model of the Atmosphere," *Monthly Weather Review,* Vol. 93, pp. 727–798.

Yu, C.-C., and Heinrich, J. C., 1986, "Petrov-Galerkin Methods for the Time-Dependent Convective Transport Equation," *International Journal of Numerical Methods in Engineering,* Vol. 23, pp. 883–901.

On the Wall-Pressure Spectrum Under a Three-Dimensional Boundary Layer

Ronald L. Panton[1]

Introduction

The pressure under a three-dimensional turbulent boundary layer is a function of wall position and time $p(x_1, x_3, t)$. Regard x_1 as the free-stream direction and x_3 as the secondary direction. Fourier transforms with regard to time and space produce a spectrum

$$\Phi(k_1, k_3, \omega) \tag{1}$$

Long ago Taylor recognized that the dominant process in turbulence statistics is the convection of a nearly frozen pattern of fluctuations. The corresponding Fourier model is the superposition of waves of wavenumber **k** traveling with phase speed **c**. Thus, the independent variables **k**, **c** are more closely related to Taylor's hypothesis than the variables **k**, ω. In two-dimensional layers convection is only in the x_1 direction with the phase speed

$$c_1 \equiv \omega / k_1 \tag{2}$$

Defining a phase velocity in three-dimensional layers poses a dilemma because the spectrum has three independent variables, k_1, k_3, ω, whereas there are four variables in k_1, k_3, c_1, c_3. The information in a spectrum $\Phi(k_1, k_3, \omega)$ is insufficient to allow four variables. Another issue is that the inviscid motions in a two-dimensional turbulent wall layer produce a mean velocity profile $U(y)$ that correlates in the form

[1] J. H. Herring Professor, Mechanical Engineering Department, University of Texas, Austin, TX 78712. Fellow ASME.

Contributed by the Fluids Engineering Division of THE AMERICAN SOCIETY OF MECHANICAL ENGINEERS. Manuscript received by the Fluids Engineering Division April 25, 1997; revised manuscript received March 2, 1998. Associate Technical Editor: P. R. Bandyopadhyay.

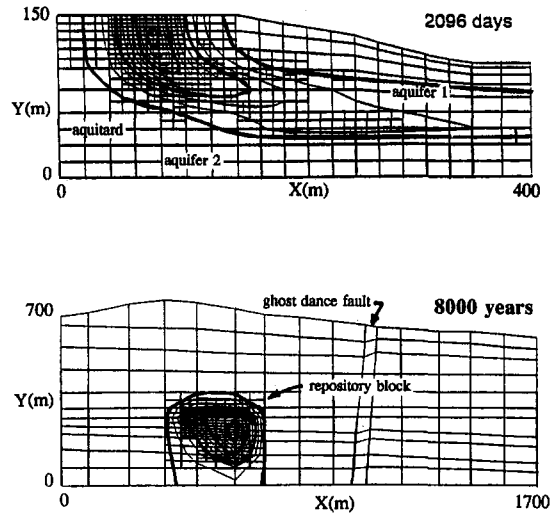

Fig. 2 Groundwater media and species transport (a) saturated media (Savannah river site); (b) unsaturated media (Yucca Mountain)

when using non-adapting finite element and finite difference methods.

2) Subsurface Transport of Toxic Material

(a) Saturated Case. Transient dispersion in saturated porous media is simulated using mesh adaptation for a buried leaking container (constant source). Figure 2(*a*) shows the final adapted mesh and concentration contours after 2096 days. The initial mesh contained 171 elements—which is coarse. Hydraulic conductivities typical of the strata found at the Savannah River Site were used (Pepper and Stephenson, 1995). In aquifer 1, $k_{xx} = 1.10$ (m/day), $k_{yy} = 6.0 \times 10^{-3}$; in the aquitard, $k_{xx} = 1.0 \times 10^{-7}$ and $k_{yy} = 6.0 \times 10^{-5}$. In aquifer 2, the conductivities are $k_{xx} = 1.20$ and $k_{yy} = 6.0 \times 10^{-5}$. Several adaptations have occurred during the transient solution of the contaminant transport. The final mesh contains 684 elements. The concentration has slowed its vertical descent and is being transported horizontally along the upper surface of the aquitard.

(b) Unsaturated Case. Groundwater flow and species transport within unsaturated porous media is calculated for a constant source in a representative cross-section of the proposed Yucca Mountain Repository for nuclear waste. Figure 2(*b*) shows the final adapted mesh and concentration contours after 8000 years. The initial mesh contained 165 elements. Conductivities typical of the strata found at Yucca Mountain were used, e.g., $k_{xx} = k_{yy} = 7.0 \times 10^{-4}$ (m/day). A constant infiltration rate of 0.1 mm/yr was assumed at the top boundary. After several adaptations, the final mesh contained 495 elements. Model results indicate that the concentration begins to reach the water table (bottom boundary) after approximately 8000 years.

Conclusions

The development and implementation of an h-adaptive algorithm with a general finite element solver has been achieved for predicting species transport and dispersion within complex problem geometries. Coupling h-adaptation with a Petrov-Galerkin finite element algorithm produces very accurate solutions while minimizing computer time and storage demands.

The finite element method, when coupled with h-adaptation, is well suited for calculating atmospheric and groundwater transport. Future research efforts will include the use of Delaunay triangulation (with the ability to produce hexahedrals), and h-p adaptation.

References

Devloo, P., Oden, J. T., and Pattani, P., 1988, "An h-p Adaptive Finite Element Method for the Numerical Simulation of Compressible Flow," *Computational Methods in Applied Mechanics and Engineering,* Vol. 70, pp. 203–235.

Domenico, P. A., and Schwartz, F. W., 1990, *Physical and Chemical Hydrogeology,* Wiley, New York.

Pepper, D. W., 1990, "A 3-D Numerical Model for Predicting Mesoscale Windfields over Vandenberg Air Force Base," *Final Report USAF/AFSC F04701-89-C-0051,* Advanced Projects Research, Inc., Moorpark, CA.

Pepper, D. W., and Carrington, D. B., 1995, "An h-Adaptive Finite Element Model for 3-D Atmospheric Transport Prediction," *3rd International Air Pollution Conference,* Porto Carras, Greece, Sept. 26–28.

Pepper, D. W., and Stephenson, D. E., 1995, "An Adaptive Finite Element Model for Calculating Subsurface Transport of Contaminant," *Ground Water,* Vol. 33, No. 3, pp. 486–496.

Pielke, R. A., 1984, *Mesoscale Meteorological Modeling,* Academic Press, Orlando, FL.

Smagorinsky, J., Manabe, S., and Holloway, J. L., 1965, "Numerical Results from a Nine-Level General Circulation Model of the Atmosphere," *Monthly Weather Review,* Vol. 93, pp. 727–798.

Yu, C.-C., and Heinrich, J. C., 1986, "Petrov-Galerkin Methods for the Time-Dependent Convective Transport Equation," *International Journal of Numerical Methods in Engineering,* Vol. 23, pp. 883–901.

On the Wall-Pressure Spectrum Under a Three-Dimensional Boundary Layer

Ronald L. Panton[1]

Introduction

The pressure under a three-dimensional turbulent boundary layer is a function of wall position and time $p(x_1, x_3, t)$. Regard x_1 as the free-stream direction and x_3 as the secondary direction. Fourier transforms with regard to time and space produce a spectrum

$$\Phi(k_1, k_3, \omega) \tag{1}$$

Long ago Taylor recognized that the dominant process in turbulence statistics is the convection of a nearly frozen pattern of fluctuations. The corresponding Fourier model is the superposition of waves of wavenumber **k** traveling with phase speed **c**. Thus, the independent variables **k**, **c** are more closely related to Taylor's hypothesis than the variables **k**, ω. In two-dimensional layers convection is only in the x_1 direction with the phase speed

$$c_1 \equiv \omega / k_1 \tag{2}$$

Defining a phase velocity in three-dimensional layers poses a dilemma because the spectrum has three independent variables, k_1, k_3, ω, whereas there are four variables in k_1, k_3, c_1, c_3. The information in a spectrum $\Phi(k_1, k_3, \omega)$ is insufficient to allow four variables. Another issue is that the inviscid motions in a two-dimensional turbulent wall layer produce a mean velocity profile $U(y)$ that correlates in the form

[1] J. H. Herring Professor, Mechanical Engineering Department, University of Texas, Austin, TX 78712. Fellow ASME.

Contributed by the Fluids Engineering Division of THE AMERICAN SOCIETY OF MECHANICAL ENGINEERS. Manuscript received by the Fluids Engineering Division April 25, 1997; revised manuscript received March 2, 1998. Associate Technical Editor: P. R. Bandyopadhyay.

$$F\left(\frac{y}{\delta}\right) = \frac{U(y) - U_\infty}{u_*} \tag{3}$$

Here U_∞ is the free-stream velocity, δ the layer thickness, and u^* the friction velocity. For two-dimensional layers Panton and Robert (1993) found negligible Reynolds number influence in the spectrum when k_1, and $c_1 \equiv \omega/k_1$ were used as variables and the phase velocity was expressed in a defect form analogous to Eq. (3); that is, $C(y/\delta) \equiv [c_1(k_1) - U_\infty]/u*$.

Phase Velocity and Spectra in Skewed 3-D Layers

As a preliminary step consider a eddy that produces the Fourier pressure component

$$\exp[i(\tilde{k}_1\tilde{x}_1 + \tilde{k}_3\tilde{x}_3)] \tag{4}$$

The $\tilde{x}_i$ coordinate system is attached to the eddy and x_i denotes wall coordinates. If the eddy travels over the wall with a velocity c_1, c_2, the coordinates are related by

$$x_1 = \tilde{x}_1 + c_1 t$$

$$x_3 = \tilde{x}_3 + c_3 t \tag{5}$$

Let $\mathbf{k} = (k_1, k_3)$ and $\mathbf{c} = (c_1, c_3)$. Substituting Eq. (5) into Eq. (4) yields the perturbation as

$$\exp[i(\mathbf{k}\cdot\mathbf{x} - \mathbf{k}\cdot\mathbf{c}t)] \tag{6}$$

There are two important facts about Eq. (6). First, the frequency at a point on the wall is given by

$$\omega = \mathbf{k}\cdot\mathbf{c} = |\mathbf{k}|\,|\mathbf{c}|\cos(\Theta) \tag{7}$$

Here Θ is the angle between the vectors $\mathbf{k}$ and $\mathbf{c}$. Second, it is only the component of phase velocity parallel to $\mathbf{k}$ that is important. One cannot distinguish perturbations with different $\mathbf{c}$ but the same $\mathbf{k}\cdot\mathbf{c}$. In three-dimensions the same frequency can be produced by different wavelengths traveling in different directions with different speeds.

In light of Eq. (7), one is led to generalize the phase speed definition as

$$c_k \equiv |\mathbf{c}|\cos(\Theta) = \omega/k \quad \text{where} \quad k = |\mathbf{k}| \tag{8}$$

In the special case of two-dimensional flow Eq. (8) reduces to Eq. (2). The subscript on c_k is used to indicate that it is actually only the component of $\mathbf{c}$ in the direction of $\mathbf{k}$.

The definition Eq. (8) can be used for a three-dimensional flow to convert frequency information into a format with wavenumber and phase velocity

$$\Phi = \Phi(k_1, k_3, \omega \Rightarrow kc_k) = \Phi(k_1, k_3, c_k) \tag{9}$$

Later on in this report the polar form of Eq. (9) will be employed.

$$\Phi = \Phi(k, \alpha, c_k) \tag{10}$$

where $k = \sqrt{k_1^2 + k_3^2}$ and $\alpha = \arctan(k_1/k_3)$.

The nature of turbulent boundary layers is that there is a ridge of dominant Φ values called the convective ridge. A useful three-dimensional definition for convection velocity is to seek a maximum of $\Phi(k, \alpha, c_k)$ in α-c_k space for constant k.

$$\Phi_{\max}(k) = \max_{\alpha \text{ and } c_k} \text{over } [\Phi(k, \alpha, c_k)]$$

$$\Phi_{\max}(k) = \Phi(k, \alpha_{\max}(k), c_{k\_\max}(k)) \tag{11}$$

A definition such as this relies on the physical nature of turbulence for validity.

Witting's Spectrum Model

Witting (1986) produced a model of $\Phi(k_1, k_3, \omega)$ that is physically based. To simulate turbulent eddies, dipoles are distributed across the boundary layer. The dipole strengths vary with the distance from the wall, but their transport velocity is taken to be a constant. Witting's model has many qualitative features in accord with measurements and is a good basis for generalization.

The following chain of equations constitute Witting's two-dimensional model.

$$\Phi(k_1, k_3, \omega) = \langle p^2\rangle \frac{\delta_*^3}{U_t}\frac{A\hat{\omega}^2}{\xi^5}\frac{3}{8}\mathbf{I}(X_{\max}, X_{\min}) \tag{12}$$

$$\xi = \hat{k} + C_o|\hat{\omega} - \hat{k}_1| \tag{13}$$

$$X_{\max} = \xi\delta_{\max}/\delta^*; \quad X_{\min} = \xi\delta_{\min}/\delta^* \tag{14}$$

$$\hat{k}_1 = k_1\delta^*; \quad \hat{k}_3 = k_3\delta^* \tag{15}$$

$$\hat{k} = (\hat{k}_1^2 + \hat{k}_3^2)^{1/2}; \quad \hat{\omega} = \omega\delta^*/U_t \tag{16}$$

$$\langle p^2\rangle = \int_{-\infty}^{\infty}\int_{-\infty}^{\infty}\int_{-\infty}^{\infty}\Phi dk_1 dk_3 d\omega \tag{17}$$

$$A = \frac{C_o}{\pi}\frac{1}{[1 + 2/(3C^2)]\ln(\delta_{\max}/\delta_{\min})} \tag{18}$$

$$\mathbf{I}(X_{\max}, X_{\min}) = \int_{X_{\min}}^{X_{\max}} x^4\exp(-2x)dx$$

$$= [(\tfrac{1}{2}x^4 + x^3 + \tfrac{3}{2}x^2 + \tfrac{3}{2}x + \tfrac{3}{4})\exp(-2x)]_{X_{\min}}^{X_{\max}} \tag{19}$$

The spectrum can be nondimensionalized by $\langle p^2\rangle\delta^{*3}/U_t$, leaving only C_o, $\delta_{\max}/\delta^*$, and $\delta_{\min}/\delta^*$ to be specified. The constant C_o sets the level of the convective ridge by adjusting the decay of the dipole strengths, while $\delta_{\max}/\delta^*$, and $\delta_{\min}/\delta^*$ are the maximum and minimum positions of the dipoles. They regulate contributions to the largest and smallest wavenumber. Because the velocity profile (Eq. (3)) scales on δ, it is a better nondimensionalizing scale than δ^*. Another item is the use of U_t as a scale in Eqs. (12) and (15). This is mathematically clean in the model (because the transport velocity is constant), but not as natural from a theoretical standpoint as u_*.

Model Spectrum for 3-D Layers

Returning now to the Witting model, one can convert to a model in the wavenumber and phase velocity form. First, consider the frequency. As discussed previously, a convective process is well represented by a phase speed. This is done by Eq. (8) $\omega = c_k k$, Note that spectrum relations Eqs. (12)–(13) contain the flow direction wavenumber k_1 explicitly, but that k_3 only occurs in the scalar magnitude k. To gain insight, consider a two-dimensional flow, but let the coordinate system be skewed so that x_1 is not in the flow direction (as assumed in writing Eqs. (12) through (19)). Introduce distinct transport velocity components U_{t1} and U_{t3} for each direction. The total magnitude is still called U_t. The flow direction wavenumber component is now given by the inner product. $k_1 = (\mathbf{k}\cdot\mathbf{U}_t)/U_t$. Hence, this expression should replace k_1 in Eq. (13). Since the magnitude of the wavenumber is independent of a coordinate system k remains in Eq. (13) as is. Witting's model written in wavenumber-phase velocity variables for an axis system in an arbitrary direction is given by replacing Eq. (13) by

$$\xi = k\delta^* + C_o\frac{U_\infty}{U_t}\left|k\delta^*\frac{c_k}{U_\infty} - k_1\delta^*\frac{U_{t1}}{U_\infty} - k_3\delta^*\frac{U_{t3}}{U_\infty}\right| \tag{20}$$

Another modification is factoring the transport velocity U_t so that the free-stream velocity U_∞ appears. Since the model constant C_o is arbitrary, the new combination C_oU_∞/U_t is just an-

other arbitrary constant. Replacing Eq. (13) by Eq. (20) produces a $\mathbf{k} - c_k$ spectrum for a two-dimensional layer measured in a coordinate system that is not aligned with the flow.

The simplest approach to a three-dimensional layer is to assume two regions: an outer region, δ_{mid} to $\delta_{\max}$, where the flow is aligned with the free stream, and an inner region, $\delta_{\min}$ to δ_{mid}, where the flow is skewed and has a smaller transport velocity. Each region has its own constant transport velocity: U_{o1}, $U_{o3} = 0$, U_{i1}, U_{i3}. Reviewing the derivation of the Witting model shows that two distinct transport velocities can be accommodated for by splitting the integral, Eq. (10). Let

$$\xi_o = k\delta^* + C_o \frac{U_\infty}{U_t}\left| k\delta^* \frac{c_k}{U_\infty} - k_1\delta^* \frac{U_{o1}}{U_\infty}\right| \tag{21}$$

$$\xi_i = k\delta^* + C_o \frac{U_\infty}{U_t}\left| k\delta^* \frac{c_k}{U_\infty} - k_1\delta^* \frac{U_{i1}}{U_\infty} - k_3\delta^* \frac{U_{i3}}{U_\infty}\right| \tag{22}$$

$$X_{o\_\max} = \xi_o\delta_{\max}/\delta^*; \quad X_{o\_\min} = \xi_o\delta_{\text{mid}}/\delta^* \tag{23}$$

$$X_{i\_\max} = \xi_i\delta_{\text{mid}}/\delta^*; \quad X_{i\_\min} = \xi_i\delta_{\min}/\delta^* \tag{24}$$

The three-dimensional spectrum is

$$\tilde{\Phi}(k, \alpha, c_k) = \frac{\Phi U_c^2}{\langle p^2\rangle \delta_*^3 U_\infty^2} = \tilde{\Phi}_o + \tilde{\Phi}_i \tag{25}$$

$$= \frac{8A}{3}\left(\frac{\omega\delta^*}{U_\infty}\right)^2 [\xi_o^{-5}\mathbf{I}(X_{o\_\max}, X_{o\_\text{mid}}) + \xi_i^{-5}\mathbf{I}(X_{o\_\text{mid}}, X_{o\_\min})] \tag{26}$$

Here the constant A is the same as before, Eq. (18). Logically, a defect form such as $C = (c_k - U_\infty)/u_*$ is preferred, but can only be tentatively proposed since scaling laws for three-dimensional layers are not certain.

Illustrative Example

The concept of expressing a pressure spectrum in the polar form of wavenumber-phase velocity space and defining a convection velocity magnitude and direction by Eq. (11) was tested by a model example (experimental results are not available). The constants chosen for the calculation were similar to those used by Witting: $C_o = 8$, $\delta_{\max}/\delta^* = 4.0$, $\delta_{\text{mid}}/\delta^* = 1.0$, $\delta_{\min}/\delta^* = 0.04$, $U_{o1}/U_\infty = 1.0$, $U_{o3}/U_\infty = 0.0$, $U_{i1}/U_\infty = 0.433$, $U_{i3}/U_\infty = 0.25$. This represents a layer with a uniform velocity of unity from $\delta_{\max}/\delta^* = 4.0$ to $\delta_{\text{mid}}/\delta^* = 1$. The inner region from $\delta_{\text{mid}}/\delta^* = 1.0$ to $\delta_{\min}/\delta^* = 0.04$ has a velocity of 0.5 skewed at an angle of 30 deg to the outer flow. Results for $\Phi(k, \alpha, c_k)$ will be presented in a series of contour plots in the $\alpha - c_k$ plane for constant wavenumber. In these plots the maximum value is the convection velocity magnitude $c_{k\_\max}(k)$ and direction $\alpha_{\max}(k)$.

One expects the convective velocity $\mathbf{c}_{k\_\max}(k)$ to be like the outer transport velocity at low k, changing to be like the inner transport velocity at high k. The $k\delta^* = 0.05$ plot, Fig. 1, has perfect symmetry about $\alpha = 0$ and the same convection velocity as the outer flow. Three-dimensional effects become evident as one proceeds to higher wavenumbers. Figure 2, at $k\delta^* = 5.0$, shows two distinct local maxima at about $c_k = 1.0$, $\alpha = 0$ and $c_k = 0.5$, $\alpha = 0.52$ (30 deg). The major maximum is the outer region transport velocity $c_k = 1.0$, $\alpha = 0$. As one proceeds to higher wavenumbers, the inner layer becomes more prominent and the outer layer effect is superimposed in a thin band. By a wavenumber of $k\delta^* = 10$, only inner layer effects can be seen. All higher wavenumbers, such as $k\delta^* = 50$, Fig. 3, would be expected to have only inner effects. The convection velocity then is $c_{k\_\max} = 0.5$, $\alpha = 0.52$ (30 deg). These are the inner region transport velocities.

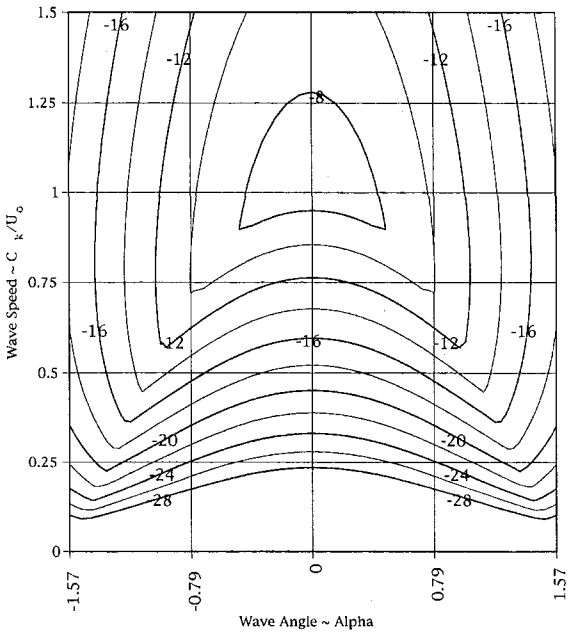

Fig. 1 Contour plot of ϕ_{pp} values as a function of wave speed and wave angle for fixed wavenumber magnitude; $k\delta^* = 0.05$

The spectra associated with each integration region are so distinct and pronounced that the transition region, that region of k where both regions contribute, consists of two separate peaks. Likewise there is not a smooth transition from an overall

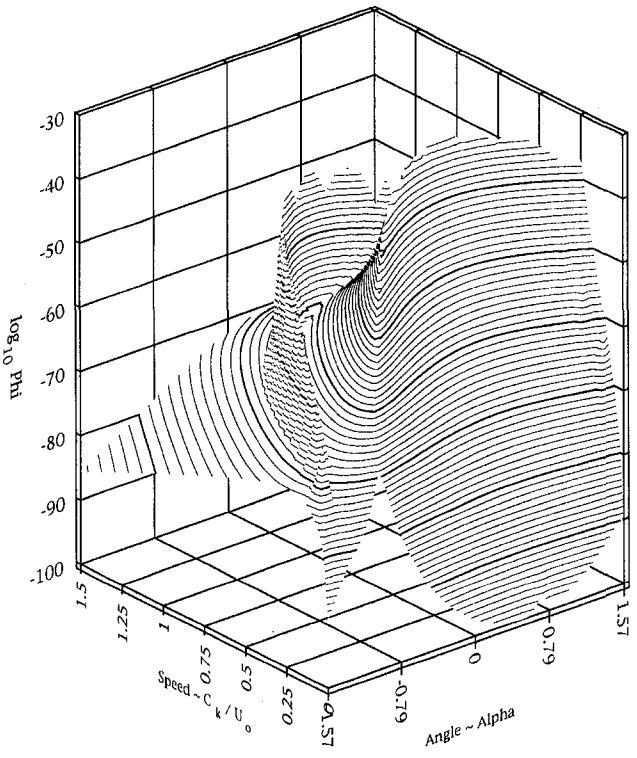

Fig. 2 Contour plot of ϕ_{pp} values as a function of wave speed and wave angle for fixed wavenumber magnitude; $k\delta^* = 0.5$

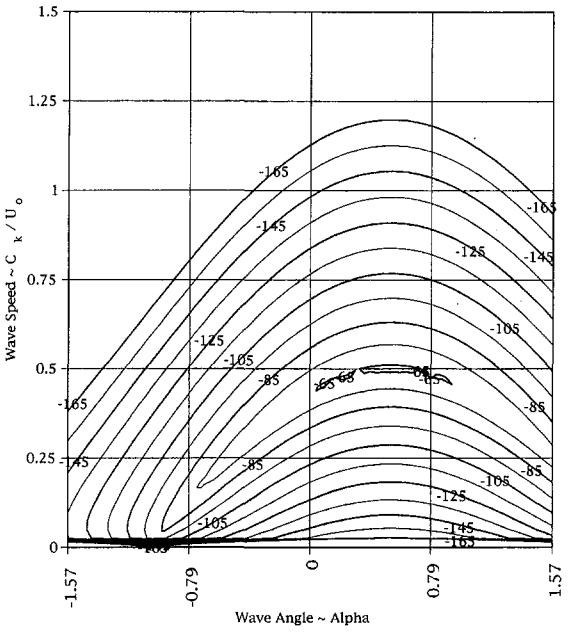

Fig. 3 Contour plot of ϕ_{pp} values as a function of wave speed and wave angle for fixed wavenumber magnitude; $k\delta^* = 50$

convection velocity of (1, 0) to (0.433, 0.25). The velocity (1, 0) has Φ_{max}, then for a slightly higher k, Φ_{max} is at (0.433, 0.25). Because a real boundary layer has a continuous range of convection velocities, not just two, one would expect a much smoother transition in the actual situation.

Summary

Wall-pressure spectra may be converted from variables $\omega - \mathbf{k}$ to variables $c_k - \mathbf{k}$ using the definition, $c_k \equiv |\mathbf{c}| \cos(\Theta) = \omega/k$, The component of $\mathbf{c}$ in the direction $\mathbf{k}$ is sufficient for use as an independent variable in pressure spectra. A three-dimensional convection velocity, $c_{k\_max}(k)$, $\alpha_{max}(k)$, is well defined as the point where $\Phi = \Phi_{max}$ for given k. These ideas were tested in a simple model of a three-dimensional boundary layer based on two regions that have different transport velocities. The model is an extension of Witting's two-dimensional model. As one would expect, the low-wavenumber spectrum is dominated by the outer region and the high-wavenumber portion by the inner region. The transition spectrum is a mixture of both events and shows a double peak structure. Such an abrupt transition is not expected in the real experimental spectrum because the mean velocity profile is continuous. Hence, although the phase speed and convection velocity definitions are viable, the two layer model is inadequate to represent the true spectrum. This indicates that a finer division of the region is needed, preferable integration over a continuous transport velocity function.

Acknowledgment

This work was supported by Office of Naval Research grant No. N00014-94-1-0109, grant monitor Dr. L. Patrick Purtell.

References

Panton, R. L., and Robert, G., 1994, "The Wavenumber A Phase Velocity Representation for the Turbulent Wall-Pressure Spectrum," ASME JOURNAL OF FLUIDS ENGINEERING, Vol. 116, pp. 477–483.

Witting, J. M., 1986, "A Spectral Model of Pressure Fluctuations at a Rigid Wall Bounding an Incompressible Fluid, Based on Turbulent Structures in the Boundary Layer," *Noise Control Engineering Journal,* Vol. 26, pp. 28–43.